Universitat Autònoma de Barcelona

Polarimetric methods for the image enhancement in biological applications

Albert Van Eeckhout Alsinet

Polarimetric methods for the image enhancement in biological applications

Albert Van Eeckhout Alsinet

Submitted in fulfillment of

the requirements for the degree of

Doctor of Physics

Thesis supervisors:

Dr. Juan Campos

Dr. Angel Lizana

Departament de Física

Universitat Autònoma de Barcelona

Universitat Autònoma de Barcelona

Bellaterra, 2021

Als meus pares, al meu germà i a l'Andrea

This work has been financed by the following research projects:

i) Development of advanced optical instrumentation for applications in image polarimetry and surface metrology by fringe deflectometry. FIS2015-66328-C3-1-R. Ministerio de Economía y Competitividad.

ii) Development of advanced polarimetric instrumentation for the characterization of materials and tissues; and surface metrology by deflectometry. RTI2018-097107-B-C31. Ministerio de Economía y Competitividad.

A. Van Eeckhout thanks the Ministerio de Economía y Competitividad for the grant "*Ayudas para contratos predoctorales para la formación de doctores 2016*". BES-2016-077952

Agraïments

Durant la realització d'aquesta tesi he conegut a diverses persones que m'han ajudat a créixer personal i professionalment, així com a divertir-me i gaudir de la investigació. Juntament a aquestes persones he viscut molts moments que em faran recordar aquesta etapa amb nostàlgia i felicitat. Per aquests motius, vull donar les gracies a totes aquelles persones que m'ha acompanyat en aquest procés.

En particular, vull agrair de manera especial als meus directors de tesi, el Juan i l'Angel, l'haver-me ajudat en totes les etapes d'aquesta tesi i l'haver estat sempre disponibles quan em sorgien dubtes i necessitava ajuda.

Al Juan, per fer-me sentir part del grup des del primer moment i fer-me partícip en moltes de les reunions. Gràcies per valorar sempre les idees que em sorgien encara que aquestes poguessin ser una bajanada. També vull agrair-te l'haver-me acompanyat als diferents congressos i fer que aquestes experiències noves fossin més familiars, així permetent-me desfruitar-les al màxim. A més, amb tu he aprés a programar millor i a controlar els diferents instruments del laboratori, sempre des de la positivitat i el realisme.

A l'Angel, per creure amb mi des del primer moment i per la seva generositat a l'hora de proposar que aparegués com a primer autor en els meus primers articles publicats, així com permetrem codirigir diversos TFG. També per ajudar-me a millorar substancialment l'escriptura d'articles. No podria contar la quantitat d'hores que has dedicat a corregir escrits meus per després dir-me que es notava una millora en l'escriptura. Aquestes respostes em donaven molts ànims encara que jo no veia la millora per enlloc. També et vull agrair especialment tots els moments en els que em començava a estressar i en els que aquest estres desapareixia gracies a parlar amb tu. Comentar com el barça feia l'inútil a la *Lliga de Campions* ajudava a desestressar-se.

També vull agrair tot el suport i l'acompanyament rebut per part del grup d'òptica de la UAB. En particular...

A la Marifí, per ajudar-me a comprendre com funciona tot el mon acadèmic i també per tots els consells que m'ha anat donant i que m'han resultat molt útils. Al Juan Carlos, per ensenyar-me diferents eines informàtiques, com el *Mendeley*, que m'han facilitat endinsar-me en el mon acadèmic. Al Pep, per ensenyar-me noves maneres de veure la ciència. A la Verònica, pel suport en la docència de l'assignatura *"Mecànica i Ones".* Al Jordi, per mostrar-me com funciona el programa de doctorat i resoldre'm els dubtes i contratemps relacionats amb aquest. Al Francesc, per introduir-me en el mon de la divulgació.

Als companys del despatx, per tots els moments de bromes, debats i visualitzacions de vídeos de *Youtube* que eren necessaris per evadir-me temporalment de la tesi i així poder ser més productiu en les hores d'investigació. Especialment a la Irene i al Haolin que són les persones amb les que he compartit més temps en el despatx. A la Irene, per permetre'm que la distragués amb temes d'actualitat i per ajudar-me amb la burocràcia de l'inici del doctorat. Al Haolin, per fer-me riure molt sovint i per compartir unes pizzes boníssimes de la *pizzeteria*. També al Kamil, a l'Emanuel, al Fabian i a la Carla, amb qui he compartit moltes hores al laboratori i algun *asado argentino* que estava boníssim. Especialment vull agrair-li a la Carla l'haver-me ajudat a realitzar moltes de les mesures utilitzades en aquesta tesi. Llàstima que la pandèmia ens hagi privat compartir el despatx i tenir anècdotes al respecte.

Als antics quàntics, JuanLu, Dani, Gerard Pelegrí, Gerard Queraltó i Josep, per distreure'm alguns migdies i parlar una mica de tot. Vull agrair-li també al JuanLu l'haver-me ajudat en les meves primeres classes com a docent en la universitat. També als nous quàntics, l'Eulàlia i el David, amb qui he compartit poc temps degut a la pandèmia, però que des de la distancia m'han ajudat a compatibilitzar millor la docència virtual amb la tesi.

Dins del departament de física, vull agrair a la Montse per guiar-me quan apareixia perdut per la secretaria i també a tots els companys del comitè d'organització de la "Trobada Anual Doctorands en Física", per tots els bons moments viscuts mentre preparàvem un congrés que malauradament (per culpa de la pandèmia) no va poder ser possible.

Durant la realització de la tesi, vaig fer una estada a "l'École polytechnique" de París. Vull donar les gracies a tots els membres del "Laboratoire de Physique des Interfaces et Couches Minces" per la seva acollida i el bon tracte. En especial a l'Enrique, per permetre'm fer aquesta estància i per la seva contribució en els meus treballs durant tota aquesta tesi. També per ajudar-me a integrar-me millor en el grup d'investigació i fer que em sentís com a casa. I al Razvigor, per ensenyar-me la polarimetria des de una vessant més teòrica.

En l'estada a París vaig conèixer diverses persones fora de la universitat que em van ajudar a fer inoblidable aquesta estada. Estic parlant principalment d'11 companys i amics del Col·legi d'Espanya, el Raul, la Loreto, l'Aitor, la Victoria, l'Ainoa, l'Álvaro, l'Ariadna, l'Asier, el Dani, la Laura (Mates) i la Laura (letras). Gracies per incitar-me a conèixer com es París i els seus voltants, per fer que cada sopar i esmorzar fos un moment de diversió, i per seguir mantenint el contacte després d'aquells mesos meravellosos.

No em vull deixar d'agrair a tots els coautors la seva contribució als articles realitzats durant el període de la tesi. En especial al Pepe, per ensenyar-me els "Índexs de Puresa Polarimètrica" (IPP) en els que es basa gran part d'aquesta tesi. A l'Emilio, la Mercè, i la Teresa, per identificar les diferents estructures que apareixen en les imatges de teixits animals i vegetals. A l'Andrés,

per compartir el seu coneixement sobre errors de mesura amb polarímetres. I al Nacho i al Claudio, per mostrar-me altres maneres d'utilitzar la polarització de la llum.

Per acabar, vull agrair a totes aquelles persones que no pertanyen al meu àmbit universitari/investigació però que han ajudat a que aquesta etapa hagi estat molt més agradable. En especial...

Al meus amics de Barcelona, Edgar, Charly, Homs, Roger, Marçal, Marta, Martí, Junia i Agnes, per ajudar-me a evadir-me de la tesis en diverses tardes/vespres tot jugant a jocs de taula, mentre preníem alguna cosa i parlàvem de l'actualitat.

A la família de l'Andrea, per donar-me ànims i preguntar-me per la tesi en tot moment encara que no acabessin d'entendre del tot el que estava fent. També per farcir-me amb *cocidos* i així tenir més energia per encarar la tesi.

A la meva família, per estar sempre pendents de mi i ajudar-me quan ho necessitava. En especial als meus pares, Divina i Joan, per ajudar-me en tot en el que em podíeu ajudar i per donar-me la seguretat de que sempre esteu quan us necessito. I també al meu germà, Joan, per ajudar-me en tota la part de classificadors i aprenentatge automàtic (*Machine learning*).

Finalment, vull agrair molt especialment a l'Andrea l'haver-me aguantat durant tota aquesta etapa, en particular, en els moment d'escriptura de la tesi en els que m'he posat més nerviós al veure que el ritme d'escriptura era més lent del que desitjava. Moltes gràcies per donar-me suport en tot moment, ajudar-me a distreure'm fent-me riure (a vegades involuntàriament) i cuidar-me en tot moment. La vida és més fàcil al teu costat.

Abstract

Since the invention of the microscope in the 17th century, the use of imaging technologies has been fundamental in the study of biological tissues. Over the centuries, new imaging technologies have been developed and implemented to enhance the visualization of tissues and ease the understanding of their structure from the measurement of some of their physical properties. In that context, polarimetry is an interesting non-contact and non-invasive optical technique that has been used for image enhancement in a wide range of fields such as astronomy, remote sensing, and characterization of materials. Moreover, polarimetry can be combined with other optical techniques to further improve the visualization of samples.

Polarimetry comprises a group of optical methods that are based on measuring the polarization of light and how it varies when interacting with samples. In this thesis, some polarimetric methods recently proposed in the literature (as well as new ones) are studied, experimentally implemented, and applied for the first time in the analysis of biological tissues to improve the visualization of animal and plant tissues.

In the field of biomedicine, the potential of polarimetry is demonstrated in a wide variety of studies. These studies are usually based on two groups of polarimetric techniques: Polarization Gating techniques and Mueller matrix-based techniques. In this thesis, we investigate the relationship between these two groups of polarimetric techniques and we propose a new generalized polarimetric method that allows the analysis of different Polarization Gating configurations from a single Mueller matrix measurement.

Concerning to the biomedical studies based on the Mueller matrix, different polarimetric properties (diattenuation, retardance, and depolarization) are analyzed from a group of observables to obtaining physical information related to the structure of biological tissues and also to enhance their visualization. In these studies, retardance is completely studied through the Lu-Chipman decomposition and the calculation of the linear retardance, the circular retardance, and the orientation of the fast axis, among others. By contrast, the analysis of depolarization content is restricted to the calculation of observables that quantify the overall depolarization of samples and do not allow the study of more specific information, as can be possible anisotropies in that depolarization process. For that reason, in this thesis, different observables that further describe the depolarization properties of the sample are studied to, afterwards, be applied for visualization enhancement of the measured animal tissues. In that sense, the parameters called Indices of Polarimetric Purity are applied to inspect animal tissues. These depolarizing observables are used to improve tissue visualization, revealing certain structures hidden in standard depolarization channels, and also to classify, with improved efficiency, different animal tissues.

Finally, we also study the use of polarimetry for the analysis of plant tissues. Unlike animal tissues, polarimetry is much less used in the plant analysis framework, being Mueller-based techniques scarcely used. For this reason, this thesis studies the potential of Mueller polarimetry for plant tissue analysis and compares the obtained results with those obtained with some commonly used polarimetric and non-polarimetric techniques. As a result, Mueller polarimetry

is an optimal polarimetric method for obtaining non-invasive images of plant tissues that, in addition, can be used as a complementary tool to other non-polarimetric optical techniques.

List of publications of Albert Van Eeckhout

Publications contained in this thesis:

Chapter 4 Analysis of polarimetric metrics for biophotonic applications

1. Angel Lizana, Albert Van Eeckhout, Kamil Adamczyk, Carla Rodríguez, Juan Carlos Escalera, Enric Garcia-Caurel, Ignacio Moreno, and Juan Campos. *Polarization gating based on Mueller matrices*, J. Biomed. Opt. **22**(5), 056004 (2017).
2. Albert Van Eeckhout, Angel Lizana, Enric Garcia-Caurel, José J. Gil, Razvigor Ossikovski, and Juan Campos. *Synthesis and characterization of depolarizing samples based on the indices of polarimetric purity*, Opt. Lett. **42**, 4155-4158 (2017).
3. Albert Van Eeckhout, Jose J. Gil, Enrique Garcia-Caurel, Javier García Romero, Razvigor Ossikovski, Ignacio Moreno, Juan Campos, and Angel Lizana. *Unravelling physical information of depolarizers*, submitted to publication.

Chapter 5 Biophotonic applications

4. Albert Van Eeckhout, Angel Lizana, Enric Garcia-Caurel, José J. Gil, Adrià Sansa, Carla Rodríguez, Irene Estévez, Emilio González, Juan Carlos Escalera, Ignacio Moreno, and Juan Campos. *Polarimetric imaging of biological tissues based on the indices of polarimetric purity*, J. Biophotonics **11**(4), e201700189 (2017).
5. Albert Van Eeckhout, Enric Garcia-Caurel, Teresa Garnatje, Mercè Durfort, Juan Carlos Escalera, Josep Vidal, José J Gil, Juan Campos, and Angel Lizana. *Depolarizing metrics for plant samples imaging*, PloS one **14**(3), e0213909 (2019).
6. Albert Van Eeckhout, Enric Garcia-Caurel, Razvigor Ossikovski, Angel Lizana, Carla Rodríguez, Emilio González-Arnay, and Juan Campos. *Depolarization metric spaces for biological tissues classification*, J. Biophotonics **13**(8), e202000083 (2020).
7. Albert Van Eeckhout, Enrique Garcia-Caurel, Teresa Garnatje, Juan Carlos Escalera, Mercè Durfort, Josep Vidal, José J. Gil, Juan Campos, and Angel Lizana. *Polarimetric imaging microscopy for advanced inspection of vegetal tissues*, Sci Rep **11**, 3913 (2021).

Other publications of Albert Van Eeckhout not contained in this thesis:

8. Angel Lizana, Haolin Zhang, Alex Turpin, Albert Van Eeckhout, Fabian A. Torres-Ruiz, Asticio Vargas, Claudio Ramirez, Francesc Pi, and Juan Campos. *Generation of reconfigurable optical traps for microparticles spatial manipulation through dynamic split lens inspired light structures*, Sci. Rep. **8**, 11263 (2018)
9. Haolin Zhang, Angel Lizana, Albert Van Eeckhout, Alex Turpin, Claudio Ramirez, Claudio Iemmi, and Juan Campos. *Microparticle Manipulation and Imaging through a Self-Calibrated Liquid Crystal on Silicon Display*, App. Sci. **8**(11), 2310 (2018).
10. Angel Lizana, Juan Campos, Albert Van Eeckhout, and Andrés Márquez. *Misalignment error analysis in polychromatic division of focal plane Stokes polarimeters*, OSA Continuum **2**(5), 1565-1575 (2019).
11. Angel Lizana, Juan Campos, Albert Van Eeckhout, and Andrés Márquez. *Influence of temporal averaging in the performance of a rotating retarder imaging Stokes polarímetre*, Opt. Expr. **28**(8), 10981-11000 (2020).

Contents

Chapter 1 Introduction

This thesis examines, for the first time, the experimental implementation of some recently proposed in literature, as well as newly developed in this thesis, polarimetric methods for the inspection of biological tissue. These polarimetric methods are applied with the aim of enhancing the visualization of biological tissues, as well as obtaining additional information useful for biomedical and botanical applications. Both polarization and depolarization properties of measured tissue samples provide relevant information for biological applications, but in this thesis, we are mainly focused on exploiting the depolarization properties of tissues. In that sense, the Indices of Polarimetric Purity (IPP) are applied, for the first time, to obtain new and relevant information from biological tissues. The IPP are a set of three observables, recently proposed by I. San José and J. J. Gil [1], that further synthesize the depolarization properties of samples. In the following chapters, we study their use for the visualization of biological tissue structures and for the automatic classification of animal tissues based on machine learning processes.

Besides depolarization properties, other polarimetric properties, as the birefringence of tissue, are also used to enhance the visualization of tissues and to determine the orientation of tissue fibers. The analysis of all these polarimetric properties is based on the calculus of polarimetric observables from the Mueller matrix. The measurement of the Mueller matrix is one of the polarimetric approaches commonly used for imaging biological tissues. However, other approaches, as for instance, Polarization Gating (PG) techniques, are also commonly used. In this thesis, we also compare the potential of polarimetric approaches commonly used in biological applications to determine which is better suited for research applications.

In this introductory chapter, we present an overview of the state of the art of optical imaging, especially in image polarimetry, in the biomedical and botanical fields. In addition, we describe some applications that motivated us to develop the research comprised in this thesis.

First, we describe in section 1.1 a collection of optical imaging techniques commonly used in biomedical and botanical applications. Then, section 1.2 overview different imaging polarimetric methods described in the specialized literature, as well as positive results obtained when using polarimetry in other fields, such as astronomy, remote sensing, and material characterization. Afterward, an overview of the studies that use polarimetric imaging techniques for biomedical applications and the medical relevance of some applications is provided in subsection 1.2.2. Subsection 1.2.3 provides an overview of the studies that use polarimetry to improve the

imaging of vegetal tissues and describes the economic interest of some botanical applications not studied with polarimetry. Finally, the main goals and the structure of this thesis are described in sections 1.3 and 1.5, respectively.

1.1 Optical imaging techniques

Imaging technologies play a fundamental role in the field of biomedicine and botany since they can be used to visualize the different structures of biological tissues and measure some of their physical properties [2–4]. The use of modern imaging technologies, which provide better visualization of measured tissues, allows a better understanding of the tissue structure and the performance of new and more detailed studies. For this reason, new and advanced imaging techniques that enhance the visualization of biological tissues by increasing the image resolution or by improving the image contrast between the different measured structures are being investigated. For instance, the stimulated emission depletion (STED) microscopy [5] is a super-resolved fluorescence technique that has overcome Abbe's diffraction limit [6] or the phase-contrast microscopy [7] which is used to improve the image contrast between adjacent structures.

In this thesis, we are focused on the use of image polarimetry techniques to improve the image contrast between the measured structures and consequently enhancing the visualization of biological tissues. Before explaining how image polarimetry works, we following describe the operation principle of the main optical imaging techniques used for the analysis of biological tissues to take a general vision of the state of the art of optical imaging in biological applications. We will also describe the operation principle of electron microscopes because they are commonly used for similar biological applications on the nanometric scale.

The operation principle of optical techniques consists of exploiting the fundamental properties of light (intensity, frequency, phase, coherence, and polarization), as well as the light-matter interaction properties (fluorescence, absorption, scattering, etc.) to improve the visualization of samples.

Simple imaging systems

At the beginning of the 17th century, the combined use of lenses was proposed to magnify the image of an object [8]. The proposed instrument was called light microscope (or optical microscope) and it is nowadays used to visualize microscopic structures. Simple light microscopes work illuminating the sample with light (usually non-polarized and non-coherent white light) and measuring the intensity of light resulting from the light-matter interaction. When the light interacts with biological tissues, part of the incident light is absorbed and scattered [4]. The absorption and scattering properties of tissues are characteristic of each sample and tend to be different for distinct tissues. Therefore, the intensity of light coming from the interaction with distinct tissue structures is usually different, allowing their distinction and recognition. Although this is the simplest optical instrument used in biology, it is responsible for very relevant findings, as for instance, the discovering of bacteria and cells [9].

Multispectral or hyperspectral imaging

The absorption and scattering processes associated with light-tissue interactions depend on the wavelength/frequency of the incident light [10]. In fact, the penetration depth is different depending on the wavelength used, being, in the case of illuminating human skin, the blue and green light more superficial than the red and the near-infrared light [11]. Therefore, the separate use of different wavelengths can be used to obtain information from superficial and deeper layers of tissue samples and also to differentiate two tissues that could be seen as equal in a particular wavelength but completely distinct in others.

Multispectral and hyperspectral imaging systems are the instruments used to measure the intensity response of a sample as a function of the wavelength [12]. They are non-contact and non-invasive optical instruments that work similarly to the simple imaging system but measuring the intensity corresponding to different wavelengths separately. In that sense, hyperspectral and multispectral imaging systems are very similar. The only difference between them is that hyperspectral systems measures a continuous range of wavelengths (e.g., 450-900 nm in steps of 1 nm) whereas multispectral systems subsets the range into different bands (e.g., 450-900 nm in 30 nm) [13]. Note that in the previous examples, the number of images per frame are 450 and 15, respectively. Thus, the amount of information is so large that it cannot be processed by a human and requires specialized software. Specialized software is even more necessary if we consider that some hyperspectral instruments are snapshots instruments that allow real-time measurements [14] (i.e., more than 25 images/s).

Among the diverse biological applications of spectral imaging techniques, they have been used to identify regional differences in oxygen saturation of blood in human retinal vessels [15] and for the automatic diagnosis of skin cancer by using machine learning tools [16]. In the latter mentioned study, the sensitivity and specificity of cancer detection take values from 75% to 85% [16] so there is room for improvement. Hyperspectral techniques have been also used for the early detection and classification of plant diseases and stress [17]. Note that for these applications spectral imaging techniques do not need sample preparation.

Raman spectroscopy

Raman spectroscopy is a non-contact and non-invasive spectral imaging technique that exploits the “Raman” scattering process to analyze the chemical composition of the measured tissue [18]. “Raman” scattering is an inelastic scattering process (i.e., the energy of the incident photon is different from the reemitted one) that was predicted by Adolf Smekal in 1923 and first observed by C.V. Raman in 1928 [18]. Similar to Rayleigh scattering, in the Raman scattering, a photon interacts with a molecule inducing a short-term transition to a virtual energy level (see Figure 1-1). However, instead of being relaxed back to the same initial state and emitting the same energy photon, like in the Rayleigh scattering process, in the Raman scattering, the molecule is relaxed to another vibrational energy state and a photon with different energy is emitted.

There are two types of Raman scatterings: Stokes and anti-Stokes scattering. Stokes Raman scattering is characterized for remitting lower energy photons and anti-Stokes Raman scattering for reemitting higher energy photons [18] (see Figure 1-1). The frequency difference between the incident photon and the reemitted one is characteristic of each molecule and its vibrational

energy levels. Therefore, illuminating the sample with a narrow bandwidth source and analyzing the spectral shift can be used to deduce the chemical composition of the analyzed sample. However, the Ramman scattering probability is very low, being the Stokes scattering the most commonly observed in biomedical research with a probability of 1 in 10^8 incident photons [18] (the Stokes scattering probability depends on the concentration of molecules, being higher with higher concentrations). Accordingly, the measured Raman signal is very low. To enhance this signal, the incident light is concentrated at a point and the measured images are taken through scanning processes. In comparison with other optical techniques as fluorescence microscopy, Raman spectroscopy usually does not need sample preparation.

As examples of biological Raman spectroscopy applications, the technique has been applied for the analysis of mineralized nodules formed *in vitro* of a bone when using different regenerative techniques [19] and for the detection of skin cancer [20]. In the latter study, the accuracy of detecting various skin oncological pathologies when using Raman spectroscopy varies from 78.4% to 100% depending on the pathology [20].

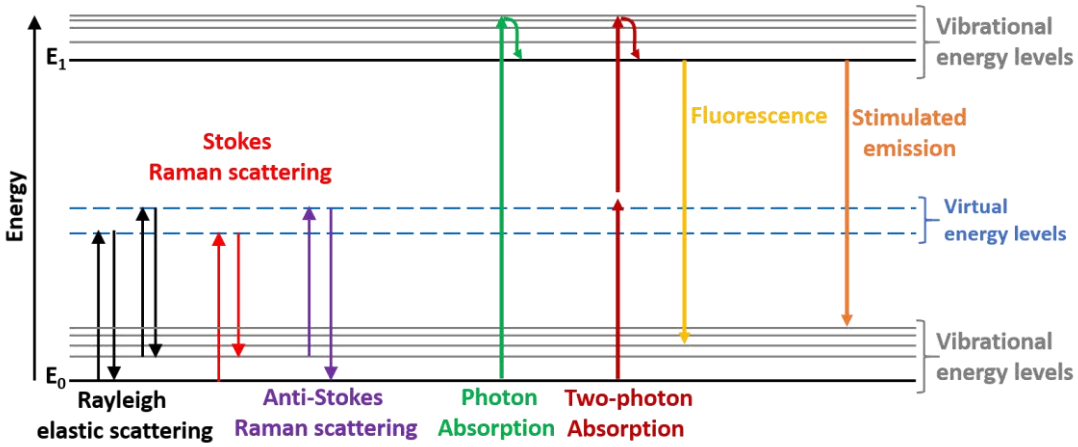

Figure 1-1. Scheme of Rayleigh scattering, Raman scattering, fluorescence, two-photon absorption and stimulated emission.

Fluorescence microscopy

Fluorescence microscopy is a non-contact imaging technique that uses the fluorescence effect produced in the measured samples to enhance the image contrast [21]. The operational principle of this technique consists of illuminating the sample with a given wavelength that must have the same energy as the absorption transition of the imaged fluorescent molecules. Then, a part of the incident photons is absorbed by these fluorescent molecules producing a molecule transition to a higher energy state E_1 (see Figure 1-1). During the next picoseconds, the molecule is relaxed to the lower vibrational state of E_1 (see Figure 1-1) and after some nano seconds, the molecule is relaxed back to the ground state E_0 emitting a fluorescent photon [21] (see Figure 1-1). The wavelength of the fluorescent photon is different from the incident one so a filter can be placed in front of the camera to only measure the fluorescent light. Consequently, only the fluorescent molecules are imaged with this technique.

In the case of measuring plant samples, many vegetal structures are composed of fluorescent molecules (fluorophores) [22]. Nevertheless, many other biological structures do not fluoresce.

In the latter cases, fluorescent dyes must be introduced in the sample, this requiring previous sample preparation. Therefore, fluorescence microscopy is an invasive technique in the case of ensuring non-fluorescent objects. Moreover, after several measurements fluorophores and fluorescent dyes can remain useless due to photobleaching processes so long-term continuous measurements are not allowed [21].

The energy of the absorbed light is always higher than the emitted fluorescent photons. Therefore, we have to illuminate the sample with shorter wavelengths. The main problem of using short wavelengths is the smaller penetration depth associated with them [11]. However, fluorescence microscopy is usually combined with confocal microscopy (following described) to image deeper layers.

As many plant present fluorescent structures, fluorescence techniques are widely used for the inspection of vegetal tissues [22–25]. For example, fluorescence microscopy has been used to study the protein dynamics in plant cells [23,24] and to study the cell patterning during the development of plant development from seeds to adult plants [25]. Fluorescence microscopy has also been used in biomedicine, for instance, to study the internal body dynamics through the intravenous administration of nanoparticles [26] and for the detection of skin cancer [20]. In the latter study, the accuracy of detecting various skin oncological pathologies when using fluorescence microscopy varies from 78.9% to 93% depending on the pathology [20].

Two-photon microscopy

Two-photon microscopy is similar to fluorescence microscopy but uses two half-energy photons to excite the molecule [3] (see Figure 1-1). After the absorption of the two photons, the fluorescence process is the same. One advantage of two-photon microscopy compared to the previously described fluorescence microscope is that lower energy photons penetrate deeper into the sample. However, the probability of two-photon absorption is much lower compared to one-photon absorption [3]. Consequently, the beam is concentrated at a point and the measured images are taken through scanning processes, like in Raman spectroscopy. In addition, the two photons must arrive nearly simultaneously (<1 fs) to be absorbed so very short pulses (e.g., femtosecond pulses) must be used. Sometimes, despite concentrating the illumination beam at a point the fluorescence signal is too low [3]. Under this scenario, the intensity of the incident beam can be increased. Nevertheless, highly concentrated beams with high intensities produce photobleaching which damages the sample [3].

The explained two-photon microscopy method is called two-photon excitation fluorescence (TPEF) and it has been used, for instance, for the in vivo imaging of a mouse brain to study Alzheimer's disease [27]. Alternatively, second-harmonic generation (SHG) is a two-photon technique similar to TPEF but in which the photon emission is an elastic process (i.e., the emitted photon has the same energy as the sum of the two incident photons energy) [3]. Unlike TPEF, SHG does not need sample preparation and does not suffers inherent photobleaching.

In biological materials, SHG is especially intense in well-organized noncentrosymmetric microcrystalline structures because the emitted light is constructively combined [3]. As an example, SHG has been used to image collagen fibers [28].

Stimulated emission depletion (STED) microscopy

In 1994, Stefan Hell published an article outlining the operation principles of the so-called stimulated emission depletion (STED) method that overcomes Abbe's diffraction limit [6]. Six years later, in 2000, he proved that STED works in practice [29,30]. STED microscopy is a fluorescence technique that is based on illuminating a point of the sample with two synchronized pulses and retrieve a superresolution image through a scanning process [5]. The scanning process can be done in the z-axis thus obtaining 3D images. The first emitted pulse is Gaussian-shaped, similar to the one used in simple fluorescence microscopy (see Figure 1-2 (a)). The photons of the first pulse are absorbed by the fluorophores (fluorescent molecules) producing a molecule transition to a higher energy state E_1 (see Figure 1-1), and in the next picoseconds, the molecule is relaxed to the lower vibrational state of E_1, like in simple fluorescence microscopy (see Figure 1-1) [5]. Then, the same point is illuminated by a second pulse before the emission of a fluorescent photon (the emission of a fluorescent photon takes some nanoseconds to occur). This second pulse is doughnut-shaped (see Figure 1-2 (b)) and produces a stimulated emission in the illuminated region (see Figure 1-1). Doughnut-shaped spots can be obtained through vortex beams and the central hole can also be obtained in the z-direction [30]. After the emission of stimulated photons, the central region remains excited (see Figure 1-2 (c)) and, after few nanoseconds, emits the fluorescent photons [5]. As the fluorescent emission area is smaller compared to the initial illuminated section, the obtained image resolution is increased. The image resolution obtained with STED microscopy in the x-y plane is 50 nm vs 250 nm obtained with confocal microscopy [5]. In the z-axis, the axial resolution of STED microscopy is 150 nm vs 550 nm obtained with confocal microscopy [5]. This increment of resolution allows the distinction of close objects as in Figure 1-2 (d) and (e) where a bacteria membrane is better outlined with STED than confocal microscopy [30].

Thanks to this nanometric resolution, the length of DNA fragments can be measured more precisely [31]. Moreover, STED allowed performing studies that were only possible with electron microscopy as the precise determination of protein sub-location and organelle quantities in the analysis of cells [32]. However, STED microscopy is an invasive technique that needs sample preparation and their measure instruments are more expensive compared to the previously described techniques because STED is more complex. Moreover, they are not able to take real-time measurements (images take ~s [5]).

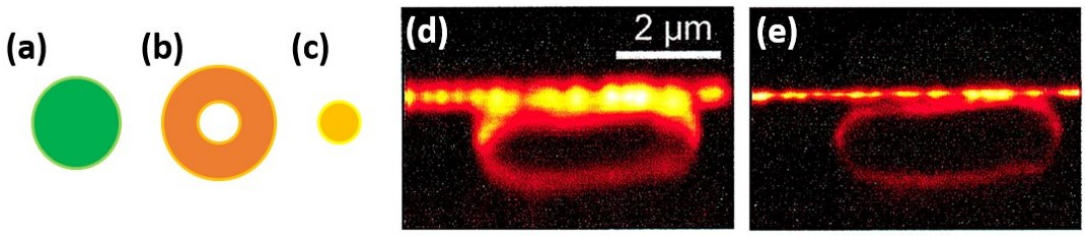

Figure 1-2. X-Y scheme of (a) excitation spot, (b) doughnut-shaped stimulated emission spot, and (c) fluorescent emission spot. Images of a membrane-labeled E. *coli* taken with (d) a confocal microscope and with (e) a STED microscope. (d) and (e) images were obtained from ref. [30].

Confocal microscopy

Confocal microscopy is a non-contact and non-invasive optical technique that is usually combined with fluorescence microscopy [33]. In fact, confocal microscopy is based on focusing the light on a point in the sample (see Figure 1-3 (a)), thus enhancing the fluorescent signal. Then, the fluorescent or the reflected light passes through a pinhole and is measured by a detector (see Figure 1-3 (a)). The particularity of this technique is that most light coming from other planes, other positions, and scattered by the sample is filtered by the pinhole and not measured (see Figure 1-3 (a)). In other words, only light coming from a particular point of the sample is measured [33].

After measuring the light coming from a point of the sample, the light is focused on other points in the sample following a scanning method, like Raman spectroscopy or STED. Like STED microscopy, confocal microscopy can take 3D images [34]. However, confocal microscopy presents a lower resolution compared to STED microscopy [5]. By contrast, confocal microscopes are cheaper instruments that can take real-time measurements (images take ~ms-s [5]).

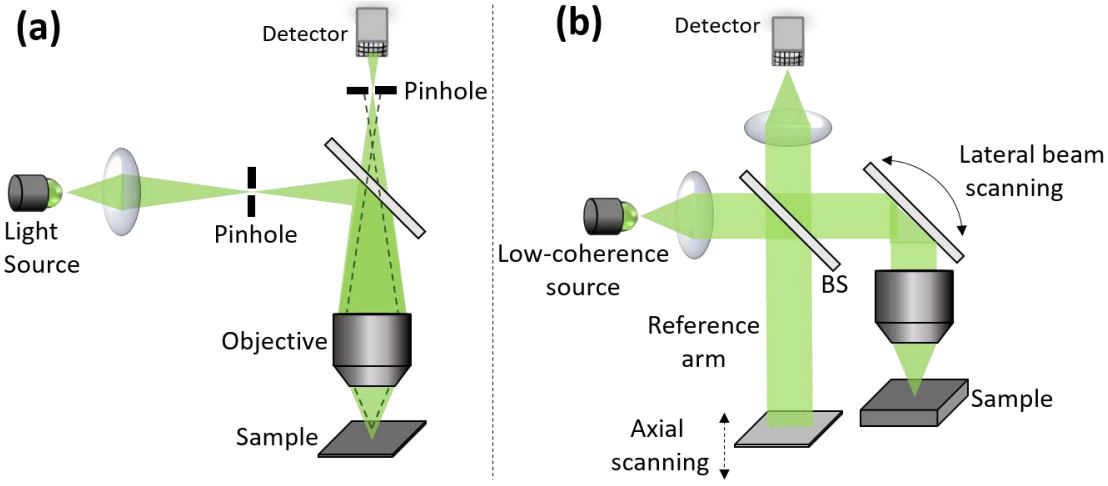

Figure 1-3. (a) Scheme of a confocal microscope. (b) Scheme of an optical coherence tomography system. BS means beam splitter.

Optical coherence tomography (OCT)

Optical coherence tomography is a scanning optical technique, like STED microscopy and confocal microscopy, that uses the coherence of light to take 3D images of semi-transparent and turbid samples [35]. This technique is based on the interferometry of low-coherence light. First, a low-coherence light beam is divided into two arms: the reference arm and the sample arm (see Figure 1-3 (b)). The reference arm is composed of a mirror that can be displaced in the beam direction. And the sample arm is composed of a lateral scanning system (a rotatable mirror in Figure 1-3 (a)) and an objective that images the sample. Then, the reflected light of each arm is recombined producing an interferometric pattern. This interferometric pattern depends on the path length as well as on any change in the refractive index [35]. Accordingly, different layers of the sample are imaged when displacing the mirror in the beam direction. Note that this interferometry is only produced if the difference in travel path lengths is less than the coherent length of light [35]. Therefore, the axial resolution of 3D images is equal to the coherent length.

In that sense, the use of broadband light sources involves that interference occurs at micrometric scales.

Compared to other scanning techniques, OCT presents lower axial resolution. However, OCT is a non-contact, non-invasive and real-time imaging technique that does not need sample preparation and which, in contrast to fluorescence microscopy, can repeat the same measurement over time [35]. Moreover, different arms can be substituted by optical fibers, this making a robust optical system applicable for *in vitro* measurements, as for instance, the measurement of colon cancer [36].

Optical coherence tomography has been regularly used in ophthalmology to detect retinal irregularities [37], and in plant biology, for instance, to study the root growth in soil [38].

Phase-contrast microscopy

Phase-contrast microscopy exploits variations of the phase of light to enhance the image contrast. It is a non-contact and non-invasive technique that does not require sample preparation [7]. Moreover, it can be used for real-time measurements and has the same resolution limitations as simple and spectral microscopy, i.e., Abbe's diffraction limit [6].

Its operational principle consists of changing the phase of light scattered by the sample in other to differentiate it from the background light. To do so, the light beam is first modified by a condenser annulus (see Figure 1-4). Then, the modified light beam interacts with the sample, being most of the light transmitted (see bright green color in Figure 1-4) and a small part scattered (see dark green color in Figure 1-4). Afterward, all the light, independently of its origin, is refocused on the camera. Now, since the path of transmitted light is known, we use a phase plate to induce a phase shift between transmitted and scattered light [7]. Finally, scattered light interferes with directly transmitted light, which creates a phase contrast. As phase is independent of the intensity, phase-contrast microscopy allows observing transparent samples. In fact, the observation of transparent samples is its main use [7].

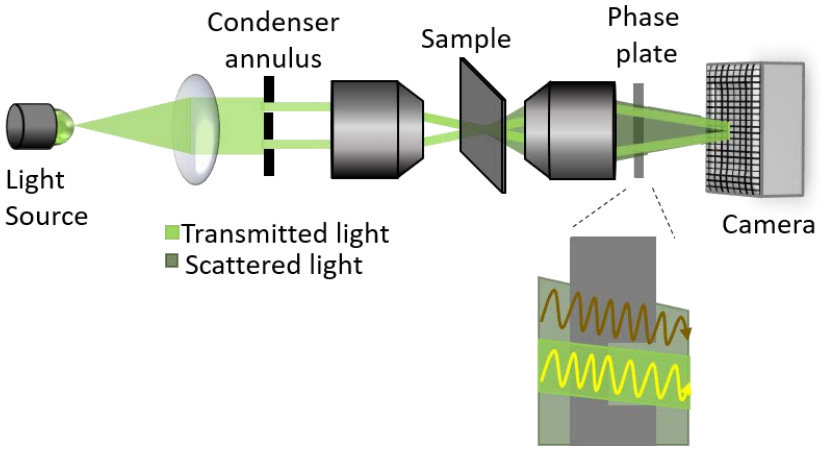

Figure 1-4. Scheme of a phase-contrast microscope.

Phase-contrast microscopy is useful to highlight the edges of measured objects because most of the scattering light is produced there. Moreover, phase-contrast images are sensitive to changes in the index of refraction and changes in the thickness of the measured sample so retrieving 3D information of samples [39]. By contrast, the measurement of thick samples is

worthless because more than 2π phase differences can occur. In addition, the measure of highly scattering samples is also worthless because scattering paths may also produce more than 2π phase differences.

For these reasons, phase-contrast microscopy is mainly used to measure thin sections of living cells because they are mostly transparent samples [39]. In addition to this application, phase-contrast is also used for biomedical applications with X-ray illumination sources because several biological samples are invisible to these wavelengths. For example, X-ray phase-contrast microscopy has been used for diagnosing rheumatoid arthritis [40] and to image ground plant parts and roots for studying dynamic and real-time processes [41].

Electron microscopy

Electron microscopy techniques are imaging techniques that were originally developed to observe inorganic materials with up to atomic resolution [35]. The two most commonly used types of electron microscopy techniques are transmission electron microscopy (TEM) and scanning electron microscopy (SEM). The operational principle of TEM is the same as a simple transmission optical microscope but uses electrons instead of photons. Accordingly, the used lenses are electromagnetic lenses and the detector is an electron detector [35]. The main issue of TEM is that it must be used to image ultrathin sections (∼100 nm). By contrast, SEM is used to measure the surface of samples so these samples have not to be thin. SEM is a scanning imaging technique that works by focusing the electrons at a point of the specimen surface. In that focused point, these primary electrons knock out electrons from the sample material. These secondary knocked-out electrons are collected by a detector and thanks to a scanning process (in which electrons are focused at different points of the specimen surface) an image of the sample surface is retrieved [35]. The resolution of SEM microscopy allows the visualization of nanometric crystals.

Although this technique provides up to the atomic resolution, the instruments are much more expensive than optical microscopes because the measurement must be performed in a vacuum chamber [35]. In addition, organic samples must be prepared before their imaging. This sample preparation follows very precise methods that usually involves a carbon coat, and which must be performed by an expert.

In biology, electron microscopy is used to measure nanometric and micrometric structures, for instance, plant stomata [42] or the composition of blood [43].

1.2 Image polarimetry

Polarization is the property of light that describes the transversal oscillation direction of electromagnetic waves [44–46]. This direction can be random (unpolarized light), in a unique and particular direction (linearly polarized light), or can variate with a circular or elliptical pattern (circularly or elliptically polarized light, respectively).

Polarimetry comprises a group of non-contact and non-invasive optical methods that measures the polarization of light as well as its modification due to light-sample interaction [44–46]. Figure 1-5 shows the basic operational principle of polarimetric techniques. In polarimetric experiments, the measured sample is illuminated with polarized light (vertical linear polarization

in Figure 1-5), and the polarized light resulting from light-sample interaction is analyzed by using one or more analyzers (diagonal linear polarization in Figure 1-5). An analyzer is an optical element (or a set of optical elements) that allows passing through only one type of polarization (several instrumental architectures can be used to analyze polarized light [47]; they are described below in section 1.3). Once light resulting from the sample is analyzed, we can determine the polarization modification produced by the sample by comparing the incident and the analyzed polarizations. In the schematized example of Figure 1-5, the sample acts as an optical rotator that rotates linearly polarized light at a given angle [45]. However, the measurement schematized in Figure 1-5 is also compatible with the fact that the sample was a linear polarizer [45]. Under this scenario, we can generate and analyze more polarization states to obtain a complete characterization of the sample's polarimetric response.

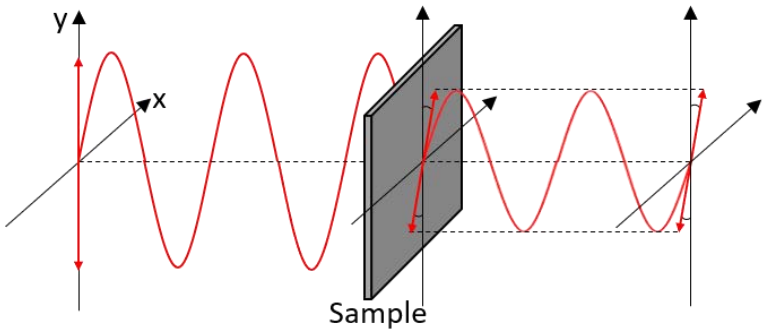

Figure 1-5. Scheme of the basic operation principle of polarimetry.

Depending on the number of generated and analyzed states we can differentiate three polarimetric approaches: Polarization Gating (PG) techniques, Stokes vector-based techniques, and Mueller matrix-based techniques.

Polarization Gating (PG) techniques

Polarization Gating techniques are the simplest polarimetric methods and consists of illuminating the sample with a certain polarization and analyzing the polarimetric response of the sample by using an analyzer with a specific polarization [48] (e.g. illuminating the sample with horizontal linearly polarized light and analyzing the amount of vertically polarized light coming from the sample). Usually, the polarization of the analyzer is the same input polarization (co-polarized configuration) or the orthogonal one (cross-polarized configuration). This group of polarimetric techniques has de benefit, in front of the methods following described, that only needs to take one image for measurement so it can be easily used for real-time applications.

Stokes vector-based techniques

Another group of polarimetric techniques are those based on the measurement of the Stokes vector [45]. Stokes vectors consist of four real parameters arranged in a vector-form that completely describe the state of polarization (SoP) of a light beam. To measure a complete Stokes vector (i.e., measure its four parameters), at least four analyzers are needed [49]. Consequently, at least four different measurements must be taken, this difficulting the real-time acquisition of Stokes images. However, real-time Stokes images can be nowadays implemented with the so called division of focal plane (DoFP) polarimeters [50–59]. DoFP polarimeters reduce the image resolution to improve the frame rate.

The operational principle of Stokes polarimetry consists of illuminating the sample with a given polarization and analyzing the polarimetric response of the sample by using four or more independent analyzers. Once measured the Stokes vector, different light polarimetric properties can be deduced from them [45]. Light depolarization is one of the most commonly analyzed polarimetric property and it is usually quantified by using the degree of polarization (DOP) [45]. Light depolarization is a statistical magnitude that can be understood as the opposite of light polarization and is associated with the randomness of the amplitudes and relative phase of the electromagnetic wave components.

Mueller matrix-based techniques

Lastly, a widespread group of polarimetric methods [1,44–46,60–73] is based on the Mueller matrix of samples [44–46]. The Mueller matrix is a 4x4 real coefficients matrix that defines how any incident polarized light beam, with a fixed wavelength and incident direction, is modified because of its interaction with the measured sample [44–46]. Accordingly, the 16 real coefficients of that matrix encode the polarimetric characteristics of the sample which can be described as a combination of three physical properties [45,46]: diattenuation-polarizance (or dichroism) - the ability to variate the intensity of the incident beam depending on their polarization and the ability to polarize light; retardance (or birefringence) – the ability to modify the type of polarization of the incident beam (e.g., modify from linearly to circularly polarized light); and depolarization – the ability to depolarize the incident beam. Under this scenario, the information of different properties can be decoupled by using different mathematical methods to obtain several observables [1,44–46,60–66,68–73]. These observables are used to analyze the polarimetric properties of samples as well as to improve the visualization of samples in imaging applications.

Diattenuation and polarizance properties are commonly described with the diattenuation **D** and polarizance **P** vectors [44–46]. To analyze the retardance of the sample, the birefringence of the sample can be completely described by operating the Lu-Chipman product decomposition [66] and calculating the total retardance (R) [66], the linear retardance (δ) [74], the angle orientation of the fast axis (θ) [74], and the optical rotation of the circular retarder, (φ) [74]. Concerning depolarization properties, a first approximation can be done with the operation of the depolarization index (P_Δ) [69] or the depolarization power (Δ) [66] which quantifies the overall depolarization of samples from a statistical point of view. However, part of depolarization information is lost when using only P_Δ or Δ, for instance, the possible dependence of sample depolarization with the input polarization (i.e, depolarization anisotropy). Interestingly, this depolarization information is not lost in other depolarization methods described in the literature which further synthesize the depolarization content of the sample, as for instance, the indices of polarimetric purity (IPP) [1], the components of purity (CP) [61], the covariance matrix eigenvalues [70], and the canonical parameters of the symmetric decomposition [72], among others. However, these metrics are not extensively used yet in biomedical applications, and to highlight their usefulness in such applications is one of the goals of this thesis. The physical meaning and the mathematical calculation of the above-cited observables will be described in detail in Chapter 2.

The operational principle to measure the complete Mueller matrix of samples consist of illuminating the sample with four or more independent polarizations and analyzing the

polarimetric response of the sample by using four or more independent analyzers. Considering that DoFP polarimeters can be used to analyze the polarization in real-time, at least four radiometric measurements are needed to retrieve the complete Mueller matrix image (8 radiometric measurements in the case of using the actual commercial DoFP polarimeters based on grid polarizers [57]). Then, taking into account the fast synchronization processes observed in STED, OCT and confocal microscopy, the fact of taking 100 images per second (25 Mueller matrix images x 4 Stokes images for each measurement) is feasible [75]. Consequently, the construction of real-time Mueller polarimeters is possible.

Regardless of the polarization technique, polarimetry always provides information that is independent of the intensity properties of the illumination light beam. In that sense, image polarimetry can distinguish objects that transmit or reflects the same amount of light but which modifies the polarized light differently, for instance, transparent samples. As an example, polarimetry can differentiate sticky tapes with different orientations [76] or organic tissues with the same reflectance but different birefringence or dichroism.

In addition, polarimetric methods can be combined with most other optical techniques to improve the obtained results. For instance, polarimetry can be combined with multispectral or hyperspectral imaging [77–79], Raman spectroscopy [80], fluorescence microscopy [81–83], second harmonic generation microscopy [84–86], or optical coherence tomography [87], among others. In the case of Raman scattering, fluorescence microscopy, and SHG microscopy, light absorbed and scattered by dipole molecules is reemitted linearly polarized with a polarization parallel to the orientation of the dipole. Therefore, the combination of second harmonic generation and polarimetry can be used to characterize the orientation of biological elements, for instance, to characterize the orientation of collagen [84–86] and muscle fibers [86]. Concerning the combination of fluorescence microscopy and polarimetry, it has been used in biomedical applications for the diagnosis of oral cancer [81] and the study of breast cancer at the cellular level [82], and to determine the orientation of cellulose fibrils in plants [83]. The combination of multispectral and hyperspectral imaging techniques with polarimetry is also very interesting because polarimetric properties of samples usually variates with the incident light wavelength. Polarization-sensitive hyperspectral imaging proved to be useful for detecting skin diseases by enhancing its visualization [78,79]. Unfortunately, polarization cannot be combined with STED microscopy because vortex beams must be circularly polarized to present the doughnut shape.

Note that most studies that combine polarimetry with other optical techniques implement PG methods [77,79,81–85] because they do not increase the acquisition time of measurements. However, other studies implement Stokes polarimetry with positive results [78,86,87]. The implementation of these polarimetric techniques in instruments that uses other optical techniques can be relatively easy to do. To make an optical instrument capable of measuring the polarization of light and how it is modified by light-sample interaction, only two sets of optical elements have to be built-in: one set capable to generate the desired polarization (called polarization state generator, PSG), and the other set capable to analyze the polarization response of the sample (called polarization state analyzer, PSA). If the PSG and the PSA can generate and analyze four independent polarization, the combined instrument is able to measure the Mueller matrix of the sample [49].

1.2.1 Image polarimetry applications

Image polarimetry proved to be useful in a wide range of fields. In the following, as an example, we review some applications in material characterization, astronomy, and remote sensing. Afterward, to motivate their use in the analysis of biological samples, we overview the use of image polarimetry for biomedical and plant applications.

Material characterization

The use of polarimetry to characterize bulk and thin-film materials is traditionally called ellipsometry [88,89]. The potential of ellipsometry was first proved by Paul Drude in 1888 when he used polarized light to analyze the optical properties of very thin metallic films and determine their thickness [90]. Recent studies usually combine ellipsometry and spectroscopy techniques for a more general characterization of analyzed materials [91,92]. In these studies, the Mueller matrix or the Jones matrix [44] of samples is measured in different angles to completely characterize their optical properties. As an example, a near-infrared Mueller matrix ellipsometer has been used to characterize strain in transparent samples [93]. Spectroscopic ellipsometers also proved to be useful for the thickness measurement of multilayer films (stack in perovskite solar cells) [94].

When light-matter interaction is produced, polarization properties of light are sensitive to the nanometric structure of measured material and some studies showed how this polarimetric information can be used to characterize the sample [95,96]. In that sense, polarimetry can be used for the study of indium nanowires deposited on silicon [95] and to characterize the optical properties of silver nanoparticles [96].

Astronomy

In astronomy studies, polarimetry often yields crucial information that is unobtainable with other optical techniques [97]. Polarimetry is mainly used for the study of stars [98–100] and for the detection and characterization of extrasolar planets [97,101]. However, polarization of light is also used in astronomy for other applications, for instance, to measure the distance of galaxies [102]. Concerning the use of polarimetry to study stars, the Sun's magnetic fields are analyzed through the measurement of light polarized via the Zeeman effect [98]. Zeeman signals show often very small amplitudes and sometimes take values smaller than the noise signal of the instrumentation [99]. Alternatively, Sun can be studied by measuring the scattering polarization associated with the Hanle effect [100]. For its side, extrasolar planets are detected by measuring the light polarized in their atmosphere because of the Rayleigh scattering process [97,101]. The polarization associated with Rayleigh scattering is especially used to study protoplanetary nebulas [101].

Remote sensing

In remote sensing, polarimetry is commonly used in combination with multispectral and hyperspectral imaging techniques to enhance the visualization of certain objects [47,103–107]. In particular, polarimetry is especially useful for distinguishing between metallic and organic objects because the former maintains the incident polarization while the latter depolarize it. In that sense, polarimetry has been used for military purposes to distinguish metallic vehicles in forest areas [47] and to detect anti-personnel mines by using an infrared camera [103]. These

latter two remote sensing applications are called passive applications because the sample is not illuminated artificially. In these cases, the sample is illuminated by the Sun's light that is polarized by the Earth's atmosphere through Rayleigh scattering processes [104]. The same passive technique is used in the study of oceans [105], forests [106], and the atmosphere [104]. Polarimetry is also used to measure the quantity of oxygen in the atmosphere [107]. Moreover, polarimetry is combined with radar techniques, for instance, for the detection of warm fronts [108] and the characterization of urban structures [109], among others.

1.2.2 Image polarimetry for biomedical applications

The potential of using polarimetry for the study of organic tissues has been provided in literature [48,79,81,82,84,85,110–148]. However, organic fibers scatter the incident light and generate depolarization. Figure 1-6 shows, in a schematic way, the light propagation in organic tissues such as human skin. Inside organic tissues, the light is scattered multiple times by fibers and other internal structures, and consequently, the incident photons follow different optical paths across the tissue. Each photon, associated with a particular path, experiences a particular polarization transformation that is different from those of the other photons. Therefore, the polarization of photons leaving the sample is different. Then, for statistics, part of the outgoing photons leaves the tissue sample in the same position and direction (see Figure 1-6), those photons reaching the same pixel of an imaging polarimeter, so their polarizations are incoherently combined. The incoherent combination of different polarizations leads to partially or fully depolarized states and part of the polarimetric information is lost. However, the measured depolarization is defined for the scattering processes which strongly depends on the density of the inherent fibers and their physical characteristics (i.e., size, shape, index of refraction, etc.) [48]. For that reason, different Monte-Carlo models have been developed to understand the relation between the intrinsic physical structure of the sample and the type of depolarization produced [149–153]. Unfortunately, this relation is a complex issue that has not been solved.

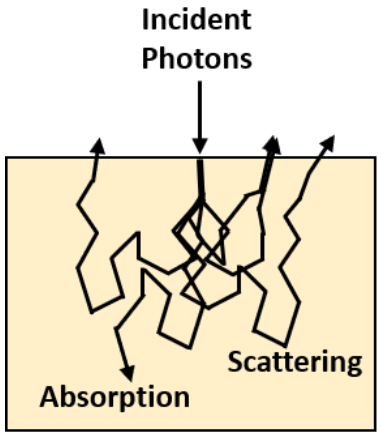

Figure 1-6. Scheme of scattering processes in biological tissues.

Although the mentioned relation is still unknown, different biological structures can produce different polarimetric responses and this information can be used to enhance their visualization. For that reason, the interest in using polarimetric methods for biomedical studies has grown during the last decades [140]. In that sense, polarimetry is used to determine the concentration of hemoglobin [113], oxygen [113], and glucose [117,141] in blood. Different concentration of

hemoglobin and oxygen variates the scattering properties of the sample thus changing light depolarization [113]. Concerning the measurement of glucose, glucose is a chiral molecule that rotates the incident polarization [117,141]. In ref. [141] human eyes are imaged to determine their glucose concentration. Other polarimetric studies takes also polarimetric images from the eyes of animals [118] and humans [119–121,142] with the aim of detecting ocular aberrations and other optical pathologies such as glaucoma [120,142]. These last studies measure the polarimetric properties of the eye's retina and show that eyes that suffer glaucoma present more depolarization than "normal" eyes. Larger depolarization levels are also observed in eyes corrected with laser *in situ* keratomileusis [143]. In this case, operated eyes also presents more irregular patterns of retardation compared to "normal" healthy eyes [143].

Polarimetry is also used to identify the orientation of tissue fibers [84–86,114,122,123]. Most of these studies use polarimetry to determine the orientation of collagen fibers because collagen presents a strong birefringence [84–86,114,122,123,144]. However, some studies showed that polarimetry can also determine the orientation of other types of biological fibers such as skeletal muscle fibers [86]. In other biomedical applications, the birefringence properties of collagen fibers are also proved to be useful to determine the structural inhomogeneities in intermediate layers of tissue samples, for instance, articular cartilages [124]. Note that SHG, a high-resolved image technique commonly used to image collagen fibers, can only measure the superficial layers of tissue samples [124].

In the biomedical field, it is difficult to diagnose of skin pathologies for pigmented lesions or darker skins [79]. In that context, the polarization of light is a property independent of the intensity that proved to be useful in dermatology for the detection of skin diseases [78,79,115,116,125,126]. Polarimetry allows an easier delimitation of the unhealth region [115] and also to perform a better diagnosis of the pathology [78,79,116,125]. Moreover, polarimetry is also able to characterize in real-time microstructural variations of skin tissues during the ultraviolet photo-damaging process [126]. Note that some of these studies (e.g., refs. [78,79]) bases their analysis on hyperspectral imaging techniques and use polarimetry to improve the visualization of the pigmented area (see Figure 1-7). In Figure 1-7 (b) light directly reflected on the surface of the skin is filtered with a linear cross-polarized PG configuration.

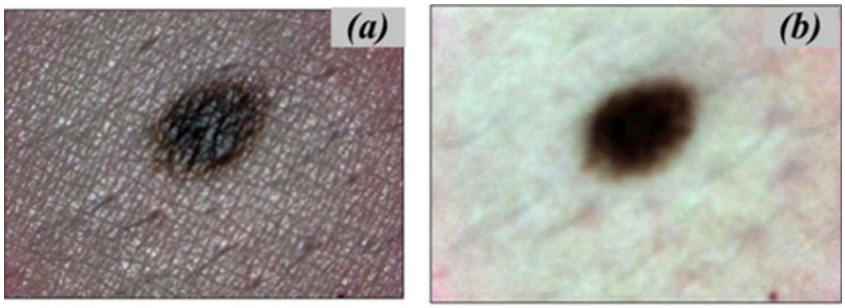

Figure 1-7. Color image of a nevus by using linear (a) co-polarized and (b) cross-polarized PG configurations. Image from ref. [79].

Nowadays, cancer detection is a very important topic in the medical field since cancer becomes the leading cause of death in 2020 with nearly 10 million deaths and 19.3 million cancer occurrences [154]. In addition, the number of cancer occurrences will grow in the next years because the world population is estimated to increase. Accordingly, the number of deaths will

also increase unless the cancer survival rate increases. In that sense, the early recognition of cancerous tissues significantly increases the probability of long-term survival [155–157]. As an example, 89.9% of patients with lung cancer survive for five or more years after the cancer diagnosis at stage I compared with 11.4% of those diagnosed at stage IV [158]. As previously said in section 1.1, different optical imaging techniques proved to be useful for the detection of cancer, but the sensitivity of these studies is around 85% [16]. Therefore, the research of new imaging methods that allows the correct early detection of malignant tissues or that eases its recognition takes a special medical interest because their use would reduce drastically the number of deaths.

In the last years, a wide number of studies proved the interest in using polarimetric imaging for the diagnosis and detection of cancer [81,82,127–132,134–136,145,146]. In particular, polarimetric imaging has been used for the diagnosis of breast cancer [82,130,146], skin cancer [131,132], cervical cancer [129,134–136], colon cancer [133], brain cancer [127], oral cancer[81], thyroid cancer [135], lung cancer [145], among others. Some of these studies are focused on using polarimetry to study carcinoma tissues at the microstructure or cellular level [82,128,130] while others image the sample from a macroscopic point of view and use the different polarimetric properties of cancer and healthy tissue to delimit the cancerous region [81,127,129,131–136,145,146]. As an example of the last group of studies, we provide in Figure 1-8 some results of ref. [135]. Figure 1-8 shows the linear retardance (δ) and the depolarization power (Δ) of a cervical carcinoma tissue. We see that birefringence and depolarization properties of cancerous and healthy regions are different. Healthy cervical tissues present a no-null linear retardance because they are well-ordered structures [135]. By contrast, cancerous cervical tissue has null linear retardance because neoplasia processes destruct and broke down these well-ordered structures [135]. Concerning depolarization properties, cancerous tissues contain denser small organelles which result in smaller depolarization [135]. Some studies analyze the different polarimetric responses between healthy and malignant tissues from an statistical point of view to automatically recognize pre-cancerous regions [129,136].

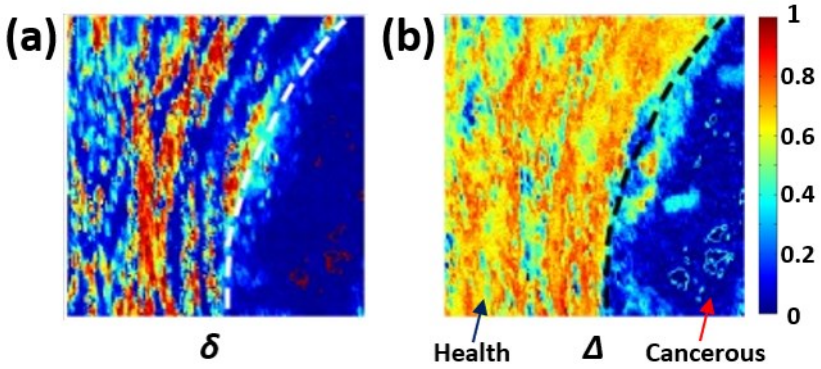

Figure 1-8. Pseudo-color image of (a) linear retardance (*δ*), and (b) depolarization power (*Δ*) of cervical carcinoma tissue. Tissue was measured at 630 nm wavelength and healthy and cancerous regions are delimited by a white and black dotted line. Images are taken from ref. [135].

Most studies that use polarimetric imaging techniques for biomedical purposes are based on two differentiated groups of methods: PG methods [48,79,81,82,84,85,110–116,145–148] and Mueller matrix-based techniques [117–139].

On the one hand, studies that use Polarization Gating techniques exploit the fact that photons directly reflected on the sample's surface maintain the incident polarization when samples are non-dichroic and non-birefringent. In that sense, many studies based on PG techniques use cross-polarized PG configurations to remove the directly reflected photons thus enhancing the visualization of deeper layers of the tissue [79,110–112,115,116,145,147,148]. For example, in ref. [79], a nevus is illuminated with linearly polarized light and when a cross-linear analyzer is used, the surface-reflected photons are filtered (see Figure 1-7 (b)). Note that when a co-linear analyzer is used, the surface-reflected photons are detected (see Figure 1-7 (a)). This study used linear polarizations, but other studies proved the interest of using circular and elliptical polarizations for image enhancement [110,111,145,148]. In particular, ref. [148] combines circular and linear PG configurations to enhance contrast and depth resolution in tissue imaging. Other studies combine linear co-polarized and cross-polarized PG configurations to determine the orientation of birefringent fibers [84,85,114].

On the other hand, a widespread number of polarization-based biomedical applications measure the Mueller matrix of tissue samples to analyze their polarimetric properties [117–120,122–132,134–139]. In that sense, birefringence and depolarization properties proved to be useful for many biomedical applications, for instance, cancer detection (see Figure 1-8). In Mueller polarimetry, these properties are studied through the calculus of different polarimetric observables. The birefringence of the sample is completely described by operating the Lu-Chipman product decomposition [66] and calculating the total retardance R [118,127,129,134], the linear retardance δ [119,124,132,138], the angle orientation of the fast axis, θ [119,124,127,134,138], and the optical rotation of the circular retarder, φ [124,138]. Concerning depolarization properties, their analysis is usually restricted to the operation of the depolarization index, P_Δ [45,69,119,124,129], or the depolarization power, Δ [66,118,127,132,134,138], both global observables that quantify the overall depolarization of samples from a statistical point of view. Note that these depolarization metrics do not measure any dependence of exiting light depolarization with the incident polarization state (i.e., they do not measure the depolarization anisotropy of the sample) so this information that could be interesting is not studied for most biomedical applications.

1.2.3 Image polarimetry for plant applications

Compared to biomedical applications, the number of studies that use polarimetry to enhance the imaging of vegetal tissue samples is much lower [83,159–176]. Despite the limited number of studies, the existing studies showed that relevant information can be obtained from the measurement of dichroism [159,169,170], birefringence [83,170–175], and depolarization [160–168,170,176] properties of vegetal samples. For example, the amount of light reflected off plant leaves is different when the incident light is polarized compared to when it is non-polarized [159,169]. Moreover, the dependence between light reflected by the leaves and the wavelength of the illumination source is also different when using polarized and non-polarized incident light [159,169]. This extra information related to light diattenuation is useful, for instance, for plant classification and characterization [169]. Diattenuation is also produced in leaf veins and can be used to determine their direction [170]. However, their diattenuation signal is weaker compared to their retardance so this application is better performed by using retardance images [170].

Birefringence information is used to characterize the structure of guard cells and their related stomata in different plant samples, including *Allium cepa* [171,172], *Nicotiana tabacum* [172], *Platycerium bifurcatum* [173], *Asplenium nidus* [173], among others [173]. Stomata are widely studied in the botanical field because they are responsible for regulating gas exchange and water loss in plants [177,178]. Figure 1-9 shows a polarization (Figure 1-9 (a)) and a non-polarization (Figure 1-9 (b)) images of an *Allium cepa* taken from ref. [172]. In the polarization image (Figure 1-9 (a)), four bright points are seen in the stomata "lips". This brightness is observed because these stomata structures retardate the incident light thus changing their polarization. This retardation can be used to study the stress and pressure of those microfibrils that compose the measured stoma [173].

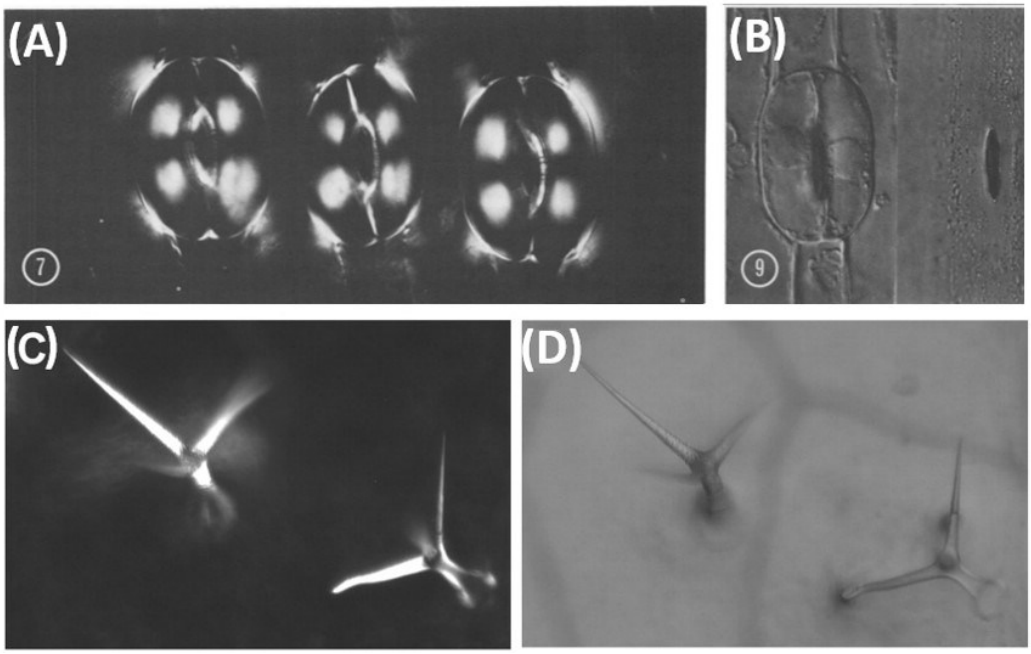

Figure 1-9. (a) Cross-polarization image of onion guard cells and their related stomata. (b) Microscopy image of an onion stoma. (c) Cross-polarization and (d) microscopy image of an *Arabidopsis thaliana* leaf. (a) and (b) images are taken from ref. [172]

In addition to guard cells and stomata, birefringence enhances the visualization of trichomes compared to using non-polarimetric microscopes [174] (see Figure 1-9 (c) and (d)). Trichomes are ideal model systems for the study of various aspects of plant cell morphogenesis [179]. Cotton fibers are trichome cells composed primarily of cellulose and their maturity can be determined by measuring their birefringence [175]. In that sense, mature fibers have more cellulose so greater birefringence [175]. Moreover, polarimetric techniques also allow determining the orientation of cellulose fibrils in plants [83].

For its side, depolarization has been used to study the photosynthesis process [165,166]. The polarimetric signature of photosynthetic pigments can be sensitive biomarkers to detect live in other planets [165]. In addition, depolarization can be used to detect water stress in plants because measured depolarization increases as plant leaves are more dehydrated [160–162]. Moreover, depolarization is also used in remote sensing to classify vegetation [163,176], to discriminate and delimit vegetal areas [167], and to distinguish land mines from the surrounding

vegetation backgrounds [164]. Note that in these remote sensing applications, polarimetry is combined with spectroscopy techniques to improve the classification results.

The above-mentioned studies that use polarization to inspect vegetal tissues are mainly based on two different approaches: PG techniques [83,171–175], and the measurement of the degree of polarization, DOP [160–163,165–167,176]. The PG techniques are mainly used to exploit the birefringence properties of vegetal structures. In turn, the degree of polarization is employed to measure the depolarization that a given polarized light suffers after its interaction with the imaged vegetal tissue. Note that when using these polarimetric techniques, only part of the birefringence or depolarization properties is studied. By contrast, Mueller polarimetry is a more general approach that allows the calculation of several retardance and depolarization observables to completely analyze these two properties from a particular Mueller matrix measurement [44–46]. However, despite the theoretical benefits, Mueller polarimetry has been scarcely used for plant applications [164,168,170].

The use of polarimetry for plant studies is minimal compared with its use in biomedical applications. Consequently, the potential of polarimetry for many plant applications is unknown. For example, polarimetry could be used for the detection of plant diseases, but its suitability in such scenario is still not studied. The detection of plant disease is a very interesting topic with economic relevance because pests and diseases are responsible for significant losses in agricultural crops thus resulting in important economic losses [180]. To give some numbers, crop losses of the major food crops (rice, wheat, maize, potatoes, etc.) due to pests and diseases were quantified between 20% to 40% [181] in 2001-2003. Therefore, the research of new imaging methods that eases the detection of diseases, preferably at early stages, takes a special economical interest.

1.3 Polarimeters

Polarimeters are the instruments used to measure the polarization properties of light and samples. Polarimeters that measure the polarization properties of light are called Stokes polarimeters whereas those used to measure sample properties are called Mueller polarimeters. Mueller polarimeters are composed of an illumination system with control to the generated state of polarization and a Stokes polarimeter that can analyze the state of polarization of measured light. In this section, we following review some of the main architectures of Stokes polarimeters: a division of amplitude polarimeters (DoAmP) [182,183], division of aperture polarimeters (DoAP) [184–186], division of focal plane (DoFP) polarimeters [50–59], polarimeters based on rotating elements [187–190], and polarimeters based on liquid crystal devices [191–194].

Division of amplitude polarimeters (DoAmP)

In DoAmP, the analyzed light beam is divided into four beams and different static analyzers (usually composed of a retarder plate and a linear polarizer) are used to measure each beam [182,183] (see Figure 1-10 (a)). Afterward, all the measured intensities are combined to retrieve the Stokes vector of the beam. This architecture has the advantage of performing simultaneous acquisitions leading to real-time measurements. However, the instrument presents large sizes compared to other options and, in the case of imaging polarimeters, four cameras are needed

thus being an expensive option compared with others. Additionally, the calibration process of these four cameras is laborious as the four images that must be combined usually present different magnifications and requires postprocessing techniques. Such postprocessing techniques must also take into account the different light absorptions and electrical responses between cameras, which can be different although being the same model.

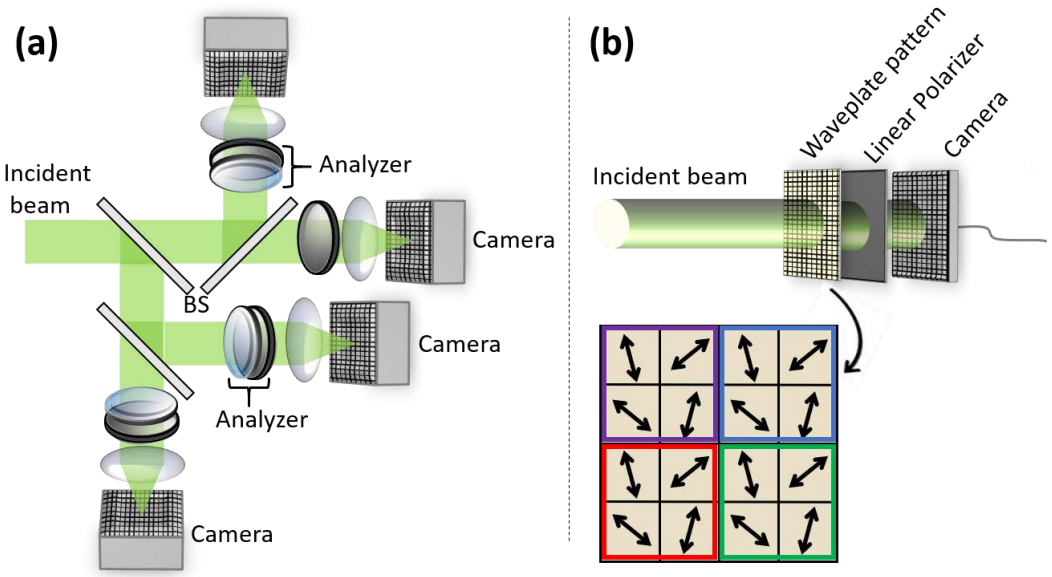

Figure 1-10. (a) Scheme of a division of amplitude polarimeter. (b) Scheme of a division of focal plane polarimeter. BS means beam splitter.

Division of aperture polarimeters (DoAP)

DoAP is an alternative architecture that presents similar characteristics to DoAmP but solving the problem of working with four different cameras. These type of polarimeters also splits the beam amplitude into four channels, they being addressed to their corresponding analyzers, but unlike DoAmP, all the resulting intensities are measured with different regions of the same camera [184–186]. Consequently, it allows the performance of compact snapshot polarimeters [186]. The main issue of DoAP polarimeters is the loss of spatial resolution with respect to DoAmP. Additionally, DoAP presents distortion, magnification, apodization, and transmission between channels due to the optical elements that split the beam.

Division of Focal plane (DoFP) polarimeters

DoFP polarimeters are compact polarimeter designs that solve the distortion, magnification, and apodization issues and allow snap-shot measurements [59]. This polarimeter is built by placing different analyzers (usually a polarization microgrid) in front of each camera pixel [50–59] (see Figure 1-10 (b)). Note that using this architecture, the resolution of the polarimetric image is lower than the standard intensity image because at least the information of four pixels must be combined to calculate the Mueller matrix (see Figure 1-10 (b) in which macropixels are represented in different colors).

Because of its miniaturized design, its construction process requires complex miniaturization techniques and high align accuracy thus resulting in very expensive polarimeters. However,

during the last years, the miniaturization industry has been growing very fast and nowadays their price is comparable with other polarimeters. This kind of polarimeters is very interesting for biomedical applications, but unfortunately, at the beginning of this thesis, a DoFP system was not available.

1.3.1 Division of time polarimeters (DoTP)

Polarimeters based on rotating elements and polarimeters based on liquid crystal devices are grouped as a division of time polarimeters (DoTP) [47] which are characterized by changing the analyzer over time (time-sequential polarimeters). This type of polarimeters works by taking measurements with different analyzers that vary over time, and after a given number of measurements (at least 4 in the case of Stokes polarimeter and 16 in the case of Mueller polarimeter) the Mueller matrix of the sample is retrieved. Note that each analyzer measurement takes time so the Mueller matrix measurements are not instantaneous, and the samples must be stationary during the measuring time. Nevertheless, although these kind of polarimeters are not the best option for real-time applications, nowadays, they can be configured to perform very fast measurements, being limited by the refresh rate of the liquid crystals (in the order of Hz for nematic liquid crystals and of kHz for ferro-electric liquid crystals [195]) or the exposure time of the camera in the case of polarimeters based on rotating elements.

Polarimeters based on rotating elements

Polarization analyzers in polarimeters based on rotating elements are mechanically modified by rotating a retarder plate or rotating a polarizer [187–190]. This type of polarimeters performs faster measurements compared to polarimeters based on liquid crystal devices and is clearly the cheapest architecture in the market. However, they present a strong disadvantage related to image acquisitions. This type of polarimeters is based on the mechanical rotation of optical elements and this mechanical rotation of the element may slightly modify the direction of the light beam so shifting the images captured with the camera (beam wander). This image shifting requires image postprocessing to be compensated.

Polarimeters based on liquid crystal devices

Polarization analyzers in polarimeters based on liquid crystal (LC) devices are modified by changing the voltage applied to liquid crystal devices thus not applying mechanical rotations [191–194]. This is because liquid crystals are based on anisotropic uniaxial molecules that are polar molecules, so tend to align with an external electric field, modifying the medium retardance with voltage. Since no mechanical rotation is applied, the captured images do not need postprocessing techniques to compensate for possible image shifts. This type of polarimeters is cheaper and easier to implement compared to DoAmP and DoAP but such polarimeters are not able to take snapshot images; they are limited by the refresh rate of the liquid crystals. Accordingly, depending on the liquid crystal device employed, faster or slower polarimeters are built.

(i) Parallel aligned nematic LC

Parallel aligned liquid crystals (PA-LC) consist of nematic liquid crystals placed between two glass substrates, and with the molecules that limit with both substrates

attached in parallel [196] (see Figure 1-11 (a)). Under this scenario, orthogonal light components experience two different indices of refraction and they are accordingly retarded, being able to modify light polarization. Importantly, when an external field is applied, LC molecules are tilted in the direction of that field. The tilted angle depends on the voltage applied, being near to 90° for high voltages (see Figure 1-11 (b)). Therefore, the effective retardance introduced by LC molecules depends on the optical axis orientation. In the case of maximum tilt, the medium acts as an isotropic medium, so PA-LC does not introduce phase shift to the light components. However, in real experimental scenarios, LC molecules never reach the perfect alignment with the external field direction, even for high voltages [196], so some residual retardance is always introduced.

In practice, PA-LC acts as a linear retarder with variable retardance δ, which can be controlled with the voltage. To swap from one state to another, PA-LC needs typically ∼10-100 ms [195]. However, the newest high-speed liquid crystal devices need ∼1ms [195] thus making possible real-time polarimeters based on PA-LC devices.

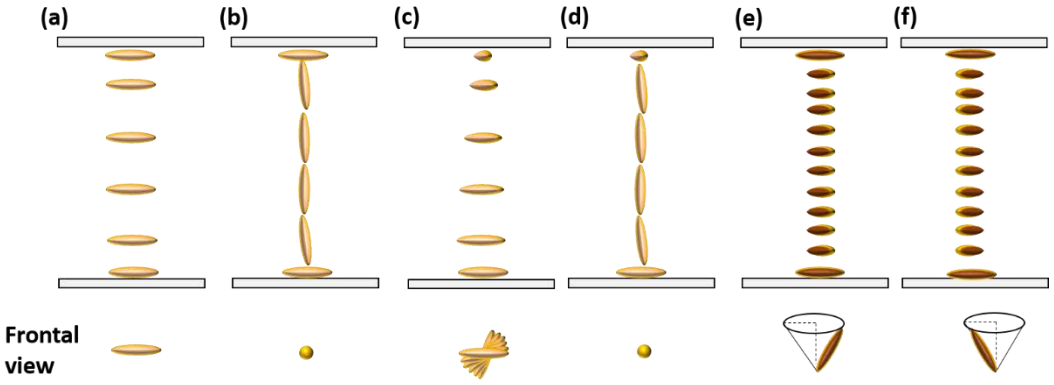

Figure 1-11. Scheme of PA-LC cell showing molecules arrangement when applying (a) no voltage and (b) high voltage. Scheme of TN-LC cell, with a twist of 75°, showing molecules arrangement when applying (c) no voltage and (d) high voltage. Scheme of ferroelectric LC cell showing molecules arrangement when applying (e) positive voltage (first stable state) and (f) negative voltage (second stable state).

(ii) Twisted nematic LC

Twisted nematic liquid crystals (TN-LC) consist of nematic liquid crystals placed between two glass substrates, and with the molecules that limit with both substrates attached in a certain angle, called twist angle [196] (see Figure 1-11 (c)). These LC devices work similarly to PA-LC but the fact global twist introduced by molecules (see Figure 1-11 (c)) produces an optical rotation to the incident light. Consequently, TN-LC acts as a combination of a linear retarder and a circular retarder (i.e., an elliptical retarder) that depends on the applied voltage [196]. The refresh rate of TN-LC is like PA-LC.

(iii) Ferroelectric LC

Ferroelectric LC consists of chiral smectic C phase molecules placed between two glass substrates [196] (see Figure 1-11 (e)). Unlike nematic liquid crystals, these chiral

molecules are not aligned when no voltage is applied. In fact, these chiral molecules are randomly oriented in a cone direction. When a certain external field is applied, chiral molecules try to be aligned parallel to its direction without leaving the mentioned cone of directions (see Figure 1-11 (e)). Therefore, when the external field is positive, chiral molecules collapse in a first stable state (see Figure 1-11 (e)) and when it is negative, chiral molecules collapse in a second stable state (see Figure 1-11 (f)). These two states can be defined in a plane and are rotated at an angle α one to the other. Consequently, ferroelectric LC acts as a linear retarder with two different orientations (θ and $\theta+\alpha$) [196]. Switching from one state to the other takes hundreds of microseconds [195].

1.4 Main goals of this thesis

Several polarimetric techniques have been developed and applied for image enhancement in biological applications (see subsections 1.2.2 and 1.2.3). Nevertheless, some metrics described in the literature that further characterize the polarization and depolarization response of tissue samples are not used. In particular, biomedical studies based on polarimetry are restricted to the measure of global depolarization observables so not measuring observables that depend on the depolarization anisotropy of the sample. On the other hand, Mueller polarimetry is scarcely used for the analysis of vegetal tissues so being a field to explore.

Under this scenario, this thesis proposes the experimental implementation of recently proposed polarimetric methods (as well as new ones) to obtain additional information from the polarization and depolarization response of biological tissues. This additional information can be used to enhance the imaging of biological tissues as well as to improve tissue classification. In that context, the main goals of this thesis are:

i. Mueller matrix and polarization gating relation: To compare the two polarimetric approaches most used in biomedical applications, i.e., Mueller polarimetry and Polarization gating techniques, and to determine a mathematical relation between them. The mathematical relation has to be experimentally tested to check if it can be used in biological applications.

ii. Complete characterization of depolarization: To experimentally analyze the physical interpretation of two sets of polarization metrics, the indices of polarimetric purity (IPP) and the components of purity (CP), that further synthesize the depolarization response of samples compared to the global observables P_Δ and Δ. The complementary aspect of both sets of parameters and their combined use to completely describe the depolarization mechanisms involved in light-matter interactions have to be also studied.

iii. IPP to enhance tissue visualization: To apply the indices of polarimetric purity, that further synthesize the depolarization response of samples, to improve the visualization of animal tissues, and to better characterize the depolarization process related to the physical structures of the tissue. In addition, the results obtained with the IPP have to be compared with those obtained with the commonly used parameters P_Δ and Δ.

iv. Depolarization information for tissue classification: To identify the best way of synthesizing the depolarization content of animal tissue samples for their automatic classification based on machine learning techniques. Accordingly, the suitability of

different sets of depolarization metrics for tissue classification must be compared. This goal includes the proposal of a classification method based on depolarization information.

v. Mueller polarimetry for plant applications: To analyze the potential of using Mueller polarimetry for the inspection of vegetal tissues and to compare the results with commonly used polarimetric and non-polarimetric optical techniques.

1.5 Structure of this thesis

The outline of this thesis is as follows:

In Chapter 2, we describe in detail the mathematical formalism used in this thesis to analyze the polarization and depolarization properties of light as well as the polarimetric properties of biological samples. In that sense, the mathematical calculations of different groups of polarimetric observables are defined based on the Mueller-Stokes formalism. We use the Mueller-Stokes formalism because it allows the description of partially and fully depolarized states.

In Chapter 3 we describe the design and experimental implementation of the image Mueller polarimeter used in most of this thesis experiments. The described polarimeter is based on Parallel Aligned Liquid Crystals (PA-LC) devices and the chapter explains its operation principle and its calibration method. Moreover, a brief explanation of the main reasons that led the research group to select this architecture is also provided.

Afterward, Chapter 4 analyzes recently proposed polarimetric methods (as well as new ones) from an experimental point of view. This chapter is divided into two differentiated studies. First, a new method to perform PG configurations based on experimentally measured Mueller matrices is proposed. The limitations and benefits of these methods are studied through phantom experiments. The fact of using phantom experiment ease the interpretation of the results because their structure is well-known. Then, a method that combines PG configurations and dichroism, retardance, and depolarization is also proposed and used to image an *ex-vivo* sample. Second, the physical interpretation of the IPP and the CP is studied through a set of simulated depolarizers. This second study comprises the analysis of the physical information associated with each set of parameters and the complementary aspect of this information. Finally, the use of the IPP is compared to P_{Δ} through the measurement of experimentally synthesized depolarizers.

Chapter 5 is divided into two differentiated sections. The first section is composed of different studies in which depolarization metrics are used to improve the results in biomedical applications. In particular, a first study describes the results obtained when using the IPP to improve the visualization of animal tissue structures. Afterward, a second study shows the use of the IPP to automatically classify different animal tissues. In this second study, other depolarization metrics, in addition to IPP, are also used for the animal tissue classification and the results are compared with those obtained with the IPP. In the second section of Chapter 5, the potential of using Mueller-based polarimetric methods to enhance the visualization of vegetal tissues is discussed through the measurement of different plant specimens. Moreover, the results obtained when using Mueller polarimetry are compared with those obtained from other polarimetric and non-polarimetric optical techniques commonly used for plant inspection.

Finally, the conclusions of this thesis are provided in Chapter 6, together with some proposals for future research.

Chapter 2 Mathematical formalism

This chapter presents the mathematical formalism used in this thesis to describe the polarized light as well as its interaction with biological samples. Starting from the well-known Mueller-Stokes formalism, the light-matter interaction is studied by means of a group of polarimetric observables that presents a well-defined physical meaning.

First of all, the concepts and notations associated with the Mueller-Stokes formalism are introduced in section 2.1. This formalism is used to describe the state of polarization of light and its interaction with media systems. Next, the descriptions of different mathematical methods that are used to analyze the polarimetric information encoded in the Mueller matrix are provided in sections 2.2, 2.3, and 2.4. In particular, the most used technique, called Lu-Chipman product decomposition, is described in section 2.2. This decomposition technique splits the polarimetric information into three matrices to analyze the content separately. However, this decomposition method has some limits regarding the analysis of the depolarization content. Accordingly, the last part of this chapter describes two groups of alternative mathematical methods that further analyze the depolarization content. The polarimetric purity parameters are presented in section 2.3 and the parameters associated with the symmetric product decomposition are provided in section 2.4.

2.1 Stokes and Mueller formalism

Polarized light and its interaction with matter can be described using different mathematical formalism such as the Jones calculus [197] based on the complex electric field components; the Berreman formalism [198] which incorporates the magnetic field; the generalized harmonic analysis introduced by Weiner [199]; or the Stokes-Mueller (S-M) formalism [200,201] based on light observables, among others. All these formalisms are different ways to describe the same phenomenon under different assumptions, and consequently, they are correlated. For example, the Stokes-Mueller formalism can be derived from temporal averages of the Jones calculus [202].

Each formalism presents its particular characteristics and applicability framework, being the Stokes-Mueller formalism better suited for the biological tissue analysis because of two main reasons. First, S-M formalism is based on light observables, whose main magnitudes arise from combinations of different intensity measurements, and this results in an easier experimental implementation. Second, most of the biological samples are highly depolarizing materials and

the Mueller-Stokes formalism not only works with fully polarized light, as the Jones calculus does [202], but it also considers partially or unpolarized light.

2.1.1 Stokes parameters

In 1858, G. G. Stokes described the state of polarization (SoP) of a light beam through four parameters [200]. These four parameters, so-called Stokes parameters, can be placed as a four-dimensional vector ***S***, so-called Stokes vector, which completely describes any SoP of polarized light, including partially polarized states.

$$\boldsymbol{S} = \begin{pmatrix} S_0 \\ S_1 \\ S_2 \\ S_3 \end{pmatrix} = \begin{pmatrix} I_{0^o} + I_{90^o} \\ I_{0^o} - I_{90^o} \\ I_{45^o} - I_{135^o} \\ I_R - I_L \end{pmatrix} \tag{2.1}$$

where S_0 is associated with the total intensity of the beam, S_1 indicates the amount of horizontal or vertical linear polarization, S_2 quantifies the amount of diagonal or anti-diagonal linear polarization, and S_3 corresponds to the amount of right-handed or left-handed circular polarization. The Stokes parameters can be defined in terms of six intensities I_{0^o}, I_{45^o}, I_{90^o}, I_{135^o}, I_R, and I_L that corresponds to the intensity measurement when analyzing the horizontal, diagonal, vertical, and anti-diagonal linear polarization, and the right-handed and left-handed circular polarization, respectively. The case of measuring six equal intensities corresponds to unpolarized light. Otherwise, we are dealing with partially or fully polarized light and its degree of polarization (*DOP*) is defined as [45,46]:

$$DOP = \frac{\sqrt{S_1^2 + S_2^2 + S_3^2}}{S_0} \tag{2.2}$$

where 0 corresponds to unpolarized light and 1 to fully polarized light. Intermediate values indicate partially polarized states.

2.1.2 Poincare sphere

From Eq. (2.1), we see that all the polarization content of the light beam is quantified with the last three parameters {S_1, S_2, S_3}. These parameters are proportional to the total intensity of the beam and it hinders the polarimetric comparison of light beams with different intensities. Accordingly, these three Stokes parameters {S_1, S_2, S_3} are normalized by S_0 resulting in three {s_1, s_2, s_3} parameters which are ranged from -1 to 1 and that are independent of the light beam intensity.

Now, any SoP of a light beam can be graphically represented in a three-dimensional space (Figure 2-1) associating each axis with the normalized {s_1, s_2, s_3} parameters [9]. Under such representation, any SoP is located within a unit sphere centered in the origin of coordinates (0, 0, 0). That sphere is known as the Poincare sphere, it was firstly proposed by H. Poincaré in 1892 [203], and it corresponds to all the physically realizable SoP. Apart from the visualization of the SoP of light beams, the Poincare sphere is useful for the visualization of its modification during light-matter interactions.

In Figure 2-1, an elliptical SoP is represented in the Poincare sphere. The SoPs can be represented in the Poincare sphere by using vectors. The modulus of these vectors (i.e. the length) corresponds to the DOP of the polarized state so the states placed at the surface of the Poincare sphere are fully polarized states (DOP=1). In contrast, the other states placed inside the sphere are partially polarized or unpolarized. In particular, unpolarized light is represented in the origin of coordinates (0,0,0) due to the 0 lengths of the vector.

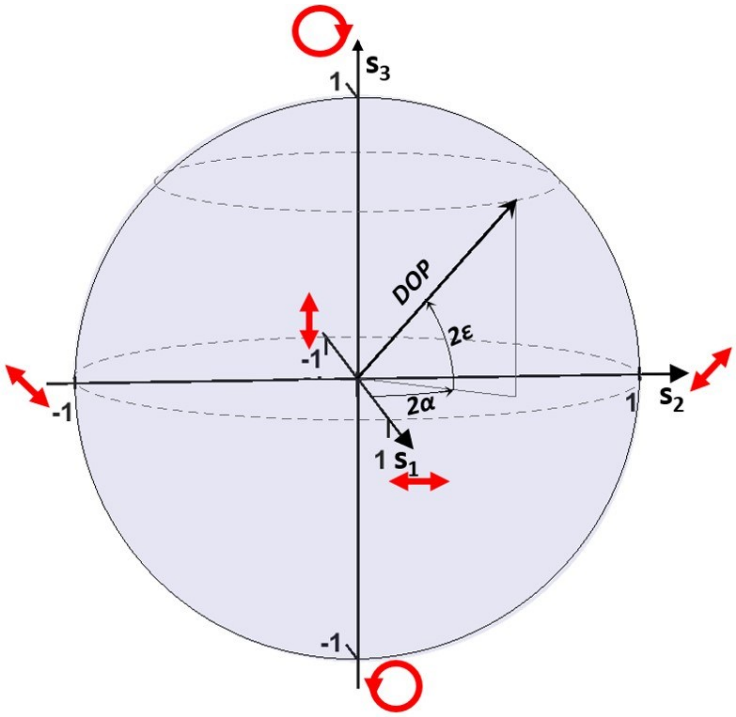

Figure 2-1. Representation of the Poincare sphere and the vector of an elliptical SoP characterized by DOP=1, α=22.5°, and ε=22.5°. The horizontal, diagonal, vertical, and anti-diagonal linear polarization, together with the right-handed and left-handed circular polarization states are represented in red near to their corresponding position at the Poincare sphere.

Apart from the modulus, the SoP vector is also characterized by a certain direction. Such direction is defined by the azimuth angle (α) and the elliptical angle (ε) as follows:

$$\boldsymbol{S} = S_0 \cdot DOP \begin{pmatrix} 1 / DOP \\ \cos(2\alpha)\cos(2\varepsilon) \\ \sin(2\alpha)\cos(2\varepsilon) \\ \sin(2\varepsilon) \end{pmatrix} \tag{2.3}$$

where 2α is the azimuthal angle between the S_1-S_3 plane at S_2=0 and the plane including both the S_3 axis and the vector pointing from the sphere center to the particular SoP, this angle being connected with the orientation of the polarization ellipse. In turn, 2ε is the angle between the S_1-S_2 plane at S_3=0 and the same plane at the S_3 value of the corresponding SoP, this angle being connected with the linearity of the polarization, being ε=45°, ε=0 and ε=-45° associated with the right-handed circular polarization, the linear polarization, and the left-handed circular polarization, respectively.

2.1.3 Mueller matrix formalism

In 1948, H. Mueller described the light-matter interaction by using the Stokes formalism and through a 4x4 matrix ***M***, so-called Mueller matrix [201]:

$$S_{out} = M \cdot S_{in} \tag{2.4}$$

where S_{in} and S_{out} are the Stokes vector before and after the light-matter interaction, and ***M*** defines the modification of the beam's polarization produced during the interaction process. It is worth noting that ***M*** does not only depend on the material characteristics, but it also depends on the wavelength, the incident beam's direction, and the output direction of the beam [44–46]. However, once these variables are fixed, the Mueller matrix ***M*** will describe how the polarization of all the possible incident beams is modified due to the light-matter interaction in linear processes. Under this scenario, the SoP of the beam after the interaction, S_{out}, can be calculated for any incident polarization state, S_{in}.

In the experimental scenario, the wavelength, the incident direction, and the output direction of the beam are usually fixed to directly relate different Mueller matrices with the material properties and its physical structures. In that case, materials can be differentiated and classified in function of their polarimetric behavior. This behavior can be described as the combination of three polarimetric properties [46]: diattenuation-polarizance (dichroism), retardance (birefringence), and depolarization.

Diattenuation describes the amount of light that is absorbed during the light-matter interaction depending on the state of polarization of the input beam [45,46], and polarizance defines the quantity of light that is polarized and the type of polarization in which it is polarized [45,46]. These two properties are related to dichroism and materials that are mainly characterized by these two properties are called diattenuators (polarizers are examples of diattenuators).

Retardance is related to the capability of materials to introduce certain phase-shift between the electromagnetic components of the input light but without changing the *DOP* or the mean intensity of the beam. The birefringent materials that are mainly characterized by this property are called retarders (e.g. quarter-wave plate or half-wave plate retarders) and present anisotropic uniaxial or biaxial properties.

Depolarization is the property of materials to depolarize light, i.e. reduce the *DOP* of the incident light beam. Materials that are mainly characterized by this property are called depolarizers (fog and smoke are examples of depolarizers for certain input wavelengths, as in the visible range).

As previously said, most materials present a combination of these polarimetric properties and all this information is encoded in the Mueller matrix. Some of this information, as the dichroic content, can be directly derived from the block expression of the Mueller matrix [204],

$$\boldsymbol{M} = \begin{pmatrix} m_{00} & m_{01} & m_{02} & m_{03} \\ m_{10} & m_{11} & m_{12} & m_{13} \\ m_{20} & m_{21} & m_{22} & m_{23} \\ m_{30} & m_{31} & m_{32} & m_{33} \end{pmatrix} = m_{00} \begin{pmatrix} 1 & \boldsymbol{D^T} \\ \boldsymbol{P} & \boldsymbol{m} \end{pmatrix} \tag{2.5}$$

where m_{00} is the mean intensity coefficient of ***M*** (i.e. transmittance or reflectance of unpolarized input states) and it presents the highest value among the **M** coefficients. ***D*** and ***P*** are three-component vectors called diattenuation vector and polarizance vector [66], respectively. The modulus of these vectors are called diattenuation, $D = \left|\boldsymbol{D}\right|$, and polarizance, $P = \left|\boldsymbol{P}\right|$ [205,206], and they are the two basic magnitudes to measure the overall dichroic content of ***M***. The magnitudes associated with the retardance and depolarization properties of ***M*** require further mathematical treatment as they are encoded in the 3x3 ***m*** submatrix. These mathematical treatments are mainly based on decomposing ***M*** into an equivalent group of matrices, each containing the specific polarimetric property of ***M***. In that way, the properties should be separated easing its interpretation. The different mathematical methods employed in this thesis are following described.

2.2 Lu-Chipman product decomposition

In 1996, S.-Y. Lu and R. A. Chipman [66] proposed to decompose the Mueller matrix ***M*** into a concatenation of three matrices each containing the main information of one of the three basic polarimetric properties,

$$\boldsymbol{M} = m_{00}\hat{\boldsymbol{M}}_{\Delta}\hat{\boldsymbol{M}}_{R}\hat{\boldsymbol{M}}_{D,} \tag{2.6}$$

where $\hat{\boldsymbol{M}}_{\Delta}$ is the normalized Mueller matrix of a depolarizer that should only contain the depolarizing information of ***M***, $\hat{\boldsymbol{M}}_{R}$ is the normalized Mueller matrix of a non-depolarizing retarder that should comprise the birefringence of ***M***, and $\hat{\boldsymbol{M}}_{D}$ is the normalized Mueller matrix of a pure diattenuator that should contain all the dichroic content of ***M.***

2.2.1 Lu-Chipman product decomposition procedure

The normalized matrix of a pure diattenuator is characterized by the three parameters of the vector ***D***, and can, in general, be defined as:

$$\hat{\boldsymbol{M}}_{D} = \begin{pmatrix} 1 & \boldsymbol{D}^T \\ \boldsymbol{D} & \boldsymbol{m}_D \end{pmatrix} \tag{2.7}$$

where $\boldsymbol{m_D}$ is the 3x3 submatrix specified by ***D***,

$$\boldsymbol{m}_D = a\boldsymbol{I}_3 + b\boldsymbol{D}\boldsymbol{D}^{\boldsymbol{T}} \tag{2.8}$$

with $a = \sqrt{1 - D^2}$, $b = 1 - \frac{a}{D^2}$ and $\boldsymbol{I}_3$ equal to the 3x3 identity matrix. The expression of the inverse of $\hat{\boldsymbol{M}}_{D}$ can be written as follows:

$$\hat{\boldsymbol{M}}_{D}^{\ -1} = \frac{1}{a^2}\begin{pmatrix} 1 & -\boldsymbol{D}^T \\ -\boldsymbol{D} & \boldsymbol{I_3} \end{pmatrix} + \frac{1}{a^2(a+1)}\begin{pmatrix} 1 & \boldsymbol{0}^T \\ \boldsymbol{0} & \boldsymbol{D}\boldsymbol{D}^{\boldsymbol{T}} \end{pmatrix} \tag{2.9}$$

The effect of the diattenuator is removed from ***M*** by multiplying the Mueller matrix with the inverse of $\hat{\boldsymbol{M}}_D$ [66]**:**

$$\boldsymbol{M}\ \hat{\boldsymbol{M}}_D{}^{-1} = m_{00}\begin{pmatrix} 1 & \boldsymbol{D}^T \\ \boldsymbol{P} & \boldsymbol{m} \end{pmatrix} \hat{\boldsymbol{M}}_D{}^{-1} = m_{00}\begin{pmatrix} 1 & \boldsymbol{0}^T \\ \dfrac{\boldsymbol{P}-\boldsymbol{m}\boldsymbol{D}}{1-D^2} & \boldsymbol{m}' \end{pmatrix} = m_{00}\hat{\boldsymbol{M}}_\Delta\hat{\boldsymbol{M}}_{\boldsymbol{R}} = \boldsymbol{M}' \quad (2.10)$$

The general expressions for a normalized pure depolarizer $\hat{\boldsymbol{M}}_\Delta$ and a normalized pure retarder $\hat{\boldsymbol{M}}_R$ are the following:

$$\hat{\boldsymbol{M}}_\Delta = \begin{pmatrix} 1 & \boldsymbol{0}^T \\ \boldsymbol{0} & \boldsymbol{m}_\Delta \end{pmatrix} \quad (2.11)$$

$$\hat{\boldsymbol{M}}_{\boldsymbol{R}} = \begin{pmatrix} 1 & \boldsymbol{0}^T \\ \boldsymbol{0} & \boldsymbol{m}_R \end{pmatrix} \quad (2.12)$$

where ***m*$_\Delta$** and ***m*$_R$** are 3x3 submatrices.

Note that $\hat{\boldsymbol{M}}_\Delta$ and $\hat{\boldsymbol{M}}_R$ present a null polarizance vector while the multiplication $\boldsymbol{M}\ \hat{\boldsymbol{M}}_D{}^{-1}$ does not. Consequently, Eq. (2.10) is impossible to accomplish taking these definitions of $\hat{\boldsymbol{M}}_\Delta$ and $\hat{\boldsymbol{M}}_R$. This issue is solved by incorporating the polarizance vector ***P*$_\Delta$** to $\hat{\boldsymbol{M}}_\Delta$.

$$\hat{\boldsymbol{M}}_\Delta = m_{00}\begin{pmatrix} 1 & \boldsymbol{0}^T \\ \boldsymbol{P}_\Delta & \boldsymbol{m}_\Delta \end{pmatrix} \quad (2.13)$$

As a result, the matrix ***M'*** can be written as:

$$\boldsymbol{M}' = m_{00}\hat{\boldsymbol{M}}_\Delta\hat{\boldsymbol{M}}_{\boldsymbol{R}} = m_{00}\begin{pmatrix} 1 & \boldsymbol{0}^T \\ \boldsymbol{P}_\Delta & \boldsymbol{m}_\Delta \end{pmatrix}\begin{pmatrix} 1 & \boldsymbol{0}^T \\ \boldsymbol{0} & \boldsymbol{m}_R \end{pmatrix} = m_{00}\begin{pmatrix} 1 & \boldsymbol{0}^T \\ \boldsymbol{P}_\Delta & \boldsymbol{m}_\Delta\boldsymbol{m}_R \end{pmatrix} \quad (2.14)$$

Now, comparing the expressions of Eqs. (2.10) and (2.14) the following definitions can be established [66]:

$$\boldsymbol{P}_\Delta = \frac{\boldsymbol{P}-\boldsymbol{m}'\boldsymbol{D}}{1-D^2} \quad (2.15)$$

$$\boldsymbol{m}' = \boldsymbol{m}_\Delta\boldsymbol{m}_R \quad (2.16)$$

The submatrices ***m*$_\Delta$** and ***m*$_R$** are symmetric ($m_\Delta = m_\Delta^T$) and orthogonal matrices ($m_R m_R^T = m_R^T m_R = I_3$), respectively, so we can take advantage of the product ***m'(m')*^{T}** as follows [66]:

$$\boldsymbol{m}'(\boldsymbol{m}')^T = \boldsymbol{m}_\Delta\boldsymbol{m}_R\ \ \boldsymbol{m}_\Delta\boldsymbol{m}_R{}^T = \boldsymbol{m}_\Delta\overbrace{\boldsymbol{m}_R\boldsymbol{m}_R{}^T}^{\boldsymbol{I}_3}\boldsymbol{m}_\Delta{}^T = \boldsymbol{m}_\Delta\boldsymbol{m}_\Delta{}^T = \boldsymbol{m}_\Delta{}^2 \quad (2.17)$$

Considering that λ_1, λ_2, and λ_3 are the eigenvalues of ***m'(m')*^{T}**, ***m*$_\Delta$** can be calculated as [66]:

$$\boldsymbol{m}_{\Delta} = \pm[\boldsymbol{m}'(\boldsymbol{m}')^T + k_2\boldsymbol{I}_3]^{-1}[k_1\boldsymbol{m}'(\boldsymbol{m}')^T + k_3\boldsymbol{I}_3] \tag{2.18}$$

with:

$$k_1 = \sqrt{\lambda_1} + \sqrt{\lambda_2} + \sqrt{\lambda_3} \tag{2.19}$$

$$k_2 = \sqrt{\lambda_1\lambda_2} + \sqrt{\lambda_2\lambda_3} + \sqrt{\lambda_1\lambda_3} \tag{2.20}$$

$$k_3 = \sqrt{\lambda_1\lambda_2\lambda_3} \tag{2.21}$$

The sign ± in Eq. (2.18) follows the sign of the determinant of ***m'***. With these last expressions the submatrix $\boldsymbol{m}_R$ is determined by inverse multiplying $\boldsymbol{m}_{\Delta}$:

$$\boldsymbol{m}_R = \boldsymbol{m}_{\Delta}^{-1}\boldsymbol{m}' = \pm[k_1\boldsymbol{m}'(\boldsymbol{m}')^T + k_3\boldsymbol{I}_3]^{-1}(\boldsymbol{m}'(\boldsymbol{m}')^T\boldsymbol{m}' + k_2\boldsymbol{m}') \tag{2.22}$$

The sign of Eq. (2.22) also follows the sign of the determinant of ***m'***.

2.2.2 Retarder parameters

Up to now, we have split the information of ***M*** into three matrices by using the Lu-Chipman decomposition [46,66]. Therefore, the dichroic information of ***M*** should be enclosed in $\boldsymbol{M}_D$, the birefringent information of ***M*** is associated with $\hat{\boldsymbol{M}}_R$ and the depolarization information of ***M*** is contained in $\hat{\boldsymbol{M}}_{\Delta}$. The dichroic content of $\boldsymbol{M}_D$ can be quantified with the vector ***D*** thus the analysis of the dichroic information does not need more mathematical treatment. Conversely, the information included in $\hat{\boldsymbol{M}}_R$ and $\hat{\boldsymbol{M}}_{\Delta}$ requires further mathematical treatment to get some observables. This subsection describes the mathematical calculation of some observables related to the $\hat{\boldsymbol{M}}_R$ matrix.

The total retardance *R* (the combination of linear and circular retardance) can be directly calculated from the trace of $\hat{\boldsymbol{M}}_R$ as follows [45,46]:

$$R = \cos^{-1}\left[\frac{tr(\hat{\boldsymbol{M}}_R)}{2} - 1\right] \tag{2.23}$$

The normalized total retardance matrix $\hat{\boldsymbol{M}}_R$ can be decomposed as the product of a linear retarder and a circular retarder (an optical rotator) [46,207].

$$\hat{\boldsymbol{M}}_R = \hat{\boldsymbol{M}}_{LR}\cdot\hat{\boldsymbol{M}}_{CR} \tag{2.24}$$

The linear retarder is characterized by the linear retardance δ (i.e. the phase difference between the fast axis and slow axis) and the orientation angle of the fast axis with respect to the horizontal θ, and its explicit expression is,

$$\hat{\mathbf{M}}_{\mathbf{LR}} = \begin{pmatrix} 1 & 0 & 0 & 0 \\ 0 & \cos^2(2\theta) + \sin^2(2\theta)\cos\ \delta & \sin(2\theta)\cos(2\theta)(1 - \cos\delta) & -\sin(2\theta)\sin\delta \\ 0 & \sin(2\theta)\cos(2\theta)(1 - \cos\delta) & \sin^2(2\theta) + \cos^2(2\theta)\cos\ \delta & \cos(2\theta)\sin\delta \\ 0 & \sin(2\theta)\sin\ \delta & \cos(2\theta)\sin\ \delta & \cos\delta \end{pmatrix} \tag{2.25}$$

and the circular retarder (optical rotator) is defined by the optical rotation φ.

$$\hat{\mathbf{M}}_{\mathbf{CR}} = \begin{pmatrix} 1 & 0 & 0 & 0 \\ 0 & \cos(2\varphi) & \sin(2\varphi) & 0 \\ 0 & -\sin(2\varphi) & \cos(2\varphi) & 0 \\ 0 & 0 & 0 & 1 \end{pmatrix} \tag{2.26}$$

Note that the multiplication of linear and circular retarders is not commutative. However, some expressions, as the following provided to calculate the optical rotation (φ) and the linear retardance (δ), are valid for both commutations ($\hat{\boldsymbol{M}}_{LR}\hat{\boldsymbol{M}}_{CR}$ and $\hat{\boldsymbol{M}}_{CR}\hat{\boldsymbol{M}}_{LR}$)[74]:

$$\varphi = tan^{-1}\left(\frac{M_{R\ 2,1}\ - M_{R\ 1,2}}{M_{R\ 1,1}\ + M_{R\ 2,2}}\right) \tag{2.27}$$

$$\delta = cos^{-1}\left(\sqrt{\left[M_{R\ 1,1}\ + M_{R\ 2,2}\ \right]^2 + \left[M_{R\ 2,1}\ - M_{R\ 1,2}\ \right]^2} - 1\right) \tag{2.28}$$

where the values between {} indicate the corresponding matrix element index.

Once the optical rotation φ is obtained, the normalized matrix of the linear retarder $\hat{\boldsymbol{M}}_{LR}$ can be calculated by inverse multiplying $\hat{\boldsymbol{M}}_{CR}$ with $\hat{\boldsymbol{M}}_{R}$. In general, the multiplication order of the matrices strongly modifies the values of $\hat{\boldsymbol{M}}_{LR}$. Therefore, both scenarios should be considered when φ≠0. In such case, the angle θ resulting from both scenarios should be compared. The angle θ can be obtained from the $\hat{\boldsymbol{M}}_{LR}$ matrix as follows [74]:

$$\theta = 0.5\tan^{-1}(r_2 / r_1) \tag{2.29}$$

where

$$r_i = (1/2\sin\delta)\sum_{j,k=1}^{3}\varepsilon_{jk}M_{\boldsymbol{LR}\{j,k\}} \tag{2.30}$$

and ε_{jk} is the Levi-Cita permutation symbol.

2.2.3 Depolarization coefficient

Unlike the retarder case, the magnitude associated with the Lu-Chipman depolarizer is limited to one coefficient so-called depolarization power Δ [66]. The coefficient indicates the average depolarizing capability of ***M*** and is given by

$$\Delta = 1 - \frac{\left|tr(\boldsymbol{m}_{\Delta})\right|}{3} \tag{2.31}$$

In the case of physically realizable matrices, the depolarization power is constrained by the $0 \le \Delta \le 1$ inequation.

Notice that the construction of Lu-Chipman $\hat{\boldsymbol{M}}_{\Delta}$ (Eq. (2.13)) is quite different from the matrix of a normalized pure depolarizer (Eq. (2.11)). First, the $\boldsymbol{m}_{\boldsymbol{\Delta}}$ of a pure depolarizer is a diagonal matrix defined by three independent parameters ($diag(\hat{d}_1, \hat{d}_2, \hat{d}_3)$) [44–46], while, in general, the Lu-Chipman $\boldsymbol{m}_{\boldsymbol{\Delta}}$ is not diagonal due to the structure of the decomposition (described in Eq. (2.6)). In fact, the $\boldsymbol{m}_{\boldsymbol{\Delta}}$ of the Lu-Chipman decomposition can be interpreted as a pure

depolarizer that is usually rotated to compensate for the presence of the retarder placed at only one side of the depolarizer [45]. Second, the Lu-Chipman $\hat{\boldsymbol{M}}_{\Delta}$ presents some dichroic content through the polarizance vector $\boldsymbol{P_{\Delta}}$ that is an artifact introduced to mathematically fit the structure of the decomposition (Eq. (2.6)). Note that these two issues are directly related to the structure of the decomposition. This structure can be reversed (leading to the *reverse product decomposition* [208]) transforming the $\boldsymbol{P_{\Delta}}$ problem into a diattenuator vector $\boldsymbol{D_{\Delta}}$ issue [208]. Subsequently, alternative decompositions and mathematical treatments that further describe the depolarizing content associated with a given $\boldsymbol{M}$ are following described.

2.3 Parameters of polarimetric purity

In this section, we describe a group of parameters that proposes an alternative approach to the depolarization phenomena to the given with the Lu-Chipman decomposition. Some of the following parameters provide analogous information to the obtained with the Lu-Chipman decomposition but with an easer mathematical treatment (they are directly calculated from the Mueller matrix parameters [45]). The other parameters are based on a completely different decomposition in which $\boldsymbol{M}$ is associated with the parallel combination of different non-depolarizing Mueller matrices [45,70]. Although the *a-priori* different approximations, the following introduced parameters are related to each other in some way and all are connected with the depolarization induced by samples.

2.3.1 Depolarization index

In 1986, ten years before the publication of the Lu-Chipman decomposition, J. J. Gil and E. Bernabeu defined the depolarization index, P_{Δ} [69] (also called the degree of polarimetric purity [209]). The depolarization index, P_{Δ}, is a global measure of the depolarization behavior of a given $\boldsymbol{M}$, like Δ, but taking the advantage of being directly calculated from the Mueller matrix parameters [69]:

$$P_{\Delta} \equiv \sqrt{\frac{(\sum_{i,j=0}^{3} m_{ij}^2) - m_{00}^2}{3m_{00}^2}}, \tag{2.32}$$

where the subindex *ij* indicates the corresponding matrix element index of $\boldsymbol{M}$ (Eq. (2.5)).

The expression of P_{Δ} (Eq. (2.32)) can be described as a generalization of the *DOP* metric to Mueller matrices. In this vein, instead of characterizing the depolarization content of light beams, the depolarization index characterizes the depolarization behavior of samples [45]. The analysis of P_{Δ} reveals that the maximum value of P_{Δ} is 1, characterizing non-depolarizing matrices, and the minimum value is 0, associated with fully depolarizing systems. Intermediate values quantify the overall random process behind the depolarizing mechanisms. This parameter is limited to the measurement of the overall depolarization and it cannot distinguish if some SoP is more or less depolarized than others. In other words, if the sample presents some anisotropy in the depolarization process.

2.3.2 Indices of Polarimetric Purity (IPP)

With this question in mind, in 2011, I. San José and J. J. Gil proposed three new parameters to describe the depolarizing content of Mueller matrices, the so-called Indices of Polarimetric Purity (IPP) [1]. IPP faces the depolarization phenomenon considering that depolarization arises from the incoherent sum of non-depolarizing sources. This consideration was previously suggested by S. R. Cloude [70], which described generally realizable Mueller matrices as an incoherent combination of four or fewer non-depolarizing matrices with different weights. S. R. Cloude called it spectral decomposition, in reference to the spectral theorem of linear algebra, and it is given by

$$\mathbf{M} = \sum_{i=1}^{4} \lambda_i \mathbf{M}_i, \tag{2.33}$$

where $\boldsymbol{M_i}$ are the non-depolarizing matrices, λ_i are the eigenvalues of the covariance matrix $\boldsymbol{H(M)}$[45,70]. Covariance matrix $\boldsymbol{H(M)}$ is a Hermitian positive semi-definite matrix that arises from a transformation of the Mueller matrix, and it is used because Mueller matrices are not Hermitian, so it cannot be ensured that they are diagonalizable, and thus, the spectral theorem is no directly applicable on them. In particular, the covariance matrix $\boldsymbol{H(M)}$ is given by [45,70]

$$\mathbf{H}(\mathbf{M}) \equiv \frac{1}{4} \sum_{i,j=0}^{3} m_{ij} (\sigma_i \otimes \sigma_j), \tag{2.34}$$

where σ represents the Pauli matrices and $\otimes$ the Kronecker product. Note that i goes from 1 to 4 because any incoherent combination of Mueller matrices can be rewritten in terms of a combination of four, or less, non-depolarizing Mueller matrices with different weights (λ_i) [70].

Once the eigenvalues of the covariance matrix are calculated, IPP are defined as follows [1,64]:

$$P_i \equiv \frac{1}{m_{00}} \sum_{k=1}^{i} k(\lambda_{k-1} - \lambda_k) \tag{2.35}$$

where i=1,2 and 3.

In the experimental scenario the measured $\boldsymbol{M}$ must be physically realizable thus its associated λ_i must be positive [210] and they must also satisfy the two following equations:

$$0 \le \hat{\lambda}_4 \le \hat{\lambda}_3 \le \hat{\lambda}_2 \le \hat{\lambda}_1 \le 1, \tag{2.36}$$

$$\sum_{i=1}^{4} \hat{\lambda}_i = 1. \tag{2.37}$$

where $\hat{\lambda}_i$ are the eigenvalues normalized by m_{00}, $\hat{\lambda}_i = \frac{\lambda_i}{m_{00}}$.

Consequently, IPP are restricted by

$$0 \le P_1 \le P_2 \le P_3 \le 1. \tag{2.38}$$

The combination of Eqs. (2.36) and (2.37) implies that the normalized $\hat{\lambda}_1$ is the only eigenvalue that can reach the value 1. Conversely, all the IPP can be equal to one and they can be equal to one simultaneously. In fact, non-depolarizing samples are associated with $P_1 = P_2 = P_3 = 1$. The opposite scenario $P_1 = P_2 = P_3 = 0$ corresponds to ideal depolarizers, $\boldsymbol{M}_{\Delta 0} = diag(m_{00}, 0, 0, 0)$.

Since IPP can be built with the covariance matrix eigenvalues, they can be interpreted in terms of the spectral decomposition of ***M***. In that sense, IPP reports the relative amounts of non-depolarizing equivalent components that a system can be assimilated with. Nevertheless, they can also be interpreted from the point of view of another decomposition, the so-called *trivial decomposition* of ***M*** [209,211],

$$\boldsymbol{M} = m_{00}[P_1 \cdot \boldsymbol{M}(\hat{\boldsymbol{H}}_1) + (P_2 - P_1) \cdot \boldsymbol{M}(\hat{\boldsymbol{H}}_2) + (P_3 - P_2) \cdot \boldsymbol{M}(\hat{\boldsymbol{H}}_3) + (1 - P_3) \cdot \boldsymbol{M}(\hat{\boldsymbol{H}}_4)] \quad (2.39)$$

where

$$\hat{\boldsymbol{H}}_k = \frac{1}{k} \sum_{i=1}^{k} (u_i \otimes u_i^{\dagger}), \quad (2.40)$$

are defined from the eigenvectors u_i associated with the eigenvalue λ_i of ***H(M)***. In that expression, *k* is equal to 1, 2, 3, or 4, and the elements of the Mueller matrix ***M*** are related to ***H*** by

$$m_{ij} = tr[(\sigma_i \otimes \sigma_j)\mathbf{H}]. \quad (2.41)$$

In the *trivial decomposition*, P_1 indicates the weight of $\boldsymbol{M}(\hat{\boldsymbol{H}}_1)$ (the only non-depolarizing matrix of Eq. (2.39)), and P_3 is directly connected with the weight of $\boldsymbol{M}(\hat{\boldsymbol{H}}_4)$ which is an ideal depolarizer ($\boldsymbol{M}(\hat{\boldsymbol{H}}_4) = diag(d_0, 0, 0, 0)$). Accordingly, P_1 indicates the amount of a non-depolarizing element that the media can be assimilated with and P_3 the amount of an ideal depolarizer that can be associated with ***M***. Otherwise, P_2 has a more difficult interpretation as it is related to the weight of the so-called 2D and 3D depolarizers [212], $\boldsymbol{M}(\hat{\boldsymbol{H}}_2)$ and $\boldsymbol{M}(\hat{\boldsymbol{H}}_3)$ respectively.

The last analysis of IPP, through the trivial decomposition, points out that IPP quantify the depolarization behavior of ***M*** but in a more detailed way than P_Δ and Δ. In fact, P_Δ can be written as a combination of IPP [1] thus resulting in that P_Δ is a general approximation of the IPP.

In order to link P_Δ with IPP, we first rewrite P_Δ as a function of λ_i by using a variety of trace properties. On the one hand, the application of the trace properties to Eq. (2.41) leads to:

$$\begin{aligned} &\sum_{i,j=0}^{3} m_{ij}^2 = \sum_{i,j=0}^{3} tr[(\sigma_i \otimes \sigma_j)\mathbf{H}]^2 = \sum_{i,j=0}^{3} tr[(\sigma_i{}^2 \otimes \sigma_j{}^2)\mathbf{H}^2] = \\ &= \sum_{i=0}^{3} tr[\overbrace{(\sigma_0 \otimes \sigma_0)}^{\mathbb{I}_{4x4}}\mathbf{H}^2] = 4tr(\mathbf{H}^2) = 4\sum_{i=0}^{3} \lambda_i{}^2 \end{aligned} \quad (2.42)$$

And, on the other hand, the trace of ***H*** (defined in Eq. (2.34)) helps to link m_{00} with λ_i.

$$tr(\mathbf{H}) = m_{00} = \sum_{i=0}^{3} \lambda_i , \tag{2.43}$$

Next, the combination of Eqs. (2.42) and (2.43) with Eq. (2.32) results in:

$$P_{\Delta} = \sqrt{\frac{4(\sum_{i=0}^{3} \lambda_i^{\,2}) - (\sum_{i=0}^{3} \lambda_i)^2}{3m_{00}^2}} \tag{2.44}$$

And finally, the eigenvalues can be substituted by the corresponding expressions of IPP (Eq. (2.35)) giving:

$$P_{\Delta} = \sqrt{\frac{2}{3}P_1^2 + \frac{2}{9}P_2^{\,2} + \frac{1}{9}P_3^{\,2}} \tag{2.45}$$

This expression shows that different combinations of IPP could lead to the same P_{Δ}. It can be explained because, unlike P_{Δ} and Δ, that give an overall measure, IPP can distinguish between different depolarizing mechanisms. In other words, it is sensitive to different polarimetric anisotropies. Such phenomenon will be experimentally analyzed in Chapter 4 and it will be exploited for biophotonic applications in Chapter 5. For the sake of visualization, Figure 2-2 represent the possible IPP combinations associated with a given P_{Δ} in the so-called Purity Space [1,213]. The Purity Space is defined as a 3D space in which each IPP parameter is associated with an axis and in which any physically realizable depolarizer can be represented. Importantly, due to the restriction given by Eq. (2.38), all realizable depolarizers are restricted into a tetrahedron at the Purity Space.

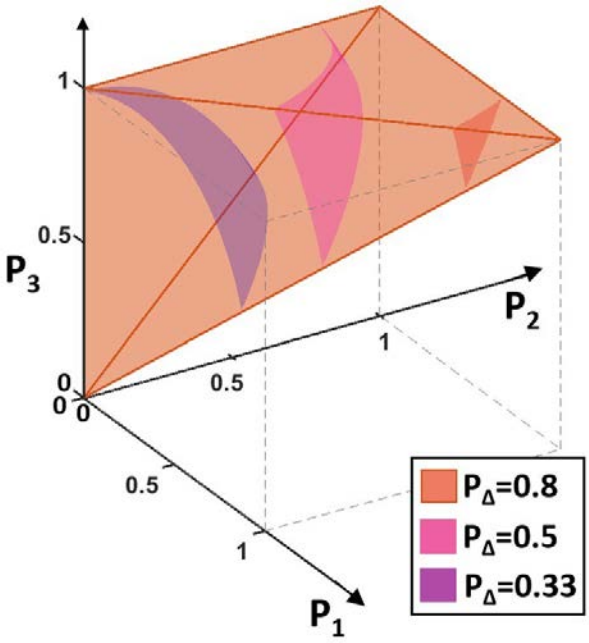

Figure 2-2. Representation of different P_{Δ} values in the Purity space. Each P_{Δ} value is associated with different colored surfaces.

In the graphical representation of the Purity Space, Figure 2-2, physically realizable Mueller matrices are represented by points and constant P_Δ values are represented by elliptical surfaces. The closer to (0,0,0) the points are, the higher is the depolarization capacity of the associated ***M***. Concerning the P_Δ surfaces, they are parameterized by the Eq. (2.45) and limited by the Purity space constraints of Eq. (2.38). Moreover, the area of the surface is minimal for P_Δ=0 and P_Δ=1, and it increases as P_Δ approaches to the value of 1/3. That value corresponds to the largest surface area. Therefore, the potential to discriminate between different depolarizer schemes of IPP vs P_Δ is maximum in the $P_\Delta \sim 1/3$ regime.

Analogously to IPP, the set of $\hat{\lambda}_i$ can also describe a space in which depolarizers, as well as P_Δ values, can be represented. Since the set of $\hat{\lambda}_i$ is made up of four parameters, the associated space should present four dimensions. However, $\hat{\lambda}_i$ associated with physically realizable Mueller matrices are limited by Eqs. (2.36) and (2.37) so each normalized eigenvalue can be written as a combination of the other three. Therefore, the degrees of freedom are reduced from four to three, and physically realizable ***M*** can be represented in a 3D space composed by using three of the four normalized eigenvalues. In that way, R. Ossikovski and J. Vizet [64] proposed the use of $\hat{\lambda}_2$, $\hat{\lambda}_3$ and $\hat{\lambda}_4$ to define the so-called *Natural depolarization space* (see Figure 2-3). The *Natural depolarization space* represented in Figure 2-3 is shaped as a tetrahedron like the Purity space. In the Natural depolarization space, like in the Purity space, depolarizers are represented by points and constant P_Δ values are represented by elliptical surfaces. Also similar to the Purity space, depolarizers with higher depolarizing capacity are near to 0 and the area of the surface increases as P_Δ is near to the 1/3 value. The main difference between the Natural space and the Purity space is related to the volume of the space, the volume of the Purity space is bigger than the Natural space volume. This is translated into a larger separation between the points that represents a group of depolarizers in the Purity space concerning the points that represents the same group of depolarizers in the Natural space.

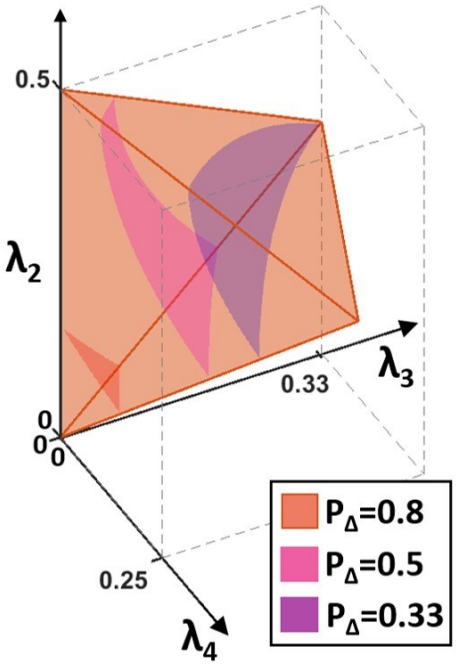

Figure 2-3. Representation of different P_Δ values in the Natural depolarization space. Each P_Δ value is associated with different colored surfaces.

2.3.3 Components of Purity (CP)

During the same year 2011, J. J. Gil decomposed P_Δ into other three new components, apart from the IPP ones, so-called Components of Purity (CP) [61]. As previously said, depolarization can be considered that arises from the incoherent combination of non-depolarizing sources. In turn, the CP focus its analysis on determining the nature of these non-depolarizing sources, i.e. the dichroic or birefringent character of the non-depolarizing sources associated with the depolarization process. As a result, two of the three parameters are the diattenuation *D* and the polarizance *P* [205,206]. According to the *D* and *P* descriptions (Eq. (2.5)), P_Δ can be written as:

$$P_\Delta = \sqrt{\frac{1}{3}P^2 + \frac{1}{3}D^2 + P_s^2} \tag{2.46}$$

where P_s is the third CP defined as [61]

$$P_s = \sqrt{\frac{\sum_{i,j=1}^{3} m_{ij}^2}{3m_{00}^2}} \tag{2.47}$$

P_s is so-called the *degree of spherical purity* [61] and it is connected with the birefringent sources behind the depolarization process. *P*, *D,* and P_s can take values from 0 to 1, but, conversely to the IPP, the three components associated with a given ***M*** can never be equal to one simultaneously. According to Eq. (2.46), the hypothetical case $P=D=P_s=1$ would overcome the condition of P_Δ to take values in the range [0,1]. The same equation (Eq. (2.46)) reveals that different CP values can lead to the same P_Δ value, similarly to the case of the IPP.

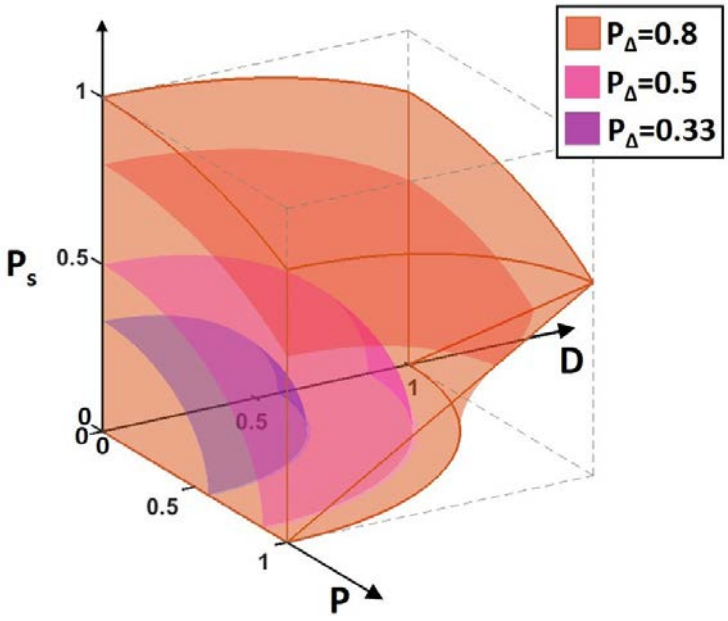

Figure 2-4. Representation of different P_Δ values in the Components of Purity space. Each P_Δ value is associated to differently colored surfaces.

For the sake of visualization and analogous to the case of IPP, the CP are represented in a 3D space associating each parameter with an axis (see Figure 2-4). It is worth noticing that a 2D

planar representation of the CP space, using the P_s and P_p (P_p is a combination of P and D, $P_p = \sqrt{(P^2 + D^2)/2}$, so-called *degree of polarizance* [61,214]) as the axis of the space, was studied in ref. [61,214]. Concerning the 3D representation displayed in Figure 2-4, depolarizers would be represented by points. The position of these points is related to the dichroic and birefringent nature of the elements involved in the depolarizing process. Note that depolarizers characterized by different dichroic and birefringent elements (different point positions of the CP space) can describe the same P_Δ value. As a result, all the possible combinations of elements that result in the same P_Δ are represented with surfaces in the CP space, this highlighting the potential of CP to discriminate between different depolarizers' physical origins. In Figure 2-4, the P_Δ=0.8, P_Δ=0.5, and the P_Δ=0.33 values are represented in the CP space to illustrate such situation. P_Δ surfaces are ellipsoids defined by Eq. (2.46) and they are limited by the following constriction, linked with the [0,1] range of P_Δ:

$$P^2 + D^2 \leq 1 + 3P_s^2 \tag{2.48}$$

We can see that, in contrast with the purity space, the area of a given P_Δ surface when it is represented in the CP space is larger as the value of P_Δ is higher. As a result, the potential of CP is higher for low depolarizing media i.e. P_Δ close to 1. This has sense because, the nearer the sample is to a pure depolarizer, the larger the loss of information (i.e., larger entropy) related to physical structures in the sample.

2.3.4 Depolarization indices of higher-order

Recently, in 2019, R. Ossikovski and J. Vizet proposed a generalization of the depolarization index defined as [64]:

$$P_\Delta^{(m)} = \sqrt{\frac{1}{4^{m-1}-1}\left[4^{m-1}\frac{tr(\boldsymbol{H}^m)}{tr(\boldsymbol{H})^m} - 1\right]} = \sqrt{\frac{1}{4^{m-1}-1}\left[4^{m-1}\sum_{i=1}^{4}\hat{\lambda}_i^m - 1\right]} \tag{2.49}$$

with m being natural numbers higher than 2. Note that the second-order index, $P_\Delta^{(2)}$, corresponds to the depolarization index, P_Δ, described in the sub-section 2.3.1. According to Eq. (2.36), the depolarization indices of higher-order associated with a physically realizable ***M*** are constrained by the following inequation.

$$0 \leq \ldots \leq P_\Delta^{(m)} \leq P_\Delta^{(4)} \leq P_\Delta^{(3)} \leq P_\Delta \leq 1 \tag{2.50}$$

In the regime of high-order depolarization indices, all the parameters can reach the value 1 simultaneously. Non-depolarizing systems are characterized by all the parameters reaching this value ($P_\Delta^{(m)} = 1$ for any value possible value m) and, by contrast, ideal depolarizers are assimilated with $P_\Delta^{(m)} = 0$ for any possible value of m. Notice that depolarization indices of higher order can be directly calculated from the covariance matrix ((2.49)), and this ***H*** matrix is a linear combination of the ***M*** elements. Therefore, its computational time is much lower than the Lu-Chipman decomposition, and it is also lower than the calculus of the covariance matrix eigenvalues.

Analogous with the IPP and CP case, a group of three $P_\Delta^{(m)}$ can be represented in a 3D space. R. Ossikovski and J. Vizet proposed the representation of the $P_\Delta^{(m)}$ parameters with the lowest

m values (i.e. $P_{\Delta}^{(m)}$ with m= 2, 3, and 4) [64]. Such space is represented in Figure 2-5. This space presents a much lower volume than the previously discussed spaces, being close to a flat space. The main interest of this space rests in its computational time that results lower than the parameters based on Mueller matrix decomposition, and also in the fact that $P_{\Delta}^{(m)}$ are a non-linear combination of λ_i and this may lead to better results in some applications.

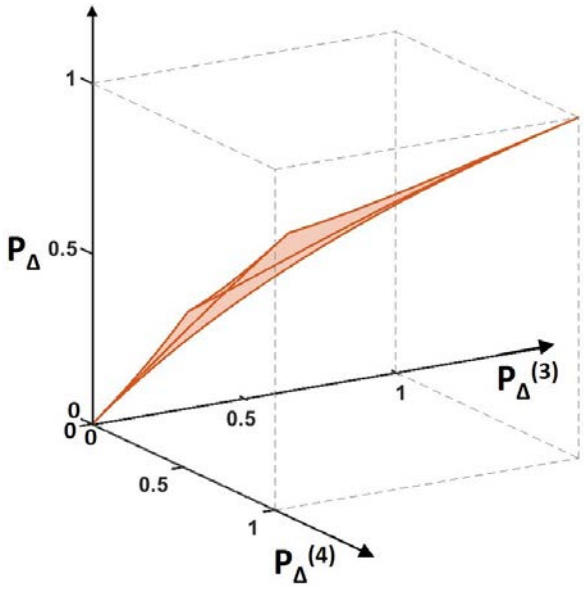

Figure 2-5. Representation of the High-order Depolarization Indices space.

2.4 Symmetric product decomposition

Up to now, we have introduced a product decomposition (Lu-Chipman decomposition) with certain limitations in the analysis of the depolarization properties of samples, and a group of alternative observables that further synthetize these depolarization properties. In this section, we will describe another product decomposition that tries to separate the depolarization content of ***M*** in a pure depolarizer matrix $\boldsymbol{M_{\Delta}}$. In the previous sub-section 2.2.3, we have seen that the structure of the depolarizer obtained from the Lu-Chipman decomposition is affected by the order of the factors in which the matrix is decomposed [208]. Such order forces to include a non-null polarizance vector in the depolarizer matrix $\boldsymbol{M_{\Delta}}$ and that vector should not appear in a matrix that is supposed to only depolarize light. Under this scenario, arises the idea of the symmetric product decomposition [72], in which the order of the elements does not depend on the sense in which we look at it and which does not need the addition of any mathematical artifact.

2.4.1 Symmetric product decomposition

The symmetric product decomposition was proposed by R. Ossikovski in 2009 [72]. It consists of decomposing the Mueller matrix into a concatenation of five matrices each characterized by only one of the three basic polarimetric properties (i.e., dichroism, birefringence, and depolarization),

$$\boldsymbol{M} = \boldsymbol{M}_{D2}\hat{\boldsymbol{M}}_{R2}\boldsymbol{M}_{\Delta d}\hat{\boldsymbol{M}}_{R1}\boldsymbol{M}_{D1} \tag{2.51}$$

where $\boldsymbol{M_{D1}}$ and $\boldsymbol{M_{D2}}$ are the matrices of two diattenuators $\hat{\boldsymbol{M}}_{R1}$ and $\hat{\boldsymbol{M}}_{R2}$ are the normalized matrices of two retarders, and $\boldsymbol{M_{\Delta d}}$ is the matrix of a pure depolarizer. Unlike the Lu-Chipman decomposition, the depolarizer is defined as a diagonal matrix without the presence of diattenuation or polarization, $\boldsymbol{M}_{\Delta d} = d_0 \cdot diag(1, \hat{d}_1, \hat{d}_2, \hat{d}_3)$. This is possible due to the symmetry of the decomposition and the central position of the depolarizer. However, not all the physically realizable matrices can be decomposed by considering $\boldsymbol{M}_{\Delta d} = d_0 \cdot diag(1, \hat{d}_1, \hat{d}_2, \hat{d}_3)$. The ones that can be decomposed using this structure are called Type I Mueller matrices [45,72]. The other physically realizable matrices that cannot be decomposed by doing this consideration are called Type II Mueller matrices and they require an alternative mathematical treatment that is described in ref. [45]. Since none of the biological measurements discussed in this thesis is a Type II Mueller matrix, the symmetric decomposition associated with Type II Mueller matrices will not be described in this thesis. Biological tissues used to be Type I Mueller samples.

The matrices of the diattenuators $\boldsymbol{M_{Di}}$, i=(1,2), are defined as

$$\boldsymbol{M}_{Di} = T_{ui} \begin{pmatrix} 1 & \boldsymbol{D}_i^T \\ \boldsymbol{D}_i & \boldsymbol{m}_{Di} \end{pmatrix} \tag{2.52}$$

with

$$T_{ui} = \frac{1}{\sqrt{1 - D_i^2}} \tag{2.53}$$

and with m_D defined in Eq. (2.8).

The use of the factor T_{ui} allows to obtain a very compact expression for the inverse of $\boldsymbol{M_{Di}}$:

$$\boldsymbol{M}_{Di}^{-1} = \boldsymbol{G}\boldsymbol{M}_{Di}\boldsymbol{G} \tag{2.54}$$

where $\boldsymbol{G}$ is well-known as the Minkowski metric, $\boldsymbol{G} = diag(1, -1, -1, -1)$. Note that Eq. (2.54) is only valid for D_i<1, which is true for most of Type I physically realizable $\boldsymbol{M}$. The other particular cases in which D_i=1 are characterized by $\boldsymbol{N}$=**0**, $\boldsymbol{N'}$=**0** or $\boldsymbol{N}$=$\boldsymbol{N'}$=**0**, with

$$\boldsymbol{N} \equiv \boldsymbol{G}\boldsymbol{M}^T\boldsymbol{G}\boldsymbol{M} \tag{2.55}$$

and

$$\boldsymbol{N}' \equiv \boldsymbol{G}\boldsymbol{M}\boldsymbol{G}\boldsymbol{M}^T \tag{2.56}$$

will be next discussed in sub-sections 2.4.1.1, 2.4.1.2, and 2.4.1.3.

Now, taking the definition of the symmetric decomposition, Eq. (2.51), we can multiply both sides of the expression by the inverse of $\boldsymbol{M_{D1}}$ to obtain

$$\boldsymbol{M}\boldsymbol{M}_{D1}^{-1} = \boldsymbol{M}\boldsymbol{G}\boldsymbol{M}_{D1}\boldsymbol{G} = \boldsymbol{M}_{D2}\boldsymbol{M}_{R2}\boldsymbol{M}_{\Delta d}\boldsymbol{M}_{R1} = \boldsymbol{M}_{D2}\boldsymbol{M}' \tag{2.57}$$

Since the depolarizer is defined diagonal and $\boldsymbol{M}_{R1}$ and $\boldsymbol{M}_{R2}$ are pure retarders, $\boldsymbol{M'}$ is structured with null diattenuation and polarizance vectors as

$$\boldsymbol{M}' = \boldsymbol{M}_{R2}\boldsymbol{M}_{\Delta d}\boldsymbol{M}_{R1} = \begin{pmatrix} d_0 & \boldsymbol{0}^T \\ \boldsymbol{0} & \boldsymbol{m'} \end{pmatrix}. \tag{2.58}$$

Thanks to the null polarizance vector of ***M'***, the first column of both sides of Eq. (2.57) is matched as

$$(\boldsymbol{MG})T_{u1}\boldsymbol{S}_1 = d_0 T_{u2}\boldsymbol{S}_2 \text{, with } \boldsymbol{S}_i = \begin{pmatrix} 1 \\ \boldsymbol{D}_i \end{pmatrix}. \tag{2.59}$$

Performing the same procedure but starting from $\boldsymbol{M}^T\boldsymbol{M}_{D2}^{-1}$ we end to an analogous expression.

$$(\boldsymbol{M}^T\boldsymbol{G})T_{u2}\boldsymbol{S}_2 = d_0 T_{u1}\boldsymbol{S}_1 \tag{2.60}$$

Now, combining Eqs. (2.59) and (2.60) the system can be decoupled to isolate $\boldsymbol{S}_1$ and $\boldsymbol{S}_2$ as two solutions of a problem with two eigenvectors associated with the same d_0^2 eigenvalue [72].

$$(\boldsymbol{M}^T\boldsymbol{GMG})\boldsymbol{S}_1 = d_0^2\boldsymbol{S}_1 \tag{2.61}$$

$$(\boldsymbol{GM}^T\boldsymbol{GM})\boldsymbol{S}_2 = d_0^2\boldsymbol{S}_2 \tag{2.62}$$

From the $\boldsymbol{S}_1$ and $\boldsymbol{S}_2$ solutions, we directly determine $\boldsymbol{D}_1$ and $\boldsymbol{D}_2$ which allow the calculus of the inverses of $\boldsymbol{M}_{D1}$ and $\boldsymbol{M}_{D2}$ by using the Eq. (2.9), like in the Lu-Chipman product decomposition. At that moment, if D_1=D_2=1 (D_i=$|\boldsymbol{D}_i|$), ***M*** is a Type II Mueller matrix, we should apply the alternative symmetric decomposition described in ref. [45]. Next, we calculate $\boldsymbol{M}' = \boldsymbol{M}_{D2}^{-1}\boldsymbol{M}\boldsymbol{M}_{D1}^{-1}$ to end the decomposition with the separation of ***m'*** utilizing the singular value decomposition SVD [72].

$$\boldsymbol{m}' = \boldsymbol{m}_{R2}\boldsymbol{m}_{\Delta d}\boldsymbol{m}_{R1} \tag{2.63}$$

where $\boldsymbol{m}_{\Delta d} = d_0 \cdot diag(\hat{d}_1, \hat{d}_2, \hat{d}_3)$ and d_0 is equal to the irradiance of the matrix ***M'*** ($d_0 = m'_{00}$). As a result,

$$\hat{\boldsymbol{M}}_{\boldsymbol{R}2} = \begin{pmatrix} 1 & \boldsymbol{0}^{\boldsymbol{T}} \\ \boldsymbol{0} & \boldsymbol{m}_{R2} \end{pmatrix},\ \boldsymbol{M}_{\Delta d} = \begin{pmatrix} d_0 & \boldsymbol{0}^{\boldsymbol{T}} \\ \boldsymbol{0} & \boldsymbol{m}_{\Delta d} \end{pmatrix},\ \hat{\boldsymbol{M}}_{\boldsymbol{R}1} = \begin{pmatrix} 1 & \boldsymbol{0}^{\boldsymbol{T}} \\ \boldsymbol{0} & \boldsymbol{m}_{R1} \end{pmatrix} \tag{2.64}$$

Now the determinant of ***M*** is calculated, and if it is smaller than *0* (det ***M*** *<0*), $\boldsymbol{M}_{\Delta d}$ and $\hat{\boldsymbol{M}}_{\boldsymbol{R}1}$ is multiplied by *diag(1,1,1,-1)* [204].

Finally, the use of the SVD creates an ambiguity with the calculus of $\boldsymbol{M}_{\Delta d}$ because any permutation of the singular values, together with the corresponding permutations of $\hat{\boldsymbol{M}}_{\boldsymbol{R}2}$ columns and $\hat{\boldsymbol{M}}_{\boldsymbol{R}1}$ rows, would give different physical solutions that, combined, result in the same ***M***. To avoid this ambiguity R. Ossikovski proposes the “minimum retardance principle” [72]. This principle consists of choosing the eigenvalue combinations associated with the $\hat{\boldsymbol{M}}_{\boldsymbol{R}1}$ with minimum retardance, i.e. the trace of $\hat{\boldsymbol{M}}_{\boldsymbol{R}1}$ is minimal (see Eq. (2.23)).

Up to now, we have described the most general scenario of Type I Mueller matrices. Following we will discuss the particular cases of Type I Mueller matrices with ***N*** and/or ***N'*** equal to ***0***.

2.4.1.1 N≠0 and N'=0

In this scenario, D_1=1 and D_2<1, thus ***M*** is a Type I Mueller matrix that corresponds to a depolarizing analyzer [72]. Accordingly, ***M*** can be written as

$$M = M_{D2} M_{\Delta 0} M_{D1} \tag{2.65}$$

where $\boldsymbol{M}_{D1}$ is a pure polarizer characterized by the diattenuation vector of ***M***, $M_{\Delta 0}$ is an ideal depolarizer, i.e. $M_{\Delta 0} = diag(d_0, 0, 0, 0)$, and $\boldsymbol{M}_{D2}$ is a diattenuator that can be derived from Eq. (2.62).

2.4.1.2 N=0 and N'≠0

Analogously to the previous case, D_1<1 and D_2=1, so that ***M*** is a Type I Mueller matrix that corresponds to a depolarizing polarizer [72]. Accordingly, the matrix can be written as Eq. (2.65) but in this case, $\boldsymbol{M}_{D2}$ is a pure polarizer characterized by the diattenuation vector of ***M*** and $\boldsymbol{M}_{D1}$ is a diattenuator that can be derived from Eq. (2.61).

2.4.1.3 N=0 and N'=0

In this case, D_1=D_2=1, so we are dealing with a pure polarizer that does not require any decomposition to be analyzed.

2.4.2 Relation between the retarders of the Symmetric and the Lu-Chipman decompositions

Apparently, the Symmetric decomposition and the Lu-Chipman decomposition are two completely different decompositions. However, we can deduce a relationship between them that involves the retarders.

Both decompositions define ***m***', the submatrix of ***M'***, as a matrix without dichroic content and containing only the birefringent and the depolarization information of ***M***. Consequently, the submatrix ***m'*** of both decompositions should be the same. Nevertheless, most of the time they are not the same because the ***M'*** of the Lu-Chipman decomposition has some residual dichroic content connected with $\boldsymbol{P}_{\Delta}$. Concerning the experiments with biological tissues performed in this thesis, the two ***m'*** obtained from a given experimental measure are very similar because the influence of $\boldsymbol{P}_{\Delta}$ is minimal. Therefore, we can approximate that both ***m'*** are the same. Under this approximation and taking the definition of **m'** in both decompositions (Eqs. (2.63) and (2.16)), we induce that

$$\boldsymbol{m}_{\Delta}\boldsymbol{m}_{R} = \boldsymbol{m}_{R2}\boldsymbol{m}_{\Delta d}\boldsymbol{m}_{R1} \Leftrightarrow \boldsymbol{m}_{\Delta} = \boldsymbol{m}_{R2}\boldsymbol{m}_{\Delta d}\boldsymbol{m}_{R1}\boldsymbol{m}_{R}^{-1} \tag{2.66}$$

Due to $\boldsymbol{m}_{\Delta}$ and $\boldsymbol{m}_{\Delta d}$ are symmetric matrices ($m_{\Delta} = m_{\Delta}^{T}$) and that the inverse matrix of retarders is equal to the transpose matrix, $\boldsymbol{m}_{R}^{-1} = \boldsymbol{m}_{R}^{T}$ (orthogonal matrices), we derive that

$$\boldsymbol{m}_{\Delta}^{2} = \boldsymbol{m}_{\Delta}(\boldsymbol{m}_{\Delta})^{T} = \boldsymbol{m}_{R2}\boldsymbol{m}_{\Delta d}\boldsymbol{m}_{R1}\boldsymbol{m}_{R}^{T}(\boldsymbol{m}_{R2}\boldsymbol{m}_{\Delta d}\boldsymbol{m}_{R1}\boldsymbol{m}_{R}^{T})^{T} =$$

$$= \boldsymbol{m}_{R2}\boldsymbol{m}_{\Delta d}\boldsymbol{m}_{R1}\boldsymbol{m}_{R}^{T}\boldsymbol{m}_{R}\boldsymbol{m}_{R1}^{T}\boldsymbol{m}_{\Delta d}^{T}\boldsymbol{m}_{R2}^{T} = \boldsymbol{m}_{R2}\boldsymbol{m}_{\Delta d}^{2}\boldsymbol{m}_{R2}^{T} = \tag{2.67}$$

$$= \boldsymbol{m}_{R2}\boldsymbol{m}_{\Delta d}\boldsymbol{m}_{R2}^{T}\boldsymbol{m}_{R2}\boldsymbol{m}_{\Delta d}\boldsymbol{m}_{R2}^{T} = (\boldsymbol{m}_{R2}\boldsymbol{m}_{\Delta d}\boldsymbol{m}_{R2}^{T})^{2}$$

Therefore, under the consideration of dealing with equal ***m'***, $\boldsymbol{m}_{\Delta}$ can be written as a function of $\boldsymbol{m}_{\Delta d}$ as following

$$\boldsymbol{m}_{\Delta} = \boldsymbol{m}_{R2}\boldsymbol{m}_{\Delta d}\boldsymbol{m}_{R2}^{T} \tag{2.68}$$

This relationship gives us the explicit diagonalization of $\boldsymbol{m}_{\Delta}$ through the retarders found in the symmetric decomposition. Note that this result is consistent with the fact that Lu-Chipman's depolarizer can be considered as a rotated depolarizer. In fact, in the case that the ***m'*** of the Lu-Chipman decomposition and the ***m'*** of the symmetric decomposition were equal, the Lu-Chipman's depolarizer would be a rotation of the diagonal depolarizer obtained from the symmetric decomposition. Moreover, comparing the expressions of Eqs. (2.66) and (2.68) we obtain the following second relation:

$$\boldsymbol{m}_{R} = \boldsymbol{m}_{R2}\boldsymbol{m}_{R1} \tag{2.69}$$

As a result, the retarder of the Lu-Chipman decomposition is equivalent to the product of the two retarders of the symmetric decomposition. So, if we knew the symmetric decomposition associated with a matrix, we could calculate its Lu-Chipman decomposition as long as the polarizance vector $\boldsymbol{P}_{\Delta} \sim \boldsymbol{0}$. Additionally, the matrix that results from the product of the two retarders of the symmetric decomposition does not depend on the order of the eigenvalues. Thus, this provides a way to establish a solid calculus of the total retardance associated with a matrix, analogous to the Lu-Chipman decomposition (subsection 2.2.2), but using the symmetric decomposition that does not require the addition of any artifact to ***m'***.

2.4.3 Type I canonical depolarization

Unlike the Lu-Chipman decomposition, the matrix of the depolarizer obtained from the symmetric decomposition of the type I Mueller matrices is diagonal with null polarizance and null diattenuation vectors. Therefore, the birefringent and dichroic content of the Mueller matrix are completely removed from the depolarizer, and it is characterized only by the depolarization and intensity properties of ***M***. The value of d_0 is related to the mean intensity of ***M***, while the depolarization of ***M*** is quantified by the normalized $\hat{d}_1$, $\hat{d}_2$, and $\hat{d}_3$ observables. These three observables are so-called type I canonical depolarization parameters, and we define them before the application of the "minimum retardance principle". The SVD ordering of the eigenvalues and the limitations related to physically realizable matrices makes that these observables must satisfy the following expressions:

$$0 \leq \hat{d}_2 \leq \hat{d}_1 \leq 1 \tag{2.70}$$

$$-\frac{1}{3} \leq \hat{d}_3 \leq \hat{d}_2 \tag{2.71}$$

From these equations is derived that $\hat{d}_1$, $\hat{d}_2$, and $\hat{d}_3$ can simultaneously achieve the value 1, as in the IPP case. This case, $\hat{d}_1 = \hat{d}_2 = \hat{d}_3 = 1$, describes non-depolarizing matrices and the ideal depolarizers are characterized by $\hat{d}_1 = \hat{d}_2 = \hat{d}_3 = 0$. From Eq. (2.71) can be also derived that, contrasting with all the other depolarizing parameters that have been presented in this thesis, the $\hat{d}_3$ values can be negative. Such negative values are produced when the determinant of ***M*** is negative too.

Finally, the type I canonical depolarization parameters can be arranged to assemble a 3D space where any type I depolarizer can be represented. Figure 2-6 is the graphical representation of this 3D so-called Type I canonical depolarization space [64]. In this space, each canonical depolarization parameter is associated with an axis, and the limit of the physically realizable space is defined by Eqs. (2.70) and (2.71). The space is shaped as a tetrahedron, like the Purity space, and it has also a similar volume. The Purity space and Type I canonical depolarization space are very similar, but it is worth noting that both spaces have been obtained by using two completely different decompositions (one is an incoherent addition of matrices and the other is a concatenation product of matrices) thus leading to different results in the experimental scenario. The suitability of each space for the tissue classification task will be studied in Chapter 5.

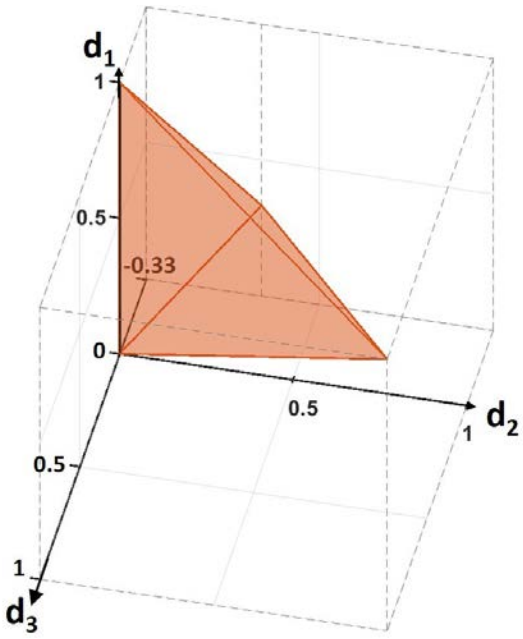

Figure 2-6. Representation of the Type I canonical depolarization space.

2.4.4 Type I Lorentz depolarization space

In 1998, A. V. Gopala Rao, K. S. Mallesh, and Sudha proposed the use of the Lorentz singular values of ***M*** to characterize its depolarizing capacity [215]. The calculus of Lorentz depolarization indices presents a computational advantage in front of the decomposition derived parameters. Their calculus avoids the generally computationally intensive tasks that the ***M*** decompositions require. This is explained because Lorentz depolarization indices do not need SVD or similar operations. Lorentz depolarization indices are based on the trace calculus of ***N*** (***N*** is described in Eq. (2.55)) and the generalized Lorentz depolarization index $L^{(m)}$ of order m ($m \geq 2$) is defined as

$$L^{(m)} = \sqrt{\frac{1}{4^{m-1}-1}\left[4^{m-1}\frac{tr(\boldsymbol{N}^m)}{tr(\boldsymbol{N})^m}-1\right]} = \sqrt{\frac{1}{4^{m-1}-1}\left[4^{m-1}\frac{\sum_{k=0}^{3}p_k^m}{\left(\sum_{k=0}^{3}p_k\right)^m}-1\right]} \tag{2.72}$$

being p_k the eigenvalues of the matrix ***N*** and k=1,2,3, and 4. Notice that Eq. (2.72) is similar to the expression of the higher-order depolarization indices $P_{\Delta}^{(m)}$ (Eq. (2.49)) but instead of using the covariance matrix ***H***, it is replaced by the ***N*** matrix. Moreover, the Lorentz depolarizing indices are limited by Eq. (2.73), which is also very similar to the constraints of $P_{\Delta}^{(m)}$ exposed in Eq. (2.50). Conversely to $P_{\Delta}^{(m)}$, non-depolarizing matrices are characterized by $L^{(m)} = 0$, and ideal depolarizers by $L^{(m)} = 1$, for any possible value of *m*.

$$0 \leq ... \leq L^{(m)} \leq L^{(4)} \leq L^{(3)} \leq L^{(2)} \leq 1 \tag{2.73}$$

In the case of the Type I matrices, the eigenvalues of the matrix ***N*** can be written in terms of the parameters of Type I canonical depolarizers. In that scenario, $p_0 = d_0^2$, $p_1 = d_1^2$, $p_2 = d_2^2$ and $p_3 = d_3^2$. Consequently, the expression of the generalized Lorentz depolarization indices can be rewritten in terms of Type I canonical depolarizer parameters.

$$L_I^{(m)} = \sqrt{\frac{1}{4^{m-1}-1}\left[4^{m-1}\frac{(1+d_1^{2m}+d_2^{2m}+d_3^{2m})}{(1+d_1^2+d_2^2+d_3^2)^m}-1\right]} \tag{2.74}$$

where the subindex I indicates that this expression is only valid for matrices that can be decomposed using the Type I symmetric decomposition.

Now, as in the $P_{\Delta}^{(m)}$ case, the first three Lorentz indices, i.e. $L_I^{(2)}$, $L_I^{(3)}$, and $L_I^{(4)}$, can be used to build a 3D space where each Type I Mueller matrix can be represented in it as a point [64]. This space is represented in Figure 2-7 and its volume is similar to the high-order depolarization indices space (Figure 2-5), i.e., the space is almost restricted to a surface. The interests of this space are the fact that its computational time results lower than the space based on the Type I decomposition parameters, and the fact that it is equivalent to a non-linear combination of Type I canonical depolarizer parameters (see Eq. (2.74)) and it may lead to better results in some applications.

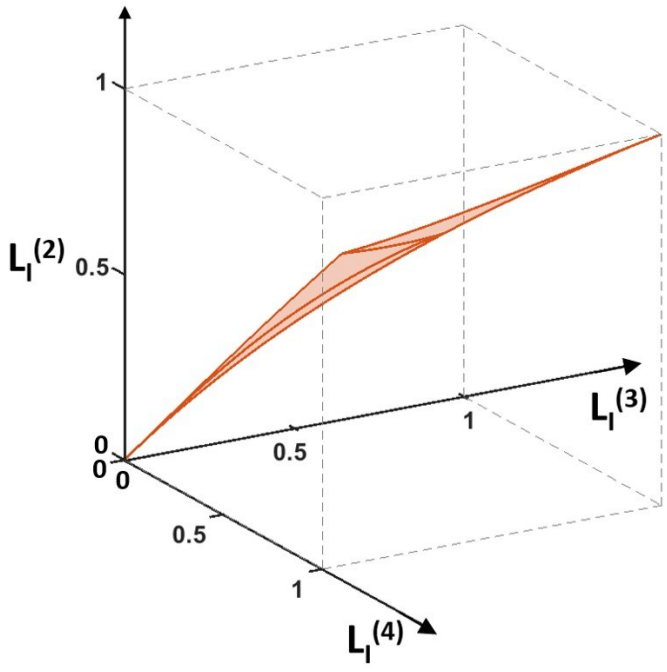

Figure 2-7. Representation of the Type I Lorentz Depolarization space.

Chapter 3 Experimental set-up

In order to measure the Mueller matrix of biological samples, an image Mueller polarimeter based on Parallel Aligned Liquid Crystals (PA-LC) was built. This chapter aims describing the image Mueller polarimeter used to measure the polarimetric response of samples and explaining its calibration method.

First, section 3.1 introduces the theory behind the measure of the Mueller matrix of samples using Mueller polarimeters. Next, the specific configuration of the Mueller polarimeters used to measure the polarimetric response of the analyzed samples of this thesis is described in section 3.2. This section also illustrates the experimental construction of the set-up built in the laboratory. Finally, section 3.3 explains the methods used to calibrate the polarimeter together with some measurement results that support the validation of such a calibration method.

3.1 Mueller matrix measurement

The measurement of sample Mueller matrices is carried out with a device called Mueller polarimeter. This instrument consists of two parts: a polarization state generator (PSG) system, capable of generating any state of polarization; and a polarization state analyzer (PSA) system, able to determine the state of polarization of an incident light beam. A general schema of the Mueller polarimeter, including the PSG and PSA systems, can be seen in Figure 3-1. Any PSG is composed of a light source and a set of optical elements that polarize the light in a specific way. For its part, the PSA consists of a set of optical elements that let pass only a specific type of polarized light followed by a detector that measures the intensity of light that has passed through the optical elements. The detector should be a pixelated-based sensor, for imaging purposes. Note that the analyzer system (PSA) can be used separately for other applications and it is known as a Stokes polarimeter [86,216,217].

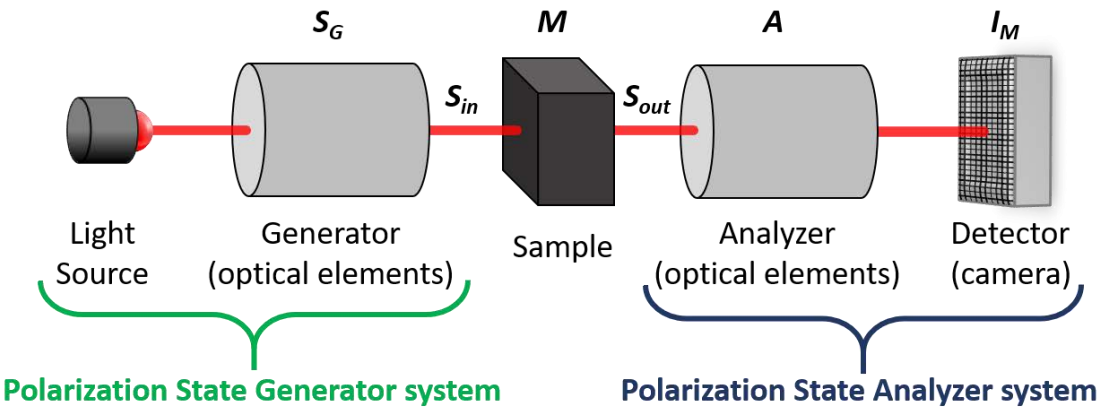

Figure 3-1. Draft of a Mueller polarimeter.

In the following, the operation principle of the PSA will be mathematically described according to ref. [68]. Given a certain SoP, $\boldsymbol{S_{out}}$, exiting from a given sample after interaction (see Figure 3-1), the intensity measured with the camera (I_q) is mathematically described as:

$$I_q = \boldsymbol{A_q}\boldsymbol{S}_{out} = a_{q0}S_0 + a_{q1}S_1 + a_{q2}S_2 + a_{q3}S_3 \tag{3.1}$$

where S_i (i=0, 1,2,3) are the coefficients of the S_{out}, $\boldsymbol{A_q}$=(a_{q0}, a_{q1}, a_{q2}, a_{q3}) characterizes the specific state of polarization analyzed by a particular configuration of the PSA (from now on, analyzer) and $\boldsymbol{A_q}/a_{q0}$ describes the normalized analyzer. Considering the use of n different analyzers, the response of the PSA to a given $\boldsymbol{S_{out}}$ can be written as:

$$\boldsymbol{I} = \begin{pmatrix} I_1 \\ I_2 \\ \vdots \\ I_n \end{pmatrix} = \boldsymbol{A}\boldsymbol{S}_{out} = \begin{pmatrix} a_{1,0} & a_{1,1} & a_{1,2} & a_{1,3} \\ a_{2,0} & a_{2,1} & a_{2,2} & a_{2,3} \\ \vdots & \vdots & \vdots & \vdots \\ a_{n,0} & a_{n,1} & a_{n,2} & a_{n,3} \end{pmatrix} \begin{pmatrix} S_0 \\ S_1 \\ S_2 \\ S_3 \end{pmatrix} \tag{3.2}$$

where $\boldsymbol{A}$ is known as the base of the analyzer (or polarimetric matrix) and $\boldsymbol{I}$ is a vector that comprises the measured intensities. Once the intensity measurement vector $\boldsymbol{I}$ and the matrix $\boldsymbol{A}$ are known (the matrix $\boldsymbol{A}$ is accurately characterized during the calibration process of PSA described in sub-section 3.3.2), the SoP, $\boldsymbol{S_{out}}$, can be determined by inverting Eq. (3.2), this leading to the following expression:

$$\boldsymbol{S_{out}} = \tilde{\boldsymbol{A}}^{-1}\boldsymbol{I} \tag{3.3}$$

where $\tilde{\boldsymbol{A}}^{-1}$ is the pseudoinverse matrix of $\boldsymbol{A}$ defined as $\tilde{\boldsymbol{A}}^{-1} \equiv \left(A^T A\right)^{-1} A^T$. Note that the pseudoinverse is used because, in general, matrix $\boldsymbol{A}$ is not a square matrix. An $\boldsymbol{A}$ matrix with a rank smaller than 4 implies that the associated PSA is incomplete and only three or fewer SoP parameters can be estimated. Accordingly, all the SoP parameters can be determined when the rank of matrix $\boldsymbol{A}$ is equal to 4 so at least four different configurations of the analyzer are required to completely retrieve $\boldsymbol{S_{out}}$.

Although all PSA configuration systems associated with rank=4 matrices can completely determine the $\boldsymbol{S_{out}}$, due to the matrix inversion in Eq. (3.3), some analyzer configurations lead to larger amplification of experimental noise from the intensity measurements to the final Stokes

parameters than others [187,192]. Therefore, the choice of a PSA basis minimizing the noise propagation is an important issue in terms of polarimeter performance. Accordingly, the PSA is calibrated based on the Conditional Number (CN) [187] and the Equally Weighted Variance (EWV) [187,192] metrics, that analyze the propagation and amplification of error. The calibration process is described below in section 3.3.

Once described how the PSA works, which is equivalent to the operation principle of the Stokes polarimeters, this operation principle is extended to describe the performance of the whole Mueller polarimeter instrument.

Let us start with the Mueller-Stokes description of the light-matter interaction (Eq. (2.4)) but replacing the output Stokes vector with the combination of the analyzers and intensities described in Eq. (3.3):

$$\boldsymbol{S_{out}} = \tilde{\boldsymbol{A}}^{-1}\boldsymbol{I} = \boldsymbol{M}\cdot\boldsymbol{S_{in}} \tag{3.4}$$

Then, we consider the case of illuminating the sample with different *k* well-known states of polarizations controlled with the PSG system. Using the S-M formalism, the different *k* incident SoPs are written in the different columns of a newly defined matrix $\boldsymbol{S_G}$ (the generator base) and, accordingly, the measured intensities related to each *k* incident SoP will be written in the different columns of a newly defined matrix $\boldsymbol{I_M}$.

$$\tilde{\boldsymbol{A}}^{-1}\boldsymbol{I}_M = \tilde{\boldsymbol{A}}^{-1}\begin{pmatrix} I_{1,1} & I_{1,2} & \cdots & I_{1,k} \\ I_{2,1} & I_{2,2} & \cdots & I_{2,k} \\ \vdots & \vdots & \ddots & \vdots \\ I_{n,1} & I_{n,2} & \cdots & I_{n,k} \end{pmatrix} = \boldsymbol{M}\boldsymbol{S_G} = \boldsymbol{M}\begin{pmatrix} S_{0,1} & S_{0,2} & \cdots & S_{0,k} \\ S_{1,1} & S_{1,2} & \cdots & S_{1,k} \\ S_{2,1} & S_{2,2} & \cdots & S_{2,k} \\ S_{3,1} & S_{3,2} & \cdots & S_{3,k} \end{pmatrix} \tag{3.5}$$

Finally, the Mueller matrix of the measured sample is estimated by using the pseudoinverse of $\boldsymbol{S_G}$.

$$\tilde{\boldsymbol{A}}^{-1}\boldsymbol{I}_M\tilde{\boldsymbol{S}}_G^{-1} = \boldsymbol{M} \tag{3.6}$$

The dimensionalities of the matrices $\boldsymbol{A}$, $\boldsymbol{I_M}$, and $\boldsymbol{S_G}$ are *nx4*, *nxk,* and *4xk*, respectively. For the same reasons above-mentioned with the PSA, the rank of $\boldsymbol{A}$ and $\boldsymbol{S_G}$ matrices must be equal to 4 to completely determine all the coefficients of the Mueller matrix. Accordingly, at least 16 independent intensities must be measured to calculate all the parameters of the Mueller matrix.

The error amplification to the calculated $\boldsymbol{M}$ coefficients depends on the analyzers of $\boldsymbol{A}$, like in the case of Stokes polarimeters, but in this case, it also depends on the SoPs of $\boldsymbol{S_G}$ that have been used to illuminate the sample. Consequently, the PSG is also calibrated by minimizing the CN and EWV figures of merit. The calibration method of PSG will be deeply described in subsection 3.3.1.

It is worth noting that, the mathematical calculation described in this section considers a monopixel detector. In the case of using a camera as a detector to retrieve the Mueller matrix of an image, the same calculation process must be performed for each individual pixel.

3.2 Experimental image Mueller polarimeter based on parallel aligned liquid crystals

Several architectures of polarimeters can be considered to satisfy the PSA schema of Figure 3-1 [47]: a division of amplitude polarimeters (DoAmP) [182,183], division of aperture polarimeters (DoAP) [184,185], polarimeters based on rotating elements [187–190], polarimeters based on liquid crystal devices [191–194], and division of focal plane (DoFP) polarimeters [50–59], among others. In the following we explain the main reasons why we built a polarimeter based on liquid crystal devices.

First, at the beginning of the thesis, polarimeters based on rotating elements and polarimeters based on liquid crystal devices appeared to be the cheapest and easiest choices to build polarimeters. Nowadays the price of DoFP polarimeters is much more accessible but it was not at the beginning of this thesis. Second, the fact that Mueller matrix measurements with these two architectures are not instantaneous and that samples must be stationary during the measurement is not a problem for the experiments performed in this thesis as we deal with stationary *ex-vivo* samples and non-organic samples. Finally, we chose using LC devices in front of rotating elements because mechanical rotation of optical elements may slightly modify the direction of the light beam so shifting the images captured with the camera (beam wander).

We chose also a design based on LC for the PSG for the same reasons discussed before, as well as for symmetry and ease of control considerations.

3.2.1 Mueller Polarimeter based on parallel aligned liquid crystals

The instrument used in this thesis is composed of liquid crystals in the PSG and PSA sections (see Figure 3-2 and Figure 3-4). In particular, the PSG and PSA are both composed of one linear polarizer (LP) and two parallel aligned liquid crystals (PA-LC). PA-LC are materials that behave as linear retarders but the phase difference between the fast axis and the slow axis (δ) can be modified with the application of different voltages [192]. The dependence of δ with the applied voltage is a continuous function thus allowing the achievement of any retardance that is contained in the retardance range of the material, more than 2π in our case, by properly applying the specific voltage.

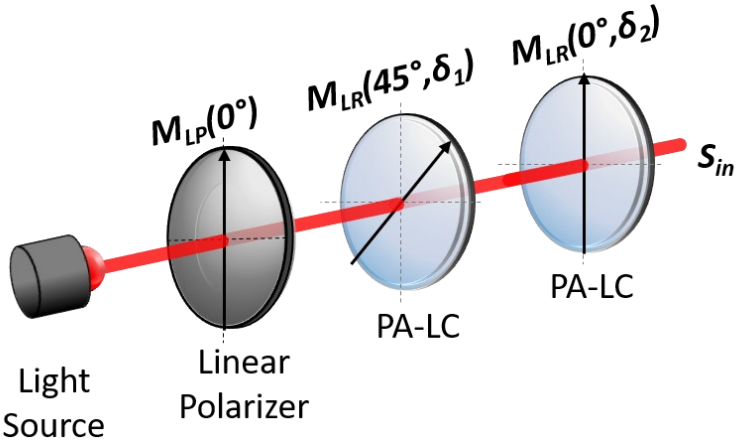

Figure 3-2. Scheme of the polarization state generator (PSG) system based on parallel aligned liquid crystals (PA-LC).

Figure 3-2 shows the scheme of the polarization state generator implemented in our set-up. It consists of a non-polarized and collimated light source (LS) followed by a linear polarizer oriented with the vertical reference of the lab, a first PA-LC oriented at 45° concerning the same reference, and a second PA-LC oriented at 0°. Given this configuration, the state of polarization of the beam at the output of the PSG ($\boldsymbol{S}_{in}$) is written as follows:

$$\boldsymbol{S}_{in} = \boldsymbol{M}_{LR}(0^{\circ},\delta_2)\boldsymbol{M}_{LR}(45^{\circ},\delta_1)\boldsymbol{M}_{LP}(0^{\circ})\boldsymbol{S}_{LS} \tag{3.7}$$

where $\boldsymbol{M}_{LR}$ and $\boldsymbol{M}_{LP}$ are, respectively, the Mueller matrices of a linear retarder and a linear polarizer [45,46], $\boldsymbol{S}_{LS}$ is the Stokes vector of the non-polarized light source, and δ_1 and δ_2 are the linear retardance of the first and second PA-LC respectively, that depend on the addressed voltage. According to Eq. (3.7), $\boldsymbol{S}_{in}$ can be written in terms of δ_1 and δ_2 as:

$$\boldsymbol{S}_{in} = \begin{pmatrix} 1 & 0 & 0 & 0 \\ 0 & 1 & 0 & 0 \\ 0 & 0 & \cos(\delta_2) & -\sin(\delta_2) \\ 0 & 0 & \sin(\delta_2) & \cos(\delta_2) \end{pmatrix} \begin{pmatrix} 1 & 0 & 0 & 0 \\ 0 & \cos(\delta_1) & 0 & \sin(\delta_1) \\ 0 & 0 & 1 & 0 \\ 0 & -\sin(\delta_1) & 0 & \cos(\delta_1) \end{pmatrix} \frac{1}{2} \begin{pmatrix} 1 & -1 & 0 & 0 \\ -1 & 1 & 0 & 0 \\ 0 & 0 & 0 & 0 \\ 0 & 0 & 0 & 0 \end{pmatrix} \begin{pmatrix} I_{LS} \\ 0 \\ 0 \\ 0 \end{pmatrix} \tag{3.8}$$

$$\boldsymbol{S}_{in} = \frac{I_{LS}}{2} \begin{pmatrix} 1 \\ -\cos(\delta_1) \\ -\sin(\delta_1)\sin(\delta_2) \\ \sin(\delta_1)\cos(\delta_2) \end{pmatrix} \tag{3.9}$$

The expression of $\boldsymbol{S}_{in}$ (Eq. (3.9)) can be normalized by the constant term ($\boldsymbol{I}_{LS}/2$) which allows the resulting polarization states to be represented in the Poincare sphere (see Figure 3-3).

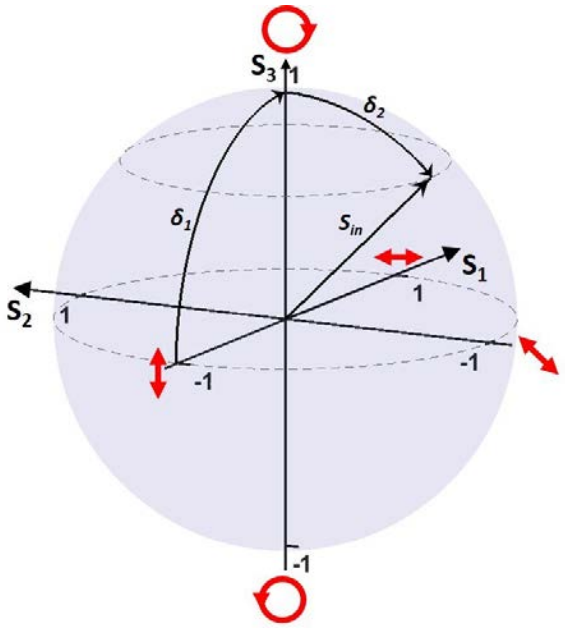

Figure 3-3. Representation of $\boldsymbol{S}_{in}$ in the Poincare sphere.

The $\boldsymbol{S}_{in}$ obtained with this configuration is usually represented over the surface of the Poincare sphere, in which the fully polarized states of polarization are located. The position of the resulting polarization in the sphere surface is determined with the angles δ_1 and δ_2: the angle δ_1 defines the direction of the projection of $\boldsymbol{S}_{in}$ in the S_1-S_3 plane and δ_2 describes the direction

of its projection in the S_2-S_3 plane. Note that relations in Eq. (3.9) define spherical coordinates, with δ_1 and δ_2 as angles. Therefore, since the linear retardances, δ_1 and δ_2 depend on the applied voltage and such retardances can get values in the range of more than 2π, any state of polarization can be generated by properly applying the associated voltage.

The polarization state analyzer system based on PA-LC is made up of the same optical elements as the PSG system (two PA-LC and a LP) but arranged in the reverse order. The optical elements of PSA are ordered with the PA-LC oriented at 0° first, followed by a PA-LC oriented at 45° and a vertical polarizer (analyzer). The Mueller matrix of this construction can be written as:

$$\boldsymbol{M}_A = \boldsymbol{M}_{LP}(0^{\circ})\boldsymbol{M}_{LR}(45^{\circ},\delta_1)\boldsymbol{M}_{LR}(0^{\circ},\delta_2) \tag{3.10}$$

$$\boldsymbol{M}_A = \frac{1}{2}\begin{pmatrix} 1 & -\cos(\delta_1) & -\sin(\delta_1)\sin(\delta_2) & -\sin(\delta_1)\cos(\delta_2) \\ -1 & \cos(\delta_1) & \sin(\delta_1)\sin(\delta_2) & \sin(\delta_1)\cos(\delta_2) \\ 0 & 0 & 0 & 0 \\ 0 & 0 & 0 & 0 \end{pmatrix} \tag{3.11}$$

These optical elements are followed by a detector, or a camera in the case of image polarimeters, that measures the intensity of the analyzed beam (see Figure 3-4). According to Eq. (3.11), the amount of intensity measured with the camera depends on the light attenuated by the optical elements of the PSA (i.e., the mean intensity coefficient and the diattenuation parameters defined in the first row of $\boldsymbol{M_A}$). Therefore, this first row of $\boldsymbol{M_A}$ constitutes the analyzer vector $\boldsymbol{A}$ and depends on δ_1 and δ_2 as follows:

$$\boldsymbol{A} = \frac{1}{2}(1 \quad -\cos(\delta_1) \quad -\sin(\delta_1)\sin(\delta_2) \quad -\sin(\delta_1)\cos(\delta_2)) \tag{3.12}$$

Like in the case of the PSG, any analyzer $\boldsymbol{A}$ can be obtained by properly selecting the voltage applied to the PA-LC devices. Therefore, this configuration allows generating and analyzing any state of polarization by properly selecting the voltage applied to the PA-LC devices.

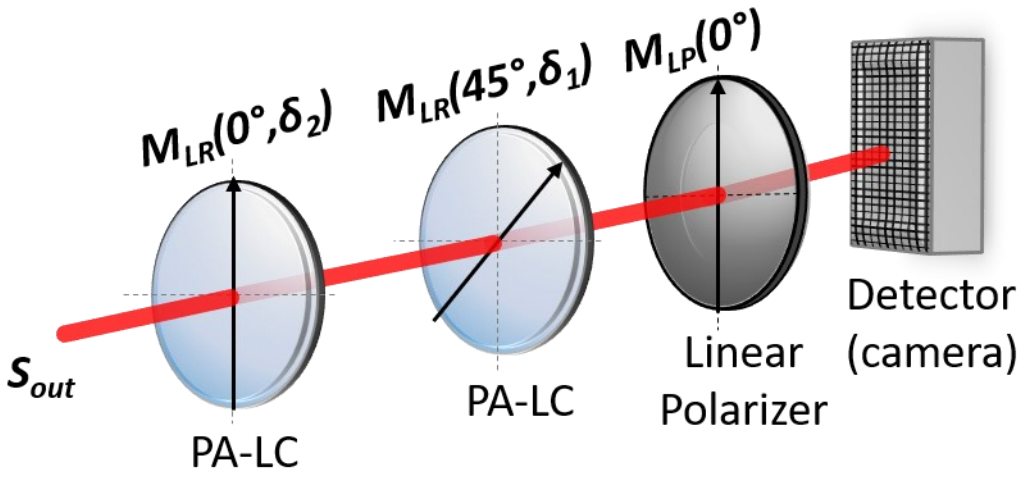

Figure 3-4. Scheme of the polarization state analyzer (PSA) system based on parallel aligned liquid crystals (PA-LC).

3.2.2 Experimental implementation of the image Mueller polarimeter

The implemented image Mueller polarimeter based on PA-LC uses a four wavelength (625 nm, 590 nm, 530 nm, and 470 nm) high-power LED source (LED4D067) operated by a DC4104 driver and distributed by Thorlabs. The use of LED sources prevents the presence of speckle effects because LED bandwidths are in the order of tens of nm and the speckle effect is produced with coherent light sources of tenths of nm bandwidths [218–220]. The speckle effect is commonly observed when illuminating scattering media, e.g., biological samples, with laser beams [218–220]. The opposite case of using sources with broad bandwidth is also harmful to the measurements because the dependence of the linear retardance (δ) of PA-LCs with the wavelength results in an increment of the error at measuring the Mueller matrix of samples. The variety of wavelengths that comprises the bandwidth range are differently retarded so producing different SoPs, and these SoPs, corresponding to different wavelengths of the bandwidth, are incoherently combined in the camera producing an effective depolarized SoP. Depolarizing SoPs increases the error propagation at measuring the Mueller matrix of samples [187,192].

Figure 3-5 plots the dependence of the LEDs intensity with the wavelength and Table 3-1 provides characteristic parameters of these dependencies: the full width half maximum (FWHM) to quantify the bandwidth of the LEDs, and the wavelength associated with the highest intensity peak of the LEDs intensity distributions. Table 3-1 reveals that the bandwidths of 470 nm and 530 nm LEDs, FWHM of 25 nm and 33 nm respectively, are higher than the bandwidth of 590 nm and 625 nm LEDs, 18 nm for both LEDs.

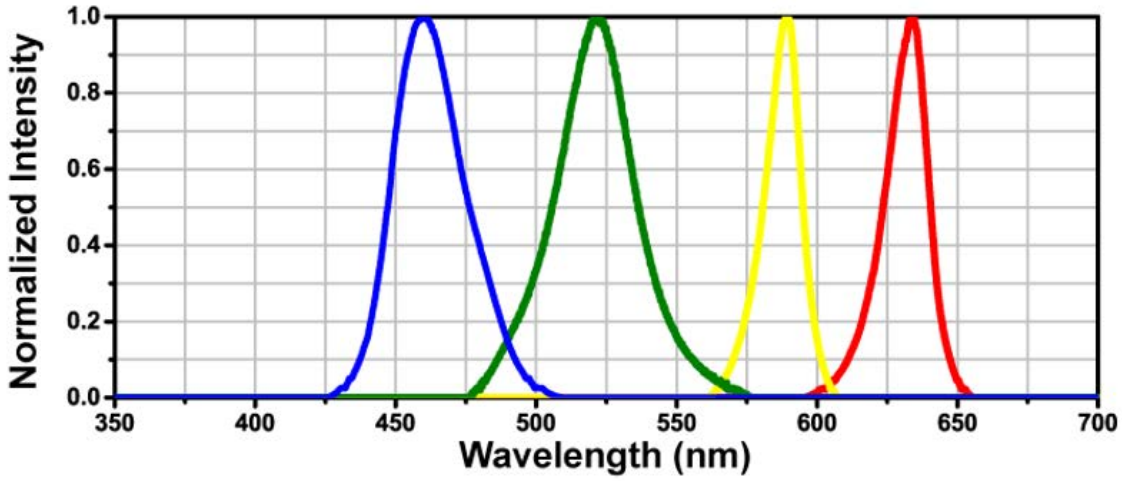

Figure 3-5. Normalized intensity vs wavelength for the four LEDs that comprise the LED4D067 light source [221]. Different color lines are associated with different LED: 625 nm is represented with a red line, 590 nm with yellow, 530 nm with green, and 470 nm with blue.

Nominal Wavelength	Bandwidth (FWHM)	Peak of the distribution
470 nm	25 nm	460 nm
530 nm	33 nm	522 nm
590 nm	18 nm	588 nm
625 nm	18 nm	633 nm

Table 3-1. Full with half maximum (FWHM) and Peak of the distribution of the four LEDs that comprise the LED4D067 light source [221].

As previously said, higher bandwidths result in further depolarized SoPs. For that reason, we have measured the DOP of generating 0°, 45°, 90°, and 135° linear polarized beams, and right-handed and left-handed circular polarized beams, and we have calculated the mean DOP value among the generated beams for each wavelength. The mean DOP values are provided in Table 3-2. Such results indicate that, on average, the DOP of the generated SoPs decreases with the wavelength of the LED source. This DOP tendency is also observed between the red (625 nm; 0.987 mean DOP) and yellow (590 nm; 0.970 mean DOP) LEDs but they have the same bandwidth so other physical properties apart from the light source bandwidth are involved in this trend. The phenomenon may be connected with the dependence of the retardance of the PA-LCs with the wavelength [222]. In this way, the variation of such function increases as the wavelength is shorter [222], and consequently, for the same bandwidth, the variety of SoPs generated with a certain combination of voltages with shorter wavelength sources is higher than the generated with larger wavelength sources. Thus, as previously said, this assortment of generated SoPs will be incoherently combined and resulting in a depolarized beam. The DOP value of this depolarized beam is lower as more different the incoherently combined SoPs are, so shorter wavelength presents lower DOP values.

Nominal Wavelength	Mean DOP (without filter)	Average DOP (with filter)
470 nm	0.816 ± 0.005	0.966 ± 0.005
530 nm	0.945 ± 0.005	0.982 ± 0.005
590 nm	0.970 ± 0.005	0.983 ± 0.005
625 nm	0.987 ± 0.005	-

Table 3-2. Mean DOP value of the 6 generated SoPs with the different LEDs that comprise the LED4D067 light source with and without 10 nm dielectric filters.

To offset this effect and generate SoPs with higher DOP (less depolarization), we filter the light of the blue, green, and yellow channels with dielectric bandwidth filters. These filters are characterized by a FWHM of 10 nm and central wavelengths of 470 nm, 530 nm, and 590 nm, respectively (FB470-10, FB530-10, and FB590-10, distributed by Thorlabs). The mean DOP values of the SoPs generated using the dielectric filters are provided in Table 3-2. Note that we have not used any bandwidth filter for the 625 nm LED as we have considered that his DOP value was acceptable.

The light of the LED source is conducted through a liquid light guide that is connected with a beam collimator (LLG5A1-A distributed by Thorlabs) to properly control the direction of the light (see Figure 3-6). After the collimator, the beam is polarized with a Glan–Thompson prism-based linear polarizer (by CASIX), and the polarization of this beam is modified by two liquid crystal variable retarders with temperature control (LVR–200–400-700-1L-TSC and D5020-20 controller by Meadowlark Optics) following the scheme of Figure 3-2.

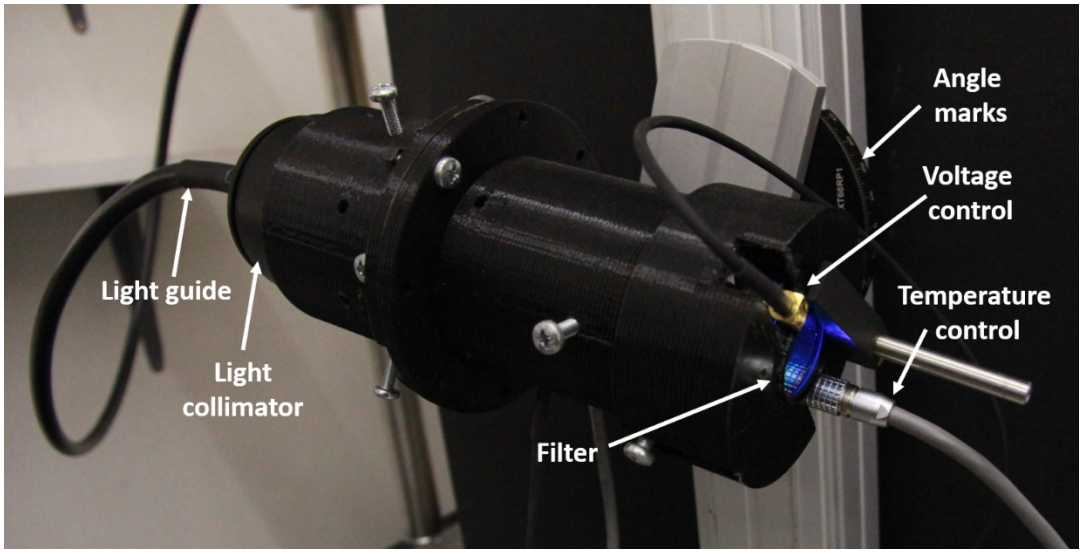

Figure 3-6. Photographic image of the PSG belonging to the experimental Mueller matrix polarimeter.

The retardance of the PA-LC changes with the temperature and the ambient temperature of the laboratory is not constant. It may differ more than 15° between summer and winter and can also fluctuate some degrees during the whole day. For that reason, we need a temperature control that maintains the temperature of the PA-LC at 30°. The temperature control system works by heating the PA-LC to the desired temperature and keeping it constant. Unfortunately, if the ambient laboratory temperature overcomes the 30°, the temperature control would not be able to decrease the PA-LC temperature. Under this scenario, we cannot perform experiments. Hopefully, this scenario is quite exceptional in our laboratory conditions.

The optical elements of the PSG are assembled in a black holder made with a 3D printer (see Figure 3-6). That holder protects the optical elements from the environment (dust, stray light, scratches, blows, etc.) and makes the PSG easy to handle. Note that the 3D printed design presents a space at the output of the PSG to place the dielectric filters for the blue, green, and yellow channels (see Figure 3-6).

Similar to the PSG, the PSA is also assembled in a black holder made with a 3D printer (see Figure 3-7). Within this holder, the optical elements observed in Figure 3-4 are placed following the same scheme. The PA-LCs used for the PSA are the same type as those used in the PSG while the polarizer is a dichroic sheet polarizer (by Meadowlark) instead of a Glan–Thompson polarizer. In the PSA, we have not used the Glan–Thompson prism-based linear polarizer because it reduces the image aperture and it can generate some distortions to the measured images. Next, a TECHSPEC® high-resolution microscope objective (distributed by Edmund Optics), with a focal length of 35 mm, is placed between the linear polarizer and the camera to

image the region of interest of the sample on the CCD camera. The camera is an Allied Vision Manta G-504B and it is characterized for being a 5 Megapixel GigE Vision camera with the Sony ICX655 CCD sensor. The camera has a 2452 × 2056 resolution and a pixel size of 3.45 µm × 3.45 µm. The combination of that pixel size and the 35 mm focal length of the objective results in a spatial resolution of ~20 µm.

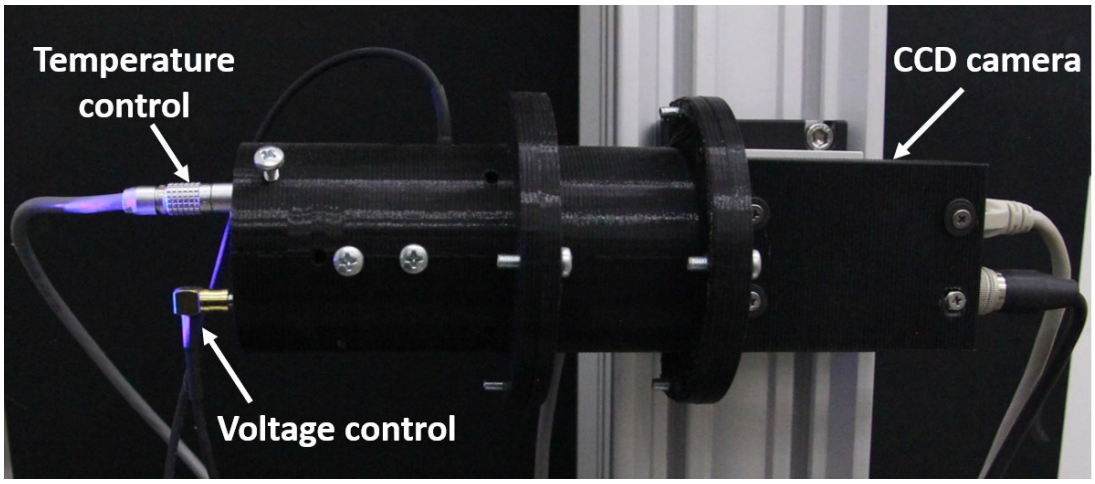

Figure 3-7. Photographic image of the PSA belonging to the experimental Mueller matrix polarimeter.

To perform the experiments of this thesis, the PSG and the PSA are fixed on vertical optical rails. In the case of the PSG, the rail presents angle marks that allow illuminating the sample in different angles with an error of ±1° (see Figure 3-6). The PSA is also rotatable but with lower precision (see Figure 3-7). According to the rotation capability, the set-up allows sample measurements in reflection and transmission (see Figure 3-8). In the reflection measurements (see Figure 3-8 (a)), we fix the illumination angle at ~30° with respect to the horizontal reference of the lab (the light impinges the sample at ~60° concerning the lab vertical z-axis), and we collect the light resulting from the interaction that is scattered in the vertical direction. Under this configuration, the sample is placed on a sample holder that can be displaced in the vertical z-axis to control the distance between the sample and the PSA and properly image the sample on the CCD camera. In the case of transmission (see Figure 3-8 (b)), the PSG and PSA are horizontally aligned and the sample is properly imaged by displacing the sample holder in the x-direction.

For the measurement of each image Mueller matrix, we illuminate the sample with 6 different SoPs and we analyze the response of the sample using a basis composed of 6 SoPs. To measure all the combinations of the generated SoPs and the analyzer SoPs we take intensity images of 36 different polarimetric configurations. The transition of one configuration to another needs the modification of the voltage applied to the PA-LCs to obtain different retardances by modifying the orientation of the PA-LC molecules. The change in the orientation of the PA-LC molecules is not instantaneous and takes ~100 ms. Therefore, as we measure 36 different configurations, our Mueller matrix measurement would take in the best scenario 3.6 s. However, we perform 8 images at each configuration to reduce the noise measured with the camera. For each camera image, the order to take an image has to be given by the computer,

with the delay in electronic communication that this entails. As a result, the image Mueller matrices measured with this instrument take around 1 minute each.

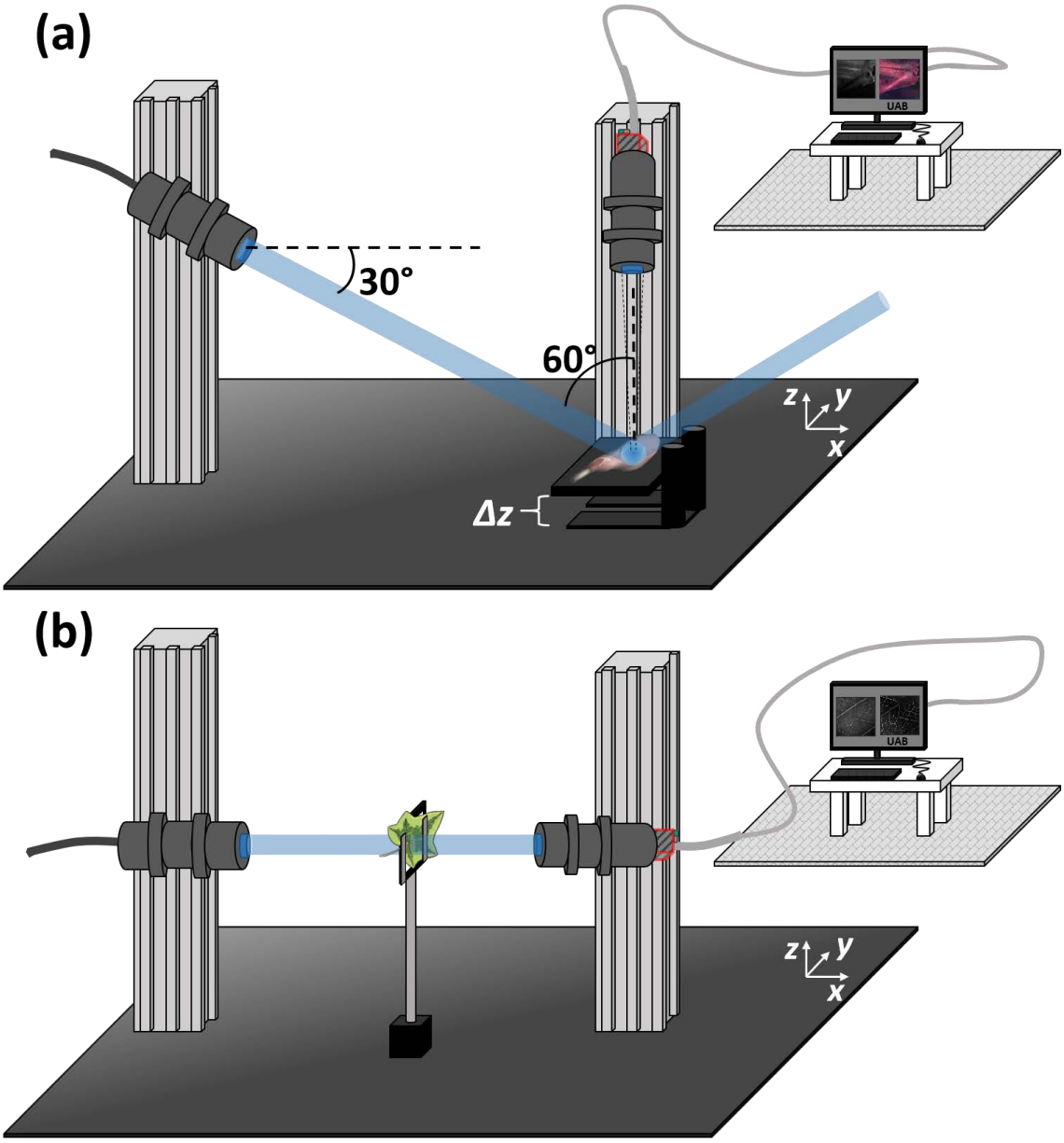

Figure 3-8. Scheme of the Mueller polarimeter working in (a) Reflection and (b) Transmission.

3.3 Calibration and validation

The experimental implementation of the set-up may introduce some deviations to the theoretical predictions. These deviations must be calibrated and taken into account to properly measure the Mueller matrix of samples. In the following, we describe the method used to calibrate the PSG and the PSA for the sake of measuring Mueller matrices with low noise propagation and high accuracy.

3.3.1 PSG calibration

The calibration of the set-up and, in particular, the calibration of the PSG takes the commercial polarimeter distributed by Thorlabs *PAX5710VIS-T* as a reference. This polarimeter is a point (mono-pixel) polarimeter based on a rotating wave plate that is used to calibrate the PSG. In this vein, the desired SoP is generated with the PSG and measured with the commercial polarimeter. The voltages addressed to the PSG are corrected until the expected SoP is measured with the commercial one. According to the data provided by the manufacturer [221], the instrument has a ±0.5% of accuracy at measuring DOP, and the normalized Stokes parameters s_1, s_2, and s_3, are measured with an accuracy <0.005. Once the PSG is calibrated, the polarization state generator is used to calibrate the PSA. Therefore, the quality performance of the employed reference (Thorlabs polarimeter) is to achieve a suitable PSG-PSA system calibration. For that reason, the performance of the commercial polarimeter is checked every few months.

The PSG calibration method consists of aligning the PSG with the *PAX5710VIS-T* polarimeter and measure the state of polarization generated with different voltages. If the SoP is not the desired, the voltages applied to the PA-LCs are changed and the newly generated state is also measured. This iterative process lasts until achieving the desired base and it is performed manually so not all the voltage combinations are explored. In fact, after the first approximations, the calibration process only explores the combination of voltages connected with polarization states that are close to the desired calibration base. Note that this calibration must be conducted for each wavelength used with the polarimeter, as same polarizations are set with different voltages at the PSG-PSA systems, due to the liquid crystal retardance dependence with de voltage.

The desired calibration of the generator base, $\boldsymbol{S_G}$, is composed of 6 SoPs (generators): four linear polarizations oriented at 0°, 45°, 90°, and 135°, and two circular polarizations rotating in the right-handed and left-handed directions. We go after this 6 SoPs base because it reduces the noise propagation regarding an optimal 4 SoPs base due to the redundant data. Moreover, it is more robust in terms of calibration error (differences between the real and the calibrated SoPs) [192].

As said in section 3.1, the rank of $\boldsymbol{S_G}$ must be equal to 4 to allow the measurement of the 16 components of the Mueller matrix but different bases that satisfy the rank 4 usually lead to different error amplification. In the case of using a 6 SoPs base, ref. [192] probed that the bases with the lowest noise propagation have their SoPs uniformly distributed over the surface of the Poincare sphere and their location matches the position of the vertices of a regular octahedron. This is the case of the desired base so it should be ideal for the Mueller matrix measurements in terms of error amplification.

To evaluate the propagation and amplification of this noise we use the Conditional Number (CN) [187] and the Equally Weighted Variance [187,192] metrics. Both metrics were designed to evaluate the error propagation for Stokes polarimeters (related to analyzer bases) but its use and interpretation can be extrapolated to Mueller polarimeters, i.e., they can also be applied to study the error amplification connected with the generator base [192].

CN is a figure of merit that analyses how far is a matrix from a singular matrix and this is connected with the way that such a matrix amplify error after inversion (the ideal case is a unitary matrix, that does not amplify error, and the worst scenario is a singular matrix)[187], and it is calculated as [187],

$$CN(\boldsymbol{W}) = tr(\boldsymbol{W}^T\boldsymbol{W})^{1/2} \tag{3.13}$$

where $\boldsymbol{W}$ is the matrix of the base (i.e., $\boldsymbol{S_G}$ or $\boldsymbol{A}$ for PSG and PSA in our study case), *tr* indicates the trace calculus, and the superindex $^{\mathrm{T}}$ the transpose of the matrix. Smaller CN values indicate smaller error amplification, being $\sqrt{3}$ the minimum physically achievable value for polarimetric systems, associated with an optimal base. The values of CN are independent of the number of SoPs *n* that compose the base, so it does not consider the improvement in the error amplification that is obtained when using more than 4 SoPs [187,192].

Conversely, this improvement is considered with the EWV metric. EWV is another figure of merit that provides a global estimation of the error propagation derived from the retrieval of the Mueller matrix from the measured intensity images. In particular, the EWV is the summation of the variances of the Stokes parameters σ_{Si}^2 that indicates the noise propagation connected to each Stokes parameter. The EWV is calculated as [187,192],

$$EWV(\boldsymbol{W}) = \sum_{i=0}^{3}\sigma_{Si}^2 = \sum_{i=0}^{3}(\sum_{j=0}^{n}q_{ij}^2) \tag{3.14}$$

where q_{ij} are the elements of the pseudoinverse matrix of the base $\boldsymbol{Q} = \tilde{\boldsymbol{W}}^{-1}$ and *n* are the number of SoPs of the base. Like in the CN case, smaller EWV values indicate smaller noise amplification. However, the EWV does not have a unique minimal value associated with the optimal architecture of the base. The optimal minimal value decreases as the number of polarization states *n* implemented with the base increases. It is produced as a consequence of the overlapping of information that involves the use of more than 4 polarization states.

As an example, Table 3-3 shows the CN and EWV values of optimal bases composed of 4 and 6 polarization states [187,192]. We see that the CN values are the same while the EWV value of the 6 SoPs base is reduced by 33% concerning the value of the 4 SoPs base. This means that the overall error amplification is reduced by 33% with a 6 SoPs base due to the redundant information [192]. Note that, as expected, the optimal EWV is reduced with the number of polarization states that comprise the base while the optimal CN is maintained equal so EWV is more appropriate for measurements with bases with more than four polarization states due to its dependence on *n* [192]. In addition, EWV is also more appropriate for the study of bases with partially polarized states because of the average approach of its calculus that reflects the difference of having one, two, three, or more depolarizing states. For example, the use of a base with one or two equally depolarized states is not differentiated with the CN as it only measures the worst scenario and it is equivalent in both cases. Conversely, these two bases would be distinguished using the EWV as the overall error amplification is higher when using a base with two depolarized states. Despite the benefits of using EWV, the information connected with the CN is unique and compatible so we use both for the analysis of the experimental bases.

Generator base	Optimal 4 SoPs base	Optimal 6 SoPs base	625 nm base	590 nm base	530 nm base	470 nm base
CN	1.73	1.73	1.77	1.80	1.81	1.83
EWV	10	6.67	7.07	6.99	7.04	7.64

Table 3-3. Values of the CN and EWV metrics for the optimal 4 and 6 SoPs bases and the experimental 625 nm, 590 nm, 530 nm, and 470nm calibrated bases for the PSG.

Following the calibration method above described we achieved the calibrated bases for the 625 nm, 590 nm, 530 nm, and 470 nm illumination LEDs (see Figure 3-9). Note that each channel, related to different LEDs, must be calibrated individually as the retardance of PA-LC devices variates with the wavelength.

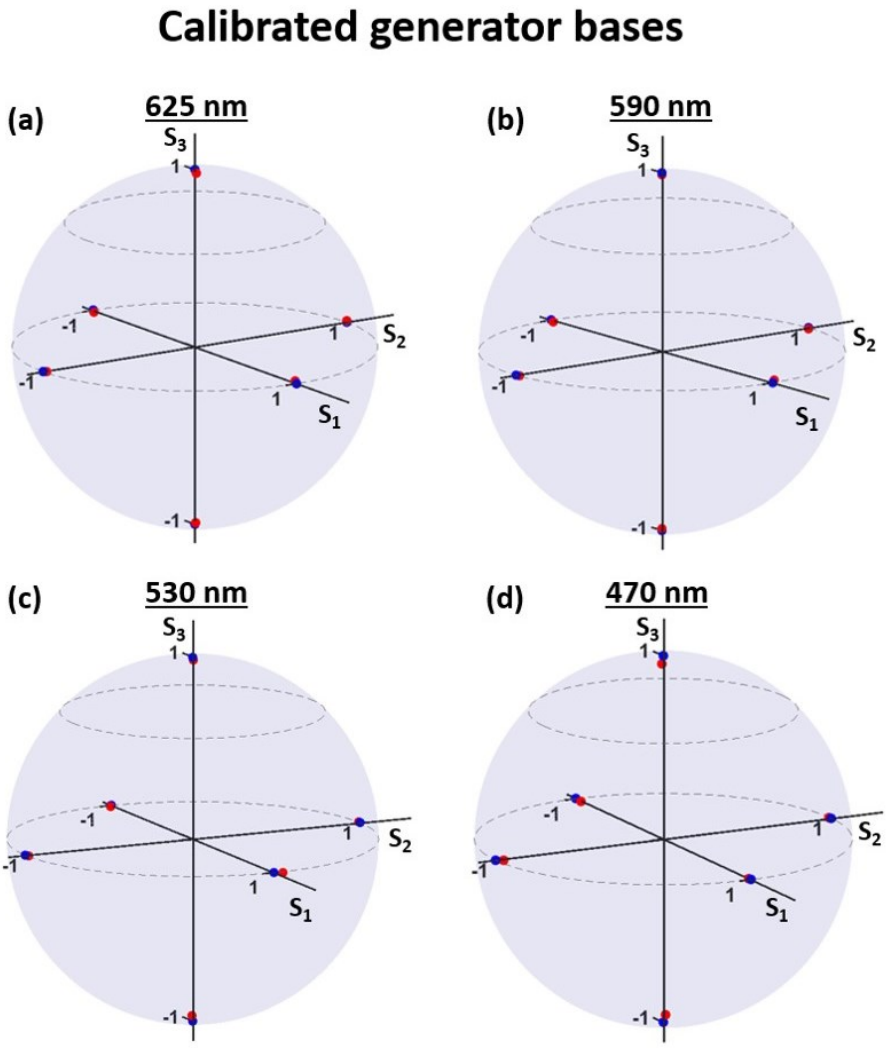

Figure 3-9. Experimental generator base calibrated at (a) 625 nm, (b) 590 nm, (c) 530 nm, and (d) 470 nm. Experimental generators are represented in red and the ideal (theoretical) ones in blue.

Figure 3-9 represents the experimental generators obtained after the calibration process in the Poincare sphere using red points. The desired SoPs for the generator, i.e., the ideal SoPs, are also represented in the Poincare spheres of Figure 3-9 using blue points. Note that the generators obtained after the calibration are very similar to the ideal ones (in other words, they

are placed very close to the ideal ones in the Poincare sphere). The only difference is that they are placed slightly deeper in the Poincare sphere as they are slightly depolarized. This depolarization is traduced in a small increment of the error propagation. It is observed with the CN and the EWV values, which are slightly higher than the ideal case (see Table 3-3). However, the CN values are always lower than 2 and the EWV values lower than 8, both considered good values. These small depolarization values measured in the calibrated SoPs can be associated to experimental errors as for instance, a not perfectly collimated beam (exiting SoPs dependence with the angle of incidence to the liquid crystals panels) or SoPs differences, due to retardance differences, associated to the source beam bandwidth.

3.3.2 PSA calibration

The calibration of the PSA is made with the PSG that has been previously calibrated. The calibration method consists of illuminating the PSA with the different polarized states of the generator base and retrieve the analyzer state associated with a pair of voltages thanks to the knowledge of the Mueller matrix of the air. The described scenario is written with the S-M formalism as

$$\boldsymbol{I}_i = \begin{pmatrix} I_{i1} \\ I_{i2} \\ \vdots \\ I_{in} \end{pmatrix} = \boldsymbol{A}_i \boldsymbol{M}_{air} \boldsymbol{S}_G \tag{3.15}$$

where $\boldsymbol{I_{in}}$ are the measured intensities related to different generated beams, $\boldsymbol{A_i}$ is the stokes vector of the analyzer, and the Mueller matrix of the air corresponds to the 4x4 identity matrix. According to this expression, the SoP of the analyzer base can be retrieved by multiplying the measured intensities by the pseudoinverse matrix of the generator base,

$$\boldsymbol{A_i} = \boldsymbol{I}_i \tilde{\boldsymbol{S}}_G^{-1}. \tag{3.16}$$

If the state of polarization of the analyzer differs from the desired one, the value of the voltages applied are manually changed and the new analyzer is measured again. This process is repeated until we reach six pairs of voltages that result in the preferred analyzer base: four linear polarizations oriented at 0°, 45°, 90°, and 135°, and two circular polarizations rotating in the right-handed and left-handed directions.

The experimental analyzer bases obtained after the calibration process of the PSA are represented with red points in the Poincare spheres of Figure 3-10. The ideal analyzer base is also represented in the Poincare spheres of Figure 3-10 but using blue points instead. Most analyzers are located very close to the ideal position except the linear vertical and horizontal analyzers. The location of the latter analyzers differs significantly from the desired position. These differences are a consequence of the architecture of the PSA and its sensitivity to possible misalignment errors produced during its construction. The Mueller polarimeter architecture based on PA-LC described in section 3.2 can, in theory, generate and analyze any state of polarization. However, any misalignment during the construction of the polarimeter impossibilities configuration of some reduced number of polarization states for the PSG and PSA systems. In that sense, the vertical and horizontal polarizations are the polarization states that appear more sensitive to that misalignments.

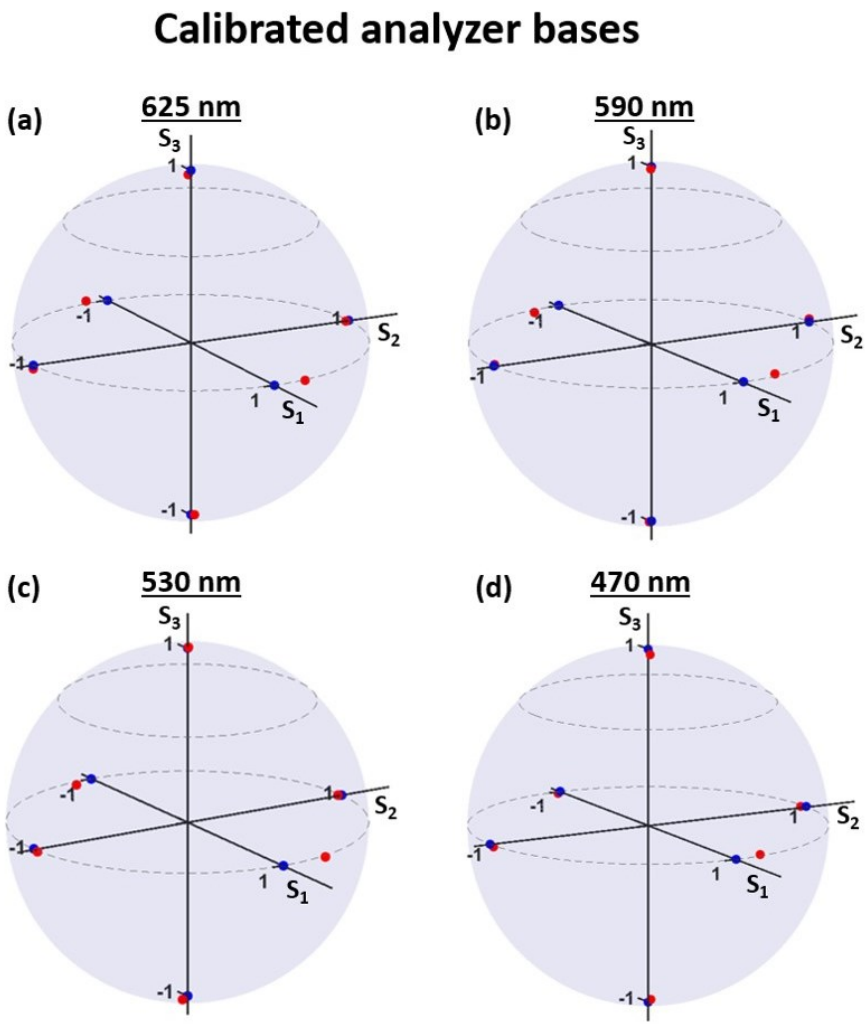

Figure 3-10. Experimental analyzer base calibrated at (a) 625 nm, (b) 590 nm, (c) 530 nm, and (d) 470 nm. Experimental analyzers are represented in red and the ideal (theoretical) ones in blue.

Our PSA presents some misalignments during its construction that impossibilities getting vertical and horizontal linear analyzers. The impossibility to reach these completely vertical and horizontal analyzers results in an increase of error propagation at measuring given polarized states (it is observed at comparing the CN values of the analyzer bases, Table 3-4, with the values obtained with the base of the generator, Table 3-3, which grow an ~8%). Nevertheless, the increase is more moderate at analyzing the overall error propagation, i.e., the EWV, which grows ~5%. Despite the increase of error propagation, the CN values of the analyzer bases are always lower than 2 and the EWV values lower than 8, both considered good values and ensuring a nice performance of the polarimeter.

Analyzer base	Optimal 6 SoPs base	625 nm base	590 nm base	530 nm base	470 nm base
CN	1.73	1.95	1.94	1.95	1.85
EWV	6.67	7.27	7.28	7.12	7.46

Table 3-4. Values of the CN and EWV metrics for the optimal 6 SoPs base and the experimental 625 nm, 590 nm, 530 nm, and 470nm calibrated bases for the PSA.

3.3.3 Experimental Mueller matrix image polarimeter validation

To validate the experimental calibration of the Mueller matrix image polarimeter implemented, we have measured a linear polarizer using the four wavelength channels of the instruments: 625 nm, 590 nm, 530 nm, and 470 nm. The normalized Mueller matrices of a horizontal linear polarizer measured with the different calibrated channels of the Mueller polarimeter are provided in Table 3-5. The values obtained at measuring the linear polarizer are slightly different from the theoretical ones [45],

$$M_{LP} = \begin{pmatrix} 1 & 1 & 0 & 0 \\ 1 & 1 & 0 & 0 \\ 0 & 0 & 0 & 0 \\ 0 & 0 & 0 & 0 \end{pmatrix} \tag{3.17}$$

where $\boldsymbol{M_{LP}}$ is the Normalized Mueller matrix of a horizontal linear polarizer. The value differences between the elements of the theoretical Mueller matrix and the elements of the measured matrices are provided in Table 3-6. Such differences are written as percentages of the element value range (the range goes from -1 to 1) and they are considered the experimental error produced at measuring the sample. To evaluate this error we have calculated the mean error made at measuring the elements of $\boldsymbol{M}$ (the error of the m_{00} element is not considered for this calculus) and the error related to the worst measured element. Using both metrics we observe that the error obtained with the 625nm, 590nm, and 530 nm channels is similar, while the error obtained with the 470 nm channel is almost double (see Table 3-6). It is in line with the mean DOP of the generator base (Table 3-2). In any case, the error produced at measuring a Mueller matrix element is smaller than 3%.

Channel	**625 nm**	**590 nm**
$\boldsymbol{M_{LP}}$	$\begin{pmatrix} 1 & 0.998 & 0.015 & 0.038 \\ 1.007 & 1.011 & 0.013 & 0.038 \\ -0.017 & -0.017 & -0.002 & -0.007 \\ -0.001 & -0.001 & 0.009 & 0.005 \end{pmatrix}$	$\begin{pmatrix} 1 & 0.996 & -0.002 & 0.034 \\ 0.983 & 0.982 & -0.002 & 0.034 \\ -0.017 & -0.018 & -0.002 & -0.006 \\ -0.007 & -0.007 & 0.004 & -0.002 \end{pmatrix}$
Channel	**530 nm**	**470 nm**
$\boldsymbol{M_{LP}}$	$\begin{pmatrix} 1 & 0.996 & 0.008 & 0.034 \\ 0.989 & 0.990 & 0.010 & 0.035 \\ -0.003 & -0.004 & -0.009 & -0.007 \\ -0.004 & -0.003 & 0.003 & -0.011 \end{pmatrix}$	$\begin{pmatrix} 1 & 1.012 & -0.019 & 0.059 \\ 0.954 & 0.971 & -0.015 & 0.054 \\ 0.007 & 0.010 & -0.006 & -0.004 \\ -0.044 & -0.046 & -0.003 & 0.003 \end{pmatrix}$

Table 3-5. Normalized Mueller matrix of a horizontal linear polarizer measured using the different calibrated channels (625 nm, 590 nm, 530 nm, and 470 nm) of the complete image Mueller polarimeter.

Channel	**625 nm**	**590 nm**	**530 nm**	**470 nm**
Mean error (%)	**0.60**	**0.59**	**0.52**	**1.19**
Absolute error (%)	**1.91**	**1.70**	**1.76**	**2.96**

Table 3-6. The mean and the absolute errors produced at measuring the element indices of the polarizer Mueller matrix with the calibrated image Mueller polarimeter.

In order to test the error of this set-up when measuring the birefringence of samples, we measured the total retardance of a quarter-waveplate (QWP) at 625 nm. The total retardance measured at 625 nm was 90.1 degrees (see Table 3-7), 0.1 degrees more than the theoretical value (90 deg). Afterward, we have measured the retardance of the same quarter-waveplate at 590 nm, 530 nm, and 470 nm wavelengths (see Table 3-7). As observed in Table 3-7, the retardance of the measured quarter-waveplate variates with the wavelength, being higher for shorter wavelengths. To evaluate the error associated with the measurement of total retardance, we have measured the total retardance of the same quarter-waveplate at the same wavelength (625 nm, 590 nm, 530 nm, and 470 nm) but with the commercial Thorlabs polarimeter (*PAX5710VIS-T*). The obtained results (Table 3-7) are taken as a reference and the difference between the measured retardances are associated with the error of our image Mueller polarimeter to measure the total retardance. The retardance difference at each wavelength is provided in Table 3-7. According to the obtained results, the error at measuring the total retardance of an optical element is always lower than 1.5 degrees.

Channel	625 nm	590 nm	530 nm	470 nm
Retardance measured with Mueller polarimeter (deg)	**90.1**	**98.8**	**110.2**	**132.4**
Retardance measured with commercial polarimeter (deg)	**91.5±0.5**	**98.3±0.5**	**111.2±0.5**	**131±0.5**
Retardance difference	**1.4**	**0.5**	**1**	**1.4**

Table 3-7. Retardance of a quarter-waveplate at 625 nm measured using the different calibrated channels (625 nm, 590 nm, 530 nm, and 470 nm) of the complete image Mueller polarimeter and the commercial Thorlabs *PAX5710VIS-T*. The difference in the measured retardance is also provided.

Although we have presented two optical elements to test the performance of the implemented polarimeter (linear polarizer and quarter-waveplate), it has been validated with a larger number of samples, dichroic and retarders at different orientations, and the error range obtained is represented by the two examples presented in this subsection.

Chapter 4 Analysis of polarimetric metrics for biophotonic applications

This chapter describes the experimental application of recently proposed polarimetric methods (as well as new ones) for the first time in biological tissues inspection. These methods have been analyzed through the measurement of phantom samples that try to mimic the properties of biological tissues. These samples present the advantage, in comparison with the regular biological tissue samples, that their structure is well-known thus easing the interpretation of the results. A better comprehension of these polarimetric techniques allows us to better understand some phenomena observed in the ex-vivo experiments performed in the next Chapter 5.

This chapter inspects the potential of two polarimetric techniques and accordingly it is divided into two main sections: the implementation of Polarization Gating (PG) techniques from measured Mueller matrices is described in section 4.1; and section 4.2 details the study and interpretation of two sets of depolarization parameters, the Indices of Polarimetric Purity (IPP) and the Components of Purity (CP), through *ad-hoc* synthesized depolarizers.

4.1 Polarization Gating and Mueller matrix relation

Polarimetric-based techniques can be used to obtain physical information from biological samples (such as tissue fiber orientation, tissue recognition, surface roughness, detection of spatial inhomogeneities, etc.), as well as to enhance the contrast of biomedical images. A group of polarimetric methods applied for biological tissue inspection is the so-called Polarization Gating (PG) techniques [48,79,81,82,84,85,110–116,145–148]. These techniques exploit the fact that the sample response may depend on the SoP of the light used to illuminate the sample. Usually, PG experiments are based on illuminating the sample with a certain polarization state and analyze the polarimetric sample response by using analyzers with the same polarization or with the orthogonal one (e.g. illuminating the sample with light horizontally polarized and analyzing the amount of horizontally or vertically polarized light of the sample response). This configuration is not restricted to linear polarization as some studies provide the interest of using circular and elliptical polarizations to improve the image contrast [110,111,145,148].

Another widespread group of polarimetric techniques is based on the measurement of the Mueller matrix and the analysis of the information encoded in the 16 real coefficients of that matrix [44–46]. These techniques, also widely used for tissue inspection [117–139], provide information about the birefringent, dichroic, and depolarizing behavior of samples and they are considered in the literature as a different approach than PG techniques.

In the following, we will demonstrate that the information obtained by PG and Mueller matrix-based methods is not independent, but PG can be derived from the measurements of the Mueller matrix. In particular, we will provide analytical expressions in which different PG configurations are written in terms of the 16 real coefficients of ***M*** (section 4.1.1). Next, we will experimentally validate these relations by performing a phantom experiment and comparing the results obtained at measuring certain PG configurations using the standard method with those obtained from the combination of measured ***M*** coefficients (section 4.1.2). The study comprises the analysis of different PG configurations based on linear and circular polarizations. Finally, we propose the combination of PG and ***M*** techniques this highlighting the advantages of using Mueller-based PG configurations in front of using the common PG techniques (section 4.1.3). These new combined techniques are discussed with two experiments: (1) a phantom and (2) an ex-vivo based experiments.

4.1.1 Mathematical derivation of polarization gating configurations from the Mueller matrix

In this subsection, we briefly describe some PG configurations commonly used for biomedical imaging and tissue inspection, and we also discuss the potential of this technique in that field (subsection 4.1.1.1). Afterward, we provide the analytical expression that relates the discussed PG configurations with the 16 real coefficients of ***M*** (subsection 4.1.1.2).

4.1.1.1 Polarization Gating configurations

When polarized light illuminates biological tissues we can distinguish different kinds of photons at light exiting the sample, depending on their optical path into the tissue (see Figure 4-1). Some of the photons are reflected at the surface of the tissue (according to ref. [148] we call them surface-reflected photons, S_L), and the others penetrate inside the sample, they being scattered by the tissue (Figure 4-1). The change in polarization, as well as, the optical path of the scattered photons will strongly depend on different parameters of the sample, such as the size of the tissue fibers, the wavelength of the photons, the polarization of the input light, among others. For that reason, the information about the characteristics of the sample and the information of some structures that may be placed inside the tissue sample is encoded in the detected photons due to light-matter interactions. In that sense, we can differentiate two types of scattered photons depending on their penetration depth: polarization maintaining photons, P_L, which reports the information related to superficial layers of the tissue, and photons reaching deeper layers of the sample, which are fully depolarized due to multiple scattering events (depolarized photons, D_L) (see Figure 4-1). Both groups of photons encode the information of the scattering events but in the case of D_L this information cannot be analyzed as the photons are fully depolarized, this leading to a loss of information (i.e., an entropy increase). As a consequence, P_L photons are very interesting in terms of tissue interpretation, as they usually provide the most significant information of the studied sample.

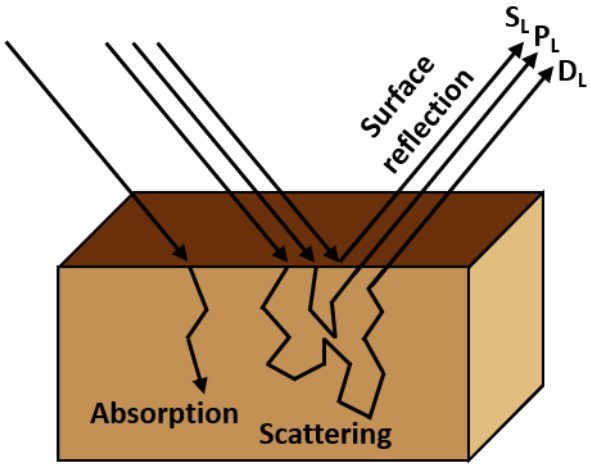

Figure 4-1. Scheme of photon interactions with biological tissues.

In the case of imaging tissue samples in reflection, the contribution of S_L, P_L, and D_L photons is mixed. The contribution of S_L photons is significantly reduced in the out-of-ballistic measurements, but a residual group of S_L photons is always present in tissue measurements due to inhomogeneities of the tissue surface that produce direct reflections in any arbitrary analyzing direction. Under this scenario, polarization gating techniques try to isolate the information of the P_L photons by eliminating the non-desired S_L and D_L contributions.

One typical PG configuration (let us label it as C1) consists of illuminating the sample with a vertical or horizontal linear polarization (e.g., horizontal polarization) and analyze the same type of polarization (horizontal polarization). This typical configuration removes half of the D_L contribution while maintaining the S_L, P_L, and the other half of the D_L contributions. Note that the contribution of the S_L is still present in the C1 configuration, but it can be removed by analyzing the orthogonal polarization (vertical polarization, following the same example). We label this cross linear configuration as C2. Images measured with that cross linear configuration efficiently filter the S_L contribution, most of the P_L contribution, and half of the D_L contribution, thus imaging half of the D_L photons. Now, by calculating the difference between C1 and C2 (C1-C2, let us call it LC) we completely remove the D_L photons thus obtaining images with only the S_L and P_L contributions. The image contrast of sample structures in LC images is improved concerning the contrast of C1 but it still presents S_L photons that degrade the final image contrast.

Recent studies propose the use of the same configurations but using circular or elliptical polarizations to improve the quality of the final image [110,111,145,148]. Unlike the case of linear polarizations, when using elliptical or circular polarizations for the input beam, the polarization of photons surface reflected becomes the orthogonal one. Therefore, considering elliptical light, the PG configuration analogous to C1 (co-elliptical configuration, let us call it C3) filter the S_E contribution (subindex E means elliptical polarization) and half of the D_E contribution thus measuring a mix of P_E and D_E photons. On the other hand, the PG configuration analogous to C2 (cross-elliptical configuration, let us call it C4) mostly eliminates the P_E contribution and reduces the contribution of D_E to the half but imaging the S_E instead and part of the D_E photons. The C3 and C4 difference (C3-C4, let us call it EC) measures only the contribution of S_E and P_E like the LC configuration. However, elliptically and circularly polarized light hold the polarization

state during more scattering events compared with the linearly polarized light thus being better suited for the analysis of deeper structures [148]. Note that in the case of using PG configuration based on diagonal linear polarized light (let us call them $C1_{45}$ and $C2_{45}$, respectively for co and cross configurations), the surface reflection of diagonally polarized light is also orthogonal thus the measured photons are analogous to the ones measured with the C3 and C4 configurations (i.e., P_L and D_L for $C1_{45}$, and S_L and D_L for $C2_{45}$).

Other approaches combine PG measurements based on circular and linear polarized light to improve the contrast of the final image [148]. In ref. [148], the authors propose the combination of the LC and EC techniques to eliminate the contribution of the photons reflected at the surface (S_L and S_E). In particular, they suggest calculating the sum of LC and EC ([C1-C2]+[C3-C4]= P_L+S_L+P_E-S_E) but adding a constant β multiplying the LC term to compensate the difference of light surface reflected between linear and elliptical polarizations (Eq. (4.1)). Note that the value of the constant β must be experimentally determined for each ellipticity and each kind of sample.

$$f = \beta[C1 - C2] + [C3 - C4] \tag{4.1}$$

By properly determining the value of β within the function *f*, the contributions of the S_L and S_E photons, together with the D_L and D_E photons are removed, and the images show only the combination of polarization-maintaining photons P_L and P_E.

4.1.1.2 Derivation of the analytical expressions of polarization gating configurations by using the Mueller matrix formalism

The PG configurations that have been presented in the previous section are devised to highlight the polarization response of samples after controlled light-matter interactions, this improving the sample image contrast. These interactions can be described by using the Mueller-Stokes formalism [200,201], as shown in Chapter 2. In that way, the polarization response of the sample to a given input polarized light can be written in terms of ***M*** as shown in Eq. (2.4) and written in terms of the ***M*** coefficients as indicated in the following expression (the SoP of light can be defined in terms of the azimuth angle (α) and the elliptical angle (ε) as described in Eq. (2.3)):

$$\boldsymbol{S}_{out} = \boldsymbol{M}\cdot\boldsymbol{S}_{in} = \begin{pmatrix} m_{00} + m_{01}\cos 2\varepsilon\cos 2\alpha + m_{02}\cos 2\varepsilon\sin 2\alpha + m_{03}\sin 2\varepsilon \\ m_{10} + m_{11}\cos 2\varepsilon\cos 2\alpha + m_{12}\cos 2\varepsilon\sin 2\alpha + m_{13}\sin 2\varepsilon \\ m_{20} + m_{21}\cos 2\varepsilon\cos 2\alpha + m_{22}\cos 2\varepsilon\sin 2\alpha + m_{23}\sin 2\varepsilon \\ m_{30} + m_{31}\cos 2\varepsilon\cos 2\alpha + m_{32}\cos 2\varepsilon\sin 2\alpha + m_{33}\sin 2\varepsilon \end{pmatrix}. \tag{4.2}$$

where $\boldsymbol{S}_{out}$ is the Stokes vector describing the polarization of light exiting from the sample. Afterward, the $\boldsymbol{S}_{out}$ response is projected on the polarization analyzer as described in section 3.2. In the case of experimental PG measurements, only one analyzer is used. The analyzer of the PG configurations is usually set equal to the input polarization (let us call $\boldsymbol{A}_{co\text{-}elliptical}$, related to the co-elliptical configuration) or orthogonal to the input polarization (let us call $\boldsymbol{A}_{cross\text{-}elliptical}$). According to Eq. (3.1) the intensity measured with the co-elliptical configuration is written in terms of ***M*** coefficients as follows,

$$
\begin{aligned}
&I_{co-elliptical} = \mathbf{A}_{co-elliptical} \cdot \mathbf{S}_{out} = m_{00} + m_{01}\cos 2\varepsilon \cos 2\alpha + m_{02}\cos 2\varepsilon \sin 2\alpha + \\
&m_{03}\sin 2\varepsilon + m_{10}\cos 2\varepsilon \cos 2\alpha + m_{11}\left(\cos 2\varepsilon \cos 2\alpha\right)^2 + m_{12}\left(\cos 2\varepsilon\right)^2 \cos 2\alpha \sin 2\alpha + \\
&m_{13}\cos 2\varepsilon \cos 2\alpha \sin 2\varepsilon + m_{20}\cos 2\varepsilon \sin 2\alpha + m_{21}\left(\cos 2\varepsilon\right)^2 \cos 2\alpha \sin 2\alpha + \\
&m_{22}\left(\cos 2\varepsilon \sin 2\alpha\right)^2 + m_{23}\cos 2\varepsilon \sin 2\alpha \sin 2\varepsilon + m_{30}\sin 2\varepsilon + \\
&m_{31}\cos 2\varepsilon \cos 2\alpha \sin 2\varepsilon + m_{32}\cos 2\varepsilon \sin 2\alpha \sin 2\varepsilon + m_{33}\left(\sin 2\varepsilon\right)^2,
\end{aligned}
\tag{4.3}
$$

where $\boldsymbol{A}_{co\text{-}elliptical}$ is the $\boldsymbol{S}_{in}$ transpose vector and $I_{\text{co-elliptical}}$ is the intensity corresponding to the projection of S_{out} on $\boldsymbol{A}_{co\text{-}elliptical}$.

A similar operation but projected on the cross-elliptical analyzer ($\boldsymbol{A}_{cross\text{-}elliptical}$) is performed for PG configurations with orthogonally polarized detectors. The analyzer corresponding to the orthogonal polarization is obtained by applying the following transformations to the co-elliptical analyzer, $\boldsymbol{A}_{co\text{-}elliptical}$: $\varepsilon \rightarrow -\varepsilon$ and $\alpha \rightarrow \alpha + \pi/2$. The intensity resulting from this configuration becomes,

$$
\begin{aligned}
&I_{cross-elliptical} = \mathbf{A}_{cross-elliptical} \cdot \mathbf{S}_{out} = \begin{pmatrix} 1 & -c\cos 2\varepsilon \cos 2\alpha & -\cos 2\varepsilon \sin 2\alpha & -\sin 2\varepsilon \end{pmatrix} \cdot S_{out} = \\
&m_{00} + m_{01}\cos 2\varepsilon \cos 2\alpha + m_{02}\cos 2\varepsilon \sin 2\alpha + m_{03}\sin 2\varepsilon - m_{10}\cos 2\varepsilon \cos 2\alpha - \\
&m_{11}\left(\cos 2\varepsilon \cos 2\alpha\right)^2 - m_{12}\left(\cos 2\varepsilon\right)^2 \cos 2\alpha \sin 2\alpha - m_{13}\cos 2\varepsilon \cos 2\alpha \sin 2\varepsilon - \\
&m_{20}\cos 2\varepsilon \sin 2\alpha - m_{21}\left(\cos 2\varepsilon\right)^2 \cos 2\alpha \sin 2\alpha - m_{22}\left(\cos 2\varepsilon \sin 2\alpha\right)^2 - \\
&m_{23}\cos 2\varepsilon \sin 2\alpha \sin 2\varepsilon - m_{30}\sin 2\varepsilon - m_{31}\cos 2\varepsilon \cos 2\alpha \sin 2\varepsilon - \\
&m_{32}\cos 2\varepsilon \sin 2\alpha \sin 2\varepsilon - m_{33}\left(\sin 2\varepsilon\right)^2.
\end{aligned}
\tag{4.4}
$$

Finally, we calculate the difference between Eqs. (4.3) and (4.4) to write the EC configuration in terms of the $\boldsymbol{M}$ coefficients.

$$
\begin{aligned}
&I_{co-elliptical} - I_{cross-elliptical} = 2\cos 2\varepsilon\left[m_{10}\cos 2\alpha + m_{20}\sin 2\alpha\right] + \\
&2\left(\cos 2\varepsilon\right)^2\left[m_{11}\left(\cos 2\alpha\right)^2 + m_{22}\left(\sin 2\alpha\right)^2 + \cos 2\alpha \sin 2\alpha\left(m_{12} + m_{21}\right)\right] + \\
&+2\cos 2\varepsilon \sin 2\varepsilon\left[\cos 2\alpha\left(m_{13} + m_{31}\right) + \sin 2\alpha\left(m_{23} + m_{32}\right)\right] + 2\sin 2\varepsilon\left[m_{30} + m_{33}\sin 2\varepsilon\right]
\end{aligned}
\tag{4.5}
$$

According to Eqs. (4.3), (4.4) and (4.5), it is possible to retrieve the different PG configurations that have been described in the previous section from the measured $\boldsymbol{M}$ coefficients by properly selecting the ε and α values. Therefore, the measurement of the experimental Mueller matrix equals the measurement of any experimental PG configuration and any PG combination, becoming then, a more general approach.

In the following, we will derive the specific PG configurations that have been presented in the previous section 4.1.1.1 in terms of the $\boldsymbol{M}$ coefficients. Let us start with the linear configurations, that correspond to the cases where the ellipticity is zero (ε=0°). The example of $C1_{45}$ and $C2_{45}$ configurations provided in section 4.1.1.1 consists of illuminating the sample with diagonally polarized light (α=45°), so ε and α are substituted accordingly in Eqs. (4.3) and (4.4), this leading to the next expressions,

$$
I_{co-elliptical}(\varepsilon = 0, \alpha = 45°) = C1_{45} = m_{00} + m_{02} + m_{20} + m_{22} \tag{4.6}
$$

and

$$I_{cross-elliptical}(\varepsilon=0,\alpha=45°)=C2_{45}=m_{00}+m_{02}-m_{20}-m_{22}. \tag{4.7}$$

The difference between these two expressions (Eqs. (4.6) and (4.7)) leads to the LC_{45} configuration expression,

$$LC_{45}=C1_{45}-C2_{45}=2[m_{20}+m_{22}]. \tag{4.8}$$

Next, we derive the C3, C4, and EC expressions in terms of the measured ***M*** coefficients. In that way, we select elliptically polarized PG configuration with arbitrary ellipticity, ε, but with an azimuth angle defined equal to α=45°. Therefore, we substitute these parameters in Eqs. (4.3), (4.4), and (4.5), this reducing the expressions to,

$$\begin{aligned}&I_{co-elliptical}(\varepsilon,\alpha=45°)=C3=m_{00}+\cos 2\varepsilon\left[m_{02}+m_{20}\right]+\\&\sin 2\varepsilon\left[m_{03}+m_{30}\right]+\cos 2\varepsilon\sin 2\varepsilon\left[m_{23}+m_{32}\right]+m_{22}\left(\cos 2\varepsilon\right)^2+m_{33}\left(\sin 2\varepsilon\right)^2,\end{aligned} \tag{4.9}$$

$$\begin{aligned}&I_{cross-elliptical}(\varepsilon,\alpha=45°)=C4=m_{00}+\cos 2\varepsilon\left[m_{02}-m_{20}\right]+\\&\sin 2\varepsilon\left[m_{03}-m_{30}\right]-\cos 2\varepsilon\sin 2\varepsilon\left[m_{23}+m_{32}\right]-m_{22}\left(\cos 2\varepsilon\right)^2-m_{33}\left(\sin 2\varepsilon\right)^2,\end{aligned} \tag{4.10}$$

and

$$\begin{aligned}&I_{co-elliptical}(\varepsilon,\alpha=45°)-I_{cross-elliptical}(\varepsilon,\alpha=45°)=C3-C4=\\&2\cos 2\varepsilon\left[m_{20}+m_{22}\cos 2\varepsilon\right]+2\cos 2\varepsilon\sin 2\varepsilon\left[\left(m_{23}+m_{32}\right)\right]+2\sin 2\varepsilon\left[m_{30}+m_{33}\sin 2\varepsilon\right].\end{aligned} \tag{4.11}$$

Note that we can calculate an arbitrary elliptical PG configuration by changing the ε parameter in Eqs. (4.9), (4.10), and (4.11). As expected, for ε=0°, the expressions correspond to the linear case (Eqs. (4.6), (4.7), and (4.8)). Alternatively, for ε= 45°, we end up with the following expressions that correspond to circularly polarized PG configurations,

$$I_{co-elliptical}(\varepsilon=45°)=C3=m_{00}+m_{03}+m_{30}+m_{33}, \tag{4.12}$$

$$I_{cross-elliptical}(\varepsilon=45°)=C4=m_{00}+m_{03}-m_{30}-m_{33}, \tag{4.13}$$

and

$$I_{co-elliptical}(\varepsilon=45°)-I_{cross-elliptical}(\varepsilon=45°)=C3-C4=2[m_{30}+m_{33}]. \tag{4.14}$$

It is worth noting that the expressions of circularly polarized PG configurations do not depend on the α value as circular polarization is independent of this parameter.

Finally, by following the same formulation, we can obtain the analytical expression of the function *f* (defined in Eq. (4.1)) in terms of the ***M*** coefficients. Accordingly, Eq. (4.1) becomes,

$$\begin{aligned}&f=\beta\cdot[C1-C2]+[C3-C4]=\beta\cdot[I_{co-elliptical}(\varepsilon=0,\alpha=0)-I_{cross-elliptical}(\varepsilon=0,\alpha=0)]+\\&[I_{co-elliptical}(\varepsilon,\alpha=0)-I_{cross-elliptical}(\varepsilon,\alpha=0)]=2\beta\left[m_{10}+m_{11}\right]+\\&2\cos 2\varepsilon\left[m_{10}+\cos 2\varepsilon m_{11}\right]+2\cos 2\varepsilon\sin 2\varepsilon\left[\left(m_{13}+m_{31}\right)\right]+2\sin 2\varepsilon\left[m_{30}+m_{33}\sin 2\varepsilon\right].\end{aligned} \tag{4.15}$$

4.1.2 Experimental polarization gating configurations based on measured Mueller matrices

Once the expression that relates the PG configurations with the ***M*** coefficients has been derived, such expression can be used to obtain multiple PG configurations from the experimentally measured Mueller matrix of a sample. In principle, as theoretically demonstrated in the previous section, the results obtained with this method should be the same as measuring a certain PG configuration. In this section, we measure a reference sample by using the two discussed methods, PG configuration and Mueller-based PG configuration, and we analyze the differences between the results obtained from both methods to experimentally probe the theoretical relation above-presented.

As a reference sample, we take a tank filled with intralipid diluted in water and a ruler submerged obliquely in that tank (see Figure 4-2). In particular, we use a plastic tank sized 15.5 cm × 7.5 cm × 5 cm that is filled with intralipid (20%, Sigma-Aldrich, France) diluted in water with a concentration of 0.1%. Intralipid is an emulsion of soybean oil, egg phospholipids, and glycerin currently used to provide calories to humans through an intravenous. In this experiment, the intralipid dilution mimics the scattering properties of real biomedical tissues, e.g. human skin. According to ref. [110], under this concentration of intralipid, we mimic a tissue with a sample penetration depth at the millimeter scale.

The optical properties of this intralipid dilution variates in time due to the segregation of lipids and our Mueller polarimeter can only measure stationary samples. However, the segregation process of this solution evolves slowly, taking times of few hours while the polarimetric measurements are performed in seconds to a minute depending on the PG method employed. Therefore, we can assume that the optical properties of the intralipid dilution remain constant during the measurement process.

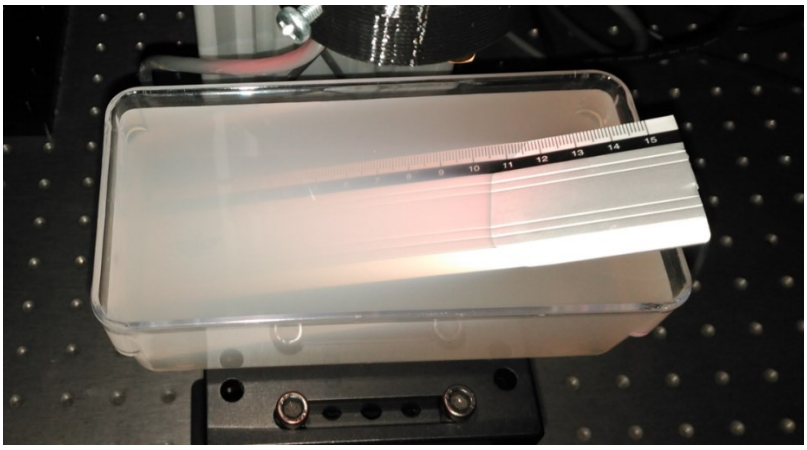

Figure 4-2. Reference sample consisting of a tank filled with intralipid diluted in water and a ruler submerged obliquely.

The measurements are performed using the image Mueller polarimeter described in Chapter 3. For this experiment, we used the red channel, 625 nm, as its penetration depth is the largest among the available channels. To analyze the viability of the proposed Mueller-based PG technique we measured the sample in two configuration regimes. On the one hand, we use the imaging polarimeter to measure the Mueller matrix of the sample in reflection following the

procedure described in section 3.2. Afterward, following the Eqs. (4.6), (4.7), (4.12), and (4.13), we calculate the $C1_{45}$, $C2_{45}$, C3, C4, $C1_{45}$-$C2_{45}$, and C3-C4 PG configurations from the measured Mueller matrix (Figure 4-3 (a), (c), (e), (g), (i), and (k), respectively). On the other hand, the same set-up is used to measure the same PG configuration but using the standard process (direct Polarization Gating configuration) for the comparison (Figure 4-3 (b), (d), (f), (h), (j), and (l), respectively). The standard method of measuring PG configurations is similar to the process of measuring the Mueller matrix but with three remarkable differences: (1) the sample is illuminated with only one SoP instead of the six used for the ***M*** measurement; (2) only one SoP, the same or the orthogonal, is analyzed, instead of the six analyzers used for the ***M*** measurement; and (3) standard PG configurations do not require mathematical post-processing. These differences involve a reduction of the measurement time to the point of allowing real-time acquisitions.

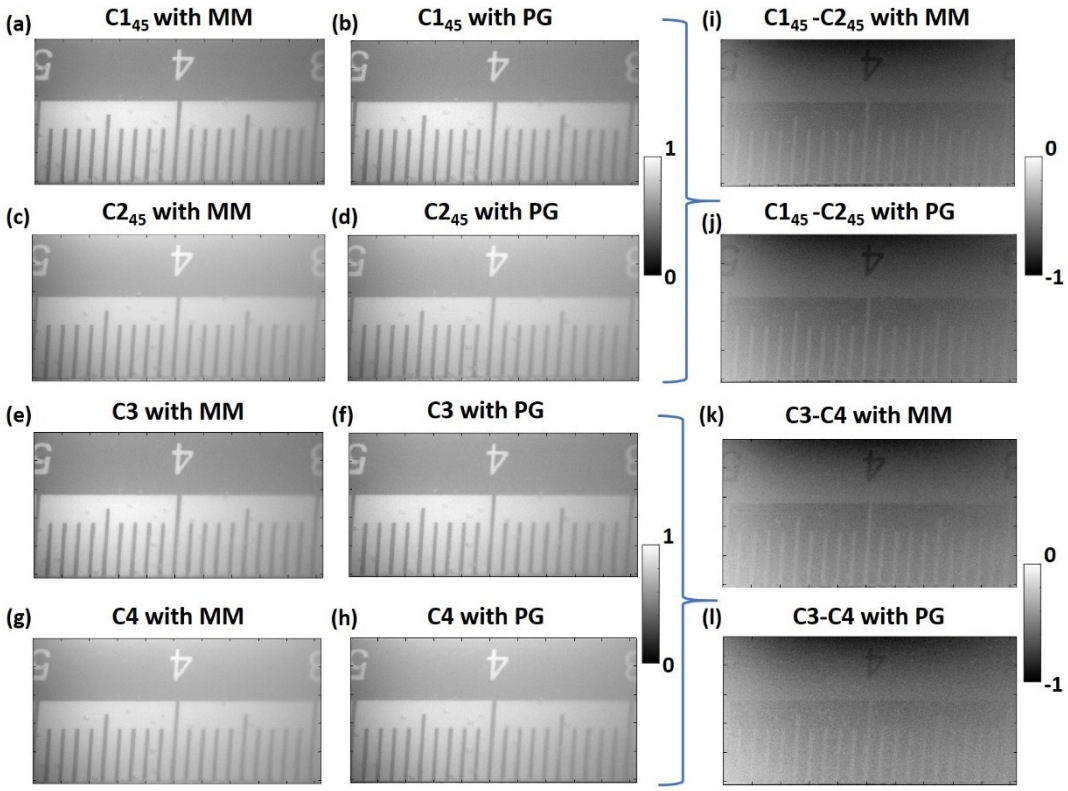

Figure 4-3. Images of different PG configurations of the ruler submerged obliquely within an intralipid dilution obtained from ***M*** coefficients (a, c, e, g, i, and k); and standard PG procedures (b, d, f, h, j, and l).

Images obtained from two methods (standard PG and ***M***-based PG) are shown in Figure 4-3. To ease the comparison of the results, the images have been normalized. For the normalization, pixels have been divided by the highest absolute intensity value of their corresponding image. In the case of configurations based on processing the difference between two images ($C1_{45}$-$C2_{45}$ and C3-C4), their calculation is carried out with the non-normalized $C1_{45}$, $C2_{45}$, C3, and C4 images, and the normalization is applied after that operation. Note that most normalized images take values from 0 to 1 except the $C1_{45}$-$C2_{45}$ and C3-C4 images that take values from 0 to -1. The negative values of the $C1_{45}$-$C2_{45}$ and C3-C4 images come from the greater amount of orthogonally polarized surface reflection photons, S_L and S_E, associated with diagonal and

circularly-polarized illumination, regarding the polarization-maintaining scattered photons P_L and P_E. The orthogonally polarized photons are filtered in the $C1_{45}$ and C3 configurations but detected in the $C2_{45}$ and C4 configurations. In contrast, $C1_{45}$ and C3 measure the polarization-maintaining photons P_L and P_E that are filtered in the cross-elliptical channels. As the amount of polarization-maintaining photons is lower than the number of photons reflected at the surface of the measured sample, cross-elliptical ($C2_{45}$ and C4) images present higher intensity values than co-elliptical ones ($C1_{45}$ and C3), and, accordingly, their difference ($C1_{45}$-$C2_{45}$ and C3-C4) take negative values.

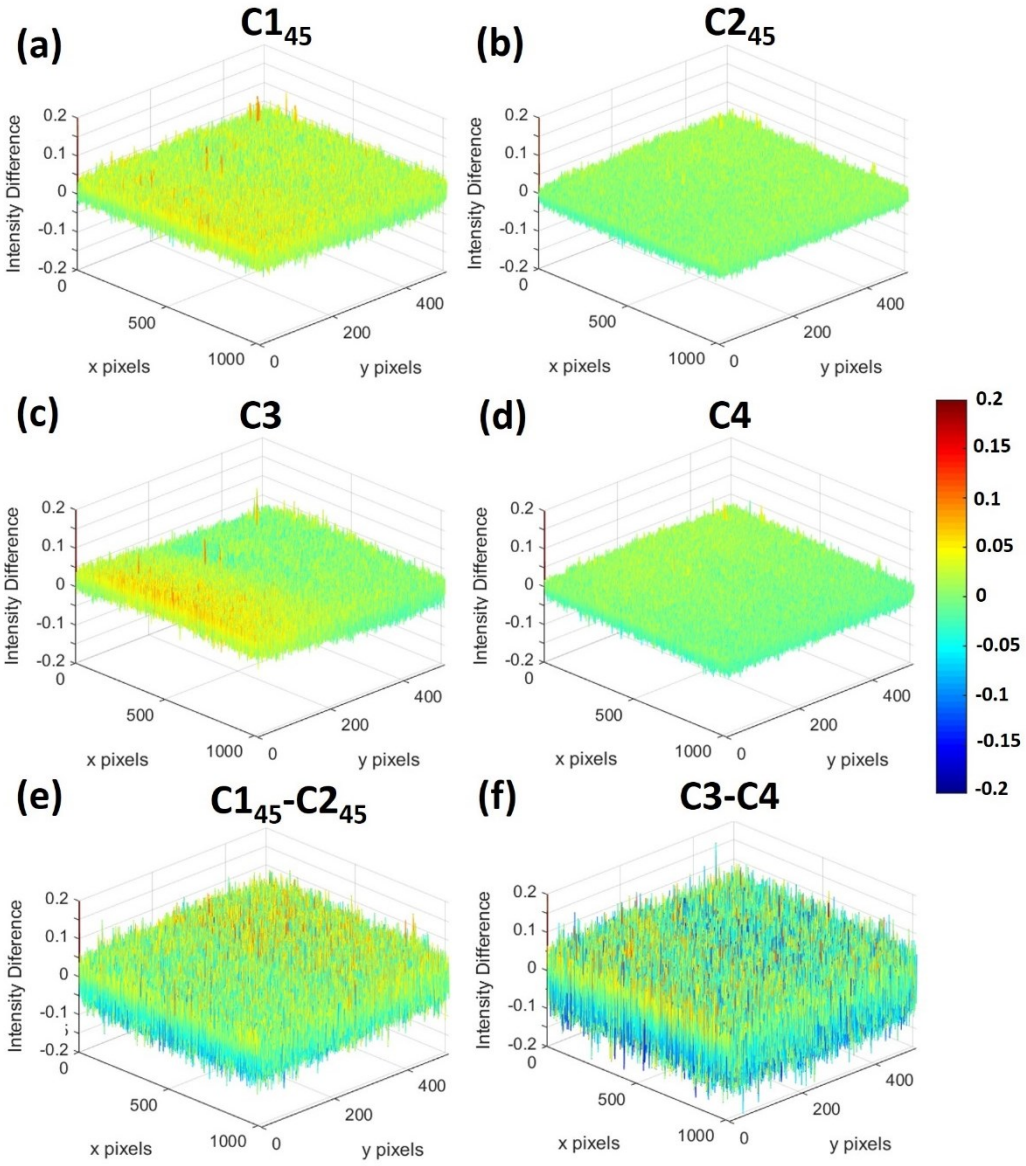

Figure 4-4. Intensity difference between the normalized images of Mueller-based and standard PG configurations: (a) $C1_{45}$, (b) $C2_{45}$, (c) C3, (d) C4, (e) $C1_{45}$-$C2_{45}$, and (d) C3-C4.

Figure 4-3 shows that the results obtained from combining the ***M*** coefficients and the ones obtained with standard PG techniques are equivalent, as can be see from the similarity between corresponding images. To quantify the similitude of the results, we evaluate the direct

difference between each pair of normalized images that represent the same PG configuration. Figure 4-4 shows the pixel-to-pixel intensity difference between normalized images of Mueller-based and standard PG configurations. In the case of directly measured PG channels ($C1_{45}$, $C2_{45}$, C3, and C4) the absolute difference values are lower than 0.05, being an error lower than the 5% of the intensity range of the image (normalized images that take values from 0 to 1). We mainly attribute these differences to random noise in the intensity measurement. For the C1-C2 and C3-C4 configurations, the absolute difference takes higher values than the directly measured PG channels, but they are lower than 0.1 (10% of the intensity range). The increment of the error values observed in the C1-C2 and C3-C4 configurations are attributed to the error propagation linked to their C1-C2 and C3-C4 operation.

To further quantify the differences obtained by using the ***M***-based technique in front of using the standard PG configuration method, the mean values of the absolute intensity difference between Figure 4-3 images are calculated and provided in Table 4-1. The mean absolute intensity differences are lower than 0.05 (5%) for all the measured configurations, being lower than 0.02 (2%) for the directly measured PG channels ($C1_{45}$, $C2_{45}$, C3, and C4, see Table 4-1). The standard deviations (σ) corresponding to the absolute intensity difference in images shown in Figure 4-4 are also provided in Table 4-1. The error fluctuations pixel-to-pixel, which is quantified through the standard deviation (σ), take values around 75% of their corresponding mean intensity differences. Taking into account that the standard deviation is calculated using the absolute value, thus avoiding negative values, the standard deviation results fit the values expected for random noise.

PG configuration	Mean absolute intensity difference	σ
$C1_{45}$	**0.018**	**0.013**
$C2_{45}$	**0.010**	**0.008**
C3	**0.020**	**0.014**
C4	**0.012**	**0.009**
$C1_{45}$-$C2_{45}$	**0.026**	**0.020**
C3-C4	**0.041**	**0.031**

Table 4-1. Mean absolute intensity difference and standard deviation (σ) for the different PG configurations analyzed in Figure 4-4.

The latter-described experimental results show the equivalence between standard PG configurations and the same PG configurations obtained from the ***M*** coefficients, validating the theoretical results presented in subsection 4.1.1. The only difference between these techniques is associated with measurement noise. However, noise errors can be reduced by time-averaging different intensity images for both methods. In addition, the errors can be reduced even more for Mueller matrix measurement by generating and analyzing more than 6 SoPs (i.e., adding data redundancy in the Mueller matrix determination process).

4.1.3 Combination of Polarization gating and Mueller matrix techniques

Up to now, we have evidenced the equivalence between ***M***-based and standard PG configurations. Hereafter we explore some advantageous properties of the Mueller matrix that

lead to new PG applications. First, through the study of different phantom experiments, we analyze the scope of using a single measurement, the determination of the ***M*** coefficients, to calculate (without the necessity of measuring) a wide number of PG configurations through phantom experiments. Second, we propose a new technique that combines the Lu-Chipman decomposition [66] and the PG formalism presented in 4.1.1. This new technique is used to enhance the image contrast of an *ex-vivo* sample (chicken neck).

4.1.3.1 PG dependence with the ellipticity (Phantom experiment)

First, we want to note that by using the standard PG method, each new PG configuration that wants to be implemented requires conducting new measurements. Conversely, with the new proposed approach, arbitrary PG configurations can be directly calculated by properly operating the Mueller matrix coefficients without needing new extra experimental measurements. As an example, we use the measured Mueller matrix of the ruler submerged obliquely in an intralipid dilution to implement the function *f* (Eq. (4.15)). For this example, we use β=1 and we do not restrict the analysis to one particular ellipticity (ε) value, but we compute all the ellipticities from ε=-45° to ε=+45° with 1° steps. This leads to the calculation of 182 PG configurations (91 measurements for C3 configurations with different values of ε + 91 measurements for C4 configurations with different values of ε; note that C1 and C2 configurations are particular cases of C3 and C4 PG configurations with ε=0°). Importantly, if the standard PG method were used, 182 experimental measurements should be done to perform the equivalent experiment. As illustrative examples, Figure 4-5 (a) and (b) show the images obtained for the cases corresponding to ε=+22.5° and ε=0°, respectively. The image associated with ε=+22.5° (Figure 4-5 (a)) is better contrasted than the obtained for ε=0° (Figure 4-5 (b)), so the image contrast present certain dependence with the ellipticity ε selected for the PG configuration. This is connected with the polarimetric differences between S_L and S_E photons and the higher penetration depth of circularly polarized photons [145,148].

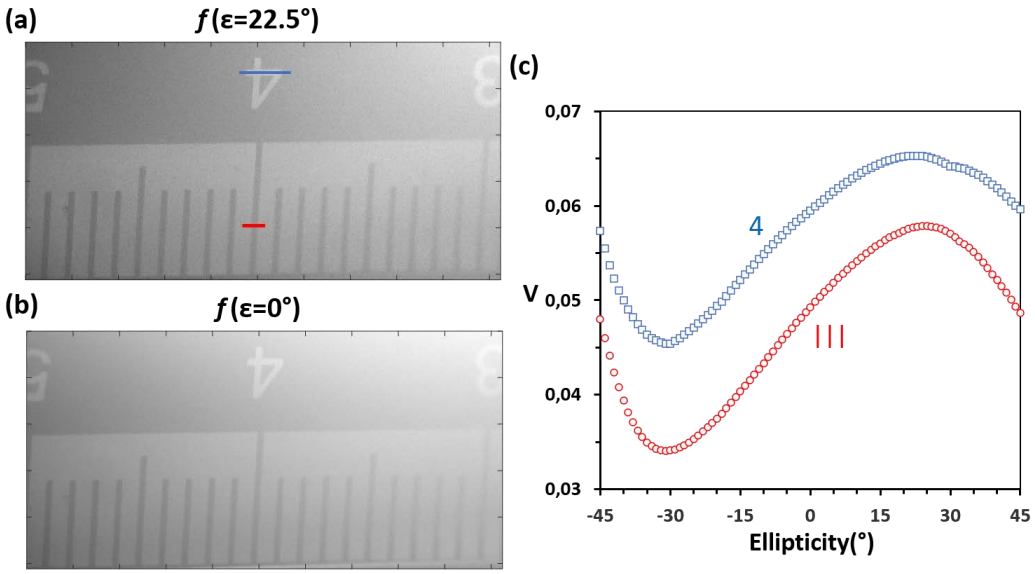

Figure 4-5. Image of *f* PG configuration with β=1 for (a) ε=22.5° and (b) ε=0°. (c) Visibility (V) vs ellipticity angle (ε) for the number 4 and a ruler millimeter tick mark. The cross-sections of the number 4 and the ruler millimeter tick mark are represented with blue and red lines.

To quantify the image contrast observed at different regions of the sample we compute the visibility *V* (Eq.(4.16)) for two cross-sections placed at the number 4 and at a ruler tick mark, respectively (see Figure 4-5 (a)).

$$V = \frac{I_{\max} - I_{\min}}{I_{\max} + I_{\min}} \tag{4.16}$$

where $I_{\max}$ and $I_{\min}$ are the maximum and minimum intensity values of the cross-section.

The dependence of the visibility with the ellipticity for the two cross-sections is plotted in Figure 4-5 (c). Figure 4-5 (c) reveals that the best visibility values are obtained using $\varepsilon \approx 22.5°$. Usually, PG experiments are restricted to configurations based on linear or circular polarizations due to their simplicity. However, other non-explored polarizations can provide better results in terms of image contrast, as seen in this example with $\varepsilon \approx 22.5°$. In addition, the particular experiments that operate with circularly or elliptically polarized light are commonly restricted to the use of positive ellipticities, considering that the results obtained with negative ellipticities are equivalent. However, Figure 4-5 (c) shows that the visibility for $\varepsilon = -30°$ is smaller than the one obtained with $\varepsilon = 30°$. Therefore, the results obtained using negative ellipticities have not to be equal to their corresponding positive ellipticities.

The last phenomenon is emphasized when measuring the same ruler submerged in intralipid but with two cellophane tapes stuck in different orientations (see Figure 4-6). Cellophane tapes are linear retarders with certain birefringence that depends on their thickness and that is related to the tensions of the constituent polymers introduced during the fabrication process. For this experiment, we measure the sample by using the standard PG method with the red channel (625-nm light). In particular, we measure the standard C3-C4 PG configuration by illuminating the sample with right-handed circularly polarized light (Figure 4-6 (c)) and with left-handed circularly polarized light (Figure 4-6 (d)). Figure 4-6 (c) and (d) present three differentiated regions that are not observed in the previous PG measurements (Figure 4-3). These differentiated regions are the result of combining cellophane retarders with different orientations that induce distinct polarization variations. Note that these regions are differently contrasted by using the equivalent positive and negative ellipticities (ε=+45°, right-handed circular light, and ε=-45°, left-handed circular light), like the observed in the previous experiment for ε=±30° (Figure 4-5 (c)). However, in this new experiment, the differences are observed when using the traditional and standard PG method, so the differences cannot be attributed to any artifact coming from the computational process associated with the ***M***-based PG technique.

The visibility of the number 4 in C3-C4 images is an extreme example of that phenomenon. It is clearly visible for the right-handed circular PG configuration (Figure 4-6 (c)), but it is completely indistinguishable when using the left-handed circular PG configuration (Figure 4-6 (d)). To highlight the image differences, Figure 4-6 (b) shows the intensity values of the cross-sections respectively marked with black and red lines in Figure 4-6 (c) and (d). The cross-section values obtained with ε=+45° are represented with black empty squares and the values associated with ε=-45° are drawn with red-filled circles. Both PG configurations are characterized by linear distributions that tend to zero as the ruler goes deeper into the intralipid dilution. To highlight the linear distributions, we have drawn the linear regression associated with ε=-45° and ε=+45° (red and black lines, respectively). The data behavior distribution related

to the contrast obtained with ε=+45° (black squares) is distinguished from ε=-45° case (red circles) for describing a sharp jump related to the contrast associated to the visible number 4 (difference in the cross-section between the polarimetric response of the pixels into the number 4 with those associated to the background). This occurs because the polarization that comes from the interaction of circularly and elliptically polarized light with linear retarders (as cellophane tapes) is usually different when using incident light with positive helicity compared to the use of light with negative helicity. For example, the interaction of right-handed circularly polarized light with a quarter-wave plate retarder may result in horizontally polarized light, while the left-handed polarized light ends in vertically polarized light at interacting with an equally oriented quarter-wave plate retarder. In addition, the dissimilar polarization modification of retarders must be combined with any anisotropic behavior of the ruler itself. Therefore, different helicities must be explored at measuring PG configurations to probe that some information is not missed in the arbitrary selection of the helicity.

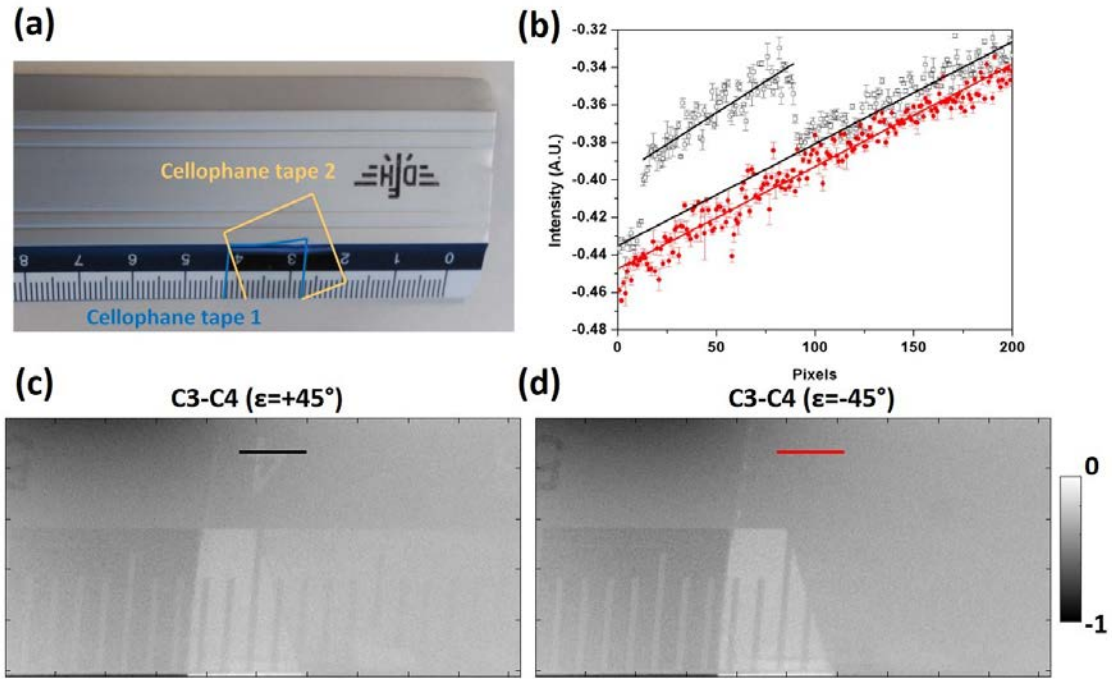

Figure 4-6. (a) Ruler with two stuck cellophane tapes. (b) Cross-section values of the black and red lines of pictures (c) (black empty squares) and (d)(red-filled circles). Images of C3-C4 PG configuration for (c) right-handed and (d) left-handed circularly polarized light.

The results shown in this subsection prove that the use of PG configurations obtained from the Mueller matrix of the sample, give access to a wide number of polarization gating configurations, as all possible PG configurations can be easily simulated, without the necessity of experimentally implementing each one of them (as occurs with standard PG methods). This is a very useful result, as usually, only few well-known PG configurations are experimentally implemented in applications (typically, co-linear, cross-linear, co-circular, and cross-circular), and we have probed that maximum contrast of certain structures can be obtained by particular elliptical based PG configuration, that can be easily tested with the proposed approach.

4.1.3.2 PG configuration based on Lu-Chipman matrices (*Ex-vivo* experiment)

At this point, we have already that the ***M***-based approach is a generalization of the standard PG technique and we have also proved the importance of using different ellipticities in the PG configurations. In this subsection, we propose a technique that combines the above-discussed PG configurations with the Mueller matrix decompositions. This new technique is discussed through the inspection of an ex-vivo chicken neck (Figure 4-7). In particular, we have analyzed a region of interest (ROI, squared in red in Figure 4-7) that contains different biological structures such as muscles and nerves. It is worth noting that muscles and nerves are fibrous based structures so their polarimetric properties tend to be anisotropic, i.e., their interaction with light usually variates with the orientation of the incident polarized light.

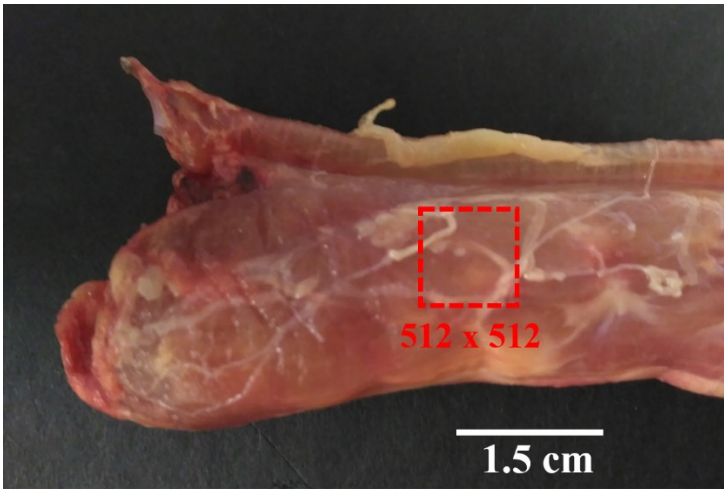

Figure 4-7. Inspected *ex-vivo* chicken neck. The red square delimits the imaged region of interest.

The technique we propose starts with the measurement of the Mueller matrix of the sample. We measured the ***M*** of the *ex-vivo* sample using the 470 nm light because larger wavelengths, as 625 nm, enters deeper into the sample than shorter ones [11], and we mainly want to inspect biological structures placed at the surface of the sample. Figure 4-8 (a) shows the experimental Mueller matrix of the chicken neck. As can be observed in Figure 4-8 (a), the contrast of the biological structures included in the imaged ROI, as muscles and nerves, varies between the different image coefficients. The image coefficients of the measured ***M*** are individually normalized by their maximum value and the mean values of each coefficient are provided at the left of the image to illustrate the weight of each coefficient. The first coefficient (m_{00}) is the reflectance of the sample for unpolarized input states and their values are always bigger than the other coefficients. For this sample, the mean value of m_{00} is more than 6 times bigger than the highest mean value of the other matrix coefficients (see Figure 4-8) so we deal with a sample with a non-negligible depolarizing behavior. Conversely, the diattenuation content encoded in the first row of the matrix is more limited.

To continue exploring the polarimetric properties of the sample, we apply the Lu-Chipman decomposition (described in Section 2.2) which decomposes the Mueller matrix into a concatenation of three basic ***M***: a diattenuator ***M*** ($\boldsymbol{M_D}$), a retarder ***M*** ($\boldsymbol{M_R}$), and a depolarizer ***M*** ($\boldsymbol{M_\Delta}$). As an illustrative example, the image coefficients of $\boldsymbol{M_R}$ are exhibited in Figure 4-8 (b). The representation of $\boldsymbol{M_R}$ is restricted to the 3x3 sub-matrix that comprises the significant

polarimetric content. The coefficients of the first row and the first column are always equal to zero (as pure retarders do not present diattenuation or polarizance responses), excluding the first coefficient that is always equal to one. As already done with ***M***, the mean values of image coefficients are also provided at the left matrix.

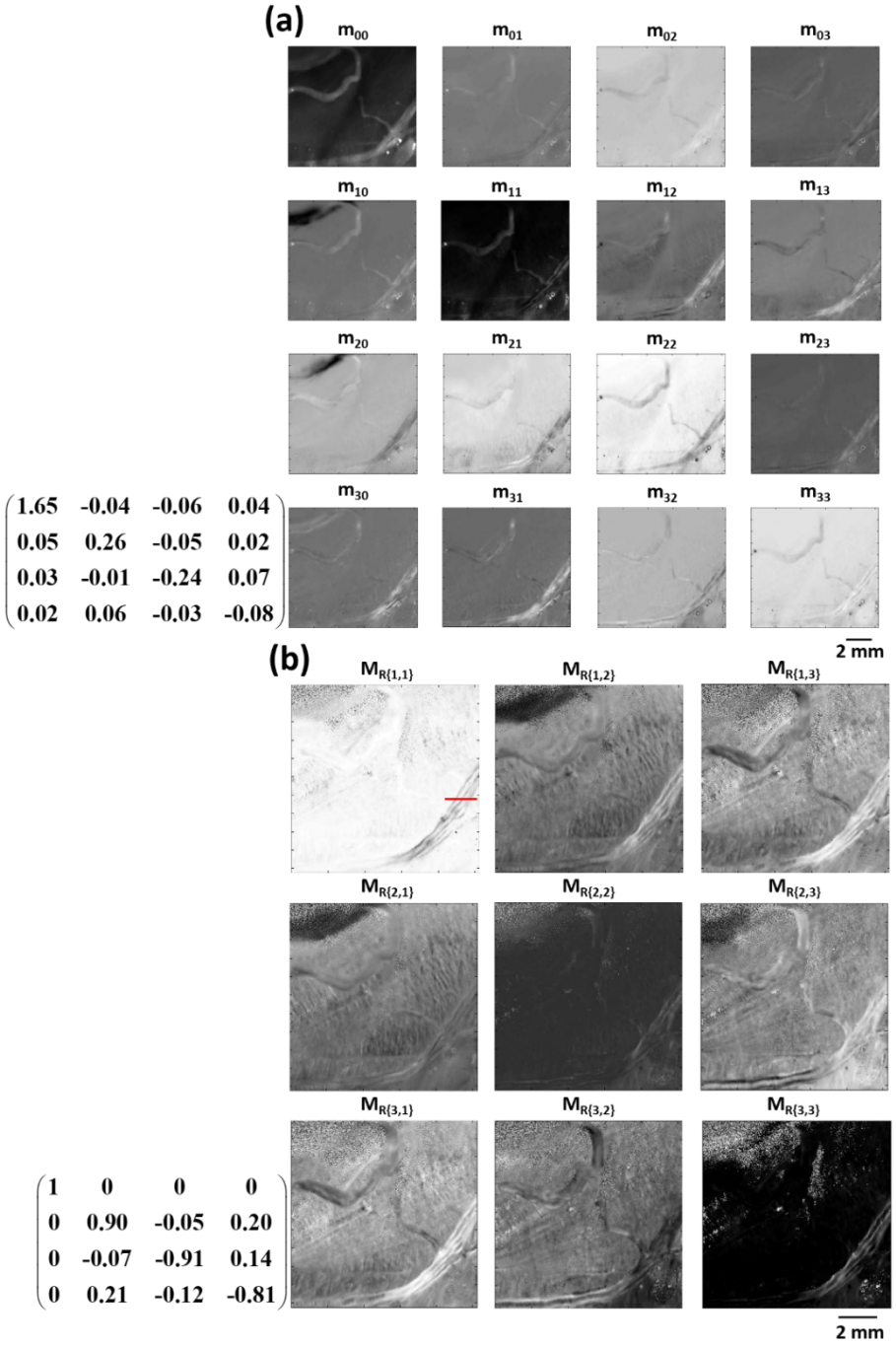

Figure 4-8. (a) Experimental Mueller matrix of the chicken neck inspected with 470 nm light and (b) 3x3 submatrix of the Lu-Chipman retarder, $\boldsymbol{M}_R$. The matrices placed at the left of the image matrices provide the mean value of their image coefficients. The values between {} indicate the corresponding matrix element index.

Note that $\boldsymbol{M}_D$, $\boldsymbol{M}_R$, and $\boldsymbol{M}_\Delta$, provide separately the diattenuation, retardance, and depolarization information of the sample, respectively. Accordingly, the image contrast stated

in the $\boldsymbol{M_R}$ coefficients is related to different birefringent structures, as collagen fibers, and their different orientation. For the chicken neck (Figure 4-8 (b)) we see that the retardance content of the nerve is considerably different from the muscle, this being better contrasted in some regions of the $\boldsymbol{M_R}$ image coefficients than in the image coefficients of $\boldsymbol{M}$. We have also calculated $\boldsymbol{M_D}$, and $\boldsymbol{M_\Delta}$ but their image coefficients are less contrasted than the $\boldsymbol{M}$ and $\boldsymbol{M_R}$.

The contrast observed with the nerve is quantified through Figure 4-9. Figure 4-9 plots the values of the cross-section marked with a red line in Figure 4-8 (b) for different image coefficients. In particular, the image shows the values corresponding to the coefficient with the best nerve visibility of the matrices $\boldsymbol{M}$, $\boldsymbol{M_D}$, $\boldsymbol{M_R}$, and $\boldsymbol{M_\Delta}$ ($\boldsymbol{m_{33}}$, $\boldsymbol{M_{D\{3,0\}}}$, $\boldsymbol{M_{R\{3,3\}}}$, and $\boldsymbol{M_{\Delta\{2,1\}}}$, respectively; the values between {} indicate the corresponding matrix element index).

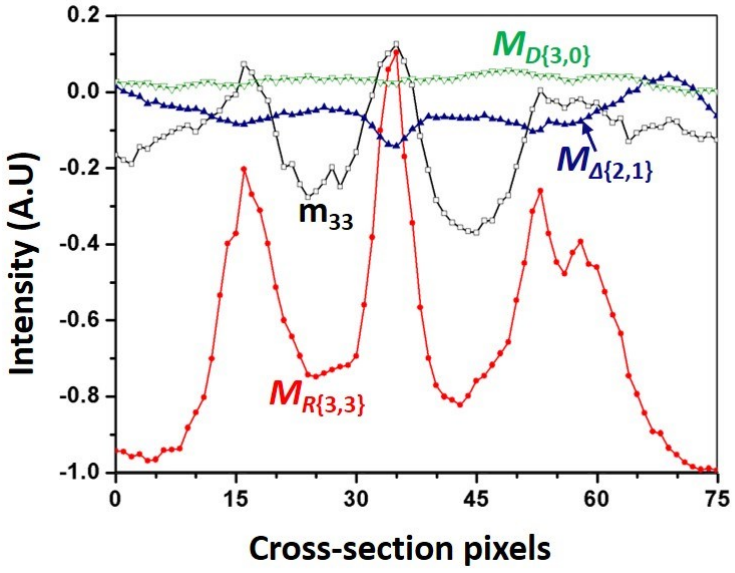

Figure 4-9. Cross-section values of the segment represented with a red line in Figure 4-8 (b) corresponding to the coefficients that provides the best visibility for the $\boldsymbol{M}$ (black empty squares), $\boldsymbol{M_D}$ (green empty triangles), $\boldsymbol{M_R}$ (red-filled circles), and $\boldsymbol{M_\Delta}$ (blue-filled triangles).

In agreement with the previous qualitative discussion, the nerve is more contrasted in the image coefficients of $\boldsymbol{M}$ (black empty squares) and $\boldsymbol{M_R}$(red-filled circles) than in the other image coefficients. The different sections of the nerve are separated by picks that are larger in the $\boldsymbol{M_{R\{3,3\}}}$ so this section of the nerve is better contrasted in this retardance coefficient. Conversely, these details are completely hidden in the diattenuation coefficient ($\boldsymbol{M_{D\{3,0\}}}$) that presents a completely flat intensity distribution (see green empty triangles), this revealing that the studied nerve does not present a dichroic response. The depolarization information shows an intermediate scenario: the central pick is still detected in the depolarization parameter ($\boldsymbol{M_{\Delta\{2,1\}}}$, see blue-filled triangles in Figure 4-9) but the other details are missed.

Next, we propose to combine matrices retrieved through the Lu-Chipman decomposition with the $\boldsymbol{M}$-based PG technique. In particular, we propose to use the expressions employed to

compute the PG configurations from the Mueller matrix coefficients but using the decomposed $\boldsymbol{M_D}$, $\boldsymbol{M_R}$, and $\boldsymbol{M_\Delta}$ coefficients instead of the original non-decomposed $\boldsymbol{M}$ matrix.

As an example, we have calculated the PG configuration f with β=1 from the measured $\boldsymbol{M}$, $\boldsymbol{M_D}$, $\boldsymbol{M_R}$, and $\boldsymbol{M_\Delta}$ of the *ex-vivo* chicken neck (Figure 4-10). The images are calculated considering ε=45° (left-handed circular light).

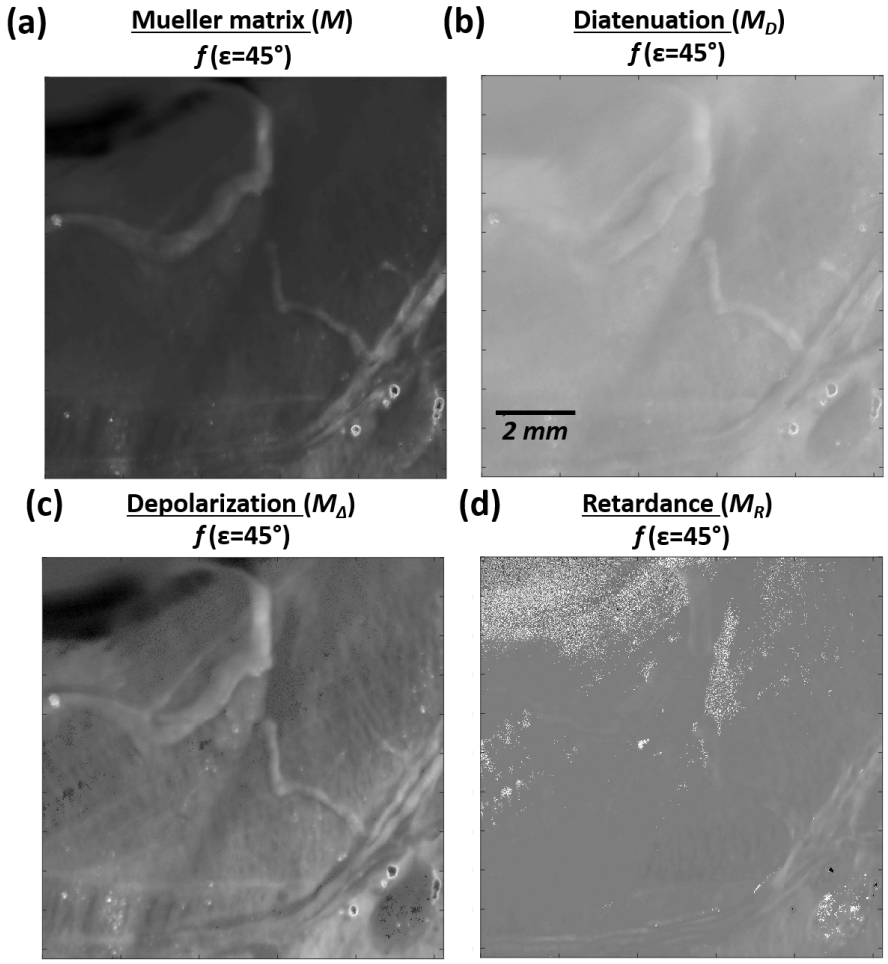

Figure 4-10. Image of $f_\circ$ PG configuration for ε=45° that is calculated with the coefficients of (a) $\boldsymbol{M}$, (b) $\boldsymbol{M_D}$, (c) $\boldsymbol{M_\Delta}$, and (d) $\boldsymbol{M_R}$. β is fixed equal to 1.

In the regular PG image (Figure 4-10 (a)), we can identify the same biological structures observed in the $\boldsymbol{M}$ coefficients (Figure 4-8 (a)). However, these structures are less contrasted than in some of the $\boldsymbol{M}$ coefficients as, for instance, the first coefficient (m_{00}). For the other PG configurations based on the Lu-Chipman matrices, we can distinguish two differentiated results.

On the one hand, diattenuation (Figure 4-10 (b)) and retardance (Figure 4-10 (d)) PG-based images have provided analogous or worst results to the ones obtained with their respective coefficients. The f based on the Lu-Chipman's diattenuator is low contrasted, like their coefficients. Similarly, the PG image of the retarder is also low contrasted, worst results compared to the coefficient $\boldsymbol{M_{R\{3,3\}}}$ (Figure 4-8 (b)) in which the nerve is clearly delimited.

On the other hand, better results have been obtained with the depolarization matrix (Figure 4-10 (c)). In this case, the linear combination of the coefficients gives better resolved biological

structures. Thanks to the use of the function *f* (Eq. (4.15)), we can recognize some roughness of the muscle skin not detected in the Mueller matrix coefficients (Figure 4-8 (a)). These rough muscle structures have not been detected either in the regular *f* function, so the proposed technique has improved the quality image in such a term.

In summary, the Mueller matrix approach is a generalization of the PG techniques that allows the use of more complex mathematical tools that further synthesize the polarimetric information of the sample. Some of the mathematical tools that can be implemented on the Mueller matrix technique, as the Lu-Chipman decomposition, can be combined with the PG techniques to improve the image contrast and reveal new information. Moreover, the Mueller matrix approach allows the study of different PG configurations (e.g., the study of the image contrast as a function of the ellipticity of the incident light) without needing more than one ***M*** measurement. For all the above-mentioned reasons, we recommend using the Mueller matrix approach as it results more suitable for biological imaging applications.

4.2 Characterization of depolarizing samples based on the indices of polarimetric purity and the components of purity

In the previous section, we have observed that the measured *ex-vivo* tissue acts as a depolarizer when interacting with the polarized light. This feature is not restricted to the measured tissue but most biomedical tissue samples are characterized presenting certain depolarization properties. Organic tissues are mainly composed of fibers [48,126,129,130] and light is partially scattered at interacting with these fibers. The scattering process is repeated multiple times inside the media before leaving the sample and the scattered photons with different paths may leave the sample in the same position and in the same direction. When these photons are measured with a polarimeter, their corresponding different polarizations of each one are incoherently combined and the photon mixture ends in partially or fully depolarized light. The measured depolarization strongly depends on the fiber characteristics. Therefore, some intrinsic structural information of scattering media can be inferred from light depolarization measurements and be used in some applications, for example in the early diagnosis of some diseases [48,129,130].

Polarization-based techniques are non-contact techniques that can be used to retrieve the physical characteristics of the biological tissue samples. Usually, the description of the polarimetric properties of the sample is based on the Mueller-Stokes formalism because it is the most appropriate frame to describe partially and fully depolarized states. Under this formalism, the depolarizing information is encoded in the 16 elements of the Mueller matrix and further mathematical treatment is required to extract it. Nowadays, a diverse group of mathematical treatments, resulting in different depolarization metrics, are available in the literature to study the scattered tissues from different points of view [1,44–46,60–73], as randomness, entropy, or stochastic behavior, among others. However, the link between these macroscopic metrics and the physical characteristics of tissues is a complex issue to be solved. A commonly used metric to inspect the depolarization property is the so-called depolarization index, P_Δ (also called the degree of polarimetric purity [209]). This metric is described in section 2.3.1 and quantifies the random process behind the scattering interactions. However, it cannot distinguish between different physical structures that lead to the same overall depolarization. Alternatively, these

structures may be distinguished using the Indices of Polarimetric Purity, IPP (described in section 2.3.2), and the Components of Purity, CP (described in section 2.3.3), which are two groups of metrics that are connected with P_Δ and that further synthesize depolarizing content.

In this section, we provide the relation between CP and IPP, and we show that the combination of CP and IPP gives the complete information of the depolarization properties of scattering systems [214] (sub-section 4.2.1). Next, we discuss their use for the analysis of the scattering phenomena through a collection of illustrative and easy to interpret examples (sub-section 4.2.2). These examples are based on the incoherent combination of different non-depolarizing elements (retarders and diattenuators). Finally, we experimentally build different depolarising systems that highlight the potential of using IPP in front of P_Δ.

4.2.1 Indices of polarimetric purity and components of purity relation

According to the description of CP and IPP provided in section 2.3, both metrics provide further physical interpretation than P_Δ and further quantitative characterization of depolarizers. However, we might want to consider whether the two spaces are equivalent, leading to the same information, or on the contrary, they are more or less suitable for a particular group of depolarizers. This topic is not resolved in literature, and authors may indistinctly use P_Δ, IPP, or CP. To answer this question, we first connect CP and IPP by equaling Eqs. (2.45) and (2.46),

$$3P_\Delta^2 = P^2 + D^2 + 3P_s^2 = 2P_1^2 + \frac{2}{3}P_2^2 + \frac{1}{3}P_3^2 \tag{4.17}$$

In Eq. (4.17), each parameter can be calculated from the other five so we have five degrees of freedom. Therefore, at least two of the three IPP or CP parameters are independent of the value of the other parameters, and accordingly, the information provided by IPP and CP should be different and compatible in some way.

According to the Mueller matrix formalism, the information related to the polarimetric response of a given medium can be provided with a set of sixteen independent magnitudes with clear physical interpretation, those magnitudes being encoded in the sixteen elements of the Mueller matrix, **M**. One of this magnitude is the Mueller matrix element m_{00} that is the mean intensity coefficient of ***M***; other ten quantities are related to retardance and orientation direction properties; and the remaining five magnitudes are related to depolarization and enpolarization [223] properties. Enpolarization implies the existence of dichroism, i.e. diattenuation and polarizance, in the probed media, and it is related to the fact that some depolarizers can increase the degree of polarization of certain incident polarization states while decreasing the degree of polarization of the remaining ones [214,223,224]. Therefore, *D* and *P* (described in section 2.1.3) are two of the magnitudes related to enpolarization properties that together with the three IPP (P_1, P_2, and P_3) may compose the above-mentioned group of five independent magnitudes that completely describe the depolarization properties of the sample. Note that taking this set of five parameters (*D*, *P,* P_1, P_2, and P_3) in Eq. (4.17) we can readily calculate the depolarization index P_Δ, and the index of spherical purity P_S [211,214]. It is remarkable that other relevant depolarizing parameters as the Cloude's entropy S [70] or the overall purity index (PI) [62] can be calculated using the same set of parameters, as they completely describe the depolarizing behavior of samples.

Another point of view is based on the representation of the CP and the IPP in a 3D space. Under that scenario, the physically realizable matrices must be represented in a limited space (the constraints of the spaces are marked in orange in Figure 2-2 and Figure 2-4), and the shape and volume of these spaces are different for each representation. In both representations, P_Δ values are represented with ellipsoid surfaces but these surfaces are described with different equations (Eq. (2.45) for the IPP-based Purity space and Eq. (2.46) for the Component space). As the shape of the spaces and the area of the P_Δ surfaces are different, the information that they provide should be as well different in some way.

To better understand this crucial point, let us revise a particular case when the depolarization index equals 1 (P_Δ=1), the case of non-depolarizing samples. In such a scenario, any non-depolarizing system is always represented at the same point in the Purity space (1,1,1), but it can be represented at some point of a wide surface of possible polarimetric samples in the Component space. This makes sense because as said above, CP provides a physical interpretation of samples constituents (so we can study the dichroism or birefringence contribution corresponding to different non-depolarizing samples), but this case has no further interpretation in terms of IPP, as non-depolarizing media do not introduce randomness to an incident beam. As it will be shown in the following, the opposite case, different depolarizers corresponding to a single point in the Component space, whereas being associated to a surface in the Purity Space, is also possible. In the following, and with the aim of better understanding the differences and complementarity between these two depolarizing spaces, we are interested in studying the following two scenarios: 1) depolarizers with identical CP but different IPP, and 2) depolarizers with identical IPP but different CP; because they illustrate the benefits of the different metrics. It is worth highlighting that these are two limit scenarios in which either IPP or CP are the only metrics that give relevant information but in general, both metrics provide significant information of depolarizing properties of the samples and should be used together to completely characterize depolarizers.

4.2.2 IPP and CP analysis through synthetized depolarizers

The collection of depolarizers that accomplish one of the two limit scenarios is simulated by incoherently combining dichroic and birefringent elements. The fact of using these well-known elements eases the interpretation of the results and clarifies the CP and IPP discussion. The simulation is grounded on the idea that depolarization can be observed as the incoherent combination of non-depolarizing elements [225,226]. Following this consideration, any depolarizer can be described as the summation of up to four non-depolarizing Mueller matrices [209,210,225,227]:

$$\boldsymbol{M} = \sum_{i=1}^{4} \alpha_i \boldsymbol{M}_i \tag{4.18}$$

where $\boldsymbol{M}_i$ are Mueller matrices of non-depolarizing elements and α_i are the different weights of matrices. In the experimental scenario, α_i correspond to the percentage of light that passes through (or is reflected to) each element composing the sample and reaches the same position of the detector. The combination is restricted to four elements as the combination of more elements can be reduced to an equivalent combination of four non-depolarizing elements [210].

4.2.2.1 Depolarizers characterized by the same CP but different IPP

From the simulated depolarizers, we first analyze a collection of depolarizers giving rise to the same values for the CP but discriminated by different IPP. In particular, we start with depolarizers without dichroism (P=D=0). This group of depolarizers is characterized by P_S being the only CP different from 0, and equal to P_Δ (the latter is according to Eq. (4)). As a consequence, each value of P_Δ is associated with a single point at the CP space, always located in the P_S axis, see Figure 4-11. Conversely, their representation in the Purity space is not restricted to one dimension and, as seen in Figure 4-11, depolarizers related to the same P_S value can be represented at different locations of the Purity space. Note that these depolarizers are arranged at certain locations over a surface (marked in green in Figure 4-11). This surface is built with all the IPP combinations that result in the same P_Δ=0.58 value and each point of the surface can be associated with different depolarizers that are indistinguishable using the CP and P_Δ but differentiable through the IPP.

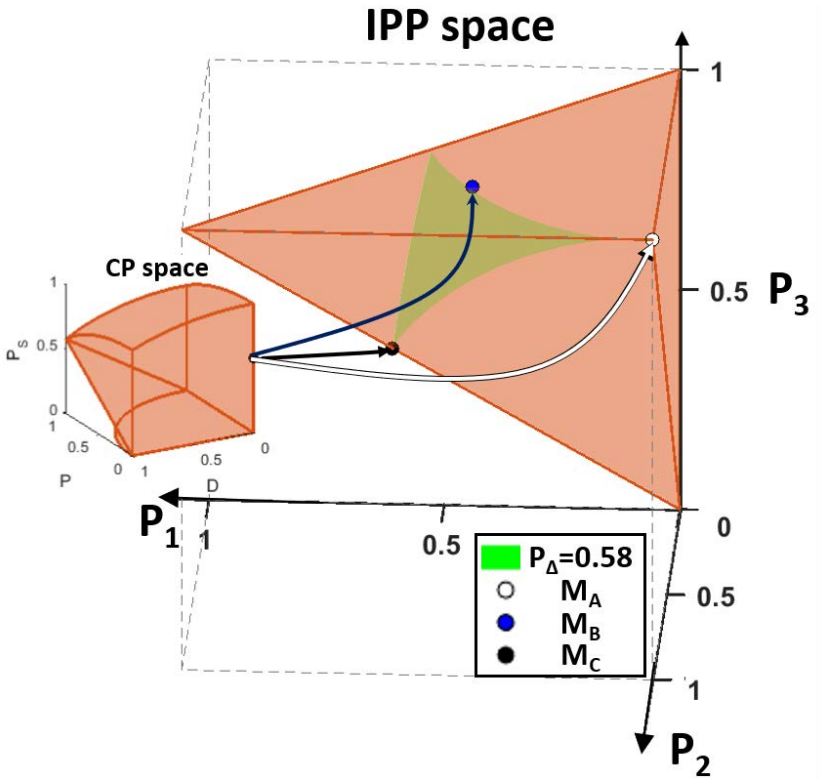

Figure 4-11. Representation of depolarizers that presents the same CP but different IPP in the Component and Purity spaces. The presented case with P_S=P_Δ=0.58 is an illustrative example.

To the sake of clarity, the simulated non-dichroic depolarizers (P=D=0) are constructed according to the following expression that is based on Eq. (4.18):

$$\boldsymbol{M} = \alpha_1 \boldsymbol{M}_{air} + \alpha_2 \boldsymbol{M}_{HWP(0°)} + \alpha_3 \boldsymbol{M}_{HWP(45°)} + \alpha_4 \boldsymbol{M}_{HWP(45°)} \boldsymbol{M}_{HWP(0°)} \tag{4.19}$$

where $\boldsymbol{M_{air}}$ is the Mueller matrix of the air (the identity matrix), and $\boldsymbol{M_{HWP(0°)}}$ and $\boldsymbol{M_{HWP(45°)}}$ are the Mueller matrices of a half-wave plate with their fast axis oriented at 0 and 45 degrees concerning the horizontal reference axis of the laboratory. Eq. (4.19) is a general expression for

the synthesis of non-dichroic depolarizers because it allows the construction of non-dichroic depolarizers with any physically feasible combination of IPP through the use of different weights combinations.

Three particular depolarizers are simulated according to Eq. (4.19), all of them fulfilling the condition of non-dichroic depolarizers (P=D=0 and P_S=P_Δ). They are labeled as $\boldsymbol{M_A}$, $\boldsymbol{M_B}$, and $\boldsymbol{M_C}$. Their Mueller matrices, as well as their construction, and their IPP, CP, and P_Δ values, are shown in Table 4-2. In addition, they are represented with points in the Purity and Component spaces of Figure 4-11. The three non-dichroic depolarizers present the same CP and P_Δ values, but their corresponding IPP values are significantly different (see Table 4-2). Accordingly, they are represented in the same location in the Component space, while their different IPP values are visually appreciable (and thus, discriminated) as different points that are placed at the same P_Δ surface of the Purity space (see Figure 4-11). The differences of such depolarizers in terms of IPP are connected with the ability of samples to randomize the input light polarization in different ways (some input fully polarized states are more depolarized than others, and those depend on each particular sample).

For the sake of visualization, the two different cases of SoPs that result from light-matter interactions of polarized light with two different depolarizers are represented in the Poincare Sphere (resulting in ellipsoids, according to refs. [45,228]) and shown in Figure 4-12. In particular, we have represented the SoPs resulting from the interaction of any fully polarized input state of polarization with the $\boldsymbol{M_B}$ and ***Mc*** depolarizers (intense blue ellipsoids), respectively in Figure 4-12 (a) and (b).

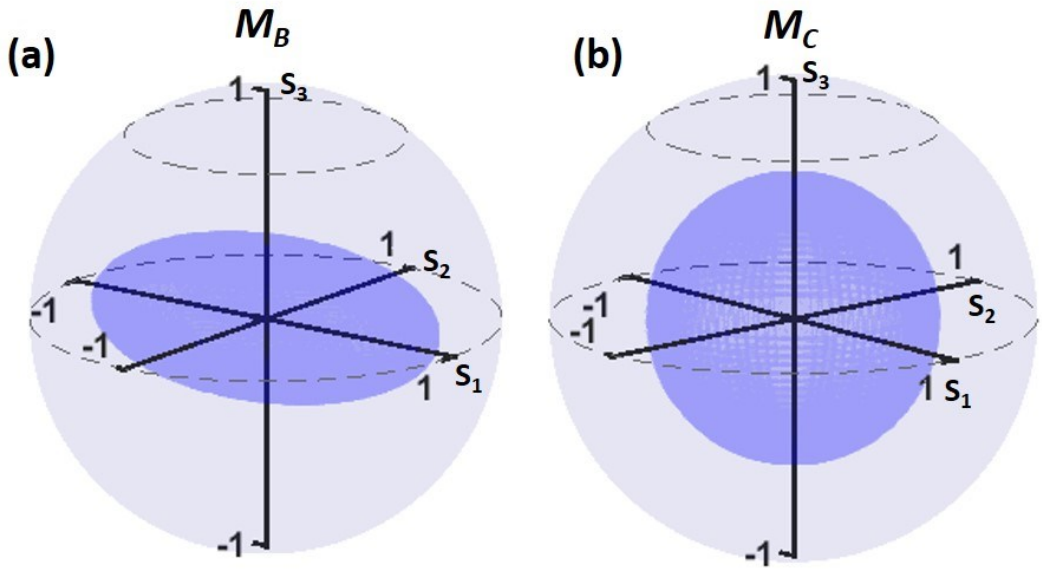

Figure 4-12. Ellipsoids of (a) $\boldsymbol{M_B}$ and (b) ***Mc*** depolarizers.

$\boldsymbol{M_C}$ depolarizer is represented with a sphere, so it does not present depolarizing anisotropy (i.e., all input polarizations are equally depolarized, so the sphere is equally shrunk). In contrast, $\boldsymbol{M_B}$ is represented with an ellipsoid that illustrates how diagonal and circular polarizations are more depolarized than the horizontally polarized states (i.e., SoPs described with S_2 and S_3 parameters are more depolarized than the ones described with S_1). Samples presenting different values for this kind of depolarization anisotropy (i.e., whose Mueller matrices lead to different

ellipsoids [45,228]), are always represented by different IPP. Under this scenario, differences in the IPP values are connected with the specific depolarizer structure. In the case of non-dichroic depolarizers, they usually come from combining retarder elements (note that the absence of dichroic elements results in *D* and *P* equal to 0). Also, note that the number of combined elements limits the values of the IPP. In our particular case of study, $\boldsymbol{M_A}$ is the combination of two non-depolarizer elements thus being impossible to reach values of P_2 smaller than 1 (Table 4-2) [45,227]. Conversely, the other depolarizers are constructed with more elements leading to P_2 values smaller than 1.

Mueller Matrices								
M_A				M_B				M_C
$\begin{pmatrix} 1 & 0 & 0 & 0 \\ 0 & 1 & 0 & 0 \\ 0 & 0 & 0 & 0 \\ 0 & 0 & 0 & 0 \end{pmatrix}$				$\begin{pmatrix} 1 & 0 & 0 & 0 \\ 0 & 0.809 & 0 & 0 \\ 0 & 0 & 0.5 & 0 \\ 0 & 0 & 0 & 0.309 \end{pmatrix}$				$\begin{pmatrix} 1 & 0 & 0 & 0 \\ 0 & 1/\sqrt{3} & 0 & 0 \\ 0 & 0 & 1/\sqrt{3} & 0 \\ 0 & 0 & 0 & 1/\sqrt{3} \end{pmatrix}$
M_D				M_E				M_F
$\frac{2}{3}\begin{pmatrix} 1 & 1/2 & 0 & 0 \\ 1/2 & 0 & 0 & 0 \\ 0 & 0 & 1/2 & 0 \\ 0 & 0 & 0 & -1/2 \end{pmatrix}$				$\frac{2}{3}\begin{pmatrix} 1 & 1/2 & 0 & 0 \\ 1/2 & 1/2 & 0 & 0 \\ 0 & 0 & 0 & 0 \\ 0 & 0 & 0 & -1/2 \end{pmatrix}$				$\frac{2}{3}\begin{pmatrix} 1 & \frac{1}{2} & 0 & 0 \\ \frac{1}{2} & \frac{1}{\sqrt{3}} & 0 & 0 \\ 0 & 0 & \frac{-1}{4\sqrt{3}} & 0 \\ 0 & 0 & 0 & \frac{-1}{4\sqrt{3}} \end{pmatrix}$
	Depolarization Parameters							**Depolarizer synthesis**
	P_1	P_2	P_3	P_Δ	P	D	P_S	
M_A	**0.00**	**1.00**	**1.00**	**0.58**	**0.00**	**0.00**	**0.58**	$\frac{1}{2}\mathbf{M}_{air} + \frac{1}{2}\mathbf{M}_{HWP(0°)}$
M_B	**0.40**	**0.71**	**1.00**	**0.58**	**0.00**	**0.00**	**0.58**	$\frac{3+\sqrt{5}}{8}\mathbf{M}_{air} + 1/4\mathbf{M}_{HWP(0°)} + \frac{3-\sqrt{5}}{8}\mathbf{M}_{HWP(45°)}$
M_C	**0.58**	**0.58**	**0.58**	**0.58**	**0.00**	**0.00**	**0.58**	$\frac{3+\sqrt{3}}{4\sqrt{3}}\mathbf{M}_{air} + \frac{\sqrt{3}-1}{4\sqrt{3}}(\mathbf{M}_{HWP(0°)} + \mathbf{M}_{HWP(45°)} + \mathbf{M}_{HWP(45°)}\mathbf{M}_{HWP(0°)})$
M_D	**0.00**	**1.00**	**1.00**	**0.58**	**0.50**	**0.50**	**0.41**	$2/3\mathbf{M}_{LP(0°)} + 1/3\mathbf{M}_{HWP(45°)}$
M_E	**0.40**	**0.71**	**1.00**	**0.58**	**0.50**	**0.50**	**0.41**	$2/3\mathbf{M}_{LP(0°)} + 1/6(\mathbf{M}_{HWP(0°)} + \mathbf{M}_{HWP(45°)})$
M_F	**0.58**	**0.58**	**0.58**	**0.58**	**0.50**	**0.50**	**0.41**	$2/3\mathbf{M}_{LP(0°)} + \frac{\sqrt{3}}{9}\mathbf{M}_{HWP(0°)} + \frac{3-\sqrt{3}}{18}(\mathbf{M}_{HWP(45°)} + \mathbf{M}_{HWP(45°)}\mathbf{M}_{HWP(0°)})$

Table 4-2. Mueller matrices, depolarizer synthesis, and IPP, CP, and P_Δ values of the $\boldsymbol{M_A}$, $\boldsymbol{M_B}$, $\boldsymbol{M_C}$, $\boldsymbol{M_D}$, $\boldsymbol{M_E}$, and $\boldsymbol{M_F}$ depolarizers. $\boldsymbol{M_{air}}$ is the Mueller matrix of the air, $\boldsymbol{M_{HWP}}$ is the Mueller matrix of a half-wave plate and $\boldsymbol{M_{LP}}$ is the Mueller matrix of a linear polarizer. The orientation of the elements is marked within the () brackets and all the angles are referenced concerning the horizontal axis of the laboratory.

The group of depolarizers that are represented in the same place in the Component space but distributed over different locations of the Purity space is not restricted to non-dichroic depolarizers. In fact, non-dichroic depolarizers are a particular case of a more general group of depolarizers, those that satisfy the $D=P\geq 0$ condition. Next, we briefly analyze a subgroup of this type of depolarizers that presents the same diattenuation ($D(\boldsymbol{M_1})=D(\boldsymbol{M_2})$). To synthesize this type of depolarizers we use a similar expression to Eq. (4.19) but replacing the air with a horizontally oriented linear polarizer, $\boldsymbol{M_{LP(0°)}}$:

$$\boldsymbol{M} = \alpha_1 \boldsymbol{M}_{LP(0°)} + \alpha_2 \boldsymbol{M}_{HWP(0°)} + \alpha_3 \boldsymbol{M}_{HWP(45°)} + \alpha_4 \boldsymbol{M}_{HWP(45°)} \boldsymbol{M}_{HWP(0°)} \tag{4.20}$$

As an example, we simulate the $\boldsymbol{M_D}$, $\boldsymbol{M_E}$, and $\boldsymbol{M_F}$. Their corresponding IPP, CP, and P_Δ values, their Mueller matrices, and their synthesis are shown in Table 4-2. As observed with non-dichroic depolarizers, all the new examples ($\boldsymbol{M_D}$, $\boldsymbol{M_E}$, and $\boldsymbol{M_F}$) share the same CP value but are described by different IPP (see Table 4-2). Note that one of these examples, the depolarizer labeled $\boldsymbol{M_D}$, corresponds to a Type-II depolarizer (defined by the alternative canonical form [45,229]). Some techniques used to analyze depolarizers, as the symmetric decomposition [45], needs alternative mathematical treatment to work with Type-II matrices [45], but this is not the case of IPP which can be calculated using the same algorithm.

4.2.2.2 Depolarizers characterized by the same IPP but different CP

In the previous section, we have proved that within the set of depolarizing media accomplishing the condition D=P, there exist depolarizer subgroups in which the most suitable metrics to characterize their performance are the IPP. From now on, we discuss the opposite situation, i.e., a collection of depolarizers sharing the same IPP but completely differentiated at using CP. Accordingly, to have the same P_Δ and IPP values the group of depolarizers must present the same randomness associated with the depolarizing process but they must be composed of different physical elements to have different CP values.

The first group of depolarizers we discuss are another subgroup of depolarizing media accomplishing the condition D=P but, in that case, taking different diattenuation ($D(\boldsymbol{M_1})\neq D(\boldsymbol{M_2})$). One case of study that satisfies the described conditions is the composed of the $\boldsymbol{M_A}$ and $\boldsymbol{M_D}$ systems (Table 4-2). Both are defined with the same IPP but different CP. In this example, $\boldsymbol{M_A}$ does not involve dichroic elements in the construction while the construction of $\boldsymbol{M_D}$ does (Table 4-2). As a result, the diattenuation of $\boldsymbol{M_A}$ is non-existent ($D=0$) while $\boldsymbol{M_D}$ presents certain diattenuation, so being two different systems in terms of CP. Conversely, the polarized light that interacts with the media results depolarized in a certain way, which depends on the incident state of polarization, which turns out similar in terms of DOP, and outcomes to the same IPP values. Other examples presenting the same phenomenon are the $\boldsymbol{M_B}$ and $\boldsymbol{M_C}$ systems compared with $\boldsymbol{M_E}$ and $\boldsymbol{M_F}$, respectively (Table 4-2). These examples are just the limit case in which one of the depolarizers does not present diattenuation, but the same scenario can be obtained when dealing with depolarizers with certain non-negligible dichroic content. These types of structures can be synthesized by combining different dichroic elements or by combining such dichroic elements with some birefringent elements. As a simple example, we will discuss a collection of depolarizers construed by combining a horizontal linear polarizer (dichroic element) and a half-wave plate oriented at 45° (birefringent element) and that follows this expression:

$$\boldsymbol{M} = \alpha_1 \boldsymbol{M}_{LP(0°)} + (1-\alpha_1) \boldsymbol{M}_{HWP(45°)} \tag{4.21}$$

Note that Eq. (4.21) is a particular case of Eq. (4.20) in which α_2 and α_4 are equal to 0 and $\alpha_3=1-\alpha_1$.

By modifying the value of α_1 we can build a collection of depolarizers with different P_Δ, thus with different overall depolarizing capability. The P_Δ, IPP, and CP metrics obtained with different α_1 values are graphically represented in Figure 4-13 (P_Δ and IPP in Figure 4-13 (a) and CP in Figure 4-13 (b)). The analysis of Fig. 4(a) shows that, under this construction, we can build two different depolarizers with different α_1 but with the same P_Δ values (e.g., the red horizontal line shows the particular case P_Δ= 0.64). This ambiguity is also observed when using the IPP. Note that we are combining only two elements, so P_2 and P_3 are always equal to 1 thus limiting P_Δ from 0.577 to 1. Conversely to IPP, CP allow for distinguishing which element (dichroic or birefringent) is more significant in the weighted sum (see Figure 4-13 (b), where *P* and *D* functions do not present a minimum, so there is no ambiguity between the depolarizers collection).

As an example, the Mueller matrices of the two particular depolarizers leading to the same P_Δ=0.64 value, labeled as $\boldsymbol{M_G}$ and $\boldsymbol{M_I}$, are provided in Table 4-3, together with their depolarization parameters (IPP, CP, and P_Δ) and their construction. As expected, $\boldsymbol{M_G}$ and $\boldsymbol{M_I}$ share the same IPP values but they are defined by different CP values. To visualize these results, both depolarizers are represented in the IPP and CP spaces of Figure 4-14 (blue and cyan points). Note that both depolarizers are located to a single point in the Purity space (P_1=0.33, P_2=1, and P_3=1) but they are distributed over the P_Δ=0.64 surface in the Component space (represented in green in Figure 4-14). In particular, they are distributed over the intersection between the P_Δ=0.64 surface and the *P*=*D* plane (it is represented in red in Figure 4-14 and it indicates the region of the CP space connected to depolarizers accomplishing the *P*=*D* condition).

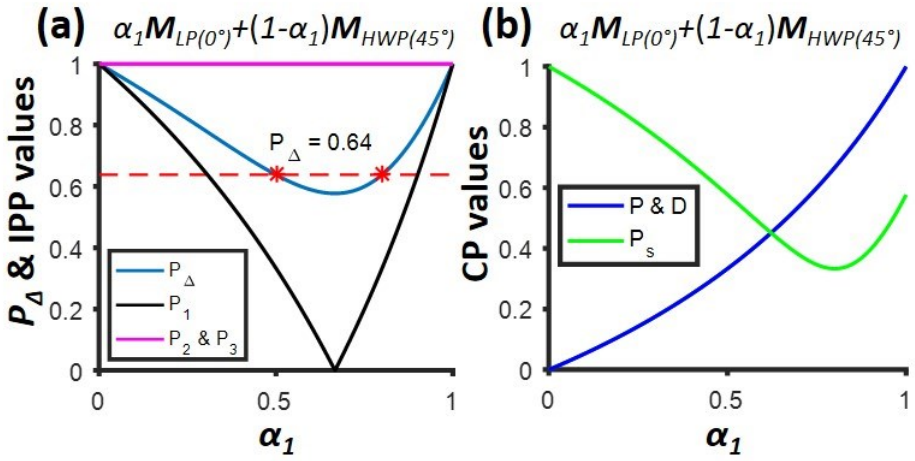

Figure 4-13. Graphical representation of (a)P_Δ, and IPP, and (b) CP values vs α_1 obtained following Eq. (4.21). The red horizontal line represents the particular case PΔ=0.64.

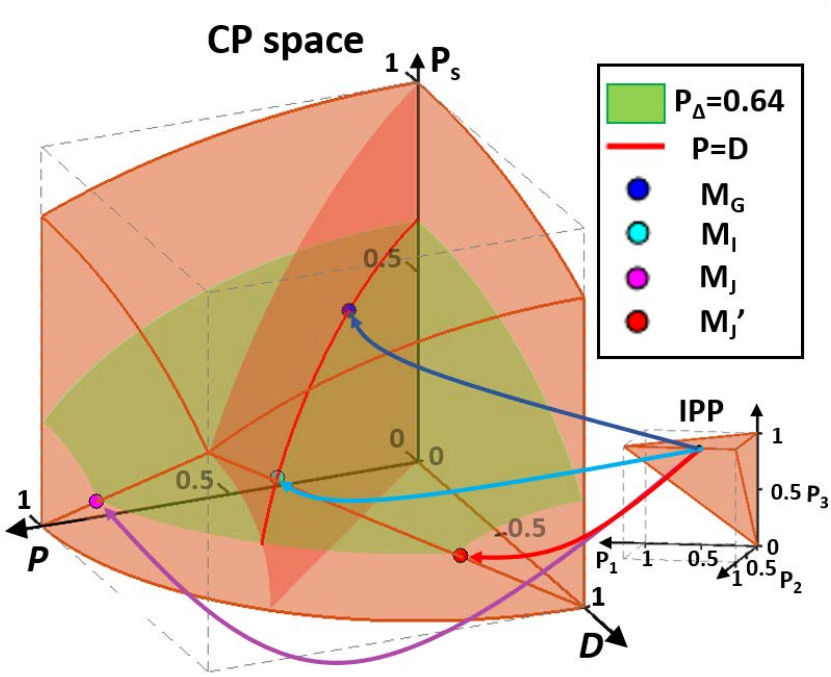

Figure 4-14. Representation of depolarizers that presents the same IPP but different CP in the Purity and Component spaces. The presented case with P_Δ=0.64 is an illustrative example.

Up to now, we have built depolarizers showing the same diattenuation and polarizance so placed at the *P=D* plane. However, depolarizing systems accomplishing the condition $P \neq D$ can also be equivalent by IPP but discriminated by CP. To synthesize this type of depolarizers we have modified Eq. (4.20) by replacing the horizontally oriented half-wave plate, $\boldsymbol{M}_{HWP(0°)}$, with the dichroic element $\boldsymbol{M}_{LP(0°)} \cdot \boldsymbol{M}_{HWP(45°)}$:

$$M = \alpha_1 \boldsymbol{M}_{LP(0°)} + \alpha_2 \boldsymbol{M}_{LP(0°)} \boldsymbol{M}_{HWP(45°)} + \alpha_3 \boldsymbol{M}_{HWP(45°)} + \alpha_4 \boldsymbol{M}_{HWP(45°)} \boldsymbol{M}_{HWP(0°)} \quad (4.22)$$

$\boldsymbol{M}_J$ is an example of a depolarizer built with Eq. (4.22). Its Mueller matrix, construction, and IPP, CP, and P_Δ values are provided in Table 4-3. The same depolarizer $\boldsymbol{M}_J$ but illuminated in a reverse way (i.e, with the incident and emerging beam directions interchanged) is calculated according to refs. [45,230]. We label the $\boldsymbol{M}_J$ *reverse Mueller matrix* as $\boldsymbol{M}_J$**'**. Its Mueller matrix, construction, and IPP, CP, and P_Δ values are also provided in Table 4-3. The forward ($\boldsymbol{M}_J$) and the reverse ($\boldsymbol{M}_J$**'**) Mueller matrices comparison (Table 4-3) shows that when a given sample is illuminated in a reverse way, the corresponding diattenuation D_r is equal to the polarizance corresponding to the same system illuminated in the forward configuration P_f, i.e., $D_r=P_f$. Likewise, the polarizance measured in the reverse mode P_r is equal to the diattenuation in the forward illumination direction D_f ($P_r=D_f$). In other words, the diattenuation and polarizance response of a given system are interchanged if measured in the forward or the reverse modes, being the diattenuation and the polarizance the two sides of the same coin [209]. Knowing this, and taking into account that *D* and *P* are two of the three axes of the Component space, CP necessarily have to be able to discriminate between systems measured in the forward and reverse configurations of depolarizers accomplishing the $P \neq D$ condition. Conversely, IPP metrics

are invariant to forward and reverse transformations [212,231] so they are unable to discriminate between polarimetric systems that are being forward or reverse illuminated.

Mueller Matrices			
M_G	M_I	M_J	M_J'
$\frac{3}{4}\begin{pmatrix} 1 & \frac{1}{3} & 0 & 0 \\ \frac{1}{3} & \frac{-1}{3} & 0 & 0 \\ 0 & 0 & \frac{2}{3} & 0 \\ 0 & 0 & 0 & \frac{-2}{3} \end{pmatrix}$	$\frac{3}{5}\begin{pmatrix} 1 & \frac{2}{3} & 0 & 0 \\ \frac{2}{3} & \frac{1}{3} & 0 & 0 \\ 0 & 0 & \frac{1}{3} & 0 \\ 0 & 0 & 0 & \frac{-1}{3} \end{pmatrix}$	$\frac{1}{2}\begin{pmatrix} 1 & \frac{1}{3} & 0 & 0 \\ 1 & \frac{1}{3} & 0 & 0 \\ 0 & 0 & 0 & 0 \\ 0 & 0 & 0 & 0 \end{pmatrix}$	$\frac{1}{2}\begin{pmatrix} 1 & 1 & 0 & 0 \\ \frac{1}{3} & \frac{1}{3} & 0 & 0 \\ 0 & 0 & 0 & 0 \\ 0 & 0 & 0 & 0 \end{pmatrix}$

	Depolarization Parameters							Depolarizer synthesis
	P_1	P_2	P_3	P_Δ	P	D	P_S	
M_G	0.33	1.00	1.00	0.64	0.33	0.33	0.58	$\frac{1}{2}\mathbf{M}_{LP(0°)} + \frac{1}{2}\mathbf{M}_{HWP(45°)}$
M_I	0.33	1.00	1.00	0.64	0.67	0.67	0.33	$\frac{4}{5}\mathbf{M}_{LP(0°)} + \frac{1}{5}\mathbf{M}_{HWP(45°)}$
M_J	0.33	1.00	1.00	0.64	1.00	0.33	0.19	$\frac{2}{3}\mathbf{M}_{LP(0°)} + \frac{1}{3}\mathbf{M}_{LP(0°)}\mathbf{M}_{HWP(45°)}$
M_J'	0.33	1.00	1.00	0.64	0.33	1.00	0.19	$diag(1,1,1,-1)\cdot\mathbf{M}_J^T\cdot diag(1,1,1,-1)$

Table 4-3. Mueller matrices, depolarizer synthesis, and IPP, CP, and P_Δ values of the M_G, M_I, M_J, and M_J' depolarizers. M_{air} is the Mueller matrix of the air, M_{HWP} is the Mueller matrix of a half-wave plate and M_{LP} is the Mueller matrix of a linear polarizer. The orientation of the elements is marked within the () brackets and all the angles are referenced concerning the horizontal axis of the laboratory. The superindex ^{T} indicates the transpose matrix.

For the sake of visualization, these two systems are represented in the CP space Figure 4-14 (M_J is represented with a magenta point and M_J' with a red point). Under such representation, we observe how they are placed over the constant P_Δ=0.64 surface, symmetrically distanced with respect to the D=P plane. This phenomenon is not restricted to this example but it can be generalized to any pair of forward-reverse pair of depolarising systems. In that sense, the D=P vertical plane divides the Component space into two sub-spaces. Any depolarizer represented at each side of the plane has its reverse version located at the other side in the mirrored position. Accordingly, any forward or reverse depolarizing systems with $P \neq D$ can be distinguished by using the Component space (or CP) but not with the Purity space (or IPP) as their capability to depolarize an input beam is equivalent.

4.2.3 Characterization of experimentally synthesized depolarizers through IPP

For the sake of completeness, we have experimentally built some depolarizers based on the idea of incoherently combining different non-depolarizing elements [225,226]. The idea behind the experiment consists of illuminating different non-depolarizing elements (linear polarizers and retarder plates) and incoherently mixing the light that outcomes from these light-matter interactions.

To do so, the set-up described in Chapter 3 is properly modified (see Figure 4-15). We changed the light source for a 627 nm and 25 nm bandwidth LED (Red LUXEON Rebel) to obtain a more expanded and better-collimated beam. The light emitted by this source is collimated through a collimator system composed of two convergent lenses. The focal lengths for these

lenses are approximately 38 mm and 40 mm, respectively. This collimated beam is polarized through the PSG and the polarized light is the one that interacts with the sample (see Figure 4-15). As we deal with a new light source, the PSG was properly calibrated by following the same method described in section 3.3. The intensity of the light that impinges the sample was too high so we placed a linear polarizer between the light source and the PSG to control the intensity of the beam. The intensity is adjusted by rotating the linear polarizer. This newly added linear polarizer does not affect the PSG calibration because the beam is collapsed into a vertically polarized state when facing the first optical element of the PSG (the linear polarizer).

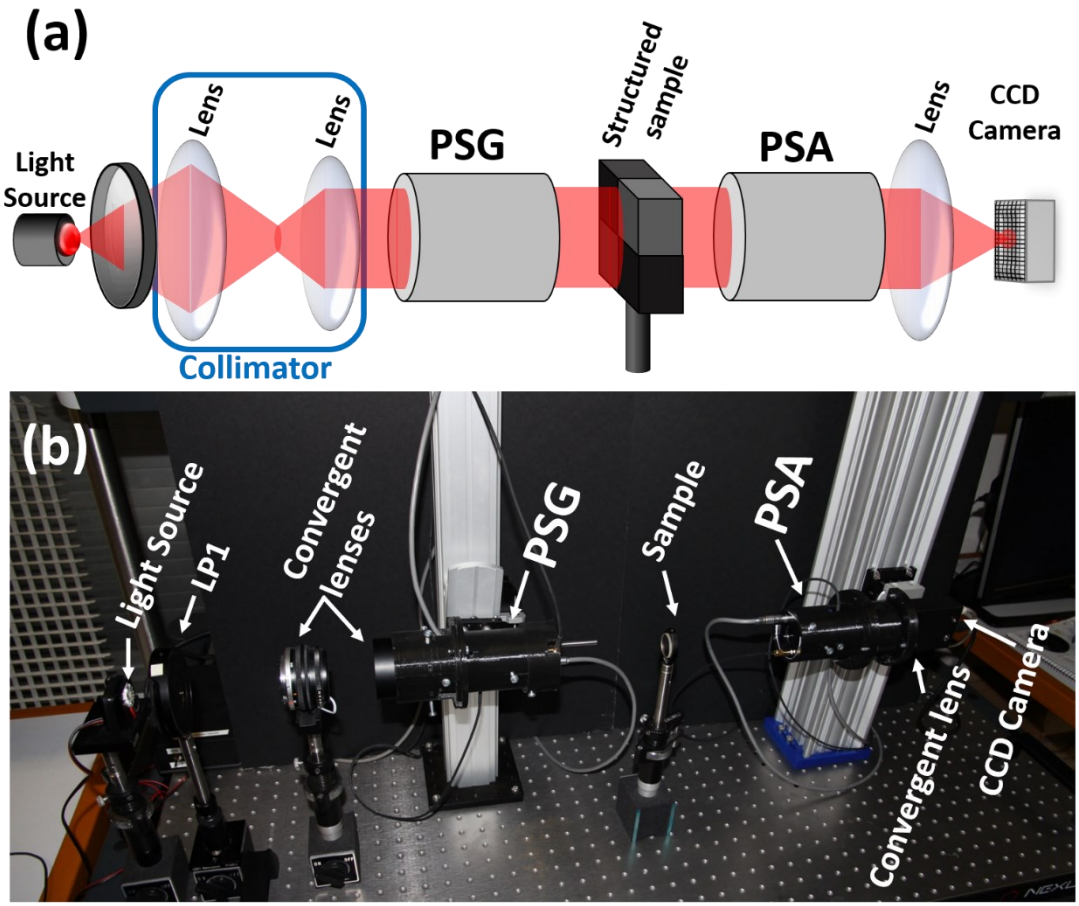

Figure 4-15. (a) Scheme of the set-up and (b) picture of the experimental Mueller polarimeter.

Most of the depolarizing samples employed in this experiment are composed of different spatially distributed optical elements (Figure 4-16). The way that light interacts with each of these optical elements is different thus resulting in an output collimated beam comprising a polarization spatial distribution.

All the experimental measurements were made in transmission and the light transmitted by samples is analyzed through the PSA. Note that the spatial polarization distribution coming from the different polarimetric elements of the sample results in spatial variations in the intensity distribution of the beam after the polarization analysis of the PSA. Finally, the analyzed light is incoherently combined in a small region of the CCD camera through the same high-resolution objective used in the regular set-up (more information in section 3.2.2). Under this scenario,

when we converge the light through the objective we are incoherently adding these intensities thus reproducing the physical scenario described in Eq. (4.18), and thus, experimentally sintetizing depolarizers.

To converge the collimated beam in a small region of the CCD camera, the objective focuses on infinity. As a result, the LED source is imaged on the CCD camera (the image of the LED source measures approximately 0.7x0.7 mm^2; 200x200 pixels) being a non-punctual spot. To work with this spot size, we averaged the measured Mueller matrices of the 200x200 pixels before calculating the depolarization parameters (Table 4-4). This averaging process was compared with the value obtained at averaging the depolarization parameters of each of the 200x200 pixels and the results obtained with both methods are equivalent.

In the following, we study three synthesized depolarizers, labeled as $\boldsymbol{M}_\alpha$, $\boldsymbol{M}_\beta$, and $\boldsymbol{M}_\gamma$, that experimentally probe the potential of IPP to analyze and classify depolarizers. In particular, we analyze three depolarizers that have been synthesized according to Eq. (4.18). Each depolarizer is constructed with different polarimetric elements spatially separated. These elements correspond to the different $\boldsymbol{M}_i$ terms of Eq. (4.18), and the α_i values are the percentage of light that impinges each element and that can be controlled by spatially shifting these elements.

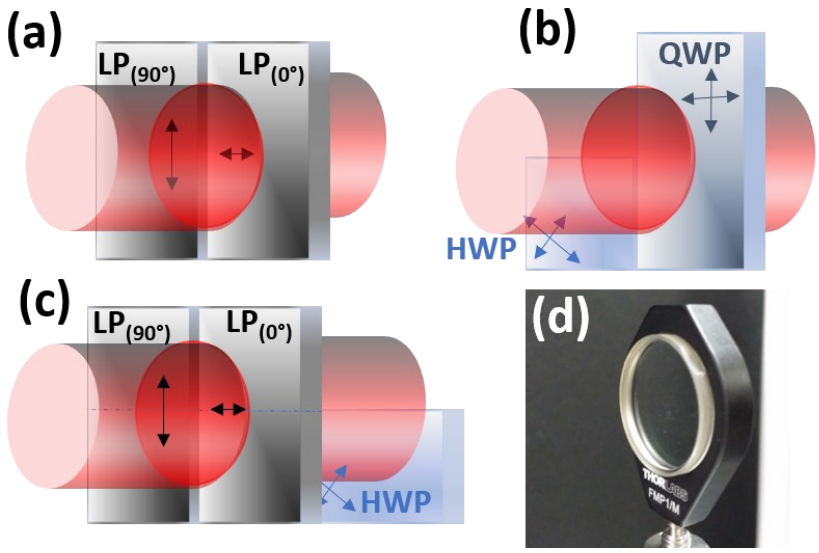

Figure 4-16. Scheme of samples: (a) $\boldsymbol{M}_\alpha$, (b) $\boldsymbol{M}_\beta$, and (c) $\boldsymbol{M}_\gamma$. (d) Picture of sample $\boldsymbol{M}_\delta$. LP: linear polarizer, HWP: half-wave plate, QWP: quarter-wave plate. The orientation of LPs is marked within the () brackets and all the angles are referenced concerning the horizontal axis of the laboratory.

First, sample $\boldsymbol{M}_\alpha$ (sketched in Figure 4-16 (a)) is built by combining two linear polarizers: a horizontally oriented polarizer ($\boldsymbol{M}_{LP(0°)}$) and a vertically oriented polarizer ($\boldsymbol{M}_{LP(90°)}$). The two elements are equally illuminated, i.e., half of the light goes through the horizontal polarizer and the other half through the vertical polarizer. Accordingly, the Mueller matrix of this sample is written as,

$$\mathbf{M}_{\alpha} = \alpha_1 \mathbf{M}_{LP(0°)} + \alpha_2 \mathbf{M}_{LP(90°)} = \frac{1}{2}\begin{pmatrix} 1 & 0 & 0 & 0 \\ 0 & 1 & 0 & 0 \\ 0 & 0 & 0 & 0 \\ 0 & 0 & 0 & 0 \end{pmatrix}. \quad (4.23)$$

where α_1 and α_2 values are both equal to ½ according to their percentage of illumination. The theoretical and experimentally measured IPP and P_Δ values are provided in Table 4-4. Note that P_2 and P_3 values are equal to 1 as we combine only two non-depolarizing elements. As previously said, more than two elements must be combined to be able to reach lower P_2 and P_3 values.

Depolarizer	Theory				Experiment			
	P_1	P_2	P_3	P_Δ	P_1	P_2	P_3	P_Δ
M_α	**0.00**	**1.00**	**1.00**	**0.58**	**0.07**	**0.93**	**1.00**	**0.56**
M_β	**0.40**	**0.71**	**1.00**	**0.58**	**0.40**	**0.70**	**1.00**	**0.59**
M_γ	**0.00**	**0.00**	**0.00**	**0.00**	**0.05**	**0.19**	**0.25**	**0.13**
M_δ	**-**	**-**	**-**	**-**	**0.01**	**0.05**	**0.09**	**0.04**

Table 4-4. Theoretical and experimental results of the depolarizing systems studied.

Second, sample $\boldsymbol{M}_\beta$ (sketched in Figure 4-16 (b)) is constructed by combining three elements thus allowing P_2 values smaller than 1 (see Table 4-4). In particular, it is synthesized with a quarter-have plate with the fast axis vertically oriented ($\boldsymbol{M}_{QWP(90°)}$), with a half-have plate with the fast axis oriented at -45° with respect to the horizontal reference ($\boldsymbol{M}_{HWP(-45°)}$) and with air ($\boldsymbol{M}_{air}$). The illumination is divided into ½ for the $\boldsymbol{M}_{QWP(0°)}$, ¼ for the $\boldsymbol{M}_{HWP(-45°)}$, and ¼ for the air, so α_1, α_2, and α_3 take these respective values. Therefore, the Mueller matrix of the second experimentally synthesized depolarizer is:

$$\mathbf{M}_{\beta} = \alpha_1 \mathbf{M}_{QWP(90°)} + \alpha_2 \mathbf{M}_{HWP(-45°)} + \alpha_3 \mathbf{M}_{air} = \begin{pmatrix} 1 & 0 & 0 & 0 \\ 0 & 1/2 & 0 & 0 \\ 0 & 0 & 1/2 & -1/2 \\ 0 & 0 & 1/2 & 0 \end{pmatrix}. \quad (4.24)$$

The comparison of $\boldsymbol{M}_\alpha$ and $\boldsymbol{M}_\beta$ depolarizers shows that in theory these two samples are described with the same depolarization index but completely different P_1 and P_2 values. Concerning the experimental results, these two depolarizers could be differentiated using P_Δ but the difference observed between the IPP values is much higher (0.33 P_1 difference, 0.23 P_2 difference vs 0.03 P_Δ difference; Table 4-4). Therefore, the classification potential of IPP is proved higher than P_Δ for the $\boldsymbol{M}_\alpha$ and $\boldsymbol{M}_\beta$ depolarizers. Note that the experimental and the theoretical results are in agreement but present small differences. We mainly attribute these small differences to the non-uniform distribution of the beam and possible misalignments of the polarimetric elements during the synthesis of the depolarizer.

Finally, we synthesize an ideal depolarizer (P_Δ=P_1=P_2=P_3=0), labeled as $\boldsymbol{M}_\gamma$ (sketched in Figure 4-16 (c)). $\boldsymbol{M}_\gamma$ is comprised by the sample $\boldsymbol{M}_\alpha$ followed by an equally weighted combination of a half-wave plate ($\boldsymbol{M}_{HWP(-45°)}$) and air (see Figure 4-16 (c)). The half-wave plate is placed in a way that interacts with half of the light coming from the vertical polarizer and half of the light coming

from the horizontal polarizer. Under that architecture, the other light passes through the air. Accordingly, the Mueller matrix of the synthesized ideal depolarizer is:

$$\mathbf{M}_{\gamma} = \alpha_1 \mathbf{M}_{LP(0^\circ)} + \alpha_2 \mathbf{M}_{LP(90^\circ)} + \alpha_3 \mathbf{M}_{HWP(-45^\circ)} \mathbf{M}_{LP(0^\circ)} + \alpha_4 \mathbf{M}_{HWP(-45^\circ)} \mathbf{M}_{LP(90^\circ)} = \frac{1}{2} \begin{pmatrix} 1 & 0 & 0 & 0 \\ 0 & 0 & 0 & 0 \\ 0 & 0 & 0 & 0 \\ 0 & 0 & 0 & 0 \end{pmatrix} \quad (4.25)$$

where $\alpha_1=\alpha_2=\alpha_3=\alpha_4=¼$ according to the percentage of light that passes through each combination of elements. Note that all the coefficients of the Mueller matrix of $\boldsymbol{M}_{\gamma}$, like ideal depolarizers, are equal to 0, except for the m_{00} coefficient. Therefore, using this construction we should build an ideal depolarizer.

The experimental implementation of $\boldsymbol{M}_{\gamma}$ does not reach the ideal $P_\Delta=P_1=P_2=P_3=0$ values but values lower than 0.25 in all the cases (see Table 4-4). In fact, the implementation of ideal depolarizers following the proposed method is more sensitive to misalignments than the accomplishment of the two previous constructions, because the implementation of this case involves a larger number of polarimetric elements. Therefore, it is expected to observe more differences between the experimental and theoretical results.

We end this study by comparing the results obtained with $\boldsymbol{M}_{\gamma}$ and the experimental IPP and P_Δ values of a commercial achromatic depolarizer labeled as $\boldsymbol{M}_{\delta}$ (DPU-25-A-Quartz-Wedge Achromatic Depolarizer distributed by Thorlabs; Figure 4-16 (d)). We see that although the $\boldsymbol{M}_{\delta}$ results are closer to 0 they do not reach that value. It may be caused for the measurement error of the polarimeters (provided in section 3.3.3).

In summary, we highlight the utility and physical significance of considering IPP and CP sets of descriptors for the analysis of depolarizing systems as biological tissue samples. Both sets of parameters provide overall information on the depolarization features of a given material sample, in such a manner that the degree of polarimetric purity P_Δ is obtained through respective weighted square averages of the IPP and the CP (Eqs. (2.45) and (2.46)). These two groups of metrics constitute three-dimensional spaces (the Component space and the Purity space) that together, give complete information of the mechanisms that generate the depolarization in any given medium, allowing its better polarimetric interpretation. On the one hand, the Purity space and the IPP report the relative amounts of non-depolarizing equivalent components that a system can be assimilated with and the depolarization anisotropy associated with the sample. On the other hand, CP space reports the optical effects of dichroism and birefringence implicated in the depolarizing process. Therefore, the first space provides a more probabilistic view of polarimetrically equivalent systems, while the second one provides a conception linked to the polarimetric nature of the scatterers involved in the medium.

We have observed, by means of limit examples, the compatibility of both approaches and their high degree of independence (5 independent parameters from the existing 6). In particular, we have seen how non-dichroic ($D=P=0$) depolarizers are better characterized with IPP while forward and reverse illuminated dichroic depolarizers with $D \neq P$ are identified as equal structures with IPP but differentiated with CP. For the case of depolarizers accomplishing the

condition (*D=P>0*), IPP or CP can be better suited for its identification depending on which other depolarizers you compare them with (i.e., $D(\boldsymbol{M_1})=D(\boldsymbol{M_2})$ or $D(\boldsymbol{M_1}) \neq D(\boldsymbol{M_2})$).

Moreover, the study also provides the regions where IPP and CP acquire better discriminatory potential. IPP is better for intermediate depolarizing systems ($0.2<P_\Delta<0.6$) and CP for low depolarizing structures ($P_\Delta>0.6$). Therefore, we propose the complementary use of both spaces simultaneously for the analysis of depolarizing systems.

Finally, we have experimentally proved the discriminatory potential of IPP in front of P_Δ through the experimental synthesis of depolarizing samples. In that way, we have built two depolarizers identified as "identical" through the P_Δ metric but discriminated as different structures with IPP. In addition, we have proposed a method to experimentally synthesize depolarizers and we have explored the limits of this method through the synthesis of an ideal depolarizer. The experimental depolarizer that has been built to mimic an ideal depolarizer, achieved by using the proposed method, reached a value of $P_\Delta=0.13$ ($P_\Delta=0$ for an ideal depolarizer).

The description provided in this section is based on artificially constructed depolarizing systems, but the results can be extrapolated to real depolarizers as, biomedical tissue samples, which in most cases, are highly scattering and depolarizing systems. Consequently, this study becomes relevant for the analysis of the physical mechanisms causing depolarization in biological tissue samples.

Chapter 5 Biophotonic applications

In the previous chapter, the measurement of the Mueller matrix is shown to be optimal for the inspection of the polarimetric properties of samples compared to the use of PG techniques. In addition, it also illustrates the potential of using the indices of polarimetric purity (IPP, a set of three parameters calculated from the Mueller matrix) to study the depolarization that is produced by samples. We demonstrated, based on simulations and theoretical experiments, that the indices of polarimetric purity further synthesize the depolarization information when compared to the commonly used depolarization index, P_{Δ}. According to these results, this chapter analyzes the potential of using Mueller polarimetry, and especially the IPP metrics, for the study of biological tissues.

The chapter is divided into two main sections: in the first section (section 5.1), Mueller polarimetry is used to inspect biological tissues of animal origin, and in the second section (section 5.2), the same polarimetric techniques are experimentally implemented to analyze plant tissues. In section 5.1, the studies are focused on exploiting the depolarization information encoded in the Mueller matrix to obtain new and more detailed physical information from the animal tissues. In particular, we studied the use of IPP to (i) improve the imaging and visualization of animal tissue samples (subsection 5.1.1) and (ii) to automatically classify different animal tissues (subsection 5.1.2). In section 5.2, the potential of Mueller polarimetry for plant imaging is discussed and compared with other polarimetric and non-polarimetric optical techniques that are commonly used.

5.1 Polarization techniques for biomedical tissue applications

The interest of using polarimetric techniques to obtain information from animal tissues, principally for biomedical purposes, has been proved in several works [48,79,81,82,84,85,110–148]. Nowadays, polarimetry is applied in medical applications as, for instance, the evaluation of skin diseases [78,79,115,116,125,126], the prevention from eye disorders [119,120,142], the early cancer recognition [81,82,127–132,134–136,145,146], among others.

Some of these works are based on the use of PG techniques [48,79,81,82,84,85,110–116,145–148], while others are performed through measuring the Mueller matrix [117–139]. In the previous chapter, we demonstrated that PG techniques are a particular case of the Mueller matrix polarimetry. Therefore, the next studies following provided are based on the experimental implementation of Mueller matrix techniques.

The Mueller matrix of a sample is a 4x4 matrix that describes their polarimetric response [45,46]. This polarimetric response encodes, in a mixed way, information of three physical properties: diattenuation, retardance, and depolarization. In the case of the biomedical field, some authors have shown that relevant knowledge can be obtained from the analysis of the retardance and depolarization properties of biological tissues [111,122,123,129,138,143,144, 153]. In these studies, retardance properties are explored by using several metrics (total retardance R, the linear retardance δ, the angle orientation of the fast axis, θ, the optical rotation of the circular retarder, φ, etc.) but the study of depolarization is usually limited to the use of the depolarization index, P_Δ [45,69,119,124,129], or the depolarization power, Δ [66,118,127,132,134,138], both being a global measure of the depolarization (these retardance and depolarization parameters are described in detail in Chapter 2). In the following subsections, we analyze other depolarization-based metrics to enhance the image contrast of samples and to obtain new and more detailed physical information of animal tissue samples.

5.1.1 Indices of polarimetric purity for biomedical tissue imaging

In this first study, the indices of polarimetric purity (IPP) are experimentally implemented to further characterize the depolarization behavior of measured animal *ex-vivo* tissues and to enhance the image contrast obtained at imaging these tissues. In principle, IPP should provide new information related to the anisotropic nature of the depolarization that may help us to easier recognize some tissue structures or reveal other structures not visible with the commonly used polarimetric metrics.

The work is grounded on the polarimetric analysis of three samples: (A) a non-standardized dissection of a rabbit leg, (B) an endocardial view of a dissected lamb heart, and (C) an undissected lamb kidney. The study starts (section 5.1.1.1) with the analysis of the ***M*** of sample A and the calculus of the images corresponding to the commonly used metrics *D*, *R, Δ* (the latter two obtained from the Lu-Chipman decomposition [66]), and the depolarization index, P_Δ. Next, the IPP of sample A are calculated and the resulting images are compared with those obtained with the previous standard ***M*** methods (section 5.1.1.2). Finally, the study shows some special cases that highlight the benefits of using IPP (section 5.1.1.3), being the IPP capable of revealing structures not observed in the other analyzed observables.

5.1.1.1 Polarimetric analysis based on the Lu-Chipman decomposition and the P_Δ metric

The Mueller matrix of a non-standardized dissection of a rabbit leg (sample A) was measured using the Mueller polarimeter described in Chapter 3 operated in the reflection configuration. The tissue was measured by using the blue channel (470 nm) because we wanted to inspect biological structures placed at the surface of the sample and larger wavelengths penetrate deeper into the scattering sample [11]. The measured Mueller matrix of sample A is shown in Figure 5-1.

Figure 5-1 shows the 16 coefficients that comprise the ***M*** of a region that includes a bone, a striated muscle, and connective tissue from tendons. The first coefficient of the ***M***, m_{00}, indicates the amount of unpolarized light that is reflected by different structures. Accordingly, the image corresponding to the m_{00} coefficient is equivalent to the intensity image that we would obtain with a standard non-polarimetric instrument. For the sake of visualization, this image is shown enlarged in Figure 5-2 (a). In this intensity image, we can distinguish a striated

muscle, pictured in gray, an elongated tendon that is located horizontally over the muscle (it is pictured in white and marked with a blue arrow in Figure 5-2 (a)) and the sample holder, observed in black at the bottom of the image. Note that the bottom side of the image presents lower intensity levels resulting from the non-flatness and the inhomogeneity performance of the sample. This inhomogeneity produces some direct reflections during the sample imaging that saturates the CCD camera. Accordingly, the illumination power of the image was kept low to avoid possible damage to the CCD camera and ensure the correct measurement of the polarization (note that saturated pixels lead to non-physically realizable Mueller matrices that do not describe the physical properties of the analyzed sample). As a result, the illumination of the bottom side of the sample is very low, making it very difficult to recognize tissue structures directly from the intensity image. However, polarimetric information is mostly independent of the intensity used during the ***M*** measurement.

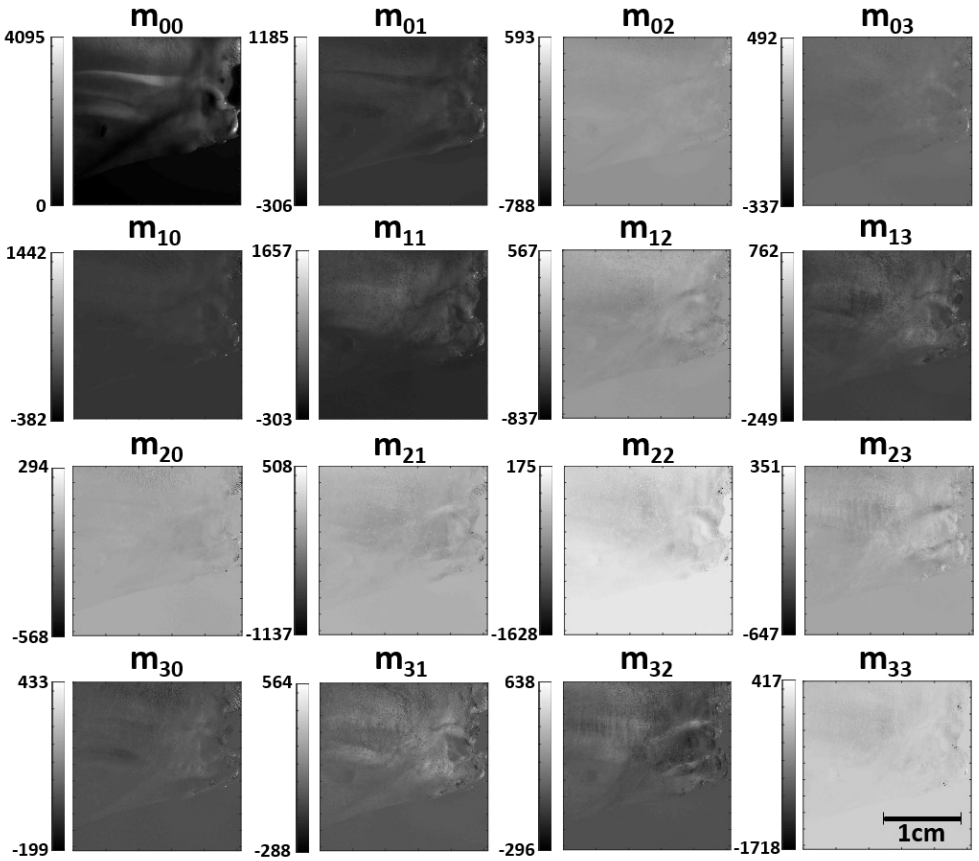

Figure 5-1. Mueller matrix of a region of a non-standardized dissection of an *ex-vivo* rabbit leg (sample A).

The polarimetric information of the sample is encoded in the other 15 coefficients of ***M***. Some structures not observed in the regular intensity image (m_{00}) can be barely appreciated in some of the 15 coefficients of Figure 5-1. Anyway, the efficient recognition of these structures is not possible using these coefficients so further mathematical treatment is required.

Accordingly, we apply the Lu-Chipman product decomposition (described in Chapter 2) to enhance the image contrast of these structures and allow their recognition. The Lu-Chipman decomposition splits ***M*** into a concatenation of three matrices, each containing the information

of one of the main polarimetric properties: the diattenuation properties are mainly contained in $\boldsymbol{M_D}$, retardance information is comprised in $\boldsymbol{M_R}$, and the depolarization behavior of $\boldsymbol{M}$ is described by $\boldsymbol{M_\Delta}$.

The obtained diattenuator matrix $\boldsymbol{M_D}$ from sample A is mostly equivalent to an identity matrix so the diattenuation effects of the sample are minimal and can be neglected. As the diattenuation does not provide significant information (not improving the image contrast), the corresponding image is not shown. In contrast, the retardance and the depolarization matrices, $\boldsymbol{M_R}$ and $\boldsymbol{M_\Delta}$, take results completely different from the identity matrix, thus giving significant information of the tissue structures. This result is in agreement with other studies in the literature also showing that relevant information is mainly connected to retardance and depolarization properties when studying biological tissues [119,133–135,138].

For the sake of the analysis, we have calculated and represented in Figure 5-2 the global retardance R (Figure 5-2 (b)) from $\boldsymbol{M_R}$ (Eq. (2.23)) and the depolarization power Δ (Figure 5-2 (c)) from $\boldsymbol{M_\Delta}$ (Eq. (2.31)). The first quantifies the global birefringence of the sample without distinguishing between linear and circular retardance, and the latter measures the global depolarization capability of the sample. In addition, we have also calculated the depolarization index P_Δ (Figure 5-2 (d); Eq. (2.32)), which also gives information about global depolarization capability of the sample, like Δ, but is calculated directly from $\boldsymbol{M}$. In fact, the P_Δ=1-Δ relation is fulfilled in the case non-dichroic samples ($D=P=0$). For the sake of comparison, the standard intensity image is also displayed in Figure 5-2 (a).

The image associated with the total retardance R (Figure 5-2 (b)) is completely different from the regular intensity image (Figure 5-2 (a)). In Figure 5-2 (b), most of the tissue structures observed in the m_{00} are not visible. In particular, the elongated tendon pictured in white in Figure 5-2 (a), which is placed over the muscle, is now indistinguishable from the surrounding muscle fibers. In that case, the tendon and the surrounding muscle present similar birefringent behavior. The total retardance of both tissues is close to 180°. Note that non-dichroic and non-birefringent materials measured in reflection are characterized for a birefringence of 180° as they introduce a sign change at the S_2 and S_3 Stokes coefficients of the input light (for instance, right-handed circularly polarized light is transformed to left-handed polarized light after reflection). Therefore, this tendon and the surrounding muscle do not induce extra retardation to the incident light beyond those associated with the reflection configuration. In contrast, a thin tendon, marked with a blue arrow in Figure 5-2 (b), presents a differentiated retardance of ∼120°. This tendon is almost invisible in Figure 5-2 (a) but is clearly highlighted in the retardance image (Figure 5-2 (b)) thanks to its particular retardance. Tendons are comprised of wire-like bundles of collagen fibers arrays and this collagen fiber organization gives tendons a certain degree of birefringence. This degree of birefringence depends on the density of fibers, this being lower in the case of large tendons (seen in Figure 5-2 (a)) than in the case of thin tendons (contrasted in Figure 5-2 (b)). In addition, the large tendon is nearer to the tendon-muscle transition, and during this transition, some tendon fibers are replaced by muscle fibers. The combination of these two factors results in a similar birefringence response of the large tendon and its surrounding muscle.

Following with the analysis of the depolarization content, the calculus of Δ and P_Δ lead to images (Figure 5-2 (c) and (d)) quite similar to the intensity image Figure 5-2 (a) but that reveal

some structures not seen in the latter. In both Figure 5-2 (c), and (d), we can distinguish the muscle, the large tendon, and the background, like in the case of Figure 5-2 (a). This means that depolarization mechanisms of the measured muscle and tendon are different enough to be visualized as different structures. In contrast to Figure 5-2 (a), some structures placed at the bottom half of the image are much better contrasted by using these depolarization-based metrics (see Figure 5-2 (c) and (d)). This occurs because pictures based on Δ and P_Δ metrics indicate the capability of different structures to depolarize the incident light and this depolarization capability is independent of the illumination intensity used to image the sample. As a result, the edge between the background corresponding to the sample holder and the rabbit leg is now clearly delimited in Figure 5-2 (c) and (d). Moreover, a nutritious channel of the bone (marked with red arrows in Figure 5-2 (c) and (d)) and a bone crest diagonally crossing the bottom of the sample image (marked with green arrows in Figure 5-2 (c) and (d)), can be better visualized in these depolarization-based images.

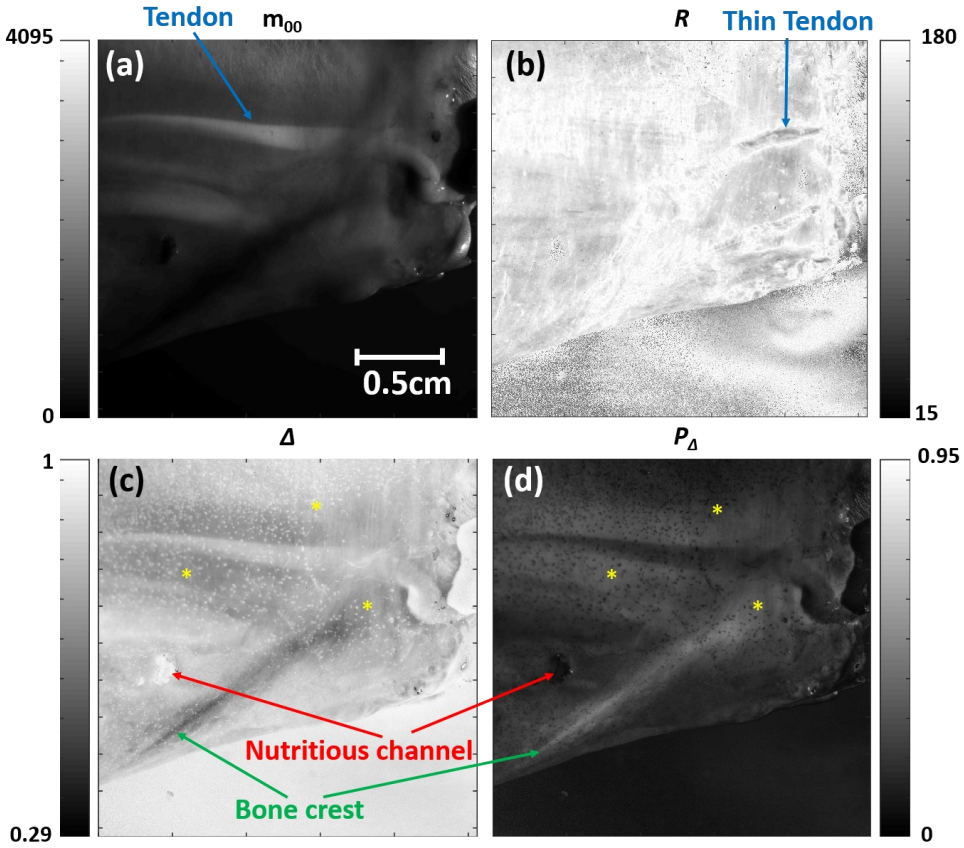

Figure 5-2. (a) Intensity (m_{00} channel), (b) retardance R, (c) depolarization power, Δ, and (d) depolarization index, P_Δ images of a rabbit leg (sample A).

Besides the improved visualization of structures, Δ and P_Δ images (Figure 5-2 (c) and (d)) reveal a spotted structure spread across the sample (see zones around the yellow asterisks, "*", as examples) that is not observed in the m_{00} and R images (Figure 5-2 (a) and (b)). This means that these structures and their surroundings have the same reflectivity and the same birefringence behavior but they differently depolarize light. The measured sample comprises a porous bone placed below the muscle. These spotted arrangements that arise from different

zones of the image may correspond to the location of the nutritious foramina of the corresponding porous bone.

As a corollary of this section, we want to highlight the extra information that can be obtained when using polarimetric observables in front of using the regular intensity images and how this new information can reveal some structures hidden in regular intensity images. For example, a spotted structure that may be related to the location of nutritious foramina is revealed when the global depolarization capability of sample A is analyzed.

5.1.1.2 IPP for the contrast enhancement of animal tissues

In the preceding subsection, we have performed a first polarimetric analysis of sample A based on the most commonly used metrics. From now on, the IPP will be experimentally implemented for three main reasons: (1) IPP further synthesize the depolarization information of the sample as discussed in section 4.2; (2) the mathematical implementation of IPP (described in section 2.3.2) is easier to implement than other metrics as it does not require product decompositions; and (3) IPP-based images may lead to better visualization of tissue structures.

Accordingly, the three IPP parameters (P_1, P_2, and P_3) are calculated from the $\boldsymbol{M}$ of sample A (Figure 5-1), and the obtained images are pictured in Figure 5-3 (a)-(c), respectively. In addition, due to the interesting interpretation of the so-called *trivial decomposition* of $\boldsymbol{M}$ [209,211] (discussed in section 2.3.2), the P_2-P_1 and P_3-P_2 differences are also operated. As the P_3-P_2 results do not provide an enhancement in image contrast, we only show the image of P_2-P_1 (Figure 5-3 (d)).

The structures that are contrasted in the P_1, P_2, and P_3 images (Figure 5-3 (a)-(c)) are the same as the observed in Figure 5-2 (c) and (d). This similitude in the results was expected as all five parameters analyze the depolarization capability of the sample. However, Δ and P_Δ parameters are two metrics that measure the global depolarization capability of the sample while P_1, P_2, and P_3 also quantify possible anisotropies in the depolarization process, thus better highlighting structures that depolarize light in a non-isotropic way. In our case of study, the thin tendon highlighted in Figure 5-2 (b) and not visualized in the intensity image (Figure 5-2 (a)) is still visible in the P_2 image (Figure 5-3 (b)). Another example of these contrast differences in polarimetric channels is observed in the P_1 channel (Figure 5-3 (a)) in which the spots of nutritious foramina (the regions containing these spots are marked with yellow asterisks in Figure 5-3 (a)) are better contrasted compared to the P_Δ image. Note that P_Δ can be calculated from the three P_1, P_2, and P_3 parameters (Eq. (2.45)). Therefore, for a given structure, the image contrast obtained with the P_Δ will be always equal (in the case of isotropic depolarization) or lower (in the case of anisotropic depolarization) to the best result obtained with IPP. The best image contrast obtained with a given IPP is mixed with the other two IPP, reducing the final image contrast of the corresponding P_Δ image. Accordingly, it is worth exploring the IPP at analyzing biomedical samples, at least to improve the image contrast of some tissue structures.

In addition, the analysis of some combinations of the IPP parameters, as the difference P_2-P_1 (Figure 5-3 (d)) which has its physical interpretation (discussed in section 2.3.2), can lead to the better visualization of some structures. For example, the thin tendon that is barely visualized in the P_2 image (see the blue arrow in Figure 5-3 (b)) is better contrasted in the P_2-P_1 channel (blue arrow in Figure 5-3 (d)). Moreover, the spotted-like structures that may be related to the

nutritious foramina and that are always represented with the same color in the other depolarization channels (in black in P_Δ, P_1, P_2, and P_3 images, and in white in the Δ image) appears represented in two different shades (white and black) in the P_2-P_1 channel (see Figure 5-3 (d)). For the sake of visualization, a zoom of the region of interest (ROI) marked with a yellow rectangle in Figure 5-3 (d) is shown in Figure 5-3 (e). The different shades of the spots indicate that those pores are physically different (white and black correspond to a different pore typology) because they present different depolarization anisotropies. Since cortical bone porosity can arise both from small cortical vessels and from the inherent structure of the cortical bone itself, we hypothesize that this white-black variation that means different depolarization anisotropies may be related to the depth of the pore and consequently, to its physiological origin.

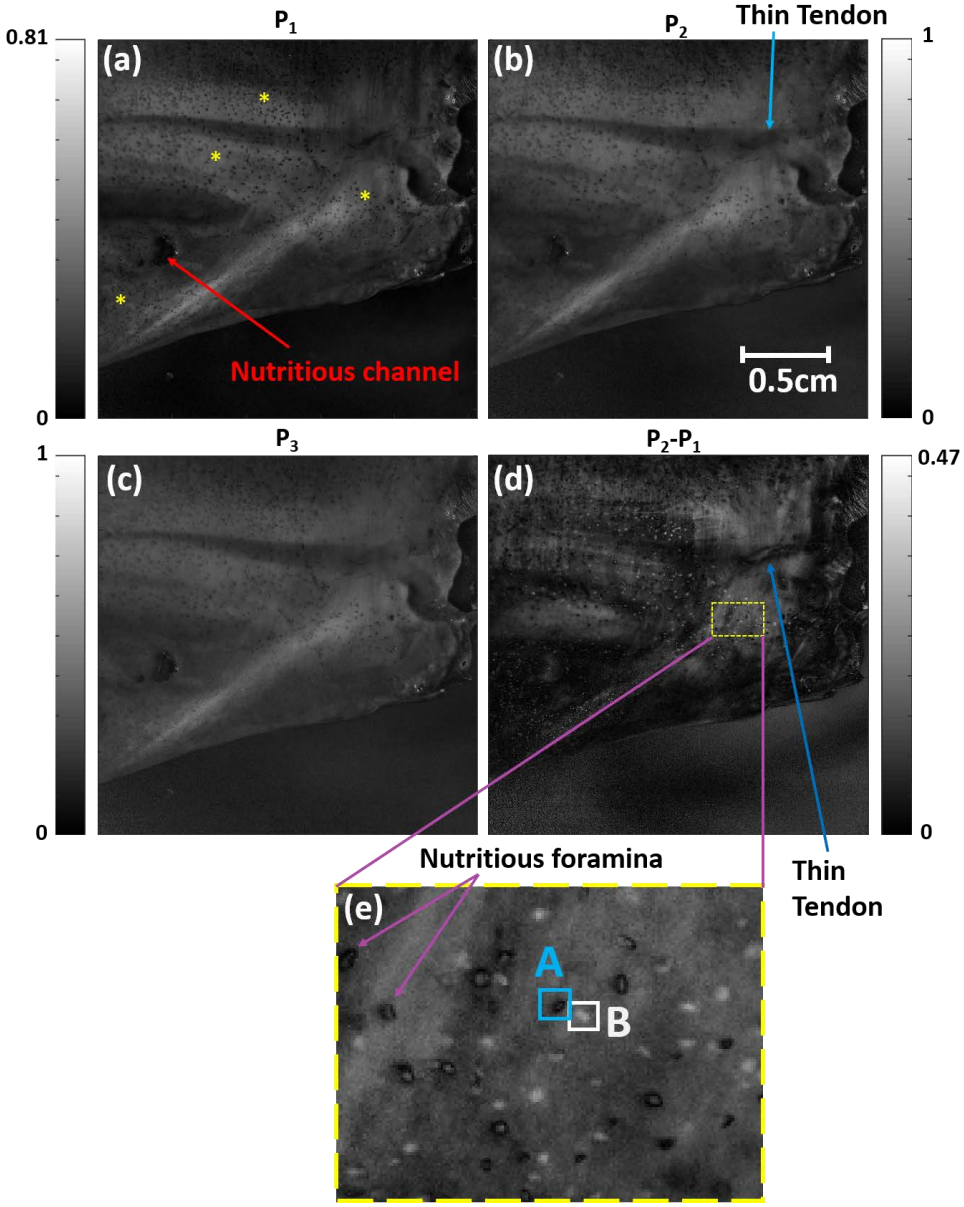

Figure 5-3. (a) P_1, (b) P_2, (c) P_3, and (d) P_2-P_1 images of a rabbit leg (sample A). (e) Zoomed image of the region of interest that is marked in yellow in (d).

To analyze the image contrasts obtained with each of the metrics images (i.e., m_{00}, R, Δ, P_Δ, P_1, P_2, P_3, and P_2-P_1) from a quantitative point of view, we have calculated the visibility V of two different cortical bone pores (labeled as, A and B in Figure 5-3 (e)). The pore A is pictured in black in the P_2-P_1 channel and it is located inside the blue square of Figure 5-3 (e). Alternatively, pore B is colored in white in the P_2-P_1 channel and it is situated inside the white square of Figure 5-3 (e). All the pixels in each square (10x10 pixels) are used to calculate the V according to,

$$V = \frac{I_{\max} - I_{\min}}{I_{\max} + I_{\min}} \tag{5.1}$$

where I_{max} is the maximum value of the pixels comprised in the evaluated region (10x10 pixels), and I_{min} is the minimum value. The value of V ranges from 0 to 1, being 0 related to uncontrasted pores and 1 associated with highly contrasted pores. In most of the images, the I_{min} corresponds to a pixel value of the pore and I_{max} to the value of one pixel of the surrounding. However, for the square B of the P_2-P_1 channel and the pores of the Δ image, the I_{min} corresponds to a value of one pixel of the surrounding and I_{max} to a pixel value of the pore.

The particular values of the visibility V for the m_{00}, R, Δ, P_Δ, P_1, P_2, P_3, and P_2-P_1 channels are provided in Table 5-1. The analysis of Table 5-1 shows that the visibility of the bone pores variates with the polarimetric metric selected. The pore A is best contrasted by using the P_2-P_1 channel (V=0.84), followed by the use of P_2 and P_1 metrics (V=0.35 and V=0.34, respectively). In the case of the pore B, the P1 (V=0.45) and the P_2-P_1 (V=0.44) channels are the best suited for their visualization. Note that in both cases, the image contrast is higher with the IPP channels than with the depolarization index P_Δ; the visibility of the pore A is tripled, and the visibility of the pore B is doubled. In summary, the contrast of the cortical bone pores is significantly improved by using IPP.

	m_{00}	R	Δ	P_Δ	P_1	P_2	P_3	P_2-P_1
Pore A	**0.07**	**0.07**	**0.13**	**0.29**	**0.34**	**0.35**	**0.25**	**0.84**
Pore B	**0.08**	**0.11**	**0.11**	**0.22**	**0.45**	**0.11**	**0.21**	**0.44**

Table 5-1. Visibility values V of the pores A and B squared in Figure 5-3 (e).

Last but not least, we propose the use of pseudo-colored images to encode simultaneously the information of all three IPP in one image for its easier visualization. The pseudo-color method is based on the *purity space* concept, shown in Figure 2-2. In the *purity space*, different depolarizers are represented by points located at different zones of a 3D space. The proposed pseudo-color representation consists of associating the red-green-blue (RGB) colors, i.e., the basic light colors, to each *purity space* axis, P_1, P_2, and P_3. In this way, points located at different positions of the *purity space* tetrahedron, thus corresponding to different depolarizers, are displayed with different colors (see Figure 5-4). Under this scenario, the color of each pixel, $C_{pix}(x,y)$, is calculated following the expression:

$$C_{pix}(x,y) = (\alpha_1 P_1(x,y); \alpha_2 P_2(x,y); \alpha_3 P_3(x,y)) \tag{5.2}$$

where $P_1(x,y)$, $P_2(x,y)$, and $P_3(x,y)$ are the x and y pixels of the corresponding IPP images, i.e., Figure 5-3 (a), (b), and (c), respectively. Note that we have added the weights α_1, α_2, and α_3, to the different red, green, and blue channels, respectively. These weights provide certain

flexibility to the method, allowing us to compensate for the usually lower values of P_1 compared to those of P_2 and P_3 and which do not cover the 0 to 1 range. For example, if we measure a sample with most of the P_1 values lower than 0.33 we can set $\alpha_1=3$ to saturate the P_1 values that are larger to 0.33 (i.e., representing it with the maximum red illumination), increasing the color difference between, for instance, P_1=0.1 and P_1=0.2 pixels. If these two P_1 values correspond to two particular structures, we would stand out the visualization of these structures.

Note that the combination of weights chosen for the pseudo-colored representation is not unique and it can be optimized to improve the image contrast of certain structures. However, their optimization to achieve the best results is out of the scope of this study, and we only propose few combinations useful for our particular goals. Moreover, the figure of merit described in Eq. (5.2) is not the unique way to synthesize the IPP information in a pseudo-colored image.

In Figure 5-4 we provide two pseudo-colored images obtained from different figures of merit. First, Figure 5-4 (a) is obtained from Eq. (5.2) with α_1=3, α_2=1, and α_3=1. This combination of weights maximizes the relevance of the P1 channel, thus highlighting the large tendon, the bone crest, and the nutritious channel seen in Figure 5-3 (a). The spots that may be related to the cortical bone pores are also seen (see Figure 5-4 (a)), but the discrimination between the two types of pores (white and black spots of Figure 5-3 (d)) is here lost. In addition, the structure of the thin tendon, first identified in Figure 5-2 (b), is hardly visualized in Figure 5-4 (a). At this point, other combinations of weights or the use of new figures of merit can be explored to increase the contrast of the last-mentioned biological structures. In our case, we have used another figure of merit based on the P_2-P_1 and P_3-P_2 differences of the so-called *trivial decomposition* of $\boldsymbol{M}$ [209,211]. The new approximation is operated as:

$$C_{pix}(x,y) = (\alpha_1 P_3(x,y); \alpha_2(P_2(x,y) - P_1(x,y)); \alpha_3(P_3(x,y) - P_2(x,y))) \tag{5.3}$$

Note that Eq. (5.3) is a non-orthogonal base composed of three terms ranged from 0 to 1. This new figure of merit is useful to highlight the differences between the IPP parameters.

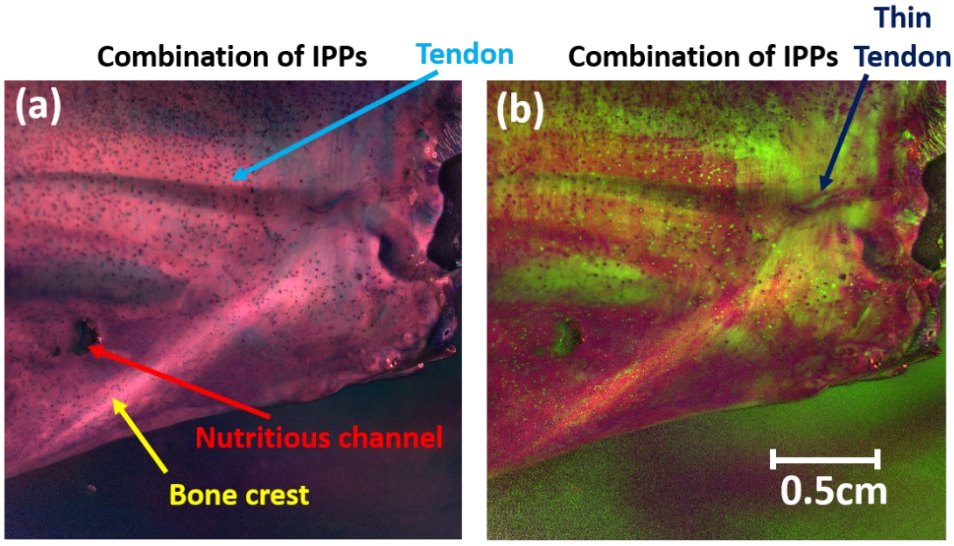

Figure 5-4. Pseudocolored image based on (a) Eq. (5.2) for α_1=3, α_2=1, and α_3=1, and (b) Eq. (5.3) for α_1=2, α_2=2, and α_3=1.

Figure 5-4 (b) pictures the image obtained from Eq. (5.3) with α_1=2, α_2=2, and α_3=1. We see that this second pseudo-colored image presents a differentiated visualization compared to those obtained when using the Eq. (5.2) with α_1=3, α_2=1, and α_3=1 (Figure 5-4 (a)). On the one hand, the bone pore discretization, which is lost in Figure 5-4 (a), is now observed through red-green spots. Moreover, the visualization of the thin tendon has been improved in Figure 5-4 (b). By contrast, although the nutritious channel, the large tendon, and the bone crest are still visible, they are poorly visualized because the weight of P_1 is reduced.

Note that aside from the visualization improvement of pseudo-colored images, each color is associated with the physical information of the sample. They are related to the depolarization capability of the biological tissue and the anisotropic behavior of that depolarization.

5.1.1.3 IPP for the contrast enhancement of animal tissues: some interesting *ex-vivo* cases

Up to now, we have analyzed in detail the polarimetric (polarization and depolarization) properties of a rabbit leg sample (labeled as sample A). The contrast obtained from different polarimetric metrics has been quantified and compared, this providing the interest of using the indices of polarimetric purity, IPP, for the analysis of animal tissue samples. However, the study has been performed through the study of a particular case, and the image contrast obtained with the IPP depends on the physical structure and composition of the measured tissues. Therefore, the discussed example could be a rare instance. In particular, the higher the depolarizing anisotropy of the biological structures analyzed, the larger the suitability of the IPP metrics. To show this fact, we show in the following other extra examples where IPP are especially suitable to enhance and reveal structures not observed by using other metrics.

In particular, we provide two new examples based on the measurement of completely distinct tissues that show the potential of using IPP. In these examples, the image contrast is improved, but some structures are also revealed with the IPP-based methods.

The first example consists of measuring a ROI of a dissected lamb heart (sample B) including an endocardium-covered heart muscle and connective tissue that is rich in subvalvular apparatus (Figure 5-5). In particular, the lamb heart was cut into two parts to image the inner section. The inner part comprises some cardiac muscles, heart valves, and cardiac cavities (Figure 5-5). In analogy with the previous study, sample B is analyzed by using the same methods previously discussed in subsections 5.1.1.1 and 5.1.1.2. However, the measurements were taken in the 625 nm channel because it penetrates deeper into the tissue [11] allowing the visualization of internal structures as blood vessels. Figure 5-5 summarizes the results by showing the regular intensity image (the coefficient m_{00}; Figure 5-5 (a)), the retardance image R (Figure 5-5 (b)), the depolarization index image P_Δ (Figure 5-5 (c)), and a pseudo-colored image based on Eq. (5.2) and α_1=3, α_2=1, and α_3=1 (Figure 5-5 (d)).

In the intensity image (Figure 5-5 (a)) we observe some papillary muscles and a solid myocardium. Like in the case of sample A, the intensity image of sample B has certain regions darker than others due to the non-flatness of the measured sample and the oblique illumination. Concerning the retardance image (Figure 5-5 (b)), it indicates certain birefringence variation among the different tissues but this variation is not enough to visually recognize the different tissue structures. By contrast, the depolarization index P_Δ (Figure 5-5 (c)) shows a significant improved image in which the heart valves and cardiac cavities are better contrasted and some

details of the papillary muscles are enhanced (see the connective rich insertion sites close to the red "*"). Finally, the pseudo-colored image based on the IPP provides the best results (Figure 5-5 (d)). The visualization of the papillary muscles and the solid myocardium is improved, together with the contrast of the heart valves and cardiac cavities. In addition, the pseudo-color image based on IPP makes also visible the heart blood capillaries (see Figure 5-5 (d)) that are hardly visible or completely hidden in the other channels not based on the IPP (Figure 5-5 (a)-(c)). It is worth highlighting that the colors used in Figure 5-5 (d) are not only useful to better visualize the tissue structures but they also provide information about the depolarization anisotropy. This information is related to the intrinsic depolarization mechanism of the constituent sample tissues and cannot be retrieved when using the global depolarization parameters (P_Δ and Δ). In other words, the red color of the capillaries and the blue color of the papillary muscles (see Figure 5-5 (d)) indicate that the depolarization mechanisms of these tissues are different, so their structures must be physically different.

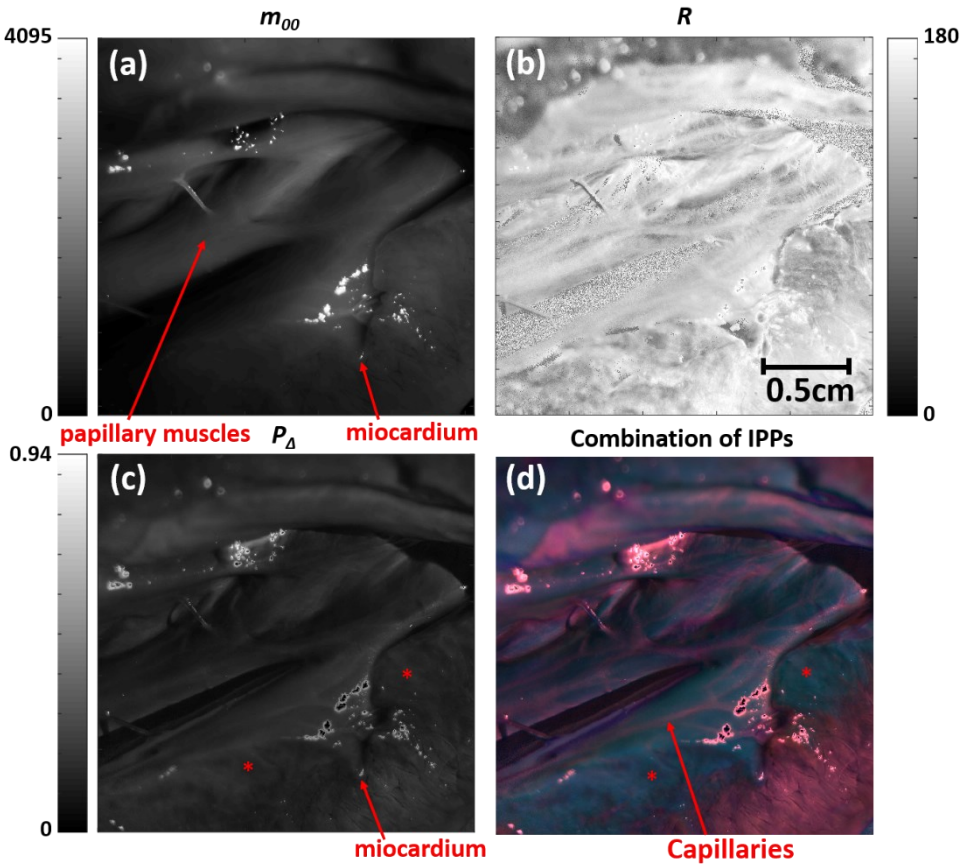

Figure 5-5. (a) Intensity (m_{00} channel), (b) retardance R, (c) depolarization index image P_Δ, and (d) the pseudo-colored images of a dissected lamb heart (sample B). The pseudo-colored image is calculated with Eq. (5.2) for α_1=3, α_2=1, and α_3=1, and the asterisks "*" points to connective rich insertion sites.

Finally, a second biological sample, an undissected lamb kidney (sample C), is analyzed by using the same polarimetric methods. Experimental images analogous to Figure 5-5 but taken from sample C are provided in Figure 5-6. The intensity image (Figure 5-6 (a)) is mostly dark because the measured kidney is characterized by a highly hydrated and significantly curved

surface that saturates the CDD camera in some regions. The hydration of the surface produces small water droplets with significantly larger reflectance than the tissue and the curved surface makes light to be directly reflected in some regions. Consequently, the kidney structures are hardly seen in Figure 5-6 (a).

By turn, the retardance property does not depend on the intensity used during the measurement thus revealing the surface of kidney tissue (see red arrow in Figure 5-6 (b)), and the renal hilum (see purple arrow in Figure 5-6 (b)). However, the left part of the image is not recognizable due to the high percentage of error (white noise) related to measuring it at very low intensities. This error is amplified by the calculation of *R*. In addition, certain parts limiting the two recognized structures are also not well-defined.

Conversely, the edges of the renal hilum that delimits it with the surface kidney tissue are perfectly visualized in the P_Δ image (Figure 5-6 (c)). In this depolarization, channel, the renal hilum is colored darker than the surface kidney tissue. Therefore, the renal hilum is, on average, more depolarizing than the surface kidney tissue. Besides these structures, we observe, in the P_Δ image, a spotted-like structure distributed all over the kidney (see the red arrow in Figure 5-6 (c)). This spotted-like structure corresponds to the stellar veins of the kidney.

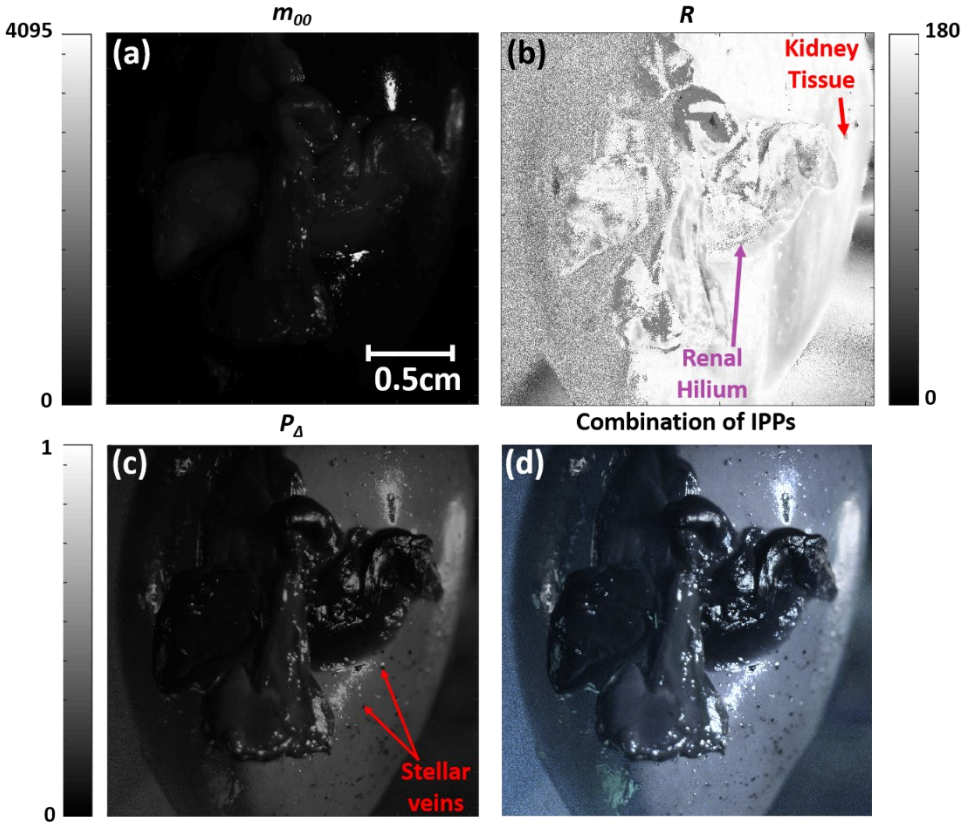

Figure 5-6. (a) Intensity (m_{00} channel), (b) retardance *R*, (c) depolarization index image P_Δ, and (d) the pseudo-colored images of a full rabbit kidney (sample C). The pseudo-colored image is calculated with Eq. (5.4) for α_1=1, α_2=1, and α_3=1.

The visualization of the stellar veins is improved in the pseudo-color image based on the IPP (Figure 5-6 (d)). Figure 5-6 (d) is obtained through operating the next figure of merit with α_1=1, α_2=1, and α_3=1.

$$C_{pix}(x,y) = \left\{ \alpha_1 \left(\frac{P_1(x,y) + P_2(x,y) + P_3(x,y)}{3} \right); \alpha_2 \left(\frac{P_2(x,y) + P_3(x,y)}{2} \right); \alpha_3 P_3(x,y) \right\} \quad (5.4)$$

Like Eq. (5.3), Eq. (5.4) is a non-orthogonal base composed of three terms ranged from 0 to 1. We see that the image obtained with the IPP combination (Figure 5-6 (d)) leads to a significant enhancement of image contrast compared with P_Δ. In particular, the details of the renal hilum and the limits of the left part of the kidney are now perfectly visualized in the pseudo-color image.

In summary, the results discussed in this study show the potential of using Mueller-based polarimetric methods to obtain new information from biological tissues and enhance the contrast in biomedical imaging. In particular, the results provided in sections 5.1.1.2 and 5.1.1.3 exhibit the interest in using IPP for the analysis of the depolarization produced by tissue samples. It has been shown that IPP not only provides an enhancement in the image contrast of some tissues but, in certain cases, they can also reveal some structures not visible in the commonly analyzed depolarization metrics neither in regular intensity images. Moreover, IPP gives further physical information about the depolarization process than the depolarization index, P_Δ. This additional information, which is related to the isotropic or anisotropic way in which the sample depolarizes incident light, is connected with the intrinsic structure of the measured tissue (discussed in detail in section 4.2). For all the above reasons, and because the mathematical algorithm of IPP has an easier implementation than other metrics, we recommend the use of IPP in the polarimetric analysis based on the measurement of the Mueller matrix.

5.1.2 Depolarization spaces for biomedical tissue identification and classification

Once the advantages of using the IPP to image animal tissues have been discussed, we go one step further and we study their potential to automatically identify and classify different tissues through machine learning processes.

The identification and classification of tissues is a recurrent topic in the biomedical domain [16,20,36,48,129,136,232–235]. The correct recognition of tissues acquires a special interest, especially if these tissues are malignant and are detected in the early stages of the disease [155–157,236]. The early tissue recognition increased the probability of long-term survival [155–157]. For example, 99.6% of people with melanoma skin cancer survive their disease for five or more years after the stage I diagnosis compared with the 70.6% of patients diagnosed at stage III [158]. In the case of lung cancer, this 5-years survival rate is 56.6% for patients diagnosed at stage I compared with the 2.9% of those diagnosed at stage IV [158]. And, for rectal cancer, the rate is 89.9% for patients diagnosed at stage I compared with 11.4% of those diagnosed at stage IV [158]. Therefore, the use of early recognition methods, preferably non-invasive, leads to a significant reduction in the number of deaths.

Under this scenario, polarimetry-based techniques are interesting tools for classification as they are non-invasive techniques that can be combined with other optical-based techniques, as for instance, with multispectral or hyperspectral imaging [77–79], Raman spectroscopy [80],

fluorescence microscopy [81–83], second harmonic generation microscopy [84–86], or optical coherence tomography [87], among others. Moreover, as seen in the previous section 5.1.1, polarimetry allows the recognition of some structures not distinguished using the regular intensity method.

To classify tissues, a significant collection of tissues (a statistical sample) is first measured. The measured sample collection must comprise tissues of all the classifiable categories, preferably to a similar extend. Afterward, the obtained results are used to build a classifier that can recognize the different tissue structures. Usually, the built classifier is a supervised classifier (it means that each type of tissue is known *a priori*). Finally, the generated classifier is used to automatically recognize other uncategorized samples. The efficiency of the classifier can be evaluated based on the percentage of tissue samples that have been properly classified.

In the case of building a classifier based on the Mueller polarimetry, the Mueller matrix of each tissue is measured and the polarimetric information is used to build the classifier. In a general case, we would use the dichroism, retardance, and depolarization information to classify the different tissues. However, this study is aimed to find the best way to synthesize the depolarization content to classify the measured tissues so depolarization metrics are the only ones used. This means that the results presented in this section could even be further improved by considering metrics that take into account other physical properties of samples.

The following study analysis is not limited to the evaluation of the IPP results and its comparison with those of the commonly used P_Δ. To make a more general study, the classification results obtained with other depolarization-based metrics are also analyzed. In particular, we will also study the efficiency of other four classifiers based on different sets of three parameters each: the ***H*** matrix eigenvalues (λ_i), the high-order depolarization indices ($P_\Delta^{(m)}$), the type I canonical parameters (d_i), and the type I high-order Lorentz parameters ($L^{(m)}$). This collection of metrics are a nice representation of the most relevant indicators to analyze depolarization that can be nowadays found in the literature [64]. Note that each of these sets of parameters comprises a 3D depolarization space, like the IPP do (all these depolarization spaces have been compiled by Ossikovski and Vizet in ref. [64] and their mathematical formalism is described in Chapter 2). Finally, the efficiency of these different depolarization spaces is compared between them, in terms of tissue classification, and according to the classification results, we identify the depolarization space best suited for tissue classification. Three depolarization spaces turn out to be better for the discrimination and classification of the examined tissues.

The outline of this classification study is as follows: in subsection 5.1.2.1, we explain the methodology that is followed to perform the automatic recognition of three different biological tissues. In particular, we introduce the depolarizing spaces used to build the classifiers, the main characteristics of the analyzed tissues, the data acquisition process, and the types of supervised classifiers used to automatically recognize the different tissues. In subsection 5.1.2.2, we analyze, from a qualitative point of view, the potential and viability of depolarizing spaces for tissue classification. The discussion is based on the representation in the different depolarizing spaces of the experimental data obtained from *ex-vivo* measurements. Next, the information of each depolarization space is used to build the classifiers and their percentage of well-classified

tissues is used as a reference to compare them from a quantitative point of view (subsection 5.1.2.3). Finally, the experimental information of tissues corresponding to different wavelengths is combined to improve the percentage of well-classified tissues (subsection 5.1.2.4).

5.1.2.1 Experimental methodology

The experiment starts by measuring the Mueller matrix image of 120 samples (40 tendons, 40 muscles, and 40 myotendinous junctions) by using the image Mueller polarimeter described in Chapter 3. All the samples were obtained from 20 different chicken thighs, and they were measured by using the same procedure to ensure similar decomposition conditions (the sample preparation procedure is detailed in the following subsection 5.1.2.1.2). The collection of tissues were measured at three different wavelengths, 470, 530, and 625 nm, and, for each wavelength, we have applied a data selection procedure to choose a region of interest (ROI) only composed of pixels of the desired tissue (the ROI selection procedure is detailed in the following subsection 5.1.2.1.4). Each ROI is composed of 150 x 150 pixels, i.e., $2.25 \cdot 10^4$ pixels, and note that each pixel corresponds to a Mueller matrix. Therefore, we work with a database of 2.7 million Mueller matrices. This huge amount of information describes the polarimetric response of different examined tissues.

Once selected the 2.7 million Mueller matrices, the aforementioned collection of depolarization metrics is calculated from each $\boldsymbol{M}$. Then, a randomized section of the pixels (1% of the total data, i.e., $2.7 \cdot 10^4$ pixels) is used to build the supervised classifier. Finally, the other 99% of pixels are used to test the efficiency of the classifiers generated from the different depolarization metrics. Note that we know *a-priori* the type of tissue associated with each pixel so we can determine the percentages of well-classified tissues when using each group of metrics. It is worth mentioning that we are measuring chicken thighs for the ease of sample acquisition, but this classification method can be extrapolated to other tissues such as human tissues for biomedical purposes.

5.1.2.1.1 *3D Depolarization spaces*

In this study, we compare the classification potential of the depolarization index, P_Δ, and five sets of three depolarization metrics each: the $\boldsymbol{H}$ matrix eigenvalues (λ_i), the indices of polarimetric purity (IPP), the high-order depolarization indices ($P_\Delta^{(m)}$), the type I canonical parameters (d_i), and the type I high-order Lorentz parameters ($L^{(m)}$). As previously said, each of these five sets comprises a 3D Depolarization space in which any physically realizable depolarizer can be represented (see Figure 5-7). We consider that the depolarization spaces elected for this work are the most representative of those compiled in ref. [64]. The mathematical foundations of each depolarization space are reviewed in sections 2.3 and 2.4.

The five depolarization spaces can be divided into two groups: those derived from the $\boldsymbol{H}$ matrix eigenvalues; and those based on the type I canonical depolarizer. The first group is constituted by three spaces: (i) the natural depolarization space (Figure 5-7 (a)), composed of three $\boldsymbol{H}$ matrix eigenvalues (λ_2, λ_3, and λ_4); (ii) the purity space (Figure 5-7 (b)), comprised of three IPP (P_1, P_2, and P_3) that are linear combinations of the $\boldsymbol{H}$ matrix eigenvalues (the relation between the IPP and the $\boldsymbol{H}$ eigenvalues is shown in section 2.3.2); and (iii) the high-order indices depolarization space (Figure 5-7 (c)), composed of three depolarization indices of higher order (

P_Δ, $P_\Delta^{(3)}$, and $P_\Delta^{(4)}$) which are non-linear combinations of the ***H*** matrix eigenvalues (the relation between $P_\Delta^{(m)}$ and the ***H*** eigenvalues is provided in section 2.3.4).

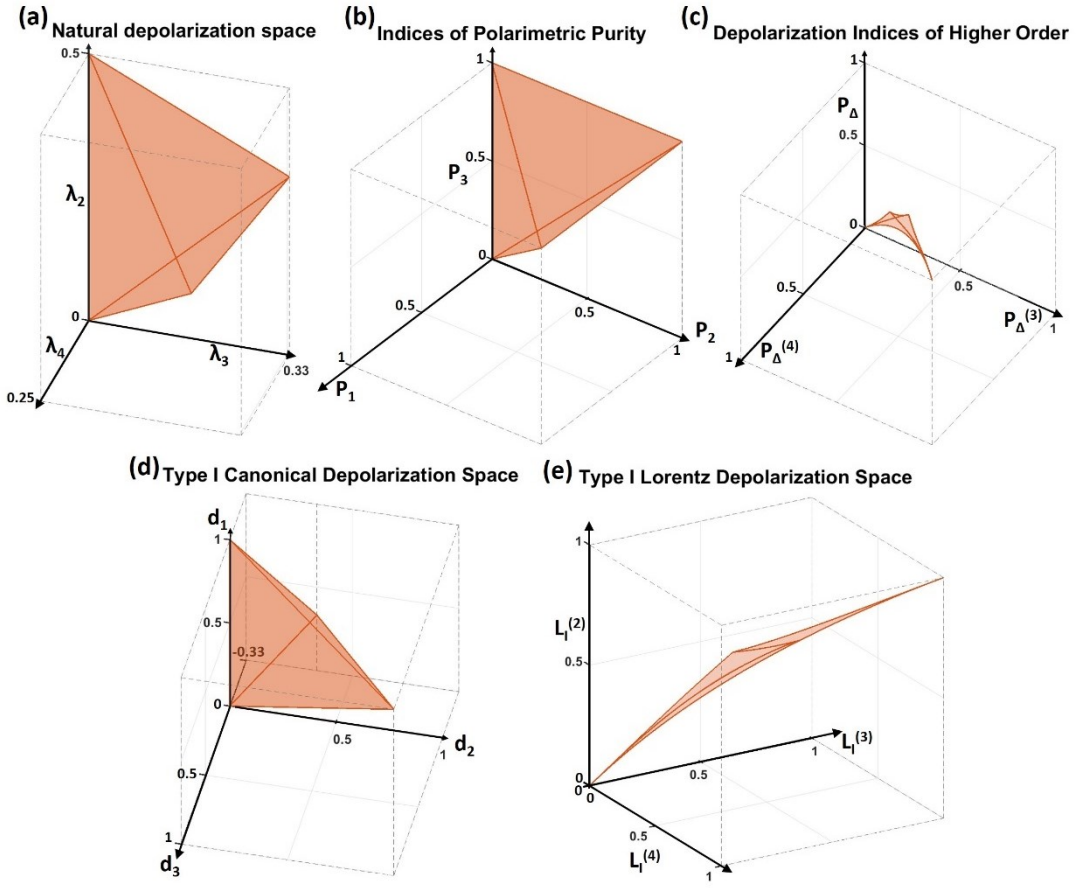

Figure 5-7. Representation of the (a) natural depolarization space, (b) purity space, (c) high-order indices depolarization space, (d) type I canonical depolarization space, and (e) type I Lorentz depolarization space.

On the other hand, the latter group of depolarization spaces comprises: (i) the type-I canonical depolarizer space (Figure 5-7 (d)), comprised of three type-I canonical depolarizer parameters (d_1,d_2 and d_3); and (ii) the type-I Lorentz space (Figure 5-7 (e)), built with three high-order Lorentz indices ($L^{(2)}$, $L^{(3)}$, and $L^{(4)}$) which are non-linear combinations of the type-I canonical depolarizer parameters (the relation between $L^{(m)}$ and the d_i is shown in section 2.4.4).

5.1.2.1.2 *Sample preparation*

Twenty chicken thighs were dissected to obtain the 120 measured samples. In particular, we obtained 2 tendons, 2 muscle, and 2 myotendinous samples from each chicken thigh. In total, 40 muscles, 40 tendons, and 40 myotendinous junctions samples. To ensure similar decomposition conditions, chicken thighs were acquired from the same commercial brand and were dissected 1-2 days before their expiration date. Afterward, the dissected samples were frozen at -16°C to significantly slow down their decomposition process until their measurement. Before measuring them, tissue samples were defrosted for 3 hours. Finally, all samples were placed in similar orientations on a black sample holder to minimize possible sample to sample difference produced by distinct orientations of the tissue fibers.

5.1.2.1.3 *Inspected tissue description*

The classification study is aimed at identifying and discriminating three different tissues: (i) muscles (Figure 5-8 (a)), (ii) tendons (Figure 5-8 (c)), and (iii) myotendinous junctions (Figure 5-8 (b)). These tissues have different physiological functionalities, so their biological composition and physical structure are distinct.

Muscles are soft tissues composed of contractile myofibrils organized in bundles (Figure 5-8 (d)) [237]. These bundles are arranged in the same direction and are surrounded by sheets of connective tissues constituting sets of muscle fibers. In our particular experiment, we measured skeletal muscles which contain different subtypes of muscle fibers [237]. The sets of muscle fiber are also surrounded by sheets of connective tissues and the final sheet of connective tissue that completely encloses the muscle fibers is called fascia and is rich in primary collagen. The same fascia also encloses the tendon and the myotendinous junction that is connected with the muscle. The main function of the fascia is to separate the tissues from the neighboring. Moreover, facia can also resist unidirectional tensions, related to muscle contractions, due to the orientation of their collagen fibers.

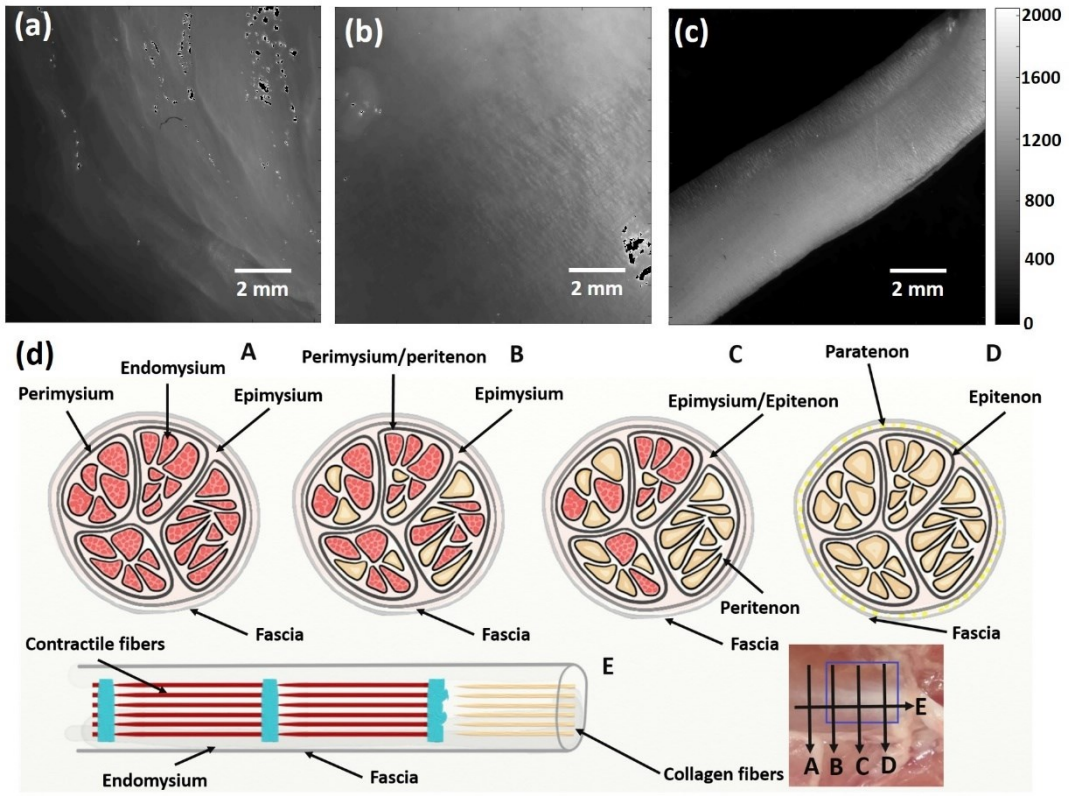

Figure 5-8. Intensity images that were taken at 625 nm of an inspected (a) muscle, (b) myotendinous junction, and (c) tendon. (d) Scheme of the muscle-tendon transition [238] in which "A" is the cross-section of a muscle, "B" and "C" are the cross-sections of the myotendinous junctions, "D" is the cross-section of a tendon, and "E" is a longitudinal representation of the muscle-tendon transition. The position and directions of the different cross-sections ("A"-"E") are represented with arrows over an RGB intensity image of a muscle-tendon transition (the image is located at the right-bottom of the figure).

Tendons are non-contractile mesodermal tissues that connect muscles to bones [238]. Their structure is similar to the muscle, i.e., composed of bundles organized parallel and in the same direction as the connected muscle ones, but with the bundles containing clusters of type I collagen fibers [239,240] (Figure 5-8 (d)). The presence of type I collagen fibers gives tendons the capacity of withstanding unidirectional tensions. Tendons are also differentiated from muscles for being enclosed by paratenon in addition to the fascia. Paratenon is an irregular cushion of fibroadipose tissue found under the fascia [241,242].

The myotendinous junction is the tissue that exists at the connections between tendons and muscle. It is basically the tissue that completes the transition from muscles to tendons. As a result, the myotendinous junction combines fibers of both, tendon and muscle, tissues (Figure 5-8 (d)). In particular, myotendinous junctions are made of bundles aligned in the same direction as muscle and tendons, but that contain a mixture of clusters of contractile (muscle) and collagen (tendon) fibers [238]. The different types of fibers are clustered in different and separated fascicles, and the percentage of each type of fascicle is progressively changing during the muscle-tendon transition [243,244]. The percentage of contractile fibers is higher in sections that are nearer to the muscle and lower in sections close to the tendon. Finally, the set of bundles that constitutes the myotendinous junction are covered by the same fascia that surrounds the connected muscle and tendon.

5.1.2.1.4 *ROI selection procedure*

The experimental measurement of the studied tissues consisted of taking Mueller images of 512x512 pixels in size at three different wavelengths (470 nm, 530 nm and 625 nm). In some cases, these images contained other elements in addition to the desired tissue itself, thus a selection of a region of interest (ROI) that only contains the desired tissue was performed before starting the classification method. For instance, Figure 5-9 (a) comprises the tendon to be classified, which covers an important part of the image, but it also contains some regions corresponding to the imaging of the sample holder (image background; top-left and bottom-right corners). Figure 5-9 (a) was taken at the 470 nm wavelength.

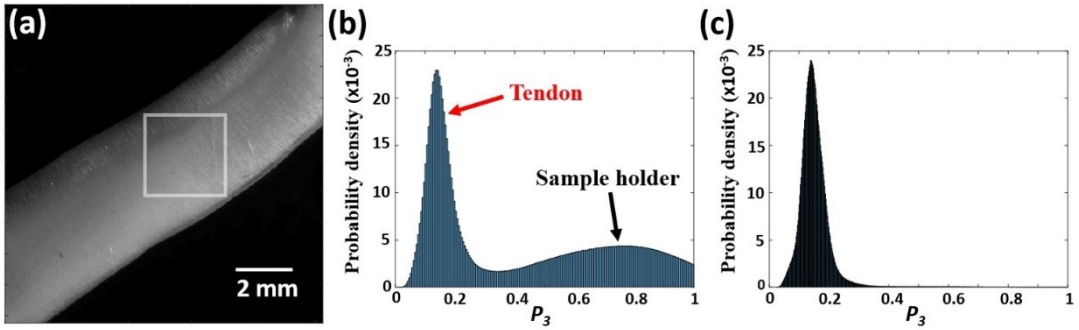

Figure 5-9. (a) Intensity image that was taken at 625 showing a portion of a tendon (grey) placed on a sample holder (black). ROI area of 150x150 pixels in size is highlighted by a white square. Histogram of the 470 nm P_3 index obtained from (b) the full area image and (c) the ROI. Horizontal axes of the histograms are split into (b) 200 parts with steps of 0.05 and (c) 500 parts with steps of 0.02, respectively.

The ROIs are square regions of the original Mueller image of 150x150 pixels in size and which, in principle, only contain the response of the studied tissue (see the white square in Figure 5-9 (a)). To be sure that the selected ROI exclusively contained pixels associated with the tendon so the background response was removed, different depolarization parameters (those discussed in subsection 5.1.2.1.1 and Chapter 2) were calculated from both the original full area image (512x512 pixels) and the ROI image (150x150 pixels). Afterward, their histograms were calculated and analyzed to prove that they only contain the response of the desired tissues (probability density vs depolarization metric). Continuing with the previous example of the tendon of Figure 5-9 (a), the histograms of the P_3 index (defined in section 2.3.2) corresponding to the 512x512 pixels of the Mueller image and to the 150x150 pixels (ROI area) are shown in Figure 5-9 (b) and (c), respectively. The histogram of the original Mueller image (Figure 5-9 (b)) reveals two differentiated contributions: (i) the tendon response, centered at P_3=0.15 and with a width of ∼0.1; and (ii) the background contribution, centered at P_3=0.8 and with a width of ∼0.4. Once identified the background contribution, the influence of the background in the ROI data was checked to be non-existent or reduced to a residual impact. Analyzing Figure 5-9 (c), we see that the ROI contribution can be mainly associated with the tendon response and the background contribution can be considered as non-existent or non-significant.

We want to highlight that this process is followed to select the ROI of each analyzed tissue sample: 40 tendons, 40 muscles, and 40 myotendinous junctions.

5.1.2.1.5 *Supervised classifiers*

The quantitative study discussed in subsection 5.1.2.3 is based on the use of supervised classifiers built from different depolarizing metrics. To build the classifiers, the data coming from the selected ROIs, related to different tissues, is randomly split into two groups. The first group, let us called it training data, comprises 1% of the experimental data (27 thousand data pixels) and is used to build the classifier. To avoid a possible statistical bias related to the use of different sizes of data sampling in the training of the classifier, training data comprises the same amount of data from each tissue type (9 thousand data pixels). From its side, the other 99% of data (around 2.7 million data pixels, let us call it test data) is used to test the performance of the classifiers (i.e., analyze the percentage of well-classified tissues).

The measured data probably takes different statistical distributions in the different depolarization spaces. The type of these data distributions may influence and benefit the efficiency of certain algorithms of supervised classifiers. Consequently, to minimize this fact and strictly associate the differences in the results with the use of different depolarization spaces, three different supervised classifiers are used in this study: (i) tree classifier [245], (ii) linear discriminant classifier [246], and (iii) k-nearest neighbors (kNN) classifier [247].

(i) Tree classifier

The tree classifier is a multi-decision model that can be recognized by its tree-like scheme [245]. The tree-like scheme is composed of decision nodes that have several brunches emerging from it, and end nodes that associate the end of a brunch with a classified item [245]. In our experiment, we have implemented the function of MATLAB called *fitctree* (it is found in the “Statistics and Machine Learning Toolbox”) to build a tree classifier. The function *fitctree* is based on nominal decision nodes that output with

the “true” or “false” answer. Accordingly, they only have two emerging brunches. The process to train the classifier consists of modifying and adding nodes until all the training data is correctly classified.

(ii) Linear discriminant classifier

The linear discriminant classifier is a probabilistic method that generates a multi-dimensional threshold, based on the linear combination of the input parameters, to separate the analyzed data into their different classes. Unlike the preceding tree classifier, the linear discriminant classifier usually does not perfectly classify all the trained data. This may occur because the different classes cannot be separated by hyperplanes. In particular, its training consists of minimizing the figure of merit called the classification cost of the training data [246],

$$\hat{y} = \underset{y=1,\ldots,K}{\arg\min} \sum_{k=1}^{K} \hat{P}(k \mid x) C(y \mid k) \tag{5.5}$$

where $\hat{y}$ is the predicted classification, K is the number of classes (3 in our case: tendon, muscle, and myotendinous junction), $\hat{P}(k \mid x)$ is the posterior probability of class k for an observation x, and $C(y|k)$ is the cost of classifying an observation into a class y when its true class is k. Such classification cost is equal to 0 ($C(y|k)$=0) when y and k are the same class (i.e., the observation is well classified), and $C(y|k)$=1 when y and k are different classes (i.e., the observation is wrong classified).

The mathematics of the posterior probability of Eq. (5.5) is defined by the statistical data distribution adopted to build the classifier. In our experiment, we have implemented the function of MATLAB called *fitcdiscr* (it is also found in the “Statistics and Machine Learning Toolbox”) that assumes that the data distribution is a multivariate normal. Accordingly, the posterior probability is calculated as [246],

$$\hat{P}(k \mid x) = \frac{P(x \mid k) P(k)}{P(x)}, \tag{5.6}$$

where $P(c)$ is a normalization constant calculated from the summation over k of $P(x|k)P(k)$, $P(k)$ is the prior probability of class k, and $P(x|k)$ is the density of a multivariate normal distribution,

$$P(x \mid k) = \frac{1}{\left(2\pi \left|\Sigma_k\right|\right)^{1/2}} \exp\left(-\frac{1}{2} \left(x - \mu_k\right)^T \Sigma_k^{-1} \left(x - \mu_k\right) \right), \tag{5.7}$$

where μ_k is the mean value of the data distribution of class k, Σ_k is its corresponding covariance matrix, and $|\Sigma_k|$ and Σ_{k-1} are the determinant and inverse matrix of Σ_k, respectively.

(iii) k-nearest neighbors (kNN) classifier

The kNN classifier is a non-parametric method based on identifying the k points of the training data that are located nearest, in a N-dimensional space, to the unidentified sample to classify it [247]. Usually, the nearest training data points do not behave to the

same class. Under this scenario, the uncategorized sample is associated with the class that is predominant among the nearest training data points, i.e., the class that is most repeated in the surroundings of the location of the unclassified sample in the *N*-dimensional space.

In our experiment, we have implemented the function of MATLAB called *fitcknn* also included in the "Statistics and Machine Learning Toolbox". To apply this function, we must set two variables: the number of *k* nearest data points and the formula used to evaluate the distance between points. For this study, we have used *k*=50 and the Euclidean distance,

$$d = \sqrt{\sum_{j=1}^{N} \left(x_j - y_j \right)^2} \tag{5.8}$$

where the subindex *j* indicates different variables (in our case different depolarization metrics, e.g., P_1, P_2, or P_3), x_j is a *j* metric value of the tested data, and y_j is the corresponding metric value of the classifiable data.

5.1.2.2 Depolarization spaces for animal tissue classification: a qualitative analysis.

The analysis starts by calculating the metrics that comprise the different depolarization spaces introduced in subsection 5.1.2.1.1 from the 2.7 million Mueller matrices corresponding to the different pixels of the 120 measured samples ROIs (150x 150 pixels each). In this way, 15 values (3x5 depolarization spaces) are obtained for each pixel, thus describing its corresponding depolarization capability. To visualize this huge amount of information (2.7 million pixels x 3 metric values x 5 depolarization spaces), we represented each pixel in the different 3D depolarization spaces by using different points (see Figure 5-10). In particular, the depolarization information of the 2.7 million pixels is represented in the natural depolarization space (Figure 5-10 (a)); the indices of polarimetric purity space (also known as purity space [1,213], Figure 5-10 (b)); the high order depolarization index space (Figure 5-10 (c)); the type I canonical depolarization space (Figure 5-10 (d)); and the type I Lorentz depolarization space (Figure 5-10 (e)). The different colors of the points indicate that the depolarization information of the represented pixel corresponds to a tendon (red), a muscle (green), or a myotendinous junction tissue (blue). For a better interpretation of the results, the edges of the depolarization spaces, delimiting the zone of physically realizable depolarizers, are also represented (purple lines). Note that some spaces are significantly bigger in volume than others. Consequently, the distance between points can be larger in these bigger spaces, which may be useful for tissue discrimination. This feature explains some results shown further on.

Samples were measured at three different wavelengths (470 nm, 530 nm, and 625 nm) and the same procedure described above was followed for each channel. The results obtained at measuring the tissue samples at 625 nm are shown in Figure 5-10. The results of the analogous measurements done at 470 nm and 530 nm wavelength are not represented because the resulting figures are very similar to Figure 5-10. In all the cases, the points seem to be mixed and tend to spread around the space starting from highly depolarizing regions (see Figure 5-10). Comparing the different spaces, we observe that the volume of some spaces, the high-order depolarization index space (Figure 5-10 (c)), and the type I Lorentz space (Figure 5-10 (e)) is almost occupied by dots whereas the other three spaces (the natural, IPP and type I canonical

spaces; Figure 5-10 (a), (b), and (d), respectively) keep some physically realizable region empty. It is worth noting that the first two spaces are based on non-linear combinations of the ***H*** eigenvalues and the type I canonical depolarizer parameters and the other three are constructed from linear combinations.

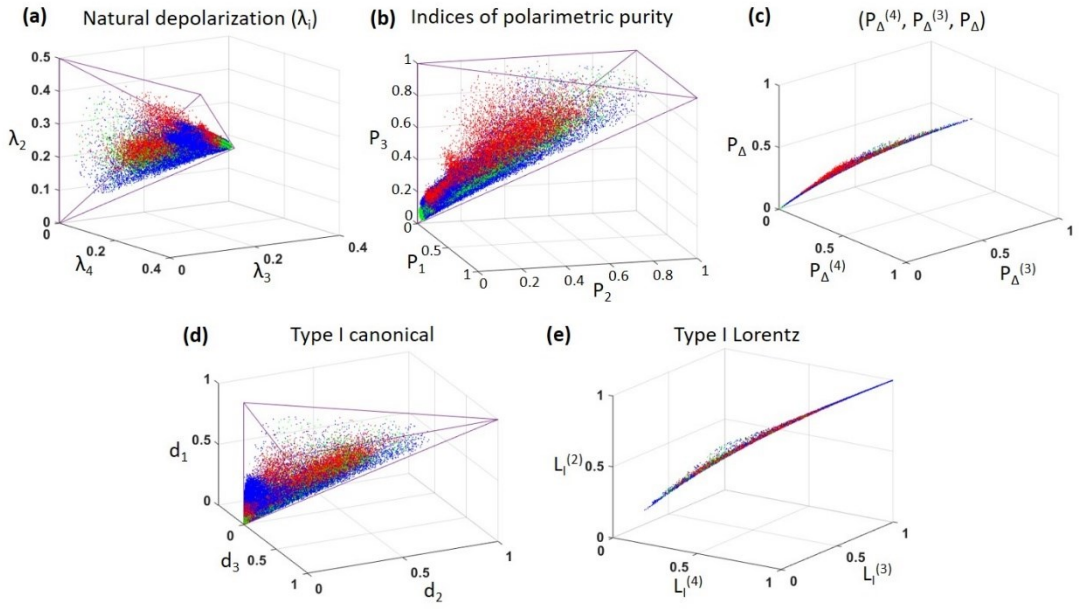

Figure 5-10. 3D representation of the experimental depolarization data measured at 625 nm for tendons (red), muscles (green), and myotendinous junction tissues (blue). Data is represented by points in the depolarization spaces: (a) natural depolarization space; (b) IPP space (purity space); (c) high order depolarization index space; (d) type I canonical depolarization space; and (e) type I Lorentz depolarization space.

The interpretation of the tissue data depolarizing dispersion based on Figure 5-10 can lead to interpretation errors as dots can be superposed. Under this representation, thousands of pixels with similar values are represented by using the same point and it may be misunderstood as one-pixel information. Therefore, different dots in those spaces may be linked to different occurrence weights (quantity of pixels represented per space position), and such information is lost in Figure 5-10. Consequently, 3D nonsymmetric ellipsoids built from the tissue data are represented in the different spaces to better visualize the data distribution (Figure 5-11, Figure 5-12, and Figure 5-13). These nonsymmetric ellipsoids are defined by a three-dimensional central value and six semiaxis values, the laters associated with different directions with respect to the center of the ellipsoid (we call them nonsymmetric ellipsoids because the semiaxis usually takes different values). The center of the ellipsoid corresponds to the median values of the data distributions corresponding to the three metrics of each depolarization space. The six semiaxes are calculated from the corresponding first and ninth deciles and their difference with the median. The positive semiaxis is twice the difference between the ninth decile and the median value, i.e., 2x(9_{th}decile - median), and the negative semiaxis is twice the difference between the median value and the first decile, i.e., 2x(median - 1_{th}decile). Under this description,

approximately 90% of the tissue data (from 86% to 91% depending on the space and tissue) is located inside the volume of the corresponding nonsymmetric ellipsoid. Figure 5-11, Figure 5-12, and Figure 5-13 show the nonsymmetric ellipsoids corresponding to the raw data obtained at measuring the samples at 625 nm, 530 nm, and 470 nm, respectively.

For the sake of visualization, the axis range of Figure 5-11, Figure 5-12, and Figure 5-13 are a portion of the full space range. Note that the axis represents from 10% to 40% of the full space range, and therefore, 90% of the data is concentrated in a reduced region of the physically realizable space. In fact, the majority of the data (90%) is located in a zone associated with highly depolarizing samples, i.e., they are close to the (0,0,0) coordinate in the IPP space (Figure 5-11 (b), Figure 5-12 (b), and Figure 5-13 (b)), the high order depolarization index space (Figure 5-11 (c), Figure 5-12 (c), and Figure 5-13 (c)), and the type I canonical depolarization space (Figure 5-11 (d), Figure 5-12 (d), and Figure 5-13 (d)), near to the (1,1,1) coordinate in the type I canonical depolarization space (Figure 5-11 (e), Figure 5-12 (e), and Figure 5-13 (e)), and near to the (0.25,0.25,0.25) coordinate in the natural depolarization space (Figure 5-11 (a), Figure 5-12 (a), and Figure 5-13 (a)).

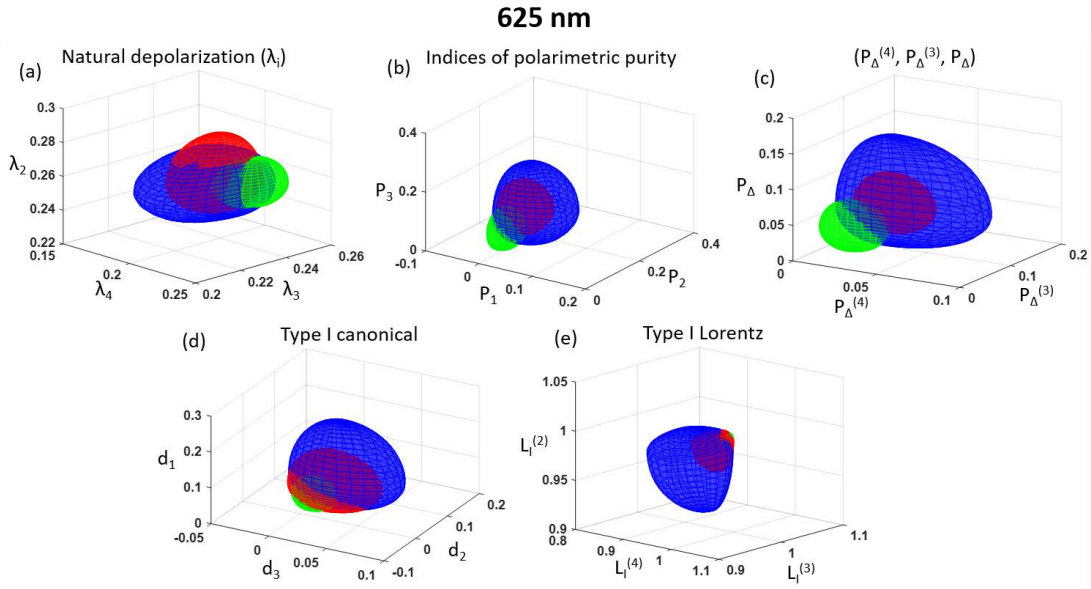

Figure 5-11. 3D representation of the experimental nonsymmetric ellipsoids (described by the median value and the first and ninth deciles of the depolarization data) for tendons (red), muscles (green), and myotendinous junction tissues (blue) measured at 625 nm. Data is represented by points in the depolarization spaces: (a) natural depolarization space; (b) IPP space; (c) high order depolarization index space; (d) type I canonical depolarization space; and (e) type I Lorentz depolarization space.

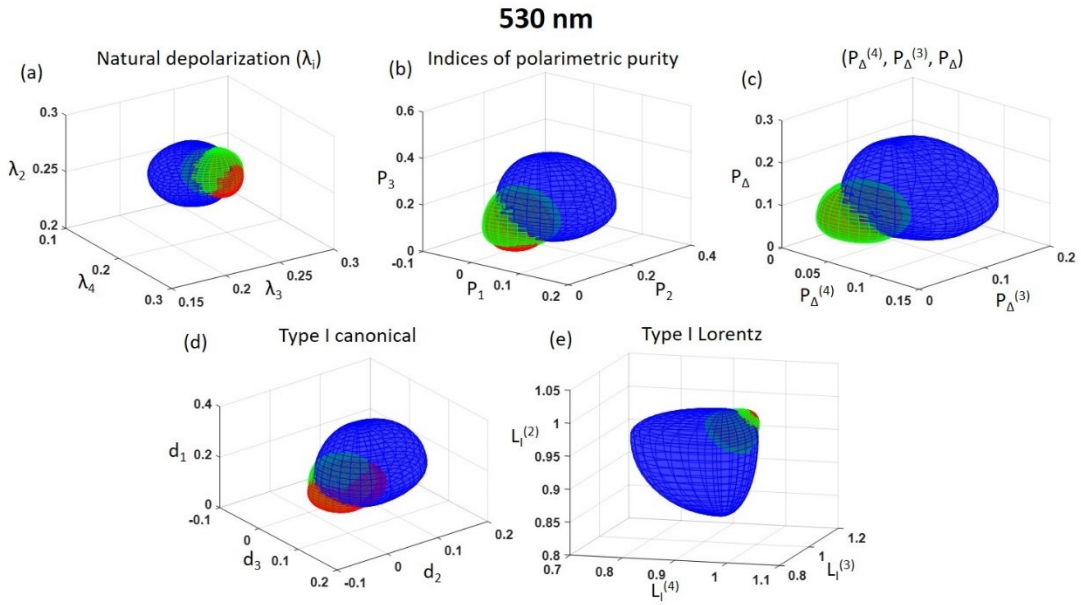

Figure 5-12. 3D representation of the experimental nonsymmetric ellipsoids (described by the median value and the first and ninth deciles of the depolarization data) for tendons (red), muscles (green), and myotendinous junction tissues (blue) measured at 530 nm. Data is represented by points in the depolarization spaces: (a) natural depolarization space; (b) IPP space; (c) high order depolarization index space; (d) type I canonical depolarization space; and (e) type I Lorentz depolarization space.

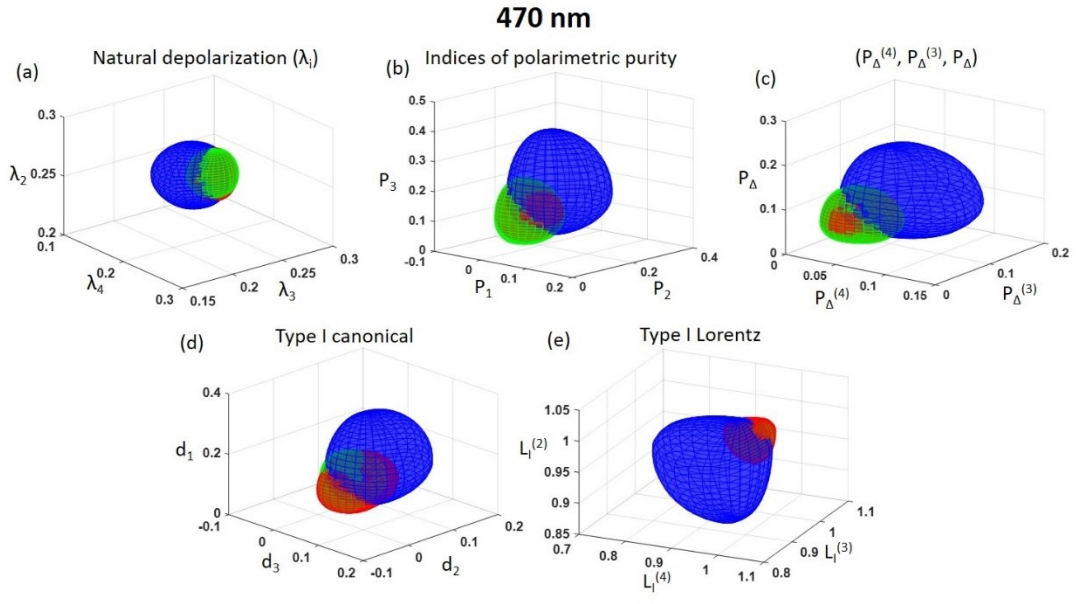

Figure 5-13. 3D representation of the experimental nonsymmetric ellipsoids (described by the median value and the first and ninth deciles of the depolarization data) for tendons (red), muscles (green), and myotendinous junction tissues (blue) measured at 470 nm. Data is represented by points in the depolarization spaces: (a) natural depolarization space; (b) IPP space; (c) high order depolarization index space; (d) type I canonical depolarization space; and (e) type I Lorentz depolarization space.

The spreading of data visualized in Figure 5-10 and represented with ellipsoids-like constructions in Figure 5-11, Figure 5-12, and Figure 5-13 may be related to the interactions of polarized light with different chicken samples or with different zones (structures) of the same non-uniform sample. In that sense, such spreading may be attributed to the non-flatness of the sample, to slightly different decomposition states due to handling variations from sample to sample (slightly disparities in defrosting times, possible dissimilar dissection durations, etc.), or simply, to biological differences between chicken samples. However, the points that are located farthest from the ellipsoid are related to noise measurements, mainly produced by direct reflections that saturate the camera thus deriving in wrong polarimetric measurements. These direct reflections mainly come from sample irregularities and water microdroplets.

The representations based on nonsymmetric ellipsoids (Figure 5-11, Figure 5-12, and Figure 5-13) illustrate the distribution of the depolarization response of different tissue samples. Under these representations, separated ellipsoids without volume overlapping imply that at least 90% of the pixels corresponding to the ellipsoids tissue can be correctly classified. Therefore, the ideal scenario would be the representation of three completely separated ellipsoids that would lead to more than 90% of true positives. In our experiment, the results obtained with 625 nm light (Figure 5-11) indicates that the muscle (marked in green) gives a depolarization response, in the IPP and high-order depolarization spaces (Figure 5-11 (b) and (c)), distinguishable from the tendon and the myotendinous junction. Therefore, the amount of well-classified muscles, in these two spaces, should be higher than the number of correctly identified tendons and myotendinous junction tissues. The latter should present a significant uncertainty due to the overlap of their depolarization response. Alternatively, the tendon and the myotendinous junction can be better distinguished when using the spaces based on type I canonical depolarization parameters (Figure 5-11 (d) and (e)). Under these spaces, the uncertainty between identifying myotendinous junction and tendon tissue should be similar to the uncertainty of differentiating tendons and muscles as their ellipsoids are similarly overlapped.

By contrast, the depolarization response of the analyzed tissues is completely different for 530 nm and 470 nm wavelength (Figure 5-12 and Figure 5-13). For both wavelengths, the expected capability to well-classify myotendinous junctions is higher than the other two tissues. In this case, the tendon and the muscle ellipsoids are completely overlapped whereas the ellipsoid corresponding to the myotendinous junction is only partially overlapped (Figure 5-12 and Figure 5-13). Such observation is coincident for both wavelength, 530 nm and 470nm, and all the explored depolarizing spaces. These results highlight the significance of using polarimetric data obtained at different wavelengths for tissue classificatory purposes.

At this point, we can anticipate that the mixture of the 625 nm, 530 nm, and 470nm measurements would lead to a significant improvement in the classification results. This improvement should be more substantial in the eigenvalue-based spaces because they present a complete overlap between the tendon and the myotendinous junction ellipsoids at 625nm and a complete overlap between the tendon and the muscle ellipsoids at 530 and 470 nm. The combination of these dissimilar data should break the uncertainty observed in the different wavelength channels thus significantly increasing the number of well-classified tissues.

Last but not least, the analysis of Figure 5-11, Figure 5-12, and Figure 5-13 illustrate the depolarization response of different tissues at 625 nm, 530nm, and 470nm, respectively. In

particular, we see that the muscle is the most depolarizing tissue for all three wavelengths because the corresponding green ellipsoid is located close to the pure depolarizer (0,0,0) coordinate in Figure 5-11 (b)-(d), Figure 5-12 (b)-(d), and Figure 5-13 (b)-(d), and close to the (1,1,1) coordinate in Figure 5-11 (e), Figure 5-12 (e), and Figure 5-13 (e). By following the same reasoning, the myotendinous junction is the lowest depolarizing tissue and the analyzed chicken tendons are characterized by an intermediate depolarization capability. Note that the depolarization capability of studied tissues is connected with their structure (described in subsection 5.1.2.1.3). In that sense, the differentiated depolarization response may be related to collagen fibrils, which have a characteristic polarimetric response [84–86,114,122,123,144] and are present in the myotendinous junctions and tendinous tissues but not in muscles. However, this relationship must be further investigated and it is beyond the scope of this study.

5.1.2.3 Depolarization spaces for animal tissue classification: a quantitative analysis.

Once the depolarization results have been qualitative analyzed, a quantitative analysis is performed to identify the depolarization space best suited to properly classify biological tissues. In particular, three different supervised classifier algorithms, the tree classifier [245], the discriminant classifier [246], and the kNN classifier [247] (all described in subsection 5.1.2.1.5) are used to build different classifiers that should automatically recognize the imaged tissues from the experimental Mueller matrices. The percentages of well-classified tissues for each wavelength, supervised classifier algorithm, and set of depolarization metrics are provided in Table 5-2. The percentages presented in Table 5-2 are the mean probability to properly identify the three tissues, i.e., the global percentage of correctly identified tissues among all predictions. Such percentages have an error of ±1% due to the random selection of the test data.

Wavelength	*Supervised classifier*	H eigenvalue-based depolarization metrics				Type I canonical-based depolarization metrics	
		$\lambda_2,\lambda_3,\lambda_4$	P_1,P_2,P_3	P_Δ, $P_\Delta^{(3)}$, $P_\Delta^{(4)}$	P_Δ	d_1,d_2,d_3	$L^{(2)},L^{(3)},L^{(4)}$
625 nm	*Tree*	58	58	55	53	52	50
	Discriminant	59	59	60	57	57	55
	kNN(50)	**65**	**65**	**62**	**60**	**60**	**55**
530 nm	*Tree*	51	51	47	46	55	50
	Discriminant	54	54	51	49	62	49
	kNN(50)	**59**	**59**	**53**	**50**	**64**	**50**
470 nm	*Tree*	52	52	48	46	52	48
	Discriminant	56	55	52	41	60	49
	kNN(50)	**60**	**59**	**54**	**52**	**62**	**49**

Table 5-2. Percentage of well-classified tissues as a function of the wavelength, the depolarization metrics, and the supervised classifier. Bold numbers indicate the best classification results for each wavelength and group of depolarization metrics.

The results shown in Table 5-2 indicate that the tree and the linear discriminant classifiers are fewer efficient than the kNN algorithm for tendon, myotendinous junction, and muscle

tissues classification. Note that the same observation is repeated for all three wavelengths. Moreover, although the used classifier algorithms show different classification efficiencies, for a particular wavelength, the order of depolarization metrics from the least to the most suitable for tissue classification, i.e., with the lowest to the highest percentage of well-classified tissues, is the same regardless of the supervised classifier algorithm selected for the analysis. Consequently, from now on, the quantitative analysis will be based on the kNN results because the interpretation is the same independently on the supervised classifier algorithm and the kNN classifier lead to the best classification results.

The classification results provided in Table 5-2 have been obtained by using metrics based on ***H*** eigenvalues (columns 3 to 6) and type I canonical depolarization parameters (columns 7 and 8). Note that the study is not restricted to the analysis of depolarization spaces but we have also provided the results obtained with the depolarization index, P_Δ, because it is widely used in the literature [45,69,119,124,139]. In the following, we start the analysis of the results through the comparison of the classification efficiencies of the ***H*** eigenvalue-based metrics (columns 3-6). Next, we evaluate the classification efficiencies associated with the depolarization spaces based on type I canonical depolarizer parameters (columns 7 and 8). And finally, we compare the classification results of the best-suited depolarization spaces of each type to end with a global conclusion.

First of all, we see that, among the sets of metrics based on the ***H*** eigenvalues, P_Δ presents the worst results for all three wavelengths (see column 6 vs columns 3-5). In particular, the high order depolarization indices (column 5) lead to an increment of 2% to 3% (depending on the wavelength) of classification success probability with respect to the use of the P_Δ. Concerning the difference in the percentage of well-classified tissues between using the ***H*** eigenvalues (column 3) or the IPP (column 4) compared to the P_Δ, the two depolarization spaces classifies correctly a 5% (for 625nm), 8% (for 530 nm) and 9% (for 470 nm) more tissues. It is worth noting that these results come from a particular case based on three tissues and the classification potential of depolarizing metrics strongly depends on the properties of the analyzed tissues. However, the obtained results indicate a clear tendency in which depolarization spaces are better suited for tissue classification than the P_Δ (depolarization spaces provide better results). Therefore, the IPP are not only better than P_Δ for the visualization of certain tissue structures, as discussed in the previous subsection 5.1.1, but they are also better for tissue classification.

Once determined that the use of ***H*** eigenvalue-based spaces (columns 3-5) gives an increment of classification success compared to the use of P_Δ (column 6), we check the percentages of well-classified tissues obtained with these three depolarization spaces to establish the set of metrics better suited for tissue classification. In this way, we see that high-order depolarization indices (column 5) classify a lower percentage of tissues than the other two spaces, ***H*** eigenvalues and the IPP (columns 3 and 4, respectively). In addition, we observe that, taking into account the 1% error associated with the experiment, the latter two sets of metrics have equivalent classification results.

High order depolarization indices are a non-linear combination of the ***H*** eigenvalue-based (more details in Chapter 2). We have the intuition, although we do not have any mathematical proof, that the lower classification efficiency observed in the high order depolarization space is related to the non-linear construction of high order depolarization indices. After applying the

non-linear transformation on the natural space (Figure 5-10 (a)), the volume of the resultant space, the high order depolarization space (Figure 5-10 (c)), is smaller in comparison. Such volume reduction usually implies compression of the data points and this compression may difficult the discrimination of tissues. We would like to emphasize that this is a heuristic approximation based on this experiment and other experiments may invalidate this discussion. However, similar classification efficiency reduction results are also observed in the other space based on non-linear operations (the type I Lorentz space, column 8 in Table 5-2), as will be further discussed.

In contrast, the IPP present the same classification efficiency as the natural depolarization space (***H*** eigenvalues) and we think that it is produced because such indices are a linear combination of the ***H*** eigenvalues. Some of the used classifier algorithms define the thresholds that delimit the region of each class based on linear combinations of the input variables, for example, the linear discriminant classifier. Therefore, the use of IPP and the ***H*** eigenvalues data should be seen as equivalent information when using this type of classifiers. Under this scenario, according to the results provided in Table 5-2, we recommend the use of ***H*** eigenvalues and IPP for tissue classification as they present the best results. In the case of only using one of both spaces, we recommend the use of IPP because they have an easier interpretation and a larger space volume. The IPP interpretation becomes easier because lower IPP values always indicate more depolarization capability [1,45], whereas lower ***H*** eigenvalues values can be related to lower or higher depolarization capabilities, depending on the eigenvalue [45,70]. For its side, the larger volume of the IPP space improves the visualization of different tissues due to larger distances between points.

Concerning the classification results of the depolarization spaces based on the type I canonical depolarizer parameters (columns 7 and 8 in Table 5-2), we see that the type I canonical depolarization space (d_1, d_2, and d_3) presents remarkably better results than the type I Lorentz depolarization space. The type I Lorentz depolarization space can be considered as a non-linear transformation of the type I canonical depolarization space and its space volume is smaller compared to those of the latter space. Consequently, we consider, in analogy with the previous discussion, that this volume reduction, which comes from the non-linear transformation, compresses the information and results in a reduction of the success classified tissues. Under this scenario, we recommend the use of type I canonical depolarization space in front of the type I Lorentz depolarization to classify tissues. Note that other non-linear combinations may modify the distribution of measured results in such a manner that the classification of the measured tissues is improved compared to type I canonical depolarizer space. However, it is not the case of type I Lorentz depolarization space.

Finally, we compare, in terms of classification success, the depolarization spaces that take the best classification results; those based on ***H*** eigenvalues (Natural depolarization and IPP spaces) with those based on type I canonical depolarizer parameters (type I canonical depolarizer space). For the sake of simplification, and because of the equivalence in classification efficiency of the two best spaces based on ***H*** eigenvalues, we focus the comparison study on only one of the two spaces based on ***H*** eigenvalues, in particular, the IPP space. The comparison in terms of classification efficiency of the IPP and the type I canonical depolarization parameters is more complex than those performed previously because the most efficient space to classify

the measured tissues depends on the wavelength (see Table 5-2). IPP shows the best efficiency results for the 625 nm illumination whereas the metrics best suited to classify tissues at 530 and 470 nm wavelengths are the type I canonical parameters.

To analyze the possible origin of these results, we must analyze the mathematical and physical differences between IPP and type I canonical depolarizer parameters (d_i). In that sense, ref. [64] provides a linear relation between d_i and the ***H*** eigenvalues (λ_i) that is accomplished for non-dichroic Mueller matrices (i.e., without diattenuation and polarizanze content). Accordingly, the classification potential of IPP and d_i should be equivalent for non-dichroic Mueller matrices as both sets of metrics are linear combinations of the ***H*** eigenvalues. However, the relation between d_i and λ_i is more complex for dichroic Mueller matrices, this relation not being described in the literature and still remaining unknown. d_i are obtained from the central depolarizer matrix in the symmetric decomposition [72]. In theory, the hole diattenuation and retardance content of the decomposed Mueller matrix is separated and encoded in the other four matrices of the decomposition. Therefore, the d_i should be independent of the dichroism of the sample thus not encoding the enpolarization phenomena [223]. In contrast, IPP takes into account the enpolarization properties of samples at analyzing the depolarization behavior and, accordingly, different no-null diattenuation and polarizance values influence the measured IPP (the non-linear relation between IPP, *D,* and *P* is shown in Eq. (4.17)). As a result, different *D* and *P* may influence the classification potential of IPP.

To further study the possible influence of *D* and *P* in the classification results, we have calculated the probability histograms of *D* and *P* for the three tissue samples (tendons, muscles, and myotendinous junctions) and for the three wavelengths (625 nm, 530 nm, and 470 nm). Results are shown in Figure 5-14. For the sake of visualization, the histogram lines are pictured following the same colors as the previous figures, i.e., the red color is associated with tendon results, muscles are related to green lines, and the myotendinous junctions results are colored in blue. In addition, the histograms are displayed with different graphics arranged in two rows and three columns. The first row corresponds to the diattenuation results and the second row to the polarizance data. The different columns are associated with different wavelengths, ordered as 625nm, 530 nm, and 470 nm, from left to right.

The diattenuation histograms indicate that the diattenuation is very similar for all tissues and wavelengths (Figure 5-14 (a)-(c)), with picks within 0 and 0.02 values in all the cases. Therefore, diattenuation does not provide any relevant information that helps the distinction or classification of the measured tissues. In fact, it acts as a source of “information noise” that reduces the classification efficiency when it is used for this task (note that we are talking about this particular example but diattenuation can be very useful to classify other type of tissues). In the case of IPP, this diattenuation information is mixed somehow so the effect of *D* reduces their classification efficiency (the 64% of type I canonical success vs the 59% of IPP for 530 nm seen in Table 5-2). This efficiency reduction is compensated in some channels by the polarizance content. In particular, it is compensated in the 625 nm and 470 nm channels.

First, for the 625 nm illumination, the polarizanze response of tendons is significantly different from the other two tissues (Figure 5-14 (d)). The mean polarizance of tendons is around 0.3 while the mean polarizance of the other two tissues is around 0.1. This difference is such that tendons may be identified, with high levels of success, by only using the polarizanze results

at 625 nm. Like in the case of diattenuation information, the polarizance information is also mixed in some way in the IPP, but, as polarizance gives relevant information in terms of distinguishability, it increases the classification efficiency of IPP for the 625 nm channel (Table 5-2). As a result, for 625 nm, IPP presents 65% of well-classified tissues vs the 60% obtained with the type I canonical depolarizer parameters.

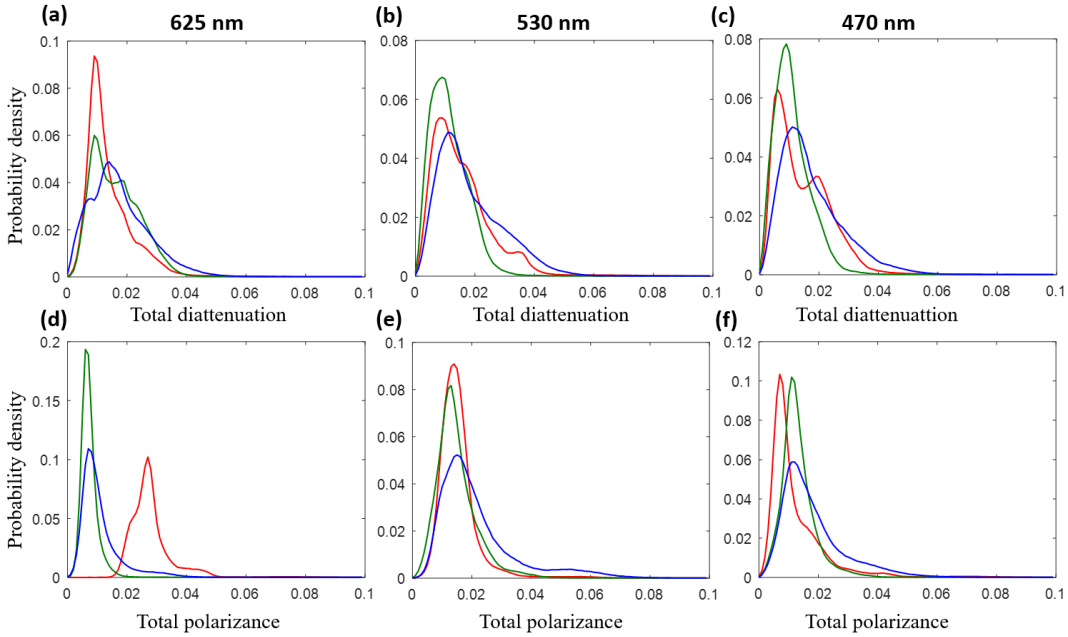

Figure 5-14. Histogram of the total diattenuation of tendons (red), muscles (green), and myotendinous junction tissues (blue) at (a) 625 nm, (b) 530 nm, and (c) 470 nm wavelength. Histogram of the total polarizance of the same tissues at (d) 625 nm, (e) 530 nm, and (f) 470 nm.

Second, when using the 530 nm channel, the polarizance response is almost the same for all tissues (Figure 5-14 (e)), like what happens with diattenuation (Figure 5-14 (a)-(c)). Consequently, the polarizance information acts as a "noise" when mixed in the IPP this amplifying the loss of classification efficiency induced by the diattenuation. As a result, the percentage of tissue classification success is 5% lower for IPP in the 530 nm case (59% of IPP vs 64% of type I canonical; Table 5-2).

Finally, an intermediate case is observed when illuminating the sample with light of 470 nm wavelength. For 470 nm illumination, the polarizance response leads to slight tissue discrimination (Figure 5-14 (f)) but it is not enough to compensate for the contribution of the irrelevant diattenuation information. As a result, the difference in terms of classification success between the IPP and d_i is 3% of the measured tissues (59% vs 62%, respectively, in Table 5-2).

In summary, among the studied depolarizing metrics, the ***H*** eigenvalues, the IPP, and the type I canonical depolarizer parameters appear to be the sets of depolarizing metrics best suited to classify tissues. The efficiency of different spaces would depend on the polarimetric properties of the samples. In that sense, if samples do not have dichroic content, all three spaces should lead to equivalent results. However, when the Mueller matrix of samples is characterized by a non-null diattenuation or polarizance vectors, the potential of each space would depend on the

discriminatory potential introduced by the diattenuation and the polarizance. If the diattenuation and polarizance information is useful for tissue discrimination, we recommend the use of the IPP or ***H*** eigenvalues values metrics as they give better results. In contrast, when the contribution of diattenuation and porlarizance is irrelevant, we recommend the use of type I canonical depolarizer parameters.

Concerning the other spaces based on non-linear transformations (the high order depolarization index and the type I Lorentz depolarizer space), we observe that their classification efficiencies are lower with respect to the other spaces. We relate these worst results to the reduction in volume produced by the non-linear transformation. However, we base our hypothesis on this particular case and these spaces might produce better results at classifying other tissues.

Although the high order depolarization space takes the worst results compared to the other two ***H*** eigenvalue-based depolarization spaces, the use of these depolarization spaces always improves the percentages of well-classified tissues obtained with P_Δ. Therefore, we recommend the use of the ***H*** eigenvalue-based depolarization spaces, and in particular, the use of the IPP space, in front of P_Δ for tissue classification.

5.1.2.4 Depolarization spaces for animal tissue classification: wavelengths combination.

Before ending with this classification study, we propose combining all the information obtained at measuring the tissues at the three different wavelengths (625nm, 530nm, and 470 nm) to improve the classification results [248]. In this way, we use the algorithm of the kNN supervised classifier [247] (described in subsection 5.1.2.1.5) to build different classifiers based on the combined data of all three wavelengths. In particular, we have built six different classifiers; each made from the six different depolarizing metrics previously studied. The percentages of well-classified tissues are provided in Table 5-3.

Wavelength	*Supervised classifier*	H eigenvalue-based depolarization metrics				Type I canonical-based depolarization metrics	
		$\lambda_2,\lambda_3,\lambda_4$	P_1,P_2,P_3	P_Δ, $P_\Delta^{(3)}$, $P_\Delta^{(4)}$	P_Δ	d_1,d_2,d_3	$L^{(2)},L^{(3)},L^{(4)}$
625 nm + 530 nm +470 nm	*kNN(50)*	86	86	78	76	76	72

Table 5-3. Percentage of well-classified tissues by using the combination of all three wavelengths (625 nm, 530 nm, and 470 nm) and the kNN supervised classifier as a function of the depolarization metrics.

The efficiency of the classifiers is significantly improved when using the combined information of all three wavelengths (Table 5-3). In particular, the IPP classification results is increased from the 65% of well-classified tissues, obtained in the best scenario of using the information of one wavelength (in that case the 625 nm; Table 5-2), to the 86% of well-classified tissues achieved with the wavelength combination (column 4 in Table 5-3). In other words, 21% of all the measured pixels that are wrongly classified when using only one wavelength, are properly classified when using the combined information of the three wavelengths. Note that for this experiment with three tissues, randomly distributed data would result in 33% of well-classified tissues.

The results of successfully classified tissues are in agreement with the discussions stated in the previous subsection. The depolarization index (column 6 in Table 5-3) continues showing the worst results among the ***H*** eigenvalue-based depolarization metrics, and the non-linear spaces (high order depolarization space, column 5 in Table 5-3, and type I Lorentz space, column 8 in Table 5-3) also present lower efficiency values than the natural space (column 3 in Table 5-3) and the type I canonical depolarizer space (column 7 in Table 5-3). However, the classification efficiency of type I canonical depolarizer parameters is equivalent to P_Δ (both classify correctly the 76% of the analyzed pixels). This result does not contradict the discussions stated in the previous subsection but it indicates that the enpolarizance information of the measured tissues is useful for their distinction.

In the general application of polarimetry to classify tissues, the analysis would not be restricted to the use of depolarization metrics but diattenuation, polarizance and retardance metrics would be also explored. Under this scenario, although using the type I canonical depolarizer parameters, the enpolarization information would be also taken into account because of the presence of the diattenuation and polarizance information. In fact, the separate use of the enpolarization information may be beneficial in the cases in which it does not helps to discriminate against tissues because it can be removed to not reduce the efficiency of the classifier. For that reason, we cannot recommend the preferred use of the ***H*** eigenvalues or the IPP in front of type I canonical depolarizer parameters. What we recommend, based on the last results, is the use of the combined measurements at different wavelengths to improve the classification results. Note that the use of multiwavelength measurements could be taken to the extreme which leads to the combination of polarization and multispectral measurement techniques.

5.2 Polarization techniques for plant applications

The studies discussed in the previous section show the interest in using polarimetric-based techniques for biomedical applications, specifically, the potential of using the indices of polarimetric purity (IPP) which synthesizes the depolarization information of samples in three parameters. In particular, such studies illustrate the benefits of using these polarimetric techniques to enhance the image contrast in biomedical tissue imaging and to automatically and efficiently recognize them. In the following, we explore the use of polarimetric techniques in other biological tissue samples, specifically, in plant samples.

The use of polarized light to characterize different structures of vegetal samples has already been investigated in the literature with positive results [83,159–176]. Most of the works show the utility of exploiting the birefringence [83,170–175] and depolarization [160–168,170,176] properties of vegetal samples for botanical applications. Nevertheless, other works also show an interest in studying their dichroism [159,169,170]. Among the works presented in the literature, birefringence has been used to characterize different plant structures as, for instance, the structure of guard cells and their related stomata [171–173], or the structure of trichomes [174]. In addition, birefringence has also been applied for the analysis of plant cell maturity [175]. Alternatively, depolarization has been used to evaluate the plant stress [160,161], to study the photosynthesis process [165,166], and in remote sensing, as an aid to vegetation classification [176] or to discriminate of land mines from vegetation backgrounds [164].

To date, the most used approach to analyze the birefringence of plant samples is based on PG techniques [83,171–175]. On the other hand, most of the plant works that study the depolarization take the DOP metric as a reference to measure it [160–163,165–167,176]. These two polarimetric techniques lead to take relevant information of the constituent characteristics of plant samples, the reason why they have been applied, but their use is limited to the analysis of certain birefringence or depolarization properties respectively. In contrast, Mueller polarimetry is a more general approach that leads the analysis of birefringence and depolarization information through the same measurement, as discussed in section 4.1. Moreover, Mueller polarimetry leads to analyze more birefringence or depolarization than PG and DOP techniques. Despite these benefits, Mueller polarimetry has been scarcely applied for plant analysis [164,168,170]. This situation contrasts with the extensive use of Mueller polarimetry in biomedical applications [117–120,122–132,134–139].

In the following, we will show the potential of Mueller polarimetry for the analysis of plant samples. In particular, we will illustrate its interest through the measurement of different leaf samples. In subsection 5.2.1, we compare the results obtained by using the DOP with those obtained from the Mueller-based observables IPP and P_{Δ}. And in subsection 5.2.2, we study the structure of a particular plant leaf at different macroscopic and microscopic scales by measuring the Mueller matrix and evaluating the polarization and depolarization observables. The corresponding polarimetric results, which provide interesting information about the physical properties of the vegetal tissue, are compared with the results obtained with other commonly used optical techniques as phase contrast or fluorescence microscopy, this comparison providing some interesting aspects of using Mueller polarimetry.

5.2.1 Depolarization index and indices of polarimetric purity for plant imaging

This subsection is aimed to compare the use of the degree of polarization (DOP; described in section 2.1) with the use of the depolarization index (P_{Δ}) and the indices of polarimetric purity (IPP) for plant inspection. P_{Δ} and IPP are obtained from Mueller matrix measurements (both described in section 2.3) and measure the depolarization properties of the sample.

The following comparison will be grounded on the experimental measurement of a *Hedera maroccana* McAll. (*Araliaceae*) leaf (Figure 5-15). *Hedera maroccana* is a climbing plant widely used for ornamental purposes and it is mainly characterized by the presence of foliar trichomes [249]. It is native to the Atlantic coast of Morocco but also grows on the Mediterranean coast where the measured specimen is taken. We deposited an herbarium voucher of the examined species in the Herbarium of the Botanical Institute of Barcelona (*Hedera maroccana*, BC843411).

The *Hedera maroccana* leaf pictured in Figure 5-15 (b) was measured in transmission by using the setup described in Chapter 3. In particular, it was measured in the 530 nm illumination channel, this resulting in a transmission of ∼44% of the incident light. To measure the DOP of the different structures of the leaf, we first measured the stokes vector related to certain polarized incident light, e.g., horizontally polarized light, and from it, we operate the DOP by means of Eq. (2.2). Concerning the measurement of the Mueller matrix, it was measured in transmission following the procedure described in Chapter 3. Note that, taking into account the use of instruments with analogous technology, for example, setups based on the same PA-LC devices, DOP measurements are, at least, 4 times faster than Mueller-based metrics. This occurs

because in DOP measurements the sample is illuminated with only one polarization state instead of the multiple illumination SoPs of Mueller measurements.

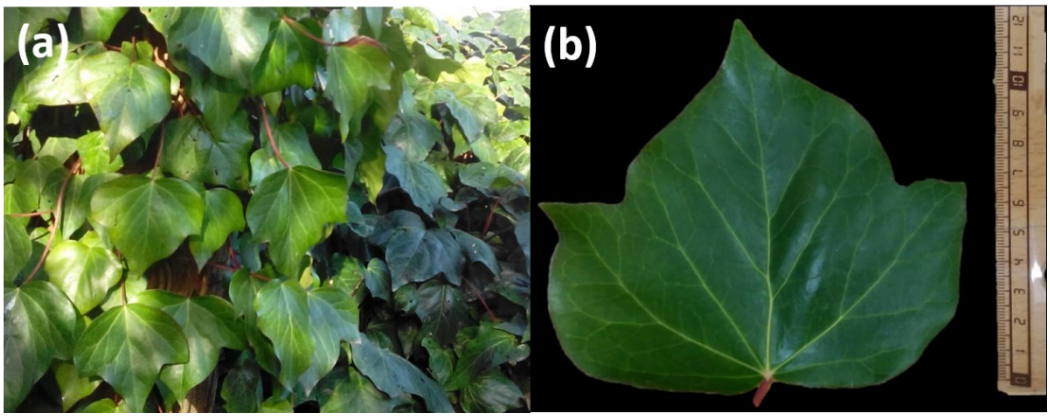

Figure 5-15. Plant sample used for the present study: (a) *Hedera maroccana* plant; (b) *Hedera maroccana* measured leaf.

This comparison study is divided into two parts: First, we analyze the imaging results obtained from the DOP metric by studying the image contrast (subsection 5.2.1.1), and second, we take this image contrast result as a reference to compare with P_{Δ} and IPP images and evaluate their potential in the plant analysis (subsection 5.2.1.2).

5.2.1.1 Plant image contrast obtained with DOP measurements

The experiment starts by measuring the DOP (Figure 5-16) corresponding to a region of interest (ROI), 2.2 x 2.2 cm in size (1024 x 1024 pixels), of the *Hedera maroccana* leaf seen in Figure 5-15. Since the DOP may depend on the SoP of the incident light, we measured the degree of polarization for three different incident SoPs: light linearly polarized in the horizontal direction (Figure 5-16 (b)), light linearly polarized in the diagonal direction (45° to the horizontal; Figure 5-16 (c)), and, left-handed circularly polarized light (Figure 5-16 (d)). Note that the selection of incidents SoPs was arbitrary and the only reason why we chose this set of SoPs is that they are quite commonly used and that they are also linearly independent of each other. However, other bases accomplish the same criteria and could be chosen instead.

In order of comparison, in Figure 5-16 (a), we picture the leaf intensity image with the same ROI. This image corresponds to the transmission of the sample when it is illuminated with 530 nm unpolarized light. The transmitted light captured in Figure 5-16 (a) reveals the presence of the primary (major) and secondary (thinner) veins of the leaf, which are responsible for transporting water and nutrients. Primary veins result highly contrasted while the secondary veins are less visible, being some parts of those veins completely invisible. By contrast, DOP images (Figure 5-16 (b)-(d)) clearly define the limits of primary and secondary veins. In addition, DOP images clearly emphasize the vascular bundles of some primary and secondary veins.

Note that, for DOP images, the contrast of different veins strongly depends on their direction and the state of polarization of the incident light. This fact is clearly observed when comparing the visible veins of Figure 5-16 (b)-(d). As an example, we focus our attention on two leaf veins pointed by yellow arrows in Figure 5-16 (c) and (d). The vein pointed out in Figure 5-16 (c) is

highly contrasted when illuminating the sample with 45° linearly polarized light, but it is much more difficult to see in the DOP images taken with linear horizontal polarization (Figure 5-16 (b)) and left-handed circular polarization (Figure 5-16 (d)). A similar case but this time well contrasted in Figure 5-16 (c) and (d) and completely invisible in Figure 5-16 (b) occurs with the vein pointed out in Figure 5-16 (d).

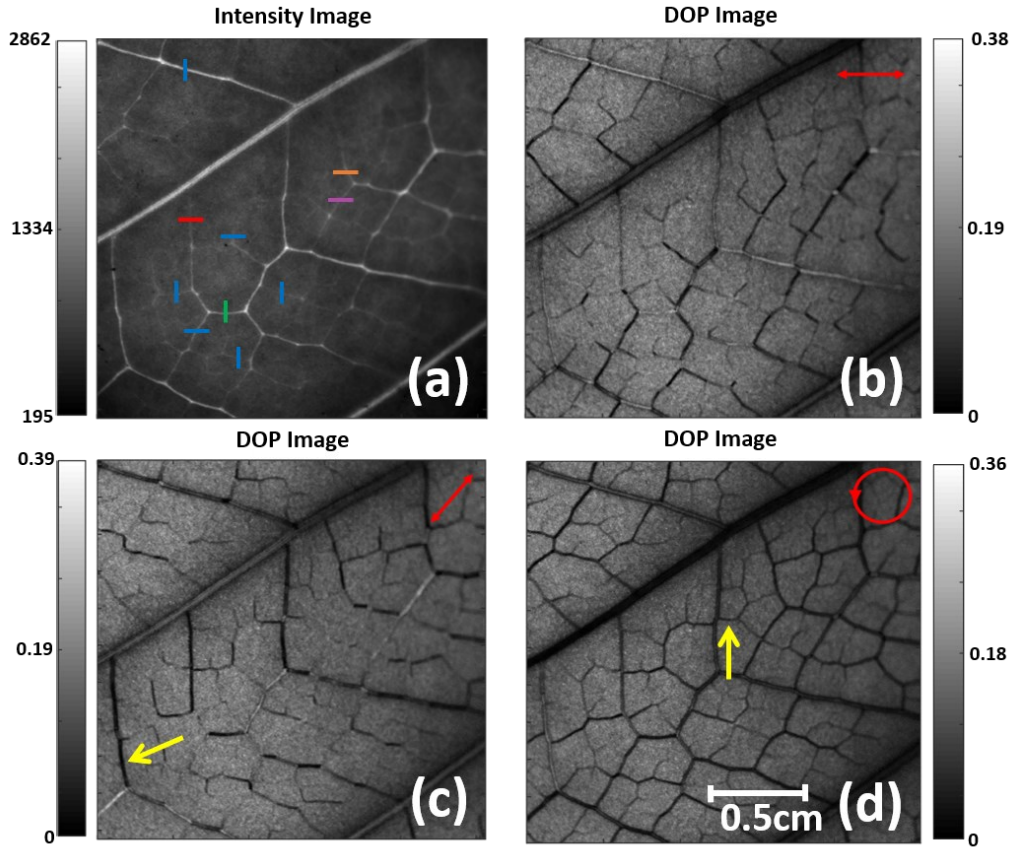

Figure 5-16. (a)Transmitted non-polarized intensity image of the *Hedera maroccana.* DOP image for the incident light (b) linearly polarized in the horizontal direction, (c) linearly polarized at 45° to the horizontal, and (d) left-handed circularly polarized. The type of incident SoPs is schematized in red in the top-right of the image.

In general, we see that when the veins are oriented parallel or perpendicular to the polarized direction of the incident linearly polarized light, the veins are low contrasted. Conversely, the visibility of the veins seems to be maximal when they are oriented at 45° regarding the direction of the incident polarization. In terms of depolarization, veins depolarize more the polarized light oriented at 45° with respect to their direction. This dependence is usually related to the presence of uniformly oriented anisotropic (birefringent or dichroic) structures. In that sense, cellulose fibrils provide a prominent birefringent response in plants (as well as dichroism when some pigments are present), particularly, the microcrystals from which cellulose fibrils are made [83,250,251]. These fibrils are oriented in the direction of the veins and this generates an anisotropy in that direction that may explain the non-isotropic depolarization illustrated in the DOP images. The depolarization dependence with the vein orientation is not observed in the case of using circularly polarized light Figure 5-16 (d) as it does not present any predominant direction. Consequently, the maximum image contrast is reduced compared with those obtained

with linearly polarized light, but it is kept sufficient to simultaneously visualize most of the veins (note that the veins that are seen in Figure 5-16 (d) present similar image contrast). This DOP dependence with the incident polarization deserves special attention because the election of the incident polarization in most of the botanical works present in literature is arbitrary. In fact, the majority of polarization-based botanical studies only analyze the DOP generated when illuminating the sample with linearly polarized states because they are simpler to generate (they can be generated by simply using a linear polarizer). Note that according to the previous results the measured DOP is more sensitive to this type of polarized light.

To further study the DOP dependence with the incident polarization state, we have measured the Mueller matrix of the *Hedera maroccana* leaf. Subsequently, according to the $\boldsymbol{S_{out}} = \boldsymbol{M} \cdot \boldsymbol{S_{in}}$ relation (Eq. (2.4)), we have calculated the output SoPs corresponding to illuminating the sample with different *N* input polarizations and, afterward, we have calculated the DOP associated with the different *N* output SoPs.

We first analyze the incidence of illuminating the sample with differently oriented linear polarized states. In particular, we study the variation of the DOP corresponding to four vein sections of the *Hedera maroccana* leaf (marked in red, orange, purple, and green in Figure 5-16). To do so, we have evaluated the interaction with the sample of 360 differently oriented linear polarized states. Their Stokes vector is described following the next equation:

$$\begin{aligned} & S_k = (1 \quad \cos 2\theta_k \quad \sin 2\theta_k \quad 0)^T \\ & \begin{cases} \theta_k = k{\cdot}\Delta\theta; \Delta\theta = \dfrac{\pi}{N_\theta} \\ \quad k = 1,\ldots,N_\theta \end{cases} \end{aligned} \tag{5.9}$$

where θ_k is the azimuth of the Stokes vectors [203], that ranges from 0 to π, and N_θ is the number of equally spaced steps into which the θ range is divided. In our study, we take N_θ=360 thus leading to 0.5 deg steps.

The DOP values corresponding to the different orientations of the incident linear polarized light are graphically represented in Figure 5-17. In particular, we represent the average DOP values of three consecutive pixels corresponding to the four vein sections (marked in red, orange, purple, and green in Figure 5-16) as a function of the angle of the incident linear SoP.

The graphical representation of the DOP in Figure 5-17 shows a strong variation of the DOP as a function of the angle of the input linear polarized light. The data distribution is similar to a double angle shifted sinusoidal function, i.e., $\sin(2\theta \pm \Delta\theta)$, which is characterized by presenting two minimums and two maximums in the range of 0 to 180°. The same pattern of two maximums and two minimums is observed for the four different veins, but the position of these maximums and minimums is different for each vein. In the analysis of Figure 5-16, we saw that the depolarization of the vein was maximal (i.e., minimum DOP value) at 45°. Accordingly, veins are oriented at +45° or -45° with respect to the polarization angle with a minimum DOP value. Unfortunately, the distribution presents two minimums, so we have two possible results.

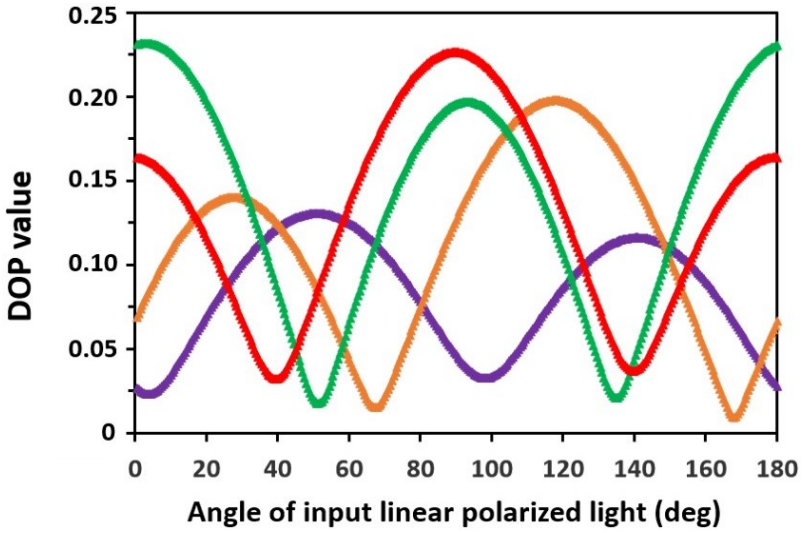

Figure 5-17. DOP values in function of the angle of the incident linear polarized light. Red, orange, purple, and green marks (triangles) correspond to sections marked with the same color in Figure 5-16 (a).

Now, taking attention to the maximum values, we see that, for each vein, one of the function maximums present higher values compared to the other (higher DOP values mean lower depolarization). This lowest depolarization is achieved when the input polarization is parallel to the orientation of the veins. When polarized light interacts with the leaf veins, part of the light is absorbed by dipoles and reemitted, maintaining the SoP of light during the process, i.e., the reemitted light is defined with the same polarization state as the absorbed. The assiduity of this phenomenon depends on the alignment between the dipole and the polarized state, being more frequent when both elements are parallel-oriented [252]. Due to the directional structure of the vein, the majority of the dipoles are parallel oriented or orthogonally oriented to the vein direction, being the first scenario more predominant. As larger the number of dipoles oriented in the vein direction, the higher the amount of absorbed and reemitted light when the vein is illuminated with parallelly polarized light. At this stage, it is worth noting that the SoP measured by the camera corresponds to the incoherent superposition of light reemitted by the dipoles and light scattered by other structures. As a result, the measured DOP is higher for an input polarization oriented in parallel to the vein direction because the camera measures more of these polarization-maintaining reemitted photons.

Following the same reasoning, the DOP measured is minimal when illuminating the sample with light polarized at 45° regarding the vein direction because the dipoles that are parallel and orthogonal to the vein absorbs the input light with the same probability and this results in the measure of the incoherent combination of the similar amount of parallelly and orthogonally polarized photons. Note that the measured DOP is not 0 because there are more parallel dipoles than orthogonal, so there are more parallelly polarized photons, this leading to a certain degree of polarized light content.

Based on the above-stated discussion, we have considered that the maximal DOP angle corresponds to the direction of the vein. The orientation angles of the four analyzed veins measured from Figure 5-16 and those obtained by using this polarization approach are provided in Table 5-4. The results are equivalent, showing a perfect correlation.

Segment	Vein orientation with respect to the lab horizontal (deg)	θ of the input linear polarization (deg) corresponding to the maximum DOP
Green	**3±1**	**3±0.5**
Purple	**51±1**	**51±0.5**
Red	**89±1**	**90±0.5**
Orange	**119±1**	**117.5±0.5**

Table 5-4. Orientation of different veins of the measured *Hedera maroccana* leaf (marked in green, purple, red, and orange in Figure 5-16 (a)) and the azimuth angle of the incident linearly polarized light corresponding to the maximum DOP value.

To generalize this study, we evaluated the interaction of a collection of *N* input polarizations that are widely distributed along the whole surface of the Poincare sphere. In particular, these input states are distributed along the Poincare sphere by shaping a spiral curve on the surface Figure 5-18. They are described by following the next expression [191]:

$$S_k = (1 \quad \cos 2\theta_k \cos 2\varepsilon_k \quad \sin 2\theta_k \cos 2\varepsilon_k \quad \sin 2\varepsilon_k)^T$$
$$\begin{cases} \varepsilon_k = k{\cdot}\Delta\varepsilon - \dfrac{\pi}{4}; \Delta\varepsilon = \dfrac{\pi}{2{\cdot}N_\varepsilon{\cdot}N_\theta} \\ \theta_k = k{\cdot}\Delta\theta; \Delta\theta = \dfrac{\pi}{N_\theta} \\ k = 1,\ldots,N_\varepsilon{\cdot}N_\theta \end{cases} \tag{5.10}$$

where θ_k and ε_k are the azimuth and the ellipticity of the Stokes vectors [203], that ranges from 0 to π and from -π/4 to π/4, respectively. The range of θ is divided into N_θ steps and N_ε defines the number of generated SoPs that presents the same θ value but different ε. In Figure 5-18, N_ε corresponds to the number of circles around the S_3 axis.

For our analysis, we used N_θ=20 and N_ε=10 to generate the 200 input polarization states that are represented with black dots over the Poincaré sphere in Figure 5-18.

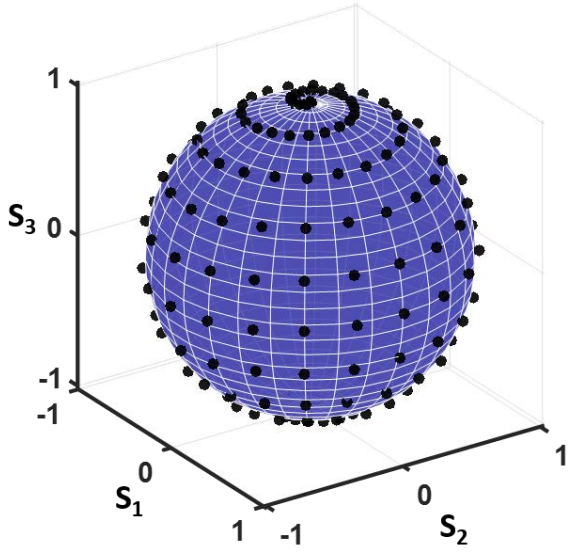

Figure 5-18. Representation of the set of N=200 generated SoPs on the Poincare sphere.

The collection of the different DOP images obtained from the output SoPs corresponding to the generated set of input SoPs is arranged in a video that can be found in the open-access ref. [249]. The visualization of this video evidences the strong relation between the depolarization produced by the veins and the incident polarization state, especially for linear incident polarizations. To quantify the image contrast obtained when using the different input polarizations, we use the figure of merit of the visibility (V),

$$V = \frac{I_{\max} - I_{\min}}{I_{\max} + I_{\min}} \tag{5.11}$$

where $I_{\max}$ and $I_{\min}$ are the maximum and minimum values of the analyzed cross-section. The visibility values of two sections, those marked in green and purple in Figure 5-16 (a), are represented in Figure 5-19 (a) as a function of the incident *k* SoPs. Note that, as stated above, the visibility will depend on the orientation of the veins. In our case, the selected veins are oriented at 45 degrees to each other so presenting a complementary visibility distribution (see Figure 5-19 (a)). In other words, the *k* SoPs that correspond to maximum visibility values for one vein (e.g., the vein marked in purple) are related to minimum values for the other (the vein marked in green). In the case of using linear polarizations, the difference between a maximum and a minimum, i.e., the pick-to-valley visibility, is approximately 0.65 (from 0.15 to 0.80) for both veins. This complementary maximum and minimum behavior is also observed when illuminating the sample with elliptical input SoPs (*k* values close to 0 and close to 200), but in this case, the pick-to-valley visibility is reduced to approximately 0.3 (from 0.45 to 0.75).

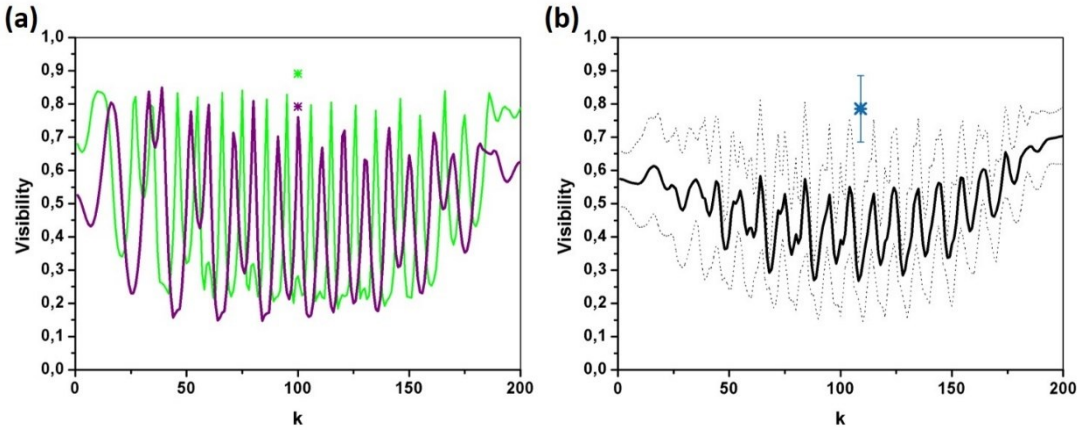

Figure 5-19. Visibility values corresponding to DOP-based images related to 200 *k* different input polarized states. (a) Visibility of the green and purple cross-section in Figure 5-16 (a). (b) Mean visibility of the 10 cross-sections marked in Figure 5-16 (a). Dashed lines correspond to the standard deviations and asterisks (*) indicate the P_2-P_1 visibility values.

For the sake of completeness, we have also calculated the visibility of 8 additional arbitrary selected vein segments (the red, orange and 6 blue segments in Figure 5-16 (a)). Afterward, we have calculated the average visibility value of the 10 studied segments (the two above analyzed and the 8 other segments). To calculate the average visibility values, we have applied the Eq. (5.11) to the selected cross-sections and then we have calculated the mean value of these 10 visibilities. The mean visibility results as a function of the input *k* SoP are represented as a

continuous black line in Figure 5-19 (b). The dashed lines in Figure 5-19 (b) corresponds to the standard deviation calculated from the 10 visibility values for each input k SoP.

Considering the 10 segments (Figure 5-19 (b)), we see that the visibility fluctuations observed in Figure 5-19 (a) are considerably reduced. It was expected as we are averaging the visibility of differently oriented veins thus reducing the influence of the polarization state direction (some low visibility values related to certain orientations are compensated with high visibility values related to other orientations). We can also compare the overall visibility obtained with linear and circular polarizations. In that sense, the mean visibility values are always below 0.7, being lower when illuminating the sample with linearly polarized light (75-125 k values). In turn, the standard deviation values are higher at such polarizations (for linear polarizations).

In summary, the above-provided results demonstrate that the contrast of DOP-based images strongly depends on the input polarization, being more sensitive to linearly polarized light. Moreover, for a certain input polarization, some structures are highlighted whereas others can result practically invisible. Accordingly, the selection of the input polarization is not trivial and the optimal state of polarization should be optimized for each particular structure. Considering that most of the botanical works that are based on the analysis of the DOP use a unique incident polarization (usually a linear polarization), our study suggests that some biological structures could be under-contrasted with such an approach. Under this scenario, it is important to find other polarimetric metrics simultaneously leading to a suitable contrast for all the analyzed biological structures, independently of their orientation.

5.2.1.2 Plant image contrast obtained with P_Δ and IPP measurements

Some of the metrics that are calculated from the Mueller matrix are independent of the orientation of the measured sample [212]. For example, the total retardance R, the diattenuation D, the polarizance P, the depolarization index P_Δ and the indices of polarimetric purity (IPP; P_1, P_2 and P_3) are observables invariant under rotations [212]. In the following, we focus our analysis on the use of P_Δ and IPP parameters because they are invariant to rotations and they work with the depolarization content like the DOP.

For the comparison with DOP-based images (Figure 5-16 (b)-(d)), we provide, in Figure 5-20 (a)-(d), the P_Δ, P_1, P_2 and P_3 images corresponding to the same ROI of the *Hedera maroccana* leaf. We see that the veins of the leaf are differently contrasted when using the different Mueller-based parameters (Figure 5-20 (a)-(d)). This is produced because each of the calculated metrics measures different depolarizing properties of the sample. P_Δ measures the overall depolarization capability of the sample [69], whereas IPP are related to the anisotropy of this depolarization, i.e., if some incident polarizations are more depolarized than others [1,64]. From these four parameters (P_Δ, P_1, P_2 and P_3), the P_1 channel (Figure 5-20 (b)) shows the best image contrast results. In the P_1 channel, we can clearly visualize the primary and secondary veins whereas some secondary veins are difficult to visualize in the P_2 and P_3 channels. The different P_1 values of veins and the surrounding structures indicate that their way to depolarize the incident light is different. The low P_1 values of veins indicate that they are characterized by the incoherent combination of different non-depolarizing polarimetric responses, i.e., different non-depolarizing Mueller matrices, and none of these responses predominate over the others [209,211]. In contrast, the P_1 values of the surrounding structures mean that they present a predominant non-depolarizing polarimetric response. Note that, due to the structure of this

sample, the P_1 channel gives the best results but P_2 and P_3 can lead to the best results when measuring other botanical samples. This is not the case of P_Δ because it is calculated by combining the three IPP (Eq. (2.45)) and the combination of the best contrasted IPP parameter with the other two always decreases the optimal image contrast.

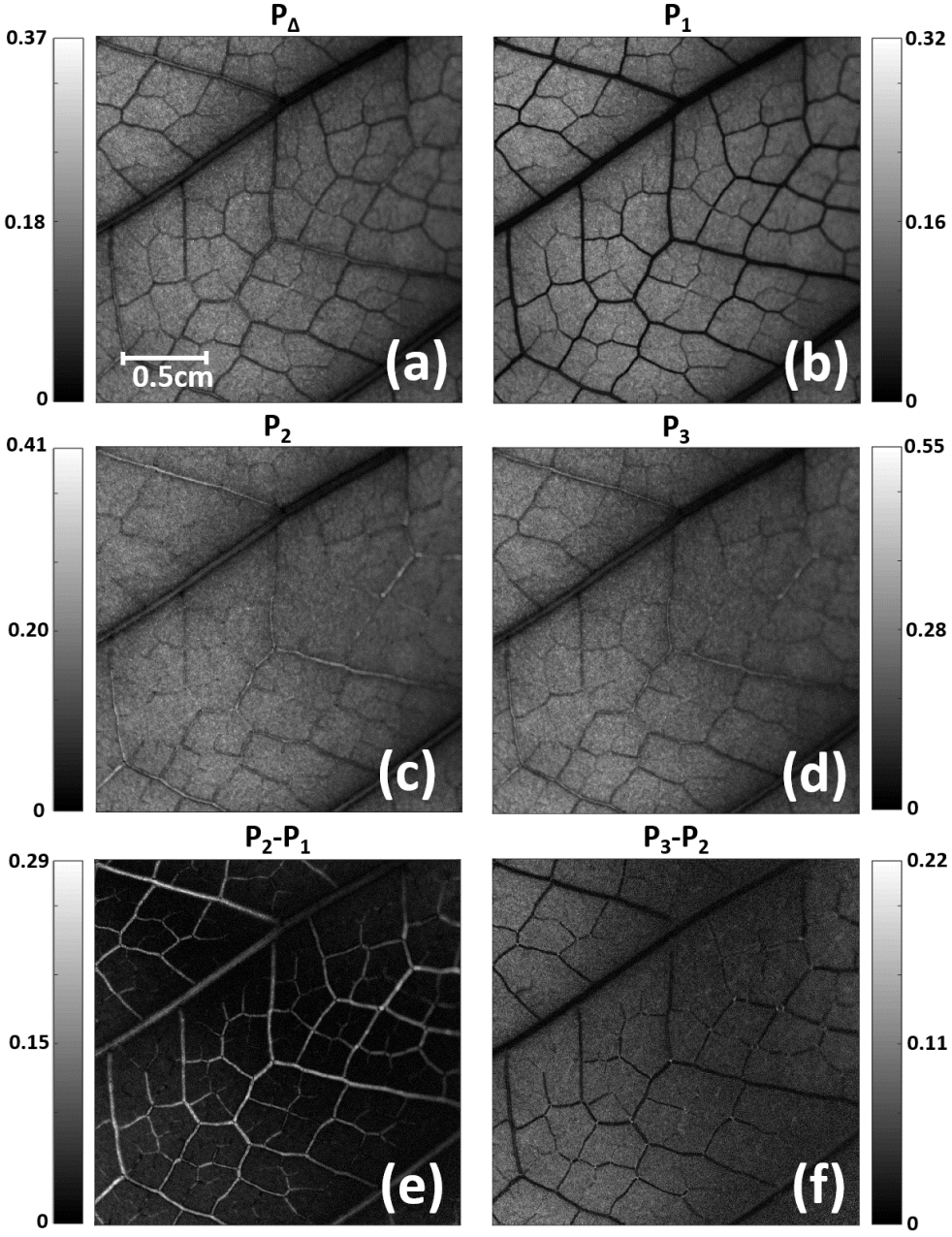

Figure 5-20. (a)P_Δ, (b) P_1, (c) P_2, (d) P_3, (e) P_2-P_1, and (f) P_3-P_2 images of a ROI of the *Hedera maroccana* leaf pictured in Figure 5-15 (b).

By comparing the P_1 image (Figure 5-20 (b)) with the DOP-based images (Figure 5-16 (b)-(d)), we realize that the visualization of veins in the P_1 channel is similar to the visualization of the best-contrasted veins in the DOP-based images. However, independently of their orientations, all the veins in the Mueller-based image are well-contrasted (with a similar contrast). This is a much better scenario than that observed in DOP-based images, in which a significant contrast variation was observed between the different veins present in the image. This is explained

because the P_1 parameter depends on the depolarization anisotropy of the sample but it is independent of the preferent direction of this anisotropy. In contrast, the DOP is affected by the preferent direction of depolarization anisotropies, this being the origin of the different image contrasts. Note that we are dealing with a particular case in which the veins of the *Hedera maroccana* present a depolarization anisotropy in which linearly polarized light is depolarized differently depending on its orientation. However, other structures may present anisotropies between linear and circular polarizations. Under this scenario, the DOP measurements based on linear polarized states would not be affected by this anisotropy, thus not identifying that characteristic. Conversely, this type of anisotropy would be detected when using the IPP.

In addition to the IPP, we evaluate the P_2-P_1 and P_3-P_2 differences. The images corresponding to the P_2-P_1 and P_3-P_2 channels are represented in Figure 5-20 (e) and (f). The direct differences between P_2-P_1 and P_3-P_2 have their particular physical interpretation; P_2-P_1 corresponds to the weight of a 2D depolarizer that can be assimilated with the sample and P_3-P_2 to the weight of a 3D depolarizer [209,211]. In practice, P_2-P_1 and P_3-P_2 are both equal to 0 for depolarizers that do not have depolarizing anisotropy and at least one of them is different from 0 in the opposite scenario. In Figure 5-20 (e), veins are very well defined because the surrounding structures take values close to 0 (represented in black) whereas veins do not (represented in white). Accordingly, veins present some type of anisotropy. In particular, P_2-P_1 values different from 0 indicate that veins are characterized by a depolarizing anisotropy in which incident light with a specific polarization is less depolarized than others. In the particular case of the measured veins, the linearly polarized light that is oriented parallel or orthogonally to the vein direction is less depolarized. In contrast, the other structures of the leaf do not present this type of anisotropy so their P_2-P_1 value is equal to 0. This distinct physical interaction leads to an image contrast of veins visually higher than those obtained with the DOP.

To quantify the image contrast of the ***M***-based images, we calculate the visibility value (Eq. (5.11)) corresponding to the P_Δ, P_1, P_2, P_3, P_2-P_1 and P_3-P_2 channels for the two segments marked in green and purple in Figure 5-16 (a). The obtained results are summarized in Table 5-5. For the sake of comparison, we have also provided the visibility value corresponding to the m_{00} channel (regular intensity; Figure 5-16 (a)). Table 5-5 reveals that the best visibility values are obtained in the P_1 and P_2-P_1 channels. This result was expected because the corresponding images provide the best visualization of the *Hedera maroccana* veins.

Segment	m_{00}	P_Δ	P_1	P_2	P_3	P_2-P_1	P_3-P_2
Purple	**0.28**	**0.26**	**0.68**	**0.25**	**0.19**	**0.79**	**0.65**
Green	**0.1**	**0.34**	**0.71**	**0.16**	**0.18**	**0.89**	**0.54**

Table 5-5. Visibility values corresponding to different polarimetric observables for the segments marked in green and purple in Figure 5-16 (a).

Comparing these visibility values with those obtained in DOP-based image, we see that the best visibility value obtained with ***M***-based techniques for the purple vein (0.79 for the P_2-P_1 channel) is lower than the best result obtained with DOP-based images (0.85 for the k=39 input polarization state; see Figure 5-19 (a)). In contrast, the P_2-P_1 visibility value corresponding to the green vein (0.89 according to Table 5-5) is larger than the best result obtained with DOP-based images (0.84 for the k=166 input polarization state; see Figure 5-19 (a)). To ease this comparison,

the P_2-P_1 visibility values are represented in Figure 5-19 by using asterisks (*). Note that the P_2-P_1 visibility values are represented with only one asterisk for each segment because their result is unique and does not depend on the incident polarized state. In fact, the experimental Mueller matrix can be understood as the measurement of the polarization light-sample interaction of all the possible incident polarizations (i.e., the polarimetric transfer function) so thinking in its dependence with the input polarization has no sense. Although their unique result, the visibility corresponding to different veins can be different due to different physical characteristics, as vein thickness, percentage of water, etc., that lead to distinct depolarizing behavior. This is the case of the purple and green veins that have a difference in the visualization of 0.1 for the P_2-P_1 channel (0.79 vs 0.89, respectively) and 0.03 for the P_1 channel (0.68 vs 0.72, respectively). In any case, these visualization differences are much lower than those obtained with DOP-based images (∼0.65 for linear input polarizations and ∼0.3 for circular input polarization).

Finally, in analogy with the DOP-based study previously discussed, we have calculated the average visibility of the same 10 segments for the P_2-P_1 channel (the purple, green, red, orange, and 6 blue segments in Figure 5-16 (a)). The mean value is represented in Figure 5-19 (b) with a blue asterisk, as well as their corresponding error bars that correspond to the standard deviation. We see that the mean visibility value for P_2-P_1 (0.77, blue asterisk) is higher than those obtained with DOP-based images (black curve). Therefore, we choose (and recommend), for the analysis of plants, the use of depolarization metrics based on the Mueller matrix, in particular, the use of IPP, in front of the degree of polarization.

We want to note that these results correspond to a particular *Hedera maroccana* sample. However, we repeated the same experiment on other 5 *Hedera maroccana* leaves by using the same and other two wavelengths (470 nm and 625 nm) and all the results were in agreement with what was stated in this section.

In summary, we presented the benefits of using the depolarization information obtained from the measure of the Mueller matrix for botanical applications. In particular, we showed that the value of P_Δ and IPP metrics do not depend on the orientation of the analyzed structures whereas the degree of polarization does. In addition, the overall visualization obtained with the P_2-P_1 channel is better than those obtained by measuring the DOP, emphasizing the suitability of these $\boldsymbol{M}$-based parameters for plants imaging. The unique disadvantage of using Mueller techniques for botanical applications in front of measuring the DOP is the necessity of a more complex setup that has a higher cost and that needs more acquisition time to complete a Mueller matrix measurement. In the case that these two factors are not a problem, we highly recommend the use of Mueller techniques for botanical applications. Mueller techniques could be applied, for instance, in plant characterization and taxonomy, for the analysis of the hydric stress, or for the early detection of diseases, among others.

5.2.2 Polarimetric imaging of plant samples at different scales

For the moment, DOP and PG techniques are the two polarimetric methods most used for plants inspection [160–167,169,171,172,174–176]. However, in the preceding study, we showed the benefits of using Mueller-based techniques for botanic applications instead of using DOP (subsection 5.2.1). In addition, we experimentally demonstrated, in section 4.1, that PG techniques are a particular case of the Mueller matrix measurement. Note that, although the

experiments described in section 4.1 are based on the measurement of phantom and animal samples, the PG-***M*** relation is also valid for botanical studies. According to these results, the measure of the Mueller matrix can be understood as a generalization of the two more commonly used polarimetric techniques for plant inspection: the DOP and the PG-based methods. The Mueller matrix allows to perform the DOP and PG studies from the same experimental Mueller matrix measurement, and also further polarimetric studies not available with these two methods as, for instance, the complete analysis of the birefringence (fast axis orientation, linear retardance, circular retardance, …) or a detailed study of the depolarization anisotropy. In other words, the Mueller matrix leads to more complete polarimetric analyses than DOP and PG. For these reasons, we conclude that Mueller matrix techniques are better suited for plant inspection.

Once we determined the optimal polarimetric tools to analyze plant samples, we study, in the following, we study the possible advantages of using these polarimetric techniques in the botanical framework, in comparison with other optical techniques commonly used in such research field. In particular, we compare the results obtained by using the Mueller polarimetry with those obtained with multi-wavelength measurements [12,17], phase-contrast microscopy [7,41] and fluorescence microscopy[22–25] techniques. We want to emphasize that this study is focused on analyzing the utility of polarimetric techniques for the imaging of plants. For that reason, polarimetry will be used to obtain information from a plant sample, a leaf of *Epipremnum aureum*. Although measuring a specific specimen, this study wants to go beyond the analysis of a particular case and proposes the use of Mueller polarimetry, alone, or in combination with other complementary techniques (such as multiwavelength, fluorescence microscopy, phase contrast microscopy, etc.) to improve the image quality and characterization accuracy in plants imaging. In other words, the goal of this study is twofold: (1) to illustrate the interest of using the Mueller polarimetry in the botanical framework, and (2) to analyze for the first time the depolarization content of microscopic structures through the use of the IPP metrics.

To the sake of completeness, the *Epipremnum aureum* leaf is studied at different scales: millimetric and micrometric. The measure at different scales allows us to correlate some structures that are observed at both scales, but which are easier to identify in the micrometric scale.

The contents of the present study are organized as follows. First, we describe the measured specimen and the instrumentation used to image it (subsection 5.2.2.1). Second, we show a set of polarimetric images based on the Mueller matrix formalism and we compare them with those obtained by using multi-wavelength images (subsection 5.2.2.2). This study is performed at the millimetric scale. Third, the interest and relevance of using polarimetric-related images at the micrometric scale are discussed by comparing polarimetric microscope images with those taken with a fluorescence microscope and a phase-contrast microscope, the latter commonly used in botany to characterize vegetal tissues (subsection 5.2.2.3). Finally, the same leaf is measured at the nanometric scale with a scanning electron microscope to validate the microscopic observations (subsection 5.2.2.4).

5.2.2.1 Materials and Methods

In this subsection, we describe the measured plant sample and the collection of instruments used to image it based on different techniques. In particular, the sample was measured with a multi-wavelength imaging system, an imaging macroscopic polarimeter, a polarimetric microscope, a fluorescence microscope, a phase-contrast microscope, and an electron microscope.

5.2.2.1.1 *Sample description*

We measured an *Epipremnum aureum* (Linden & André) G.S.Bunting leaf (Fig. 1(b)). This species belongs to the *Araceae family* and it is also known as *Pothos aureus* Linden & André. These evergreen climbing plants (see Fig. 1(a)) native to Southeast Asia and Australia are mainly cultivated with an ornamental purpose. The older leaves usually look perforated and often have translucent spots along the midrib [253]. An herbarium voucher of the studied species is deposited in the Herbarium of the Botanical Institute of Barcelona (BC843412).

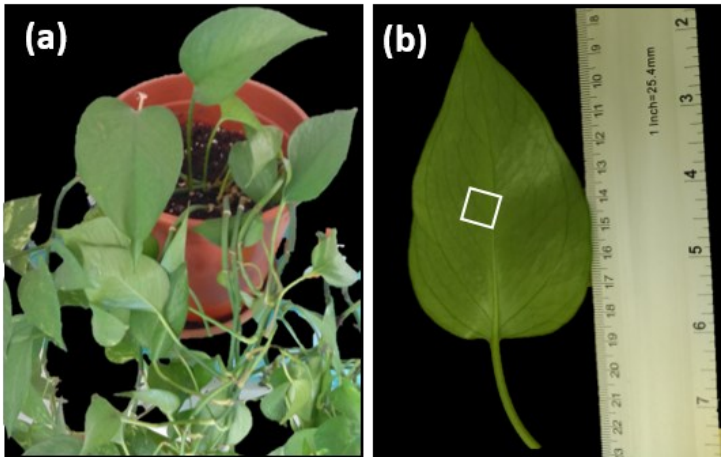

Figure 5-21. Plant sample used for the present study: (a) *Epipremnum aureum* plant; (b) *Epipremnum aureum* measured leaf.

5.2.2.1.2 *Multi-wavelength imaging system*

The multi-wavelength imaging system is the same instrument described in Chapter 3 but used to only measure the intensity response of the sample when illuminated with unpolarized light. The instrument was used in the transmission configuration.

5.2.2.1.3 *Imaging macroscopic polarimeter*

The imaging polarimeter is the instrument described in Chapter 3. For this study, the sample was measured in transmission with the 530 nm channel.

5.2.2.1.4 *Polarimetric microscope*

To obtain polarimetric images at the microscopic scale we used a multimodal imaging Mueller polarimetric microscope (Figure 5-22). The used instrument is a multimodal microscope because it can image the real and the Fourier planes. The standard microscope images correspond to the image plane, while the images obtained in the Fourier plane correspond to the angular distribution of light captured by the camera (light transmitted and scattered by the sample). To ease the switch between real and Fourier image mode, a Bertrand lens is placed in the optical paths [254]. Particularly, in this work, the sample was only imaged in the real plane.

To illuminate the sample, the instrument uses a white light LED source that is filtered by a narrow-band spectral filter (centered at 533nm wavelength and with a spectral bandwidth of 15 nm). Before reaching the sample, the light is polarized by the polarization state generator (PSG; see Figure 5-22). Then, the polarized light interacts with the sample, and the resulting polarization state is analyzed by the polarization state analyzer (PSA). Both, the PSG and the PSA are based on ferroelectric liquid crystals [255] and can generate and analyze, respectively, any state of polarization.

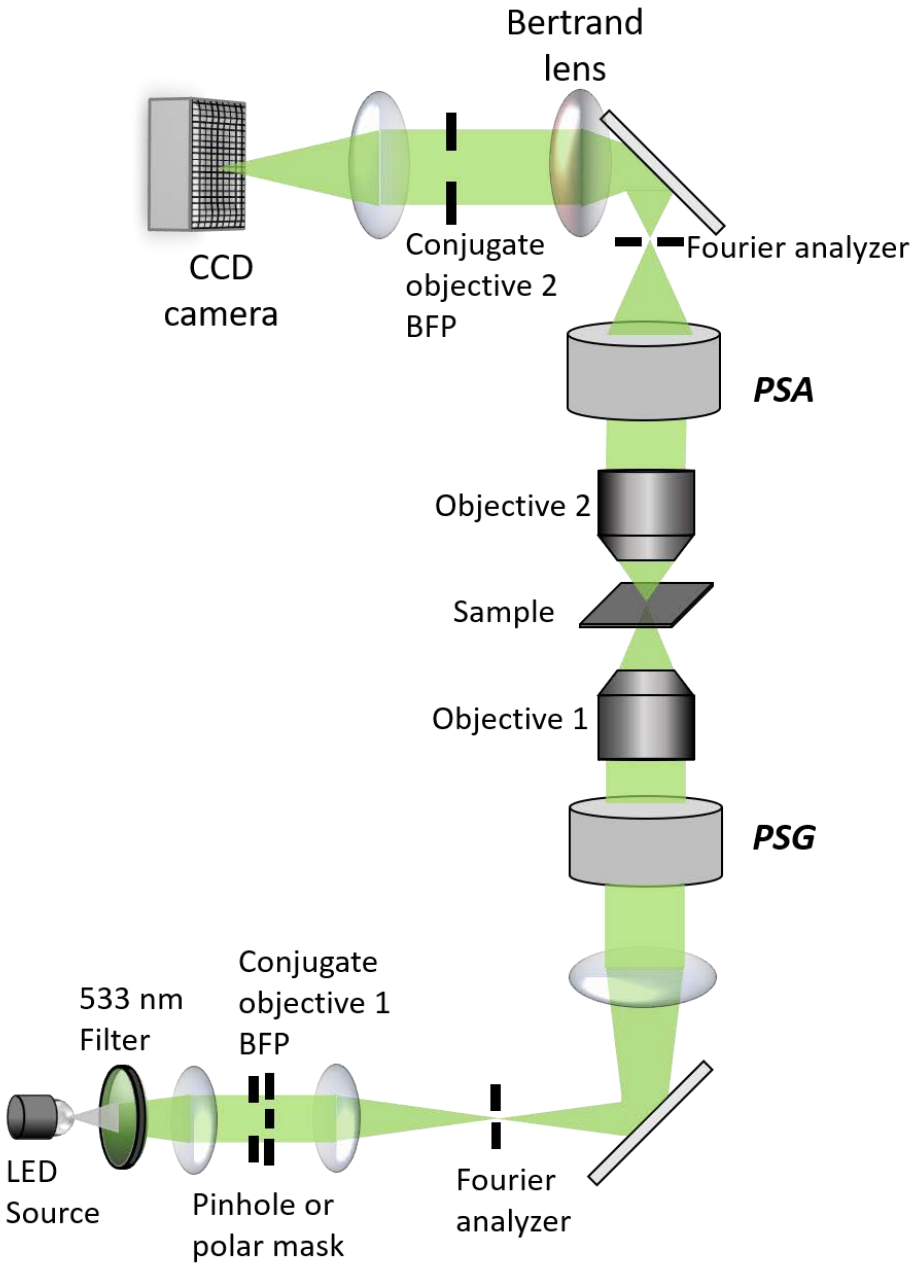

Figure 5-22. Scheme of the multimodal imaging Mueller polarimetric microscope in the transmission configuration.

The leaf measurements with this polarimetric microscope were performed in transmission; being the sample paced between two identical microscope objectives (see Figure 5-22). One of the objectives is used to illuminate the sample and the other is used for imaging it. Depending

on the desired resolution and the numerical aperture, objectives with different magnifications are used: 50x, 20x, or 5x.

A series of aligned lenses are used, in the illumination and imaging arms, to create conjugates of the back-focal planes (BFP) of their respective objectives. The direction and aperture of the beam can be controlled by placing pinholes in these conjugates of the BFP. In our experiment, the sample is illuminated with a normal incident beam with an aperture of 5° thanks to a 500 µm diameter pinhole that is placed in the conjugate of the BFP of the illumination objective. In contrast, no pinhole was put in the imaging arm to capture more scattered light and thus optimizing the sensitivity of depolarization measurements.

5.2.2.1.5 *Fluorescence microscope*

A commercial *Olympus Fluoview 1000* microscope (Figure 5-23) was used to take the fluorescence images. The instrument allows illuminating the sample with six different wavelengths or with multiple combinations of them. The illumination sources are three diode lasers (405, 559, and 635 nm) and a multiline argon laser that can illuminate the sample with three different wavelengths (458, 488, and 515 nm). Light is absorbed by the fluorescent sample (leaf properly treated with fluorescent dyes) and reemitted with other wavelengths. To distinguishing this reemitted light from those reflected, we use filters with a different central wavelength than the incident light. For this work, images were taken by using simultaneously the *Olympus U-MWU2*, *U-MNB2*, and *U-MWG2* filters which are centered at 330 nm, 470 nm, and 510 nm, respectively. The equipment allows the acquisition of images in up to four channels simultaneously. Three different photomultipliers (PMT) can capture the fluorescent and/or reflected light, and an additional external detector can measure the transmitted light. The equipment allows imaging different regions of the sample and different depths thanks to their accurate x, y, z control. In addition, they can take images in real-time. Therefore, we can say that this equipment has 5 degrees of versatility: three for space, one for time, and one for wavelength. The fluorescence images were taken in the reflection configuration.

Figure 5-23. Image of the commercial Olympus Fluoview 1000 microscope. The image is taken from ref. [256].

5.2.2.1.6 *Phase-contrast microscope*

The commercial *Olympus Fluoview 1000* microscope (Figure 5-23) used to obtain the fluorescence image is also used to obtain the phase-contrast images. For the phase-contrast imaging, the instrument is equipped with the annulus and phase ring placed above and below

the illumination and imaging objectives, respectively. The phase-contrast images were taken in the transmission configuration.

5.2.2.1.7 *Scanning electron microscope*

The measurements at the nanometric scale were made with the scanning electron microscope (Jeol JSM-7100F; Figure 5-24) of the Centros Científicos y Tecnológicos (CCiT) of the University of Barcelona. The electron microscope images have a resolution that ranges from 100 to 500 nm depending on the selected magnification. Before imaging the leaf sample with the electron microscope, they were dehydrated with alcohol of increasing graduation until absolute alcohol was used. Next, the leaf samples were taken to the critical point and covered with special coal after thermal evaporation [253].

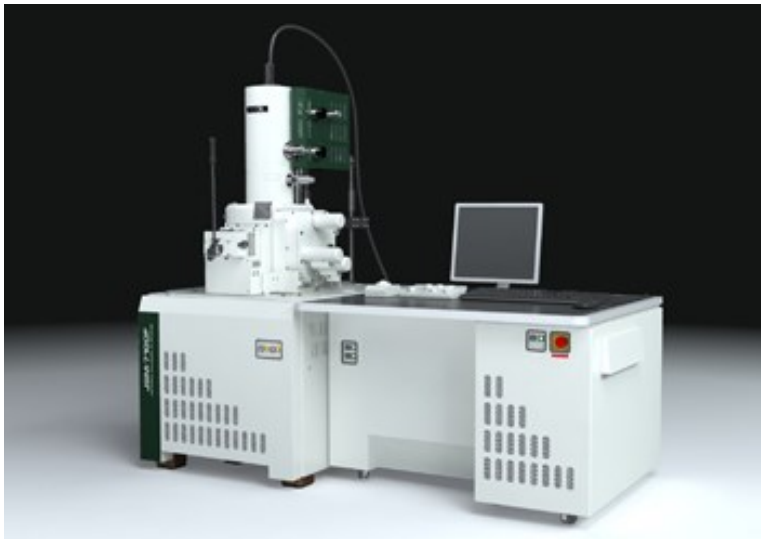

Figure 5-24. Image of the commercial scanning electron microscope Jeol JSM-7100F. The image is taken from ref. [257].

5.2.2.2 Millimetric scale

In this subsection, we show the most relevant results obtained after measuring the *Epipremnum aureum* leaf (Figure 5-21 (b)) at the millimeter scale [258]. These results were obtained by measuring a region of interest (ROI), marked with a white square in Figure 5-21 (b), with the multi-wavelength imaging system and the macroscopic polarimeter (both described in the previous subsection 5.2.2.1). The multiwavelength imaging system serves to image the sample at different wavelengths and identify variations in light absorption with the incident wavelength. In this study, the sample was imaged at four different wavelengths: 470, 530, 590, and 625 nm. The corresponding intensity images are provided in Figure 5-25 (a)-(d), respectively.

Intensity images of Figure 5-25 correspond to a ROI of 2.2x2.2 cm^2 in size with a resolution of 22 μm. The instrument is used to image, in transmission configuration, the lower part of the leaf surface, i.e., the part seen in Figure 5-21 (b). Under this configuration, the ROI is characterized by including primary, secondary, and tertiary veins. The primary vein (the midrib) is visible in the top-left corner in Figure 5-25 (a)-(d). For its side, secondary veins branch from the primary vein crossing the leaf from the top to the bottom. Tertiary veins branch from the secondary veins but are more difficult to perceive due to their reduced image contrast. In addition, a white-spotted structure is observed randomly spread across the whole surface of the

leaf. Such spots can be related to small microdroplets of water located on the leaf surface. Now, because of the similar image contrast of pictures in Figure 5-25 images, it can be said that, in this particular case, the multiwavelength technique does not bring a significant improvement over using a single wavelength beyond certain variations in the image contrast of veins.

The polarimetric analysis of the leaf starts by measuring the Mueller matrix corresponding to the same ROI (marked with a white square in Figure 5-21 (b)) at 530 nm. From the Mueller image, we calculate different polarimetric metrics (or observables) that give information related to the dichroism, retardance, and depolarization properties of the plant structures. In particular, dichroism is studied through the polarizance P, and the diattenuation D parameters; the total retardance R, the linear retardance δ, the angle of the fast axis θ, and the optical rotation φ of the Lu-Chipman retarder are calculated to analyze the retardance properties; and the depolarization index P_Δ, the IPP (P_1, P_2, and P_3) and their differences (P_2-P_1 and P_2-P_2) are evaluated to inspect the depolarization behavior of the measured structures. The analysis of the depolarization includes the calculus of the IPP because, as seen in the preceding work (subsection 5.2.1), plant structures may not depolarize light in the same way for all the incident polarizations (i.e., plant structures may present some depolarization anisotropy) and this phenomenon is not distinguished by using the P_Δ metric. In contrast, IPP can discern those structures that depolarize homogenously the incident light and those that depolarize it anisotropically. It is worth emphasizing that the way in which light is depolarized is closely related to the composition of the plant structures at the micrometric and nanometric scale.

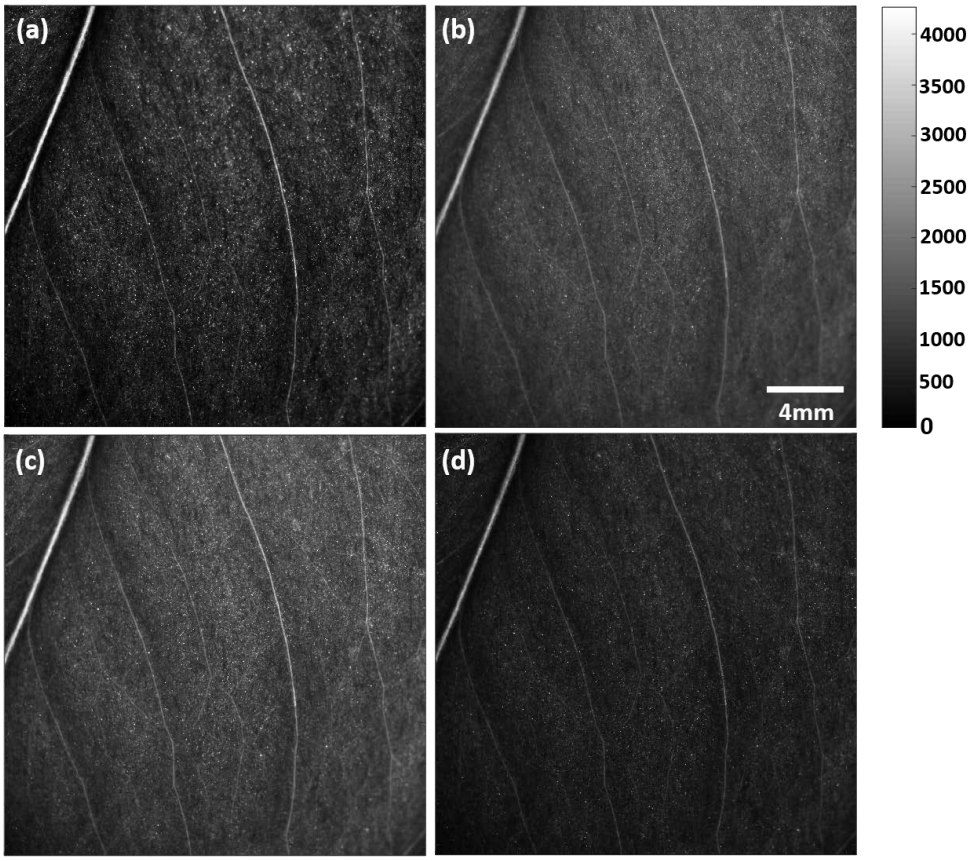

Figure 5-25. Multiwavelength image of the *Epipremnum aureum* leaf measured in transmission at (a) 470 nm, (b) 530 nm, (c) 590 nm, and (d) 625 nm wavelength.

Polarization and depolarization observables corresponding to the most representative images are provided in Figure 5-26. Concerning dichroism properties, we have provided in Figure 5-26 (a) the image of the diattenuation *D*. Except for the primary vein and a spotted-like structure uniformly distributed across the surface of the leaf, the imaged leaf is characterized for presenting a null or close to null diattenuation. The origin of the spotted-like structure will be discussed further on. Regarding the retardance properties, veins are described with a differentiated linear retardance response (the sinus of the linear retardance is provided in Figure 5-26 (b)). Note that the image of the optical rotation (circular retardance) is not shown because it is not relevant for the studied specimen. In the case of the depolarization properties, the P_Δ image is shown in Figure 5-26 (c), the P_1 image in Figure 5-26 (d), and the P_2-P_1 image in Figure 5-26 (e). As previously said, other IPP and combinations of IPP have been evaluated but their results are worse in terms of image contrast than those shown in Figure 5-26.

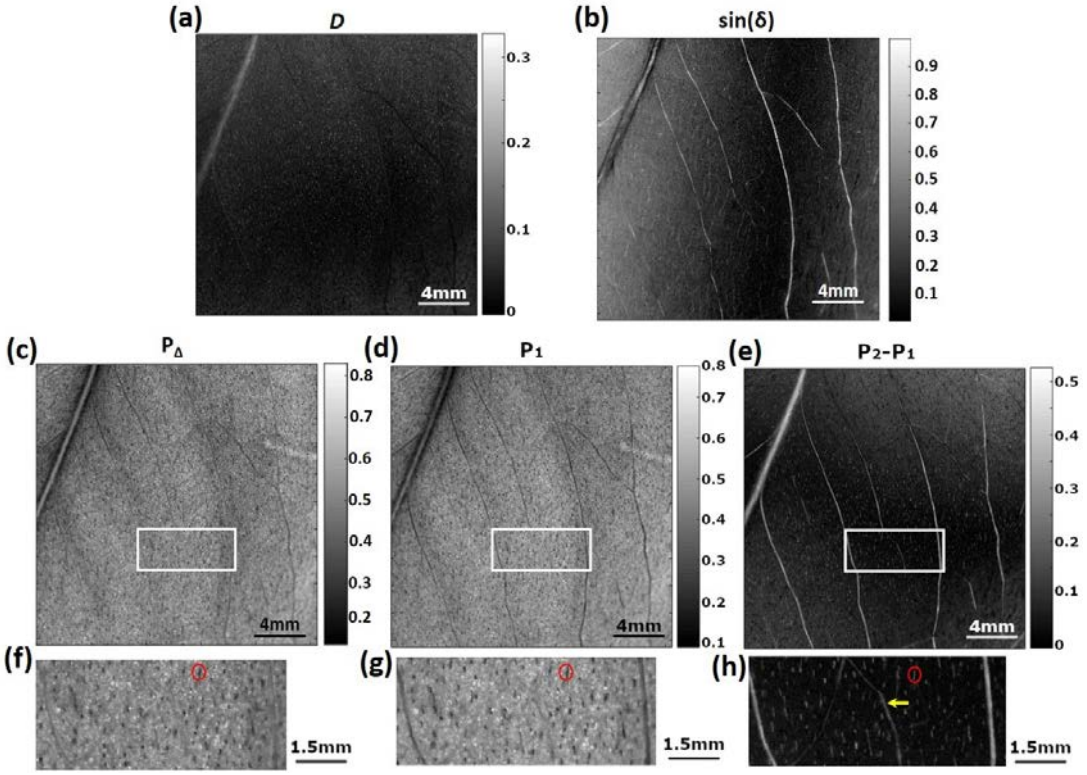

Figure 5-26. Polarimetric images of the *Epipremnum aureum* leaf measured at 530 nm wavelength. The pictures were obtained by using different channels: (a) diattenuation; (b) sinus of linear retardance δ; (c) P_Δ; (d) P_1; and (e) P_2-P_1. For the sake of visualization, (f), (g), and (h) are zoomed images of delimited regions (by the white rectangles) in Figure 5-26 (c), (d), and (e), respectively.

The image contrast between two adjacent structures has been quantified by using the figure of merit of visibility *V* (Eq. (5.11)). Visibility values range from 0 (no contrast) to 1 (maximum contrast). As a reference to compare the visibility between the 530 nm intensity image (Figure 5-25 (b)) and the images based on the polarization and depolarization metrics (Figure 5-26 (a)-(h)), we evaluate the visibility of the tertiary vein located at the middle of the white rectangle in Figure 5-26 (e). For the sake of visualization, zoomed images of the regions marked with a white rectangle in Figure 5-26 (c)-(e) are provided in Figure 5-26 (f)-(h), respectively. In Figure 5-26 (h),

the vein used as a reference is marked with a yellow arrow. The three best visibility values correspond to the P_2-P_1 channel (Figure 5-26 (e) and (h); V=0.52), followed by the sinus of the retardance (Figure 5-26 (b); V=0.42) and ending with the intensity image (Figure 5-25 (b); V=0.17). Note that in the P_Δ channel (Figure 5-26 (f)), the tertiary vein cannot be seen whereas the P_2-P_1 channel presents the best visibility values. This is explained because the overall depolarization of the tertiary vein and its surrounding is similar, but their anisotropic depolarization response is different.

To further visualize their different depolarization anisotropy, we have represented in Figure 5-27 the P_Δ and IPP values of both structures (the vein and its surrounding – the leaf lamina). In particular, Figure 5-27 shows the values corresponding to 10x30 pixels around the tertiary vein (marked with a yellow arrow in Figure 5-26 (f)). The P_Δ values are represented in a one-dimensional plot (Figure 5-27 (a)) in which yellow points correspond to vein pixels and black points to background cells. Regarding the IPP results, they are represented in the *purity space* [1,213] following the same color criteria.

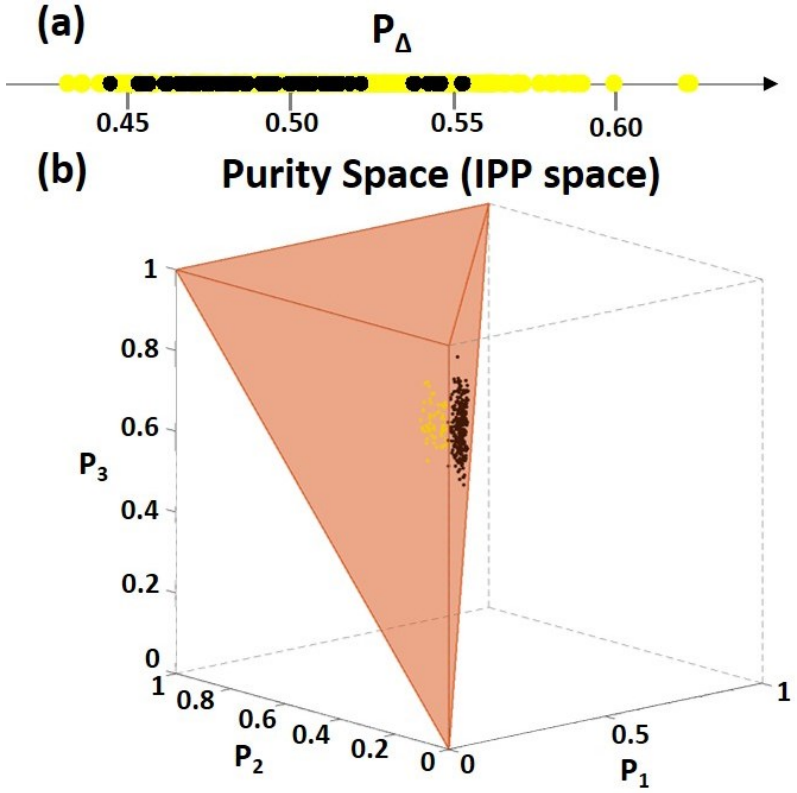

Figure 5-27. (a) Representation of P_Δ values of a 10x30 pixels region around the tertiary vein arrowed in yellow in Figure 5-26 (h). (b) Representation of the corresponding IPP values in the Purity Space. Yellow spots correspond to vein pixels and black spots to those associated with leaf lamina (background cells).

In Figure 5-27 (a), the P_Δ values of the vein (yellow points) and the values corresponding to the surrounding cells (black points) appear mixed (they are overlapping in the P_Δ value range of 0.45-0.55). Therefore, these two different plant structures (vein and leaf lamina) cannot be distinguished when using this metric. Conversely, these two groups of points are spatially separated in the *purity space* (Figure 5-27 (b)). Therefore, they could be automatically

identifiable, with no errors, as two distinct tissues. This is another example that supports the benefits of using the extra information obtained at calculating the IPP.

Besides the veins, a spotted-like structure, that is uniformly distributed over the entire leaf surface, is also seen in the depolarization-based images. In contrast to the tertiary vein, this spotted-like structure is observed in all the depolarization channels (Figure 5-26 (c)-(h)), even in those that have not been shown. These structures size from 50 µm to 300 µm and are located at different positions concerning the water microdroplets observed in the intensity images (Figure 5-25) so their physical origin is different. In fact, these structures tend to present certain spatial organization, they being orientated in the same direction as the closest secondary veins. Unlike this, such spatial organization was not observed in the water microdroplets present in the regular intensity images (Figure 5-25) that shown a random distribution. For that reason, we think that these spots will be an intrinsic characteristic structure of the leaf. The *Epipremnum aureum* species belongs to the *Araceae family*, and this family of plants tends to present raphides. In our particular case, we suppose we are measuring inulin raphides. Inulin is a type of polysaccharide that crystallizes in needle-shaped crystals that tend to group to form raphides and which is found in parenchymal cells in some plant species [258]. In the next two subsections, we prove, thanks to the measurements at the micrometric and nanometric scale, that the observed spots are really the inulin raphides.

The use of polarimetric images as diattenuation (Figure 5-26 (a)) also allows their visualization. The total diattenuation of the spotted structures ranges from 0.1 to 0.2 whereas the background cells have diattenuation values close to 0. Although diattenuation allows the visualization of inulin raphides, their image contrast is lower in the diattenuation images than in the depolarization-based images. To compare the images, we have calculated the visibility value of the raphide circled in red in Figure 5-26 (f)-(h) for the different channels. As a result, the visibility of this particular raphide is 0.18 for the D channel, 0.29 for the P_Δ channel, 0.39 for the P_1 channel and 0.51 for the P_2-P_1 channel. Therefore, we can say that the visualization of these structures is clearly improved when using polarization and depolarization observables by comparing their visibility values with the very low value of 0.09 for intensity images.

At this point, we want to emphasize that as states before, the bright dots observed in the intensity image do not correspond to the inulin raphides but they are more likely water microdroplets related to the humidity of the leaf. To confirm the different origin of these bright dots, we measured other leaves corresponding to other plant specimens with and without raphides [258] (*Arum italicum* Mill., *Hedera helix* L., *Hibiscus syriacus* L., *Photinia × fraseri* Dress, *Prunus dulcis* (Mill.) D.A.Webb, *Spathiphyllum* sp., and *Vitis vinifera* L.). The bright dots have been observed in all kinds of measured plants, regardless of whether or not they are characterized by presenting raphides. Conversely, the elongated and spatially oriented spots only observed by polarimetric means have been only detected in those species containing inulin raphides.

In summary, the examples discussed in this subsection illustrate how the use of polarization and depolarization-based images such as the orientation of the birefringence or the IPPs, can provide images with higher image contrast than images taken under non-polarized light. Moreover, it is shown that polarimetric-based images can reveal structures, such as the inulin raphides, which are simply overlooked when unpolarized light is used.

5.2.2.3 Micrometric scale

In the preceding subsection, we showed how images taken with a macroscope imaging polarimeter can provide information about the structure and organization of matter in vegetal tissues. In this subsection, the potential of the proposed approach is further studied following an analog approach but at the microscopic scale by comparing standard microscopy techniques with polarimetric microscopy. Our goal is not only to demonstrate the kind of information that can be obtained thanks to polarization, but also, we would like to highlight the relevance of polarimetric microscopy by comparing it with other microscopy techniques considered as an advanced state of the art in botany. We want to note that this is not an exhaustive compilation of microscopy techniques but rather we want to compare a representative group of techniques to illustrate the potential and interest of using Mueller polarimetry.

The comparative study is illustrated by the measurement of a piece of the same *Epipremnum aureum* leaf analyzed in the preceding subsection with the different microscopic techniques. We start showing how polarimetric microscope images, with a spatial resolution of 650 nm, can complete and enhance the information retrieved with the macroscopic image polarimeter. An example of polarimetric microscope images of the *Epipremnum aureum* leaf showing an inulin raphide is presented in Figure 5-28. These images were taken with the multimodal microscope (described in subsection 5.2.2.1.4) working in transmission and with the lower part of the leaf surface (the part pictured in Figure 5-21 (b)) facing the imaging objective. The regular intensity image of the inulin raphide obtained with non-polarized light can be seen in Figure 5-28 (a). In the intensity image, it is possible to distinguish a set of epidermal cells that surrounds a stoma (circled in black in Figure 5-28 (a)). Stomata are micrometric structures that can be located at the upper or lower surfaces of plant leaves (depending on the species) and which regulate the gas exchange and water loss in plants [178]. Note that stomatal functionality is a key leaf structure, especially in the context of climate change produced by the increase of CO_2 emissions. An elongated structure that appears blurred (circled in red in Figure 5-28 (a)) can be seen close to the stoma. It corresponds to an inulin raphide and it appears blurred because it is located inside the leaf, and thus, slightly out of the focal plane. Due to the blurry, it is difficult to specify the edges that limit the raphide.

The Mueller matrix of the same section of the leaf was measured with the same multimodal polarimetric microscope. To get specific information on the polarization and depolarization properties of the leaf structures, different observables have been calculated from the Mueller matrix, like in the macroscopic case. The evaluated observables are the same as in the preceding subsection and, analogously, only the most representative results will be discussed. Concerning depolarization, the images corresponding to the P_Δ, P_1 and P_2-P_1 channels are shown in Figure 5-28 (b)-(d). P_1 and P_2-P_1 channels present the best results in terms of image contrast and physical information. The P_Δ image is provided for the sake of comparison because of its more common use in Mueller polarimetry. Concerning polarization observables, Figure 5-28 (e) shows the total diattenuation *D,* and the sinus of the linear retardance is shown in Figure 5-28 (f). The first gives information related to the dichroism properties of the imaged plant structures and the latter provides information about their birefringence. Other observables related to retardance properties as the optical rotation φ are not provided because the imaged structures do not present circular retardance.

The inulin raphide is characterized by a differentiated polarimetric response compared with the surrounding leaf cells (see Figure 5-28 (b)-(f)). Thanks to this particular polarimetric response the edges of the raphide can be clearly distinguished. In fact, the upper region of the raphide that could be confused with plant cells is now clearly seen with the polarization and depolarization observables. This fact is highlighted in the P_1 channel (Figure 5-28 (c)) because the way that raphides depolarize the light is different from the aqueous surrounding cells. In particular, raphides depolarizes light in a more anisotropic way. To give some numbers, the average P_1 value of the white square section of the raphide (squared in Figure 5-28 (c)) is 0.11 whereas the average value of the yellow square section, corresponding to the surrounding cells, is 0.29.

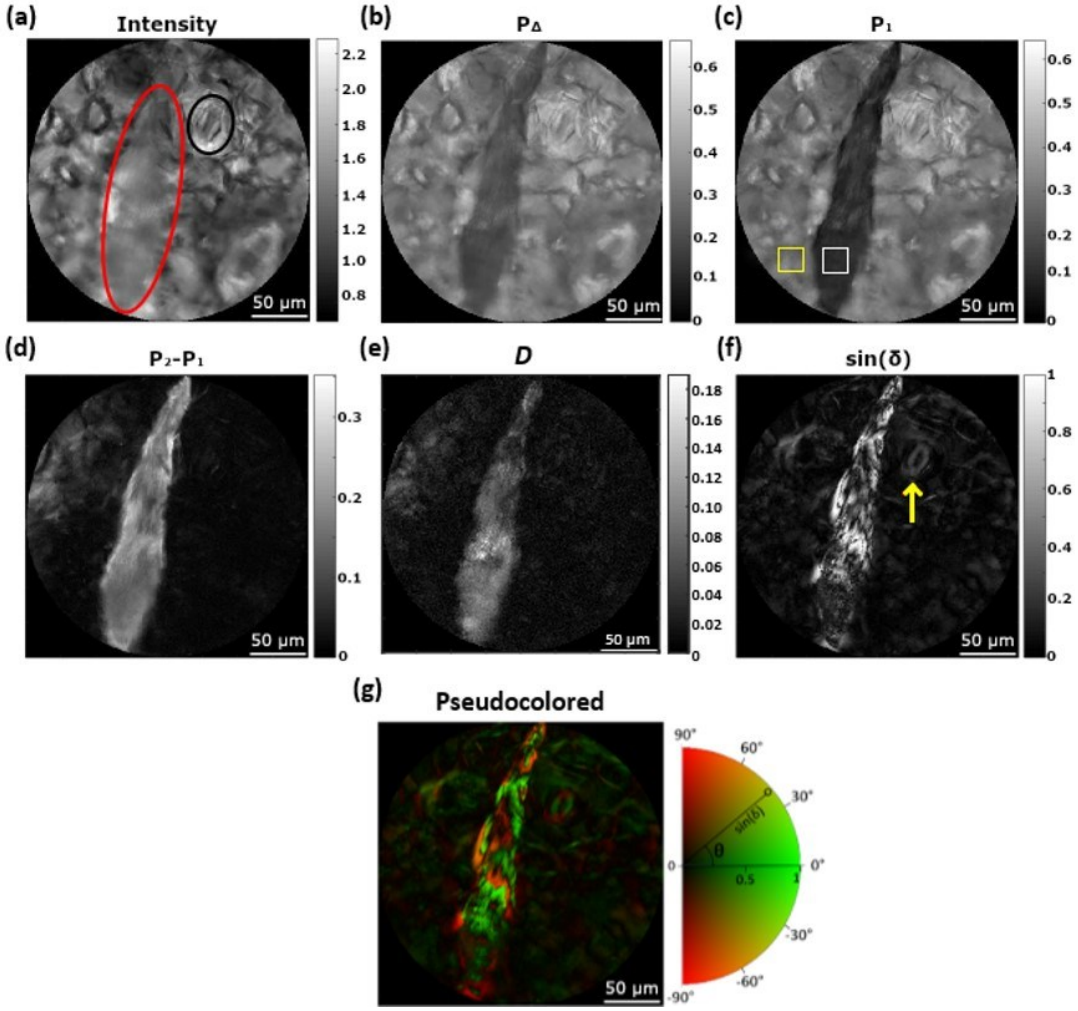

Figure 5-28. Polarimetric image of an inulin raphide belonging to a small piece of the *Epipremnum aureum* leaf measured at the 533 nm wavelength. The pictures were obtained by using different channels: (a) Intensity; (b) P_Δ; (c) P_1; (d) P_2-P_1; (e) diattenuation *D*; (f) sinus of linear retardance δ; and (f) pseudocolored image in which the color indicates the direction of the fast axis (θ) and the brightness depends on the sinus of linear retardance δ.

The average value of the squared sections can be used to calculate the visibility (Eq. (5.11)) between the inulin raphide and the background cells (cells of the lamina leaf). In this case, the

maximum and minimum intensities are replaced by the average intensities corresponding to squared sections. The resultant visibility for the P_1 channel is V=0.41. The same process is repeated for the other channels (Figure 5-28 (a)-(e)) and the resultant visibilities are provided in Table 5-6. Note that the visibility is significantly improved when using the polarization and depolarization observables (visibilities from 0.24 to 0.72) compared with the non-polarization images (V=0.03), being the best visibilities achieved with the diattenuation (V=0.7) and the P_2-P_1 (V=0.72) channels. It is worth pointing out that the visibility of the raphide variates considerably between different regions of the diattenuation image compared to the more uniform results observed in the depolarization-based images. Consequently, depolarization observables are better suited for the identification of these raphides.

Among the depolarization observables, those based on the IPP have significantly better visualization values (0.41 and 0.72) than those corresponding to the P_Δ image (0.24, see table Table 5-6). Therefore, raphides are easier to recognize when using these IPP observables so they are recommended for this task. The origin of the better contrast results observed when using the IPP arises from the anisotropic way that raphides depolarized the incident light.

	Intensity	P_Δ	P_1	P_2-P_1	D
Visibility	**0.03**	**0.24**	**0.41**	**0.72**	**0.70**

Table 5-6. Visibility of the raphide imaged in Figure 5-28 for the different channels

Besides the particular dichroism and depolarization shown by raphides, they also present a differentiated birefringence. However, such birefringence shows a strong spatial dependence, this not allowing the perfect recognition of the raphide edges. Alternatively, other plant structures as guard cells and their related stomata can be highlighted when using the birefringence information (Figure 5-28 (f)).

The imaged section of the leaf (Figure 5-28) contains a stoma of ~50µm length located close to the analyzed raphide (marked with a yellow arrow in Figure 5-28). The guard cells (the "lips" of this stoma") present a characteristic linear retardance of 17 degrees. This retardance comes from an alignment of cellulose myofibrils inside the walls [173]. The cellulose myofibrils of young and healthy guard cells tend to be aligned thus showing regular patterns. Unlike this, dead or non-functional guard cells have distended walls and present distorted patterns with low retardance [173]. To further study the birefringence properties of stomas, a pseudocolored image combining the linear retardance information δ and the orientation of the fast axis (θ) is shown in Figure 5-28 (g). The color of the image illustrates the direction of the fast axis while the brightness of this color shows the linear retardance corresponding to each pixel. Figure 5-28 (g) reveals a radial orientation of the fast axis (radial color variation), but its analysis is difficult due to its low brightness. Despite its characteristic birefringent response, this stoma is hard to visualize because the raphide saturates the image with its higher birefringence response.

For that reason, another section of the leaf containing stomata but without the presence of inulin raphides was imaged with the polarimetric microscope. An analogous pseudocolored image corresponding to this section is shown in Figure 5-29 (a). This section corresponds to an area of the leaf containing three stomata and where the cell walls are clearly visible with the pseudocolored technique. For the sake of visualization, a zoomed view of the area circled in blue in Figure 5-29 (a) is shown in Figure 5-29 (b). The circled area contains a stoma surrounded by

epidermal cells. Some structures as the inner thick walls and the stomata pore are clearly distinguished in Figure 5-29 (b). Note that this degree of definition is not observed in the intensity images (Figure 5-28). Additionally, the linear retardance of the stoma of Figure 5-29 (b) is radially orientated (the orientation is represented with different colors), being the fast axis parallel to the direction of the "lips" at each position. This directionality together with the absolute linear retardance value can be used to analyze the strain produced in the guard cells of the stoma [173].

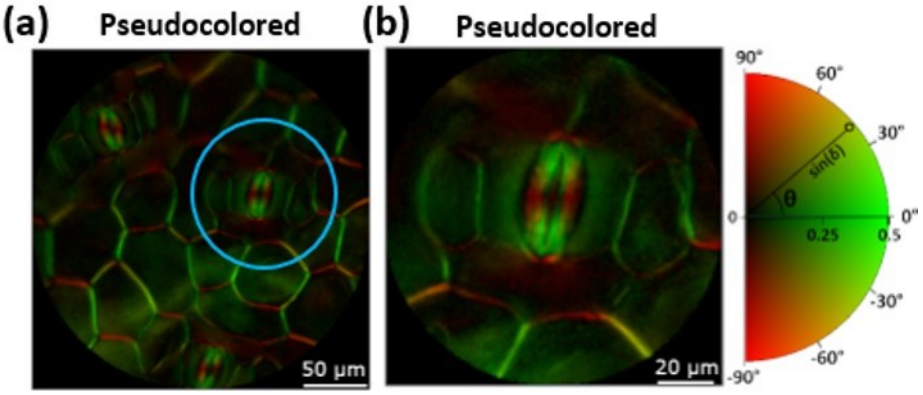

Figure 5-29. (a) Pseudocolored image of a collection of stomata and (b) the zoomed image of the region circled in blue. The color of the image illustrates the direction of the fast axis while the brightness is related to the linear retardance.

Before ending with the polarimetric measures, we want to highlight a relevant characteristic of polarimetric imaging we reported for the first time, the ability to highlight some structures located out of focus. This property will be next discussed through a particular example; the measurement of a region of the leaf containing an inulin raphide but this time with the obverse part of the leaf facing the imaging objective (Figure 5-30). These images were taken focusing on the obverse surface of the leaf so the inulin raphide is completely defocused because it is placed inside the leaf. The corresponding standard intensity image is shown in Figure 5-30 (a). In this intensity image, the walls of epidermal cells can be recognized and the raphide, which is located out of focus, appears considerably blurred, this difficulting its identification. In fact, the visibility of the raphide is approximately 0 (calculated by using the data corresponding to the yellow and white squared areas of Figure 5-30 (c)). In contrast, when the same region is measured with the polarization and depolarization observables, particularly diattenuation (Figure 5-30 (b)) and P_2-P_1 (Figure 5-30 (c)), the presence of the raphide is clearly revealed. The visibilities for the diattenuation channel and for the P_2-P_1 channel are equal to V=0.60 and V=0.67, respectively. Like in the preceding case, the visualization is similar for both channels but, for this experiment, the depolarization channels also seem to be better because the visibility value is uniform across the raphide unlike the case of the diattenuation image.

Despite the raphide remains out of focus, it interacts with light that passes through the sample and depolarizes it. The depolarization contribution of the raphide is mixed with other light-matter interactions, thus minimizing it. However, the depolarization of the raphide is an information channel so different that it allows its recognition even when it is out of focus. Thanks to this we could focus our image on some specific layer of the sample to not lose resolution and

at the same time revealing some out-of-focus structures. This would be useful when the users do not have prior information on samples.

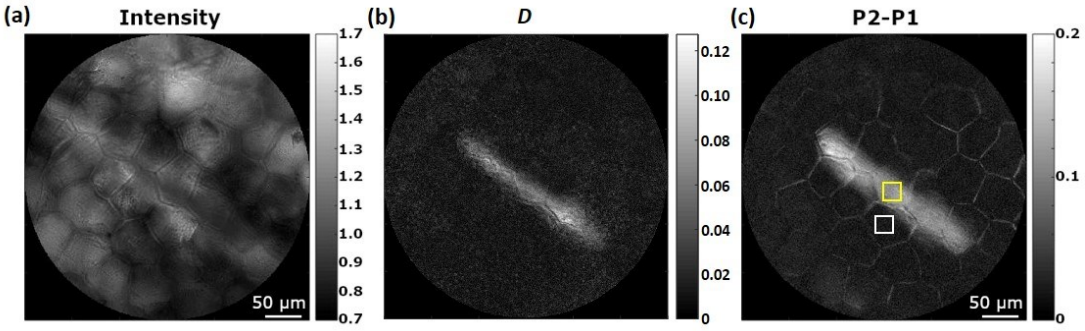

Figure 5-30. (a) Intensity, (b) diattenuation, and (c) P2-P1 images of a defocused inulin raphide of an *Epipremnum aureum* leaf.

The preceding microscopic images highlight the interest in using polarimetric microscopy for botanical applications as, for instance, the characterization of plants. In the case of the *Epipremnum aureum* species, polarimetry significantly improves the visualization of raphides and provides relevant information about the birefringence properties of stomata that can be connected with mechanical properties. Stomata have been studied in depth in the botanical field due to their important role [177,178] (they regulate the gas exchange and the water loss in plants) and because they can be used to determine the productivity of plants by analyzing their use of water [259]. Moreover, the density and size of stomata are characteristic of each plant so they can be used for plant characterization. Typically, stomata measurements consist of covering the leaf surface with a silicon rubber impression technique [260] and then using the silicon impression as a mold to create a positive replica of the leaf surface by using nail varnish [261]. Under this scenario, polarimetry is presented as an alternative technique that is non-invasive and faster. In addition, polarimetry brings new information that can be related to the physical properties of the sample as, for instance, the directionality of the birefringence observed in stomata cell walls which is connected with the mechanical strain [173]. Raphides imaged in Figure 5-28 and Figure 5-30 correspond to inulin raphides. In the industry, inulin is used for nutritional and medical applications [262,263]. Like stomata, the size and density of raphides can be used to characterize and classify plant species [264,265]. In fact, inulin raphides are particularly frequent in the *Araceae* family. These crystal raphides are commonly observed with electron microscopes. However, we have seen that they have a particular and characteristic polarimetric response that allows their easy recognition by using polarimetric microscopy. In particular, their diattenuation takes values from 0.1 to 0.2 whereas other plant structures present values close to 0. Moreover, they are suitable to be characterized with IPP metrics, as their depolarization is anisotropic, i.e., it depends on the SoP of the incident light, while other plant cells depolarize light more homogenously.

For the moment, we have discussed some properties of the Mueller polarimetric microscopy and the possible advantages of applying it in botanical applications. In particular, we have illustrated the benefits of using Mueller polarimetric microscopes compared with standard microscopes. However, botanical studies are not restricted to the use of standard microscopes and other microscopy techniques as phase-contrast microscopy and fluorescence microscopy

are commonly used. For the sake of comparison, images of the same specimen were taken by using phase-contrast microscopy and fluorescence microscopy.

Phase-contrast microscopy works separating the directly transmitted light and the scattered light by modifying the phase of the latter and thus generating a phase difference [7]. Then, the direct and the scattered light are coherently combined before reaching the camera, this emphasizing the edges of the measured structures. This microscopic technique also detects small variations in the thickness or refractive index (the latter can be related to differences in the density) among adjacent zones. Due to its high sensitivity, it is commonly used to image almost transparent samples that are difficult to visualize when using standard microscopes.

For the sake of comparison with polarimetric images, representative images of stomata and raphides that were taken with the phase-contrast microscope (the *Olympus Fluoview 1000* commercial microscope) are shown in Figure 5-31 (a) and (b). Figure 5-31 (a) shows a collection of three stomata that are clearly visible (V=0.38; calculated over the regions marked in red and green in Figure 5-31 (a)). In fact, some chloroplasts of guard cells can be seen in Figure 5-31 (a). These chloroplasts were not seen in polarimetric microscopy images, being the phase-contrast microscopy better suited for inspecting these organelles. Conversely, in this example, raphides are less contrasted in phase-contrast microscopy as observed in Figure 5-31 (b). The visibility of the imaged raphide is V=0.14 (calculated over the regions marked with white and yellow squares in Figure 5-31 (b)) compared to the V=0.72 obtained with polarimetric techniques. Polarimetric microscopy benefits from the fact that light depolarized by raphides depends on the state of polarization of the incident light, phenomena that phase-contrast microscopy is unable to measure as it is based on using unpolarized light. In addition, the multiple observables measured in Mueller polarimetry permits color encoding techniques that may help the visualization of structures. The latter cannot be done with the phase-contrast images as they are restricted to one channel. Another reason that may explain the less contrasted raphides obtained with the phase-contrast imaging technique is the fact that these raphides are not thin structures. In these cases, the phase differences can be larger than 2π leading to a grayscale representation that is non-linearly related to the thickness or refractive index of the sample. However, this characteristic of phase-contrast microscopy can be useful for other applications as the imaging of stomata. Stomata are seen with similar visibility in Figure 5-31 (b) than in Figure 5-31 (a) although the presence of inulin raphides.

As observed, phase contrast and polarimetry give complementary information of samples so both could be used as complementary techniques for the study of plants. For instance, phase microscopy could be used to image stomata with slightly better results and polarimetry could be used to study the birefringence of stomata and their relation with the strain produced in guard cells.

The same area of the leaf is imaged with the same *Olympus Fluoview 1000* microscope but working in the fluorescence mode. The corresponding set of three stomas are shown in Figure 5-31 (c) and the fluorescence image of the raphide is shown in Figure 5-31 (d). The characteristics of the fluorescent emission of light lead to highly resolved structures compared with the other techniques. For instance, some details of stomata as the chloroplasts of guard cells are clearly seen in Figure 5-31 (c) thanks to their fluorescent reaction. Although the observed improvement in the visualization of stomata reached by using fluorescence

microscopy, polarimetry methods still arise as an interesting approach for their study because some physical properties are related to polarimetric observables, e.g., the mechanical stress of cell walls and the birefringence. Concerning the raphide, its visualization (Figure 5-31 (d)) is worse compared with those obtained with the depolarization observables Figure 5-28 (b)-(d). Therefore, although raphides can be seen in fluorescence images, polarimetry is the optimal optical technique to inspect them.

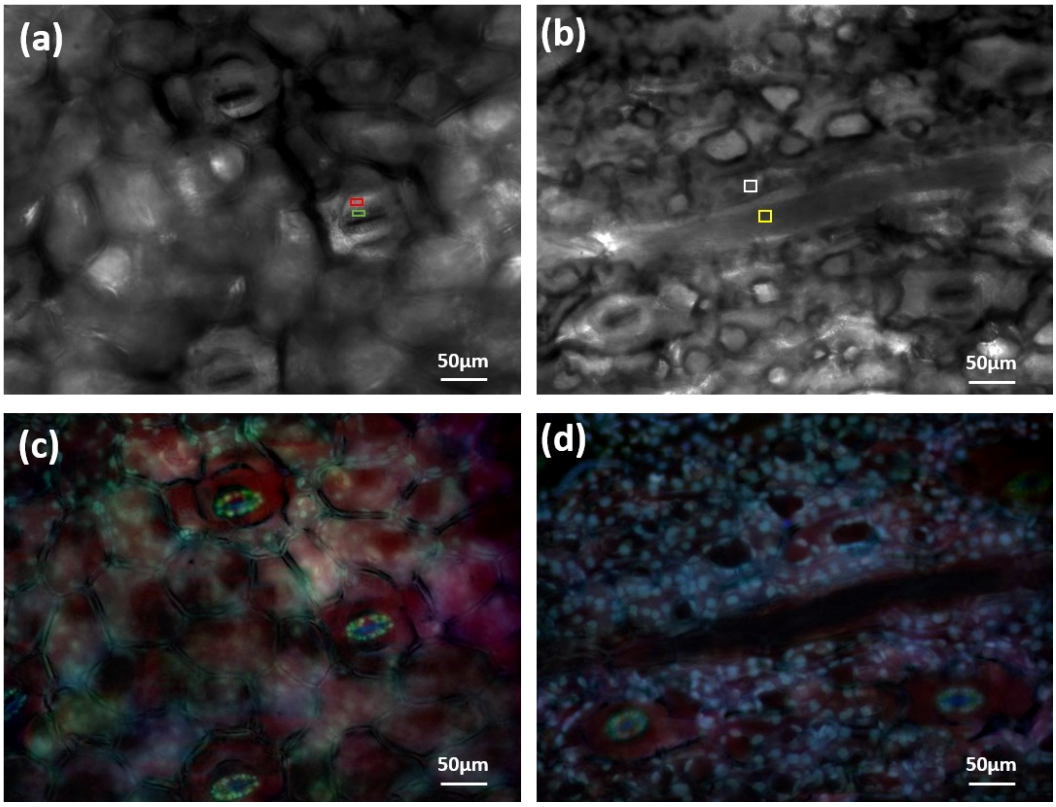

Figure 5-31. Phase-contrast images of different areas of an *Epipremnum aureum* leaf with (a) a collection of stomata and (b) an inulin raphide. Fluorescence images of the same areas that contain (c) a collection of stomata and (d) an inulin raphide.

Like in the case of phase-contrast, fluorescence techniques are also compatible with polarimetric techniques and can be used as complementary tools. Fluorescence microscopy works better with thin samples because, in thick samples, the fluorescence light emitted by dyes or fluorescent structures of the sample as chloroplasts is more probable to be scattered this degrading the spatial resolution of the image. However, this issue can be reduced by using the confocal configuration as in the present experiment. In contrast, polarimetric techniques use this scattered light to obtain information from the sample, as long as the scattered light is not excessive. We want to highlight that in addition to the above, polarimetric methods are less invasive than fluorescent microscopy, as they do not require manipulation of samples with fluorophores (fluorescent dyes), and with a proper image polarimeter, they could even be used for *in situ* measurements, without the need of transporting the samples into a laboratory.

The comparison performed in this subsection shows the compatibility of the analyzed optical techniques and that each technique has its pros and cons. Concerning to polarimetric

microscopy, the main issue is that to complete a Mueller matrix image measurement, it needs the capture of multiple images. This reducing the number of measures per time and, accordingly, difficulting the real-time measurements. In our case, the measurement of a Mueller image lasts around 1 minute. However, recent advances in polarimetry instrumentation (faster liquid crystal panels, pixelated polarization cameras, etc.) are making these instruments suitable for real-time applications. On the other hand, polarimetry leads to the enhancement of image contrast obtained at measuring certain structures, for instance, inulin raphides. Moreover, polarimetric microscopy brings information about the polarimetric response of samples which is directly related to their intrinsic structure. Polarimetric information can be very useful as it comes from interactions at the microscopic scale but can be observed at the macroscopic scale. Inulin raphides are a clear example of this; their polarimetric interaction comes from the microcrystals that comprise the raphide but their polarimetric response was also measured by using the macroscopic polarimeter (Figure 5-26). An additional advantage of polarimetry is its possible combination with the other optical techniques within the same equipment [85]. In fact, polarimetry can be introduced in other instruments by only adding a PSG and a PSA, thus performing minimal modifications [85]. In relation, it is worth mentioning that some architectures of polarimeters are very compact [59,186] this easing outdoors polarimetric experiments.

5.2.2.4 Nanometric scale

Finally, the presence of inulin raphides on the *Epipremnum aureum* leaves is verified by using a scanning electron microscope (SEM) to take high-resolution images of the same plant leaves. Representative images of inulin raphides sections from the analyzed *Epipremnum aureum* leaves are provided in Figure 5-32 (a) and (b). Note that the raphide showed in Figure 5-32 (b) was broken during the sample preparation. Preparing the sample without affecting the integrity of raphides is very complicated because they are located inside the leaf. This difficult sample preparation contrast with the simplicity of using polarimetric microscopy. The SEM images also confirm the presence of inulin raphides in *Epipremnum aureum* leaves. Two stomas with open and closed pores, respectively, are also imaged with the SEM, and the corresponding pictures are shown in Figure 5-32 (c) and (d). Thanks to the high resolution of electron microscopy several tinny salt crystals, not observed with the previous optical techniques, can also be recognized around the stoma with the closed pore Figure 5-32 (d).

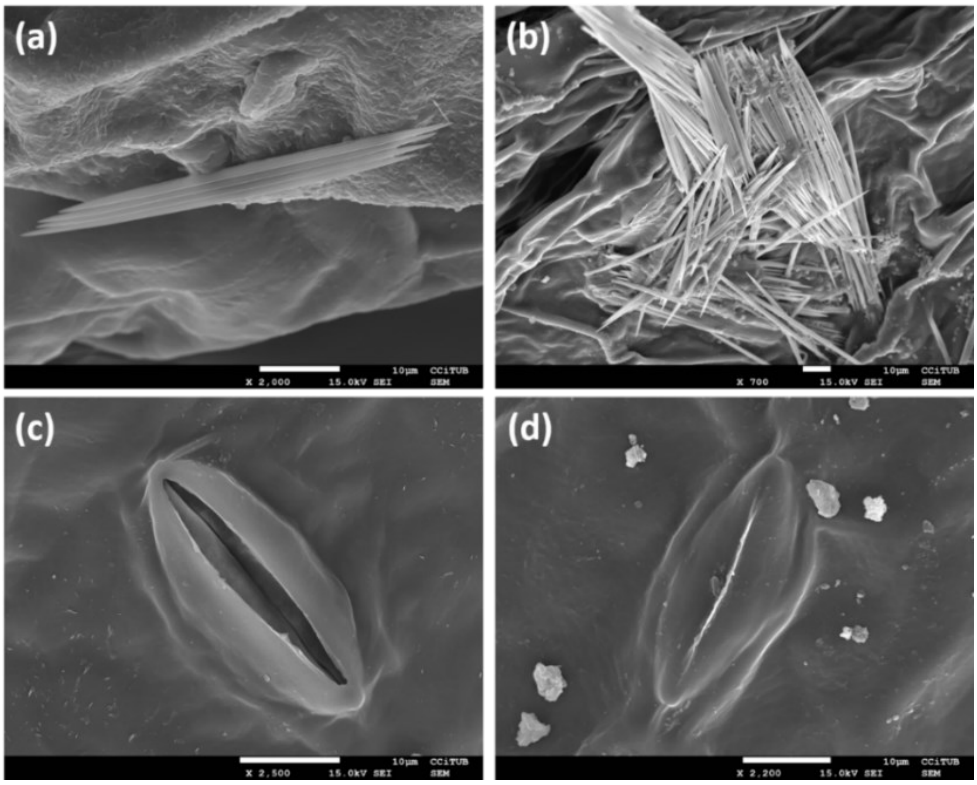

Figure 5-32. (a) and (b) Scanning electronic microscope (SEM) images showing sections of raphides located inside the *Epipremnum aureum* leaf. SEM images of stomata with (c) open and (d) closed pores are also shown.

Chapter 6 Conclusions

In this thesis, recently proposed and new polarimetric methods were studied, experimentally implemented and applied for the first time in biological tissue inspection to obtain additional information from the polarization and depolarization response of biological tissues. First, the relation between PG and Mueller matrix techniques was studied by measuring phantom samples that try to mimic the properties of biological tissues. Polarization gating techniques were proved to be a particular case of the Mueller matrix, so the use of the Mueller matrix is preferred. Then, the interpretation of the indices of polarimetric purity (IPP) and the components of purity (CP), both related to depolarization properties, was discussed through a set of simulated and experimentally synthesized samples. IPP and CP have the advantage, in comparison with the commonly used depolarization metrics P_Δ and Δ, that further synthesize the depolarization content of samples giving information about the anisotropy of the depolarization and the nature of the physical structures involved in the depolarization process. Once understood some properties of these metrics, they (as well as other Mueller matrix methods) were applied to inspect biological tissues of animal and plant origin.

In the case of inspecting animal tissues, the studies were meant to exploit the depolarization properties of the sample through the use of IPP metrics. IPP enhanced the image contrast of tissue structures, revealing certain structures hidden when using the standard polarimetric techniques. Moreover, IPP were also used to automatically classify animal tissues through machine learning processes. Under the latter scenario, IPP improved the percentage of well-classified tissues compared to the depolarization index P_Δ.

In the case of inspecting plants, the different studies provided were aimed to compare Mueller techniques with other polarimetric and non-polarimetric imaging methods. Mueller polarimetry showed some advantages, in comparison with other optical techniques, that highlight its potential for the inspection of plant tissue.

This last chapter summarizes the main results presented in this thesis and the corresponding conclusions (section 6.1). In addition, this chapter also proposes future applications and future research that can be done concerning the depolarization content of biological tissue samples (section 6.1.4.2).

6.1 Summary and conclusions

We highlight the following main conclusions from each chapter:

6.1.1 Mathematical formalism

Chapter 2 was aimed to review the Mueller-Stokes formalism as well as the Mueller decompositions and metrics used in this thesis. This thesis is based on the Mueller-Stokes formalism because it can describe partially and completely depolarized states. Starting from the description of the state of polarization (SoP) of a light beam through the Stokes vector, the different metrics and concepts were derived. First, the main properties of the polarized light and the main metrics used to analyze them were defined. For example, the mathematical description of the degree of polarization was provided. The degree of polarization is used in several plant studies, as well as in this thesis, to analyze the depolarization of light beams coming from the sample. In addition, the Poincare sphere representation, which is used across the thesis to provide a visual representation of light SoPs, was also described in this chapter.

Afterward, light-matter interaction was described by using the Mueller matrix. The Mueller matrix was defined as a 4x4 component matrix that relates the Stokes vector of the light beams before and after light-matter interaction, so it describes how the polarized light is modified during such light-matter interaction. This Mueller matrix is characteristic of each sample and, analogously to polarized light, the main polarimetric properties of the samples and the main metrics used to analyze them were defined. In this way, the diattenuation D and polarizance P were defined for the study of dichroism. For the analysis of the retardance and depolarization properties, more complex mathematical formalisms were needed as these properties appear encoded in the Mueller matrix.

Lu-Chipman decomposition was described as a method to separate the dichroism, retardance, and depolarization properties of the sample in three matrices. The mathematical implementation of the Lu-Chimpan decomposition was completely detailed. From the retardance matrix of the Lu-Chipman decomposition, we defined different metrics that are used in the thesis to analyze the retardance of samples. In particular, we mathematically described the total retardance (R), the linear retardance (δ), the optical rotation (φ), and the angle of the fast axis with respect to the horizontal direction (θ). Concerning the depolarization matrix of the Lu-Chimpan decomposition, it contained other properties besides depolarization, for example, a polarizance vector. In addition, only one metric was defined; the depolarization power Δ that quantifies the overall depolarization capability of samples. Owing to the last two reasons, other depolarization metrics were explored.

The mathematical description and the physical interpretation of the depolarization index (P_Δ), the covariance matrix eigenvalues, the indices of polarimetric purity (IPP), the components of purity (CP), and the depolarization indices of a high order were provided. P_Δ gives information about the overall depolarization capability of samples whereas the other four sets of metrics further synthesize this depolarization information. Moreover, the latter four sets of metrics can be used to build four different 3D spaces in which any physically realizable depolarizer can be represented. Mathematical relationships between the P_Δ and the IPP and between the P_Δ and

the CP were also provided. Note that the IPP is used in most of the studies discussed in this thesis.

Finally, an alternative Mueller matrix decomposition, the symmetric decomposition, was also defined. In particular, the detailed mathematical implementation corresponds only to type I matrices because the decomposition of type II matrices was not necessary for this thesis. Regarding the retardance content, we described a direct relation between the retardance matrices of the symmetric decomposition and the retardance matrix of the Lu-Chipman decomposition. We demonstrated how the latter is equal to the product of the two retardance matrices of the symmetric decomposition if samples do not present dichroism. Concerning the depolarization matrix of Type I symmetric decomposition, it does not contain any artifact and is defined by three parameters. These three parameters further synthesize the depolarization information compared to the Δ. Like the other sets of parameters, the latter depolarization parameters can be used to build a 3D space in which any physically realizable depolarizer can be represented. Last but not least, we described the Lorentz depolarization space based on a non-linear combination of these three depolarizer parameters.

6.1.2 Experimental set-up

The image Mueller polarimeter used in this thesis to measure biological samples is based on Parallel Aligned Liquid Crystals (PA-LC) panels. In Chapter 3, we described the experimental implementation of this Mueller polarimeter and the mathematical theory behind its operation principle. Regarding its operation principle, the measurement of a Mueller matrix consists of illuminating the sample with different generated polarized states and analyzing the outcoming light by using different polarization analyzers. Both the generated and analyzed states were described as a collection of Stokes vectors that comprise the generator and analyzer bases. These generator and analyzer bases were defined with two matrices, the $\boldsymbol{S_G}$ and $\boldsymbol{A}$, respectively. Once the matrices of these two bases are calibrated, they could be pseudoinversed to retrieve the Mueller matrix of the measured sample from the corresponding intensity measures. To retrieve the 16 coefficients of the Mueller matrix, the rank of the $\boldsymbol{S_G}$ and $\boldsymbol{A}$ matrices must be equal to 4. Accordingly, at least 16 independent intensity measurements, corresponding to different four generated and analyzed states, must be taken for a complete Mueller matrix measurement.

Several architectures could be implemented to build an image Mueller polarimeter. We reviewed most of these architectures and described the pros and cons of each one. Due to the relatively low cost, the easy implementation, and the fact of no using mechanical elements, we chose to build our setup based on liquid crystals. In particular, it was based on PA-LC devices.

The PSG of our setup is composed of a linear polarizer oriented at 0° with respect to the vertical of the lab, followed by two PA-LCs oriented at 45° and 0°, respectively. The PSA is composed of the same elements but arranged in inverse order. Thanks to this configuration, we can set fully polarized states for the generation and analysis systems in a controlled way.

Our image Mueller polarimeter can measure samples in reflection and transmission at four different wavelengths (625nm, 590 nm, 530 nm, and 470nm). The instrument uses an illumination system based on LED sources that prevent the speckle effect but generate partially depolarized states due to their broad bandwidths (in comparison with lasers). The fact of

illuminating the sample with partially depolarized states increases the error in the measurement of Mueller matrices so bandwidth filters of 10nm were used to reduce the effective depolarization obtained. As a result, the average *DOP* obtained in the worst case is equal to 0.966, corresponding to the 470 nm. By using this instrument, we can take Mueller images of regions of ~4.9x4.1 cm^2 with a resolution of ~20μm.

Before imaging the sample, the setup was calibrated based on the condition number (CN) and the equally weighted variance (EWV) figures of merit. Both figures of merit were described in detail in this chapter. The calibration process was performed for each wavelength and consist of calibrating the PSG with a commercial polarimeter and then use the calibrated PSG to calibrate the PSA. The calibrated generator and analyzer bases were composed both of six SoPs. When using 6 SoPs for both bases, the acquisition of Mueller images takes approximately 1 minute so only stationary samples can be measured. Finally, the calibrated bases were validated through the measurement of a polarizer and a retarder plate. As a result, the error in one coefficient was lower than the 3% of the total range in the worst case (measurement at 470 nm) and the error in the measurement of the total retardance is always lower than 1.5 degrees, both values that we consider acceptable for our work.

6.1.3 Analysis of polarimetric metrics for biophotonic applications

Recently proposed polarimetric methods (as well as new ones) were studied through controlled experiments in Chapter 4. First, an analytical expression that relates the polarization gating (PG) technique with the 16 coefficients of the Mueller matrix was proposed. Thanks to this analytical expression, any PG configuration can be calculated from the Mueller matrix. Therefore, instead of measuring several PG configurations, we could perform a single measurement of the Mueller matrix of the samples and obtain the equivalent information by applying the aforementioned expression. In addition, the Mueller matrix opens the possibility to use other analytical tools as, for instance, the Mueller matrix decompositions.

This analytical relation was experimentally proved by measuring a phantom sample. Several images corresponding to different PG configurations were taken by using both the standard method and the Mueller-based method. The obtained results were equivalent, presenting minimal differences that were attributed to the measurement noise. This noise error was higher in the case of using the method based on the Mueller matrix due to the error propagation. However, noise error could be reduced in the Mueller matrix measurement by using generator and analyzer bases with more SoPs (i.e., adding data redundancy), leading to negligible noise error. In conclusion, the experimental results proved the equivalence between the standard PG method and the PG method based on the Mueller matrix.

We also proved the relevance of using PG configurations based on elliptically polarized light and the importance of analyzing the positive and negative ellipticities. In particular, we showed that when using a particular PG gating configuration, the best result in terms of image contrast may correspond to an incident elliptical polarized state. Note that most PG experiments only analyze linearly polarized light, or at best circularly polarized light, so the application of PG techniques may not be optimized in these experiments. In addition, we also proved that positive and negative ellipticities may not lead to the same results so both ellipticities should be always inspected. This fact was emphasized with an experiment in which one object target (the number

4) was clearly observed when using right-handed circularly polarized light, but it was completely invisible when using left-handed circularly polarized light.

In the case of using the standard PG method, the measurement of PG configurations based on different incident ellipticities implies different measurements. By contrast, the equivalent results are obtained by only performing one measurement if using the PG method based on the Mueller matrix. Therefore, the latter method is better suited for research applications.

Finally, we proposed a new technique that combines the PG configurations with the Mueller matrix decompositions. This new technique was used to image an *ex-vivo* chicken neck and the best results were obtained with the depolarization information. This last experiment emphasizes that the Mueller matrix approach is a generalization of the PG techniques which allows the use of more complex mathematical tools leading to richer information, as for instance, the use of Mueller matrix decompositions or its combination with PG methods, that further synthesize the polarimetric information of the sample. Accordingly, Mueller matrix techniques are more suitable for biological imaging applications.

Once studied the relation between the PG and the Mueller matrix, we analyzed the indices of polarimetric purity (IPP) and the components of purity (CP), two sets of parameters that describe the depolarization content of samples. Both sets of metrics encode the information corresponding to the overall depolarization capability of a given sample in such a manner that the parameters could be combined to obtain the degree of polarimetric purity P_Δ. However, these two sets of metrics constitute two different three-dimensional spaces (the Component space and the Purity space) that further synthesize this depolarization information.

We show how the way in which these spaces synthesize the depolarization information is completely different. On the one hand, the IPP give information about the depolarization anisotropy associated with the sample and the relative weights of non-depolarizing components that a system can be assimilated with. Note that IPP indicate the presence of depolarization anisotropy but not the predominant direction of this anisotropy. On the other hand, CP indicates the dichroism and birefringence behavior of the effects involved in the depolarization process, i.e., the nature of these elements. This information is complementary so the two groups of metrics can be used together to completely describe the mechanisms that produce the depolarization in any sample.

The complementary aspect of IPP and CP is highlighted when the IPP are written in term of CP. Five of the six parameters are independents, for instance, *D, P,* and the three IPP (this base could be used as a reference to describe the depolarization of a sample). Moreover, the Purity and the CP spaces are completely different. This difference leads to regions where IPP and CP acquire better discriminatory potential compared to P_Δ: IPP is better for intermediate depolarizing samples ($0.2< P_\Delta<0.6$) and CP for low depolarizing systems ($P_\Delta>0.6$).

To further study the complementarity of IPP and CP, we simulated a group of depolarizers that represent limit cases. From these simulations we concluded that non-dichroic ($D=P=0$) depolarizers are better characterized with IPP whereas forward and reverse illuminated dichroic depolarizers with $D \neq P$ are distinguishable with CP but not with IPP. In the case of dichroic depolarizers with $D=P$, both sets of metrics should be used as their potential depends on which depolarizer you compare them with (i.e., $D(\boldsymbol{M_1})=D(\boldsymbol{M_2})$ or $D(\boldsymbol{M_1}) \neq D(\boldsymbol{M_2})$). Therefore, we

propose the complementary use of both spaces simultaneously for the analysis of depolarizing systems.

Finally, the discriminatory potential of IPP compared to P_Δ is proved through experimentally synthesized depolarizers. Two experimentally synthesized depolarizers were described with the same P_Δ value but different IPP. We want to emphasize that this phenomenon, same P_Δ value but different IPP, corresponds to two samples with the same overall depolarization but with different depolarization anisotropy, i.e., the input polarization states are depolarized differently. In addition, it is worth noting that these are experimental results and although being based on artificially synthesized depolarizers, the same phenomena could be seen in other samples as biomedical tissues. Last but not least, we proposed a method that allows the construction of experimentally synthesized depolarizers. We proved that highly depolarization systems can be synthesized by using this method, e.g., the synthesis of an ideal depolarizer that reached a value of P_Δ=0.13 (P_Δ=0 for a theoretical ideal depolarizer).

6.1.4 Biophotonic applications

Chapter 5 is meant to apply the Mueller matrix for biophotonics application. Chapter 5 is divided into two main sections: one corresponding to the inspection of animal tissues and the other to the study of tissues of plant origin. Analogously, the conclusions will also be divided into the same two sections.

6.1.4.1 Polarization techniques for biomedical tissue applications

Mueller polarimetry is widely used for animal tissues inspection but most of the studies only analyze the overall depolarization properties of samples and ignore possible depolarization anisotropy characteristics. For that reason, our works were mainly focused on studying metrics that better exploit this depolarization information.

First, we studied the experimental implementation of IPP for imaging animal tissues. The experiment started measuring the Mueller matrix of a rabbit leg and calculating some commonly used polarimetric observables (D, R, Δ, and P_Δ). We highlighted the interest of using Mueller polarimetry for tissue inspection by showing that some structures not observed in regular intensity images were revealed with polarimetric observables, e.g., a thin tendon and a spotted structure spread across the muscle. In addition, extra information, related to the physical structure of tissues was obtained with these polarimetric observables. Afterward, we calculated the IPP corresponding to the same Mueller matrix image and their results were compared with those of Δ and P_Δ, both commonly used depolarization observables. We proved that IPP may enhance the image contrast of some structures compared to Δ and P_Δ. In addition, we demonstrated that IPP may also reveal some structures or characteristics not observed in commonly studied polarized-based images. Moreover, as demonstrated in the previous chapter, IPP gives further information about the depolarization anisotropy of light that is connected with the structure and composition of the measured tissue. The latter information is not provided by Δ and P_Δ. Finally, we proposed a method that encodes the IPP information in one pseudocolored image in order to allow the visualization of the depolarization anisotropy information. Under this representation, each color corresponds to a particular depolarization response so the pseudocolored image can be used to visualize the depolarization properties of the sample.

Moreover, we showed that thanks to this representation, structures unseen in the Δ and P_Δ channels are clearly distinguishable in the pseudocolored image.

As a summarizing conclusion, we proved that IPP lead to better results for the inspection of animal tissues compared to the commonly used depolarization techniques (Δ and P_Δ) so their use is recommended.

In a second study, different sets of depolarization parameters were used to automatically recognize and classify different animal tissues. In particular, five different sets of parameters (the so-called depolarization spaces), together with the P_Δ metric, were used to classify three different animal tissues: tendons, muscles, and myotendinous junctions. The image Mueller matrices of 120 samples (40 for each tissue) were measured at three different wavelengths (470 nm, 530 nm, and 625 nm) and the different depolarization metrics were calculated. Then, the raw data corresponding to each measured pixel and the corresponding non-symmetric ellipsoids were represented in the different depolarization spaces for qualitative analysis. According to the obtained results, the three studied tissues are proved to be highly depolarizing structures (P_Δ<0.25) being the muscle the most depolarizing tissue, followed by the tendon and the myotendinous junction. The depolarization response of muscles and myotendinous junctions was similar for all the wavelengths but tendons showed a completely different response at 625 nm compared to 470 nm and 530 nm. This caused two different scenarios: (i) muscles were easier to classify when using the 625 nm wavelength because the depolarization response of tendons and myotendinous junctions is very similar at this wavelength; and (ii) myotendinous junctions were easier to classify when using the 470 nm and 530 nm wavelengths because the depolarization response of tendons and muscles is very similar at these wavelengths.

Afterward, the data corresponding to the different depolarization spaces was used to build several supervised classifiers. The percentage of well-classified tissues was used as a reference to quantify the suitability of depolarization spaces for the classification task. In that sense, the metrics based on the eigenvalues of the covariance matrix (***H***) were first compared. We showed that depolarization spaces provided better classification results than P_Δ, so the use in tissue classification studies of depolarization spaces, especially of the IPP metrics, is recommended. Concerning the spaces based on the ***H*** eigenvalues, the best results were obtained for the ***H*** eigenvalues and the IPP, being the latter recommended as they provide an easier physical interpretation. Regarding the spaces based on type I canonical depolarizer parameters, the highest classification efficiency is obtained with the type I canonical space.

Then, the results of the ***H*** eigenvalues/IPP and the type I canonical space were compared to determine the set of metrics most suited for the classification task. The set of metrics with the best percentage of well-classified tissues depended on the illumination wavelength. This occurs because the IPP and the ***H*** eigenvalues are influenced by the enpolarization of the sample, so they are influenced by the D and P of the sample, while the type I canonical depolarizer parameters are not. Therefore, when measuring non-dichroic samples (D=P=0) the potential of the three spaces is similar. In the opposite case, the efficiency of the spaces will be determined by the discriminatory potential of D and P. In that sense, samples presenting discriminating polarizance or diattenuation information are better classified by using the ***H*** eigenvalues/IPP, whereas type I canonical parameters better classify the tissues when samples present nondiscriminating polarizance or diattenuation information. Under this scenario, for tissue

classification, we recommend the use of the proposed depolarization spaces (***H*** eigenvalues, IPP or type I canonical space) together with the standard dichroic and brirrefigence parameters (*D*, *P*, *R*, *δ*,…).

Finally, we proved that polarimetry can be combined with other techniques as the multiwavelength measurements and we showed that the combination of polarimetric information corresponding to different wavelengths significantly improves the classification results.

Under this scenario, we want to emphasize that the classification method applied for the classification of animal tissue can be also applied in the early detection of disease, for instance, early cancer recognition or fungus detection in vegetal tissues.

6.1.4.2 Polarization techniques for plant applications

Unlike the case of animal tissues, Mueller polarimetry is barely used for plant tissue inspection, so our studies were mainly focused on studying the potential of using Mueller polarimetry compared to other polarimetric and non-polarimetric techniques.

First, we compared, through the measurement of a particular *Hedera maroccana* leaf, some depolarization-based Mueller parameters (P_Δ and IPP) with the degree of polarization (DOP), commonly used to study the depolarization produced by a leaf. We showed that DOP can strongly depend on the input polarization as well as on the orientation of the sample if the sample presents depolarization anisotropy. This variation causes that some structures may be highlighted whereas others are minimally visible. Therefore, the selection of the incident polarization is not trivial and various incident polarization states should be used to have a general vision of the sample.

By contrast, the values of P_Δ and IPP are unique and do not depend on the orientation of the sample. Consequently, similar structures present a more uniform image contrast in these channels. Concerning the analyzed Mueller-based channels, IPP channels showed higher image contrast compared to P_Δ channels. In particular, the P_2-P_1 channel showed the best visualization of leaf veins. Concerning DOP images, between all the veins present in the leaf, the image contrast of a small number of them was slightly better than those obtained with the P_2-P_1 channel. However, the overall contrast of most veins in the DOP image was dramatically lower than that of the P_2-P_1 channel, thus emphasizing the suitability of Mueller polarimetry for plants imaging.

In addition, the measured Mueller matrix can be used to calculate DOP images. By using this technique, we can take advantage of the DOP dependence with the incident polarization state to recognize some properties of the sample as, in our case, the direction of the veins. As a result, the unique disadvantage of Mueller polarimetry is the necessity of a more complex setup that wastes more time for each measurement. Therefore, if this is not a relevant issue, Mueller polarimetry should be applied instead.

In a second study, we illustrated the benefits of using Mueller polarimetry for botanical applications through the polarimetric measurement of a particular specimen, an *Epipremnum aureum*, at different scales: millimetric and micrometric. The same sample was also measured with other optical techniques and the obtained results were compared. At the millimetric scale,

we showed how polarimetry is capable to reveal some structures not seen in multiwavelength intensity images as the inulin raphides. Moreover, we also proved the interest in using the IPP for plant inspection as they revealed some veins not observed in the P_{Δ} channel.

At the millimetric scale, different inulin raphides and stomata were imaged using an image Mueller microscope, a phase-contrast microscope, and a fluorescence microscope. According to the results, we proved that some structures are better visualized in polarimetric-based images, for example, inulin raphides, whereas other structures are better visualized when using the other microscope techniques, e.g., stomata. However, we also showed that although stomata are better contrasted when using other optical techniques, for instance, fluorescence microscopy, the polarimetric images give information about the birefringence properties of the stomata which are connected with their intrinsic structure and that may be related to their mechanical strain. Note that the latter information can be useful for certain studies and it is only available by performing polarimetric measurements. In addition, we showed that polarimetry leads to the visualization of some structures, e.g., inulin raphides, that are commonly analyzed through electronic microscopes, being polarimetry a cheaper technique that does not need sample preparation. In the case of inulin raphides, their polarimetric response is very significant, and as a consequence, their structure is recognizable even being out of the image focal plane.

Mueller polarimetry is a relatively cheap technique that may be implemented in very compact architectures that ease outdoor experiments. Moreover, Mueller polarimetry provides different information of samples than other optical techniques, being complementary to them. Note that Mueller polarimetry can be combined with other optical techniques by implementing minimal modifications in the equipment.

Under this scenario, we think that Mueller polarimetry is an interesting tool that may be applied in several botanical applications as plant characterization, detection of plant diseases, analysis of hydric stress, among others.

6.2 Proposal for future research

- Identify a direct relation between the indices of polarimetric purity and the type of depolarization anisotropy. This relation can be studied in samples with and without dichroism. In addition, a more precise relationship between the IPP and the structure of the sample can be studied through polarization-sensitive Monte-Carlo simulations.
- Propose new Mueller-based metrics that describe the preferent directionality of the depolarization anisotropy.
- Build a real-time Mueller polarimeter. It could be a compact instrument to perform outdoor studies or a polarimetric microscope to make precision measurements. The PSA of this instrument would be probably a DoFP polarimeter.
- Improve the classification method by including other metrics as the CP and apply it in the early detection of diseases as early cancer recognition.
- Study different plant applications of the Mueller polarimetry as the early detection of plant diseases, the detection of the hydric stress in plants, or fungus recognition, among others.

List of acronyms

Acronym	Meaning
CCD	Charge-Coupled Device
CCiT	Centros Científicos y Tecnológicos
CN	Conditional Number
CP	Components of Purity
DoAmP	Division of Amplitude Polarimeter
DoAP	Division of Aperture Polarimeter
DoFP	Division of Focal Plane
DOP	Degree of Polarization
DoTP	Division of Time Polarimeter
EWV	Equally Weighted Variance
FWHM	Full Width Half Maximum
HWP	Half-Wave Plate
IPP	Indices of Polarimetric Purity
kNN	k-Nearest Neighbors
LC	Liquid Crystal
LED	Light-Emitting Diode
LP	Linear Polarizer
LS	Light Source
M	Mueller matrix
OCT	Optical Coherence Tomography

PA-LC	Parallel Aligned Liquid Crystal
PG	Polarization Gating
PI	Purity Index
PMT	Photomultipliers
PSA	Polarization State Analyzer
PSG	Polarization State Generator
QWP	Quarter-Wave Plate
RGB	Red-Green-Blue
ROI	Region of Interest
S-M	Stokes-Mueller
SEM	Scanning Electron Microscopy
SHG	Second Harmonic Generation
SoP	State of Polarization
STED	Stimulated Emission Depletion
TEM	Transmission Electron Microscopy
TN-LC	Twisted Nematic Liquid Crystal
TPEF	Two-Photon Excitation Fluorescence

Bibliography

1. I. San José and J. J. Gil. *Invariant indices of polarimetric purity: Generalized indices of purity for n × n covariance matrices*, Opt. Commun. **284**(1), 38–47 (2011).
2. A. R. Kherlopian, T. Song, Q. Duan, M. A. Neimark, M. J. Po, J. K. Gohagan, and A. F. Laine. *A review of imaging techniques for systems biology*, BMC Syst. Biol. **2**(1), 74 (2008).
3. R. Carriles, D. N. Schafer, K. E. Sheetz, J. J. Field, R. Cisek, V. Barzda, A. W. Sylvester, and J. A. Squier. *Invited Review Article: Imaging techniques for harmonic and multiphoton absorption fluorescence microscopy*, Rev. Sci. Instrum. **80**(8), 081101 (2009).
4. S. Jacquemoud and S. Ustin. *Leaf Optical Properties* (Cambridge University Press, 2019).
5. S. Pujals, N. Feiner-Gracia, P. Delcanale, I. Voets, and L. Albertazzi. *Super-resolution microscopy as a powerful tool to study complex synthetic materials*, Nat. Rev. Chem. **3**(2), 68–84 (2019).
6. E. Abbe. *Beiträge zur Theorie des Mikroskops und der mikroskopischen Wahrnehmung*, Arch. für Mikroskopische Anat. **9**, 413–418 (1873).
7. C. J. R. Sheppard. *Microscopy: Phase Contrast Microscopy*, Encycl. Mod. Opt. **3**, 103–110 (2004).
8. A. Van Helden, S. Dupre, and R. Van Gent. *The Origins of the Telescope.* (2011).
9. B. Amos. *Lessons from the history of light microscopy*, Nat. Cell Biol. **2**(8), E151–E152 (2000).
10. H. Zhang, D. Salo, D. M. Kim, S. Komarov, Y.-C. Tai, and M. Y. Berezin. *Penetration depth of photons in biological tissues from hyperspectral imaging in shortwave infrared in transmission and reflection geometries*, J. Biomed. Opt. **21**(12), 126006 (2016).
11. F. H. Mustafa and M. S. Jaafar. *Comparison of wavelength-dependent penetration depths of lasers in different types of skin in photodynamic therapy*, Indian J. Phys. **87**(3), 203–207 (2013).
12. H. F. Grahn and P. Geladi. *Techniques and Applications of Hyperspectral Image Analysis* (John Wiley & Sons, 2007).
13. C. Veys, J. Hibbert, P. Davis, and B. Grieve. *An ultra-low-cost active multispectral crop diagnostics device*, in 2017 IEEE SENSORS (2017), pp. 1–3.
14. N. A. Hagen and M. W. Kudenov. *Review of snapshot spectral imaging technologies*, Opt. Eng. **52**(9), 1–23 (2013).
15. A. M. Shahidi, S. R. Patel, J. G. Flanagan, and C. Hudson. *Regional variation in human retinal vessel oxygen saturation*, Exp. Eye Res. **113**, 143–147 (2013).

16. L. Rey-Barroso, F. J. Burgos-Fernández, X. Delpueyo, M. Ares, S. Royo, J. Malvehy, S. Puig, and M. Vilaseca. *Visible and extended near-infrared multispectral imaging for skin cancer diagnosis*, Sensors (Switzerland) **18**(5), 1441 (2018).
17. A. Lowe, N. Harrison, and A. P. French. *Hyperspectral image analysis techniques for the detection and classification of the early onset of plant disease and stress*, Plant Methods **13**(1), 80 (2017).
18. K. J. I. Ember, M. A. Hoeve, S. L. McAughtrie, M. S. Bergholt, B. J. Dwyer, M. M. Stevens, K. Faulds, S. J. Forbes, and C. J. Campbell. *Raman spectroscopy and regenerative medicine: a review*, npj Regen. Med. **2**(1), 12 (2017).
19. E. Gentleman, R. J. Swain, N. D. Evans, S. Boonrungsiman, G. Jell, M. D. Ball, T. A. V Shean, M. L. Oyen, A. Porter, and M. M. Stevens. *Comparative materials differences revealed in engineered bone as a function of cell-specific differentiation*, Nat. Mater. **8**(9), 763–770 (2009).
20. Y. A. Khristoforova, I. A. Bratchenko, O. O. Myakinin, D. N. Artemyev, A. A. Moryatov, A. E. Orlov, S. V. Kozlov, and V. P. Zakharov. *Portable spectroscopic system for in vivo skin neoplasms diagnostics by Raman and autofluorescence analysis*, J. Biophotonics **12**(4), e201800400 (2019).
21. J. W. Lichtman and J.-A. Conchello. *Fluorescence microscopy*, Nat. Methods **2**(12), 910–919 (2005).
22. L. Donaldson. *Autofluorescence in Plants*, Molecules **25**(10), (2020).
23. T. Chen, D. Ji, and S. Tian. *Variable-angle epifluorescence microscopy characterizes protein dynamics in the vicinity of plasma membrane in plant cells*, BMC Plant Biol. **18**(1), 43 (2018).
24. C. A. Konopka and S. Y. Bednarek. *Variable-angle epifluorescence microscopy: A new way to look at protein dynamics in the plant cell cortex*, Plant J. **53**(1), 186–196 (2008).
25. M. Ovečka, D. von Wangenheim, P. Tomančák, O. Šamajová, G. Komis, and J. Šamaj. *Multiscale imaging of plant development by light-sheet fluorescence microscopy*, Nat. Plants **4**(9), 639–650 (2018).
26. D. Sonin, E. Pochkaeva, S. Zhuravskii, V. Postnov, D. Korolev, L. Vasina, D. Kostina, D. Mukhametdinova, I. Zelinskaya, Y. Skorik, E. Naumysheva, A. Malashicheva, P. Somov, M. Istomina, N. Rubanova, I. Aleksandrov, M. Vasyutina, and M. Galagudza. *Biological Safety and Biodistribution of Chitosan Nanoparticles*, Nanomater. (Basel, Switzerland) **10**(4), 810 (2020).
27. J. Skoch, G. A. Hickey, S. T. Kajdasz, B. T. Hyman, and B. J. Bacskai. *In vivo imaging of amyloid-beta deposits in mouse brain with multiphoton microscopy*, Methods Mol. Biol. **299**, 349–363 (2005).
28. P. J. Campagnola, A. C. Millard, M. Terasaki, P. E. Hoppe, C. J. Malone, and W. A. Mohler. *Three-dimensional high-resolution second-harmonic generation imaging of endogenous structural proteins in biological tissues*, Biophys. J. **82**(1 Pt 1), 493–508 (2002).
29. The Royal Swedish Academy of Sciences. (June 2021). *How the optical microscope became a nanoscope*, retrieved from https://www.nobelprize.org/uploads/2018/06/popular-chemistryprize2014.pdf.
30. T. A. Klar, S. Jakobs, M. Dyba, A. Egner, and S. W. Hell. *Fluorescence microscopy with diffraction resolution barrier broken by stimulated emission*, Proc. Natl. Acad. Sci. **97**(15), 8206–8210 (2000).
31. N. Kim, H. J. Kim, Y. Kim, K. S. Min, and S. K. Kim. *Direct and precise length measurement of single, stretched DNA fragments by dynamic molecular combing*

and STED nanoscopy, Anal. Bioanal. Chem. **408**(23), 6453–6459 (2016).
32. A. Jaiswal, C. H. Hoerth, A. M. Zúñiga Pereira, and H. Lorenz. *Improved spatial resolution by induced live cell and organelle swelling in hypotonic solutions*, Sci. Rep. **9**(1), 12911 (2019).
33. J. Jonkman, C. M. Brown, G. D. Wright, K. I. Anderson, and A. J. North. *Tutorial: guidance for quantitative confocal microscopy*, Nat. Protoc. **15**(5), 1585–1611 (2020).
34. A. D. Elliott. *Confocal Microscopy: Principles and Modern Practices*, Curr. Protoc. Cytom. **92**(1), e68 (2020).
35. M. Li, S. Landahl, A. R. East, P. Verboven, and L. A. Terry. *Optical coherence tomography—A review of the opportunities and challenges for postharvest quality evaluation*, Postharvest Biol. Technol. **150**, 9–18 (2019).
36. L. van Manen, J. Dijkstra, C. Boccara, E. Benoit, A. L. Vahrmeijer, M. J. Gora, and J. S. D. Mieog. *The clinical usefulness of optical coherence tomography during cancer interventions*, J. Cancer Res. Clin. Oncol. **144**(10), 1967–1990 (2018).
37. D. Thomas and G. Duguid. *Optical coherence tomography—a review of the principles and contemporary uses in retinal investigation*, Eye **18**(6), 561–570 (2004).
38. C. J. Larimer, E. H. Denis, J. D. Suter, and J. J. Moran. *Optical coherence tomography imaging of plant root growth in soil*, Appl. Opt. **59**(8), 2474–2481 (2020).
39. Z. Kong, X. Zhu, S. Zhang, J. Wu, and Y. Luo. *Phase contrast microscopy of living cells within the whole lens: spatial correlations and morphological dynamics*, Mol. Vis. **18**, 2165–2173 (2012).
40. A. Momose, W. Yashiro, K. Kido, J. Kiyohara, C. Makifuchi, T. Ito, S. Nagatsuka, C. Honda, D. Noda, T. Hattori, T. Endo, M. Nagashima, and J. Tanaka. *X-ray phase imaging: from synchrotron to hospital*, Philos. Trans. A. Math. Phys. Eng. Sci. **372**(2010), 20130023 (2014).
41. C. Karunakaran, R. Lahlali, N. Zhu, A. M. Webb, M. Schmidt, K. Fransishyn, G. Belev, T. Wysokinski, J. Olson, D. M. L. Cooper, and E. Hallin. *Factors influencing real time internal structural visualization and dynamic process monitoring in plants using synchrotron-based phase contrast X-ray imaging*, Sci. Rep. **5**, 12119 (2015).
42. Z.-J. Guan, S.-B. Zhang, K.-Y. Guan, S.-Y. Li, and H. Hu. *Leaf anatomical structures of Paphiopedilum and Cypripedium and their adaptive significance*, J. Plant Res. **124**(2), 289–298 (2011).
43. J. A. Terzakis, E. Santagada, A. Hernandez, and M. Taskin. *Scanning electron microscopy of peripheral blood smears: comparison of normal blood with some common leukemias*, Ultrastruct. Pathol. **29**(1), 19–28 (2005).
44. E. Garcia-Caurel, R. Ossikovski, M. Foldyna, A. Pierangelo, B. Drévillon, and A. De Martino. *Advanced mueller ellipsometry instrumentation and data analysis*, in Ellipsometry at the Nanoscale (Springer-Verlag Berlin Heidelberg, 2013), pp. 31–143.
45. J. J. Gil Pérez and R. Ossikovski. *Polarized Light and the Mueller Matrix Approach*. 1st Ed. (CRC Press, 2016).
46. D. H. Goldstein. *Polarized Light*. 3rd Ed. (CRC Press, 2011).
47. J. S. Tyo, D. L. Goldstein, D. B. Chenault, and J. A. Shaw. *Review of passive imaging polarimetry for remote sensing applications*, Appl. Opt. **45**(22), 5453–5469 (2006).

48. V. V. Tuchin. *Tissue Optics: Light Scattering Methods and Instruments for Medical Diagnosis*. 3rd Ed. (SPIE Press, 2015).
49. A. Peinado, A. Lizana, and J. Campos. *Design of polarimeters based on liquid crystals and biaxial crystals for polarization metrology*, Opt. Pura y Apl. **49**(4), 167–177 (2016).
50. W.-L. Hsu, G. Myhre, K. Balakrishnan, N. Brock, M. Ibn-Elhaj, and S. Pau. *Full-Stokes imaging polarimeter using an array of elliptical polarizer*, Opt. Express **22**(3), 3063–3074 (2014).
51. J. Guo and D. Brady. *Fabrication of thin-film micropolarizer arrays for visible imaging polarimetry*, Appl. Opt. **39**(10), 1486–1492 (2000).
52. V. Gruev, J. Van der Spiegel, and N. Engheta. *Dual-tier thin film polymer polarization imaging sensor*, Opt. Express **18**(18), 19292–19303 (2010).
53. H. Kikuta, H. Haccho, K. Iwata, T. Hamamoto, H. Toyota, and T. Yotsuya. *Real-time polarimeter with a form-birefringent micro retarder array*, in Optical Engineering for Sensing and Nanotechnology (ICOSN 2001) (2001).
54. X. Zhao, A. Bermak, F. Boussaid, and V. G. Chigrinov. *Liquid-crystal micropolarimeter array for full Stokes polarization imaging in visible spectrum*, Opt. Express **18**(17), 17776–17787 (2010).
55. G. Myhre, W.-L. Hsu, A. Peinado, C. LaCasse, N. Brock, R. A. Chipman, and S. Pau. *Liquid crystal polymer full-stokes division of focal plane polarimeter*, Opt. Express **20**(25), 27393–27409 (2012).
56. N. Gu, B. Yao, L. Huang, and C. Rao. *Design and Analysis of a Novel Compact and Simultaneous Polarimeter for Complete Stokes Polarization Imaging with a Piece of Encoded Birefringent Crystal and a Micropolarizer Array*, IEEE Photonics J. **10**(2), 1–12 (2018).
57. J. Qi, C. He, and D. S. Elson. *Real time complete Stokes polarimetric imager based on a linear polarizer array camera for tissue polarimetric imaging*, Biomed. Opt. Express **8**(11), 4933–4946 (2017).
58. A. Lizana, J. Campos, A. Van Eeckhout, and A. Marquez. *Misalignment error analysis in polychromatic division of focal plane Stokes polarimeters*, OSA Contin. **2**(5), 1565–1575 (2019).
59. X. Tu, S. McEldowney, Y. Zou, M. Smith, C. Guido, N. Brock, S. Miller, L. Jiang, and S. Pau. *Division of focal plane red–green–blue full-Stokes imaging polarimeter*, Appl. Opt. **59**(22), G33–G40 (2020).
60. R. Espinosa-Luna, E. Bernabeu, and G. Atondo-Rubio. *Q(M) and the depolarization index scalar metrics*, Appl. Opt. **47**(10), 1575–1580 (2008).
61. J. J. Gil. *Components of purity of a Mueller matrix*, J. Opt. Soc. Am. A **28**(8), 1578–1585 (2011).
62. A. Tariq, P. Li, D. Chen, D. Lv, and H. Ma. *Physically Realizable Space for the Purity-Depolarization Plane for Polarized Light Scattering Media*, Phys. Rev. Lett. **119**(3), 033202 (2017).
63. A. Tariq, H. He, P. Li, and H. Ma. *Purity-depolarization relations and the components of purity of a Mueller matrix*, Opt. Express **27**(16), 22645–22662 (2019).
64. R. Ossikovski and J. Vizet. *Eigenvalue-based depolarization metric spaces for Mueller matrices*, J. Opt. Soc. Am. A **36**(7), 1173–1186 (2019).
65. C. J. R. Sheppard, A. Bendandi, A. Le Gratiet, and A. Diaspro. *Eigenvectors of polarization coherency matrices*, J. Opt. Soc. Am. A **37**(7), 1143–1154 (2020).
66. S.-Y. Lu and R. A. Chipman. *Interpretation of Mueller matrices based on polar decomposition*, J. Opt. Soc. Am. A **13**(5), 1106–1113 (1996).

67. R. Ossikovski. *Differential matrix formalism for depolarizing anisotropic media*, Opt. Lett. **36**(12), 2330–2332 (2011).
68. R. A. Chipman. *Polarimetry*, in Handbook of Optics: Devices, Measurements, and Properties, 2nd Ed. (McGraw-Hill, 1995).
69. J. Jorge Gil and E. Bernabeu. *Depolarization and polarization indices of an optical system*, Opt. Acta (Lond). **33**(2), 185–189 (1986).
70. S. R. Cloude. *Group theory and polarisation algebra*, Optik (Stuttg). **75**, 26–36 (1986).
71. R. A. Chipman. *Depolarization index and the average degree of polarization*, Appl. Opt. **44**(13), 2490–2495 (2005).
72. R. Ossikovski. *Analysis of depolarizing Mueller matrices through a symmetric decomposition*, J. Opt. Soc. Am. A **26**(5), 1109–1118 (2009).
73. R. Ossikovski. *Alternative depolarization criteria for Mueller matrices*, J. Opt. Soc. Am. A **27**(4), 808 (2010).
74. N. Ghosh, M. F. G. Wood, and I. A. Vitkin. *Mueller matrix decomposition for extraction of individual polarization parameters from complex turbid media exhibiting multiple scattering, optical activity, and linear birefringence*, J. Biomed. Opt. **13**(4), 1–14 (2008).
75. A. Le Gratiet, A. Mohebi, F. Callegari, P. Bianchini, and A. Diaspro. *Review on Complete Mueller Matrix Optical Scanning Microscopy Imaging*, Appl. Sci. **11**, 1632 (2021).
76. P. Li, D. Lv, H. He, and H. Ma. *Separating azimuthal orientation dependence in polarization measurements of anisotropic media*, Opt. Express **26**(4), 3791 (2018).
77. Y. Zhao, Q. Peng, C. Yi, and S. G. Kong. *Multiband Polarization Imaging*, J. Sensors **2016**, 5985673 (2016).
78. A. S. Alenin, L. Morrison, C. Curiel, and J. S. Tyo. *Hyperspectral measurement of the scattering of polarized light by skin*, in Polarization Science and Remote Sensing V (2011).
79. F. Vasefi, N. MacKinnon, R. B. Saager, A. J. Durkin, R. Chave, E. H. Lindsley, and D. L. Farkas. *Polarization-sensitive hyperspectral imaging in vivo: A multimode dermoscope for skin analysis*, Sci. Rep. **4**, 1–10 (2014).
80. A. Frigout, M. Richert, and R. Ossikovski. *From polarized to polarimetric Raman spectroscopy*, EPJ Web Conf. **5**, 6002 (2010).
81. E. Gnanatheepam, U. Kanniyappan, K. Dornadula, A. Prakasarao, and G. Singaravelu. *Polarization gating technique extracts depth resolved fluorescence redox ratio in oral cancer diagnostics*, Photodiagnosis Photodyn. Ther. **30**, 101757 (2020).
82. A. N. Yaroslavsky, X. Feng, A. Muzikansky, and M. R. Hamblin. *Fluorescence Polarization of Methylene Blue as a Quantitative Marker of Breast Cancer at the Cellular Level*, Sci. Rep. **9**(1), 940 (2019).
83. J. P. Verbelen and S. Kerstens. *Polarization confocal microscopy and congo red fluorescence: A simple and rapid method to determine the mean cellulose fibril orientation in plants*, J. Microsc. **198**(2), 101–107 (2000).
84. T. Yasui, Y. Tohno, and T. Araki. *Characterization of collagen orientation in human dermis by two-dimensional second-harmonic-generation polarimetry*, J. Biomed. Opt. **9**(2), 259–264 (2004).
85. K. Reiser, P. Stoller, and A. Knoesen. *Three-Dimensional Geometry of Collagenous Tissues by Second Harmonic Polarimetry*, Sci. Rep. **7**(1), 2642 (2017).

86. N. Mazumder and F. J. Kao. *Stokes polarimetry-based second harmonic generation microscopy for collagen and skeletal muscle fiber characterization*, Lasers Med. Sci. (2020).
87. J. F. de Boer, C. K. Hitzenberger, and Y. Yasuno. *Polarization sensitive optical coherence tomography - a review [Invited]*, Biomed. Opt. Express **8**(3), 1838–1873 (2017).
88. R. M. A. Azzam and N. M. Bashara. *Ellipsometry and Polarized Light* (North-Holland, 1977).
89. A. De Martino, E. Garcia-Caurel, J.-P. Gaston, and L. Yan. *Application of Spectroscopic Ellipsometry and Mueller Ellipsometry to Optical Characterization*, Appl. Spectrosc. **67**(1), 1–21 (2013).
90. P. Drude. *Ueber die Gesetze der Reflexion und Brechung des Lichtes an der Grenze absorbirender Krystalle*, Ann. Phys. **268**(12), 584–625 (1887).
91. M. Losurdo, M. Bergmair, G. Bruno, D. Cattelan, C. Cobet, A. de Martino, K. Fleischer, Z. Dohcevic-Mitrovic, N. Esser, M. Galliet, R. Gajic, D. Hemzal, K. Hingerl, J. Humlicek, R. Ossikovski, Z. V Popovic, and O. Saxl. *Spectroscopic ellipsometry and polarimetry for materials and systems analysis at the nanometer scale: state-of-the-art, potential, and perspectives*, J. Nanopart. Res. **11**(7), 1521–1554 (2009).
92. S. Richter, M. Rebarz, O. Herrfurth, S. Espinoza, R. Schmidt-Grund, and J. Andreasson. *Broadband femtosecond spectroscopic ellipsometry*, Rev. Sci. Instrum. **92**(3), 33104 (2021).
93. L. M. S. Aas, P. G. Ellingsen, and M. Kildemo. *Near infra-red Mueller matrix imaging system and application to retardance imaging of strain*, Thin Solid Films **519**(9), 2737–2741 (2011).
94. M. Hasan, K. Lyon, L. Trombley, C. Smith, and A. Zakhidov. *Thickness measurement of multilayer film stack in perovskite solar cell using spectroscopic ellipsometry*, AIP Adv. **9**(12), 125107 (2019).
95. H. W. Yeom, S. Takeda, E. Rotenberg, I. Matsuda, K. Horikoshi, J. Schaefer, C. M. Lee, S. D. Kevan, T. Ohta, T. Nagao, and S. Hasegawa. *Instability and Charge Density Wave of Metallic Quantum Chains on a Silicon Surface*, **82**(24), 4898–4901 (1999).
96. J. M. Flores-Camacho, L. D. Sun, N. Saucedo-Zeni, G. Weidlinger, M. Hohage, and P. Zeppenfeld. *Optical anisotropies of metal clusters supported on a birefringent substrate*, Phys. Rev. B **78**(7), 75416 (2008).
97. F. Snik and C. U. Keller. *Astronomical Polarimetry: Polarized Views of Stars and Planets BT - Planets, Stars and Stellar Systems: Volume 2: Astronomical Techniques, Software, and Data*, in T. D. Oswalt and H. E. Bond, eds. (Springer Netherlands, 2013), pp. 175–221.
98. N. Uribe-Patarroyo, A. Alvarez-Herrero, R. L. Heredero, J. C. Del Toro Iniesta, A. C. López Jiménez, V. Domingo, J. L. Gasent, L. Jochum, and V. Martínez Pillet. *IMaX: A polarimeter based on liquid crystal variable retarders for an aerospace mission*, Phys. Status Solidi **5**(5), 1041–1045 (2008).
99. D. O. Suárez. *Polarimetric Observations of the Sun BT - Astronomical Polarisation from the Infrared to Gamma Rays*, in R. Mignani, A. Shearer, A. Słowikowska, and S. Zane, eds. (Springer International Publishing, 2019), pp. 147–172.
100. J. Trujillo Bueno, J. Štěpán, and R. Casini. *The Hanle Effect of the Hydrogen Lyα Line for Probing the Magnetism of the Solar Transition Region*, Astrophys. J. **738**(1), L11 (2011).

101. J. Hough. *Polarimetry: A powerful diagnostic tool in astronomy*, Astron. Geophys. **47**(3), 3.31-3.35 (2006).
102. W. ~B. Sparks. *A Direct Way to Measure the Distances of Galaxies*, Astrophys. J. **433**, 19 (1994).
103. F. J. Iannarilli Jr., H. E. Scott, and S. H. Jones. *Passive IR polarimetric hyperspectral imaging contributions to multisensor humanitarian demining*, in Proc.SPIE (2001), **4394**.
104. O. Dubovik, Z. Li, M. I. Mishchenko, D. Tanré, Y. Karol, B. Bojkov, B. Cairns, D. J. Diner, W. R. Espinosa, P. Goloub, X. Gu, O. Hasekamp, J. Hong, W. Hou, K. D. Knobelspiesse, J. Landgraf, L. Li, P. Litvinov, Y. Liu, A. Lopatin, T. Marbach, H. Maring, V. Martins, Y. Meijer, G. Milinevsky, S. Mukai, F. Parol, Y. Qiao, L. Remer, J. Rietjens, I. Sano, P. Stammes, S. Stamnes, X. Sun, P. Tabary, L. D. Travis, F. Waquet, F. Xu, C. Yan, and D. Yin. *Polarimetric remote sensing of atmospheric aerosols: Instruments, methodologies, results, and perspectives*, J. Quant. Spectrosc. Radiat. Transf. **224**, 474–511 (2019).
105. J. Chowdhary, B. Cairns, F. Waquet, K. Knobelspiesse, M. Ottaviani, J. Redemann, L. Travis, and M. Mishchenko. *Sensitivity of multiangle, multispectral polarimetric remote sensing over open oceans to water-leaving radiance: Analyses of RSP data acquired during the MILAGRO campaign*, Remote Sens. Environ. **118**, 284–308 (2012).
106. R. Hegedüs, A. Barta, B. Bernáth, V. B. Meyer-Rochow, and G. Horváth. *Imaging polarimetry of forest canopies: how the azimuth direction of the sun, occluded by vegetation, can be assessed from the polarization pattern of the sunlit foliage*, Appl. Opt. **46**(23), 6019–6032 (2007).
107. S. Ding, J. Wang, and X. Xu. *Polarimetric remote sensing in oxygen A and B bands: sensitivity study and information content analysis for vertical profile of aerosols*, Atmos. Meas. Tech. **9**(5), 2077–2092 (2016).
108. S. C. Keppas, J. Crosier, T. W. Choularton, and K. N. Bower. *Microphysical Properties and Radar Polarimetric Features within a Warm Front*, Mon. Weather Rev. **146**(7), 2003–2022 (2018).
109. T. L. Ainsworth, D. L. Schuler, and J.-S. Lee. *Polarimetric SAR characterization of man-made structures in urban areas using normalized circular-pol correlation coefficients*, Remote Sens. Environ. **112**(6), 2876–2885 (2008).
110. A. Da Silva, C. Deumié, and I. Vanzetta. *Elliptically polarized light for depth resolved optical imaging*, Biomed. Opt. Express **3**(11), 2907–2915 (2012).
111. S. P. Morgan and I. M. Stockford. *Elimination of surface reflections in polarization imaging of superficial tissue*, in Annual International Conference of the IEEE Engineering in Medicine and Biology - Proceedings (2002).
112. Y. Liu, Y. L. Kim, and V. Backman. *Development of a bioengineered tissue model and its application in the investigation of the depth selectivity of polarization gating*, Appl. Opt. **44**(12), 2288–2299 (2005).
113. M. P. Siegel, Y. L. Kim, H. K. Roy, R. K. Wali, and V. Backman. *Assessment of blood supply in superficial tissue by polarization-gated elastic light-scattering spectroscopy*, Appl. Opt. **45**(2), 335–342 (2006).
114. B. Yang, P. Y. Lee, Y. Hua, B. Brazile, S. Waxman, F. Ji, Z. Zhu, and I. A. Sigal. *Instant polarized light microscopy for imaging collagen microarchitecture and dynamics*, J. Biophotonics **14**(2), e202000326 (2020).
115. L. Graham, Y. Yitzhaky, and I. Abdulhalim. *Classification of skin moles from optical spectropolarimetric images: a pilot study*, J. Biomed. Opt. **18**(11), 111403

(2013).
116. S. L. Jacques, S. Roussel, and R. Samatham. *Polarized light imaging specifies the anisotropy of light scattering in the superficial layer of a tissue*, J. Biomed. Opt. **21**(7), 071115 (2016).
117. L.-H. Lin, Y.-L. Lo, C.-C. Liao, and J.-X. Lin. *Optical detection of glucose concentration in samples with scattering particles*, Appl. Opt. **54**(35), 10425–10431 (2015).
118. V. N. Du Le, I. Saytashev, S. Saha, P. F. Lopez, M. Laughrey, and J. C. Ramella-Roman. *Depth-resolved Mueller matrix polarimetry microscopy of the rat cornea*, Biomed. Opt. Express **11**(10), 5982–5994 (2020).
119. K. M. Twietmeyer, R. A. Chipman, A. E. Elsner, Y. Zhao, and D. VanNasdale. *Mueller matrix retinal imager with optimized polarization conditions*, Opt. Express **16**(26), 21339–21354 (2008).
120. J. M. Bueno. *Measurement of parameters of polarization in the living human eye using imaging polarimetry*, Vision Res. **40**(28), 3791–3799 (2000).
121. J. M. Bueno and P. Artal. *Polarization and retinal image quality estimates in the human eye*, J. Opt. Soc. Am. A **18**(3), 489–496 (2001).
122. J. Chue-Sang, Y. Bai, S. Stoff, M. Gonzalez, J. Gomes, A. Gandjbakhche, V. V. Chernomordik, and J. C. Ramella-Roman. *Use of Mueller matrix polarimetry and optical coherence tomography in the characterization of cervical collagen anisotropy*, J. Biomed. Opt. **22**(8), 1–9 (2017).
123. K. A. Montejo, J. Chue-Sang, Y. Bai, S. Stoff, N. Holness, M. Gonzalez, J. Gomes, A. Gandjbakhche, V. V. Chernomordik, and J. C. Ramella-Roman. *Use of Mueller matrix colposcopy in the characterization of cervical collagen anisotropy*, J. Biomed. Opt. **23**(12), 1–9 (2017).
124. P. G. Ellingsen, M. B. Lilledahl, L. M. S. Aas, C. de L. Davies, and M. Kildemo. *Quantitative characterization of articular cartilage using Mueller matrix imaging and multiphoton microscopy*, J. Biomed. Opt. **16**(11), 116002 (2011).
125. D. Fricke, M. Wollweber, and B. Roth. *Mueller matrix measurement system for skin polarimetry as additional module for non-contact dermatoscopy*, in 2019 Conference on Lasers and Electro-Optics Europe and European Quantum Electronics Conference, CLEO/Europe-EQEC 2019 (2019).
126. Y. Dong, H. He, W. Sheng, J. Wu, and H. Ma. *A quantitative and non-contact technique to characterise microstructural variations of skin tissues during photo-damaging process based on Mueller matrix polarimetry*, Sci. Rep. **7**(1), 14702 (2017).
127. P. Schucht, H. R. Lee, H. M. Mezouar, E. Hewer, A. Raabe, M. Murek, I. Zubak, J. Goldberg, E. Kövari, A. Pierangelo, and T. Novikova. *Visualization of White Matter Fiber Tracts of Brain Tissue Sections with Wide-Field Imaging Mueller Polarimetry*, IEEE Trans. Med. Imaging **39**(12), 4376–4382 (2020).
128. Y. Wang, H. He, J. Chang, C. He, S. Liu, M. Li, N. Zeng, J. Wu, and H. Ma. *Mueller matrix microscope: a quantitative tool to facilitate detections and fibrosis scorings of liver cirrhosis and cancer tissues*, J. Biomed. Opt. **21**(7), 71112 (2016).
129. M. Kupinski, M. Boffety, F. Goudail, R. Ossikovski, A. Pierangelo, J. Rehbinder, J. Vizet, and T. Novikova. *Polarimetric measurement utility for pre-cancer detection from uterine cervix specimens*, Biomed. Opt. Express **9**(11), 5691–5702 (2018).
130. B. Liu, Y. Yao, R. Liu, H. Ma, and L. Ma. *Mueller polarimetric imaging for characterizing the collagen microstructures of breast cancer tissues in different genotypes*, Opt. Commun. **433**, 60–67 (2019).

131. D. L. Le, D. T. Nguyen, T. H. Le, Q.-H. Phan, and T.-T.-H. Pham. *Characterization of healthy and cancerous human skin tissue utilizing Stokes–Mueller polarimetry technique*, Opt. Commun. **480**, 126460 (2021).
132. E. Du, H. He, N. Zeng, M. Sun, Y. Guo, J. Wu, S. Liu, and H. Ma. *Mueller matrix polarimetry for differentiating characteristic features of cancerous tissues*, J. Biomed. Opt. **19**(7), 76013 (2014).
133. A. Pierangelo, A. Benali, M.-R. Antonelli, T. Novikova, P. Validire, B. Gayet, and A. De Martino. *Ex-vivo characterization of human colon cancer by Mueller polarimetric imaging*, Opt. Express **19**(2), 1582–1593 (2011).
134. A. Pierangelo, A. Nazac, A. Benali, P. Validire, H. Cohen, T. Novikova, B. H. Ibrahim, S. Manhas, C. Fallet, M.-R. Antonelli, and A.-D. Martino. *Polarimetric imaging of uterine cervix: a case study*, Opt. Express **21**(12), 14120–14130 (2013).
135. C. He, H. He, J. Chang, Y. Dong, S. Liu, N. Zeng, Y. He, and H. Ma. *Characterizing microstructures of cancerous tissues using multispectral transformed Mueller matrix polarization parameters*, Biomed. Opt. Express **6**(8), 2934–2945 (2015).
136. J. Rehbinder, H. Haddad, S. Deby, B. Teig, A. Nazac, T. Novikova, A. Pierangelo, and F. Moreau. *Ex vivo Mueller polarimetric imaging of the uterine cervix: a first statistical evaluation*, J. Biomed. Opt. **21**(7), 071113 (2016).
137. K. U. Spandana, K. K. Mahato, and N. Mazumder. *Polarization-resolved Stokes-Mueller imaging: a review of technology and applications*, Lasers Med. Sci. **34**(7), 1283–1293 (2019).
138. M. K. Swami, S. Manhas, P. Buddhiwant, N. Ghosh, A. Uppal, and P. K. Gupta. *Polar decomposition of 3 x 3 Mueller matrix: a tool for quantitative tissue polarimetry*, Opt. Express **14**(20), 9324–9337 (2006).
139. J. Qi and D. S. Elson. *Mueller polarimetric imaging for surgical and diagnostic applications: a review*, J. Biophotonics **10**(8), 950–982 (2017).
140. T. Novikova, I. Meglinski, J. C. Ramella-Roman, and V. V. Tuchin. *Special Section Guest Editorial: Polarized Light for Biomedical Applications*, J. Biomed. Opt. **21**(7), 071001 (2016).
141. R. Rawer, W. Stork, and K. D. Müller-Glaser. *Polarimetric methods for measurement of intra ocular glucose concentration*, Biomed. Tech. (Berl). **47**, 186–188 (2002).
142. O. K. Naoun, V. L. Dorr, P. Allé, J.-C. Sablon, and A.-M. Benoit. *Exploration of the retinal nerve fiber layer thickness by measurement of the linear dichroism*, Appl. Opt. **44**(33), 7074–7082 (2005).
143. J. M. Bueno, E. Berrio, and P. Artal. *Corneal polarimetry after LASIK refractive surgery*, J. Biomed. Opt. **11**(1), 14001 (2006).
144. K. Komatsu, L. Mosekilde, A. Viidik, and M. Chiba. *Polarized light microscopic analyses of collagen fibers in the rat incisor periodontal ligament in relation to areas, regions, and ages*, Anat. Rec. **268**(4), 381–387 (2002).
145. B. Kunnen, C. Macdonald, A. Doronin, S. Jacques, M. Eccles, and I. Meglinski. *Application of circularly polarized light for non-invasive diagnosis of cancerous tissues and turbid tissue-like scattering media*, J. Biophotonics **8**(4), 317–323 (2015).
146. R. Patel, A. Khan, R. Quinlan, and A. N. Yaroslavsky. *Polarization-sensitive multimodal imaging for detecting breast cancer*, Cancer Res. **74**(17), 4685–4693 (2014).
147. P. Shukla and A. Pradhan. *Polarization-gated imaging in tissue phantoms: Effect*

of size distribution, Appl. Opt. **48**(32), 6099–6104 (2009).
148. S. Sridhar and A. Da Silva. *Enhanced contrast and depth resolution in polarization imaging using elliptically polarized light*, J. Biomed. Opt. **21**(7), 071107 (2016).
149. J. C. Ramella-Roman, S. A. Prahl, and S. L. Jacques. *Three Monte Carlo programs of polarized light transport into scattering media: part II*, Opt. Express **13**(25), 10392 (2005).
150. J. C. Ramella-Roman, S. A. Prahl, and S. L. Jacques. *Three Monte Carlo programs of polarized light transport into scattering media: part I*, Opt. Express **13**(12), 4420 (2005).
151. E. Du, H. He, N. Zeng, C. Liu, Y. Guo, R. Liao, M. Sun, Y. He, and H. Ma. *Characteristic features of mueller matrix patterns for polarization scattering model of biological tissues*, J. Innov. Opt. Health Sci. **7**(1), 1350028 (2014).
152. Y. Zhang, B. Chen, and D. Li. *Propagation of polarized light in the biological tissue: a numerical study by polarized geometric Monte Carlo method*, Appl. Opt. **55**(10), 2681–2691 (2016).
153. P. Li, H. R. Lee, S. Chandel, C. Lotz, F. K. Groeber-Becker, S. Dembski, R. Ossikovski, H. Ma, and T. Novikova. *Analysis of tissue microstructure with Mueller microscopy: logarithmic decomposition and Monte Carlo modeling*, J. Biomed. Opt. **25**(1), 015002 (2020).
154. Global Cancer Observatory. (May 2021). *Global Cancer Observatory: Cancer Today. Lyon: International Agency for Research on Cancer*, retrieved from https://gco.iarc.fr/today/home.
155. M. Rue, E. Vilaprinyo, S. Lee, M. Martinez-Alonso, M. dia Carles, R. Marcos-Gragera, R. Pla, and J. A. Espinas. *Effectiveness of early detection on breast cancer mortality reduction in Catalonia (Spain)*, BMC Cancer **9**(1), 326 (2009).
156. E. Vilaprinyo, T. Puig, and M. Rue. *Contribution of early detection and adjuvant treatments to breast cancer mortality reduction in Catalonia, Spain*, PLoS One **7**(1), e30157 (2012).
157. R. C. N. van den Bergh, S. Loeb, and M. J. Roobol. *Impact of Early Diagnosis of Prostate Cancer on Survival Outcomes*, Eur. Urol. Focus **1**(2), 137–146 (2015).
158. Office for National Statistics. (June 2021). *Cancer survival in England - adults diagnosed - Office for National Statistics*, retrieved from https://www.ons.gov.uk/peoplepopulationandcommunity/healthandsocialcare/conditionsanddiseases/datasets/cancersurvivalratescancersurvivalinenglandadultsdiagnosed.
159. L. Grant, C. S. T. Daughtry, and V. C. Vanderbilt. *Polarized and non-polarized leaf reflectances of Coleus blumei*, Environ. Exp. Bot. **27**(2), 139–145 (1987).
160. V. C. Vanderbilt, L. Grant, and C. S. T. Daughtry. *Polarization of Light Scattered by Vegetation*, Proc. IEEE **73**(6), 1012–1024 (1985).
161. V. I. Kharuk and V. V. Yegorov. *Polarimetric indication of plant stress*, Remote Sens. Environ. **33**(1), 35–40 (1990).
162. G. Rondeaux and M. Herman. *Polarization of light reflected by crop canopies*, Remote Sens. Environ. **38**(1), 63–75 (1991).
163. L. Grant, C. S. T. Daughtry, and V. C. Vanderbilt. *Polarized and specular reflectance variation with leaf surface features*, Physiol. Plant. **88**(1), 1–9 (1993).
164. F. Stabo-Eeg, D. Letalick, O. Steinvall, and M. Lindgren. *Discriminating land mines from natural backgrounds by depolarization*, in Electro-Optical Remote Sensing, Photonic Technologies, and Applications II (2008).
165. S. V. Berdyugina, J. R. Kuhn, D. M. Harrington, T. Šantl-Temkiv, and E. J. Messersmith. *Remote sensing of life: Polarimetric signatures of photosynthetic*

pigments as sensitive biomarkers, Int. J. Astrobiol. **15**(1), 45–56 (2016).
166. Joseph Priestley. *Photosynthesis, Two Centuries after Its Discovery by Joseph Priestley* (Springer Science & Business Media, 1972).
167. K. Arai and Y. Nishimura. *Polarization model for discrimination of broad and needle shaped leaves and estimation of LAI using polarization measurements*, Adv. Sp. Res. **44**(4), 510–516 (2009).
168. S. N. Savenkov, R. S. Muttiah, E. A. Oberemok, A. V Priezzhev, I. S. Kolomiets, and A. S. Klimov. *Measurement and interpretation of Mueller matrices of barley leaves*, Quantum Electron. **50**(1), 55–60 (2020).
169. V. C. Vanderbilt, C. S. T. Daughtry, and L. L. Biehl. *Is there spectral variation is the polarized reflectance of leaves?*, in Polarization: Measurement, Analysis, and Remote Sensing XI (2014).
170. C. H. L. Patty, D. A. Luo, F. Snik, F. Ariese, W. J. Buma, I. L. ten Kate, R. J. M. van Spanning, W. B. Sparks, T. A. Germer, G. Garab, and M. W. Kudenov. *Imaging linear and circular polarization features in leaves with complete Mueller matrix polarimetry*, Biochim. Biophys. Acta - Gen. Subj. **1862**(6), 1350–1363 (2018).
171. B. A. Palevitz and P. K. Hepler. *Cellulose microfibril orientation and cell shaping in developing guard cells of Allium: The role of microtubules and ion accumulation*, Planta **132**(1), 71–93 (1976).
172. E. Zeiger and P. K. Hepler. *Production of Guard Cell Protoplasts from Onion and Tobacco*, Plant Physiol. **58**(4), 492–498 (1976).
173. I. Shtein, Y. Shelef, Z. Marom, E. Zelinger, A. Schwartz, Z. A. Popper, B. Bar-On, and S. Harpaz-Saad. *Stomatal cell wall composition: Distinctive structural patterns associated with different phylogenetic groups*, Ann. Bot. **119**(6), 1021–1033 (2017).
174. V. Bischoff, S. Nita, L. Neumetzler, D. Schindelasch, A. Urbain, R. Eshed, S. Persson, D. Delmer, and W. R. Scheible. *TRICHOME BIREFRINGENCE and its homolog AT5G01360 encode plant-specific DUF231 proteins required for cellulose biosynthesis in arabidopsis*, Plant Physiol. **153**(2), 590–602 (2010).
175. R. L. Long, M. P. Bange, S. G. Gordon, and G. A. Constable. *Measuring the Maturity of Developing Cotton Fibers using an Automated Polarized Light Microscopy Technique*, Text. Res. J. **80**(5), 463–471 (2010).
176. P. J. Curran. *Polarized visible light as an aid to vegetation classification*, Remote Sens. Environ. **12**(6), 491–499 (1982).
177. W. Yan, Y. Zhong, and Z. Shangguan. *Contrasting responses of leaf stomatal characteristics to climate change: a considerable challenge to predict carbon and water cycles*, Glob. Chang. Biol. **23**(9), 3781–3793 (2017).
178. C. J. Gao, X. J. Xia, K. Shi, Y. H. Zhou, and J. Q. Yu. *Response of stomata to global climate changes and the underlying regulation mechanism of stress responses*, Zhiwu Shengli Xuebao/Plant Physiol. J. **48**(1), 19–28 (2012).
179. B. Schwab, U. Folkers, H. Ilgenfritz, and M. Hülskamp. *Trichome morphogenesis in Arabidopsis*, Philos. Trans. R. Soc. Lond. B. Biol. Sci. **355**(1399), 879–883 (2000).
180. S. Savary, A. Ficke, J. N. Aubertot, and C. Hollier. *Crop losses due to diseases and their implications for global food production losses and food security*, Food Secur. **4**(4), 519–537 (2012).
181. E. C. Oerke. *Crop losses to pests*, J. Agric. Sci. **144**(1), 31–43 (2006).
182. E. Compain and B. Drevillon. *Broadband division-of-amplitude polarimeter based*

on uncoated prisms, Appl. Opt. **37**(25), 5938–5944 (1998).
183. C. Negara, Z. Li, T. Längle, and J. Beyerer. *Simplified Stokes polarimeter based on division-of-amplitude*, in Photonics and Education in Measurement Science 2019 (2019).
184. J. L. Pezzaniti and D. B. Chenault. *A division of aperture MWIR imaging polarimeter*, in Polarization Science and Remote Sensing II (2005).
185. T. Mu, C. Zhang, and R. Liang. *Demonstration of a snapshot full-Stokes division-of-aperture imaging polarimeter using Wollaston prism array*, J. Opt. (United Kingdom) **17**(12), 125708 (2015).
186. H. Luo, K. Oka, E. Dehoog, M. Kudenov, J. Schiewgerling, and E. L. Dereniak. *Compact and miniature snapshot imaging polarimeter*, Appl. Opt. **47**(24), 4413–4417 (2008).
187. D. S. Sabatke, M. R. Descour, E. L. Dereniak, W. C. Sweatt, S. A. Kemme, and G. S. Phipps. *Optimization of retardance for a complete Stokes polarimeter*, Opt. Lett. **25**(11), 802–804 (2000).
188. Á. Lizana, J. Campos, A. Van Eeckhout, and A. Márquez. *Influence of temporal averaging in the performance of a rotating retarder imaging Stokes polarimeter*, Opt. Express **28**(8), 10981–11000 (2020).
189. D. H. Goldstein. *Mueller matrix dual-rotating retarder polarimeter*, Appl. Opt. **31**(31), 6676–6683 (1992).
190. J. S. Tyo. *Design of optimal polarimeters: Maximization of signal-to-noise ratio and minimization of systematic error*, Appl. Opt. **41**(4), 619–630 (2002).
191. A. Peinado, A. Lizana, and J. Campos. *Optimization and tolerance analysis of a polarimeter with ferroelectric liquid crystals*, Appl. Opt. **52**(23), 5748–5757 (2013).
192. A. Peinado, A. Lizana, J. Vidal, C. Iemmi, and J. Campos. *Optimization and performance criteria of a Stokes polarimeter based on two variable retarders*, Opt. Express **18**(10), 9815–9830 (2010).
193. A. Peinado, A. Lizana, J. Vidal, C. Iemmi, and J. Campos. *Optimized Stokes polarimeters based on a single twisted nematic liquid-crystal device for the minimization of noise propagation*, Appl. Opt. **50**(28), 5437–5445 (2011).
194. N. J. Pust and J. A. Shaw. *Dual-field imaging polarimeter using liquid crystal variable retarders*, Appl. Opt. **45**(22), 5470–5478 (2006).
195. Meadowlark Optics. (June 2021). *Meadowlark Optics, Polarization Solutions*, retrieved from https://www.meadowlark.com/index.php.
196. A. Peinado Capdevila. *Design of polarimeters based on liquid crystals and biaxial crystals for polarization metrology*. Universitat Autònoma de Barcelona (2014).
197. R. C. Jones. *A New Calculus for the Treatment of Optical SystemsI Description and Discussion of the Calculus*, J. Opt. Soc. Am. **31**(7), 488–493 (1941).
198. D. W. Berreman. *Optics in Stratified and Anisotropic Media: 4×4-Matrix Formulation*, J. Opt. Soc. Am. **62**(4), 502–510 (1972).
199. N. Wiener. *Generalized harmonic analysis*, Acta Math. **55**, 117–258 (1930).
200. G. G. Stokes. *On the compoisition and resolution of streams of polarised light from different sources*, Trans. Cambridge Philos. Soc. **9**, 399 (1852).
201. H. Mueller. *The foundation of optics*, J. Opt. Soc. Am. **38**(7), 661 (1948).
202. N. G. Parke. *Optical Algebra*, J. Math. Phys. **28**(1–4), 131–139 (1949).
203. H. Poincare. *Theorie Mathematique de La Lumiere* (XII. Gauthier-Villars, Paris, 1892).
204. Z. F. Xing. *On the deterministic and non-deterministic mueller matrix*, J. Mod. Opt. **39**(3), 461–484 (1992).

205. G. R. Bird and W. A. Shurcliff. *Pile-of-Plates Polarizers for the Infrared: Improvement in Analysis and Design*, J. Opt. Soc. Am. **49**(3), 235–237 (1959).
206. W. A. Shurcliff. *Polarized Light* (Harvard University Press, 2013).
207. S. Manhas, M. K. Swami, P. Buddhiwant, N. Ghosh, P. K. Gupta, and J. Singh. *Mueller matrix approach for determination of optical rotation in chiral turbid media in backscattering geometry*, Opt. Express **14**(1), 190–202 (2006).
208. R. Ossikovski, A. De Martino, and S. Guyot. *Forward and reverse product decompositions of depolarizing Mueller matrices*, Opt. Lett. **32**(6), 689–691 (2007).
209. J. J. Gil. *Polarimetric characterization of light and media*, Eur. Phys. J. Appl. Phys. **40**(1), 1–47 (2007).
210. S. R. Cloude. *Conditions For The Physical Realisability Of Matrix Operators In Polarimetry*, in Proc. SPIE 1166, Polarization Considerations for Optical Systems II, R. A. Chipman, ed. (International Society for Optics and Photonics, 1990).
211. J. J. Gil. *Review on Mueller matrix algebra for the analysis of polarimetric measurements*, J. Appl. Remote Sens. **8**(1), 081599 (2014).
212. J. J. Gil. *Invariant quantities of a Mueller matrix under rotation and retarder transformations*, J. Opt. Soc. Am. A **33**(1), 52–58 (2016).
213. J. J. Gil, J. M. Correas, P. A. Melero, and C. Ferreira. *Generalized polarization algebra*, Monogr. del Semin. Matemático García Galdeano **33**, 161–167 (2004).
214. J. J. Gil. *Structure of polarimetric purity of a Mueller matrix and sources of depolarization*, Opt. Commun. **368**, 165–173 (2016).
215. A. V. G. Rao, K. S. Mallesh, and Sudha. *On the algebraic characterization of a Mueller matrix in polarization optics. I. Identifying a Mueller matrix from its N matrix*, J. Mod. Opt. **45**(5), 955–987 (1998).
216. S. Li, N. Quan, C. Zhang, T. Mu, and B. Hu. *Stokes polarimeter for the measurement of full linearly Stokes parameters with immunity to Gaussian and Poisson noise*, Optik (Stuttg). **175**, 8–16 (2018).
217. K. Singh, N. Tabebordbar, A. Forbes, and A. Dudley. *Digital Stokes polarimetry and its application to structured light: Tutorial*, J. Opt. Soc. Am. A **37**(11), C33–C44 (2020).
218. X. Yang, Y. Pu, and D. Psaltis. *Imaging blood cells through scattering biological tissue using speckle scanning microscopy*, Opt. Express **22**(3), 3405–3413 (2014).
219. P. Jain and S. E. Sarma. *Measuring light transport properties using speckle patterns as structured illumination*, Sci. Rep. **9**(1), 11157 (2019).
220. Z. Wang, X. Jin, and Q. Dai. *Non-invasive imaging through strongly scattering media based on speckle pattern estimation and deconvolution*, Sci. Rep. **8**(1), 9088 (2018).
221. Thorlabs. (April 2021). *Thorlabs, Inc. - Your Source for Fiber Optics, Laser Diodes, Optical Instrumentation and Polarization Measurement & Control*, retrieved from https://www.thorlabs.com/.
222. N. P. Schnoor, R. C. Niemeier, A. L. Woods, and J. D. Rogers. *Calibration of liquid crystal variable retarders using a common-path interferometer and fit of a closed-form expression for the retardance curve*, Appl. Opt. **59**(34), 10673–10679 (2020).
223. T. Tudor. *On the enpolarization/depolarization effects of deterministic devices*, Opt. Lett. **43**(21), 5234–5237 (2018).
224. R. Simon. *Nondepolarizing and degree polarization*, Opt. Commun. **77**(5–6), 349–354 (1990).

225. S. Cloude. *Polarisation: Applications in Remote Sensing* (Oxford University Press, 2010).
226. I. San José and J. J. Gil. *Retarding parallel components of a Mueller matrix*, Opt. Commun. **459**, 124892 (2020).
227. J. J. Gil and I. San José. *Polarimetric subtraction of Mueller matrices*, J. Opt. Soc. Am. A **30**(6), 1078–1088 (2013).
228. R. Ossikovski, J. J. Gil, and I. San José. *Poincaré sphere mapping by Mueller matrices*, J. Opt. Soc. Am. A **30**(11), 2291–2305 (2013).
229. R. Ossikovski. *Canonical forms of depolarizing Mueller matrices*, J. Opt. Soc. Am. A **27**(1), 123 (2010).
230. Z. Sekera. *Scattering Matrices and Reciprocity Relationships for Various Representations of the State of Polarization*, J. Opt. Soc. Am. **56**(12), 1732–1740 (1966).
231. A. Schönhofer and H. G. Kuball. *Symmetry properties of the Mueller matrix*, Chem. Phys. **115**(2), 159–167 (1987).
232. V. V. Tuchin, L. V. Wang, and D. A. Zimnyakov. *Optical Polarization in Biomedical Applications* (Springer-Verlag Berlin Heidelberg, 2006).
233. M. Nagendran, D. P. Riordan, P. B. Harbury, and T. J. Desai. *Automated cell-type classification in intact tissues by single-cell molecular profiling*, Elife **7**, e30510 (2018).
234. J. M. Gálvez, D. Castillo, L. J. Herrera, B. S. Román, O. Valenzuela, F. M. Ortuño, and I. Rojas. *Multiclass classification for skin cancer profiling based on the integration of heterogeneous gene expression series*, PLoS One **13**(5), e0196836 (2018).
235. L. Marcu, S. A. Boppart, M. R. Hutchinson, J. Popp, and B. C. Wilson. *Biophotonics: the big picture*, J. Biomed. Opt. **23**(3), 021103 (2017).
236. N. J. Dhinagar and M. Celenk. *Early diagnosis and predictive monitoring of skin diseases*, in 2016 IEEE Healthcare Innovation Point-of-Care Technologies Conference (HI-POCT) (2016).
237. S. Schiaffino and C. Reggiani. *Fiber types in Mammalian skeletal muscles*, Physiol. Rev. **91**(4), 1447–1531 (2011).
238. A. Van Eeckhout, E. Garcia-Caurel, R. Ossikovski, A. Lizana, C. Rodríguez, E. González-Arnay, and J. Campos. *Depolarization metric spaces for biological tissues classification*, J. Biophotonics **13**(8), e202000083 (2020).
239. D. L. Butler, E. S. Grood, F. R. Noyes, and R. F. Zernicke. *Biomechanics of ligaments and tendons*, Exerc. Sport Sci. Rev. **6**, 125–181 (1978).
240. J. Kastelic, A. Galeski, and E. Baer. *The multicomposite structure of tendon*, Connect. Tissue Res. **6**(1), 11–23 (1978).
241. R. James, G. Kesturu, G. Balian, and A. B. Chhabra. *Tendon: Biology, Biomechanics, Repair, Growth Factors, and Evolving Treatment Options*, J. Hand Surg. Am. **33**(1), 102–112 (2008).
242. D. J. S. Hulmes. *Building collagen molecules, fibrils, and suprafibrillar structures*, J. Struct. Biol. **137**(1–2), 2–10 (2002).
243. B. Charvet, F. Ruggiero, and D. Le Guellec. *The development of the myotendinous junction. A review*, Muscles. Ligaments Tendons J. **2**(2), 53–63 (2012).
244. H. Asahara, M. Inui, and M. K. Lotz. *Tendons and Ligaments: Connecting Developmental Biology to Musculoskeletal Disease Pathogenesis*, J. Bone Miner. Res. **32**(9), 1773–1782 (2017).
245. L. Breiman, J. H. Friedman, R. A. Olshen, and C. J. Stone. *Classification and Regression Trees* (Chapman & Hall, 1984).

246. Y. Guo, T. Hastie, and R. Tibshirani. *Regularized linear discriminant analysis and its application in microarrays*, Biostatistics **8**(1), 86–100 (2007).
247. T. M. Mitchell. *Machine Learning* (McGraw Hill, 1997).
248. A. Van Eeckhout, E. Garcia-Caurel, R. Ossikovski, A. Lizana, C. Rodríguez, E. González, and J. Campos. *Depolarizing spaces for biological tissue classification based on a wavelength combination*, in Proc. SPIE 11363, Tissue Optics and Photonics (2020).
249. A. Van Eeckhout, E. Garcia-Caurel, T. Garnatje, M. Durfort, J. C. Escalera, J. Vidal, J. J. Gil, J. Campos, and A. Lizana. *Depolarizing metrics for plant samples imaging*, PLoS One **14**(3), e0213909 (2019).
250. R. H. Newman, L. M. Davies, and P. J. Harris. *Solid-state 13C nuclear magnetic resonance characterization of cellulose in the cell walls of Arabidopsis thaliana leaves*, Plant Physiol. **111**(2), 475–485 (1996).
251. A. Mendoza-Galván, T. Tejeda-Galán, A. B. Domínguez-Gómez, R. A. Mauricio-Sánchez, K. Järrendahl, and H. Arwin. *Linear birefringent films of cellulose nanocrystals produced by dip-coating*, Nanomaterials **9**(1), 45 (2019).
252. M. Kerker. *The Scattering of Light and Other Electromagnetic Radiation* (Academic Press, 1969).
253. A. Van Eeckhout, E. Garcia-Caurel, T. Garnatje, J. C. Escalera, M. Durfort, J. Vidal, J. J. Gil, J. Campos, and A. Lizana. *Polarimetric imaging microscopy for advanced inspection of vegetal tissues*, Sci. Rep. **11**(1), 3913 (2021).
254. J. A. Kurvits, M. Jiang, and R. Zia. *Comparative analysis of imaging configurations and objectives for Fourier microscopy*, J. Opt. Soc. Am. A **32**(11), 2082–2092 (2015).
255. T. Yoo. *Application d'un imageur polarimétrique multimodal pour l'étude de la réponse optique de milieux et de microstructures diffusantes*. Université Paris Saclay (2018).
256. Servei de Microscòpia. (May 2021). *Olympus Fluoview 1000*, retrieved from https://sct.uab.cat/microscopia/content/olympus-fluoview-1000.
257. JEOL. (May 2021). *Announcement of JSM-7100F New FE SEM - High performance analytical tool with improved observation and analysis functions*, retrieved from https://www.jeol.co.jp/en/news/detail/20120130.347.html.
258. A. Van Eeckhout, E. Garcia-Caurel, T. Garnatje, J. C. Escalera, M. Durfort, J. Vidal, J. J. Gil, J. García-Romero, R. Ossikovski, I. Moreno, J. Campos, and A. Lizana. *Retrieving physical information of depolarizing systems*, in Proc. SPIE 11646, Polarized Light and Optical Angular Momentum for Biomedical Diagnostics (2021).
259. T. Lawson and M. R. Blatt. *Stomatal size, speed, and responsiveness impact on photosynthesis and water use efficiency*, Plant Physiol. **164**(4), 1556–1570 (2014).
260. J. D. B. Weyers and L. G. Johansen. *ACCURATE ESTIMATION OF STOMATAL APERTURE FROM SILICONE RUBBER IMPRESSIONS*, New Phytol. **101**(1), 109–115 (1985).
261. D. Fanourakis, H. Giday, R. Milla, R. Pieruschka, K. H. Kjaer, M. Bolger, A. Vasilevski, A. Nunes-Nesi, F. Fiorani, and C. O. Ottosen. *Pore size regulates operating stomatal conductance, while stomatal densities drive the partitioning of conductance between leaf sides*, Ann. Bot. **115**(4), 555–565 (2015).
262. N. Kaur and A. K. Gupta. *Applications of inulin and oligofructose in health and nutrition*, J. Biosci. **27**(7), 703–714 (2002).
263. M. A. Mensink, H. W. Frijlink, K. Van Der Voort Maarschalk, and W. L. J.

Hinrichs. *Inulin, a flexible oligosaccharide I: Review of its physicochemical characteristics*, Carbohydr. Polym. **130**, 405–419 (2015).
264. K. Kubitzki. *The Families and Genera of Vascular Plants. Volume VI. Flowering Plants. Dicotyledons. Celastrales, Oxalidales, Rosales, Cornales, Ericales.* (Springer, Heidelberg, 2004).
265. J. Pinela, A. M. Carvalho, and I. C. F. R. Ferreira. *Wild edible plants: Nutritional and toxicological characteristics, retrieval strategies and importance for today's society*, Food Chem. Toxicol. **110**, 165–188 (2017).

Papers of this doctoral thesis

Journal of Biomedical Optics

BiomedicalOptics.SPIEDigitalLibrary.org

Polarization gating based on Mueller matrices

Angel Lizana
Albert Van Eeckhout
Kamil Adamczyk
Carla Rodríguez
Juan Carlos Escalera
Enric Garcia-Caurel
Ignacio Moreno
Juan Campos

SPIE.

Angel Lizana, Albert Van Eeckhout, Kamil Adamczyk, Carla Rodríguez, Juan Carlos Escalera, Enric Garcia-Caurel, Ignacio Moreno, Juan Campos, "Polarization gating based on Mueller matrices," *J. Biomed. Opt.* **22**(5), 056004 (2017), doi: 10.1117/1.JBO.22.5.056004.

Polarization gating based on Mueller matrices

Angel Lizana,[a,*] Albert Van Eeckhout,[a] Kamil Adamczyk,[a] Carla Rodríguez,[a] Juan Carlos Escalera,[a] Enric Garcia-Caurel,[b] Ignacio Moreno,[c] and Juan Campos[a]
[a]Universitat Autònoma de Barcelona, Grup d'Òptica, Physics Department, Bellaterra, Spain
[b]Université Paris-Saclay, LPICM, CNRS, École Polytechnique, Palaiseau, France
[c]Universidad Miguel Hernández, Department of Materials Science, Optics and Electronics Technology, Elche, Spain

Abstract. We present mathematical formulas generalizing polarization gating (PG) techniques. PG refers to a collection of imaging methods based on the combination of different controlled polarization channels. In particular, we show how using the measured Mueller matrix (MM) of a sample, a widespread number of PG configurations can be evaluated just from analytical expressions based on the MM coefficients. We also show the interest of controlling the helicity of the states of polarization used for PG-based metrology, as this parameter has an impact in the image contrast of samples. In addition, we highlight the interest of combining PG techniques with tools of data analysis related to the MM formalism, such as the well-known MM decompositions. The method discussed in this work is illustrated with the results of polarimetric measurements done on artificial phantoms and real *ex-vivo* tissues. [DOI: 10.1117/1.JBO.22.5.056004]

Keywords: polarization gating; Mueller matrix; biological tissue; polarimetric image contrast.

Paper 170020R received Jan. 13, 2017; accepted for publication Apr. 17, 2017; published online May 10, 2017.

1 Introduction

In the last decade, polarimetric information has proven to be useful for biological tissues inspection.[1–3] As a result, polarimetric-based techniques are nowadays being applied in multiple scenarios, such as cancer detection and stage identification,[4–8] to enhance image contrast in skin diseases,[9–11] for human eye examination,[12,13] for diabetes diagnosis as well as therapy,[14,15] etc.

There are different ways to extract sample information from polarimetric measurements (such as surface roughness, tissue spatial inhomogeneities, biological material recognition, optical properties of turbid tissues, tissue depth metrology, subsurface examination, etc.), as well as to enhance the contrast of images taken from the sample. A widespread polarimetric technique applied for biological tissues inspection is the so-called polarization gating (PG).[16–20] Essentially, PG techniques exploit the fact that samples respond differently depending on the polarization state of the light used to probe it. The basic PG configuration consists of using linear polarization for illumination and detection [linear polarization gating (LPG)] stage. Then, LPG images can be combined to provide a new processed image, for instance, by subtracting the images captured with parallel and with crossed polarizers. To further improve image contrast, recent studies have provided the interest of generalizing LPG techniques with the use of elliptical polarization, i.e., elliptical polarization gating (EPG).[17,19]

Another group of polarimetric methods is based on the measurement of the Mueller matrix (MM) of the sample, and the subsequent analysis of the polarimetric content which is encoded in the corresponding 16 real MM coefficients.[21] These techniques, which provide, in principle, a different polarimetric approach than those given by PG techniques, are used by a number of authors for biological tissues inspection.[5,7,8,12,13]

In this paper, we demonstrate that information provided by PG techniques can be alternatively obtained from the experimental MM of the sample. In particular, we derive an analytical expression, which consists of a linear combination of different Mueller coefficients, and we show how a set of PG configurations can be considered as particular cases of the derived analytical expression. The desired PG configuration is then obtained by properly tuning some control parameters, such as the azimuth or the ellipticity of the input and analyzing states of polarization. In addition, we highlight the interest of using MM measurements instead of particular PG configurations. First, due to the MM-based analytical expression, we show in this work that we can extract the polarimetric information of a sample corresponding to multiple PG configurations without the necessity of experimentally measuring each one of them. Instead of this, only the measurement of the experimental MM of the sample is required with our method. Second, Mueller measurements not only allow building a more general analytical expression, but also give access to extra channels of data processing, such as those provided by the different product MM decompositions schemes[21–23] or even further, by applying recently developed methods such as those based on the differential MM.[21,23–26]

The method proposed in this paper is experimentally tested by using an imaging MM polarimeter based on liquid crystal panels. This allows the system to dynamically perform the experimental measurements without the necessity of mechanical movements. The commutation rate of the used liquid crystal panels is ~60 Hz, and the exposure time of the CCD camera that is used to register the intensity images is adapted for each sample analyzed to capture the maximum intensity without saturating the camera (the exposure time range used for measurements is between 0.004 and 0.12 s). With this experimental configuration, full polarimetric measurements can be done in

*Address all correspondence to: Angel Lizana, E-mail: angel.lizana@uab.es

1083-3668/2017/$25.00 © 2017 SPIE

few (0.4 to 2.2) seconds, which may be of interest in real-time applications. Indeed, if the methods discussed in this manuscript would be considered to be applied for real-time applications, the experimental set-up could be further optimized by using ferroelectric liquid crystal displays or photoelastic modulators.[27,28] Another interesting application for the methods discussed here is standard scanning microscopy adapted to polarimetric metrology. If these latter applications should be performed in real time, then the high-speed imaging Mueller polarimeter provided in Ref. 29 can be used, which works at the time scale of a scanning microscope.

In a sense, we think that the methods proposed in this work bring together two mathematical tools for polarimetric sample analysis (PG- and MM-based methods) that traditionally have been unlinked and may be of interest in biological applications.[16–20,30–32]

The outline of this manuscript is as follows. In Sec. 2, we first briefly describe some of the more commonly used PG configurations (Sec. 2.1). Afterward, in Sec. 2.2, we derive a general expression based on the MM coefficients of the studied sample, from which the different PG configurations described in Sec. 2.1 become individual solutions. In particular, each different PG configuration is achieved from the proposed general expression by properly tuning two control parameters in the mathematical equation, representing the azimuth and ellipticity values of the polarizations illuminating and analyzing the sample. In Sec. 3, we describe the optical scheme that is used to measure the MM of different samples, from which different PG configurations are achieved (Sec. 3.1). In addition, the description of the different samples inspected in this work is also provided (Sec. 3.2). In Sec. 4, we provide the equivalence between standard PG and PG configurations obtained from MM metrology (Sec. 4.1). Next, in Sec. 4.2, we highlight the interest of combining PG configurations with well-known MM analytical tools. Finally, the main conclusions of the work are given in Sec. 5.

2 Polarization Gating Configurations Derived from Mueller Matrix Data

In this section, we briefly describe some PG configurations currently used for tissue inspection and we discuss some of the strengths and drawbacks related to them (Sec. 2.1). The nomenclature used to label the different PG configurations described in Sec. 2.1 is that followed in Ref. 19. Afterward, we derive an analytical expression that consists of a linear combination of different functions which depend on several of the MM coefficients of the measured sample (Sec. 2.2). Note that such a relation can be interpreted as a generalization of multiple PG configurations.

2.1 *Polarization Gating Techniques*

When polarized light interacts with biological tissues, the characteristics of the produced scattered light strongly depend on different parameters, such as the sample molecules' size, the polarization of the input light, the wavelength, and the sample depth proven, among others.

One typical measuring configuration (let us call it configuration C1) consists of illuminating the analyzed sample with linear polarization and projecting the scattered light to the same input polarization (i.e., parallel polarizer-analyzer). When illuminating the sample with a linear polarization, a mixed contribution of different kind of photons is observed when measuring out of the ballistic direction.[19,33] We can subgroup them as photons reflected at the tissue surface (surface-reflected photons, S_L), photons penetrating to the subsurface but maintaining the original polarization (polarization maintaining photons, P_L), and photons reaching deeper layers of the sample, which are fully depolarized by multiple scattering events (depolarized photons, D_L).

Therefore, the C1 configuration leads to a mixture of all three kinds of S_L, P_L, and D_L photon contributions. However, as P_L photons are those that usually provide the most significant information of the studied sample, different strategies can be applied to remove the image background and to improve the image contrast, by eliminating the nondesired S_L and D_L contributions as much as possible. To this aim, some authors have proposed to combine the C1 configuration with a second measurement, where the sample is illuminated with linear polarized light and scattered light is imaged through the corresponding orthogonal linear polarization (cross linear configuration, here labeled as C2). Images recorded by using the C2 configuration (crossed polarizers) are mainly based on D_L photons, because P_L and S_L photons are efficiently filtered by the linear analyzer.[19] Under this scenario, by simply obtaining the difference, C1-C2 (let us call this PG configuration as linear configuration, LConfig), we obtain polarimetric images which are only due to P_L and S_L photons (D_L photons are removed), thus, the image quality is improved when compared with the C1 configuration by itself. However, by using the LConfig, the contribution of SL photons still degrades the image contrast to a certain extent.

To improve the final image, recent studies have suggested an interest in generalizing LPG with the use of elliptical polarization, i.e., EPG.[19,33–35] In particular, EPG presents two main benefits when compared with LPG. First, elliptical states change the sense of rotation by surface reflection, thus, specular reflection is eliminated by using a coelliptical configuration for detection. Second, elliptically polarized light holds its polarization state for a larger number of scattering events than linearly polarized light, so it is suitable for the study of sub-substrate structures.[19] In particular, when illuminating a sample with an elliptical polarization out of the ballistic direction, a mixed contribution of photons (elliptical polarization maintaining photons, P_E and depolarized photons, D_E) is observed for a coelliptical configuration (let us call it configuration C3).[19,33] Note that by using the coelliptical configuration, S_E photons are removed because they undergo a change in helicity by reflection.[19,35] On the other hand, by using a cross-elliptical configuration (i.e., illuminating with a given elliptical polarization and detecting with the orthogonal one; configuration C4), a mix of surface-reflected elliptical photons, S_E, and D_E photons, is obtained, as P_E photons are removed in the cross-elliptical configuration.[19,35] Thus, analogously to the LPG case (LConfig), by simply subtracting the C3 and C4 channels (i.e., C3-C4), the obtained images are mainly produced by P_E and S_E photons, as the nondesired contribution of D_E photons is removed by subtraction. Let us label this PG configuration (C3-C4) as an elliptical configuration (EConfig). Nevertheless, by using the EConfig, the contribution of S_E photons is still present and somewhat degrades the final image contrast.

Other PG approaches can be found in literature to improve the final image contrast. For instance, a clever approximation is derived in Ref. 19. The authors provide an analytical function that combines the above-described [(C1-C2) and (C3-C4)] PG configurations. This leads to a mixture of surface reflected and

polarization maintaining photons from linear and elliptical polarizations ($P_L + S_L + P_E - S_E$). Note that, in general, the flux for the S_L and S_E photons is different, because the portion of input light projected to the plane of incidence is different for the linear and elliptical polarization cases. However, by normalizing the amount of reflected light projected in the plane of incidence for the elliptical polarization case to that of the linear polarization case by a factor β, such that $S_E = \beta S_L$, the influence of S_L and S_E photons in the final processed image can be avoided. In particular, this function, here labeled as function f, can be calculated as follows:[19]

$$f = (C3 - C4) + \beta(C1 - C2), \tag{1}$$

where the numerical parameter β corrects the differences in the amount of light projected to the components parallel (p-polarized) and perpendicular (s-polarized) to the plane of incidence when using different ellipticities for the input state of polarization. This parameter β has to be experimentally determined for each particular elliptical configuration (C3-C4) applied in the function f.[19]

Note that by using the function f, the photons contributing to the final image are mainly those maintaining the polarization, P_L and P_E photons, while the background, related to D_L, D_E, S_E, and S_L photons, is removed.

2.2 *Polarization Gating Configurations Described Using the Mueller Matrix Formalism*

In this section, we derive an analytical expression which depends on several MM coefficients, that allows performing a number of PG configurations by properly setting a few control parameters. To this aim, we adopt the well-known Stokes–Mueller formalism.[21,22] Accordingly, the state of polarization of a fully, partial, or unpolarized light beam is described by four intensity values, usually arranged in column-form in the so-called Stokes vector. In turn, the polarimetric response of any sample can be described by its 4×4 MM, whose 16 real coefficients encode the polarimetric information of the sample. In this framework, an MM can be understood as the polarization transfer function of the medium and the interaction of light with the medium is described by the following linear system:[21,22]

$$S_{\text{out}} = M \cdot S_{\text{input}} = \begin{pmatrix} m_{00} & m_{01} & m_{02} & m_{03} \\ m_{10} & m_{11} & m_{12} & m_{13} \\ m_{20} & m_{21} & m_{22} & m_{23} \\ m_{30} & m_{31} & m_{32} & m_{33} \end{pmatrix} \cdot \begin{pmatrix} S_0 \\ S_1 \\ S_2 \\ S_3 \end{pmatrix}, \tag{2}$$

where m_{ik} are the coefficients of the MM and S_i are the different channels of the Stokes vector.

When dealing with fully polarized light beams, the normalized Stokes vector can be written as a function of the polarization angles of the polarization ellipse, i.e., the azimuth (α) and the ellipticity (ε) angles:[22]

$$S = \begin{pmatrix} 1 \\ \cos 2\varepsilon \cos 2\alpha \\ \cos 2\varepsilon \sin 2\alpha \\ \sin 2\varepsilon \end{pmatrix}. \tag{3}$$

Note that by properly selecting the values for α and ε in Eq. (3), any fully polarized state of polarization can be described. According to Eqs. (2) and (3), when a fully polarized light beam interacts with a sample, the state of polarization S_{out} of the output (transmitted, reflected or scattered) light beam can be written as follows:

$$S_{\text{out}} = \begin{pmatrix} m_{00} + m_{01}\cos 2\varepsilon \cos 2\alpha + m_{02}\cos 2\varepsilon \sin 2\alpha + m_{03}\sin 2\varepsilon \\ m_{10} + m_{11}\cos 2\varepsilon \cos 2\alpha + m_{12}\cos 2\varepsilon \sin 2\alpha + m_{13}\sin 2\varepsilon \\ m_{20} + m_{21}\cos 2\varepsilon \cos 2\alpha + m_{22}\cos 2\varepsilon \sin 2\alpha + m_{23}\sin 2\varepsilon \\ m_{30} + m_{31}\cos 2\varepsilon \cos 2\alpha + m_{32}\cos 2\varepsilon \sin 2\alpha + m_{33}\sin 2\varepsilon \end{pmatrix}. \tag{4}$$

Afterward, we can project (i.e., analyze) this output light beam, S_{out}, on a polarization detector system setting a polarization analyzer (let us call it S_{PSD}) equal to the input polarization [i.e., that set in Eq. (3)]. This situation represents a coelliptical measurement and leads to

$$\begin{aligned} I_{\text{co-elliptical}} &= S_{\text{PSD}}^{\text{T}} \cdot S_{\text{out}} \\ &= m_{00} + m_{01}\cos 2\varepsilon \cos 2\alpha + m_{02}\cos 2\varepsilon \sin 2\alpha + m_{03}\sin 2\varepsilon + m_{10}\cos 2\varepsilon \cos 2\alpha + m_{11}(\cos 2\varepsilon \cos 2\alpha)^2 \\ &\quad + m_{12}(\cos 2\varepsilon)^2 \cos 2\alpha \sin 2\alpha + m_{13}\cos 2\varepsilon \cos 2\alpha \sin 2\varepsilon + m_{20}\cos 2\varepsilon \sin 2\alpha + m_{21}(\cos 2\varepsilon)^2 \cos 2\alpha \sin 2\alpha \\ &\quad + m_{22}(\cos 2\varepsilon \sin 2\alpha)^2 + m_{23}\cos 2\varepsilon \sin 2\alpha \sin 2\varepsilon + m_{30}\sin 2\varepsilon + m_{31}\cos 2\varepsilon \cos 2\alpha \sin 2\varepsilon \\ &\quad + m_{32}\cos 2\varepsilon \sin 2\alpha \sin 2\varepsilon + m_{33}(\sin 2\varepsilon)^2, \end{aligned} \tag{5}$$

where the superscript T denotes transpose and $I_{\text{coelliptical}}$ is the intensity corresponding to the projection of S_{out} on S_{PSD}, i.e., for the coelliptical configuration.

Afterward, we operate in the same way, but now we project S_{out} onto a polarization detector system configuring the orthogonal polarization, $S_{\text{PSD}}^{\perp}$. To obtain the orthogonal polarization, it is sufficient to apply the following transformations to the polarization angles: $\varepsilon \to -\varepsilon$ and $\alpha \to \alpha + (\pi/2)$. Under this scenario, the intensity resulting from the projection of S_{out} on $S_{\text{PSD}}^{\perp}$ (i.e., cross-elliptical configuration) becomes

$$
\begin{aligned}
I_{\text{cross-elliptical}} &= (S_{\text{PSD}}^{\perp,T}) \cdot S_{\text{out}} \\
&= (\,1 \quad -\cos 2\varepsilon \cos 2\alpha \quad -\cos 2\varepsilon \sin 2\alpha \quad -\sin 2\varepsilon\,) \cdot S_{\text{out}} \\
&= m_{00} + m_{01} \cos 2\varepsilon \cos 2\alpha + m_{02} \cos 2\varepsilon \sin 2\alpha + m_{03} \sin 2\varepsilon - m_{10} \cos 2\varepsilon \cos 2\alpha - m_{11}(\cos 2\varepsilon \cos 2\alpha)^2 \\
&\quad - m_{12}(\cos 2\varepsilon)^2 \cos 2\alpha \sin 2\alpha - m_{13} \cos 2\varepsilon \cos 2\alpha \sin 2\varepsilon - m_{20} \cos 2\varepsilon \sin 2\alpha - m_{21}(\cos 2\varepsilon)^2 \cos 2\alpha \sin 2\alpha \\
&\quad - m_{22}(\cos 2\varepsilon \sin 2\alpha)^2 - m_{23} \cos 2\varepsilon \sin 2\alpha \sin 2\varepsilon - m_{30} \sin 2\varepsilon - m_{31} \cos 2\varepsilon \cos 2\alpha \sin 2\varepsilon \\
&\quad - m_{32} \cos 2\varepsilon \sin 2\alpha \sin 2\varepsilon - m_{33}(\sin 2\varepsilon)^2. \qquad (6)
\end{aligned}
$$

Finally, we perform the difference between Eqs. (5) and (6), leading to

$$
\begin{aligned}
I_{\text{co-elliptical}} - I_{\text{cross-elliptical}} &= 2 \cos 2\varepsilon[m_{10} \cos 2\alpha + m_{20} \sin 2\alpha] + 2(\cos 2\varepsilon)^2[m_{11}(\cos 2\alpha)^2 + m_{22}(\sin 2\alpha)^2 \\
&\quad + \cos 2\alpha \sin 2\alpha(m_{12} + m_{21})] + 2 \cos 2\varepsilon \sin 2\varepsilon[\cos 2\alpha(m_{13} + m_{31}) + \sin 2\alpha(m_{23} + m_{32})] \\
&\quad + 2 \sin 2\varepsilon[m_{30} + m_{33} \sin 2\varepsilon]. \qquad (7)
\end{aligned}
$$

Therefore, by measuring the experimental MM of a sample and by using Eqs. (5)–(7), it is possible to retrieve multiple PG configurations just by setting the proper values for α and ε. Note that once the MM is measured, multiple PG configurations are numerically derived without the necessity of experimentally implementing each one of them.

In the following, we derive the PG configurations described in Sec. 2.1 using the MM-based formalism. First, setting $\alpha = 0$ deg and $\varepsilon = 0$ deg (linear polarization oriented at the laboratory vertical) in Eqs. (5) and (6), they yield, respectively,

$$
I_{\text{co-linear}} = C1 = m_{00} + m_{01} + m_{10} + m_{11} \qquad (8)
$$

and

$$
I_{\text{cross-linear}} = C2 = m_{00} + m_{01} - m_{10} - m_{11}. \qquad (9)
$$

Note that Eqs. (8) and (9) are, respectively, equivalent to the configurations C1 and C2, as explained in Sec. 2.1. Accordingly, LConfig is as follows:

$$
I_{\text{co-linear}} - I_{\text{cross-linear}} = C1 - C2 = 2[m_{10} + m_{11}]. \qquad (10)
$$

Next, we select PG configurations based on elliptical polarizations with arbitrary ellipticity, ε, and the corresponding major axis parallel to one of the laboratory frame axis represented by $\alpha = 0$ deg in Eqs. (5) and (6). Thus, they are reduced, respectively, to

$$
\begin{aligned}
I_{\text{co-elliptical}} &= C3 \\
&= m_{00} + \cos 2\varepsilon[m_{01} + m_{10}] + \sin 2\varepsilon[m_{03} + m_{30}] \\
&\quad + \cos 2\varepsilon \sin 2\varepsilon[m_{13} + m_{31}] \\
&\quad + m_{11}(\cos 2\varepsilon)^2 + m_{33}(\sin 2\varepsilon)^2 \qquad (11)
\end{aligned}
$$

and

$$
\begin{aligned}
I_{\text{cross-elliptical}} &= C4 \\
&= m_{00} + \cos 2\varepsilon[m_{01} - m_{10}] + \sin 2\varepsilon[m_{03} - m_{30}] \\
&\quad - \cos 2\varepsilon \sin 2\varepsilon[m_{13} + m_{31}] - m_{11}(\cos 2\varepsilon)^2 \\
&\quad - m_{33}(\sin 2\varepsilon)^2. \qquad (12)
\end{aligned}
$$

Note that Eqs. (11) and (12) are equivalent to the EPG configurations C3 and C4, respectively, both explained in Sec. 2.1. Accordingly, different ellipticities can be set by properly selecting the angle ε. Logically, for $\varepsilon = 0$, we end up in the linear case, thus, Eqs. (11) and (12) reduce to Eqs. (8) and (9), respectively.

The EConfig described in Sec. 2.1 can be obtained by subtracting these two relations as follows:

$$
\begin{aligned}
I_{\text{co-elliptical}} - I_{\text{cross-elliptical}} &= C3 - C4 \\
&= 2 \cos 2\varepsilon[m_{10} + m_{11} \cos 2\varepsilon] \\
&\quad + 2 \cos 2\varepsilon \sin 2\varepsilon[(m_{13} + m_{31})] \\
&\quad + 2 \sin 2\varepsilon[m_{30} + m_{33} \sin 2\varepsilon]. \qquad (13)
\end{aligned}
$$

Note that we can select an arbitrary EConfig simply by changing the ε parameter in Eq. (13).

Finally, from the above-described formulation, we can also obtain the function f defined in Eq. (1) and derived in Ref. 19. To avoid the requirement of performing extra experimental measurements for the determination of the parameter β in Eq. (1), we set $\alpha = 45$ deg. By using this configuration, the amount of light projected to the p-polarized and s-polarized components is always the same, independent of the chosen ellipticity. Thus, the factor β equals to 1 in such a case. Accordingly, Eq. (7) becomes

$$
\begin{aligned}
&I(\alpha = 45 \text{ deg})_{\text{co-elliptical}} - I(\alpha = 45 \text{ deg})_{\text{cross-elliptical}} \\
&= 2 \cos 2\varepsilon[m_{20} + m_{22} \cos 2\varepsilon] + 2 \cos 2\varepsilon \sin 2\varepsilon[m_{23} + m_{32}] \\
&\quad + 2 \sin 2\varepsilon[m_{30} + m_{33} \sin 2\varepsilon]. \qquad (14)
\end{aligned}
$$

Moreover, if $\varepsilon = 0$ deg in Eq. (14), it reduces to the linear case:

$$
\begin{aligned}
&I(\alpha = 45 \text{ deg}; \varepsilon = 0 \text{ deg})_{\text{co-elliptical}} \\
&\quad - I(\alpha = 45 \text{ deg}; \varepsilon = 0 \text{ deg})_{\text{cross-elliptical}} = 2[m_{20} + m_{22}]. \qquad (15)
\end{aligned}
$$

Finally, adding Eqs. (14) and (15) leads to

$$
\begin{aligned}
f_{\text{MM}} &= (C3 - C4)|_{\alpha=45} + (C1 - C2)|_{\alpha=45} \\
&= 2[m_{20} + m_{22}] + 2 \cos 2\varepsilon[m_{20} + m_{22} \cos 2\varepsilon] \\
&\quad + 2 \cos 2\varepsilon \sin 2\varepsilon[m_{23} + m_{32}] \\
&\quad + 2 \sin 2\varepsilon[m_{30} + m_{33} \sin 2\varepsilon], \qquad (16)
\end{aligned}
$$

which provides the function f as a function of the MM coefficients.

Note that, in practice, many samples present spatial dependence of their polarimetric properties as birefringent samples that possess a principal direction. In such cases, larger image contrast may be obtained by illuminating the sample with a different azimuth angle. If this is the case, the parameter β should be experimentally determined, as described in Ref. 19.

3 Imaging Mueller Polarimeter and Sample Description

In this section, we describe the optical arrangement that is used to measure the MM of samples (Sec. 3.1), and we describe the different samples we study in the forthcoming experimental section (Sec. 3.2).

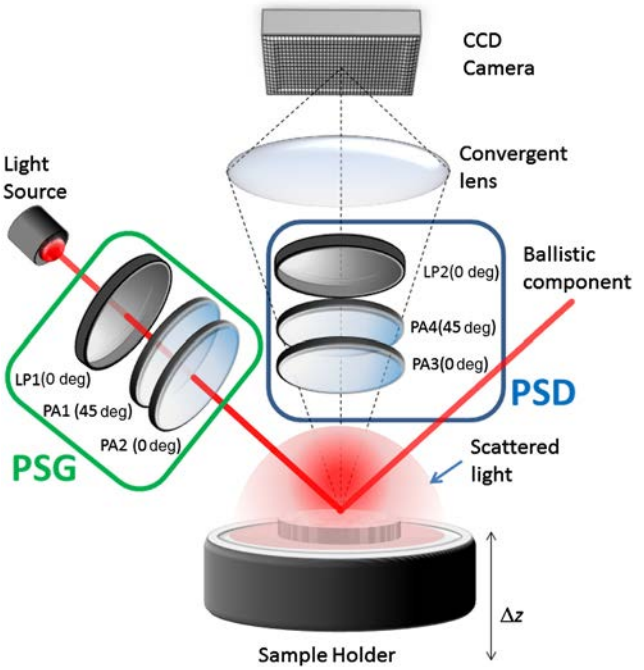

Fig. 1 Optical scheme of the used Mueller polarimeter. Video 1 shows the PG-based function f_{MM} calculated from the MM of the sample A. Different frames are related to different ellipticity values. (Video 1, MOV, 725 KB [URL: http://dx.doi.org/10.1117/1.JBO.22.5.056004.1]).

3.1 *Optical Scheme: Imaging Mueller Polarimeter*

The optical set-up used to measure MMs of different samples is a complete imaging MM polarimeter[36] based on parallel aligned liquid crystal (PA-LC) retarders. The set-up, sketched in Fig. 1, is analogous to that described in Ref. 37 but adapted for imaging polarimetry.

First, a light source illuminates a polarization state generator (PSG, marked with a green rectangle in Fig. 1), which includes a linear polarizer at 0 deg to the laboratory vertical reference axis, a first PA-LC panel (PA1), oriented at 45 deg to the laboratory vertical, and a second PA-LC panel oriented at 0 deg to the laboratory vertical (PA2). As discussed in Ref. 37, any fully polarized state of polarization can be generated with this system by adjusting the retardances of the two PA-LC panels. Then, the input light with controlled polarization illuminates a sample holder, where the sample is set, with an incident angle of ~60 deg. The sample holder can be mechanically displaced in the z direction for imaging purposes. Then, the light scattered by the sample is measured with a polarization state detector (PSD, marked with a blue rectangle in Fig. 1), which is constructed with the same optical elements as those in the PSG but with inverse order. Finally, a convergent lens images the sample on a CCD camera with a certain magnification.

Under this scenario, by properly generating a basis of known input polarizations with the PSG and measuring the corresponding Stokes vector of the scattered light with the Stokes polarimeter (PSD system), we construct a linear system [see Eq. (2)] from which the experimental MM of the sample can be obtained by applying an inversion method, as discussed in Refs. 21 and 38.

All experimental results shown and analyzed in a forthcoming section (Sec. 4) were obtained by experimentally implementing the optical scheme sketched in Fig. 1. The experimental set-up is shown in Fig. 2(a). As a light source, we used a four-wavelength high-power LED source (operated by DC4104 drivers distributed by Thorlabs). In particular, the color channels used in this work for conducting the different experimental measurements were the red channel [with a central wavelength of 625 nm and a spectral bandwidth (FWHM) of 18 nm] and the blue channel (central wavelength of 470 nm and a FWHM of 10 nm), with maximum output powers of 240 and 250 mW, respectively. To achieve a FWHM of 10 nm with the blue channel, a dielectric bandwidth filter (Thorlabs) was used. The linear polarizer in the PSG (LP1) is a Glan–Thompson prism-based polarizer (by CASIX). The linear polarizer at the PSD (LP2) is a dichroic sheet polarizer (by Meadowlark Optics). For the

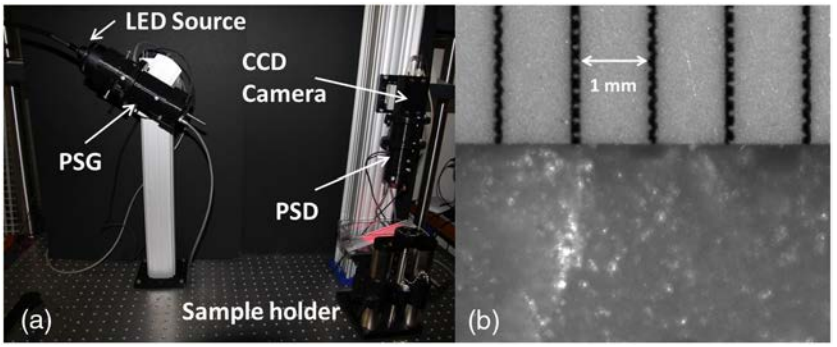

Fig. 2 (a) Picture of the experimental system; (b) image of a ruler placed on a slice of pork, for image resolution calculation. Video 2 shows the PG-based function f_{MM} calculated from the MM of the sample B. (Video 2, MOV, 603 KB [URL: http://dx.doi.org/10.1117/1.JBO.22.5.056004.2]).

liquid crystal panels in the PSG and PSA, we used four PA liquid crystal variable retarders with temperature control (LVR–200–400-700-1LTSC by Meadowlark Optics). Finally, a microscope objective images the selected sample RoI on a CCD camera. The convergent lens in Fig. 1 was a TECHSPEC® high resolution objective, distributed by Edmund Optics, with a focal length of 35 mm. The camera is an Allied Vision Manta G-504B. It is a 5 Megapixel GigE Vision camera with the Sony ICX655 CCD sensor, with a 2452 (H) × 2056 (V) resolution, and a cell size of 3.45 μm × 3.45 μm. As shown in Fig. 2(a), the PSG and PSD systems were assembled in two black holders made with a 3-D printer. These holders were designed to configure a robust and feasible full-Mueller imaging polarimeter in which the optical elements were protected from the environment (dust, misalignments, stray light, scratches, etc.).

The resolution selected for the conducted experimental measurements is described in the following. In Fig. 2(b), we picture a ruler placed on a thick slice of pork tissue. The distance between different lines is 1 mm. This distance corresponds to 52 pixels of the recorded image, leading to a spatial resolution of ~19 μm. If more resolution is desired, the sample holder can be brought closer to the objective by performing an axial displacement Δz, as indicated in Fig. 1.

3.2 *Sample Description: Phantom Experiment and Ex-Vivo Measurement*

To prove that the above discussed PG configurations can be obtained from Mueller measurements, we have performed two different experiments.

First, we have reproduced the phantom experiment described in Ref. 19. Let us call it sample A. In particular, a metallic ruler is placed obliquely on a plastic tank (15.5 cm × 7.5 cm × 5 cm). Then the tank is filled with intralipid (20%, Sigma-Aldrich, France) diluted in water [see Fig. 3(a)]. Intralipid is a lipid emulsion currently used for human intravenous use. In particular, intralipid is an emulsion of soy bean oil, egg phospholipids, and glycerin, and is available in 10%, 20%, and 30% concentrations. In the current work, this intralipid is diluted in water to a concentration of 0.1%, and the dilution is used to mimic the interaction of light with scattering tissues. For this concentration, the reduced scattering coefficients μ_s' for the red and blue channels are estimated to be of $\mu_s'|_{625\ \mathrm{nm}} = 0.63\ \mathrm{cm}^{-1}$ and $\mu_s'|_{470\ \mathrm{nm}} = 0.46\ \mathrm{cm}^{-1}$. According to Ref. 39, the corresponding anisotropy factors g of the intralipid are 0.73 and 0.83 for the 625 and 470 nm, respectively. The corresponding mean-free paths (MFPs) are $\mathrm{MFP}|_{625\ \mathrm{nm}} = 4.3$ mm and $\mathrm{MFP}|_{625\ \mathrm{nm}} = 3.7$ mm. According to the experimental results observed and described in a forthcoming section, with this configuration, we can perform macroscopic measurements with a sample penetration depth at the millimeter scale.

The second experiment is performed on an *ex-vivo* tissue (let us call it sample B). In particular, we have studied a region of interest (RoI) of a chicken neck, where different biological structures, such as muscles and nerves, are observed [see red square in Fig. 3(b)]. We want to emphasize that the region selected for measurements is fairly flat, avoiding possible image quality losses related to defocused planes.

Concerning the stability of the optical properties of the intralipid, a complementary experience, not discussed in this work, showed that the structure of an intralipid emulsion left still over time can evolve because spontaneous phase segregation (lipid/water) takes place. The process of phase segregation is very slow with a characteristic time of a few hours. Since the experiences reported here were performed in a time scale of seconds, we can, therefore, assume that the polarimetric properties of the samples remained constant throughout the measurement time.

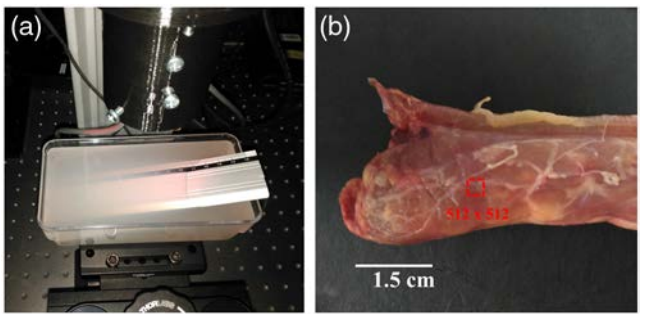

Fig. 3 (a) Tank filled with intralipid diluted in water and the metallic ruler (sample A). The sample is located in a sample holder to be measured with the polarimeter. The scattering effect is clearly observed. (b) Chicken neck for the *ex-vivo* experiment. The red square shows the measured RoI. Video 3 shows the PG-based function f_{MM} calculated from the equivalent diattenuator matrix (Di) for the sample B. (Video 3, MOV, 741 KB [URL: http://dx.doi.org/10.1117/1.JBO.22.5.056004.3]).

4 Experimental Results

In this section, we provide the equivalence between the PG configurations and those deduced from MM (Sec. 4.1). In addition, the potential of using MM to perform PG-based analysis is highlighted in Sec. 4.2, as MM channels provide extra polarimetric information that can be combined with PG techniques.

To this aim, we show and discuss experimental data obtained from measurements on the samples described in Sec. 3.2 (see Fig. 3). In particular, different measurements of the samples were performed under different PG configurations. For comparison with formulation given in Sec. 2.2, the corresponding MMs of the samples were also measured. The two sets of measurements (i.e., PG configurations and MM measurements) were obtained by using the experimental set-up described in Sec. 3.1.

4.1 *Polarization Gating Configurations Derived from Mueller Measurements*

In this subsection, we provide the equivalence between different PG configurations (Sec. 2.1) and those obtained from MM measurements (Sec. 2.2). To this aim, we have used the sample A described in Sec. 3.2. All the images provided in this subsection present a resolution of 1024 × 512 pixels and are obtained by illuminating the samples with the red channel (625 nm).

First, the MM of the sample was experimentally obtained by using the Mueller polarimeter sketched in Fig. 1. To this aim, we used a basis of six states of polarization both for illumination and detection: linear polarizations oriented at 0, 45, 90, and 135 deg to the laboratory vertical and two circular polarizations (right-handed and left-handed polarizations). The selected polarization basis stated above is commonly used due to its simplicity and because it leads to the minimum possible condition number (mathematical indicator that can be used to estimate the quality of a PSG-PSD system in terms of noise amplification) for polarimetric systems (Condition Number = 1.73).

We want to note that some authors[40,41] have proved that the intensity contrast of a particular sample can be enhanced by

selecting a direct gating configuration, where the PSG-PSD polarizations are optimized. To make this selection of the optimal PSG-PSD channels, we need to know some *a priori* polarimetric information of the sample or measure its MM. In the latter case, from the measured MM, by applying an optimization method, one can find the PSG-PSD channels that maximize the image contrast. Note that the MM-based approach we propose not only can be combined with PG configurations but could also be used to perform the optimizations proposed in Refs. 40 and 41.

From the measured MM, different PG configurations were calculated according to the formulation described in Sec. 2.2. As an example, Fig. 4 shows the results obtained for some of the PG configurations described in Sec. 2.1, obtained by using the experimental MM coefficients: configurations C1 [Fig. 4(a)], C2 [Fig. 4(c)], C3 [Fig. 4(e)], C4 [Fig. 4(g)], C1-C2 [Fig. 4(i)], and C3-C4 [Fig. 4(k)].

For comparison, the same configurations were obtained by using standard PG procedures, i.e., by setting the proper PSG-PSA configurations and recording the corresponding intensity images. Results are given in C1 [Fig. 4(b)], C2 [Fig. 4(d)], C3 [Fig. 4(f)], C4 [Fig. 4(h)], C1-C2 [Fig. 4(j)], and C3-C4 [Fig. 4(l)].

We see that the results obtained from MM or from standard PG techniques lead, in all cases, to equivalent information, because the final intensity images are very similar. To further quantify this similarity, Fig. 5 shows the absolute difference between the intensity images obtained from MM and from PG techniques for the C1 [Fig. 5(a)], C3 [Fig. 5(b)], C4 [Fig. 5(c)], and C3-C4 [Fig. 5(d)] cases.

For polarization configurations obtained from a single measurement, i.e., the C1, C2, C3, and C4 channels, the absolute error calculations were conducted as follows: (1) the $C_i(\mathrm{PG})$ image is obtained from PG measurements (the subscript i is equal to 1, 2, 3, or 4 for the C1, C2, C3, and C4 cases, respectively); (2) the $C_i(\mathrm{MM})$ image is obtained from MM measurements; (3) $C_i(\mathrm{PG})$ and $C_i(\mathrm{MM})$ are normalized to 1; and (4) the absolute error between images $[C_i(\mathrm{PG}) - C_i(\mathrm{MM})]$ is obtained pixel-to-pixel.

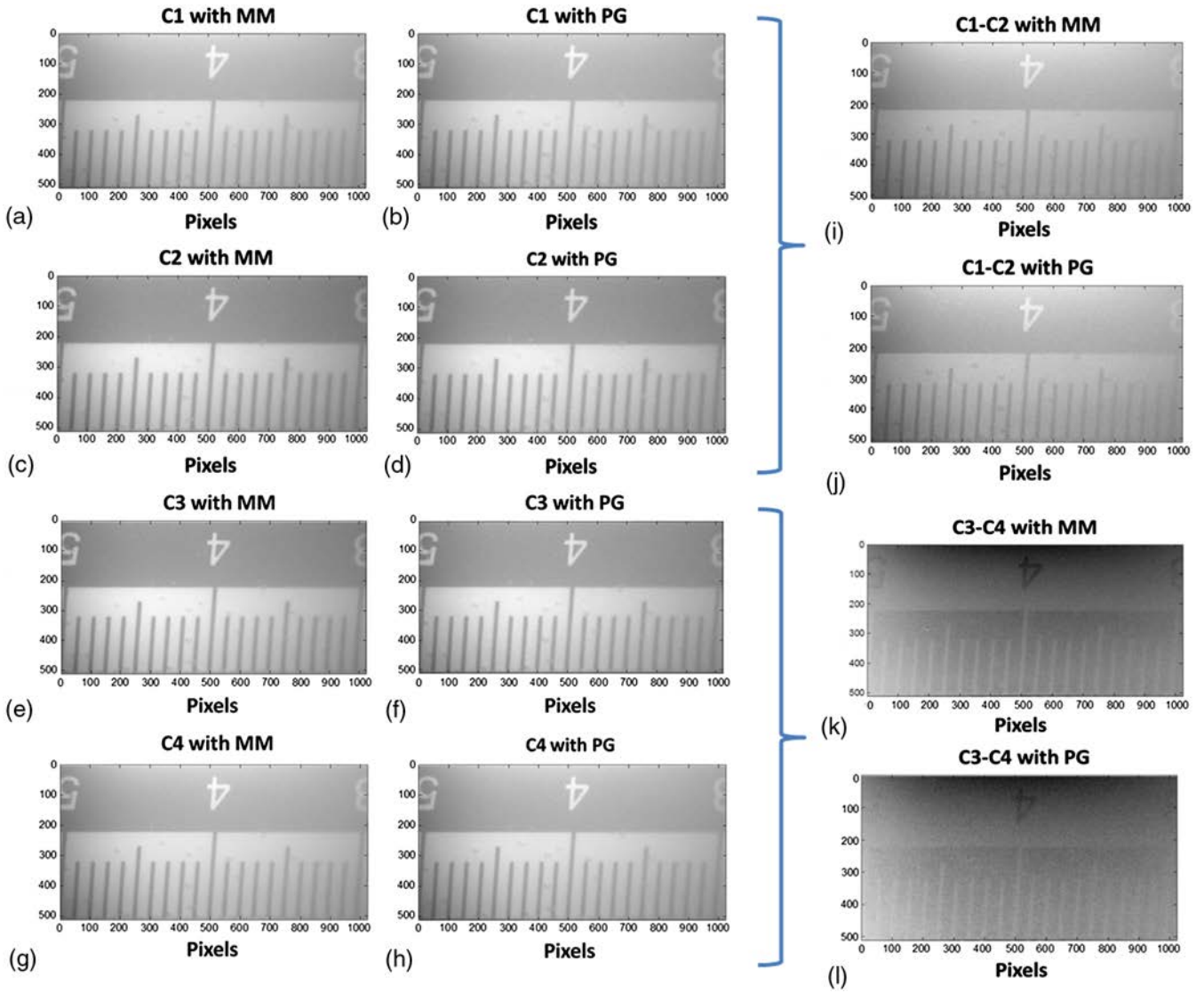

Fig. 4 Comparison between different PG configurations obtained from: MM coefficients (a, c, e, g, i, and k); and from standard PG procedures (b, d, f, h, j, and l). Video 4 PG-based function f_{MM} calculated from the equivalent depolarizer matrix (De) for the sample B. (Video 4, MOV, 974 KB [URL: http://dx.doi.org/10.1117/1.JBO.22.5.056004.4]).

For polarization configurations obtained from image processing, e.g., C1-C2 and C3-C4 channels, the absolute error calculations were conducted as follows: (1) the $C_j(\mathrm{PG})$ image is obtained from PG measurements (the subscript j is equal to 1 or 3 for the C1-C2 or the C3-C4 cases, respectively); (2) the $C_j(\mathrm{MM})$ image is obtained from MM measurements; (3) the $C_{j+1}(\mathrm{PG})$ image is obtained from PG measurements; (4) the $C_{j+1}(\mathrm{MM})$ image is obtained from MM measurements; (5) the $C_j - C_{j+1}$ channels are obtained in each case: $A = C_j(\mathrm{PG}) - C_{j+1}(\mathrm{PG})$ and $B = C_j(\mathrm{MM}) - C_{j+1}(\mathrm{MM})$; (6) the processed images A and B are normalized to 1; and (7) the absolute error between A and B is calculated as $A - B$.

In addition, the mean absolute error and standard deviation (σ) values corresponding to all the experiments shown in Fig. 4 are also provided in Table 1.

Note that for direct PG channels, i.e., C1, C2, C3, and C4 configurations, the absolute differences [Figs. 5(a)–5(c)] and the mean absolute differences (Table 1) are always smaller than 0.05. This leads to absolute differences smaller than 5% if taking into account the full images intensity range [0–1], and they can be mainly attributed to random noise at the intensity measurements. The case of PG channels obtained from image subtraction processing is also studied. We analyzed two different configurations: (i) the C1-C2 channel (i.e., "C1-C2 with MM"—"C1-C2 with PG") and (ii) the C3-C4 channel (i.e., "C3-C4 with MM"—"C3-C4 with PG"). The absolute errors between channels are always smaller than 0.1 (10%) [e.g., Fig. 5(d)]. In addition, the mean absolute errors were 0.021 and 0.041 (Table 1), and thus smaller than 0.05 (5%).

Note that the above-shown error values ensure the equivalence between standard PG configurations and PG configurations obtained from Mueller matrices. If required, these error values could be even more reduced by time-averaging different intensity images.

Finally, we want to highlight that by implementing PG configurations from MM measurements, we do not need to perform any new experiment for each extra PG configuration to be implemented. In fact, by using the mathematical formalism detailed in Sec. 2.2, a widespread number of PG configurations can be analytically obtained based on the MM coefficients.

As an example, we show the results obtained when implementing the function f_{MM}, detailed in Eq. (16), from the MM coefficients measured for the phantom experiment (i.e., ruler submerged into a tank with intralipid diluted in water; see sample A description in Sec. 3.2). Note that the ellipticity angle ε is

Table 1 Mean absolute difference and standard deviation σ for different PG channels.

Channel	Mean absolute difference	σ
C1	0.015	0.010
C2	0.026	0.019
C1-C2	0.021	0.016
C3	0.020	0.014
C4	0.012	0.009
C3-C4	0.041	0.031

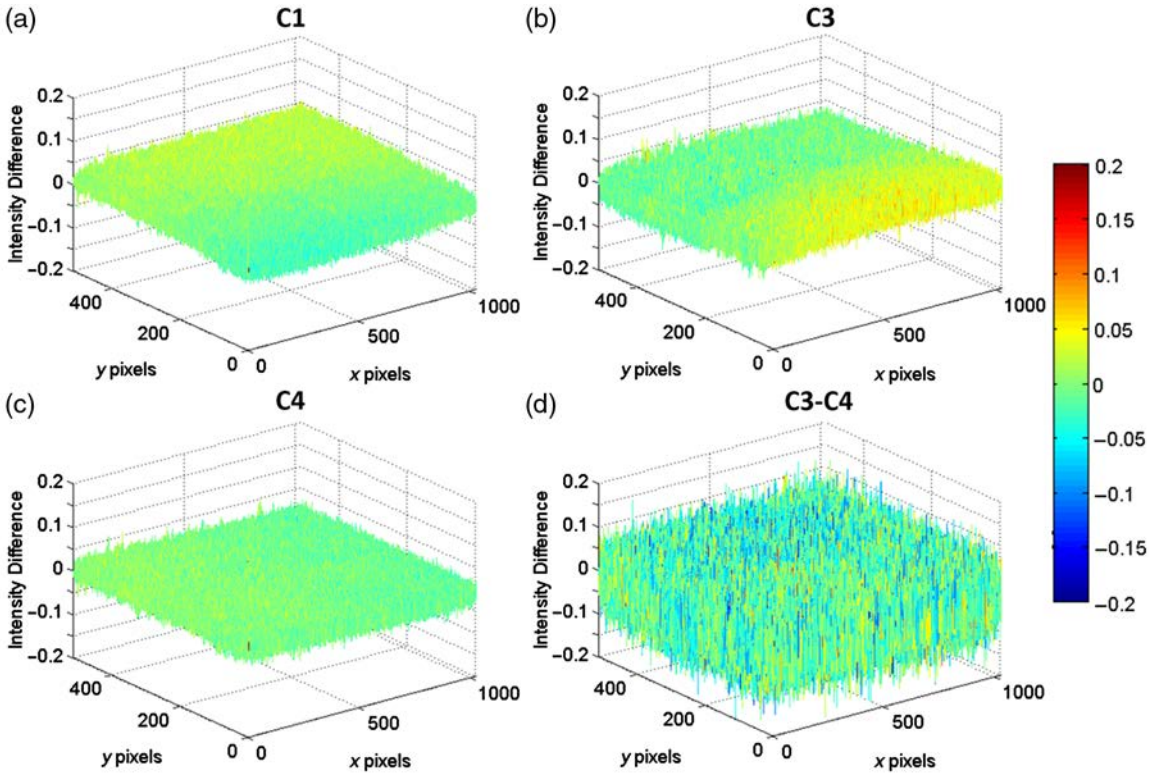

Fig. 5 Intensity absolute differences for the PG configurations: (a) C1, (b) C3, (c) C4; and (d) C3-C4. Video 5 shows PG-based function f_{MM} calculated from the equivalent retarder matrix (Ret) for the sample B. (Video 5, MOV, 1.03 MB [URL: http://dx.doi.org/10.1117/1.JBO.22.5.056004.5]).

a control parameter in Eq. (16). Therefore, in contrast to traditional PG experiments, where each ellipticity value to be tested (i.e., ellipticity for the generated and analyzed polarizations) has to be experimentally implemented, we can readily obtain such information with an arbitrary ε from measured MM coefficients [Eq. (16)]. This situation is highlighted in Video 1, where different frames show the sample A image obtained by processing the function f_{MM} as a function of the ε value, from $\varepsilon = -45$ deg to $\varepsilon = +45$ deg, with steps of 1 deg. Note that each video in this manuscript can be visualized with the corresponding link placed at the figure caption of the figure with the same number.

Images of Video 1 show the ruler submerged into the diluted intralipid and the different ruler numbers observed (i.e., 3-4-5) are related to different depths in the liquid [see Fig. 3(a)]. In particular, the number 5 is the number closer to the surface and the number 3 is the one more in depth. In agreement with other studies,[17,19] we see that larger ellipticity values ($\varepsilon \sim \pm 45$ deg) lead to a larger quantity of photons coming from deeper parts of the sample, as the number of scattering events taking place in a particular length depend on the polarization. This can be observed in Video 1 as clearer ($\varepsilon \sim +45$ deg) or darker ($\varepsilon \sim 0$ deg) image frames.

To quantify the different contrast provided by selecting different ellipticities in Eq. (16) for the phantom experiment (variations observed in Video 1), we have calculated the visibility $V = \frac{I_{\max} - I_{\min}}{I_{\max} + I_{\min}}$ for the two cross-sections shown in Fig. 6(a) (blue line for the four number and red line for the ruler tick mark), where $I_{\max}$ and $I_{\min}$ are the maximum and minimum values in the cross-section selected. We want to note that the best visibility values are obtained for an elliptical state of polarization (~30 deg). In general, PG configurations based on linear and circular polarizations are commonly used for its simplicity to be experimentally implemented. However, as shown in Fig. 6(b), these configurations will not always lead to the best contrast. If another ellipticiy needs to be tested, by using standard PG measurements, each new configuration has to be experimentally implemented, leading to a blind process. However, by using the method described in Sec. 2.2, such information can be analytically obtained, as shown in Fig. 6(b).

Note that Video 1 and data in Fig. 6 show the potential of rapidly implementing standard PG configurations from MM measurements, as this method constitutes a more general approach.

4.2 *Polarization Gating and Mueller Processing Combination*

In this section, we show the interest of performing polarimetric analysis of biological samples using MM data because this method not only allows to set multiple PG configurations from analytical expressions (shown in Sec. 4.1), but also provides new information channels (Mueller matrices, matrix decompositions, differential matrices, etc). In addition, the study provided in this section also highlights the interest of combining MM analysis tools with PG configurations.

4.2.1 *Phantom experiment*

We first performed a modification on the sample A by also considering retardance. The intralipid-ruler based experiment discussed above tries to mimic the scattering response of biological tissues. However, in general, other polarimetric responses simultaneously occur when light interacts with biological tissues. For instance, most biological tissues contain collagen fibers, which are part of the extracellular matrix and provide structural and biochemical support to the surrounding cells. Depending on the collagen degree of mineralization, collagen tissues may be rigid (e.g., bone), flexible (e.g., tendon), or present a gradient from rigid to flexible (e.g., cartilage). Moreover, collagen fibers are birefringent materials that present different retardation values for different biological structures,[42] such as those present in nerves, muscles, bones, ligaments, etc. Thus, image contrast between different tissues may be enhanced by considering polarimetric information. Some studies show that collagen fibers appear curly and anisotropic in normal stroma,[43] but they appear more stretched during early cancer progression, and they tend to be aligned parallel to the tumor border.[44] Therefore, retardation content is a valuable parameter for enhancing image contrast for biological and medical applications.

To take this fact into account and to include some retardance in the sample, the intralipid-ruler based experiment was repeated but by sticking two cellophane tape films on the ruler with different orientations, respectively [let us call it sample C;

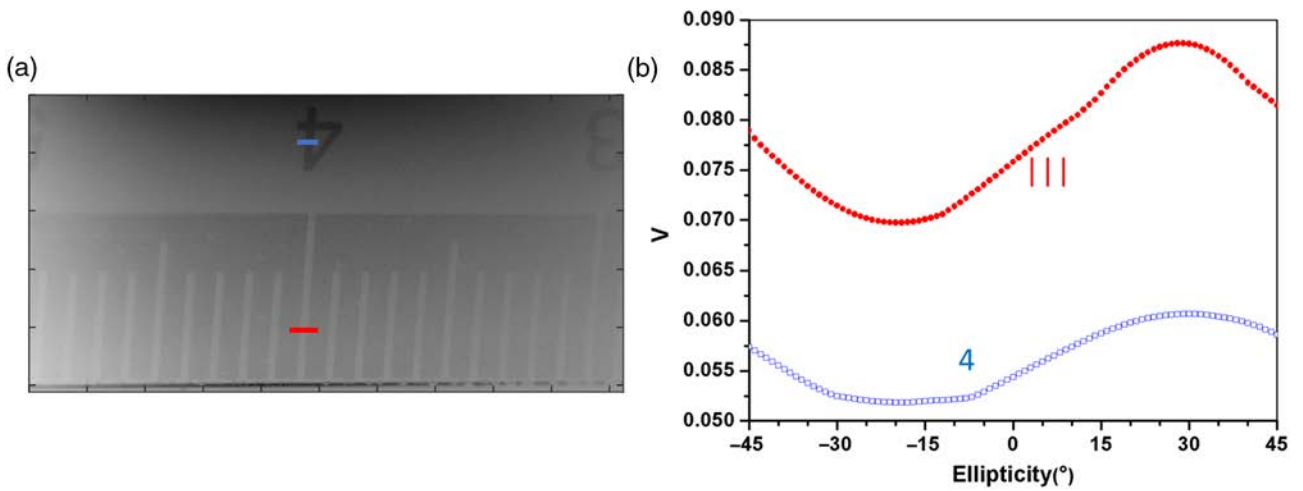

Fig. 6 (a) Cross-sections selected for the number 4 (blue line) and a ruler millimeter tick mark (red line). (b) Visibility (V) as a function of the ellipticity angle.

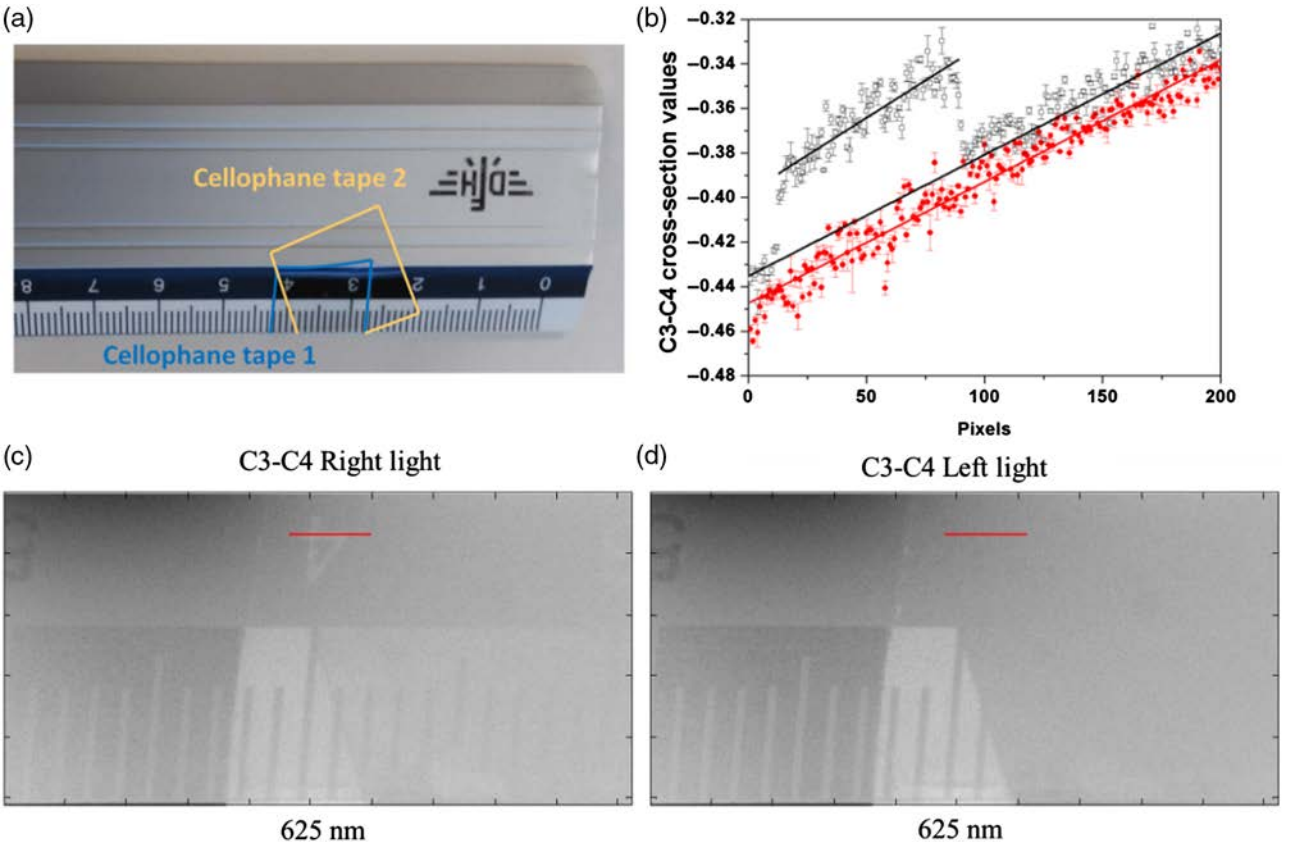

Fig. 7 (a) Ruler with stuck Scotch tapes (sample C); (b) cross-section values of the red line in panel (c) (black empty squares) and panel (d) (red circles); (c) C3-C4 PG image for right-handed circular light; and (d) C3-C4 PG image for left-handed circular light.

see Fig. 7(a)]. Note that the cellophane tape films act as linear retarders due to the stress applied on their constituent polymers during the fabrication process.

First, we have measured sample C by using traditional PG experimental techniques with the 625-nm light channel. In particular, Fig. 7(c) shows the image obtained by performing the standard PG configuration labeled as C3-C4 in Sec. 2.1, by using right-handed circular polarization for illumination. By contrast, Fig. 7(d) shows the same PG configuration but this time for a left-handed circular illumination. We can see well-differentiated zones with different intensity structures in sample C as a consequence of the polarization variations induced by the cellophane retardance. Note that these differences are not present in Figs. 4(k) and 4(l) (same PG configuration but applied on sample A). In addition, we observe that image contrast is significantly different by using right-handed [Fig. 7(c)] or left-handed [Fig. 7(d)] polarizations.

For example, the number 4 is not visible for the left-handed polarization, but it is clearly visible when using the right-handed polarization. This fact is highlighted in Fig. 7(b), where the cross-section corresponding to the red lines marked in Figs. 7(c) and 7(d) is shown. The cross-section values related to the red line in Fig. 7(c) (right-handed polarization case) go linearly to zero as we go inside the intralipid-water solution (see red circles). The linear tendency is shown by the calculated linear regression drawn as a continuous line (red line). In turn, the cross-section values for the red line in Fig. 7(d) (left-handed polarization case) have the same behaviour but show a sharp jump in the image contrast for the pixels related to the number 4 (see black squares). This situation occurs because elliptical states of polarization are modified in a different way depending on the retardation and orientation of the cellophane tape. Although some authors have pointed out the interest of using elliptical polarizations to test deeper structures in biological tissues, data shown in Fig. 7 also show the interest of optimizing the helicity of the selected polarization, because such a parameter can be important to enhance image contrast in biological tissues.

Afterward, we have calculated the MM of the sample C for 625 nm. The corresponding 16 real images are shown in Fig. 8. We want to note that the image coefficients pictured in Fig. 8 are normalized in each case by the corresponding maximum coefficient value, thus maximizing the image contrast for each particular coefficient. However, this representation does not allow us to visualize the relative intensity differences between Mueller coefficients. Thus, a matrix showing the maximum intensity value for each MM element when being normalized by the maximum value of the MM00 element is also provided as a bar chart at the left part of Fig. 8. This information allows us to identify the relative intensity magnitude between channels.

Note that the MM by itself provides different polarimetric information (MM coefficients in Fig. 8) than those related to the standard PG configurations, thus, MM coefficients provide further information that can be used and combined to enhance the sample image contrast.[45] In addition, the MM analysis allows performing a physical interpretation of the sample.[21,22] In a rough approximation, the MM coefficients in the first row and column of the matrix can be linked with the diattenuation

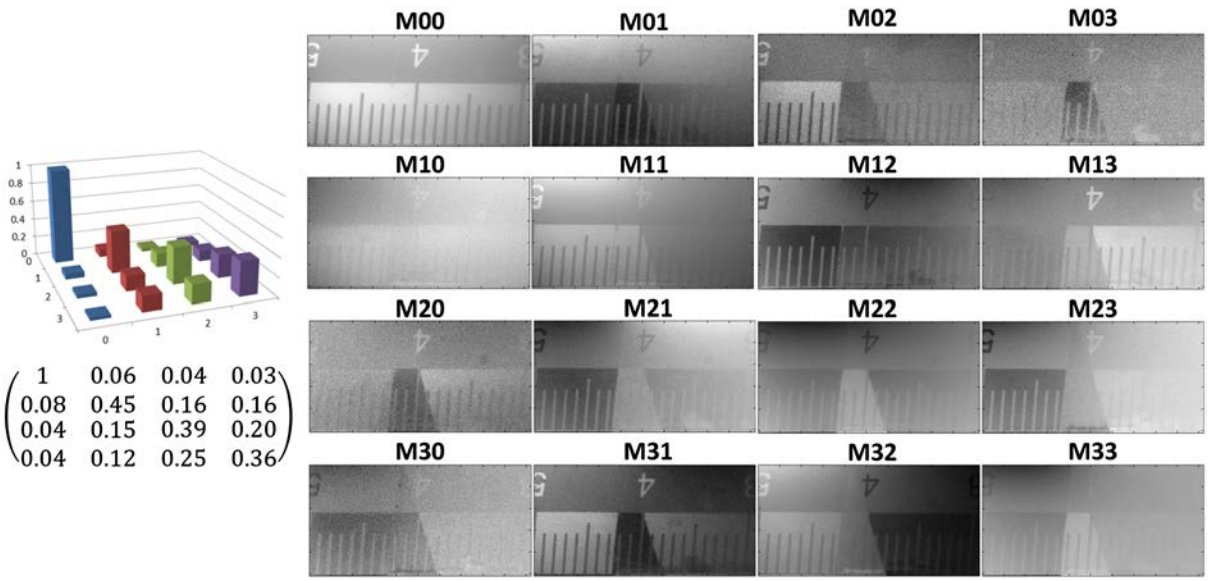

Fig. 8 Experimental MM of the sample C measured at 625 nm.

and polarizing capabilities of the sample, respectively (in the case of the sample C, mainly related to light reflections on the metallic surface of the ruler), the diagonal coefficients encode the depolarizing capability of the sample (for the sample C, mainly related with scattering events produced due to the fats present in the intralipid-water dissolution), and the bottom-right 3×3 submatrix can be linked with the retardance introduced by the sample (in sample C, due to the cellophane birefringence values).

In addition, the polarimetric content encoded on the MM of the sample can be further quantified by performing a physical model, where the properties of the sample are thought of as a combination of different pure polarimetric samples, typically, a diattenuator, a retarder, and a depolarizer. In other words, the sample can be further inspected by using well-known MM analytical tools, such as by applying MM decompositions.[21,22,46]

4.2.2 *Ex-vivo experiment*

Finally, to discuss a case which is closer to real experience than the phantom previously shown, the *ex-vivo* tissue labeled as sample B (see Sec. 3.2) was analyzed. To this aim, the MM of the sample was measured using the 470-nm channel. Some authors have provided the dependence of light penetration in biological tissues with the wavelength used.[47] In the visible range, larger wavelengths enter deeper into the skin than shorter ones. Therefore,

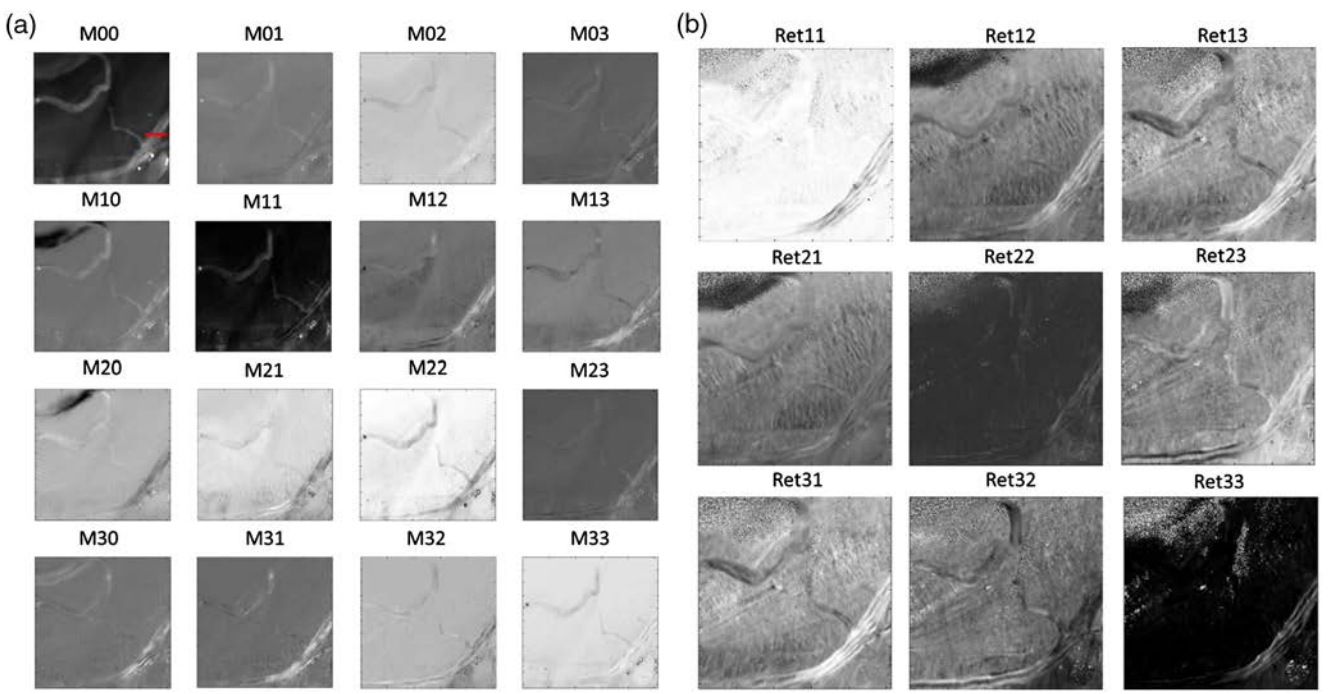

Fig. 9 (a) Experimental MM of the sample B measured at 470 nm and (b) 3×3 Mueller submatrix of the equivalent linear retarder for the sample B.

we have chosen the shorter available wavelength for illumination to mainly inspect biological structures at the sample surface.

The experimental MM for the sample B is shown in Fig. 9(a). As can be observed from the coefficient M00, which is related to the sample irradiance, the selected RoI [see Fig. 3(b)] includes different biological structures, such as muscles and nerves. It can be observed that different image coefficients lead to different contrast levels between the biological structures present in the sample [Fig. 9(a)].

In addition, to highlight the interest of using MM-based analytical tools, we have also applied the Lu–Chipman decomposition,[22] which allows us to decompose the MM of a sample as a product of three basic MMs: the MM of a diattenuator (Di), the MM of a retarder (Ret), and the MM of a depolarizer (De). As an example, the MM of the retarder (Ret) for sample B is also provided in Fig. 9(b). For a better visualization of the Ret matrix, the first row and column coefficients are removed in Fig. 9(b) because they are always zero in linear retarders. Thus, significant polarimetric content in the Ret matrix is at the 3×3 submatrix shown in Fig. 9(b).

Note that the matrix Ret only provides the retardance information of the sample (other polarimetric content has been already extracted by means of the matrix decomposition), thus, the image contrast observed in the Ret matrix channels is mainly due to retardance features of the sample. In other words, contrast obtained from the retarder matrix of biological tissues is related to retardance created by different sample structures, for instance, due to the different collagen fibers density, mineralization degree, or orientation at the different biological structures. For the sample B particular case [Fig. 9(b)], we see that the retardance content of the sample provides a noticeable contrast of the nerve ramification along the muscle in the chicken neck, this being specially highlighted in the Ret13, Ret31, Ret23, and Ret32 coefficients of the Ret matrix. In addition, the MMs of the depolarizer (De) and the diattenuator (Di) have been calculated as well, leading, in this case, to less contrast than the M and the Re matrices.

To quantify the above-stated discussion, in Fig. 10, we show the cross-sections related to the red line shown in Fig. 9 [see coefficient M00 in Fig. 9(a)]. In particular, we have calculated the visibility corresponding to the cross-line above-stated for all the Mueller coefficients and for all the coefficients of the decomposed matrices (Di, De, and Ret cases), always for the same line of the sample. The largest visibility in each case has been obtained for the M33, Ret33, De21, and Di30 coefficients. The corresponding cross-sections are provided in Fig. 10.

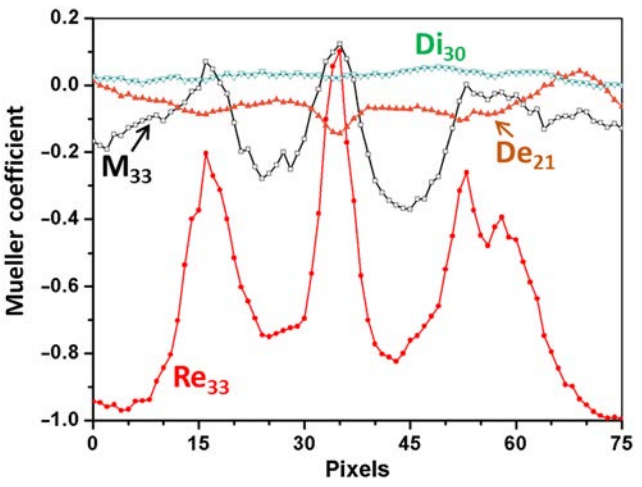

Fig. 10 Cross-sections [related to the line shown in Fig. 9(a)] corresponding to the coefficients providing the best visibility for the MM (black empty squares), the retarder (red circles), the depolarizer (brown triangles), and the diattenuator (green empty triangles).

In agreement with the qualitative discussion provided above, the best contrast for the chicken nerve [see red line in Fig. 9(a)] is obtained with the retarder matrix, where the separation between different nerve structures is highlighted by the different picks (see red circles in Fig. 10). Note that this sample detail is almost hidden in the diattenuation and the depolarization channels (green empty triangles and brown triangles, respectively, in Fig. 10).

At this point, we have shown how PG techniques based on MM measurements lead to a generalization of the standard PG methods (Secs. 2.2 and 4.1). In this subsection, we also highlighted the interest of using MM measurements for biological tissues inspection as they bring a whole new battery of analytical techniques. Last but not least, we want to discuss the interest of combining PG methods with MM analytical tools.

To this aim, we used sample B [chicken neck, see RoI in Fig. 3(b)] described in Sec. 3.2. In particular, the function f_{MM} [Eq. (16) in Sec. 2.2; PG-based relation] was calculated from the MM coefficients of sample B [data pictured in Fig. 9(a)]. In addition, to exploit the MM capabilities, the f_{MM} was calculated again but this time from the decomposed Mueller matrices, which were calculated according to the Lu–Chipman decomposition.[22] Therefore, the f_{MM} function was obtained for the diattenuator (Di), the retarder (Ret), and the depolarizer (De) Mueller matrices. As f_{MM} is an analytical expression, in all the cases, it was calculated for different ellipticity values, from -45 to $+45$ deg with steps of 1 deg. Thus, results are provided in video format. In particular, Video 2 provides the f_{MM} function calculated from the MM as a function of the ellipticity value selected. Moreover, the same function but calculated from the Di, De, and Ret matrices is given in Video 3, Video 4, and Video 5, respectively.

On the one hand, when analyzing the data obtained from the MM coefficients (Video 2), we observe certain contrast between the biological tissues present in the sample, mainly nerves and muscle tissues. Moreover, the biological structures visualization strongly depends on the ellipticity of the PG channel selected. For instance, in Video 2, we see that the nervous tissue placed at the image bottom is better visualized by using larger ellipticities ($\varepsilon \sim \pm 45$ deg), showing more clearly its ramified structure. On the contrary, surface muscle is better contrasted by using linear polarizations ($\varepsilon \sim 0$ deg).

On the other hand, better sample interpretation can be achieved by using the f_{MM} function derived from decomposed Mueller matrices. First, Video 3 provides the f_{MM} function calculated from the diattenuator matrix coefficients. As can be observed, we obtain a very poor image contrast between tissues, indicating that the analyzed structures do not present significant dichroism values (at least at the superficial layers), and polarimetric features of sample B are mainly related to birefringence and depolarizing processes. Next, the f_{MM} function calculated from the depolarizer matrix coefficients provides a noticeable image contrast between nerves and muscles (Video 4), indicating that each particular tissue scatters light in a different way. In addition, image contrast varies with the selected elliptical channel, ellipticities close to $\varepsilon \sim -45$ deg being those providing the best contrast between nerves and muscle. By contrast, the fibrillary nature of muscle tissue is

better resolved by using linear channels ($\varepsilon < \pm 10$ deg). Finally, the function f_{MM} calculated from the retarder matrix Ret also provides different polarimetric information (Video 5). By using this polarimetric information, muscle–nerve contrast is reduced when compared with data in Video 4. In addition, muscle tissue seems to be quite uniform through the whole muscle surface, leading to a uniform black image (the best muscle contrast is obtained for linear channels). Nevertheless, nerve contrast itself is significant. In fact, f_{MM} function based on the retarder data reveals a ramified structure for the nerve (in the lower part of the images), where different nerve details are discovered by using different ellipticity channels.

We want to emphasize that this particular example could be further investigated by using other analytical expressions deducted from MM coefficients, as those provided in Ref. 45, or other relevant processing techniques.

5 Conclusions

We presented an experimental method based on the calculation of the MM of samples suitable for the calculation of standard PG techniques. We proved that this method is not only equivalent to standard PG measurements, but also can be used to build general analytical expressions from which a set of PG configurations can be simultaneously obtained.

We also proved that when conducting PG measurements to inspect biological tissues, it is not only important to optimize the ellipticity of the input and analyzing states of polarization, as previously highlighted by some authors, but also to optimize the helicity of the elliptical state of polarization. This situation occurs because when polarized light interacts with complex structures, right-handed and left-handed polarizations are modified in a different way due to different media polarimetric characteristics, for instance, the retardance introduced by the media, the orientation of the extraordinary axis of the anisotropic media, etc.

Finally, we have also highlighted the interest of not only performing PG based on MM measurements but also to take advantage of all those analytical tools related to the Mueller formalism. By doing this, extra polarimetric channels and analysis techniques are available. In addition, they can be combined with standard PG methods to obtain further information.

The experimental method proposed here was tested on different samples as different phantom experiments and *ex-vivo* biological tissues, thereby providing the suitability of the method to be applied for the polarimetric analysis of samples.

Disclosures

No conflicts of interest, financial or otherwise, are declared by the authors.

Acknowledgments

We acknowledge the financial support of Spanish MINECO (FIS2015-66328-C3-1-R, FIS2015-66328-C3-3-R, and Fondos FEDER); Catalan Government (SGR 2014-1639).

References

1. T. Novikova et al., "Polarized light for biomedical applications," *J. Biomed. Opt.* **21**(7), 071001 (2016).
2. A. G. Ushenko and V. P. Pishak, "Laser polarimetry of biological tissue: principles and applications," in *Handbook of Coherent-Domain Optical Methods: Biomedical Diagnostics, Environmental and Material Science*, V. V. Tuchin, Ed., pp. 93–138, Kluwer Academic Publishers, Boston (2004).
3. V. V. Tuchin, "Polarized light interaction with tissues," *J. Biomed. Opt.* **21**(7), 071114 (2016).
4. T. Novikova et al., "Polarimetric imaging for cancer diagnosis and staging," *Opt. Photonics News* **23**(10), 26–33 (2012).
5. A. Pierangelo et al., "Polarimetric imaging of uterine cervix: a case study," *Opt. Express* **21**(12), 14120–14130 (2013).
6. O. Peresunko, T. V. Kruk, and S. B. Yermolenko, "Diagnostic value spectropolarimetry of blood plasma in patients with breast cancer," *Proc. SPIE* **9166**, 91661D (2014).
7. Y. A. Ushenko, "Investigation of formation and interrelations of polarization singular structure and Mueller-matrix images of biological tissues and diagnostics of their cancer changes," *J. Biomed. Opt.* **16**(6), 066006 (2011).
8. E. Du et al., "Mueller matrix polarimetry for differentiating characteristic features of cancerous tissues," *J. Biomed. Opt.* **19**(7), 076013 (2014).
9. Y. Yitzhaky, L. Graham, and I. Abdulhalim, "Analysis of skin moles from optical spectropolarimetric images," *Proc. SPIE* **8856**, 88562J (2013).
10. T. Yasui, Y. Tohno, and T. Araki, "Characterization of collagen orientation in human dermis by two-dimensional second-harmonic-generation polarimetry," *J. Biomed. Opt.* **9**(2), 259–264 (2004).
11. L. Graham, Y. Yitzhaky, and I. Abdulhalim, "Classification of skin moles from optical spectropolarimetric images: a pilot study," *J. Biomed. Opt.* **18**(11), 111403 (2013).
12. K. M. Twietmeyer et al., "Mueller matrix retinal imager with optimized polarization conditions," *Opt. Express* **16**(26), 21339–21354 (2008).
13. J. M. Bueno, "Measurement of parameters of polarization in the living human eye using imaging polarimetry," *Vision Res.* **40**, 3791–3799 (2000).
14. R. Rawer, W. Stork, and K. D. Müller-Glaser, "Polarimetric methods for measurement of intra ocular glucose concentration," *Biomed. Tech.* **47**, 186–188 (2002).
15. G. Purvinis, B. D. Cameron, and D. M. Altrogge, "Noninvasive polarimetric-based glucose monitoring: an *in vivo* study," *J. Diabetes Sci. Technol.* **5**(2), 380–387 (2011).
16. P. Shukla and A. Pradhan, "Polarization-gated imaging in tissue phantoms: effect of size distribution," *Appl. Opt.* **48**, 6099–6104 (2009).
17. B. Kunnen et al., "Application of circularly polarized light for non-invasive diagnosis of cancerous tissues and turbid tissue-like scattering media," *J. Biophotonics* **8**(4), 317–323 (2015).
18. C. W. Sun et al., "Polarization gating in ultrafast-optics imaging of skeletal muscle tissues," *Opt. Lett.* **26**(7), 432–434 (2001).
19. S. Sridhar and A. Da Silva, "Enhanced contrast and depth resolution in polarization imaging using elliptically polarized light," *J. Biomed. Opt.* **21**(7), 071107 (2016).
20. S. L. Jacques, S. Roussel, and R. Samatham, "Polarized light imaging specifies the anisotropy of light scattering in the superficial layer of a tissue," *J. Biomed. Opt.* **21**(7), 071115 (2016).
21. E. Garcia-Caurel et al., "Advanced Mueller ellipsometry instrumentation and data analysis," in *Ellipsometry at Nanoscale*, M. Losurdo and K. Hingerls, Eds., pp. 31–143, Springer-Verlag, Berlin (2013).
22. D. Goldstein, *Polarized Light*, 2nd ed., Marcel Dekker, New York (2003).
23. R. Ossikovski, "Differential and product Mueller matrix decompositions: a formal comparison," *Opt. Lett.* **37**(2), 220–222 (2012).
24. R. Ossikovski, "Differential matrix formalism for depolarizing anisotropic media," *Opt. Lett.* **36**(12), 2330–2332 (2011).
25. R. Ossikovski and O. Arteaga, "Statistical meaning of the differential Mueller matrix of depolarizing homogeneous media," *Opt. Lett.* **39**(15), 4470–4473 (2014).
26. N. Ortega-Quijano and J. L. Arce-Diego, "Depolarizing differential Mueller matrices," *Opt. Lett.* **36**(13), 2429–2431 (2011).
27. A. Peinado, A. Lizana, and J. Campos, "Optimization and tolerance analysis of a polarimeter with ferrolectric liquid crystals," *Appl. Opt.* **52**, 5748–5757 (2013).
28. S. Alali, A. Gribble, and I. A. Vitkin, "Rapid wide-field Mueller matrix polarimetry imaging based on four photoelastic modulators with no moving parts," *Opt. Lett.* **41**, 1038–1041 (2016).
29. A. Le Gratiet et al., "Scanning Mueller polarimetric microscopy," *Opt. Lett.* **41**(18), 4336–4339 (2016).

30. V. M. Turzhitsky et al., "Measuring mucosal blood supply *in vivo* with a polarization-gating probe," *Appl. Opt.* **47**(32), 6046–6057 (2008).
31. M. P. Siege et al., "Assessment of blood supply in superficial tissue by polarization-gated elastic light-scattering spectroscopy," *Appl. Opt.* **45**(2), 335–342 (2006).
32. Y. Liu, Y. L. Kim, and V. Backman, "Development of a bioengineered tissue model and its application in the investigation of the depth selectivity of polarization gating," *Appl. Opt.* **44**(12), 2288–2299 (2005).
33. S. P. Morgan and M. Ridgway, "Polarization properties of light backscattered from a two layer scattering medium," *Opt. Express* **7**(12), 395–402 (2000).
34. A. Da Silva, C. Deumié, and I. Vanzetta, "Elliptically polarized light for depth resolved optical imaging," *Biomed. Opt. Express* **3**(11), 2907 (2012).
35. S. P. Morgan and I. M. Stockford, "Surface-reflection elimination in polarization imaging of superficial tissue," *Opt. Lett.* **28**(2), 114–116 (2003).
36. J. S. Tyo et al., "Review of passive imaging polarimetry for remote sensing applications," *Appl. Opt.* **45**(22), 5453–5469 (2006).
37. A. Peinado et al., "Optimization and performance criteria of a Stokes polarimeter based on two variable retarders," *Opt. Express* **18**(10), 9815–9830 (2010).
38. R. A. Chipman, "Polarimetry," in *Handbook of Optics*, Chapter 22, pp. 1–37, McGraw-Hill, New York (1995).
39. H. J. van Staveren et al., "Light scattering in intralipid-10% in the wavelength range of 400-1100 nm," *Appl. Opt.* **30**(31), 4570–4514 (1991).
40. G. Anna et al., "Fully tunable active polarization imager for contrast enhancement and partial polarimetry," *Appl. Opt.* **51**, 5302–5309 (2012).
41. F. Goudail, "Comparison of maximal achievable contrast in scalar, Stokes, and Mueller images," *Opt. Lett.* **35**, 2600–2602 (2010).
42. K. Komatsu et al., "Polarized light microscopic analyses of collagen fibers in the rat incisor periodontal ligament in relation to areas, regions, and ages," *Anat. Rec.* **268**(4), 381–387 (2002).
43. M. Egeblad, M. G. Rasch, and V. M. Weaver, "Dynamic interplay between the collagen scaffold and tumor evolution," *Curr. Opin. Cell Biol.* **22**, 697–706 (2010).
44. M. W. Conklin et al., "Aligned collagen is a prognostic signature for survival in human breast carcinoma," *Am. J. Pathol.* **178**, 1221–1232 (2011).
45. H. He et al., "A possible quantitative Mueller matrix transformation technique for anisotropic scattering media," *Photonics Lasers Med.* **2**(2), 129–137 (2013).
46. J. J. Gil and R. Ossikovski, *Polarized Light and the Mueller Matrix Approach*, CRC Press, Taylor & Francis, New York (2016).
47. F. H. Mustafa and M. S. Jaafar, "Comparison of wavelength-dependent penetration depths of lasers in different types of skin in photodynamic therapy," *Indian J. Phys.* **87**(3), 203–209 (2013).

Angel Lizana received his MSc and PhD degrees in physics at the UAB in 2006 and 2011, respectively. He was a postdoctoral scientist in the École Polytechnique, France, in 2012 to 2014. His research interests include liquid crystal displays and its application to diffractive optics, as well as the implementation of polarimeters and their use in biological applications. He is an associate professor at the UAB since 2016.

Albert Van Eeckhout received his BSc degree in physics at the University of Barcelona (UB) in 2015 and his MSc degree in photonics at the Polytechnique University of Barcelona (UPC), UB, and Autonomous University of Barcelona (UAB) in 2016. He is performing his PhD in physics at the UAB since 2017 and the topic of the thesis is related to the design and implementation of optical instrumentation based on polarization to be used in biomedical applications.

Kamil Adamczyk is a student at the University of Warsaw, Poland. He graduated with a bachelor's degree in physics and chemistry in 2015 and 2016. As part of his master's programme in physics at the same university, he participated in the exchange programme at the UAB. His academic interests revolve around experimental optics, in particular polarimetry and its use in biomedical applications.

Carla Rodríguez is a final year student of the physics degree at the UAB. She is interested in optics, and particularly, in polarimetry and its use in biomedical applications.

Juan C. Escalera received his degree in physics from the University of Zaragoza, Spain, in 1982 and his MS and PhD degrees from the UAB, Spain, in 1990 and 1991, respectively. He is a research collaborator with UAB since 1988 and an associate professor with UAB since 2001. His research interests include diffraction and color image formation, liquid crystal displays, and its applications in diffractive and polarization optics.

Enric Garcia-Caurel received his PhD in physics from the UB in 2001. He is a research associate at École Polytechnique, France, since 2003 and also at Synchrotron SOLEIL since 2015. His research includes ellipsometry and polarimetry for materials science, interaction of light in turbid media for biomedical optics, development of new optical instruments in collaboration with the industry, and, exploration of new applications of polarized light. He is a senior member of SPIE.

Ignacio Moreno received his BS and PhD degrees in physics at the UAB in 1992 and 1996, respectively. He is a full professor of optics at the University Miguel Hernandez of Elche. He is currently the president of the Spanish Optical Society—SEDOPTICA. He is a fellow member of SPIE and OSA. His research interests include liquid crystal displays and its applications in diffractive and polarization optics.

Juan Campos received his MSc degree in physics at the University of Zaragoza in 1981 and his PhD at the UAB in 1986. He was a professor of optics at the UB. From 1993, he was a professor at the UAB and since 2005 he is a full professor. He has worked in image processing, pattern recognition, digital holography, color information, liquid crystals, surface metrology, and polarimetry. He is a fellow of the SPIE, OSA, and EOS.

Synthesis and characterization of depolarizing samples based on the indices of polarimetric purity

[Albert Van Eeckhout, Angel Lizana, Enric Garcia-Caurel, José J. Gil, Razvigor Ossikovski, and Juan Campos. *Synthesis and characterization of depolarizing samples based on the indices of polarimetric purity*, Opt. Lett. **42**, 4155-4158 (2017)]

DOI: https://doi.org/10.1364/OL.42.004155

Polarimetric imaging of biological tissues based on the indices of polarimetric purity

[Albert Van Eeckhout, Angel Lizana, Enric Garcia-Caurel, José J. Gil, Adrià Sansa, Carla Rodríguez, Irene Estévez, Emilio González, Juan Carlos Escalera, Ignacio Moreno, and Juan Campos. *Polarimetric imaging of biological tissues based on the indices of polarimetric purity*, J. Biophotonics **11**(4), e201700189 (2017)]

DOI: https://doi.org/10.1002/jbio.201700189

Received: 9 March 2020 | Revised: 1 May 2020 | Accepted: 8 May 2020

DOI: 10.1002/jbio.202000083

JOURNAL OF BIOPHOTONICS

FULL ARTICLE

Depolarization metric spaces for biological tissues classification

Albert Van Eeckhout[1*] | Enric Garcia-Caurel[2] | Razvigor Ossikovski[2] | Angel Lizana[1*] | Carla Rodríguez[1] | Emilio González-Arnay[3,4] | Juan Campos[1]

[1]Grup d'Òptica, Physics Department, Universitat Autònoma de Barcelona, Bellaterra, Spain

[2]LPICM, CNRS, École Polytechnique, Université Paris-Saclay, Palaiseau, France

[3]Departamento de Anatomía, Histología y Neurociencia, Universidad Autónoma de Madrid, Madrid, Spain

[4]Servicio de Anatomía Patológica, Hospital Universitario de Canarias, Santa Cruz de Tenerife, Spain

***Correspondence**
Albert Van Eeckhout and Angel Lizana, Grup d'Òptica, Physics Department, Universitat Autònoma de Barcelona, 08193 Bellaterra, Spain.
Email: albert.vaneeckhout@uab.cat (A. V. E) and
Email: angel.lizana@uab.cat (A. L.)

Funding information
Agència de Gestió d'Ajuts Universitaris i de Recerca, Grant/Award Number: 2017-SGR-001500; Ministerio de Economía y Competitividad, Grant/Award Numbers: Fondos FEDER, RTI2018-097107-B-C31

Abstract

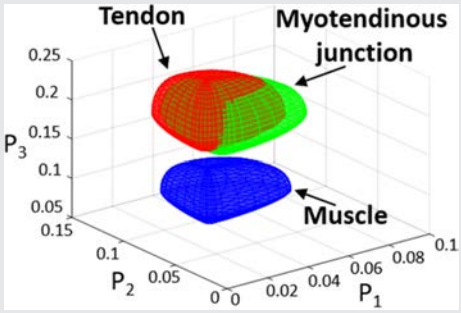

Classification of tissues is an important problem in biomedicine. An efficient tissue classification protocol allows, for instance, the guided-recognition of structures through treated images or discriminating between healthy and unhealthy regions (e.g., early detection of cancer). In this framework, we study the potential of some polarimetric metrics, the so-called depolarization spaces, for the classification of biological tissues. The analysis is performed using 120 biological ex vivo samples of three different tissues types. Based on these data collection, we provide for the first time a comparison between these depolarization spaces, as well as with most commonly used depolarization metrics, in terms of biological samples discrimination. The results illustrate the way to determine the set of depolarization metrics which optimizes tissue classification efficiencies. In that sense, the results show the interest of the method which is general, and which can be applied to study multiple types of biological samples, including of course human tissues. The latter can be useful for instance, to improve and to boost applications related to optical biopsy.

KEYWORDS

biological tissue, biomedical, depolarization, imaging, Mueller matrix, polarimetry

1 | INTRODUCTION

Identification and classification of tissues is a recurrent topic in the biomedical domain.[1–8] Successful tissue classification allows, for example, the discrimination between healthy and malignant cancers and the early detection of cancerous regions.[5–8] Under this scenario, optical-based techniques are powerful tools to classify tissues as they are noninvasive techniques and they can achieve significant classification effectiveness.[6–9]

Polarimetry appears to be a promising optical technique for biomedical applications because it can

be combined with other optical techniques, as regular imaging or multispectral imaging, providing a new complementary way of characterization.[10–16] In past studies, it has been shown for instance that polarimetry allows for the grading of skin diseases,[14–17] the determination of the organization and density of fibers in tissues,[16, 18, 19] the discrimination between healthy and malignant cancer tissues,[20–25] and the description of scattering mechanisms in biological samples,[1, 26] among others.

Polarimetric analysis is usually based on two groups of techniques: polarization gating (PG) techniques[27–29] and Mueller (**M**) matrix-based methods.[20–26, 30–33] It has been proved that PG analysis can be derived from the **M** matrix.[34] Moreover, the **M** matrix contains more quantitative information than polarization gating techniques, and thus, **M**-based methods are better suited to classify samples. In this way, the Mueller-Stokes formalism is chosen to conduct the present work.

The **M** matrix is 4-by-4 real matrix which contains the intensity, diattenuation, retardance, and depolarization information of the sample.[30–33]

$$\mathbf{M} = m_{00}\begin{pmatrix} 1 & \mathbf{D}^T \\ \mathbf{P} & \mathbf{m} \end{pmatrix}. \quad (1)$$

Some of the information can be directly derived, such as the sample irradiance, provided by the m_{00} coefficient, the diattenuation and the polarizance characteristics of the sample, the latter provided by the three-dimensional (3D) vectors **D** and **P**, respectively, in Equation (1). Conversely, the retardance and the depolarization information are mixed and encoded in the 3-by-3 **m** submatrix, and to be obtained, they require further mathematical treatment.

The depolarizing content reveals structural information of biological tissues because it is related to scattering process produced by sample constituents,[1, 2] and therefore, it stands as an ideal candidate for the classification of different tissues. The analysis of depolarizing content in biological samples is usually restricted to the depolarization index P_Δ metric.[9, 33, 35] However, other parameters called indices of polarimetric purity (IPP, composed by P_1, P_2 and P_3 parameters),[36, 37] which are calculated from the eigenvalues (λ_i) of the covariance matrix (**H**),[38, 39] present further physical interpretation, synthetization of the depolarization content, and differences between tissues, and in some cases, provide visualization of structures that are hidden by using the depolarization index.[40–42] In a recent review paper, Ossikovski and Vizet presented a compendium of existing depolarization parameters which define different depolarization metric spaces thus, giving different ways to describe the loss of polarization of light.[43]

The increasingly amount of depolarization metrics raises questions about the equivalence of different depolarization metric spaces, their mutual redundancy, and also, the possibility to select a particular depolarization parameter space, better suited than others, to classify a given type of biological tissues. This work addresses these questions for the first time, by comparing the efficiencies of different depolarization metric spaces (and other commonly used depolarization metrics) to classify different organic tissues. To this aim, we measure the Mueller matrix of a collection of ex vivo samples, from which different depolarization metrics, including those related to the depolarization spaces, are calculated. Among those metrics, we analyze their classification potential and viability to discriminate between different tissues by representing the experimental data into the so-called depolarization metric spaces. We also discuss the capability classification models based on the different depolarization metric spaces to discriminate between different tissues. According to the classification results, the best suited depolarization model to treat the data used in the discussed example is proposed.

2 | MATERIALS AND METHODS

2.1 | Depolarization metric spaces

In this work, five depolarization metric spaces (the detailed theoretical background is provided in Data S1) and the depolarization index P_Δ have been used to classify different tissues. Each space is constituted by three parameters. The spaces can be divided in two groups: the ones based on **H** matrix eigenvalues (the Natural space, the IPP space and the high-order depolarization indices space) and the ones based on the type I canonical depolarizer parameters (type I canonical space and the type I Lorentz space). These polarimetric spaces, recently provided in the literature,[43] were selected in this work to be analyzed for the first time in the framework of biophotonics, as they have the potential of provide larger insight on polarimetric properties of biological tissues than other more commonly used metrics.[43] In this context, the well-known and standardly used depolarization index P_Δ is selected as a reference, to be compared with results obtained by using the different polarimetric spaces highlighted in this work.

2.1.1 | Depolarization metric spaces based on H matrix eigenvalues

Natural space is composed by the λ_2, λ_3 and λ_4 eigenvalues of the **H** matrix[33]:

$$\mathbf{H} = \frac{1}{4}\sum_{k,l=4}^{4} m_{kl}(\sigma_k \otimes \sigma_l), \tag{2}$$

where m_{kj} are the elements of the **M** matrix, σ_k are the four Pauli spin matrices and the symbol $\otimes$ corresponds to the Kronecker product.

The IPP (P_1, P_2, P_3) are defined as a linear combination of **H** eigenvalues[37]:

$$P_n = \sum_{k=1}^{n} k\Delta\lambda_k, \text{where } \Delta\lambda_k = \lambda_k - \Delta\lambda_{k+1}, \text{and provided that } \sum_{i=1}^{4}\lambda_i = 1, \tag{3}$$

while the high-order depolarization indices (P_Δ, $P_\Delta^{(3)}$, $P_\Delta^{(4)}$) are a nonlinear combination of this eigenvalues,[43]

$$P_\Delta^{(m)} = \sqrt{\frac{1}{4^{m-1}-1}\left(4^{m-1}\sum_{k=1}^{4}\lambda_k^m - 1\right)}. \tag{4}$$

Note that the depolarization index is, in fact, the second-order depolarization index ($P_\Delta = P_\Delta^{(2)}$).

2.1.2 | Depolarization metric spaces based on the type I canonical depolarizer parameters

There is a second group of depolarization metric spaces, not based in the eigenvalues of the **H** matrix but in model matrices called canonical depolarizers. The type I canonical space is composed by three canonical parameters d_1, d_2 and d_3 obtained from the type I depolarization matrix:

$$\mathbf{M}_{\Delta d} = \mathrm{diag}(1\ d_1\ d_2\ d_3), \tag{5}$$

which is derived from the symmetric decomposition.[44]

The type I Lorentz space, described by L_I, $L_\mathrm{I}^{(3)}$ and $L_\mathrm{I}^{(4)}$, is a generalization of the Lorentz parameter.[45] The high-order Lorentz parameters are defined by a nonlinear combination of the type I canonical depolarizer parameters

$$L_\mathrm{I}^{(m)} = \sqrt{\frac{1}{4^{m-1}-1}\left[4^{m-1}\frac{1+d_1^{2m}+d_2^{2m}+d_3^{2m}}{\left(1+d_1^2+d_2^2+d_3^2\right)^m} - 1\right]}. \tag{6}$$

Note that the second order is, in fact, the Lorentz parameter.

2.2 | Experimental methodology

The experiment starts by measuring the Mueller matrices of 120 samples (40 tendons, 40 muscles and 40 myotendinous junction regions) at three different wavelengths, such as 625, 530 and 470 nm. All the samples were obtained from 20 different chicken thighs, and they were measured by using a complete Mueller matrix image polarimeter based on parallel-aligned liquid crystals retarders[41, 42, 46] (the image polarimeter is described in Data S1). In order to ensure similar tissue decomposition conditions, all tissues were submitted to the same measurement procedure (described in Data S1). Moreover, for each wavelength, the experimental matrices are analyzed and a region of interest (ROI) of 150×150 pixels, for each sample is selected to perform the classification (the ROI selection method is described in Section 2.4 of Data S1). Note that each pixel of the selected ROI image corresponds to a particular **M** matrix resulting into 2.7 million of **M** matrices. This important amount of depolarization information of a sample describes the polarimetric behavior of tissues and the results are studied by calculating the different depolarization metrics above mentioned. As above stated, we carried out the analysis by using data obtained from a collection of chicken thighs, the latter illustrates the interest of the above-mentioned polarimetric metrics to be used in the framework of tissues classification based on optical data. We selected to apply our approach on chicken thighs tissues for the ease of handling. The thighs were acquired in a local market of fresh meat and vegetables, and they were initially sold for human consumption purposes. Despite of standard conservation procedures in a fridge for a limited period, there is no particular restriction or hazard concerning their manipulation. However, note that the method could be tested on any biological sample, including human tissues which can be found in hospitals or specialized research institutions.

2.2.1 | Analyzed tissue description

The polarimetric response of the analyzed tissue strongly depends on its structure at different scales (milimeter, micrometer and nanometer). Tendon is a noncontractile mesodermal tissue that connects muscle to bone and it is prepared to resist tensions. It is mainly composed by type I collagen clustered into fascicles showing the same orientation as muscle bundles.[47-50] Muscle is a soft tissue composed by contractile myofibrils organized in bundles surrounded by sheets of connective showing an arrangement that is very similar to the one present in tendons. In the experiment, we measured skeletal muscle, which

has a structure closely related to the one present in tendon, but containing different subtypes of muscle fibers instead of type I collagen fibers.[51] The myotendinous junction shows a combination of the other two studied tissues. It is composed by fibers clustered into fascicles, as the previously described tissues, but in this case, fascicles of contractile (muscle) and collagen (tendon) are intermingled.[52, 53]

Further detailed description of tissues is provided in Data S1.

2.2.2 | Supervised classifiers

After the experimental measurements, all the depolarization information is used to build a supervised classifier using one of the three following methods: tree classifier,[54] linear discriminant classifier,[55] and k-nearest neighbors (kNN) classifier.[56] Tree classifier is a decision model based on a tree-like scheme[54]; linear discriminant classifier is a probabilistic method which finds a linear combination of different parameters capable of separating the data in different classes[55]; and the idea behind the kNN classifier is the selection of the k training data points, in the N space dimension, which are the nearest (in a smaller distance) to a given test data.[56] The three supervised classifiers methods are implemented using the "Statistics and Machine Learning Toolboox" in the MATLAB language and they are widely described in Data S1.

The whole of the results cannot be applied to build (train) the classifier, but the efficiency test of depolarization metric spaces requires the use of a fraction the original data for this task. In our study, the supervised classifier is built using 1% of all the measured data and the remaining 99% were used to use the classifier.

3 | RESULTS AND DISCUSSION

In this section, we qualitatively and quantitatively analyze the classification potential of the different depolarization metrics (described in Data S1) that are calculated from the experimental ROIs of the different measured tissues. The qualitative study is discussed in Section 3.1 by analyzing the depolarization distributions of measured tissues. The quantitative analysis is based on the use of supervised classification models (described in Data S1) to classify the experimental measurements into different tissues. We show how the classification efficiency depends on the application of different depolarization metric spaces. The obtained results are presented and discussed in Section 3.2.

3.1 | Depolarization metric spaces to classify experimental biological tissues: Qualitative analysis

The qualitative analysis starts by calculating the different depolarization metrics, described in Section 2.1, for every pixel in the corresponding polarimetric images of measured tissues. Taking the ensemble of pixels as a whole leads to a large amount of data to be treated and interpreted, that is, for each parameter we have 120 images of (150×150 pixels each) which gives 2.7 million of realizations. To better apprehend such amount of information, we represented them as a collection of points in the different 3D spaces. The kind of visual information that can be obtained in this way is illustrated in Figure 1. The figure represents the polarimetric information expressed in terms of the five parametric spaces that we compare in this study (Figure 1A-E), each space contains 2.7 million of points. Note that in the image different colors represent different tissues (red for tendon, blue for muscle and green for myotendinous junction tissue). The purple lines in each space show the limits of the corresponding physically realizable zone. Since we decided to use the same scale to represent the five spaces, it is possible to see that some of them occupy much more volume than others. The consequences of the latter will be discussed in detail further on. In order to no overextend the length of this manuscript, only results obtained for a wavelength of 625 nm are plotted and discussed as a representative case (530 and 470 nm results are provided in Data S1). The only difference between the results obtained at different wavelengths, in terms of depolarization response, is that muscle and myotendinous junction response is slightly less depolarizing for 530 and for 470 nm measurements than for 625 nm case.

By observing the representation in Figures 1A-E, we can differentiate two types of spaces depending on volume and shape. The linearly shaped spaces (natural, Figure 1A; IPP, Figure 1B) and type I canonical Figure 1D) occupy more volume than the nonlinear spaces (high-order depolarization index, Figure 1C) and type I Lorentz (Figure 1E). However, most of the available space of the nonlinear 3D spaces (Figure 1C,E) is filled by the experimental data, whereas some physically realizable regions in the linear 3D spaces are empty (Figures 1A,B,D). Although is clear that data points tend to spread in the allowed space, they are not randomly mixed, that is, points belonging to each particular class tend to group together.

Although Figure 1 gives relevant information of the sample response, it can lead to errors in the analysis due to the data dispersion and because certain dots can be superposed. To better visualize and describe the data

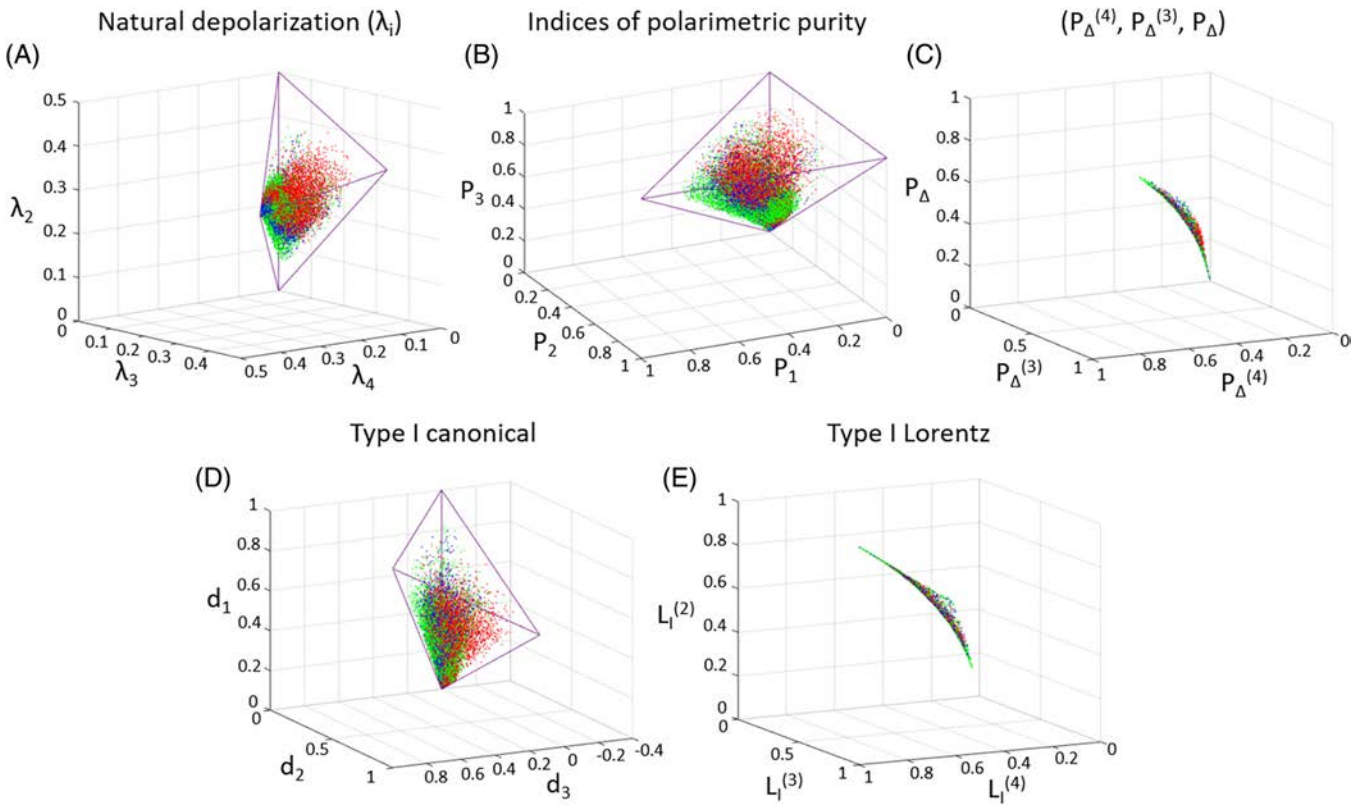

FIGURE 1 Three-dimensional representation of the experimental depolarization data collected at 625 nm for tendons (red), muscles (blue) and myotendinous junction tissues (green). The depolarization data are represented in the depolarization metric spaces: A, natural depolarization space; B, indices of polarimetric purity space; C, higher-order depolarization index space; D, type I canonical depolarization space; E, type I Lorentz depolarization space

distributions, we have calculated nonsymmetric ellipsoids representing data of different tissues at different spaces. These nonsymmetric ellipsoids are defined by a central value and six different semiaxis values, depending on their direction with respect to the center of the ellipsoid. The center of the ellipsoid corresponds to the mean value of the specific tissue data collection, and the semiaxes are calculated as the SD associated with the positive and negative values with respect to each of the three specific parameter's mean (for instance, SDs of λ_2, λ_3 and λ_4 for the natural depolarization space, or SDs of P_1, P_2 and P_3 for IPP space) (mean and SDs data can be consulted in Table S1 in Data S1). We call the ellipsoids nonsymmetric because for a given ellipsoid and a given axis, the length of the corresponding positive and negative semiaxes, do not need to be identical. Under this description, approximately 68% of tissue data are located inside of the volume of the corresponding nonsymmetric ellipsoid. Figure 2 shows the described nonsymmetric ellipsoids obtained from the raw points of the same spaces shown in Figure 1.

Note that for the sake of visualization, the axis range used in Figure 2 does not represent the full space range, but it represents the ≈10% of the physically realizable one. In other words, images in Figure 2 do not show the full space but a reduced one, where data are concentered, this particular zone being associated with a highly depolarizing behavior. Spreading of data shown in Figure 1 may be explained by different polarimetric interaction of light with tissues and nonuniformities of samples themselves. In particular, such spreading may be attributed to sample not-flatness and roughness, and to a less extent, to the different handling of chicken tissue (possible variations in defrosting times, possible pressures during dissection process, etc.) as well as biological differences between dissected chickens. However, points in Figure 1, which are located farthest from ellipsoids in Figure 2, are mostly a consequence of the measurement's noise of a discrete number of pixels, which may be produced by sample irregularities and/or direct reflections.

Figure 2 shows how the depolarization response of measured tissues is distributed over the depolarization metric spaces. Separated closed volumes without overlapping are associated to completely distinguishable tissues. Therefore, the ideal scenario in our study would correspond to three completely separated volumes (chicken muscle, myotendinous junction and tendon), that

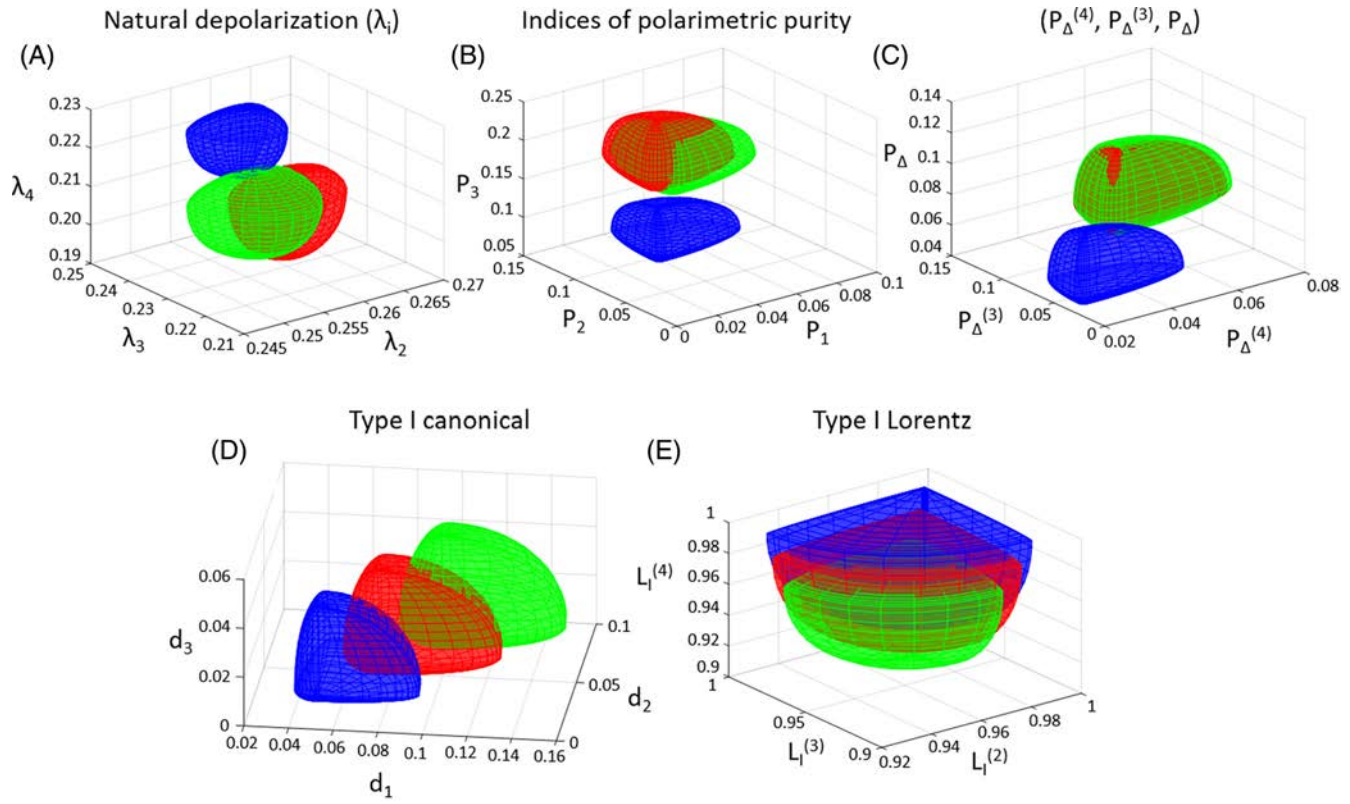

FIGURE 2 Three-dimensional representation of the experimental nonsymmetric ellipsoids (described by the mean value and the SD values) obtained for data measured at 625 nm. Data corresponding to different tissues are represented by different colors: tendon (red), muscle (blue) and myotendinous junction tissue (green). The data representation is conducted in the depolarization space: A, natural depolarization space; B, indices of polarimetric purity space; C, higher-order depolarization index space; D, type I canonical depolarization space; E, type I Lorentz depolarization space

would lead to sensitivity and specificity values for tissues discrimination of 100%. The experimental result (Figure 2) indicates that muscle gives a very distinguished response, in the eigenvalue-based spaces (Figure 2A-C), with respect to the tendon and myotendinous junction tissue. According to this result, the muscle is candidate to be well classified by using such spaces. In contrast to this, a significant uncertainty is likely to happen in the classification process between the tendon and the myotendinous junction tissue, since their response overlaps in all the spaces. From the latter, we also expect that the uncertainty in classification will be maximal in the high-order space, where the response of tendon and myotendinous junction tissue fully overlaps (Figure 2C). On the contrary, it can be expected that discrimination between tendon and myotendinous junction tissue will be optimal in the type I canonical depolarization space (Figure 2D) because the overlap between the corresponding nonsymmetric ellipsoids is minimal. At this point we can anticipate that the capacity to discriminate among different types of tissue is in connection to the tissue structures and the relative chemical composition of them. Although the structure of the analyzed tissues is very similar (all are based on arranged fibrils), tendons and myotendinous junction are both composed by collagen fascicles. Collagen fibrils provides a differentiated and characteristic polarimetric response,[15, 17] and the absence of these fibrils in muscles may produce the differentiated response observed in eigenvalue-based spaces.

Last but not least, by analyzing information in Figure 2, we can clearly see that when illumination at 625 nm is used, the muscle is the structure with larger depolarization. In particular, in Figures 2B-D, the blue ellipsoid is the one closer to the (0, 0, 0) coordinate (pure depolarizer), as well as in Figure 2E it is the ellipsoid closer to the (1, 1, 1) coordinate (note that in the type I Lorentz space, pure depolarizers are located at the position (1, 1, 1)[43]). By following the same reasoning, we note that the second tissue with larger depolarizing capability is the tendon (red ellipsoid), being the myotendinous junction tissue (green ellipsoid) the one presenting the lowest depolarizing capability. Note that although myotendinous junction response is expected to be intermediate, because its structure is a mixture of tendon and muscle fibers, the depolarization response associated to these structure lead to lower depolarization values than those exhibit by tendons and muscles.

3.2 | 3D depolarization metric spaces to classify experimental biological tissues: Quantitative analysis

Once the qualitative analysis of the results is done, a quantitative analysis is performed to identify the best suited depolarization parameters to properly classify different depolarizing tissues. The quantitative analysis is carried out by applying three classification models, tree,[54] discriminant[55] and kNN[56] (described in Data S1), to the multiwavelength results. The percentages of well-classified tissues as a function of the different depolarization metric spaces are presented in Table 1. The percentages are the mean probability to achieve a proper classification of the three tissues and they are calculated using the different models with data taken at the wavelengths 625, 530, and 470 nm, respectively. The probability results have an error of ±1% owing to the randomness of the test data selection.

The discrimination efficiency results presented in Table 1 are ordered in such a way that eigenvalue-based spaces results are presented in columns 3 to 5, and, canonical parameters-based spaces are presented in columns 7 to 8. The results obtained by using the index of depolarization are also provided (column 6) for comparison because it is one parameter widely extended in the literature.[9, 33, 35]

The efficiency results in Table 1 clearly indicate how the tree classification model is the less efficient in discriminating data whereas the kNN is the one which discriminates data the best. Moreover, for a particular wavelength, if we order the discrimination efficiencies for different depolarization metric spaces (different columns) from highest to lowest, we obtain the same result independently on the classification model selected. Therefore, kNN is selected to discuss the quantitative analysis of our results, because it is the best and because the conclusions for this particular classifier are also true for the other two.

In the following, we first compare the results obtained for the eigenvalue-based metrics (columns 3-6). Secondly, we compare the results obtained by using type I canonical parameters-based spaces (columns 7 and 8). Finally, a global conclusion, by taking into account all the spaces analyzed, is also provided.

On the one hand, by considering the efficiencies obtained by using eigenvalue-based metrics (columns 3-6), we see how the depolarization index P_Δ used alone, provides the worst results in all the cases. Therefore, it is directly deduced from the above results that the use of depolarization metric spaces instead of the depolarization index is not only better for visualization, as provided by Van Eeckhout et al. [41, 42], but also for classification. In particular, the combination of higher-order indices $P_\Delta^{(3)}$ and $P_\Delta^{(4)}$ (column 5) to the depolarization index (column 6) gives an increment of 2% to 3% (depending the wavelength) of classification success. If we compare the **H** matrix eigenvalue (column 3) or the IPP spaces (column 4) with respect to P_Δ (column 6), the efficiency increment is even more significant, with an improvement of 5% (for red channel), 8% (for blue channel) and 9% (for green channel). We would like to emphasize here that, this is a particular experiment involving three particular tissues, and the classification efficiency, as well the best depolarization metric space, will depend on the tissues under consideration. However, the obtained results clearly indicate that, regardless of the efficiency obtained for studied tissues, the use of depolarization metric

TABLE 1 Percentage of well-classified tissues as a function of the used wavelength, the classification model and the depolarization parameters

Wavelength	Classifier	Eigenvalue-based depolarization metrics				Canonical-based depolarization metrics	
		$\lambda_2, \lambda_3, \lambda_4$	P_1, P_2, P_3	$P_\Delta, P_\Delta^{(3)}, P_\Delta^{(4)}$	P_Δ	d_1, d_2, d_3	$L_I, L_I^{(3)}, L_I^{(4)}$
625 nm	Tree	58	58	55	53	52	50
	Discriminant	59	59	60	57	57	55
	kNN (50)	**65**	**65**	**62**	**60**	**60**	**55**
530 nm	Tree	51	51	47	46	55	50
	Discriminant	54	54	51	49	62	49
	kNN (50)	**59**	**59**	**53**	**50**	**64**	**50**
470 nm	Tree	52	52	48	46	52	48
	Discriminant	56	55	52	51	60	47
	kNN (50)	**60**	**59**	**54**	**52**	**62**	**49**

Bold values indicate the best classification results for each depolarization space and wavelength measurement.

spaces can improve the classification potential obtained by P_{Δ}.

Once we realize that eigenvalues-based depolarization spaces (**H** matrix eigenvalues, IPP and high-order depolarization index) provide better results in terms of tissue classification than P_{Δ}, we focus on determining which one of these three spaces is more suitable for classification. By checking the efficiencies in columns 3 to 5, we see that the worst results are obtained by the high-order space (column 5) whereas **H** matrix eigenvalues and IPP provide the best (and identical if taking into account 1% associated error) results.

We think, although we do not have to date a fundamental proof, the fact that the high-order depolarization space (column 5 in Table 1) provides not as good results as the **H** matrix eigenvalues or the IPP spaces arises from the nonlinear mathematical origin of such space. Such nonlinear combinations reduce the volume occupied by physically valid data in the parametric space, which automatically compresses the information (see Figure 1). The compression of information implies that the differences between tissue responses are reduced, thus reducing the classification efficiency. We would like to highlight that this conclusion arises from a heuristic approach, because we cannot infer the observed loss of information related to nonlinear spaces directly from the mathematical relations itself. However, we have clearly observed this tendency in the case of all the analyzed tissues and for all the wavelengths. As will be further discussed, this situation is also observed in the canonical case.

At this point, the **H** matrix eigenvalues space (column 3) and IPP space (column 4) appears to be the best options to represent depolarization information for tissue classification. Recent papers show that the IPP space can be used to provide a physical interpretation of the studied samples[36, 37, 40] together with an improvement sample visualization with respect to other parameters (**H** matrix eigenvalues or depolarization index).[41] The improvement in visualization quality and contrast is related to the increment of volume. However, as it can be seen in Table 1, the classification potential of both blocks of parameters is always the same. We think that this is because the IPP are a linear combination of eigenvalues, λ_i. Taking this in mind, as the used classification models improve the classification efficiency by conducting linear combinations of data, from the point of view of the classifiers, either IPP or λ_i are equivalent. Therefore, taking into account that **H** matrix eigenvalues space and IPP space provide identical classification results but the latter provides larger tissues visualization, then the use of the IPP space to get depolarization information for classification issues, is recommended.

On the other hand, analogously to the discussion provided above, we can perform a comparative study between results obtained using canonical-based spaces (columns 7 and 8 in Table 1). We clearly observe that the type I canonical parameters (d_i for $i = 1, 2, 3$) space provides significantly better results than the type I Lorentz parameters space. In analogy with our previous discussion, we also consider that the non-linear mathematical origin of the type I Lorentz space leads to a compression of information, and therefore to a loss in classification efficiency. Under this scenario, if canonical-based spaces have to be used, then the type I canonical parameters should be used instead of the Lorentz canonical parameters.

Finally, according to the conclusions to which we have arrived in the previous discussions, we compare, in terms of classification potential, the best space based on eigenvalues (IPP) with the best space based on canonical metrics (type I canonical parameters). By comparing these two spaces, it can be shown that the best efficiency results depend on the wavelength used. However, the type I canonical parameters space presents the best efficiency values for the 470- and 530-nm channels, the IPP space presents the best efficiency for the 625 nm case.

This efficiency dependence with the wavelength can be understood by taking into account the metrics associated to these two spaces. When the **M** matrix has no diattenuation and polarizance content, d_i parameters can be described as a linear combination of λ_i.[43] However, if the **M** matrix contains diattenuation or polarizance response, then, d_i parameters and λ_i are no more linearly related. In theory, the symmetric decomposition[44] needed to obtain the d_i parameters fully separates the diattenuation and retardance from the depolarization content, but in the case of **H** matrix eigenvalues, λ_i, this content is not completely separated. Therefore, the λ_i values are influenced by the diattenuation or polarizance.[33] Therefore, the diattenuation and polarizance of the sample can directly affect the values of λ_i and thus, their potential for classifying different tissues when using the IPP space (note that IPPs depend on λ_i; described in Data S1).

To further analyze this fact, we have calculated probability histograms for the diattenuation and polarizance present in our experimental samples (three tissues types) for the three wavelengths studied. The histograms show the proportion (probability density) of pixels with different $|\mathbf{D}|$ and $|\mathbf{P}|$ (see Equation (1)) values. Results are shown in different graphics in Figure 3 ordered in two rows and three columns. Each column of graphics in the figure corresponds to a given wavelength. Graphics in the first row of the figure correspond to diattenuation data, and graphics in the second row of the figure to

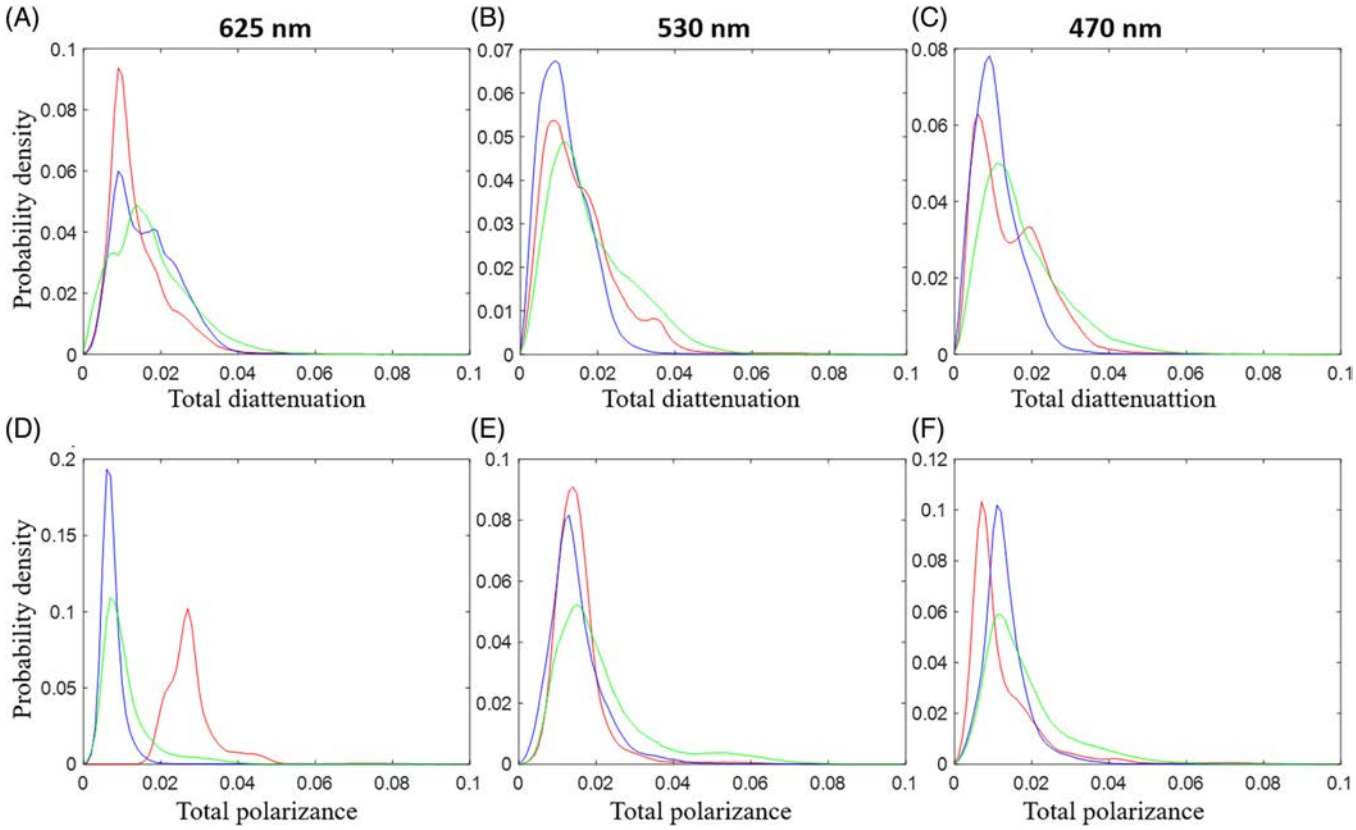

FIGURE 3 Histogram of the total diattenuation response of the different tissues using, A, 625-nm wavelength; B, 530-nm wavelength; C, 470-nm wavelength. Total polarizance response using the same, D, 625-nm wavelength; E, 530-nm wavelength; F, 470-nm wavelength. Tendon is represented in red, muscle in blue and the myotendinous junction tissue in green

polarizance data. To separate the contributions of different tissues, tendons are represented in red, muscles in blue and the myotendinous junction tissues in green.

The diattenuation histograms show that the diattenuation content of the different tissues is almost the same for all tissues and for all the wavelengths. In consequence, diattenuation cannot be used to distinguish among tissues. In this particular case, the diattenuation channel can be considered as a source of "information noise" which may hinder the performance of the classification algorithm. On the contrary, the polarizance response of tendons (red color) is significantly different from that of the other two tissues for the 625-nm channel. Moreover, the central polarizance of the tendon case decreases with the wavelength of light. In contrast, the polarizance of muscle and myotendinous junction tissue increases when wavelength shortens. This particular polarimetric behavior produces three different scenarios depending on the wavelength used to illuminate the samples.

First, distinguishable polarizance results are produced illuminating with 625 nm (Figure 3D). The mean polarizance of the tendon is 0.03, while the same characteristic of the other two tissues is approximately 0.01. Thus, polarizance gives relevant information to classify the tissue and this information is present in the λ_i. As this classification information is relevant, the polarizance improves the classification efficiency of the IPP space (with polarizance contribution) with respect that of the type I canonical parameters space (note that d_i have not polarizance contribution). Therefore, in Table 1, IPP space provides better efficiencies than type I canonical parameters space (65% and 60%, respectively) for the red channel.

Second, by using the 530-nm wavelength, the polarizance and diattenuation responses are almost the same for all the tissues studied, and thus, they do not provide relevant information. Since this irrelevant information appears in the **H** eigenvalues, λ_i, as a source of "information noise," but not in the d_i parameters, the classification efficiency of the IPP space is reduced with respect to of the type I canonical parameters space. Consequently, canonical space provides better classification efficiencies than IPP space in the 530 nm case (64% vs 59%, respectively, in Table 1).

Finally, when illuminating the tissues with 470 nm, an intermediate case between the two previous ones is observed. The polarizance response provides some new

valuable information in terms of differences between tissues, but it is not enough to counter the irrelevant information given by the diattenuation content. As a result, the IPP space classification efficiency appears to be slightly smaller than the efficiency of the type I canonical parameters (59% vs 62%, respectively, in Table 1).

Summarizing the discussion provided in Section 4.2, we can state that among the five spaces compared in this study, the IPP space and the type I canonical parameters space perform the best. In absence of diattenuation or polarizance, the IPP space and the type I canonical parameters space provide are comparable. If diattenuation and polarizance information are present and show a discrimination ability, then the IPP space can perform better than the type I canonical parameters space, However, if the samples present diattenuation or polarizance but this information does not discriminate between tissues, then, the type I canonical parameters space will lead to better classification efficiencies as it is not affected by such information. Note that the **D** and **P** content in samples may depend on wavelength, as proved in our analysis, so a multichannel analysis is recommended when possible as a good practice in the analysis of polarimetric images of tissues.

Therefore, if the classification efficiency is considered as the main metric to guide the use of the polarimetric data, then based on the results of this study for the particular sample of chicken tissues discussed here, we recommend the use of a model based on the type I canonical parameters space. This is because if the sample presents non-discriminating polarizance or diattenuation information, the type I canonical parameters space is not affected by them. On the contrary if diattenuation and polarizance provide non-negligible discrimination capacity, then the IPP-based space is to be preferred. Finally, since the evaluation IPP requires less computation time than the evaluation of the type I canonical parameters, we also recommend the use of the IPP-based space when diattenuation and polarizance are negligible.

4 | CONCLUSIONS

In this work, we discussed the efficiency of different groups of depolarizion metrics to classify tissues. Such groups of observables are composed of three depolarization parameters which are characteristic of different depolarization metric 3D spaces. They are divided into two main groups: derived from **H** matrix eigenvalues (eigenvalue-based spaces) and derived from the type I canonical depolarization parameters (canonical-based spaces).

To this aim, we measured the Mueller matrix of 120 chicken thighs. Three different tissues are studied (40 muscles, 40 tendons and 40 myotendinous junction tissues). To ensure pure tissues (ie, without contributions of other surrounding tissues type), a region of interest selecting method is applied, resulting in a collection of images of 150×150 pixels.

The analysis of the suitability of the depolarization metric spaces to classify samples is conducted from a qualitative (Section 3.1) and a quantitative (Section 3.2) point of view. The qualitative observation of the results is conducted through the visualization of the data at the studied 3D spaces. It shows that muscles are significantly differentiated from the other two tissues by using **H** matrix eigenvalues space, allowing a successful muscle classification. However, tendons and myotendinous junction tissues occupy similar regions in such spaces, being the best visualization obtained by using the type I canonical space. The quantitative analysis is performed by using three different supervised classifications models: tree classifier, linear discriminant classifier and kNN classifier. From those models, and for the particular case of the samples used in the present discussion, the higher classification efficiencies are obtained by using the kNN model, so this supervised model is selected.

Regarding to the depolarization metric spaces, we have conducted a first comparative between **H** matrix eigenvalue-based spaces, and they have also been compared with the standard depolarization index P_Δ. We have shown that depolarization spaces provide better classification efficiencies than the P_Δ, which is commonly used in polarimetric community, so the inclusion of depolarization metric spaces in polarimetric studies instead of P_Δ is highly recommended. From the eigenvalue-based spaces, the highest efficiencies are obtained for the IPP and the **H** matrix eigenvalues spaces, being the former recommended as it also provides physical interpretation of data. We have performed a second comparison between canonical spaces, the type I canonical space providing much better results than the type I Lorentz space, in terms of classification efficiency.

Finally, the two selected spaces, IPP space, and type I canonical space, are compared to determine the most suitable one to build a classification model for the studied tissues. We have observed that the best efficiencies to classify a tissue are reached by one or the other spaces depending on the wavelength illuminating the sample. This situation is explained by the relation between the values of the **H** matrix eigenvalues and the presence of diattenuation and polarizance in the sample. In the case of nonpolarizing and nondiattenuating samples, both spaces are equivalent in terms of discrimination efficiency because in such conditions the two spaces are

related by a linear combination. Moreover, it has been shown that samples presenting nondiscriminating polarizance or diattenuation information, are better classified with the type I canonical space parameters, whereas samples presenting discriminating polarizance or diattenuation information, are better classified by using the IPP space.

The method proposed in the present is general, and we believe that it can be applied to any type of sample. The fact that the use of the method has been illustrated here with a particular case of study does not imply any intrinsic limitation. Taking in account the increasing place that polarimetry is taking in biophotonics; we think that the proposed method has the potential to open new possibilities in the field and to improve the existing approaches providing a means to achieve optimal tissue classification efficiencies. Moreover, since each biological tissue (human, animal or vegetal) shows a singular polarimetric response the proposed protocol can in principle be applied to define the optimal model for the specific application. In this sense an experimental data set (Mueller matrices of the tissues under investigation) must be measured, and then used to feed the statistical data protocol discussed in this manuscript. If properly applied, the method will provide the set of observables which optimize the ability of an automatic classifier to handle the data. The fact that different data sets will eventually result in different sets of optimal observables for subsequent classification, is inherent to the optical properties of the samples themselves, and not a limitation of the method proposed here.

ACKNOWLEDGMENTS

We acknowledge the financial support of Spanish MINECO (RTI2018-097107-B-C31 and Fondos FEDER); Catalan Government (2017-SGR-001500).

ORCID

Albert Van Eeckhout https://orcid.org/0000-0003-2540-2746

REFERENCES

[1] V. V. Tuchin, *Tissue Optics: Light Scattering Methods and Instruments for Medical Diagnosis*, SPIE Press, Bellingham **2007**.
[2] V. V. Tuchin, L. Wang, D. A. Zimnyakov, *Optical Polarization in Biomedical Applications*, Springer-Verlag, Berlin Heidelberg **2006**.
[3] M. Nagendran, D. P. Riordan, P. B. Harbury, T. J. Desai, *Elife* **2018**, *7*: e30510.
[4] S. H. Youn, T. Sim, A. Choi, J. Song, K. Y. Shin, I. K. Lee, H. M. Heo, D. Lee, J. H. Mun, *Comp. Biol. Med.* **2015**, *61*(1), 92.
[5] J. M. Gálvez, D. Castillo, L. J. Herrera, B. San Román, O. Valenzuela, F. M. Ortuño, I. Rojas, *PloS One* **2018**, *13*(5), e0196836.
[6] L. van Manen, J. Dijkstra, C. Boccara, E. Benoit, A. L. Vahrmeijer, M. J. Gora, J. Mieog, *J Cancer Res. Clini. Oncol.* **2018**, *144*(10), 1967.
[7] L. Marcu, S. A. Boppart, M. R. Hutchinson, J. Popp, B. C. Wilson, *J. Biomed. Opt.* **2018**, *23*(2), 021103.
[8] Y. A. Khristoforova, I. A. Bratchenko, O. O. Myakinin, D. N. Artemyev, A. A. Moryatov, A. E. Orlov, S. V. Kozlov, V. P. Zakharov, *J. Biophoton.* **2019**, *12*(4), e201800400.
[9] V. P. Zakharov, I. A. Bratchenko, D. N. Artemyev, O. O. Myakinin, S. V. Kozlov, A. A. Moryatov, A. E. Orlov, *Neurophoton. Biomed. Spect.* **2019**, *1*, 449.
[10] J. Qi, D. S. Elson, *J. Biophotonics* **2017**, *10*, 950.
[11] I. J. Vaughn, B. G. Hoover, J. S. Tyo, *Proc. SPIE* **2012**, *8364*, 83640S.
[12] B. G. Hoover, J. S. Tyo, *Appl. Opt.* **2007**, *46*(34), 8364.
[13] G. Anna, F. Goudail, D. Dolfi, *Opt. Exp.* **2011**, *19*(25), 25367.
[14] A. S. Alenin, L. Morrison, C. Curiel, J. S. Tyo, *Proc. SPIE* **2011**, *8160*, 816014.
[15] L. Graham, Y. Yitzhaky, I. Abdulhalim, *J. Biomed. Opt.* **2013**, *18*, 111403.
[16] T. Yasui, Y. Tohno, T. Araki, *J. Biome. Opt.* **2004**, *9*, 259.
[17] Y. Yitzhaky, L. Graham, I. Abdulhalim, *Proc. of SPIE* **2013**, *8856*, 88562J.
[18] K. Komatsu, L. Mosekilde, A. Viidik, M. Chiba, *Anat. Rec.* **2002**, *268*, 381.
[19] M. Borovkova, V. A. Ushenko, A. V. Dubolazov, O. Y. Vanchulyak, O. G. Ushenko, A. V. Bykov, I. Meglinski, *PLOS One* **2019**, *14*(5), e0214494.
[20] T. Novikova, A. Pierangelo, A. De Martino, A. Benali, P. Validire, *Opt. Phot. News* **2012**, *23*, 26.
[21] A. Pierangelo, A. Nazac, A. Benali, P. Validire, H. Cohen, T. Novikova, B. H. Ibrahim, S. Manhas, C. Fallet, M. R. Antonelli, A. De Martino, *Opt. Exp.* **2013**, *21*, 14120.
[22] E. Du, H. He, N. Zeng, M. Sun, Y. Guo, J. Wu, S. Liu, H. Ma, *J. Biomed. Opt.* **2014**, *19*, 076013.
[23] V. Ushenko, A. Sdobnov, A. Syvokorovskaya, A. Dubolazov, O. Vanchulyak, A. Ushenko, Y. Ushenko, M. Gorsky, M. Sidor, A. Bykov, I. Meglinski, *Photonics* **2018**, *5*(4), 54.
[24] M. Kupinski, M. Boffety, F. Goudail, R. Ossikovski, A. Pierangelo, J. Rehbinder, J. Vizet, T. Novikova, *Biomed. Opt. Exp.* **2018**, *11*(9), 5691.
[25] B. Liu, Y. Yao, R. Liu, H. Ma, L. Ma, *Opt. Commun.* **2019**, *433*, 60.
[26] N. Ghosh, M. F. Wood, I. Vitkin, *J. Biomed. Opt.* **2008**, *3*, 044036.
[27] P. Shukla, A. Pradhan, *Appl. Opt.* **2009**, *48*, 6099.
[28] B. Kunnen, C. Macdonald, A. Doronin, S. Jacques, M. Eccles, I. Meglinski, *J. Biophoton.* **2015**, *8*, 317.
[29] C. W. Sun, C. Y. Wang, C. C. Yang, Y. W. Kiang, I. J. Hsu, C. W. Lin, *Opt. Lett.* **2001**, *26*, 432.
[30] D. Goldstein, *Polarized Light*, 2nd ed., Marcel Dekker, New York, NY **2003**.
[31] E. Garcia-Caurel, R. Ossikovski, M. Foldyna, A. Pierangelo, B. Drévillon, A. De Martino, in *Advanced Mueller Ellipsometry Instrumentation and Data Analysis* (Eds: M. Losurdo, K. Hingerls), Springer-Varlag, Berlin **2013**.
[32] R. A. Chipman, *Polarimetry: Handbook of Optics*, 2nd ed., McGrawHill, New York, NY **1995**.
[33] J. J. Gil, R. Ossikovski, *Polarized Light and the Mueller Matrix Approach*, CRC Press, Boca Raton, FL **2016**.

[34] A. Lizana, A. Van Eeckhout, K. Adamczyk, C. Rodríguez, J. C. Escalera, E. Garcia-Caurel, I. Moreno, J. Campos, *J. Biomed. Opt.* **2017**, *22*, 056004.
[35] J. J. Gil, E. Bernabeu, *Opt. Acta* **1986**, *33*, 185.
[36] J. J. Gil, J. M. Correas, P. A. Melero, C. Ferreira, *Monog. Sem. Mat. G. Galdeano* **2004**, *31*, 161.
[37] I. San José, J. J. Gil, *Opt. Commun.* **2011**, *294*, 38.
[38] S. R. Cloude, *Optik* **1986**, *75*, 26.
[39] S. R. Cloude, *SPIE Proc.* **1989**, *1166*, 177.
[40] A. Van Eeckhout, A. Lizana, E. Garcia-Caurel, J. J. Gil, R. Ossikovski, J. Campos, *Opt. Lett.* **2017**, *42*, 4155.
[41] A. Van Eeckhout, A. Lizana, E. Garcia-Caurel, J.J Gil, A. Sansa, C. Rodríguez, I. Estévez, E. González, J. C. Escalera, I. Moreno, and J. Campos, *J. Biophoton.*, *11*(14): e201700189 (**2018**)x
[42] A. Van Eeckhout, E. Garcia-Caurel, T. Garnatje, M. Durfort, J. C. Escalera, J. Vidal, J. J. Gil, J. Campos, A. Lizana, *PLoS One* **2019**, *14*(3): e0213909.
[43] R. Ossikovski, J. Vizet, J. Opt, *Soc. Am. A* **2019**, *36*, 1173.
[44] R. Ossikovski, *J. Opt. Soc. Am. A* **2009**, *26*, 1109.
[45] R. Ossikovski, *J. Opt. Soc. Am. A* **2010**, *27*, 123.
[46] A. Peinado, A. Lizana, J. Vidal, C. Iemmi, J. Campos, *Opt. Exp.* **2010**, *18*, 9815.
[47] J. Kastelic, A. Galeski, E. Baer, *Connect. Tissue Res.* **1978**, *6*, 11.
[48] D. L. Butler, E. S. Grood, F. R. Noyes, R. F. Zernucke, *Exer. Sports Sci. Rev.* **1978**, *6*, 125.
[49] R. James, G. Kesturu, G. Balian, A. B. Chhabra, *J. Hand Surg. Am* **2008**, *33*(1), 102.
[50] D. J. Hulmes, *Struct. Biol.* **2002**, *137*(1–2), 2.
[51] S. Schiaffino, C. Reggiani, *Physiol. Rev.* **2011**, *91*(4), 1447.
[52] B. Charvet, F. Ruggiero, D. Le Guellec, *Musc. Liga. Tend. J.* **2012**, *2*(2), 53.
[53] H. Asahara, M. Inui, M. K. Lotz, *J. Bone Miner. Res.* **2017**, *32* (9), 1773.
[54] L. Breiman, J. H. Friedman, R. A. Olshen, C. J. Stone, *Classification and Regression Trees*, Chapman & Hall, Boca Raton, FL **1984**.
[55] Y. Guo, T. Hastie, R. Tibshirani, *Biostatistics* **2007**, *8*(1), 86.
[56] T. Mitchell, *Machine Learning*, McGraw-Hill, New York **1997**.

SUPPORTING INFORMATION

Additional supporting information may be found online in the Supporting Information section at the end of this article.

How to cite this article: Van Eeckhout A, Garcia-Caurel E, Ossikovski R, et al. Depolarization metric spaces for biological tissues classification. *J. Biophotonics*. 2020;13:e202000083. https://doi.org/10.1002/jbio.202000083

PLOS ONE

RESEARCH ARTICLE

Depolarizing metrics for plant samples imaging

Albert Van Eeckhout[1]*, Enric Garcia-Caurel[2], Teresa Garnatje[3], Mercè Durfort[4], Juan Carlos Escalera[1], Josep Vidal[1], José J. Gil[5], Juan Campos[1], Angel Lizana[1]

1 Grup d'Òptica, Physics Department, Universitat Autònoma de Barcelona, Bellaterra, Spain, **2** LPICM, CNRS, Ecole Polytechnique, Université Paris-Saclay, Palaiseau, France, **3** Botanical Institute of Barcelona (IBB, CSIC-ICUB), Barcelona, Spain, **4** Departament de Biologia Cel·lular, Fisiologia & Immunologia, Facultat de Biologia, Universitat de Barcelona, Barcelona, Spain, **5** Universidad de Zaragoza, Zaragoza, Spain

* albert.vaneeckhout@uab.cat

Citation: Van Eeckhout A, Garcia-Caurel E, Garnatje T, Durfort M, Escalera JC, Vidal J, et al. (2019) Depolarizing metrics for plant samples imaging. PLoS ONE 14(3): e0213909. https://doi.org/10.1371/journal.pone.0213909

Editor: Patrizia Restani, Università degli Studi di Milano, ITALY

Received: October 2, 2018

Accepted: March 4, 2019

Published: March 14, 2019

Data Availability Statement: All relevant data are within the manuscript and its Supporting Information files.

Funding: This research was supported by the Spanish MINECO (FIS2015-66328-C3-1-R, FIS2015-66328-C3-3-R and fondos FEDER, all to JC); Catalan Government (SGR 2014-1639 to JC). The funders had no role in study design, data collection and analysis, decision to publish, or preparation of the manuscript.

Competing interests: The authors have declared that no competing interests exist.

Abstract

Optical methods, as fluorescence microscopy or hyperspectral imaging, are commonly used for plants visualization and characterization. Another powerful collection of optical techniques is the so-called polarimetry, widely used to enhance image contrast in multiple applications. In the botanical applications framework, in spite of some works have already highlighted the depolarizing print that plant structures left on input polarized beams, the potential of polarimetric methods has not been properly exploited. In fact, among the few works dealing with polarization and plants, most of them study light scattered by plants using the Degree of Polarization (DoP) indicator. Other more powerful depolarization metrics are nowadays neglected. In this context, we highlight the potential of different depolarization metrics obtained using the Mueller matrix (MM) measurement: the Depolarization Index and the Indices of Polarimetric Purity. We perform a qualitative and quantitative comparison between DoP- and MM-based images by studying a particular plant, the Hedera maroccana. We show how Mueller-based metrics are generally more suitable in terms of contrast than DoP-based measurements. The potential of polarimetric measurements in the study of plants is highlighted in this work, suggesting they can be applied to the characterization of plants, plant taxonomy, water stress in plants, and other botanical studies.

Introduction

Optical methods, as fluorescence microscopy or hyperspectral imaging, have proved their utility for the characterization and visualizations of plants and some of their structures [1–4]. One optical method, widely used for enhanced image contrast and characterization of samples are the polarimetric methods. However, they have barely been studied for the analysis of plants.

Polarization is a physical property of light exploited in a large number of applications, as a complementary tool to other techniques or constituting a completely different approach [5–7].

In recent decades, a large number of works have highlighted an interest in analyzing the polarimetric print left by biological samples when interacting with polarized light [8]. As a

consequence, polarimetric techniques are commonly incorporated in different fields in order to study and characterize biological samples. For instance, polarimetric methods are successfully used in some medical applications, like in calculating the sugar concentration in blood in diabetics[9], or for the early diagnosis of some types of cancer [10, 11], including skin cancer [12, 13], colon cancer [14, 15], breast cancer [16], and others [17].

Polarized light is also used for curative processes [18–20]. Medical cases being treated with polarized light include severe second degree burns [18], wounds [19], leg ulcers, psoriasis and eczema [20], and the improvement of blood's immunological response [21].

This well-known usefulness of polarized light and polarimetric techniques when dealing with biological tissues suggests their suitability in botanical applications. In the 80s, the interest in using polarized light for the characterization of botanical samples was explored by different authors [22–25]. In general, the studies were intended for remote sensing and were done to explore Degree of Polarization as an aid to vegetation classification [26]. They showed that light scattered at different leaf layers and structures presents different depolarizing characteristics and that this partially-polarized light may be described by the Stokes vector (see, for instance, [22, 27]).

After the above-mentioned pioneering works, most studies of plants based on polarimetric methods focused on the depolarization signal (as opposed to retardance or diattenuation) as it is the polarimetric channel leading to the most polarimetric sensitivity. Furthermore, nearly all works restrict their analyses to the use of the most basic depolarization metric, the Degree of Polarization (DoP) associated with the light reflected by or transmitted in plants [22, 25, 26, 28–30]. This DoP can be readily calculated from the Stokes vector parameters of the studied light [31, 32],

$$DoP = \frac{\sqrt{S_1^2 + S_2^2 + S_3^2}}{S_0}, \tag{1}$$

where the Si (i = 0,1,2,3) are the Stokes parameters of the light transmitted, reflected, or scattered by the sample. Note that throughout this manuscript we use the Stokes-Mueller (S-M) formalism to describe the polarimetric characteristics of light and/or matter. The basic concepts of the S-M formalism are taken for granted in this manuscript and more details can be found in the specialized bibliography [31–34].

Some areas of interest related to botanical applications have been explored based on DoP calculations. For instance, the DoP has been applied to determine the water stress on plants [32], to monitor crop growth [29], or to discriminate land mines from natural backgrounds [35]. The measurement of polarization properties such linear, circular dichroism and birefringence as well as the DoP of light reflected by plants has been shown to be of great importance in research related to plant photosynthesis [36–38]. The effect of polarized and unpolarized light on the growth of some plants has also been investigated [39]. Vanderbilt et al. [30] found no evidence of hyperspectral variation in the polarized portion of the reflectance in the leaves of the five species they measured.

Despite the aforementioned collection of works based on the DoP indicator, polarimetric techniques have not been consolidated in botanical applications. Rather, in the last decade, they have fallen into oblivion, with the exception of some sporadic works [30, 36–39, 40].

The above-mentioned works show that different plant structures will depolarize light differently and thus, using depolarization as an observable, can be used to visualize structural properties (or changes) which remain veiled under nonpolarized light. Recent theoretical developments have shown that the depolarization phenomena can be more accurately described using a set of parameters deduced from the Mueller matrix than with the classical DoP deduced from the Stokes vector. The parameters obtained using the Mueller matrix have

largely proved their significance in the evaluation of the depolarizing characteristics of samples, but they are not being applied in the botanical context. In fact, one of the purposes of this work is to reverse the decreasing tendency observed in recent years of botanical studies based on polarization and to show for the first time the potential of some depolarizing factors in plant imaging and characterization. We think that underscoring the significance of polarimetry in botanical applications may allow readers to adopt less destructive methods and to seek new botanical applications, which would have a high social impact, as plants are primary producers and the basis of the food chain.

In particular, we study different depolarization-related observables calculated using the Mueller matrix (MM) measurement in the botanical context. On one hand, we study the Depolarization Index P_Δ which was first proposed by J.J. Gil and E. Bernabeu [41], which constitutes a standard magnitude in the polarimetric community when dealing with depolarizers [31–34]. On the other hand, we focus on the so-called Indices of Polarimetric Purity (IPPs) [42, 43], which have been successfully used to enhance the image contrast of polarimetric images of animal tissues [44], unveiling physiologic structures which otherwise would have remained invisible. In fact, the interest in IPPs relies on the fact that each of them is sensitive to specific depolarization mechanisms. Since depolarization is related to the structure of tissues by the way they scatter light, the specificity of IPPs to different depolarization mechanisms can be used to finely discriminate among different tissue structures which scatter light in specific ways [44, 45]. The suitability of the aforementioned depolarizing factors and techniques is highlighted in this work by the study of light scattered by leaves of *Hedera maroccana*. At this point, we would like to emphasize that the choice of this particular species for this work was made because it was easily available to the authors. The choice is by no means exhaustive and shows that the use of polarized light can be extended to any type of leaf or vegetal tissue sample, provided it transmits enough light. The experimental measurements and polarimetric treatment discussed in this paper are provided to illustrate the suitability of the different depolarization indices in the study of vegetal tissues, which can be of interest in scientific and industrial areas related to, among others, pharmaceuticals, the food sector, and botany.

Material and methods

In this section, we briefly review the mathematical fundamentals of different polarimetric indicators used to analyze the studied plants (subsection 2.1). We also include a brief description of the plant used for the polarimetric analysis, the *Hedera maroccana* (subsection 2.2), and we give some experimental details of the image polarimeter used to calculate the Mueller matrix of the samples (subsection 2.3).

Mathematical background

We start first by reviewing the mathematical formulation of the depolarization metrics we use to characterize botanical samples. The depolarization index, P_Δ, is a single-number metric that characterizes the depolarization of a MM and is defined as [41, 46],

$$P_\Delta = \frac{\sqrt{\sum_{ij=0}^{3} M_{ij}^2 - M_{00}^2}}{\sqrt{3} M_{00}}, \tag{2}$$

where M_{ij} are the different coefficients of the MM. The P_Δ equals 1 for nondepolarizing samples (samples that do not decrease the degree of polarization of any totally-polarized input beam) and equals 0 for an ideal depolarizer (a sample that fully depolarizes an input beam

independently of its polarization). In fact, the P_Δ is proportional to the Euclidean distance between an ideal depolarizer and the specific depolarizer [42].

Thereafter, we review another set of depolarizing indicators that can also be obtained from the MM, three real magnitudes labelled as P_1, P_2, and P_3 (with values from 0 to 1 each), known as Indices of Polarimetric Purity (IPPs) [42–44]. The idea behind IPPs is that the response of any depolarizer can be synthesized as the incoherent sum of four nondepolarizing components. In this context, IPPs represent the relative statistical weight of each one of the pure components, which allows us to differentiate between different types of depolarizers [45, 47]. Moreover, by using these three magnitudes as a coordinate system, a new representation of depolarizers, the so-called *Purity-Space*, is obtained. This is a very intuitive space because every possible depolarizer occupies a different spatial position in a tetrahedron inscribed within the *Purity-Space* [43, 47]. Thus, the physical interpretation of IPPs further synthesizes the depolarizing information of samples because every combination of IPPs is linked to a different depolarizing mechanism [45, 48] — in contrast to the P_Δ indicator, which gives an overall depolarizing estimation.

These three IPP magnitudes are defined as follows in terms of the relative differences between the four eigenvalues (taken in decreasing order $\lambda_0 \geq \lambda_1 \geq \lambda_2 \geq \lambda_3$) of the covariance matrix H associated with the MM [43].

$$P_1 \equiv \frac{\lambda_0 - \lambda_1}{\mathrm{tr}\mathbf{H}}, P_2 \equiv \frac{\lambda_0 + \lambda_1 - 2\lambda_2}{\mathrm{tr}\mathbf{H}}, P_3 \equiv \frac{\lambda_0 + \lambda_1 + \lambda_2 - 3\lambda_3}{\mathrm{tr}\mathbf{H}} \tag{3}$$

Furthermore, the P_Δ can also be calculated from the IPPs as [43],

$$P_\Delta = \frac{1}{\sqrt{3}}\sqrt{2P_1^2 + \frac{2}{3}P_2^2 + \frac{1}{3}P_3^2}. \tag{4}$$

Nondepolarizing systems are characterized by $P_\Delta = P_1 = P_2 = P_3 = 1$. In the other limiting case, the values $P_\Delta = P_1 = P_2 = P_3 = 0$ correspond to an ideal depolarizer. In general, the indices of purity are restricted by the following inequalities [43],

$$0 \leq P_1 \leq P_2 \leq P_3. \tag{5}$$

The aforementioned depolarizing metrics (Eqs (2) and (3)) are obtained from the MM of the sample and provide more complete and meaningful information of samples than basic DoP (Eq (1)).

Plant sample description

In order to show the suitability of these MM-based metrics for experimental data, we have measured the Mueller matrix (MM) of a plant leaf. In particular, we measured a *Hedera maroccana* McAll. (Araliaceae) leaf, labelled as Sample A.

This is a climbing plant native to the Atlantic coast of Morocco. This species, which also grows in the Mediterranean area, is widely cultivated as an ornamental plant and is sometimes naturalized. The main diagnostic characteristics of this species are its foliar trichomes.

An herbarium voucher of the studied species is deposited in the Herbarium of the Botanical Institute of Barcelona (*Hedera maroccana*, BC843411). An image of the *Hedera maroccana* measured and considered in this work is given in Fig 1.

Mueller matrix polarimeter

To determine the Mueller matrix (MM) of sample A, we used the complete image polarimeter sketched in Fig 2. The polarimeter mainly consists of two arms; the first one is used for

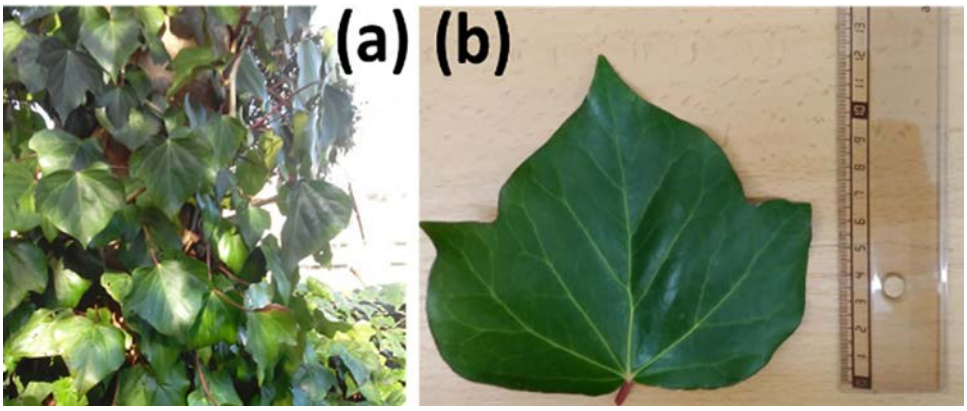

Fig 1. Plant sample used for the polarimetric analysis: (a) *Hedera maroccana* plant; (b) *Hedera maroccana* measured leaf (Sample A).

https://doi.org/10.1371/journal.pone.0213909.g001

illumination and polarization generation, while the second arm is used for imaging and polarization analysis. The sample is always placed between the two arms. Measures on sample A were always conducted in transmission configuration. What is more, the images shown in this work were conducted with the obverse of the leaf looking at the light source and the reverse looking at the CCD camera, as shown in the sketch given in Fig 2. It was also measured by flipping over the sample, i.e., with the reverse looking at light source and the obverse at the CCD camera. Results were quite similar, but the contrast obtained was slightly lower in this second case, so the first configuration was selected. Note that this is not a general result, and depending on the studied plant type, different contrast may be obtained by flipping over the sample. In fact, it will depend on the spatial distribution of the different leaf components and structures. Therefore, for each analyzed specimen, we recommend measuring both sides of leaves.

The first arm contains a light source and a Polarization State Generator (PSG) that allows for the controlling of the polarization of the light illuminating the studied sample. As a light source, we used the green channel (central wavelength of 530 nm and a FWHM of 10 nm, respectively), with a maximum output intensity of 1000 mA in both cases. To achieve a FWHM of 10 nm with the green channel, a dielectric bandwidth filter (by Thorlabs) was used. The PSG consists of a linear polarizer (LP1) oriented toward the laboratory vertical, followed by two Parallel Aligned (PA) liquid crystal panels. While the first liquid crystal panel, PA1, is placed at 45˚ to the laboratory vertical, the second one (PA2) is oriented at 0˚ to the vertical.

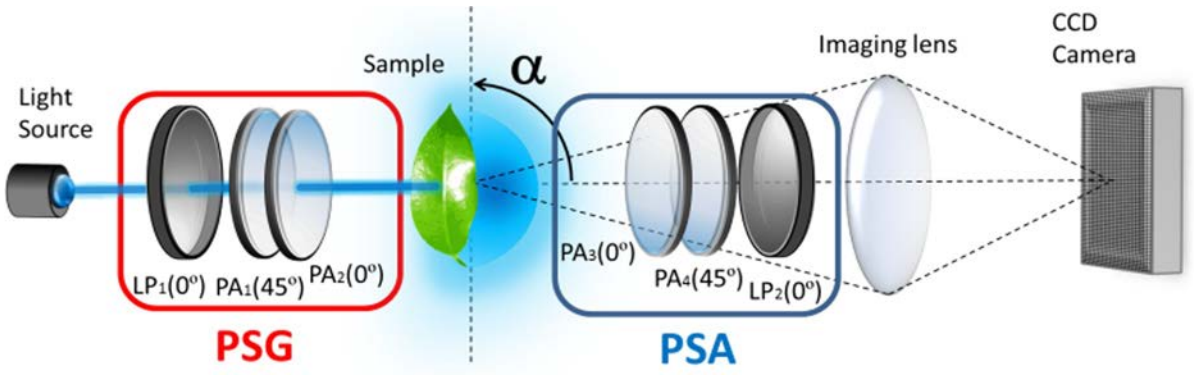

Fig 2. Scheme of the imaging polarimeter used to measure the Mueller matrices of plant leaves.

https://doi.org/10.1371/journal.pone.0213909.g002

By using this PSG scheme, and by properly addressing the voltages of the PA1 and PA2 elements, any fully-polarized state of polarization (SoP) can be generated [49]. This controlled illumination impinges a sample holder, where the botanical sample is set. Thereafter, light scattered by the sample is polarimetrically analyzed by using a Polarization State Analyzer (PSA). The PSA is composed of the same optical elements used in the PSG but is arranged in the reverse order. By using this PSA, any SoP can be measured [49].

Depending on the operation of the PSG and the PSA, the polarimeter can measure either Stokes vectors or Mueller matrices. If a single polarization state generated by the PSG is analyzed by the PSA, then the measurement corresponds to the Stokes vector representing the SoP of the beam scattered by the sample. The SoP described by this Stokes vector depends on both the initial polarization state created by the PSG and the optical response of the sample. From this SoP measurement, the corresponding DoP can be calculated according to Eq (1). On the other hand, if at least four well-different polarization states generated by the PSG and scattered by the sample are sequentially analyzed by the PSA, the collection of the resulting sixteen independent images can be used to compute the Mueller matrix of the sample [44, 50]. Note that a convergent lens images the sample plane to a CCD camera with a given magnification, so imaging polarimetry can also be performed. Moreover, the PSA system can be rotated from the specular direction (containing mainly non-scattered light) to an angle α (see Fig 2), which allows us to analyze the light scattered in different directions. A more complete discussion about the technical characteristics of the imaging polarimeter can be found in Ref. [50].

Results and discussion

A discussion of the experimental results obtained is provided below. First, we treat the images of a leaf of *Hedera maroccana* (Sample A) by calculating the corresponding Degree of Polarization (DoP) of the forward scattering. Measures were conducted in transmission configuration (leaf transmittance of ~0.44% for 530 nm). Then, we provide a discussion interpreting the contrasts seen in the image in terms of the structures found in the leaf in a botanical framework (subsection 3.1). This interpretation serves as a benchmark (or gold standard) to be compared with the images obtained using the MM-based observables in order to show their potential in the analysis of plant structures (subsection 3.2).

Plant samples contrast based on DoP measurements

In this section we discuss the DoP images obtained from Stokes vectors scattered by sample A and measured in transmission configuration ($\alpha = 90^{\circ}$ in Fig 2). Since the scattered SoPs depend on the initial polarization state, our discussion is based on a set of SoPs measured using the following incidents SoPs: linearly polarized in the horizontal direction (0LP), linearly polarized at 45° to the vertical direction (45LP), and, left-handed circularly-polarized (CP). The set of SoPs used in this work is arbitrary—they were chosen because they are linearly independent from each other and also intuitive. However, a different basis could have been chosen. The obtained images, shown in Fig 3, correspond to a Region of Interest (ROI) in the selected *Hedera maroccana* leaf (see Fig 1B) with dimensions of 1024x1024 pixels, which corresponds to an area of 2.2x2.2 cm on the leaf.

The image shown in Fig 3A corresponds to the coefficient m_{00} of the Mueller matrix of the sample, i.e. to the transmission of unpolarized light. The contrasts of this image reveal the presence of the primary (major) veins of the leaf, which constitute one of the more relevant structural features and which are even visible to the naked eye. By contrast, less visible in the intensity image but clearly defined in the DoP images (Fig 3B, 3C and 3D) are the secondary (smaller) veins. In fact, DoP images clearly stress the vascular bundles of highly basted and lignified walls.

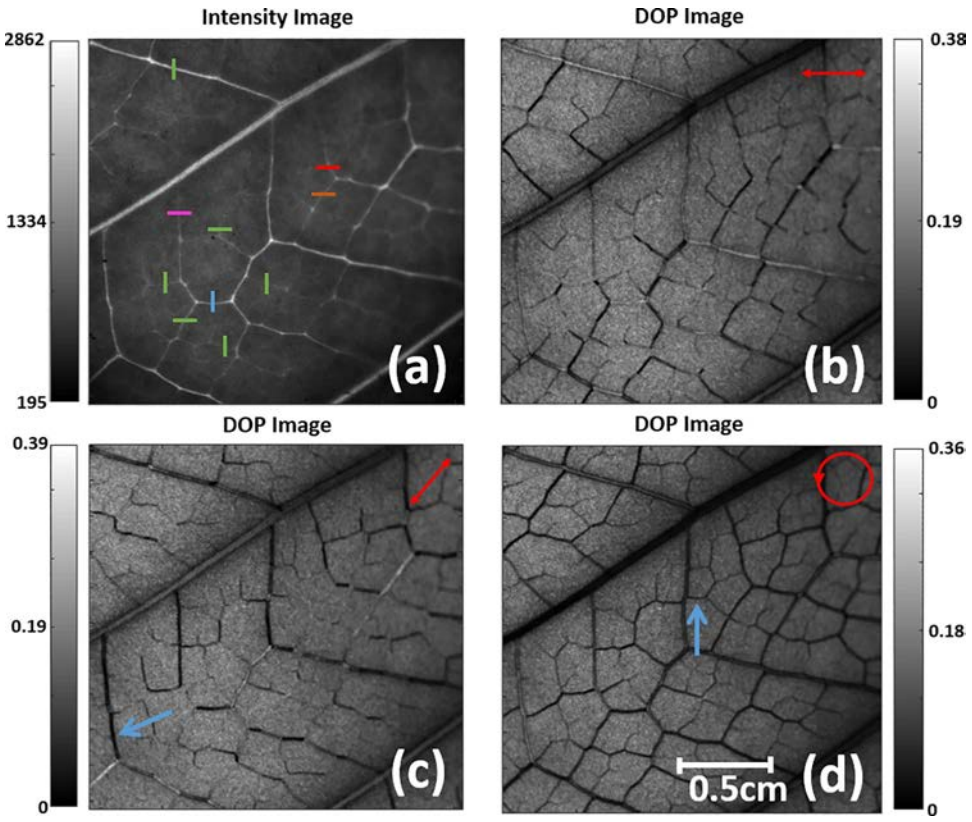

Fig 3. (a) Nonpolarized light intensity image of the Hedera maroccana (Sample A) obtained on transmission. (b)-(d) DoP image for an input polarization: (b) linear polarization at 0˚; (c) linear polarization at 45˚; (d) left-handed circular polarization. Input polarization is marked in red at the top-right corner of the images.

https://doi.org/10.1371/journal.pone.0213909.g003

It is important to notice that this improved contrast strongly depends on the selected input polarization, as the contrast among different secondary vein structures differs from one polarization to another. This fact is clearly observable by analyzing the visual information in Fig 3B (0LP), 3C (45LP), and 3D (CP). For instance, the leaf vein marked with a blue arrow in Fig 3C shows high contrast when using an input linear polarization at 45˚, whereas almost no contrast is visible when using linear polarization at 0˚ (Fig 3B) or circular polarization (Fig 3D). When a linearly-polarized incident SoP is used, the contrast enhancement depends on the vein orientation in respect to the direction of the incident SoP. In contrast, the SoP orientation dependence is somewhat suppressed when a circular polarization is used (Fig 3D), with this polarization keeping an image contrast sufficient for the visualization of tiny veins.

This spatial dependence of the contrast of the leaf structures on the input polarization by using DoP-based images deserves special attention. In fact, the selection of the input polarization in botanical polarization-based studies is, in the majority of cases, arbitrary. Linear polarizations are most commonly used because of their simplicity to be generated (only a linear polarizer is required). To generalize the physical picture suggested by the images in Fig 3, we have measured the Mueller matrix for Sample A and we have analytically calculated the output polarization corresponding to a set of N input polarizations (according to well-known input-output Stokes linear relation scheme $S_{output} = M_{sample} \cdot S_{input}$ [31, 32]). Afterwards, we calculated N DoP images corresponding to the N output Stokes array, according to Eq (1). To consider as widespread of a set of input polarizations as possible, we generated a collection of input

polarizations equally distributed along the whole Poincaré sphere surface. In particular, the collection of input polarizations tested draw a spiral-like curve covering the whole Poincaré sphere surface (see Fig 4). They are described by the following parametric relation of the Stokes vector [51]:

$$S_k = \begin{pmatrix} 1 & \cos 2\theta_k \cos 2\varepsilon_k & \sin 2\theta_k \cos 2\varepsilon_k & \sin 2\varepsilon_k \end{pmatrix}^T$$
$$\begin{cases} \varepsilon_k = k \cdot \Delta\varepsilon - \dfrac{\pi}{4}; \quad \Delta\varepsilon = \dfrac{\pi}{2N_\varepsilon N_\theta}; \\ \theta_k = k \cdot \Delta\theta; \quad \Delta\theta = \dfrac{\pi}{N_\theta}; \\ k = 1, \ldots, N_\varepsilon N_\theta \end{cases} \tag{6}$$

where the θ and ε are the azimuth and ellipticity angles, describing the polarization ellipse [32]. Whereas θ goes from 0 to π, the angle ε goes from -π/4 to π/4 (from left to right handed, respectively). The parameter N_θ is the number of steps in each circle around the S_3 axis and $N\varepsilon$ is the number of circles around the S_3 axis (see Fig 4).

In our particular calculation, we selected $N_\theta = 20$ and $N\varepsilon = 10$, so a total number of N = 200 input polarizations are sampled, which are represented as black dots on the Poincaré sphere in Fig 4.

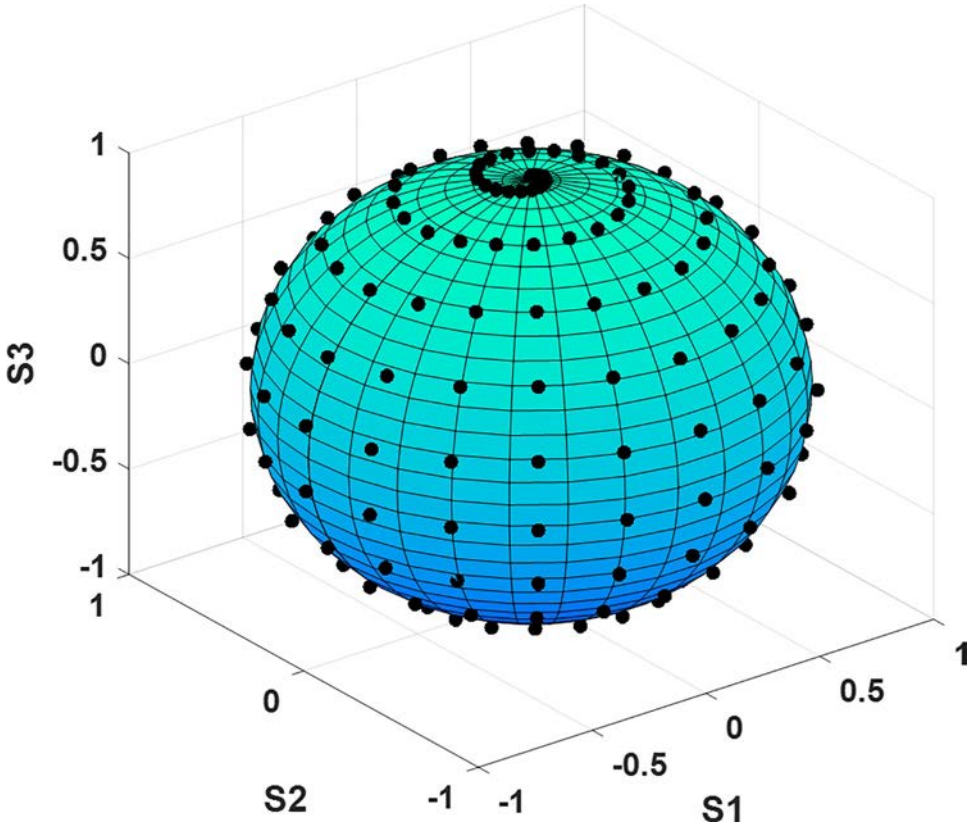

Fig 4. Poincaré sphere showing the location of the input polarizations (N = 200) used to study the dependence of the input polarization on the DoP-based images contrast.

https://doi.org/10.1371/journal.pone.0213909.g004

For the sake of visualization, the resulting collection of DoP images is arranged in video format included in the supplementary material accompanying this work (S1 Video). In fact, S1 Video consists of 200 frames where each frame shows the DoP image of Sample A calculated for a different input polarization. By varying the input polarization, we see how the contrast in different veins is modified (or even appears and disappears), and thus, S1 Video constitutes clear evidence of the high dependency of each particular leaf structure contrast on the input polarization. This dependence can be explained by the fact that veins and other structures are made of highly oriented polymers that present certain anisotropic (birefringent or dichroic) response. The components that mainly provide birefringent response in plants (as well as dichroism when some pigments are present) are the cellulose fibrils, and in particular, the microcrystals of which cellulose fibrils are made of [52–55]. These microcrystals tend to be oriented in the direction of the large structures. Oriented polymers generate a form of anisotropy (linear or circular, depending on which oriented polymer is considered) which implies that they do not isotropically scatter light in all directions of the space. This fact can explain the contrast dependence on the vein direction observed in DoP images when the illumination was linearly polarized. In contrast, since the electric field of a circular polarization vibrates with the same probability in all directions perpendicular to the propagation direction, the orientation dependence in DoP images obtained with circularly-polarized illumination is less evident. However, the maximum contrast obtained with circular polarization is half the maximum contrast obtained with linearly-polarized light.

As above-stated, we observe a clear relation between the visualization of the veins in the *Hedera marroccana* leaf and the input polarization. We further investigated this fact by analyzing the correlation between the DoP values of veins with different orientations and the input polarization orientation. To this aim, we calculated different *Hedera marroccana* DoP images corresponding to a set of different linear input polarizations, which were calculated by setting $\varepsilon_k = 0$ and $N_\theta = 200$ in Eq (6) (i.e., the 200 equispaced linear polarizations placed over the Poincaré sphere equator were evaluated). From the different DoP-based images, we calculated the averaged value of the DoP obtained at three consecutive pixels in a segment over four different veins with different orientations (see orange, red, blue and purple segments in Fig 3A). The obtained results are represented in Fig 5.

Data in Fig 5 reveals a strong dependence between the DoP values and the orientation of the input linear polarization, following an approximately sinusoidal relation. All the analyzed veins (colored segments in Fig 3A) follow the same tendency, but the positions for the DoP maximums (minimum depolarization) and minimums (maxima depolarization) are related to different orientations of the input linear polarization (i.e., there are horizontal shifts between DoP curves obtained for veins with different orientations). In fact, we observed that the orientation of the input linear polarization for which a maximum value of the DoP is measured, it is parallel (coincides) with the orientation of the vein in the leaf. This situation has sense because as commented before, veins are made of highly oriented vascular bundles (oriented organic polymers). When linear polarization is oriented parallel to the leaf veins, and for symmetry reasons, it is also likely to be oriented parallel to the global dipole of the oriented molecules from with the vein is made. Although the measurements presented in this work are done in relatively transparent spectral region, the interaction of light with matter is always present and higher when the polarization is parallel to the dipoles (from which the matter is composed) than when the polarization is perpendicular to them. So, it can be said that light will be more efficiently absorbed when it vibrates parallel to the molecules than otherwise. If absorption is enhanced, then, the amount of scattered light respect to direct light decreases because the optical path of scattered light is longer than that of direct light. Let us recall that depolarization arises because there is an incoherent superposition of direct and scattered light contributions

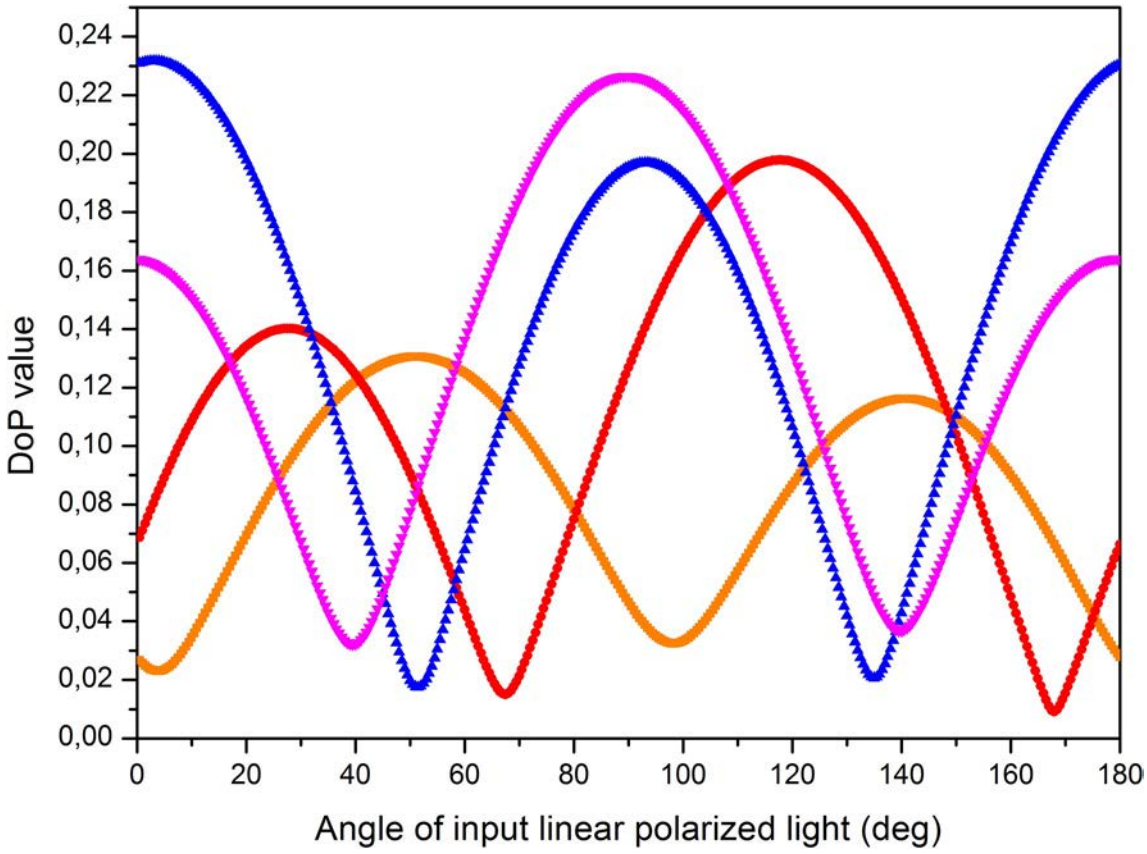

Fig 5. DoP values as a function of the input linear polarization orientations. Orange (squared), red (circle), blue (triangle) and purple (inverted triangle) curves correspond to the segments of the same color in Fig 3A.

https://doi.org/10.1371/journal.pone.0213909.g005

when it is detected by the CCD camera. If due to the above mentioned reasons the detected component related to direct light dominates, then the DoP increases (light polarization becomes purer). When light is polarized perpendicularly to the direction of molecular dipoles, the interaction of light with them (and thus, absorption and subsequent re-emission of scattered light), is also minimized. Again, in this situation, but for different reasons, the ratio between direct (non-scattered) to scattered light is favorable to the direct light component reaching the detector, which leads to an increase of the measured DoP. When light is neither parallel nor perpendicular to the material dipoles, the ratio of scattered to direct light reaching the detector increases thus leading to a decrease of the DoP. For symmetry reasons, light

Table 1. Correlations between the vein orientation and the maximum DoP value for different veins in the *Hedera maroccana* leaf (orange, red, blue and purple segments in Fig 3A).

Segments	Vein orientation with respect to the lab horizontal (deg)	Input linear orientation (in deg) for the maximum DoP
Orange	51±1	51±0.5
Red	119±1	117.5±0.5
Blue	3±1	3±0.5
Purple	89±1	90±0.5

https://doi.org/10.1371/journal.pone.0213909.t001

polarized at 45˚ with respect to the material dipoles represents a particular case for which the DoP reaches a minimum value (maxima depolarization).

To summarize this correlation between the vein angular orientation in the leaf and the orientation of the input linear polarization providing the maximum DoP value, these two quantities are provided in Table 1 for the four veins studied."

The above-stated dependence of the *Hedera maroccana* contrast with input polarization was further studied from a more quantitative point of view. To do so, the visibility V can be defined as a function of the input polarization particular index (k parameter in Eq (6)). Note that the visibility can be calculated for any arbitrary point on the image. In our case, we focused on two particular secondary veins, which are oriented at 90˚ degrees one to each other (visibility of the orange and blue segments in Fig 3A). These visibility values were obtained according to the following equation,

$$V = \frac{I_{max} - I_{min}}{I_{max} + I_{min}}, \tag{7}$$

where Imax and Imin stand for the maxima and the minima intensity of the selected segments.

The results are shown in Fig 6A, where we see the visibility value for each tested input polarization (i.e., as a function of the input polarization index k in Eq (6); ranging from 1 to 200). The orange and blue curves in Fig 6 provide the visibility values as a function of k for the orange and blue segments in Fig 3A, respectively. They reveal that the significant dependence of the image contrast as a function of the three input polarizations discussed in Fig 3 (linear polarizations at 0˚ and 45˚ and right-handed circular polarization) is generalized for all the mapped input polarizations, as provided by the high variation of the visibility observed in Fig 6A both for the orange and blue curves (with peak-to-valley visibility variations from approximately 0.15 to 0.85 in both cases). It is also clear that the maximum visibility for different structures in the leaf (orange and blue segments in Fig 3A) are obtained for different input polarizations, as shown by the peaks displacement observed between the orange and blue curves. Therefore, we confirm that the visibility of a particular plant structure depends on the input polarization (high visibility variations with the *k* parameter in Fig 6A). What is more, we also prove that different plant structures present different visibility responses to the input polarization (as shown by the different curves in Fig 6A).

For the sake of generalization, the same study was repeated using a larger number of structures. In particular, the visibility of 10 different segments arbitrarily chosen all along the whole image was calculated (see orange, blue and 8 green segments in Fig 3A). The average visibility as a function of the input polarization index k is represented as a black curve in Fig 6B. Note that for each value of k (x-axis), the value of the mean visibility is calculated in the following way: the visibility for each one of the 10 random segments is calculated, then the mean value of these 10 visibilities is obtained, and this is the value represented in Fig 6B. In addition, the corresponding upper and lower deviations, included as dashed lines, were calculated from the standard deviation.

We see that by considering different plant structures at the same time (10 segments), the corresponding mean visibility (black line) is considerably reduced. Note that if some input polarization (k value) were capable of obtaining high visibility values for the 10 plant structures at the same time, some point of the visibility black curve would be close to 1. However, we see that all the mean visibility values are lower than 0.7, with the majority of them restricted to values lower than 0.6 for all the input polarizations. This result generalizes the discussion related to Fig 6A, and confirms that a particular input polarization provides very different visibility

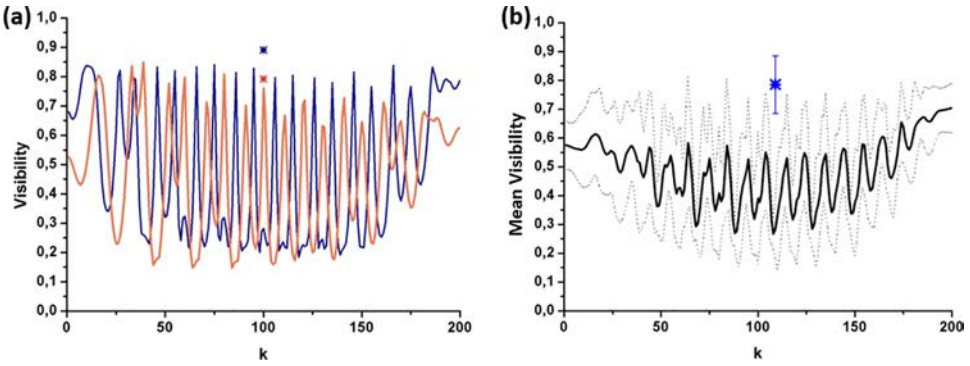

Fig 6. Visibility values calculated from DoP images corresponding to 200 different input polarizations (k parameter). (a) Orange curve and blue curve provide the visibility related to the orange and blue segments in Fig 3A, respectively; and (b) Mean visibility (black curve) as a function of the input polarization, calculated from 10 different segments (orange, blue and 8 green lines in Fig 3A) arbitrarily selected along the leaf. The corresponding standard deviations values are given by the upper and lower dashed black lines.

https://doi.org/10.1371/journal.pone.0213909.g006

values for different plant structures. The same idea is observed in the large standard deviations associated to the mean visibility values (dashed lines in Fig 6B).

In summary, the images in Figs 3 and 6 and S1 Video demonstrate that the contrast of DoP-based images is highly dependent on the input polarization, so an optimal selection of the input polarization is a crucial issue. What is more, the visibility of different spatial structures of the plant show a large variation (Fig 6B) when a particular illumination polarization is chosen. Therefore, the optimum contrast related to each specific biological structure is obtained by selecting different input polarizations. Considering the vast majority of polarimetric methods conducted on plants so far are based on DoP measurements and using a particular input polarization (usually linearly-polarized light), the above-provided study reveals that those methods never provide the best possible contrast simultaneously for all the biological structures present in the plant. Thus, the use of new techniques to better enhance the overall contrast of polarized images of plants is required.

Contrast of plant samples based on MM metrics: P_Δ and IPP indicators

In the present section, we discuss the results obtained when MM-based observables are used and we compare them with the results obtained for DoP-based images. In particular, the depolarization metrics reviewed in section 2.1 were calculated for Sample A from the experimental MM of the sample. For comparison with images in Fig 3 (DoP-based images), Sample A images for the P_Δ, P_1, P_2 and P_3 polarimetric purity indices are given in Fig 7A–7D, respectively. We see that different polarimetric channels provide different contrast visualization of the plant structures. This can be understood by taking into account the physical interpretation of these metrics. Whereas P_Δ gives a measure of an overall depolarization capability of the sample [41], i.e. it depolarizes more or less (from 0 to 1), the IPPs are related to the inherent depolarizing mechanisms of samples, and thus can differentiate among different kinds of depolarizers [42, 43, 45]. From all the obtained results, the best image contrast is achieved for the P_1 channel (Fig 7B), clearly showing the vascular bundles of highly basted and lignified walls constituting the veins in the *Hedera maroccana* sample. This contrasted visualization of the veins indicates that they scatter light in a very different way than other structures in the plant. More precisely, the veins in Sample A can be understood as equivalent depolarizers consisting of an incoherent addition of two nondepolarizing Mueller matrices [31, 32]. Note that this analysis is correct for the studied particular case of Sample A, but the best-contrasted

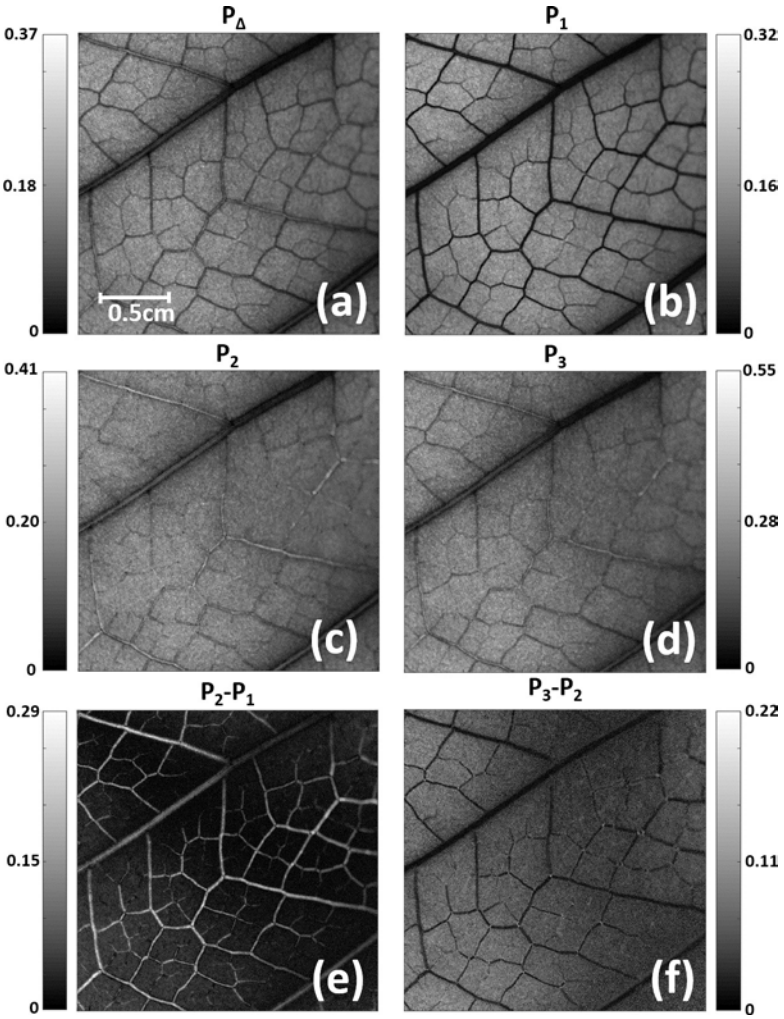

Fig 7. *Hedera maroccana* (Sample A) images obtained by using different depolarizing based indicators: (a) Depolarization Index P_Δ; (b)-(d) Indices of Polarimetric Purity (IPPs), P_1, P_2 and P_3. Sample A images obtained by combining different IPP channels: (e) P_2-P_1; and (f) P_3-P_2.

https://doi.org/10.1371/journal.pone.0213909.g007

images for other plants could be obtained with P_2 or P_3 channels if different inherent depolarizing mechanisms were predominant.

In this scenario, the study of IPPs channels is highly recommended because they synthesize and magnify the overall depolarizing information given by DoP images (section 3.1), leading to higher contrast.

By comparing the results in Fig 3 (DoP-based images) with those in Fig 7 (MM-based images), we realize that a given input polarization can enhance the polarimetric response of a particular structure of a plant with this polarization maximizing the depolarizing response of this particular biological structure. However, when different depolarizing mechanism origins (plant scatters with different densities, concentrations, organizations, sizes, etc.) are at different spatial locations, as is the usual case of a biological image, a particular polarization illumination does not reveal all the properties of the plant (check the dependence of the spatial image contrast on the input polarization in Figs 3 and 6 and S1 Video). Unlike this, by calculating the MM of the plant, the full polarimetric information is encoded in the matrix, as MMs describe the polarimetric behavior in polarimetric samples [31–34]. In this scenario, a proper decoding

Table 2. Visibility values *V* for different polarimetric indicators (different columns) corresponding to the orange and blue segments in Fig 3A.

Segment	m_{00}	P_Δ	P_1	P_2	P_3	P_2-P_1	P_3-P_2
Orange	0.1	0.34	0.71	0.16	0.18	0.89	0.54
Blue	0.28	0.26	0.68	0.25	0.19	0.79	0.65

https://doi.org/10.1371/journal.pone.0213909.t002

of the polarimetric information can reveal all characteristics of the sample. In such a situation, the analysis of a set of different depolarization metrics based on the MM arises as a promising strategy, as they provide an overall visualization of scattering structures in the plant. For instance, we have shown how, in the particular case of *Hedera maroccana*, the P_1 channel (Fig 7B) is clearly better than any DoP image obtained using any other input polarization state (Fig 3A–3D).

Although we review here the particular case of Sample A, we have also studied other plant taxa (*Spathiphyllum* sp., *Hibiscus syriacus* L., *Prunus dulcis* (Mill.) D.A.Webb, *Arum italicum* Mill.). In all these cases, MM metrics provided an overall image contrast enhancement when compared with standard DoP-based measurements. In particular, the P_1 channel tends to provide the highest contrast in the majority of studied cases.

Some authors have also pointed out that the combination of different IPP channels may lead to a visualization improvement [44, 47]. For instance, in the particular case of Sample A (Fig 7), we see how, as stated before, the P_1 channel provides a significant contrast of the plant veins, whereas these structures are more poorly contrasted in the P_2 channel (P_2 image shows quite a constant spatial intensity with blurred vein structures). Therefore, the direct differences between P_2-P_1 channels could be understood as the removing of certain image background, which leads to a possible image enhancement for some plant structures. This hypothesis is compatible with the structure of polarimetric randomness [56] given by the *characteristic* (or *trivial*) *decomposition* [57], whose coefficients are precisely the differences P_i–P_{i-1}. To test this situation, we have also calculated the P_2-P_1 (direct difference between images in Fig 7C and 7B) and P_3-P_2 (direct difference between images in Fig 7D and 7C) images for the Sample A, and the corresponding results are given in Fig 7E and 7F, respectively. We see well-contrasted images in both cases, especially for the P_2-P_1 channel (Fig 7E), leading to the best contrast of the primary and secondary veins in Sample A.

To highlight this image contrast enhancement provided by Mueller matrix-based metrics from a quantitative point of view, we have examined the visibility of the orange and blue pixel-segments studied in Fig 3. Let us now turn to the MM-based images in Fig 7. As a reminder, the two orthogonal segments set in Fig 3 are plotted again in Fig 7B. In particular, the visibility values corresponding to the direct channels P_Δ, P_1, P_2, P_3, as well as for the combined channels P_2-P_1 and P_3-P_2, were calculated according to Eq (7), and both for the orange and blue segments (i.e., we tested two different secondary veins in Sample A). The results obtained are summarized in Table 2, where we observe how the P_1 and P_2-P_1 channels are those providing the best visibility values for both the orange and blue segments. This result was expected because the P_1 and P_2-P_1 polarimetric images of the *Hedera maroccana* leaf provided the best visualization for Sample A structures (see Fig 7).

For the sake of comparison with the DoP-based images, the visibility values obtained for the P_2-P_1 images (i.e., the largest visibility values in Table 2) are represented in Fig 6A as an asterisk (an orange and blue asterisk for the orange and blue segments in Fig 7B, respectively). We want to note that the visibility calculated for the P_2-P_1 channel (asterisks in Fig 6A), or for any other MM-based metric, does not depend on the input polarization because they are calculated from the MM of the sample (see metrics in Section 2.1). In fact, the Mueller matrix can be understood as the polarimetric transfer function of the system, linearly relating the input

and output polarizations [31–34], and only depends on the polarimetric characteristics of the sample.

In the case of the vein in Sample A, highlighted in the orange segment, the visibility value for the P_2-P_1 channel is equal to 0.79 (orange asterisk in Fig 6A), with this value being very close to the maximum visibility value obtained from DoP-based images (0.85 for the value k = 39 in the orange curve in Fig 6A). On the other hand, in the case of the blue segment, the visibility value for the P_2-P_1 channel is equal to 0.89 (blue asterisk in Fig 6A), with this visibility being larger than any other visibility obtained from DoP images (the largest DoP-based visibility for the blue curve is 0.84, obtained for the polarization index value k = 166).

Therefore, unlike DoP-based methods, by using the MM-based depolarizing metrics we obtain a reasonably good visibility for the two studied segments simultaneously (more than 0.78), and without any dependence on the input polarization. In particular, despite the fact that some specific input polarization (which must be found using some optimization method) may lead to the largest visibility for a specific structure of the plant (e.g., orange segment visibility of 0.85 for the input polarization k = 39; see Fig 6A), this same input polarization will degrade the visibility of other structures in the plant (blue curve for the same k, visibility value of 0.26). Therefore, the fact that using P_Δ and IPP indicators for the full image of the plant provides a nice overall contrast without the necessity of optimizing the input polarization proves this is a more adequate approach for the characterization of plants through polarizing images.

Finally, the adequacy of MM-based metrics in the visualization of different plant structures is further highlighted by generalizing the above-described visibility study to 10 different pixel-segments arbitrarily selected along the plant (the same 10 segments shown in Fig 3A that were previously used to test veins placed at different spatial positions on the leaf, data in Fig 6B). In particular, we calculated the mean visibility (average of the visibility values for the 10 segments) corresponding to the P_2-P_1 channel. The corresponding standard deviation was also calculated. To illustrate the comparison with the DoP-based approach, the calculated mean visibility is marked with a blue asterisk in Fig 6B along with its corresponding error bar. We observe how the mean visibility obtained from the P_2-P_1 channel is significantly higher (0.77, blue asterisk in Fig 6B) than the mean visibility calculated using DoP images (black curve in Fig 6B), independently of the input polarization (k parameter). This result highlights the suitability of the MM-based depolarizing metrics for plant imaging.

Conclusion

In this work we presented the benefits of polarimetric methods for the inspection of plants. Although polarimetric methods have widely proved their suitability in biological applications, for instance in medical applications, they have not been extensively exploited in botanical applications. In particular, despite the fact some authors have studied different plants using polarized light, the number of works in this topic is not very extensive, and those that do exist mainly focus on the study of the Degree of Polarization of light dispersed by plant samples.

However, methods for polarimetric analysis of data have been largely improved in recent years. We proved how current polarimetric tools, based on the calculus of the Mueller matrix of the samples, can be beneficial in extracting information about plant structure. In fact, polarimetric tools provide images showing a larger contrast in some plant structures (or even show structures hidden in the intensity images) than nonpolarized intensity images. Furthermore, they have proven to be more suitable than polarimetric approaches based on the Degree of Polarization evaluated from the Stokes vector of scattered light.

A qualitative/quantitative polarimetric analysis of a *Hedera maroccana* leaf is provided in this work. The contrast of some leaf structures which are hidden in nonpolarized light

intensity images (such as secondary veins), can be revealed by DoP images. However, we proved that such structures, like veins with different spatial orientation, present very different visibility values as a function of the input polarization. As a consequence, no input polarization is able to provide high visualization of all structures at the same time. In contrast, we proved how some polarimetric indicators evaluated using the Mueller matrix provide a much better overall visualization of plant structures and are highly recommended over DoP-based images. In particular, the depolarization index, P_Δ, and the Indices of Polarimetric Purity, IPPs, were used to study the *Hedera maroccana*. Among these indices, we have shown that both P_1 and P_2-P_1 channels provide the best contrast of the principal and secondary vein systems of the leaf. Analyses conducted on sample A were repeated on different *Hedera maroccana* leaves (sampling of 5 leaves), obtaining analogous results.

The examples provided in this work prove that polarimetric methods can be successfully used in botanical applications and the methods described could be of interest in a wide number of botanical applications. For instance, cell membrane depolarization potential can be a transient situation due to different factors: biotic elicitor for phytoalexin production in vitro culture, effect of feeding on plant leaf, interaction between root plant and Rhizobium bacteria, etc. The analysis of polarimetric imaging of plant tissues is then a useful parameter in order to verify the membrane integrity and function. The methods could also be applied in diverse botanical areas, as for instance, in plants characterization of structures and plant taxonomy, evolution of plant specimen, hydric stress determination, and for early detection of some plant diseases.

Supporting information

S1 Video. Video consist of 200 frames where each frame shows the DoP image of *Hedera maroccana* leaf calculated for a different input polarization.
(AVI)

Author Contributions

Conceptualization: Albert Van Eeckhout, Enric Garcia-Caurel, Teresa Garnatje, Josep Vidal, Juan Campos, Angel Lizana.

Data curation: Albert Van Eeckhout.

Formal analysis: Albert Van Eeckhout, Enric Garcia-Caurel, Teresa Garnatje, Mercè Durfort, Juan Carlos Escalera, Juan Campos, Angel Lizana.

Funding acquisition: Juan Campos.

Investigation: Albert Van Eeckhout, José J. Gil.

Methodology: José J. Gil.

Project administration: Juan Campos, Angel Lizana.

Resources: Juan Campos.

Software: Juan Campos.

Supervision: Enric Garcia-Caurel, Juan Campos, Angel Lizana.

Validation: Albert Van Eeckhout.

Writing – original draft: Albert Van Eeckhout, Teresa Garnatje, Mercè Durfort, Juan Carlos Escalera, Angel Lizana.

Writing – review & editing: Albert Van Eeckhout, Enric Garcia-Caurel, Josep Vidal, Angel Lizana.

References

1. Ovečka M, von Wangenheim D, Tomančák P, Šamajová O, Komis G, and Šamaj J, Multiscale imaging of plant development by light-sheet fluorescence microscopy, Nature Plants 2018; 4: 639–650. https://doi.org/10.1038/s41477-018-0238-2 PMID: 30185982
2. Yu K-Q, Zhao Y-R, Li X-L, Shao Y-N, Liu F, et al. Hyperspectral Imaging for Mapping of Total Nitrogen Spatial Distribution in Pepper Plant. PLoS ONE 2014; 9(12): e116205. https://doi.org/10.1371/journal.pone.0116205 PMID: 25549353
3. Staedler YM, Masson D, and Schönenberger J, Plant Tissues in 3D via X-Ray Tomography: Simple Contrasting Methods Allow High Resolution Imaging. PLoS ONE 2013; 8(9): e75295. https://doi.org/10.1371/journal.pone.0075295 PMID: 24086499
4. Huisken J, Swoger J, Del Bene F, Wittbrodt J, and Stelzer E.H.K, Optical Sectioning Deep Inside Live Embryos by Selective Plane Illumination Microscopy, Science 2004; 305(5686): 1007–1009. https://doi.org/10.1126/science.1100035 PMID: 15310904
5. Noda J, Okamoto K, Sasaki Y, Polarization-maintaining fibers and their applications, J. Lightwave Techn. 1986; 4(8): 1071–1089.
6. Wolff L. B, Applications of polarization camera technology, IEEE Expert-Intell. Syst. Appl. 1995; 10(5): 30–38.
7. Xu F, Ford J.E, and Fainman Y, Polarization selective computer-generated holograms: design, fabrication, and applications, Appl. Opt. 1995; 34(2): 256–66. https://doi.org/10.1364/AO.34.000256 PMID: 20963110
8. Tuchin V. V, Polarized light interaction with tissues, J. of Biomed. Opt. 2016; 21(7): 71114.
9. Webb A.J, and Cameron B.D, The use of optical polarimetry as a noninvasive in vivo physiological glucose monitor, Proc. of SPIE 2011; 7906: 66–77.
10. Hunter M, Backman V, Popescu G, Kalashnikov M, Boone C.W, Wax A, et al. Tissue self-affinity and polarized light scattering in the Born approximation: a new model for precancer detection, Phys. Rev. Lett. 2006; 97(13): 1–4.
11. Backman V, Wallace M.B, Perelman L.T, Arendt J.T, Gurjar R, Müller M.G, et al. Detection of preinvasive cancer cells, Nature 2000; 406(6791): 35–36. https://doi.org/10.1038/35017638 PMID: 10894529
12. Backman V, Gurjar R, Badizadegan K, Itzkan L, Dasari R.R, Perelman L.T, et al. Polarized light scattering spectroscopy for quantitative measurement of epithelial cellular structures in situ, IEEE J. Sel. Topics in Quantum Electron. 1999; 5(4): 1019–1026.
13. Yaroslavsky A.N, Neel V, and Anderson R.R, Demarcation of nonmelanoma skin cancer margins in thick excisions using multispectral polarized light imaging, J. Investig. Dermatol. 2003; 121(2): 259–266. https://doi.org/10.1046/j.1523-1747.2003.12372.x PMID: 12880416
14. Roy H.K, Liu Y, Wali R.K, Kim Y.L, Kromine A.K, Goldberg M.J, et al. Four-dimensional elastic light-scattering fingerprints as preneoplastic markers in the rat model of colon carcinogenesis, Gastroenterol. 2004; 126(4): 1071–1081.
15. Pierangelo A, Benali A, Antonelli M.R, Novikova T, Validire P, Gayet B, et al. Ex-vivo characterization of human colon cancer by Mueller polarimetric imaging, Opt. Express 2011; 19(2): 1582. https://doi.org/10.1364/OE.19.001582 PMID: 21263698
16. Anwar S, Firdous S, Rehman A, and Nawaz M, Optical diagnostic of breast cancer using Raman, polarimetric and fluorescence spectroscopy, Laser Phys. Lett. 2015; 12(4): 045601.
17. Manhas S, Vizet J, Deby S, Vanel J.C, Boito P, Verdier M, et al. Demonstration of full 4×4 Mueller polarimetry through an optical fiber for endoscopic applications, Opt. Express 2015; 23(3): 3047. https://doi.org/10.1364/OE.23.003047 PMID: 25836165
18. Monstrey S, Hoeksema H, Saelens H, Depuydt K, Hamdi M, Van Landuyt K, et al. A conservative approach for deep dermal burn wounds using polarised-light therapy, Br. J. Plast. Surg. 2002; 55(5): 420–426. PMID: 12372372
19. Vanscheidt W, The effect of polarized light on wound healing, Eur. J. Plast. Surg. 2002; 24(8): 383–383.
20. Stegmann W, Behandlung des Ulcus Cruris mit Polarisiertem Licht, Phlebologie Proktologie 1985; 14: 96–97.

21. Samoilova K.A, Obolenskaya K.D, Vologdina A.V, Snopov S.A, and Shevchenko E.V, Single skin exposure to visible polarized light induces rapid modification of entire circulating blood: I. Improvement of rheologic and immune parameters, Proc. of SPIE 1998; 3569: 90–103.
22. Vanderbilt V.C, Grant L, and Daughtry C.S.T, Polarization of light scattered by vegetation, Proc. the IEEE 1985; 73(6): 1012–1024.
23. Grant L, Daughtry C.S.T, and Vanderbilt V.C, Polarized and non-polarized leaf reflectances of Coleus blumei, Environ. Exp. Bot. 1987; 27(2): 139–145.
24. Grant L, Diffuse and specular characteristics of leaf reflection, Remote Sens. Environ. 1987; 22(2): 309–322.
25. Rondeaux G, and Herman M, Polarization of light reflected by crop canopies, Remote Sens. Environ. 1991; 38(1): 63–75.
26. Curran P.J, Polarized visible light as an aid to vegetation classification, Remote Sens. Environ. 1982; 12(6): 491–499.
27. Grant L, Daughtry C.S.T, and Vanderbilt V.C, Polarized and specular reflectance variation with leaf surface features, Physiol. Plant. 1993; 88(1): 1–9.
28. Kharuk V.I, and Yegorov V.V, Polarimetric Indication of Plant Stress, Remote Sens. Environ. 1990; 33 (1): 35–40.
29. Arai K, and Nishimura Y, Polarization model for discrimination of broad and needle shaped leaves and estimation of LAI using polarization measurements, Adv. Space Res. 2009; 44(4): 510–516.
30. Vanderbilt V.C, Daughtry C.S.T, and Biehl L.L, Is there spectral variation in the polarized reflectance of leaves? Proc. of SPIE 2014; 9099: 1–6.
31. Chipman R. A, in Polarimetry: Handbook of Optics, 2nd ed, McGraw-Hill, New York, 1995.
32. Goldstein D, *Polarized Light*, 2nd ed., Marcel Dekker, New York 2003.
33. Azzam R. M. A, Bashara N. M, *Ellipsometry and Polarized Light*, North-Holland Publishing Company, Amsterdam, 1977.
34. Garcia-Caurel E, Ossikovski R, Foldyna M, Pierangelo A, Drévillon B, De Martino A, in *Advanced Mueller Ellipsometry Instrumentation and DataAnalysis* (Eds: Losurdo M., Hingerls K.), Springer-Varlag, Berlin 2013.
35. Stabo-Eeg F, Letalick D, Steinvall O, and Lindgren M, Discriminating land mines from natural backgrounds by depolarization, Proceedings of SPIE 2008; 7114: 71140H–71140H–10.
36. Berdyugina S.V, Kuhn J.R, Harrington D.M, Šantl-Temkiv T. and Messersmith E.J, Remote sensing of life: polarimetric signatures of photosynthetic pigments as sensitive biomarkers, Int. J. of Astrobiol. 2016; 15(1): 45–56.
37. Priestley J, Photosynthesis, two centuries after its discovery, in Proceedings of the IInd International Congress on Photosynthesis Research Volume I Primary reactions and electron transport (Eds. G. Forti, M. Avron and A. Melandri), Springer Science & Business Media, 2012.
38. Lucas Patty C.H, Luo D.A, Snik F, Ariese F, Jan Buma W, Loes ten Kate I, et al. Imaging linear and circular polarization features in leaves with complete Mueller matrix polarimetry, Biochimica et Biophysica Acta (BBA)—General Subjects 2018; 1862(6): 1350–1363.
39. Fiedorowicz M, and Chaczatrian G, Effect of Illumination with the Visible Polarized and Nonpolarized Light on α-Amylolysis of Starches of Different Botanical Origin, J. Agric. and Food Chem. 2003; 51(26): 7815–7819.
40. Kanaka Rao P.V, and Anjaiah J, "Polarization Imaging of Coffee Arabica," Int. J. Adv. Sci. Eng. Technol. (IJASEAT) 2017; (1): 13–15.
41. Gil J.J, Bernabéu E, Depolarization and polarization indices of an optical system, Óptica Acta 1986; 33: 185–189.
42. Gil J.J, Correas J. M, Melero P. A, and Ferreira C, Generalized polarization algebra, Monog. Sem. Mat. G. Galdeano 2004; 31: 161–167.
43. San Jose I, and Gil J.J, Invariant indices of polarimetric purity: generalized indices of purity for n× n covariance matrices, Opt. Commun. 2011; 284: 38–47.
44. Van Eeckhout A, Lizana A, Garcia-Caurel E, Gil J.J, Sansa A, Rodríguez C, et al. Polarimetric imaging of biological tissues based on the indices of polarimetric purity, J. Biophotonics 2018; 11(14): e201700189.
45. Van Eeckhout A, Lizana A, Garcia-Caurel E, Gil J.J, Ossikovski R. and Campos J, Synthesis and characterization of depolarizing samples based on the indices of polarimetric purity, Opt. Lett. 2017; 42(20): 4155–4158. https://doi.org/10.1364/OL.42.004155 PMID: 29028036
46. Chipman R.A, Depolarization index and the average degree of polarization, Appl. Opt. 2005; 44(13).

47. Gil J. J, Ossikovski R, *Polarized Light and the Mueller Matrix Approach*, CRC Press, Boca Raton, FL 2016.

48. Tariq A, Li P, Chen D, Lv D, and Ma H, Physically Realizable Space for the Purity-Depolarization Plane for Polarized Light Scattering Media, Phys. Rev. Lett. 2017; 119: 033202. https://doi.org/10.1103/PhysRevLett.119.033202 PMID: 28777609

49. Peinado A, Lizana A, Vidal J, Iemmi C, and Campos J, Optimized Stokes polarimeters based on a single twisted nematic liquid-crystal device for the minimization of noise propagation, Appl. Opt. 2011; 50 (28): 5437–5445. https://doi.org/10.1364/AO.50.005437 PMID: 22016210

50. Lizana A, Van Eeckhout A, Adamczyk K, Rodríguez C, Escalera J.C, Garcia-Caurel E, et al. Polarization gating based on Mueller matrices, J. Biomed. Opt. 2017; 22(5): 56004. https://doi.org/10.1117/1.JBO.22.5.056004 PMID: 28492853

51. Peinado A, Lizana A, and Campos J, Optimization and tolerance analysis of a polarimeter with ferroelectric liquid crystals, Appl. Opt. 2013; 52(23): 5748–5757. https://doi.org/10.1364/AO.52.005748 PMID: 23938428

52. Verbelen K., Polarization confocal microscopy and Congo Red fluorescence: a simple and rapid method to determine the mean cellulose fibril orientation in plants, J. of Microscopy 2000; 198(2):101–107.

53. Newman R. H., Davies L. M., Harris P. J., Solid-State 13C Nuclear Magnetic Resonance Characterization of Cellulose in the Cell Walls of Arabidopsis thaliana Leaves, Plant Physiol. 1996; 11(1): 475–485.

54. Pollister A.W., in Physical techniques in biological research; Volume III Part A: Cells and Tissues, 2nd ed., Academic Press, London, 1966.

55. Mendoza-Galván A., Tejeda-Galán T., Domínguez-Gómez A.B., Mauricio-Sánchez R. A., Järrendah K., and Arwin H., Linear Birefringent Films of Cellulose Nanocrystals Produced by Dip-Coating, Nanomaterials 2019; 9(1): 45.

56. Gil J. J, On optimal filtering of measured Mueller matrices, Appl. Opt. 2016; 55(20): 5449–5455. https://doi.org/10.1364/AO.55.005449 PMID: 27409325

57. Gil J. J, Polarimetric characterization of light and media: physical quantities involved in polarimetric phenomena, Eur. Phys. J. Appl. Phys. 2007; 40(1): 1–47.

scientific reports

Check for updates

OPEN

Polarimetric imaging microscopy for advanced inspection of vegetal tissues

Albert Van Eeckhout[1]✉, Enrique Garcia-Caurel[2], Teresa Garnatje[3], Juan Carlos Escalera[1], Mercè Durfort[4], Josep Vidal[1], José J. Gil[5], Juan Campos[1] & Angel Lizana[1]

Optical microscopy techniques for plant inspection benefit from the fact that at least one of the multiple properties of light (intensity, phase, wavelength, polarization) may be modified by vegetal tissues. Paradoxically, polarimetric microscopy although being a mature technique in biophotonics, is not so commonly used in botany. Importantly, only specific polarimetric observables, as birefringence or dichroism, have some presence in botany studies, and other relevant metrics, as those based on depolarization, are underused. We present a versatile method, based on a representative selection of polarimetric observables, to obtain and to analyse images of plants which bring significant information about their structure and/or the spatial organization of their constituents (cells, organelles, among other structures). We provide a thorough analysis of polarimetric microscopy images of sections of plant leaves which are compared with those obtained by other commonly used microscopy techniques in plant biology. Our results show the interest of polarimetric microscopy for plant inspection, as it is non-destructive technique, highly competitive in economical and time consumption, and providing advantages compared to standard non-polarizing techniques.

The inherent properties of light are a signifi ant source of information when used to probe the properties of vegetal tissues[1–17]. In microscopy imaging, it is common to prepare the samples to be studied in very thin sections to prevent multiple scattering of light by the different tissue structures, which can degrade image contrast and spatial resolution. Thin sections of tissues are in general almost transparent and very difficult to visualize if a contrast enhancement technique is not applied. Chemical staining is a very popular approach because of the chemical specific ty of dyes to targeted molecules in the tissues. The phase contrast technique[13] is a widely spread approach, which does not require any staining, and which can increase contrast of the thin sections proportionally to the optical thickness of the vegetal structures probed.

The use of polarized light to increase contrast in images used for vegetal tissue characterization is also a well-known approach. Contrast enhancement of images of plant structures is usually obtained using polarized light, through the measure of dichroism or birefringence[18–25]. Dichroism is related to the polarization-dependent absorption of light by plant structures and it is useful to detect specific molecules as well as to visualize how they are organized in a three-dimensional framework. Dichroism is successfully used in many studies devoted to reveal the organization and concentration of chloroplasts and related organelles in plant species[19,21]. Birefringence is generated either by anisotropic molecules (in general partially crystallized macromolecules) or by non-isotropic organization of non-necessarily anisotropic macromolecules. Birefringence has been successfully used to characterize birefringent macromolecules as cellulose, involved in distinct types of cell processes, such as cell development and aging[18], production of guard cell protoplasts[19]. Birefringence has also been used to study the structure of guard cells themselves and their related stomata[20] or to investigate the cell wall composition in phylogenetically distant groups of plants[21], and to study the structure of trichomes[22,23].

Polarimetric microscopes used for plant inspection are mostly optimized to measure dichroism or birefringence, but other polarimetric features, as depolarization, are usually neglected. Depolarization arises when photons with different polarization states incoherently reach the same area of the detector. In plants, depolarization is mainly caused by light scattered by cells, organelles, extracellular structures, and other elements that may be located within the tissue. For very thin preparations, scattering is usually low and depolarization effects

[1]Grup D'Òptica, Physics Department, Universitat Autònoma de Barcelona, 08193 Bellaterra, Spain. [2]LPICM, CNRS, Ecole Polytechnique, Institut Polytechnique de Paris, 91120 Palaiseau, France. [3]Botanical Institute of Barcelona (IBB, CSIC-ICUB), 08038 Barcelona, Spain. [4]Departament de Biologia Cellular, Fisiologia & Immunologia. Facultat de Biologia, Universitat de Barcelona, 08028 Barcelona, Spain. [5]Department of Applied Physics, University of Zaragoza, Pedro Cerbuna 12, 50009 Zaragoza, Spain. ✉email: albert.vaneeckhout@uab.cat

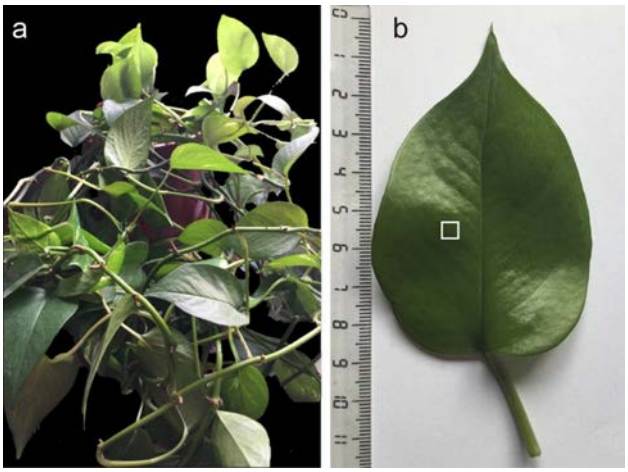

Figure 1. Plant specimen used for the present study: (**a**) *Epipremnum aureum* general view; (**b**) one of the measured *Epipremnum aureum* leaves.

are usually disregarded, however, optical characterization of plants is not always performed in such conditions. To date, the most used approach to account for depolarization introduced by plants is to measure the so-called degree of polarization (DoP) of scattered light[26–29]. Since DoP depends on the intrinsic characteristics of the constituents of plants it is a pertinent and informative observable of the state of a given specimen, reason why it has been used in preceding studies. However, a more general approach, Mueller polarimetry has been scarcely used in botany[24,25,30]. The latter situation is surprising compared to the extensive use and the still growing interest of Mueller polarimetry to study either human or animal tissues[31–36].

The goal in the present manuscript is to show that Mueller polarimetry provides both, polarization-based and depolarization-based observables and that both of them can bring interesting and independent information about the physical properties and structure of vegetal tissues. Polarization-based observables can be measured with techniques other than Mueller polarimetry, however, Mueller polarimetry has the advantage compared to other experimental approaches that it provides all the polarization-based observables and the depolarization-based ones as the result of a single measurement. The present manuscript is to be read as a general presentation of imaging Mueller polarimetry applied to plants and the evident potential benefits that botanists can obtain when implementing it in their characterization routines. Th s paper goes beyond the simple illustration of a case study and compares polarization microscopy-related images with microscopy images obtained with state-of-the art techniques commonly used to visualize and to characterize plants. We demonstrate how polarization microscopy is an excellent tool for characterization of vegetal tissues and plant sections. It is a perfect complement, and in some cases is advantageous, to standard microscopy methods, providing the potential to expand the field of optical instrumentation for the study of plants.

Results

In this work we have considered leaves from a specimen of *Epipremnum aureum* (Linden & André) G.S.Bunting belonging to the Araceae family as a case of study. A picture of said specimen is shown in Fig. 1a. Comparison of imaging polarimetry with other advanced techniques, such optical microscopy, phase contrast microscopy, fluorescent microscopy, highlights the potential of polarimetry for plant inspection. These advanced imaging methods that will be discussed in the present study are currently used in botany for plant inspection. Although the selection is not an exhaustive compilation, it is meant to be representative of the techniques used in the fi ld and they should be interpreted here as a base of comparison to help the reader to understand the potential and the interest of Mueller polarimetry. Note that other methods could be mentioned but are not available in this study, as for instance, differential contrast microscopy (DIC) that is a relevant advanced characterization technique, and that presents images like those obtained by phase contrast microscopy but emphasizing lines and edges of the sample structures by exploiting the polarization properties of light[37]. Figure 1b shows one of the leaves used for the present study. The square inside the leave highlights the area that was imaged using the above-listed microscopic techniques. A description of the plant used for the present study is found at the Methods section.

Polarimetric microscopic images of the *Epipremnum aureum* leaves were taken with a multimodal microscope working in transmission configur tion. The microscope can also be used in a way to obtain images insensitive to the polarization of light (standard optical microscope). More details of the microscope used can be found in the Methods section. An example of an image taken in non-polarized mode of the lower leaf surface of the leaf can be seen in Fig. 2a. In the latter image it is possible to distinguish the presence of a few epithelial cells, characterized by their typical polygonal shape, and a guard cell and its related stomata. These cells are located just at the lower surface of the leaf. In the image shown, there is also possible to guess the presence of an elongated structure which appears blurred because it is located inside the leaf, at a distance from the focal region longer than the depth of focus of the objective used to take the images. Because of the blurry and the lack of contrast in said image, it is not possible to perceive the details, or at least, to unambiguously identify the nature of the elongated structure.

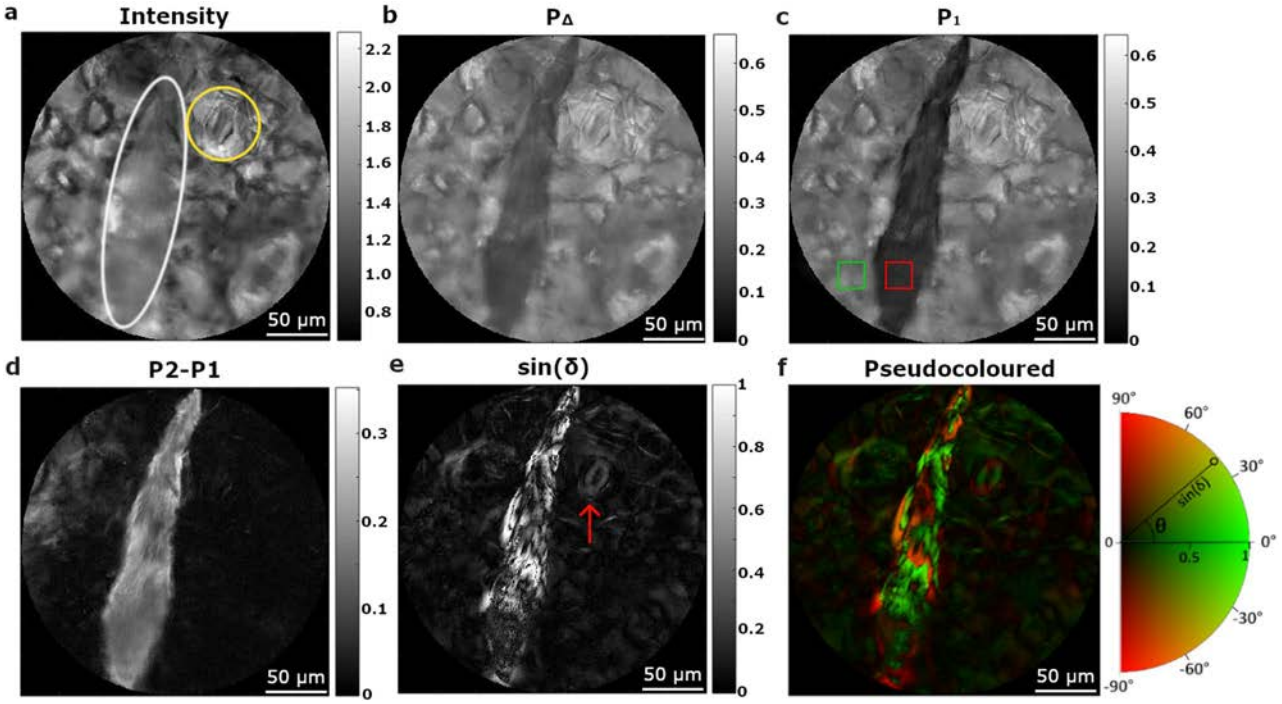

Figure 2. Polarimetric analysis of a small piece of the *Epipremnum aureum* leaf (marked with a white rectangle in Fig. 1b). Different images of an inulin raphide, situated close to a stoma, are provided, which were obtained by using different channels: (**a**) Intensity; (**b**) $P_{\Delta;}$ (**c**) P_1; (**d**) P_2–P_1; (**e**) The sinus of linear retardance δ (stoma highlighted with a red arrow); and (**f**) Pseudocoloured image encoding retardance modulus and orientation. Pseudocoloured image comprises the linear retardance of the sample (shown into a white–black scale; radius of the semi-circular colour scale), and the fast axis orientation (represented with different colours; perimeter of the semi-circular colour scale).

The same portion of the leaf was measured in polarimetric mode and the Mueller matrix image encoding the polarimetric response of the sample was obtained. To get further physical information from the measured Mueller matrix image, the latter was decomposed to obtain a set of subsequent images of polarization and depolarization metrics. Concerning depolarization, in this work it is used the depolarization index P_Δ and a set of observables (P_1, P_2 and P_3) called indices of polarimetric purity (IPPs) that give indications about the way that a medium depolarizes light. Accordingly, P_Δ and IPPs are sensitive to classify different microscopic elements according to their ability to depolarize the illuminating light. It is worth to note that P_Δ is a global depolarization measure while IPP can distinguish different depolarization anisotropies that results into the same P_Δ value. Interested readers can found, in the Methods section and in the Supplementary information, a detailed description of the polarization-depolarization observables and an algorithm to deduce them from Mueller matrices.

Figure 2b–d show the images corresponding to P_Δ, the fi st IPP, P_1, and the difference P_2–P_1, which provided highly contrasted images. Concerning polarization properties, Fig. 2e shows the sinus of the linear retardance, which gives information about the birefringence of structures in the imaged area of the leaf. In Fig. 2b–e the elongated shape of an inulin raphide can be also seen. Inulin is a type of polysaccharide which crystallizes in needle-shaped crystals; the crystals tend to group together to form raphides, which are found in parenchymal cells in some plant species. In such images, the edges of the raphide can be clearly distinguished, and the whole structure is highly contrasted with respect to the background. In fact, in the case of P_1 image (Fig. 2c), the red square section of the raphide, has an average P_1 value of 0.11 whereas the green square section, corresponding to the background, has an average P_1 value of 0.29. A compact structure such a raphide scatters light differently that the aqueous structure of the surrounding media. The fact that the values of P_1 are well clustered in two groups around 0.11 and 0.29 respectively, shows the ability of the observable P_1 to distinguish among different types of matter, which would not be possible under non-polarized light images. The case of P_2–P_1 channel in Fig. 2d is also exemplary. According to this observable, the same section of the raphide is characterized by values around 0.13 whereas the same section of the background cells shows the value 0.02. To quantify the image contrast between two structures in the image, the so-called visibility has been used as a metric. The visibility is defined by the expression: $V = |\bar{I}_{str} - \bar{I}_{back}|/(\bar{I}_{str} + \bar{I}_{back})$, with $\bar{I}_{str}$ and $\bar{I}_{back}$ being the average signal intensities of the studied biological structure (in this case the raphide) and the background cells respectively. Visibility values are between 0 (null contrast) and 1 (maximum contrast). In the analysed case, the visibility of the image between the raphide and the background is $V = 0.03$ for the intensity image (Fig. 2a), $V = 0.24$ for P_Δ (Fig. 2b), $V = 0.41$ for the P_1 observable, (Fig. 2c) and a visibility of $V = 0.72$ for P_2-P_1 case (Fig. 2d). Visibility values of different observables are calculated over the same red and green square sections (Fig. 2c) and further contrast analysis, including the study of the standard deviation of the intensity in these regions, is provided in the Supplementary information.

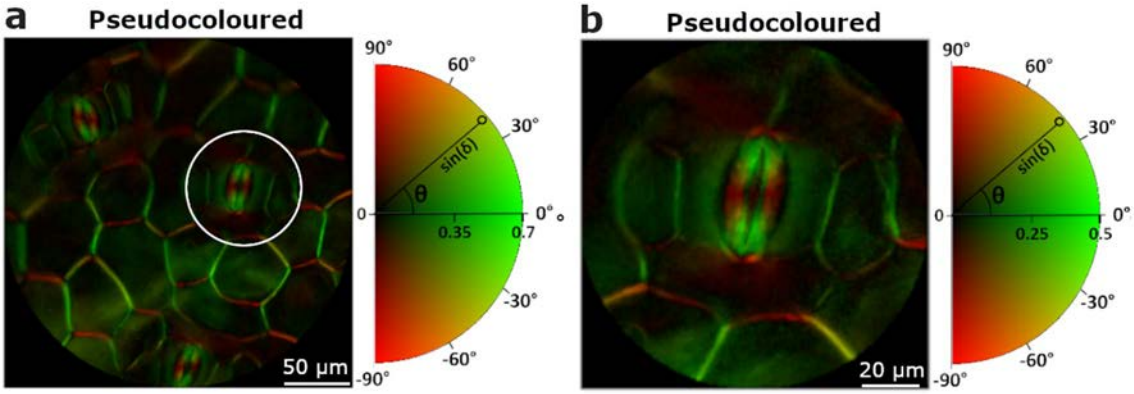

Figure 3. Pseudocoloured image of a collection of stomata and the zoomed image of a given stoma are shown in (**a**) and (**b**), respectively. The pseudocoloured image comprises the linear retardance information of the sample (shown into a white–black scale; radius of the semi-circular colour scale), and the fast axis orientation (represented with different colours; perimeter of the semi-circular colour scale).

Note that the visibility values of depolarizing observables are signifi antly better than those obtained for the polarization insensitive image. Regarding the different depolarizing observables, the visibility of the raphide is higher in the case of analysing P_1 and P_2–P_1 than P_Δ as the raphide depolarizes light in an anisotropic way. Therefore, raphides are easier to identify when using these IPPs observables than in the P_Δ case.

Raphides are not the only structures which can be highlighted thanks to polarimetric microscopy. There are for instance guard cells and their related stomata, which can also be visualized and characterized using birefringence. Birefringence in guard cells is mostly due to a preferential alignment of small cellulose microfibrils inside their walls. Young and healthy guard cells can show regular and intense birefringent pattern, on the contrary, dead or non-functional guard cells have distended walls, and show distorted or very poor birefringence patterns. The portion of the leaf shown in Fig. 2a–f contains a stoma of about ~ 50 μm stomatal length close to the raphide. Despite of being birefringent, the visibility of the stoma is lower than that of the raphide (also birefringent) and therefore somehow screened by it in the colour scale chosen to represent Fig. 2e.

While the stoma has a negligible dichroism, the raphide is characterized by 0.2 rad of linear dichroism, which indeed appeared to be oriented along the axis of said raphide. The linear dichroism in raphide may be due to the anisotropic absorption of well aligned inulin crystals which form the raphide or to the non-isotropic scattering which attenuates differently light polarized parallel or perpendicular to the major axis of the raphide. The results of a specific study to elucidate the origin of dichroism in raphides is out of the scope of the present work but will be presented elsewhere. Moreover, the non-isotropic scattering of light due to the elongated shape of the crystals may be at the origin of the non-symmetric depolarization that gives rise to the highly contrasted P_1 channel with respect to P_Δ.

A colour encoding format is an appropriate way to highlight different polarization and depolarization signatures at once in the same image[38]. For instance, Fig. 2f shows the sine of the retardance, already shown in Fig. 2e, completed with the information of the orientation of the birefringence. In a second figure, Fig. 3a, it is shown how colour encoding allows for further visualization of the stoma. The image corresponds to an area of the leaf, free of raphides, where stoma, guard cells and cell membranes are present. Colour encoding allows for a clear difference between the membranes of the guard cells and the boundaries of the stoma. The image in Fig. 3b corresponds to a zoomed view of the area encircled in Fig. 3a and shows how the structure of the stoma (the pore region) and the underlying walls of the associated guard cells can be clearly distinguished. Note that it is impossible to achieve a similar level of differentiation by using standard, non-polarimetric, visualization techniques in microscopy with unstained samples; see for instance Fig. 2a. What is more, since the colour scale in Fig. 3b is related to different orientations of the birefringence, quantitative information about strain spatial distribution can be obtained from the image[21].

Finally, we want to highlight another relevant advantage of polarimetric imaging, the ability to highlight properties and to improve visibility of objects which in standard conditions of observations may appear blurry because they are out of focus. The latter is discussed through the following example, in which the same leaf was used, but observed with the corresponding obverse face pointing to the imaging microscope objective (the opposite face than in previously discussed examples). A region of interest was selected in which a raphide was present in the fi ld of view, but instead of focusing on the raphide (inside the leaf) the image was focused on the surface of the leaf. Accordingly, in Fig. 4a, it is shown an image taken under unpolarized light to illustrate how the scene is viewed under standard visualization conditions. In this image, the epidermal cell walls are clearly visible and the raphide appears so out of focus and blurry that it is barely identifiable. The visibility of the raphide is $V \sim 0$ (the visibility is calculated by using the associated red and green squared regions of Fig. 4b). However, when the same region of the leaf is measured using polarimetry in identical imaging conditions, the presence of the raphide is clearly revealed in the P_2–P_1 channel Fig. 4b, with visibility equal to 0.67. The same image allows for the observation of the cell walls which are also contrasted respect to a black background. Cell walls and raphide are visible because both scatter light more effici tly than the bulk of the cell, and, therefore they create more light depolarization. Even though the raphide remains out of focus, it cannot be, by any means, overlooked. We

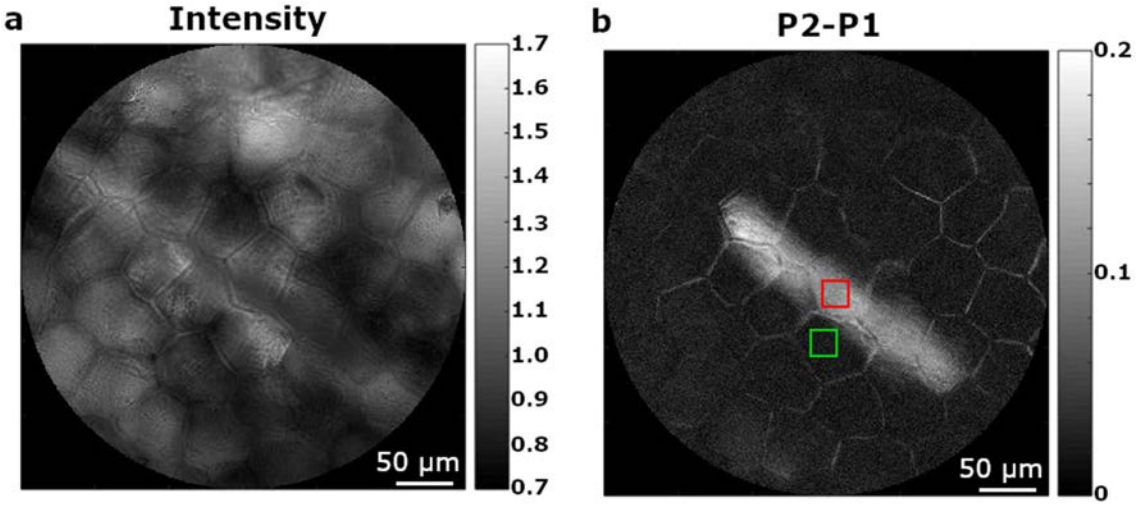

Figure 4. Figure (**a**) shows the intensity image of an inulin raphide out of focal plane (defocused). The corresponding image obtained by using the P_2–P_1 channel is provided in (**b**).

think that the ability of polarimetric imaging of showing the presence of structures, even being out of focus, is a major advantage as it allows for the identification of biological structures located at different axial planes. The later permits imaging of a given region at the focal plane without loss of resolution while revealing some out of focus structures at the same time. Th s could be helpful to users without aprioristic information of samples, as polarimetric contrast shows to be very useful to detect relevant structures which may be out of focus.

So far, in this section we have seen the improvement associated to polarimetric imaging microscopy, with special mention to the IPPs channels, when compared with standard microscopy. However, other microscopy techniques are well-stablished in biophotonics applications. For the sake of completeness, we include here a set of images taken from the same sample specimen, the *Epipremnum aureum* leaf, obtained using two of the main optical microscopy techniques used in botanic: phase contrast microscopy and fluorescence microscopy.

Phase contrast microscopy allows for the observation of unstained cells[13] and it is especially useful to explore living cells in real time because it does not need the evaluation of multiple images as in polarimetry. Phase contrast measures differences in the global phase of a light beam between adjacent zones in the sample under examination which are created by small variations in thickness and density (refractive index) among those zones. In phase contrast microscopy, birefringence is not needed to create a visible contrast between two areas of a sample. Phase contrast images of an almost transparent and non-contrasted object give to the human eye the impression of a shaded three-dimensional object. The latter implies a signifi ant improvement in the perception of the sample, and it is in part what is behind the success of this technique. Representative images of stomata and raphides imaged with the phase contrast microscope are shown in Fig. 5a,b, respectively. The leaf piece was imaged using a commercial *Olympus Fluoview 1000* phase contrast microscope described in the Methods section. Whereas the stomata are clearly visible in the phase contrast microscopy image (Fig. 5a), with a visibility of $V = 0.38$ (V is calculated over the purple and yellow regions of Fig. 5a representing the stomata and background respectively), the raphides were no so-well contrasted, presenting a visibility reduced to $V = 0.14$ (V is calculated over the red and green squared regions of Fig. 5a representing the raphide and background respectively). In Fig. 5b, the location of a raphide is highlighted by a violet ellipse to help for visualization. In this example, polarimetric images produce more contrasted and more specific images than phase microscopy. Phase contrast performed less well than polarimetry, especially in the case of images of raphides, because the light scattered by raphides depends on the polarization of the incident light and phase contrast microscopy is unable to see that phenomena as it illuminates the sample with unpolarized light. Moreover, colour encoding strategies to enhance image contrast and visibility can be applied in polarimetric imaging because polarimetry consists in multiple independent channels of information whereas in phase-contrast microscopy the information is restricted to only one channel. A second reason why phase contrast performed less well than polarimetry in the example discussed here is the fact that the sample was not thin, i.e., limited to a single monolayer of cells. In these circumstances, phase shifts larger than 2π can cumulate and produce grey scales which do not linearly relate to variations in sample thickness or density, therefore degrading the performance of the technique. Phase contrast and polarimetry can be complementary because they can be used in non-stained samples. In polarimetry, some channels are specifi to the manifestation of a property in the sample, such as retardation or dichroism. In this way, while phase-contrast provides an enhanced view of the tridimensional conformation of the object, polarimetric observables can highlight aspects related to certain specific properties of the sample.

Images of the same areas of the leaf explored under phase contrast imaging were taken with the same *Olympus Fluoview 1000* commercial microscope previously cited, operated in fluorescent mode. The use of specific dyes selected to link to the molecules that are of interest for the observations, makes fluorescence microscopy a highly specific and highly resolved technique. By using two different fluorescent dyes, images of well contrasted and differentiated stomata (Fig. 5c) and raphide (Fig. 5d) were obtained. Although the visualization of the raphide structure is comparable with that obtained by using polarimetric channels (Fig. 2b–d), the stoma image shows

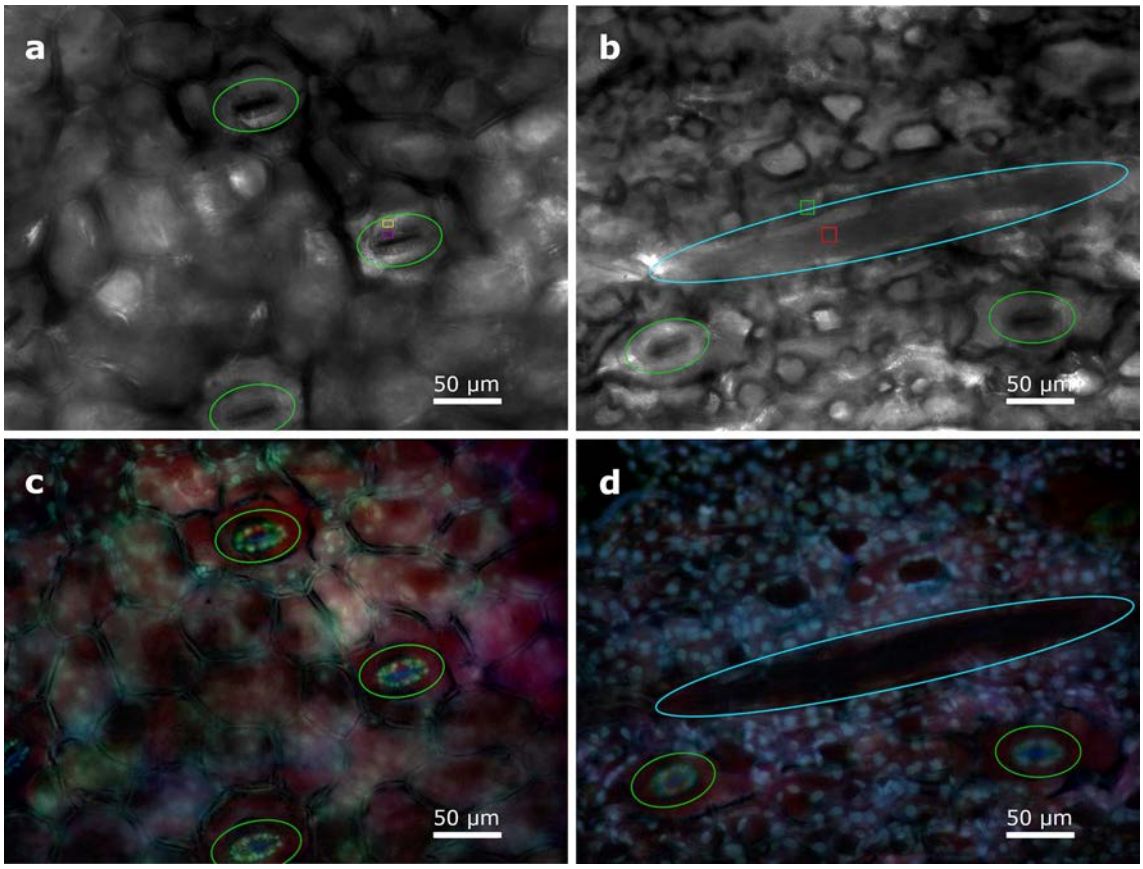

Figure 5. Images of *Epipremnum aureum* stomata obtained with a phase (**a**) and a fluorescence (**c**) microscope. Images of an *Epipremnum aureum* inulin raphide, obtained with the same phase and fluorescence microscopes (**b**,**d**), respectively.

some characteristics and details which cannot be reached by polarimetric means (Fig. 5c). However, some physical information provided by polarimetric images is not present in fluorescence image, such as mechanical stress (which in turn creates birefringence) that may occur in cell walls. Polarimetric and fluorescence techniques are compatible in the sense that both can be applied to stained samples. Staining may enhance polarimetric properties, in particular dichroism, in places where the dye links to the molecules of the sample because in many cases dyes are anisotropic and dichroic. Fluorescence microscopy works well with samples prepared as very thin sections made of a monolayer of cells. For relatively thick samples, like the one used here, the light emitted by dyes can be scattered within the tissue and then to end up by degrading the spatial resolution of the images if a confocal configuration is not used. Working with thick samples is not a problem in polarimetry, provided that an adequate separation between polarization and depolarization channels can be done as shown in this work.

Finally, the validity of the analysis performed on the *Epipremnum aureum* leaves by polarimetric methods is confirmed by high resolution images from scanning electron microscopy (SEM) taken on the same leaves of the same plant. From SEM images, we observed a concentration of inulin raphides which are in agreement in size and shape to the structures observed in Fig. 2b–d and identifi d as raphides. An electron microscope image showing a representative inulin raphide in the studied *Epipremnum aureum* plant is shown in Fig. 6a. Another inulin raphide is shown in Fig. 6b, but the size of this raphide cannot be well determined because it was broken during the sample preparation. Preparing the sample without damaging the raphides is very challenging and requires a high degree of technical expertise. The images provided by SEM also confi m the presence of stomata previously shown in Figs. 2, 3 and 5. Two stomata with open and closed pores respectively are shown in Fig. 6c,d. The presence of other structures, not detected by previous methods, such as tinny salt crystals which are observed above and around the stomata pores can also be observed due to high resolution of SEM.

Discussion

The present paper highlights the interest of polarimetric microscopy to the study of an *Epipremnum aureum* leaf, but the suitability of polarimetric methods here discussed was also observed by us in different specimens of *Hedera maroccana* McAll., *Spathiphyllum* sp., *Hibiscus syriacus* L., *Photinia* × *fraseri* Dress, *Prunus dulcis* (Mill.) D.A.Webb, *Arum italicum* Mill., *Hedera helix* L., and *Vitis vinifera* L. For completeness, microscopic polarimetric images of *Heredera Helix* and *Vitis vinifera* are provided in the Supplementary information as illustrative examples. In the case of the *Epipremnum aureum*, polarimetric channels clearly show the presence of raphides and stomata in the plant. Stomata play an important role in the interaction between plants and environment[39].

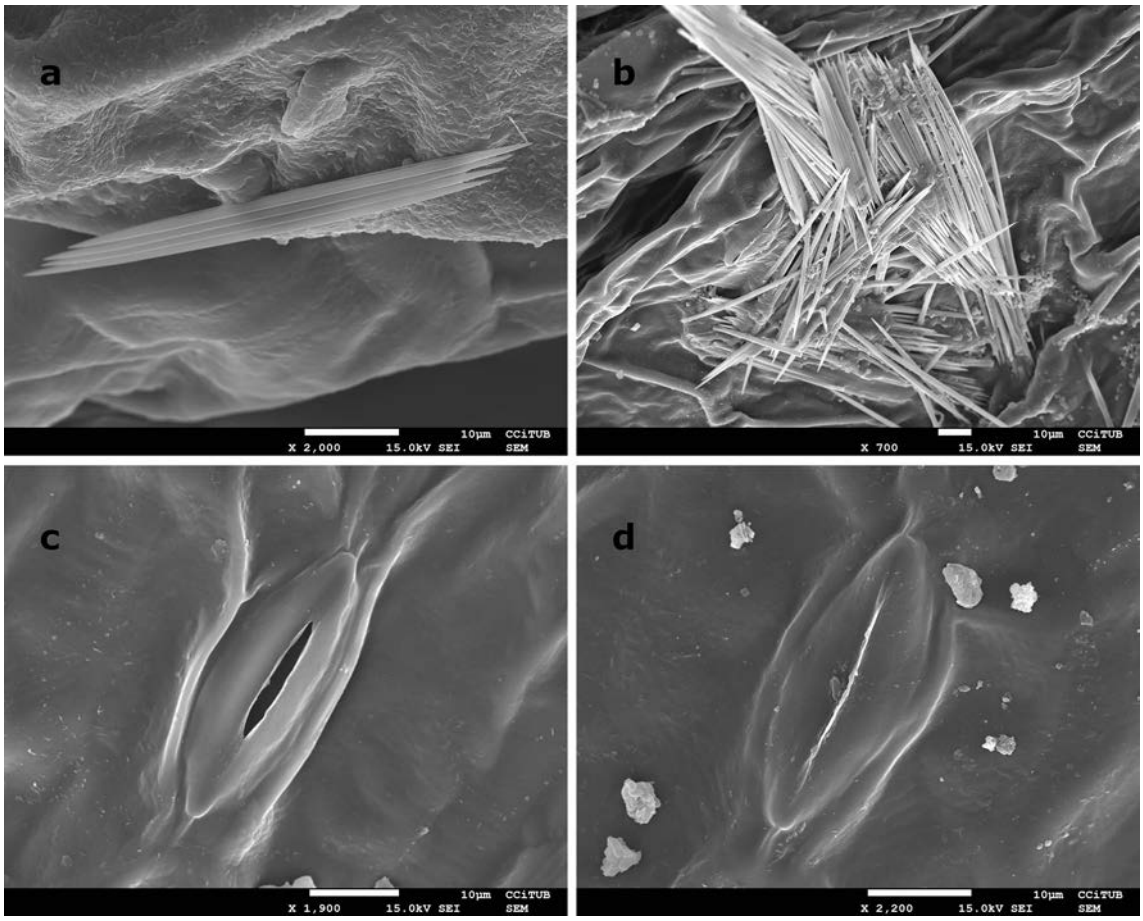

Figure 6. Scanning electron micrograph showing the ultrastructure of a bunch of inulin raphides (**a**) and (**b**) in the parenchyma cell of the studied *Epipremnum aureum* leaf. Stoma ultrastructure is also shown with an open (**c**) and closed (**d**) pore.

These structures regulate gas exchange and water loss in plants, being both key processes in a context of increase of CO_2 atmospheric concentration and water stress produced by extreme droughts. Despite the contrasting responses of stomata to climate change[40], the study of these structures in living plants is especially relevant in the current scenario to determine the plant productivity by analysing its water use efficiency[41]. Measurements of stomata are typically conducted using a silicon rubber impression technique[42] followed by a positive replica of the impression material made by using nail varnish[43]. Polarimetry is presented as a non-contact alternative technique that is faster and easier to implement. Moreover, polarimetry brings new information related with the distribution of birefringence, probably due to mechanical stain, in the stomata cell walls[21].

Raphides are present in many plant species, their abundance and morphology (size, shape…) presence together with the crystal structure and morphology seems to be characteristic of taxonomic group of plants. These structures, which may be part of the defence mechanism of the plant due to their toxicity, are particularly frequent in the Araceae family. They are used in food and pharma industries[44,45] and they have several medicinal applications, though they can also cause several side effects. In addition, the study of the raphides can be used in the characterization of some plant species and in their systematic classifi ation[46] and to inform about the toxicity of wild edible plants included in retrieval strategies[47]. Electron microscopy is routinely used to observe the crystals in detail, but the technique requires specific sample preparation. Polarimetry is presented as a non-invasive technique with an easier implementation.

The results shown in this article have been selected to illustrate the presence of different polarization and depolarization responses in plant tissues and therefore how they can be used to characterize plant sections or specific vegetal structures. Raphides are characterized by a well-defi ed depolarizing and dichroic response, and stomata by their retardance. These characteristic polarimetric responses allow for an easy identifi ation of the mentioned structures (Figs. 2, 3 and 4), while being almost invisible to the most used optical instrumentation techniques. Therefore, it has been shown how polarimetric imaging provides very practical and useful tools that allow for the visualization of some plant characteristics not observed when standard non-polarized images are used. In addition, polarimetric methods can reveal some structures hidden because they are out of focus but have a distinct polarimetric response (Fig. 4). Although elaborate sample preparation, such as clearing, fi ing, cutting, or mounting can of course help to improve image quality, they are not mandatory to do polarimetric imaging, which greatly simplify the sample handling and characterization procedures.

Thanks to the sensitivity of polarization to specific properties which are generally located in well-defi ed parts of plant, polarimetry can be complementary or even more useful than other standard characterization techniques. In fact, polarimetry can be combined with other optical techniques within the same optical instrument[35]. As an important advantage, polarimetric methods can provide unique physical information, as was the case of the non-homogeneous physical properties of the stoma revealed by polarization (Fig. 3a,b), that was hidden when using any of the other methods described in this manuscript, including electron microscopy.

The images provided by SEM (Fig. 6) confirm the results obtained by using polarimetric microscopy. Electronic images provide the best visualization of plant structures, when compared with optical techniques previously discussed. However, optical, in particular polarimetric methods are much more accessible than electronic microscope and could be used for dynamic applications (snapshot imagers). Polarimeters are based on compact (an eventually portative) optical configurations[48], which can be used for outdoors measurements.

Summarizing, the results provided in this manuscript illustrate the potential of Mueller polarimetric microscopy for plant characterization and botanical applications, and also they illustrate the benefits of the recently devised depolarization-based observables in complement of the commonly used polarization-based ones. Mueller polarimetry provides complementary information not accessed using other optical techniques, as phase contrast or fluorescent microscopy. Electron microscopy provides images with high resolution but is less practical than polarimetry or other optical methods. Moreover, polarized light microscopy is a non-invasive technique (as it is the case of fluorescent microscopy) and can be combined with other optical techniques in the same instrument just by including very feasible setups (polarimeters) in the common path of standard optical microscope setup. In addition, some image polarimeter architectures are very compact[48] and can be used outdoors, thus being valid to perform in situ and in vivo measurements of plants. Under this scenario, we think that Mueller polarimetry is a very interesting and promising technique to be used alone or in complement to other approaches to study plants.

Methods

Sample description. We measured a leaf of *Epipremnum aureum* (Linden & André) G.S.Bunting, which is a synonym of *Pothos aureus* Linden & André. Th s species, belonging to the Araceae family, occurs in forests from Southeast Asia to tropical Australia. The adult leaves are usually perforated and often have translucent spots along the midrib. These evergreen climbing plants are cultivated for their attractive foliage. A herbarium voucher of the studied species is deposited in the Herbarium of the Botanical Institute of Barcelona (BC843412). An image of the measured *Epipremnum aureum* is given in Fig. 1a. The leaf measured is shown in Fig. 1b.

The Mueller matrix approach. Polarization of light is in general modifi d when it interacts with material media. The formalism followed in this work to describe the polarimetric modifi ations is the Mueller matrix approach. Within this approach, the states of polarization of light are represented by means of four real parameters, which are the components of the so-called Stokes vector. The physical meaning of the four components of the Stokes vector is related to the ellipticity, ε, and the azimuth, θ, of the polarization ellipse[49]. The polarization ellipse is the trajectory followed by the end point of the electromagnetic fi ld when light propagates in a given media. Accordingly, the modifi ation of the polarization state produced during light-matter interactions is described by using a 4×4 matrix called the Mueller matrix, in such a manner that the Stokes vector of the output light is given by the product of the Mueller matrix and the Stokes vector of the input light.

The determination of the experimental Mueller matrix requires the use of a Mueller polarimeter, which measures the polarimetric characteristics of the sample by controlling the polarization of the illumination light and analysing the state of polarization of the light eventually modifi d during the light-matter interaction. The determination of a Mueller matrix is obtained from a set of radiometric measurements resulting from the illumination of the sample with light prepared in different polarization states, and the subsequent analysis of the polarization of imaged (or detected) light beam. This situation is mathematically described by means of the following expression:

$$\boldsymbol{I} = \boldsymbol{S}_{PSA}\boldsymbol{M}_{Sample}\boldsymbol{S}_{PSG}, \tag{1}$$

where $\boldsymbol{I}$ is a $n\times n$ matrix composed by the measured intensities, $\boldsymbol{M}_{Sample}$ is the 4×4 Mueller matrix of the sample, S_{PSG} is a $4\times n$ matrix whose n columns represent the Stokes vectors of the different polarization states used to illuminate the sample, and $\boldsymbol{S}_{PSA}$ is a $n\times4$ matrix whose rows provide the n different transposed Stokes vectors which represent the set of analysis polarization states over which the polarization state emerging from the sample is projected to be analyzed. The Mueller matrix can be derived from the Eq. (3) by calculating the pseudoinverse of the analyzer and the illumination matrices ($\tilde{\boldsymbol{S}}^{-1}_{PSA}$ and $\tilde{\boldsymbol{S}}^{-1}_{PSG}$) this leading to the following relation,

$$\boldsymbol{M}_{Sample} = \tilde{\boldsymbol{S}}^{-1}_{PSA}\boldsymbol{I}\tilde{\boldsymbol{S}}^{-1}_{PSG}. \tag{2}$$

At least four illuminating and analyzed states are needed to measure the full Mueller matrix. Therefore, at least 16 measurements are required to fully determine $\boldsymbol{M}_{Sample}$.

Polarization and depolarization metrics. In the work presented here, we make use of different polarimetric metrics to analyze the optical response of vegetal samples. These metrics are calculated from the experimental Mueller matrix and they are related to the main polarimetric content of the sample, i.e., diattenuation, retardance and the degree of depolarization. Although a few metrics can be directly gathered from the Mueller matrix, such as the diattenuation D, other metrics can be obtained after decomposition of the Mueller matrix to a set of simpler matrices. There are different types of matrix decomposition schemes, such as product, sum and differential[50,51] ones, each decomposition is adapted to particular and well-defi ed experimental conditions.

Accordingly, the choice of one or another decomposition scheme must consider the experimental conditions and the sample structure. In the context of the present work a product decomposition known as Lu-Chipman decomposition[49,50] was used to obtain the polarimetric properties from experimental data. In general, the polarimetric properties derived from different decompositions may differ to each other, the latter being due to the non-commutativity of the different algebraic operations needed to be done in order to implement the decomposition. Before doing a fi al choice to present the data of this work, the polarimetric data obtained with the Lu-Chipman decomposition, the symmetric decomposition and the differential decomposition were compared. For the case analysed in this article it was found that all the decompositions tested provided equivalent results. The choice of the Lu-Chipman decomposition was done because it provided slightly better results in terms of numerical noise compared to the symmetric decomposition, and because it can be applied for measurements in transmission and refl ction configur tions, contrarily to the differential decomposition, only valid for measurements in transmission.

The Lu-Chipman decomposition describes the Mueller matrix as a product of three 4×4 real matrices separating the main polarimetric information encoded in $\mathbf{M}$,

$$\boldsymbol{M} = \boldsymbol{M}_{\Delta}\boldsymbol{M}_{R}\boldsymbol{M}_{D}, \tag{3}$$

where $\boldsymbol{M}_{\Delta}$ represents a depolarizer, $\boldsymbol{M}_{R}$, a generalized retarder, and $\boldsymbol{M}_{D}$ is a generalized diattenuator. These matrices can be used to obtain the values of the linear and circular retardance and the linear and circular dichroism. Moreover, the orientation of the axis defining linear retardance and dichroism can also be obtained from matrices $\boldsymbol{M}_{R}$ and $\boldsymbol{M}_{D,}$ respectively. The details about the implementation of the Lu-Chipman decomposition have been largely discussed in the literature and are included in the extended information section for reader's convenience.

To characterize the depolarizing content of the botanical samples, in this study it is discussed the use of a full depolarization space instead of a single observable. A depolarization space is an abstract mathematical space made of three or more depolarization-related metrics which are not fully independent but related to each other. A depolarization space gives information not just on how much light is depolarized but also on how it is depolarized by the sample. The defin tion of a depolarization space is not unique[52,53] and a choice must be done based on multiple criteria such as discrimination power between depolarization metrics, computation time, adequacy to the physical problem treated among others[54]. The depolarization space used in this work is composed by the IPPs[55], which can be directly deduced from the measured Mueller matrix of the sample. The set of IPPs is composed of three real magnitudes labelled as P_1, P_2, and P_3 (with values from 0 to 1 each) defi ed as respective combinations of the four eigenvalues (taken in decreasing order $\lambda_0 \geq \lambda_1 \geq \lambda_2 \geq \lambda_3$) of the covariance matrix $\mathbf{H}$ which is associated with the Mueller matrix, $\mathbf{M}$[55].

$$P_1 \equiv \frac{\lambda_0 - \lambda_1}{tr\boldsymbol{H}}, P_2 \equiv \frac{\lambda_0 + \lambda_1 - 2\lambda_2}{tr\boldsymbol{H}}, P_3 \equiv \frac{\lambda_0 + \lambda_1 + \lambda_2 - 3\lambda_3}{tr\boldsymbol{H}}. \tag{4}$$

IPP parameters are restricted by the following inequalities[55],

$$0 \leq P_1 \leq P_2 \leq P_3. \tag{5}$$

The idea behind IPPs is that the response of any depolarizer can be synthesized as the incoherent sum of four components with different weights, which are regulated by the IPPs[50,56]. Accordingly, P_1 is associated with the relative portion of a non-depolarizing component, P_3 with the portion that is not fully depolarized, and P_2–P_1 measures the relative portion of a parallel component composed of an equiprobable mixture of two non-depolarizing elements[50]. In this context, IPPs allows for the differentiation between different types of depolarizers[56,57], or, in other words, between different types of depolarization mechanisms, which may unveil differences among the structures and organs in the sample tissue. In contrast to the IPP, which provide complete quantitative information of depolarization, the depolarization index P_{Δ}[58], commonly used in the polarimetric community, only provides an overall measure of the depolarizing power of the sample. Note that P_{Δ} can eventually be calculated from the IPPs as[55],

$$P_{\Delta} = \frac{1}{\sqrt{3}}\sqrt{2P_1^2 + \frac{2}{3}P_2^2 + \frac{1}{3}P_3^2}. \tag{6}$$

Optical microscope. The optical microscope is the same used in the polarimetric microscope (described below), but without the corresponding PSG and PSA.

Polarimetric microscope. Polarimetric images (Figs. 2, 3 and 4) were obtained with a multimodal microscope polarimeter. The multimodal microscope is an innovative polarimetric imaging system that can be operated in two imaging modes, the real plane, and the Fourier plane (also called conjugate space plane). In real plane imaging mode, the microscope produces images of the studied sample, while in Fourier imaging mode the images correspond to the angular distribution of light transmitted or scattered by the sample. The instrument is coupled to a white light LED as a source, followed by a narrow-band spectral filter centred at a wavelength of 533 nm with a spectral width of 15 nm. The microscope is mounted in transmission configur tion; the sample is located between two identical microscope objectives (one for imaging and another for illumination). The microscope objectives can be selected among different magnifi ations; 50×, 20×, or 5× depending on the needs of a specific esolution and a numerical aperture of a desired image.

Thanks to the use of a series of relay lenses, it is possible to create conjugates of the back-focal planes (BFP) of the illumination and imaging objectives the illumination and imaging arms, respectively. The eventual insertion of pinholes in the conjugates of the BFP of the two objectives allows for the control of the direction and the aperture of the illuminating and the imaging beam, respectively. A pinhole (500 μm diameter) is used to illuminate the samples with a beam in normal incidence with an aperture of 5°. No pinhole is inserted in the imaging arm to maximize the collection of scattered light intensity and thus to optimize depolarization sensitivity of the measurements. The relay lens system provides a conjugate of the sample plane in both; the illumination and the imaging arms, therefore, the use of pinholes in those planes, helps to defi e the shape and size of the illuminated and imaged field of view (FOV) respectively. The insertion of a Bertrand lens in the optical path of the microscope allows for an easy switch between the real and the Fourier imaging modes[59]. In the present work only images in the real plane were used. The same instrument has been applied in the past to characterize the dependence of polarization and depolarization properties as function of sample thickness[60] and digital histology of human samples to study the influence of sample thickness of polarimetric observables[61].

Fluorescence microscope. Fluorescence images are obtained by a commercial *Olympus Fluoview 1000* microscope. The system can illuminate the sample with six different wavelengths and a multiple combination of them. Among all the available wavelengths, three are generated with diode lasers (405, 559 and 635 nm) and the other three are generated with a multiline argon laser (458, 488, and 515 nm). The fluorescence images presented in this work were acquired using three filters (Olympus U-MWU2, U-MNB2, U-MWG2) which are centred at 330 nm, 470 nm, and 510 nm, respectively. The equipment allows for the acquisition of images in four channels simultaneously with a resolution of 200 nm, using a spectral detection system. The signal can be captured by three photomultipliers (PMT) for fluorescence and/or refl ction, plus an external detector for transmitted light. Captions can be made in 5 dimensions, three for space, one for time, and one for wavelength (xyztλ). The control of CO_2 delivery and temperature allows the system to carry out in-vivo experiments over time.

Phase contrast microscope. The phase contrast microscope is the same instrument used to measure the fluorescence response (the Olympus Fluoview 1000 microscope) but equipped with two phase contrast elements: a phase contrast condenser annulus located under the microscope stage, and a phase ring placed above the objective.

Electron microscope. The observations were made with a scanning electron microscope (*Jeol J7100F*) of the Centros Científicos y Tecnológicos de la Universidad de Barcelona (CCiT). The preparation of the leaves before observation was performed as follows. They were dehydrated with alcohols of increasing graduation until the absolute alcohol. Afterwards, they were brought to the critical point and were coated with a special carbon thin film deposited using thermal evaporation. The resolution of the electron microscope is of 100–500 nm depending on the selected magnifi ation.

Received: 13 October 2020; Accepted: 3 February 2021
Published online: 16 February 2021

References

1. Jacquemoud, S. & Ustin, S. *Leaf Optical Properties* (Cambridge University Press, Cambridge, 2019).
2. Truernit, E. *et al.* High-resolution whole-mount imaging of three-dimensional tissue organization and gene expression enables the study of phloem development and structure in Arabidopsis. *Plant Cell Online* **20**, 1494–1503 (2008).
3. Zeng, Y., Himmel, M. E. & Ding, S. Y. Visualizing chemical functionality in plant cell walls Mike Himmel. *Biotechnol. Biofuels* **10**, 1–16 (2017).
4. Chundawat, S. P. S. *et al.* Multi-scale visualization and characterization of lignocellulosic plant cell wall deconstruction during thermochemical pretreatment. *Energy Environ. Sci.* **4**, 973–984 (2011).
5. Potůčková, M. *et al.* Comparison of refl ctance measurements acquired with a contact probe and an integration sphere: Implications for the spectral properties of vegetation at a leaf level. *Sensors (Switzerland)* **16**, 1801 (2016).
6. Komis, G., Šamajová, O., Ovečka, M. & Šamaj, J. Super-resolution microscopy in plant cell imaging. *Trends Plant Sci.* **20**, 834–843 (2015).
7. Tamada, Y. *et al.* Optical property analyses of plant cells for adaptive optics microscopy. *Int. J. Optomechatron.* **8**, 89–99 (2014).
8. Chen, N., Rehman, S. & Sheppard, C. J. R. Advanced optical microscopy methods for in vivo imaging of sub-cellular structures in thick biological tissues. *J. Innov. Opt. Health Sci.* **07**, 1440001 (2014).
9. Timmers, A. C. J. Light microscopy of whole plant organs. *J. Microsc.* **263**, 165–170 (2016).
10. Donaldson, L. A. Auto fluorescence in plants, review. *Molecules* **25**, 2392–2412 (2020).
11. Konopka, C. A. & Bednarek, S. Y. Variable-angle epifluorescence microscopy: A new way to look at protein dynamics in the plant cell cortex. *Plant J.* **53**, 186–196 (2008).
12. Chen, T., Ji, D. & Tian, S. Variable-angle epifluorescence microscopy characterizes protein dynamics in the vicinity of plasma membrane in plant cells. *BMC Plant Biol.* **18**, 1–17 (2018).
13. Sheppard, C. J. R. Phase contrast microscopy. *Encycl. Mod. Opt.* **3**, 103–111 (2004).
14. Yano, A. & Fujiwara, K. Plant lighting system with five wavelength-band light-emitting diodes providing photon flux density and mixing ratio control. *Plant Methods* **8**, 46 (2012).
15. Blackburn, G. A. Hyperspectral remote sensing of plant pigments. *J. Exp. Bot.* **58**, 855–867 (2007).
16. Ovečka, M. *et al.* Multiscale imaging of plant development by light-sheet fluorescence microscopy. *Nat. Plants* **4**, 639–650 (2018).
17. Karunakaran, C. *et al.* Factors influencing real time internal structural visualization and dynamic process monitoring in plants using synchrotron-based phase contrast X-ray imaging. *Sci. Rep.* **5**, 1–13 (2015).
18. Palevitz, B. A. Cellulose microfibril orientation and cell shaping in developing guard cells of Allium: The role of microtubules and Ion Accumulation. *Planta* **132**, 71–93 (1976).

19. Zeiger, E. & Hepler, P. Production of guard cell protoplasts from onion and tobacco. *Plant Physiol.* **58**, 492–498 (1976).
20. Jarvis, P. G. & Mansfield, T. A. *Stomatal Physiology* (Cambridge University Press, Cambridge, 1981).
21. Shtein, I. S. *et al.* Stomatal cell wall composition: Distinctive structural patterns associated with different phylogenetic groups. *Ann. Bot.* **119**, 1021–1033 (2017).
22. Bischoff, V. *et al.* Trichome birefringence and its homolog AT5G01360 encode plant-specific DUF231 proteins required for cellulose biosynthesis in arabidopsis. *Plant Phys.* **153**, 590–602 (2010).
23. Long, R. L., Bange, M. P., Gordon, S. G. & Constable, G. A. Measuring the maturity of developing cotton fibers using an automated polarized light microscopy technique. *Textile Res. J.* **80**, 463–471 (2010).
24. Patty, C. H. L. *et al.* Imaging linear and circular polarization features in leaves with complete Mueller matrix polarimetry. *Biochim. Biophys. Acta Gen. Subj.* **1862**, 1350–1363 (2018).
25. Savenkov, S. N. *et al.* Measurement and interpretation of Mueller matrices of barley leaves. *Quantum Electron.* **50**, 55 (2020).
26. Curran, P. J. Polarized visible light as an aid to vegetation classification. *Remote Sens. Environ.* **12**, 491–499 (1982).
27. Vanderbilt, V. C., Grant, L. & Daughtry, C. S. T. Polarization of light scattered by vegetation. *Proc. IEEE* **73**, 1012–1024 (1985).
28. Yao, C., Lu, S. & Sun, Z. Estimation of leaf chlorophyll content with polarization measurements: Degree of linear polarization. *Radiat. Transfert* **242**, 106787 (2020).
29. Kharuk, V. I. & Yegorov, V. V. Polarimetric indication of plant stress. *Remote Sens. Environ.* **33**, 35–40 (1990).
30. Van Eeckhout, A. *et al.* Depolarizing metrics for plant samples imaging. *PLoS ONE* **14**, 1–19 (2019).
31. Tuchin, V. V. Polarized light interaction with tissues. *J. Biomed. Opt.* **21**, 071114 (2016).
32. Backman, V. *et al.* Detection of preinvasive cancer cells. *Nature* **406**, 35–36 (2000).
33. Novikova, T. *et al.* The origins of polarimetric image contrast between healthy and cancerous human colon tissue. *Appl. Phys. Lett.* **102**, 241103 (2013).
34. Lizana, A. *et al.* Polarization gating based on Mueller matrices. *J. Biomed. Opt.* **22**, 056004 (2017).
35. Reiser, K., Stoller, P. & Knoesen, A. Th ee-dimensional geometry of collagenous tissues by second harmonic polarimetry. *Sci. Rep.* **7**, 2642 (2017).
36. Le Gratiet, A. *et al.* Zebrafish structural development in Mueller-matrix scanning microscopy. *Sci. Rep.* **9**, 19974 (2019).
37. Pluta, M. Nomarski's DIC microscopy: A review. *Proc. SPIE* **1846** (1994).
38. Van Eeckhout, A. *et al.* Polarimetric imaging of biological tissues based on the indices of polarimetric purity. *J. Biophoton.* **11**, e201700189 (2018).
39. Gao, C. J., Xia, X. J., Shi, K., Zhou, Y. H. & Yu, J. Q. Response of stomata to global climate changes and the underlying regulation mechanism of stress responses. *Plant Physiol. J.* **48**(1), 19–28 (2012).
40. Yan, W., Zhong, Y. & Shangguan, Z. Contrasting responses of leaf stomatal characteristics to climate change: A considerable challenge to predict carbon and water cycles. *Glob. Change Biol.* **23**(9), 3781–3793 (2017).
41. Lawson, T. & Blatt, M. R. Stomatal size, speed, and responsiveness impact on photosynthesis and water use effici cy. *Plant Physiol.* **164**, 1556–1570 (2014).
42. Weyers, J. D. & Johansen, L. G. Accurate estimation of stomatal aperture from silicone rubber impressions. *New Phytol.* **101**, 109–115 (1985).
43. Fanourakis, D. *et al.* Pore size regulates operating stomatal conductance, while stomatal densities drive the partitioning of conductance between leaf sides. *Ann. Bot.* **115**(4), 555–565 (2015).
44. Kaur, N. & Gupta, A. K. Applications of inulin and oligofructose in health and nutrition. *J. Biosci.* **27**(7), 703–714 (2002).
45. Mensink, M. A., Frijlink, H. W., der Voort Maarschalk, K. & Hinrichs, W. L. J. Inulin, a flex ble oligosaccharide I: Review of its physicochemical characteristics. *Carbohydr. Polym.* **130**, 405–419 (2015).
46. Kubitzki, K. *The families and Genera of Vascular Plants. Volume VI. Flowering Plants. Dicotyledons. Celastrales, Oxalidales, Rosales, Cornales, Ericales.* (Springer, Heidelberg, 2004).
47. Pinela, J., Carvalho, A. M. & Ferreira, I. C. Wild edible plants: Nutritional and toxicological characteristics, retrieval strategies and importance for today's society. *Food Chem. Toxicol.* **110**, 165–188 (2017).
48. Luo, H. *et al.* Compact and miniature snapshot imaging polarimeter. *Appl. Opt.* **47**(24), 4413–4417 (2008).
49. Goldstein, D. *Polarized Light* 2nd edn. (Marcel Dekker, New York, 2003).
50. Gil, J. J. & Ossikovski, R. *Polarized Light and the Mueller Matrix Approach* (CRC Press, Boca Raton, 2016).
51. Garcia-Caurel, E. et al. On advanced mueller ellipsometry instrumentation and data analysis. In *Ellipsometry at the Nanoscale* (eds. Losurdo M., Hingerl K.) 31–143 (Springer, Berlin, 2013)
52. Ossikovski, R. & Vizet, J. Eigenvalue-based depolarization metric spaces for Mueller matrices. *J. Opt. Soc. Am. A* **36**, 1173–1186 (2019).
53. Sheppard, C. J. R., Bendandi, A., Le Gratiet, A. & Diaspro, A. Eigenvectors of polarization coherency matrices. *J. Opt. Soc. Am. A* **37**, 1143–1145 (2020).
54. Van Eeckhout, A. *et al.* Depolarization metric spaces for biological tissues classifi ation. *J. Biophotonics* **13**, e202000083 (2020).
55. San Jose, I. & Gil, J. J. Invariant indices of polarimetric purity. *Opt. Commun.* **284**, 38–47 (2011).
56. Van Eeckhout, A. *et al.* Synthesis and characterization of depolarizing samples based on the indices of polarimetric purity. *Opt. Lett.* **42**, 4155–4158 (2017).
57. Tariq, A., Li, P., Chen, D., Lv, D. & Ma, H. Physically realizable space for the purity-depolarization plane for polarized light scattering media. *Phys. Rev. Lett.* **119**, 033202 (2017).
58. Gil, J. J. & Bernabéu, E. Polarization and depolarization indices of an optical system. *Opt. Acta* **33**, 185–189 (1986).
59. Kurvits, J. A., Jiang, M. & Zia, R. Comparative analysis of imaging configurations and objectives for Fourier microscopy. *J. Opt. Soc. Am. A.* **32**, 2082 (2015).
60. Yoo, S. Y., Ossikovsky, R. & Garcia-Caurel, E. Experimental study of thickness dependence of polarization and depolarization properties of anisotropic turbid media using Mueller matrix polarimetry and differential decomposition. *Appl. Surf. Sci.* **421**, 870 (2017).
61. Lee, H. R. *et al.* Digital histology with Mueller microscopy: How to mitigate an impact of tissue cut thickness fluctuations. *J. Biomed. Opt.* **24**, 076004 (2019).

Acknowledgements

We acknowledge Núria Barba and the UAB microscopy service for the measurements of the plant with the *Olympus Fluoview 1000* microscope and Eva Prats for the Electron microscopy images. We also acknowledge the financial support of Spanish Ministerio de Ciencia, Innovación y Universidades (RTI2018-097107-B-C31, and Fondos FEDER); and Catalan Government (2017-SGR-001500).

Author contributions

E.G.C., J.V., J.C., and A.L. designed the study. A.V.E., T.G., and A.L. collected samples. A.V.E., E.G.C., and M.D. conducted measurements. A.V.E., E.G.C., T.G., J.C.E., J.J.G., and A.L. analyzed data. A.V.E., E.G.C., J.C.E., and A.L. drafted the manuscript. All authors reviewed the manuscript.

Competing interests
The authors declare no competing interests.

Additional information
Supplementary Information The online version contains supplementary material available at https://doi.org/10.1038/s41598-021-83421-8.

Correspondence and requests for materials should be addressed to A.E.

Reprints and permissions information is available at www.nature.com/reprints.

Publisher's note Springer Nature remains neutral with regard to jurisdictional claims in published maps and institutional affiliations.